
Syn-kinematic, water-fluxed melting and ascent of granitic magmas in the Karakoram Shear Zone, Ladakh, NW India

A thesis submitted for the degree of Doctor of Philosophy

Henning Reichardt, Dipl.-Geol. Univ.



View from Horlam La (5100 m) into the Pangong Range. The Karakoram Shear Zone runs NW-SE, parallel to the valley.

School of Geosciences
Faculty of Science
Monash University

May 2010

Addendum

- p93, caption to Fig. 2, line 3: add “Different grey scales in (b) indicate relative proportions of dark minerals (Bt + Hbl), e.g. black parts are Hbl-rich parts as shown in (c)”.
- p120, caption to Fig. 8: add “The wall trends NE (left) to SW (right)” after second sentence.
- p15, line 32: insert (Fig. 1) after “2500 km”.
- p17, line 12: insert “(Fig. 2)” after “zones”.
- p19, line 1: insert “(Fig. 3)” after “~20 Ma”.
- p20, line 5: insert “(Fig. 4)” after “area”.

Errata

- p11, line 4: insert “the” before differentiation.
- p11, line 33: “processes” for “processed”.
- p11, line 36: “shear zone” for “Shear Zone”.
- p12, line 19: insert “the” before “Himalayas”.
- p12, line 21: insert “the” before “role”.
- p12, line 28: insert space before “neosome”.
- p12, line 29: “crystallizations” for “crystallization”.
- p12, line 33: insert full stop after “rock”.
- p12, line 36: “pre-migmatization” for “pre-migmatization”.
- p13, line 3: insert “the” before grain-scale.
- p13, line 4: insert “-” before scale.
- p13, line 6: “in rocks with” for “if rocks that show”.
- p13, line 7: “will” for “would”.
- p13, line 11: insert “the” before “microscopic”.
- p13, line 13: insert “and” before “in”.
- p13, line 24: “include” for “can be found in”.
- p13, line 36: insert full stop after “Kohlstedt & Holtzman, 2009”.
- p14, line 4: delete “(Fig. 1)”.
- p14, line 18: “fractures” for “fracture”.
- p14, line 21: “as by far” for “by far as”.
- p14, line 37: “found” for “yielded”.
- p15, line 10: “between” for “of”.
- p15, line 11: delete “still nowadays”.
- p15, line 12: insert “still” before “pushing”.
- p15, line 14: “They” for “it”.
- p15, line 17: “Mountains” for “Mountains”.
- p15, line 18: insert comma after “Ladakh”.
- p15, line 23: insert comma after “Fault”.
- p15, line 30: “is” for “forms a”.
- p15, line 30: insert “a suite of” before “Mid-Cretaceous”.
- p15, line 31: “that forms” for “form a”.
- p16, line 3: delete “in”.
- p16, line 4: “consider” for “considers”.
- p16, line 9: insert “Fig. 1” after “basin”.
- p16, line 15: “plutonic complexes of the Karakoram terrane crop out north of the SSZ” for “North of the SSZ plutonic complexes of the Karakoram terrane crop out”.
- p16, line 16: “that” for “and”.
- p17, line 3: insert “the” before Karakoram”.
- p17, line 16: “have” for “has”.
- p17, line 17: delete “that have been”.
- p18, line 7: insert “the” before “Karakoram”.
- p18, line 19: “contains” for “comprises”.
- p18, line 20: delete “and in this thesis it is”.
- p18, line 21: insert “in this thesis” after “Batholith”.
- p18, line 21: “includes” for “comprises”.
- p18, line 22: “consisting” for “cosisting”.
- p18, line 24: “intruded intensely” for “intensely intruded”.
- p19, line 8: insert “their” before “migmatization”.
- p19, line 20: insert full stop after “dykes”.
- p19, line 21: delete “zone initiation”.
- p20, line 1: insert “Zone” after “Shear”.
- p20, line 11: “provides” for “gives”.
- p20, line 20: insert comma after “relief”.
- p20, line 21: “only amenable” for “leave them”.
- p20, line 32: “of” for “on”.
- p20, line 37: “repetitions” for “reptitions”.
- p21, line 8: “linkage” for “link”.
- p21, line 10: “of” for “on”.
- p21, line 32: insert “oriented” before “parallel”.
- p21, line 33: insert “the” before “trend”.
- p32, line 16: “mafic microgranular enclaves” instead “mafic magmatic enclaves”.
- p41, line 16: “Fig. 6e and f” for “Fig. 6”.
- p41, line 27: “(Fig. 6b)” for “(Fig. 6)”.
- p42, line 3: “(Fig. 3, 6a)” for “(Fig. 3, 6)”.
- p84, Table 2, first column, row 20 and row 32: “Cations” for “Kations”.
- p95, line 4: “data” for “date”.
- p99, line 43: insert “rock” before “analysis”.
- p100, line 1: insert “the” before “melanocratic”.
- p101, line 9: “Al total” for “Al tot”.
- p102, line 33: insert “the” before “case”.
- p103, line 14: “studied directly” for “directly studied”.
- p103, line 15: “by” for “due to”.
- p110, line 17: insert comma after “Typically”.
- p110, line 18: “cross-cutting” for “crosC-Sutting”.
- p110, line 22: insert comma after “continuous”.

p110, line 24: insert comma after "predictions".
p115, line 21: "from" for "form".
p116, line 4: "syn-kinematic" for "sy-kinematic".
p117, line 31: "intruded extensively" for "extensively intruded".
p119, line 22: "protruding surfaces," for "3D protrusion on the surface".
p121, line 19: "oblique" for "unconformable".
p126, line 8: delete ", perpendicular to the axial plane".
p126, line 18: insert "the" before "shear".
p126, line 19: ", and that dykes rotated synthetically" for "and synthetic rotation of dykes".
p127, line 5: "cross-cutting" for "cross-cutting".
p127, line 16: "competent" for "competent".
p128, line 13: "continuity, rare" for "continuity with".
p128, line 14: "dyke intersections" for "intersection".
p128, line 19: "the maximum shortening direction" for "the maximum elongation".
p134, line 7: "lie" for "run".

p134, line 8: "parallel to" for "along with".
p134, line 15: "lacks" for "lack".
p134, line 18: "crops out" for "outcrops".
p134, line 24: "that" for "the one".
p134, line 26: "trend" for "run".
p134, line 27: insert "to" before "and".
p134, line 27: delete "to the".
p138, line 40: "crop out" for "outcrop".
p150, line 8: "trends" for "runs".
p150, line 10: "trends" for "runs".
p150, line 14/15: delete "These are most likely (Fig. 2).".
p150, line 25: insert comma after "Geochemically".
p150, line 32: insert "the" before "Tirit".
p150, line 34: insert "the" before "Eurasian".
p150, line 37: "trend" for "run".
p175, Table Appendix C, first column, row 20, row 12: "Cations" for "Kations".
p176, Table Appendix C, first column, row 20, row 12: "Cations" for "Kations".
p177, Table Appendix C, first column, row 20, row 12: "Cations" for "Kations".
p178, Table Appendix C, first column, row 20, row 12: "Cations" for "Kations".

Copyright Notices

Notice 1

Under the Copyright Act 1968, this thesis must be used only under the normal conditions of scholarly fair dealing. In particular no results or conclusions should be extracted from it, nor should it be copied or closely paraphrased in whole or in part without the written consent of the author. Proper written acknowledgement should be made for any assistance obtained from this thesis.

Notice 2

I certify that I have made all reasonable efforts to secure copyright permissions for third-party content included in this thesis and have not knowingly added copyright content to my work without the owner's permission.

Table of Contents

Table of contents	1
Thesis Declaration	7
Acknowledgements	8
Abstract	9
Chapter I: Introduction	11
1.1 General views on granite formation and aims of the project	11
1.2 Migmatites and role of shear zones	12
1.2.1 Migmatite terminology	12
1.2.2 Melt segregation	13
1.2.3 Magma transport in shear zones	14
1.2.4 Water-fluxed melting	14
1.3 Geological background	15
1.3.1 Overview of the Karakoram Mountains and Ladakh	15
1.3.2 Geology of the study area in the Karakoram Shear Zone	17
1.4 Field laboratory Karakoram Shear Zone: addressing the research questions	20
1.5 Structure of the thesis	20
1.6 Methodology	22
Chapter II. Hybridization of granitic magmas in the source:	30
The origin of the Karakoram Batholith, Ladakh, NW India	
1. Introduction	31
2. Regional geology	32
3. Methodology	35
3.1 Geochemical analysis	35
3.2 Rb-Sr and Sm-Nd isotope geochemistry	35
3.3 U-Pb SHRIMP analysis	38
4. Field relations and anatexis in the Tangtse and Darbuk-Shyok areas	38
4.1 Meta-sedimentary sequence	39

4.2 Calc-alkaline granitoids	40
4.3 Leucogranites	40
4.4 Syndeformational melting	41
4.5 Water-fluxed melting	42
5. Evidence for magma hybridization in migmatites	43
5.1 Base of Tangtse Pluton	43
5.2 Leucogranite dykes in the Darbuk-Shyok gorge	46
6. Major and Trace Element Geochemistry	47
7. Geochronology	48
7. 1 Age of the Muglib Batholith	48
7. 2 Age of the leucogranites from the Tangtse Pluton	53
8. Rb-Sr and Sm-Nd isotope geochemistry	53
8. 1 Results	54
9. Discussion	56
9.1 Geochemical characteristics: comparison to other Miocene Himalayan leucogranites	56
9.2 Significance of water-fluxed melting	57
9.3 Age relations between leucogranites and the Muglib Batholith	57
9.4 Origin of the Muglib Batholith	58
9.5 Linking source to sink	59
9.5.1 Field relations	59
9.5.2 Implications of the isotopic signatures	61
9.6 Similar leucogranite intrusions elsewhere in the Karakoram?	62
10. Conclusions	63
Chapter III. Hornblende chemistry in meta- and diatexites and its fractionation in leucogranite magma	70
1. Introduction	70
2. Geological background	71
3. Migmatite morphology and hornblende accumulation	72
4. Petrography	74
5. Geochemistry	77
5.1 Analytical procedures	77

5.1.1 Whole rock analysis	77
5.1.2 Mineral analysis	77
5.2 Whole rock geochemistry	80
5.2.1 Major elements	80
5.2.2 Trace elements	81
5.3 Mineral Geochemistry	83
5.3.1 Major element geochemistry	83
<i>Hornblende</i>	83
<i>Plagioclase</i>	87
5.5.2 Trace element geochemistry	88
<i>Hornblende</i>	88
<i>REE patterns of other minerals</i>	91
5.6 Geochemical modelling	93
5.6.1 Batch melting	93
5.6.2 Fractional crystallization	95
5.6.3 Accumulation model	97
6. Discussion	98
6.1 REE patterns of hornblende and partition coefficients	98
6.2 The role of hornblende in magma formation	101
6.3 Adakite and TTG signatures	102
7. Conclusions	103
Chapter IV. Leucogranite magma transport from source to sink:	110
the dyke network in the Karakoram Shear Zone, NW India	
1. Introduction	110
2. Regional Geology	112
3. Water-fluxed melting and magma ascent	114
4. Magma networks from source to batholith	115
4. 1 Magma extraction networks in the anatectic zone	115
4.2 Organized network geometries	117
<i>Shear fabric dyke network</i>	119
<i>Ductile fracture and chaotic dyke networks</i>	120
4.3 Lithological contacts	121

5. Pluton growth	122
6. Regional connections: feeding the batholith	124
7. Discussion	125
7. 1 Filtering processes	125
7. 2 Magma transfer in axial planar orientation and shear fabrics	125
7.3 Intersections increasing permeability	126
7.4 Ductile fractures and apparent chaotic networks	126
7.5 Implications for magma transfer	127
8. Conclusions	128
Chapter V. Are the Shyok Suture Zone and the Karakoram Shear Zone	134
parallel in Ladakh?	
1. Introduction	134
2. Regional geology	136
2.1 Shyok Suture Zone (SSZ)	136
2.2 Karakoram Shear Zone and Pangong Metamorphic Complex	137
2.3 Ladakh Batholith	138
2.4 Muglib Batholith	139
3. Major and Trace Element Geochemistry	141
4. Geochronology	144
5. Rb-Sr and Sm-Nd isotope systematics	146
6. Discussion	147
6.1 Ladakh and Muglib Batholith similarities	147
6.2 Comparison to other batholiths	148
6.3 Position of the Shyok Suture Zone	149
7. Conclusions	150
Chapter VI. Summary and conclusions	155
1. Introduction to research outcomes	155
2. Synthesis of results	155
2.1 Water-fluxed melting	155
2.2 Hornblende geochemistry	156
2.3 Formation and orientation of magma flow networks	157

2.4 Timing of anatexis	158
2.5 Magma hybridization in the source	159
2.6 Similarities between Ladakh and Muglib Batholith	160
3. Conclusions	161
Appendix	165
A. Whole rock chemistry	165
B. U-Pb SHRIMP analysis	170
C. Electron microprobe data of hornblende	174
D. Electron microprobe data of plagioclase	179
E. LA-ICP-MS data of hornblende	181
F. LA-ICP-MS data of feldspar, biotite, clino-pyroxene, titanite and allanite	187
G. LA-ICP-MS line-scan of hornblende	189
H. Cover of Geological Society of America Bulletin	190
I. Published articles	191

General Declaration

Monash University
Monash Research Graduate School

Declaration for thesis based or partially based on conjointly published or unpublished work

General Declaration

In accordance with Monash University Doctorate Regulation 17/ Doctor of Philosophy and Master of Philosophy (MPhil) regulations the following declarations are made:

I hereby declare that this thesis contains no material which has been accepted for the award of any other degree or diploma at any university or equivalent institution and that, to the best of my knowledge and belief, this thesis contains no material previously published or written by another person, except where due reference is made in the text of the thesis.

This thesis includes 1 original paper published in peer reviewed journals and 3 unpublished publications. The core theme of the thesis is magma formation and segregation. The ideas, development and writing up of all the papers in the thesis were the principal responsibility of myself, the candidate, working within the School of Geosciences under the supervision of Roberto Weinberg. The inclusion of co-authors reflects the fact that the work came from active collaboration between researchers and acknowledges input into team-based research.

In the case of chapters 2, 3, 4 and 5 my contribution to the work involved the following:

Thesis chapter	Publication title	Publication status*	Nature and extent of candidate's contribution
2	Hybridization of granitic magmas in the source: The origin of the Karakoram Batholith, Ladakh, NW India	Published in Lithos, 2010, Vol. 116. ISSN0024-4937	70% contribution. Development of ideas, collection and interpretation of data, and writing up.
3	Hornblende chemistry in meta- and diatexites and its fractionation in leucogranite magma	In preparation for submission to the Journal of Petrology	80% contribution. Development of ideas, collection and interpretation of data, and writing up.
4	Leucogranite magma transport from source to sink: the dyke network in the Karakoram Shear Zone, NW India	In preparation for submission to the Geological Society of America Bulletin	75% contribution. Development of ideas, writing up.
5	Are the Shyok Suture Zone and the Karakoram Shear Zone parallel in Ladakh?	In preparation for submission to Lithos	80% contribution. Development of ideas, collection and interpretation of data, and writing up.

I have not renumbered sections of submitted or published papers in order to generate a consistent presentation within the thesis.

Signed:

Date:

Acknowledgements

First of all, I thank my supervisor, Roberto Weinberg for initiating this research project that gave me the opportunity to do research in such an amazing field area in the Karakoram, and for his enthusiasm about the project. I thank the Monash Research Graduate School and the Faculty of Science for financial support during my candidature. I am most grateful to my parents for their outstanding support throughout the years. I also thank all staff at the School of Geosciences who were always helpful, be it in dealings with administrative matters, or running the laboratories. From the research staff of the department I thank Massimo Raveggi for all discussions on geochemistry and geochemical modelling, Pete Betts for his relentless efforts in organizing the Broken Hill field-camps, and Andy Tomkins for co-supervision. Here I also thank Geordie Mark, for discussions in the field and co-supervision at the beginning of my research project, and Bruce Schaefer for discussions on isotope geochemistry. I also thank Ulf Andersson who I got to know on a field-trip in Finland for discussions on geochemistry. Alos thanks to Daniel Bryce for help during field work, especially for all those dyke measurements. Regarding field work in India, I want to say thank you to the people of Ladakh for hospitality, and general friendliness.

Further, I thank the PhD students I got to now in the department, many of which became friends of mine. To my office-mates a big thank you for tolerating my grumpiness during the last few months. Also thanks to my old office-mate Kyle. I thank the present and former Elwood people Pat & Sahereh, Max & Janett, Danielle, Margarete, Heather, Rob and Matilda for their friendship. I thank my brother and my sister in law for their friendship and giving me office-space during my stays in Franconia, and my all friends back in Germany for still recognizing me. Moreover, I thank the Scholte family for welcoming me in the hills. Finally and especially, I want to say thank you to my schatz Tamar who showed me many new views, and with whom spending the (almost) last 12 months was simply great.

Thanks to all of you.

Abstract

The Karakoram Shear Zone in Ladakh, NW India, forms part of a crustal-scale shear zone system that developed in response to the northward push of the Indian into the Eurasian continent. In its central part, the ~750 km long, NW-SE trending shear zone is split into two parallel mylonitic strands that bound deeply exhumed rocks of the Pangong Metamorphic Complex. This region provides a rare opportunity to study the conditions of magma formation, its segregation from the source and subsequent ascent through the crust to feed a batholith. Metamorphism at upper amphibolite facies gave rise to anatexis of a suite of calc-alkaline granitoids of the Muglib Batholith and a meta-sedimentary sequence, and to formation of leucogranite dykes, stocks and plutons. Timing of anatexis is constrained by U-Pb SHRIMP analyses on zircons and titanites of a leucogranite and two calc-alkaline granitic rocks. These yielded Miocene (~18 Ma) crystallization ages for the leucogranite and a contemporaneous Miocene metamorphic event in the Cretaceous (~71 Ma) calc-alkaline rocks. Meta- and diatexites of calc-alkaline protolith have abundant euhedral, poikilitic hornblende megacrysts in the leucosome, interpreted to be peritectic and indicative for water-fluxed conditions. Hornblende locally forms accumulations in the migmatitic source, and is generally absent in the leucogranites derived from these source rocks. REE contents in hornblende are unusual and vary between samples, and have significant influence on the REE concentrations of the magmatic products. Geochemical modelling by using own determined partition coefficients for these hornblendes, shows that retainment of hornblende in the source explains adakite-like high La_n/Yb_n and high Sr/Y values of leucogranites, without involvement of garnet in the residue. Rb-Sr and Sm-Nd isotope systematics show that magma stemming from two distinct sources, calc-alkaline granitoids with a signature indicative of a mantle source, and meta-sedimentary rocks with a stronger crustal signature, hybridized to form magmatic rocks with an intermediate hybrid isotope signature. Magma hybridization is a common feature of magmas world-wide, but how and where hybridization takes place has remained debatable. Here it is demonstrated that granite magmas hybridize already within the source by confluence into shared flow channels.

The link between anatectic rocks and the Karakoram Batholith is characterized by a transported zone dominated by dyke swarms linked to local stocks and plutons. Dykes are generally interconnected, with rare cross-cutting or truncation relationships, and have a common intersection direction parallel to the dominant mineral lineation. All dyke networks are oriented at high angles to the orientation of the axis of maximum compression during shearing, and not, as expected from the literature, at high angles to the minimum compression axis.

Isotope systematics was also used to investigate relationships between the Muglib Batholith, and the contemporaneous Ladakh Batholith to the south. The finding of similar

characteristics contrasts to expectations derived from current understanding that the Shyok Suture Zone separates the two, and that the Muglib Batholith formed at the southern margin of continental Asia. It is suggested that the two batholiths are part of the same Ladakh island arc and are therefore not separated by a suture zone. In summary, this thesis contributes to fundamental understanding of the tectonics of the region and to the origin of water-fluxed anatectic magmas, the role of hornblende and the nature of a complex magma network linking source to batholith.

Chapter I.

Introduction

1.1 General views on granite formation and aims of the project

Granite formation is a fundamental process in differentiation of Earth's crust (e.g. Bateman, 1984; Brown, 1994; D'Lemos *et al.*, 1992; Hutton, 1982; Mehnert, 1968; Pitcher, 1979; Wickham, 1987; Wyllie, 1977). The chemistry of magmatic rocks is a result of multiple processes from melting of heterogeneous source rocks, mixing of magmas, assimilation of country rocks, and fractionation processes, in the source, during transport or after final emplacement in the sink (e.g. Brown, 1994; Clemens, 2006; Harris *et al.*, 1986; Hawkesworth & Vollmer, 1979; Mehnert, 1968).

The transport of granitic magma to emplacement sites is generally thought to be achieved by either diapirism, dyking, or through ascent in shear zones. These mechanisms are rather end-members and it is expected that more than one mechanism controls the whole process (Paterson & Fowler, 1993). Today it is widely accepted that deformation is a key factor for magma transport from its source in the lower to middle crust to final emplacement in the upper crust (e.g. Brown, 1994; Brown & Solar, 1998; Rosenberg & Berger, 2001; Vigneresse, 1995). In particular, the close spatial relationship between shear zones and granites is striking (D'Lemos *et al.*, 1992; Weinberg *et al.*, 2004). Consequently it has been proposed that crustal-scale shear zones provide the required dynamics to drive melt out of the source region, the pathway for melt ascent and emplacement sites (e.g. Brown, 1994; Wagner, 2006). Shear zones may not only provide the pathways for magmas, they may also control the sites of initial melt formation and segregation (Brown & Solar, 1998). At lower to mid-crustal levels, magma (magma = melt + crystals) migration may occur pervasively through rocks at or above their solidus (Vanderhaeghe, 1999; Weinberg, 1999; Weinberg & Searle, 1998), while magma ascent through colder sub-solidus crust generally is thought to occur in dykes eventually linking to emplacement sites in dilational jogs (e.g. Clemens & Mawer, 1992; Emmerman, 1990; Petford, 1994; Weinberg, 1996).

Despite substantial advances on the topic (see review in Brown, 2007), the processes involved in initial melt formation in the anatectic source region, melt segregation and accumulation in magma escape pathways, the growth of larger networks that leave the anatectic region and transport magma through sub-solidus crust and eventually link to emplacement sites in the upper crust, are still not fully understood. The Karakoram Shear Zone, Ladakh, NW India, provides an ideal region to study these processes. Here, anatexis took place during shearing (Weinberg & Mark, 2008) and produced a swarm of dykes and irregular sheets feeding plutons and ultimately the Karakoram Batholith (Weinberg *et al.*, 2009). Focusing on this Shear Zone, this thesis contributes to the discussion by addressing the following subjects:

- The formation of melt escape pathways and interaction between magmas migrating from different source rocks into a growing network. How does the deformation regime in a shear zone influence the geometries of the magma flow networks in the anatectic source

and in the transport zone? Do these geometries observed in nature correspond to the ones from model experiments? What is the nature of magma transport zones? How do natural dykes that form escape paths and feed plutons compare to experimental and theoretical predictions?

- The geochemical evolution of the rocks subject to anatexis and the melting products in view of mineral fractionation and accumulation processes.
- The link between source and sink. How do *in situ* leucosomes in migmatites connect to intrusive dykes, local stocks and plutons, thus forming networks on the kilometric scale?
- How do magmas evolve geochemically as they separate from the source and solid fractions get filtered out? How do magmas derived from different sources interact to create hybrids?
- Regional implications of the studies of the Karakoram Shear Zone. Are the leucogranites of the Pangong Metamorphic Complex related to the voluminous Karakoram Batholith? Do calc-alkaline granites in the Pangong Metamorphic Complex relate to calc-alkaline granites of the Ladakh Batholith? If so, what are the consequences for the tectonic interpretation of crustal-scale lineaments in the Karakoram?

The following sections give an introduction to crucial aspects of melt formation, magma transport and emplacement. After a brief overview of Himalayas and the Karakoram in Ladakh, an introduction to the regional geology of my study area is presented.

1.2 Migmatites and role of shear zones

1.2.1 Migmatite terminology

In broadest terms, migmatites are partially molten rocks (Sederholm, 1907; Sederholm, 1913). In this thesis, the nomenclature of Sawyer (2008) will be used for migmatite description. Most commonly in the course of crustal thickening, high temperatures and pressures, under the presence or absence of an external water-rich fluid, give rise to partial melting of a given rock, the protolith (= paleosome), and the formation of leucosome and melanosome (=neosome). The leucosome is usually light in colour (greek; leucos = white) and consists of crystallization from a melt phase and peritectic phases, but commonly also contains entrainments from protolith or melanosome. The melanosome represents the refractory melt depleted rock, consisting of mineral phases that have not taken part in the melting reaction, phases that have not been totally consumed by melting, and peritectic minerals that remain in the source rock. Depending on the efficiency of melt segregation, the melanosome may either be strongly refractory, consisting of mainly dark (greek; melanos = dark) mafic minerals, or can be almost undistinguishable from the protolith. **With increasing** amounts of melt in the rock, the pre-migmatization fabric of the protolith is gradually erased, leading to transition from metatexite to diatexite. In metatexite, the fabric is disrupted by leucosomes but the rock remained coherent. At ~30 % melt fraction in the rock, the protolith structure is obliterated and diatexite is formed (Ashworth, 1985; Mehnert, 1968; Sawyer, 2008). In contrast to metatexite which deforms as a solid, diatexite shows magma behavior

and is capable of flowing *en masse*.

1.2.2 Melt segregation

In an anatectic region, the first occurrence of melting can be observed at grain-scale in migmatites. Connection of grain scale melt domains can be considered as the first step in the process of melt segregation. From this incipient stage onwards, melt migration is driven by pressure gradients in an anisotropic medium. Even if rocks that show no obvious anisotropy before or at the beginning of melting, external stresses would still drive melt segregation from pores into larger melt pockets thus creating anisotropies (Stevenson, 1989). Rabinowicz & Vigneresse (2004) distinguished between two competing main processes of melt segregation: compaction controlled by buoyancy contrasts and channelling controlled by external stress fields. They concluded that the latter is by far the more efficient mechanism. At microscopic scale, melt can be observed as thin films along grain boundaries, in small pockets between grains, in cracks within grains or transgranular cracks (Sawyer, 2001). The onset of melt segregation is determined by the achievement of melt interconnection (Brown, 2005). In a review of previous experiments (Arzi, 1978; Dell'Angelo & Tullis, 1988; Rutter & Neumann, 1995; van der Molen & Paterson, 1979) it has been proposed that melt interconnection (= melt connectivity transition) is achieved at a melt fraction of ~ 0.07 (Rosenberg & Handy, 2005).

Generally, melt moves down pressure gradients, and such gradients are already present at the grain scale due to anisotropies (Robin, 1979). Melt further migrates by exploring planes of potential weakness in the source rock, which can be any type of foliation, shear zones or fractures. Further migration paths are along fold limbs (high pressure sites) towards fold hinges (low pressure sites) (Sawyer, 1999). Other low pressure sites where melt can collect can be found in boudin necks. During concurrent melting and deformation, an interconnected network of layer parallel leucosomes and leucosomes oblique to the rock fabric may be formed (Marchildon & Brown, 2003; Sawyer, 2001; Vanderhaeghe, 1999). At the same time, high strain enhances the possibility of melt escape (Brown, 1995). Here, migration of melt is achieved by porous flow (Brown & Rushmer, 1997). Melt veins in favourable orientation in relation to the local stress field will widen and transport more melt, whereas veins in a less favourable orientation may be drained (Sawyer, 2001).

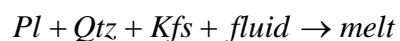
The orientation of melt channels has been subject to many experimental studies (e.g. Holtzman & Kohlstedt, 2007; Katz *et al.*, 2006; Kohlstedt & Holtzman, 2009; Rosenberg & Berger, 2001; Stevenson, 1989). Model experiments indicate that melt channels form parallel to the direction of maximum compression (Rosenberg & Berger, 2001), or at an acute angle of about 20° to the shearing direction (Holtzman & Kohlstedt 2007; Katz *et al.*, 2006; Kohlstedt & Holtzman, 2009). Melt segregation parallel to the axial plane in folds is at odds with the assumption that melt channels form preferably parallel to the direction of maximum compression (Vernon & Paterson, 2001). However, leucosomes in axial planar orientation are well documented in migmatites (Hand & Dirks, 1992; Weinberg & Mark, 2008; Vernon & Paterson, 2001). Thus, the geometries of melt pathways and how these are linked from source to sink require further investigation.

1.2.3 Magma transport in shear zones

On the crustal scale, shear zones provide the conditions for anatexis at depth, the pressure gradients to drive melt segregation and subsequent transport, as well as dilation sites for magma accumulation (Fig. 1) (e.g. Brown, 1994). The significance of shear zones starts at the incipient stages of partial melting. Shear zones act as fluid pathways (Mancktelow, 2006) and thus promote partial melting (Berger *et al.*, 2008; Burri *et al.*, 2005; Genier *et al.*, 2008; Milord *et al.*, 2001; Mogk, 1992; Pognante, 1992). Negative pressure gradients may drive melt from interconnected melt-bearing layers in migmatites and thus lead to melt accumulation in shear zones (Brown, 1994). Brown & Solar (1998) have shown that melting and shearing can be interlinked and promote each other in a feedback relation. Melt that is generated in the anatectic zone at depth may be driven by a combination of buoyancy forces and tectonic stresses from high pressure zones to low pressure zones in a process termed by Brown (1994) as strike-slip dilatancy pumping. Alternating phases of transtension and transpression may lead to magma accumulation in dilatant jogs and magma expulsion, respectively (Weinberg *et al.*, 2009). The link between the anatectic, ductily deforming lower to middle crust to the brittle upper crust is thought to be achieved via networks of dykes (e.g. Brown, 1994; D'Lemos *et al.*, 1992), possibly changing from ductile fractures to brittle-elastic fracture (Weinberg & Regenauer-Lieb, 2010). Finally, magma ascent will be halted at a structural boundary or the level of neutral buoyancy (Cruden, 1998).

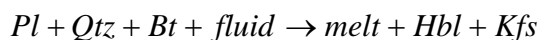
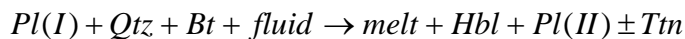
1.2.4 Water-fluxed melting

In crustal melting regimes, water absent melting is generally considered by far as the most common mechanism (e.g. Clemens & Droop, 1998; Clemens, 2006; Clemens & Vielzeuf, 1987). However, certain migmatite terrains show evidence for migmatization under water-fluxed conditions (e.g. Cruciani *et al.*, 2008; Lappin & Hollister, 1980; Kenah & Hollister, 1983; Mogk, 1992; Sawyer, 2009). Probably the most significant difference between fluid present (water-fluxed) and fluid absent melting is, beside the fluid itself, the temperature at which the melting reaction takes place. The most common fluid absent melting reactions, muscovite dehydration melting and biotite dehydration melting, require temperatures of at least 700°C and 800°C, respectively. Temperatures and pressures for water-fluxed melting in quartzo-feldspathic rocks are essentially identical to the wet granite solidus, so that melting begins at temperatures as low as 640°C and ~3 kbar (Holtz & Johannes, 1992). In the haplogranitic system, this melting reaction is



(mineral abbreviations after Kretz, 1983).

An important indication for water-fluxed melting is the presence of hornblende in leucosomes (Cruciani *et al.*, 2008; Kenah & Hollister, 1983; Lappin & Hollister, 1980; Mogk, 1992; Viruete, 1999). Melting experiments yielded that hornblende is only stable in a granitic melt when at least 5 % external water is added (Gardien *et al.*, 2000). McLellan (1988) and Lappin & Hollister (1980) suggested the following melting reactions that form hornblende:



In the presence of free water, these reactions can take place at temperatures of 700°C to 720°C (Slagstad et al., 1995). In the following, a regional geological overview of the study area in Ladakh, NW India, is given.

1.3 Geological background

1.3.1 Overview of the Karakoram Mountains and Ladakh

The Himalayas form the world's largest intracontinental mountain range that formed at an at least 2500 km long collision front of the Indian and Eurasian plates. The history of the Himalayas started some 140 Ma in Late Jurassic/ Early Cretaceous times, and still nowadays India is pushing into Eurasia in an approximately Northward movement at a rate of about 5 cm per anno (e.g. Allègre et al., 1984). The Himalayas host the highest elevations on Earth and also the largest crustal thicknesses (> 60 km in some regions). It can be divided into the Western Himalayan orogen (W of 81°E), the Central Himalayan orogen (between 81°E and 89°E) and the Eastern Himalayan orogen (E of 89°E) (Yin, 2006).

This research project is focused on an area in the Karakoram Mountains in the Western Himalayas. The study area lies in the region and former kingdom of Ladakh which today is part of the Indian state Jammu and Kashmir in the NW of the country, bordering Tibet in the NE and Pakistan in the NW. This region is of special geologic significance as it is traversed by several major tectonic elements of the Himalayas. These are the Indus Suture Zone and Shyok Suture Zone which mark two collision zones between India and Eurasia, and the Karakoram Fault which accommodates parts of the dextral extrusion of the Tibetan block in response to the Indian indentor (Avouac & Tapponnier, 1993; Matte *et al.*, 1996; Tapponnier *et al.*, 1986; Tapponnier *et al.*, 1982).

In Ladakh, rocks of the Ladakh island arc are bound by the Indus Suture Zone (ISZ), which marks the boundary between India and Eurasia, to the south and by the Shyok Suture Zone (SSZ), and it is thus sandwiched between India and Eurasia (Allègre *et al.*, 1984; Dietrich *et al.*, 1983; Frank *et al.*, 1977; Gansser, 1980; Honegger *et al.*, 1982). The Ladakh island arc forms a part of Mid-Cretaceous to Eocene calc-alkaline granitic intrusions, commonly referred to as the Trans-Himalayan plutonic belt, form a semi-continuous arcuate body over 2500 km (e.g. Allègre *et al.*, 1984; Coward *et al.*, 1986; Petterson & Windley, 1985). It is generally accepted that calc-alkaline magmatism that gave rise to the Trans-Himalaya batholiths resulted from northward subduction of Indian oceanic crust beneath the Eurasian plate in the course of closure of the Neo-Tethyan Ocean (Allègre *et al.*, 1984; Dietrich *et al.*, 1983; Honegger *et al.*, 1982; Ji *et al.*, 2009). Age data indicate that magmatic activity began at ~103 Ma and lasted until ~45 Ma. It is widely accepted that the end of magmatism marks the time of collision of India with Eurasia (Honegger *et al.*, 1982; Schärer *et al.*, 1984; Singh *et al.*, 2007; Upadhyay *et al.*, 2008; Weinberg & Dunlap, 2000). This interpretation is in agreement with the youngest marine sediments of Eocene age, after which continental

molasse was deposited in the ISZ (Brookfield & Andrews-Speed, 1984).

Collision of the Ladakh island arc and the Kohistan island arc with Eurasian (= Karakoram) margin, formed the SSZ which continues in to the NW in Pakistan as the Northern Suture Zone (Patterson & Windley, 1985). The majority of researchers considers the Kohistan and Ladakh island arcs, separated by spur of the Nanga Parbat syntaxis, as one composite Kohistan-Ladakh arc, based on geochemical, geochronological and isotopic relationships (Khan *et al.*, 2009; Petterson & Windley, 1985; Rolland *et al.*, 2002; Weinberg & Dunlap, 2000). It is debated whether the SSZ marks a second subduction zone of the Tethyan Ocean, north of the ISZ, or the closure of a back-arc basin (Coward *et al.*, 1986; Rai, 1997; Rex *et al.*, 1988; Robertson & Collins, 2002; Rolland *et al.*, 2000; Thakur *et al.*, 1981; Upadhyay, 2008). However, it is also debated whether the Ladakh island arc collided first with India, forming the ISZ, and then accreted as a composite terrane on to Eurasia, or whether the arc collided first with Eurasia, thus forming the SSZ before the ISZ (Khan *et al.*, 2009; Petterson & Windley, 1985; Upadhyay *et al.*, 1999).

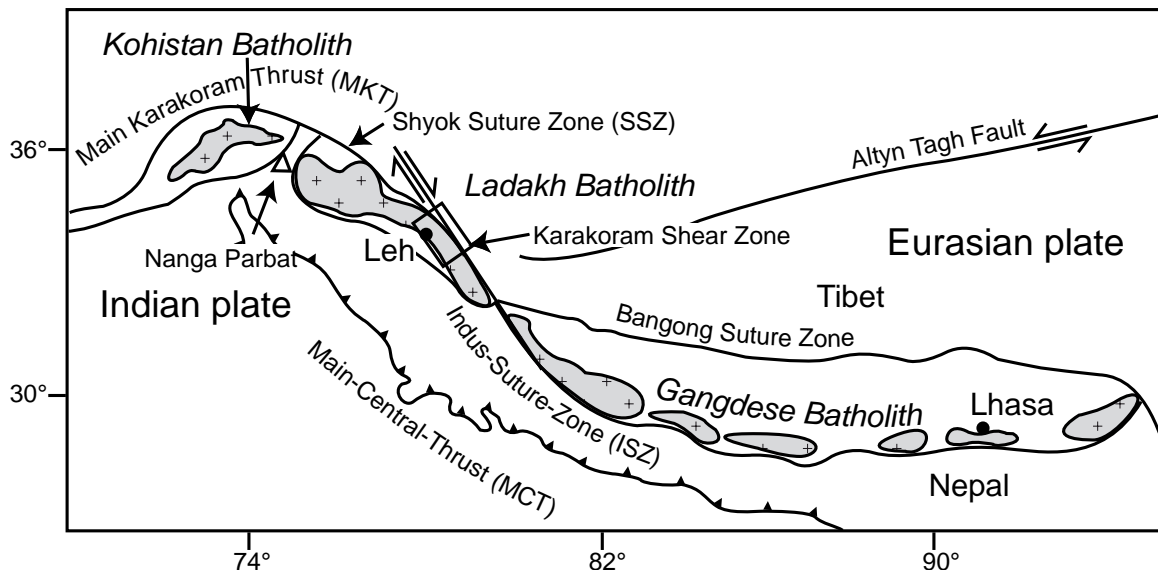


Fig. 1: Tectonic overview map showing the main terrane boundaries in the Karakoram and Himalaya. The Indian continent pushes northward into the Eurasian continent. The Nanga Parbat spur forms the northernmost promontory of India. Calc-alkaline batholiths of the Trans-Himalyan plutonic belt crop out along the Indus Suture Zone. The study area in the central part of the Karakoram Shear Zone is indicated with a frame.

North of the SSZ plutonic complexes of the Karakoram terrane crop out, forming the pre-collisional Karakoram Axial Batholith and intruded the Eurasian continental margin (~120 Ma to 55 Ma), and post-collisional granites (~25 Ma to 8 Ma) including the Baltoro granite or Karakoram Batholith (~21 to ~15 Ma) (Crawford & Searle, 1992; Crawford & Searle, 1993; Crawford & Windley, 1990; Debon *et al.*, 1987; Debon *et al.*, 1986; Desio & Zanettin, 1970; Mahéo *et al.*, 2009; Mahéo *et al.*, 2002; Parrish & Tirrul, 1989; Searle, 1992; Searle *et al.*, 1998).

Continued northward movement of the Indian plate led to formation of post-collisional fault systems. Of these, the most prominent are the >700 km dextral Karakoram Fault, the >100 km dextral Red River Fault and the >1500 km sinistral Altyn-Tagh Fault (Avouac &

Tapponnier, 1993; Lacassin, 2004; Molnar & Tapponnier, 1975; Tapponnier *et al.*, 1986; Tapponnier *et al.*, 1982). The study area here lies in the central part of the Karakoram Fault, which is henceforth named Karakoram Shear Zone because of its high grade metamorphism. The timing of initiation, total offset and long term slip-rate of the Karakoram Shear Zone are debated and highly variable, depending on the method used (see discussion in Valli *et al.*, 2007). Interestingly, the leucogranites that intruded along the Karakoram Shear Zone play a significant role in determining initiation of the shear zone in terms of whether they are syn-kinematic (Lacassin, 2004; Rolland *et al.*, 2009; Valli *et al.*, 2007) or pre-kinematic (Phillips *et al.*, 2004; Phillips & Searle, 2007; Searle, 1996).

1.3.2 Geology of the study area in the Karakoram Shear Zone

In the central part of the Karakoram Shear Zone, the shear zone is split into two parallel mylonitic shear zones. The Tangtse Shear Zone (SW strand) dips 70° NE and separates the Pangong Range that hosts the Pangong Metamorphic Complex (PMC) to the NE from the Ladakh Batholith to the SW. The Pangong Shear Zone (NE strand) is sub-vertical and separates the PMC from rocks of the Karakoram Terrane and the Karakoram Metamorphic Complex (KMC). Dextral transpressive kinematics in the Karakoram Shear zone has led to deep exhumation of the PMC in a pop up structure that thrust rocks that have been metamorphosed under upper amphibolite facies conditions over colder rocks to the SW and NE (Dunlap *et al.*, 1998; McCarthy & Weinberg, in press). The main regional foliation trends 120°-140°, parallel to the strike of the main shear strands.

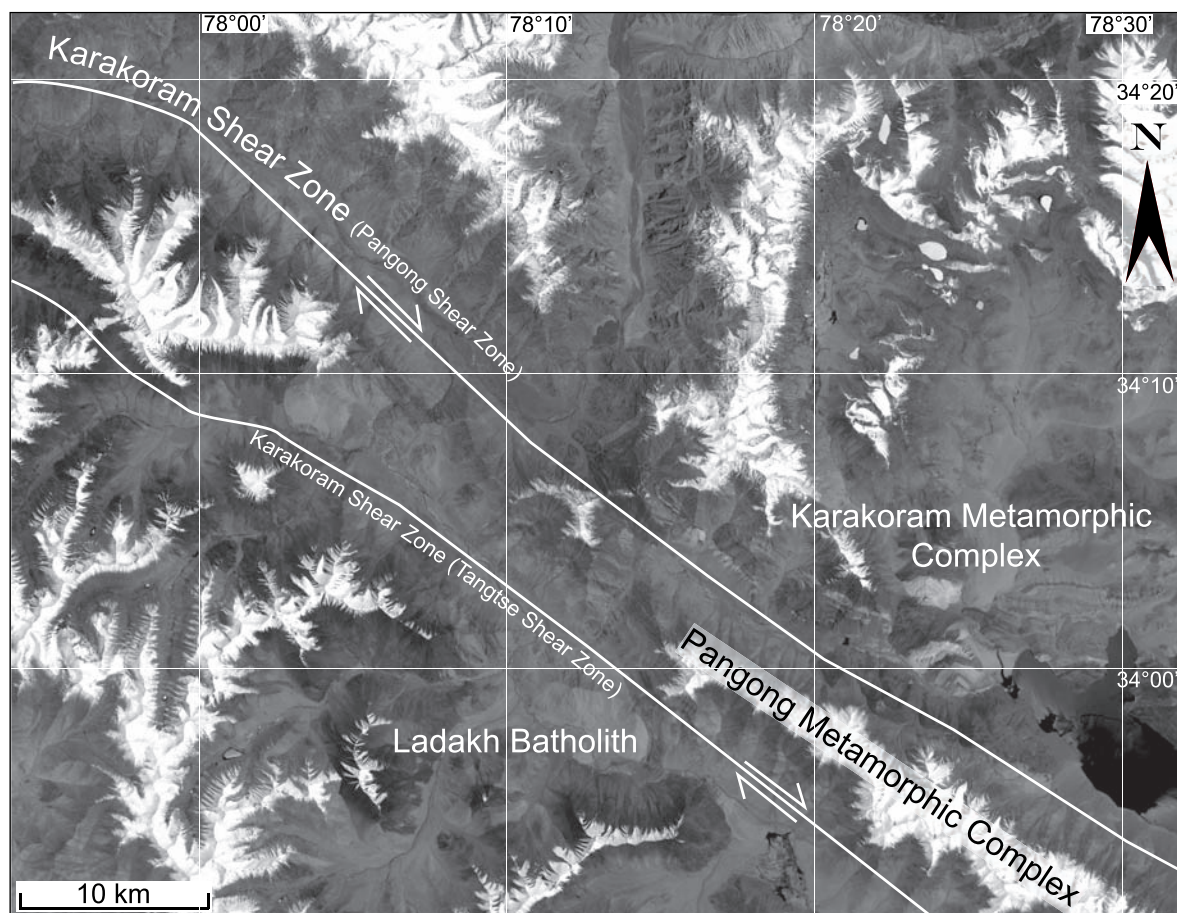


Fig. 2: Overview map of the study area. Note that valleys run parallel to the shear zones.

Rocks of the PMC show consistent dextral C-S fabrics and mineral stretching lineations of biotite and quartz trending NW, generally plunging 20–45°, rarely horizontal (Dunlap *et al.*, 1998; Weinberg *et al.*, 2000; Weinberg *et al.*, 2009). Reactivation under colder, greenschist facies conditions has been documented for the Pangong Shear Zone (McCarthy & Weinberg, in press; Rolland *et al.*, 2009; Rutter *et al.*, 2007). Changes in the stress regime have been inferred from the cooling history of Karakoram fault zone rocks. $^{40}\text{Ar}/^{39}\text{Ar}$ data shows that Karakoram Shear Zone underwent intense cooling between 17 and 13 Ma possibly due to upthrusting, followed by a phase of dominant strike-slip motion between 13 and 8 Ma (relatively slow cooling) and a change into rapid cooling (oblique thrusting) again after 8 Ma (Dunlap *et al.*, 1998). Present-day movements are reported only from the Pangong Shear Zone, while the Tangtse Shear Zone seems to be inactive (Brown *et al.*, 2002).



Fig. 3: Example of a leucogranite pluton related to anatexis in the Pangong Metamorphic Complex.

Unmetamorphosed calc-alkaline Hbl-Bt-granodiorites of the Ladakh Batholith (~50.4 to ~64 Ma; Ravikant *et al.*, 2009; Singh *et al.*, 2007; Upadhyay *et al.*, 2008) and the overlying Khardung Volcanics (~67.4 to 60.5 Ma; Dunlap & Wysoczanski, 2002) crop out immediately to the SW of the Tangtse Shear Zone. These rocks are both related to the Ladakh island arc. Rocks of the KMC to the NE of the Pangong Shear Zone consist dominantly of Grt-Bt-St-schists, marbles, amphibolites, mica-schists and psammities, and have been metamorphosed under greenschist to lower amphibolite facies (Dunlap *et al.*, 1998; McCarthy & Weinberg, in press). The PMC comprises a calc-alkaline granitoid rock suite with crystallization ages ranging between ~56 Ma and ~115 Ma, and in this thesis it is referred to as the Muglib Batholith. The PMC also comprises a meta-volcanic sequence ranging from amphibolites to Hbl-Bt schists, a meta-sedimentary sequence consisting of Bt-pelites, Bt-psammities and rare marbles, and calc-silicate rocks (Jain & Singh, 2008; Phillips *et al.*, 2004; Searle *et al.*, 1998; Weinberg & Mark, 2008). It is intensely intruded by peraluminous Bt-leucogranites and Ms-

Bt \pm Grt-leucogranites that span crystallization ages between ~ 13.5 and ~ 20 Ma (Phillips *et al.*, 2004; Ravikant *et al.*, 2009; Searle *et al.*, 1998).

It has been inferred, based on zircon inheritance in the leucogranites, that crustal anatexis of the Muglib Batholith at depths of ~ 18 - 20 km gave rise to leucogranite formation in the PMC (Searle *et al.*, 1998). Pervasive magma migration in migmatitic Bt-psammities led to formation of the Pangong Injection Complex, and coalescence of magma sheets to formation of the leucogranitic Tangtse Pluton (Weinberg & Searle, 1998). Weinberg & Mark (2008) described a layer of meta- and diatexite migmatites in the Tangtse gorge, and migmatization was interpreted as the result of syn-deformational water-fluxed melting. In these rocks, the transition from metatexite to diatexite occurred via transposition of layering into axial planar orientation, truncation of fold hinges by axial planar leucosomes and shearing parallel to the axial plane in tight to isoclinal folds. Water-fluxed melting in the PMC was found to be in agreement with thermobarometric calculations that determined peak metamorphic conditions in the Tangtse area to be at temperatures of 700 ± 20 °C at 7 ± 1 kbar (Rolland & Pêcher, 2001).

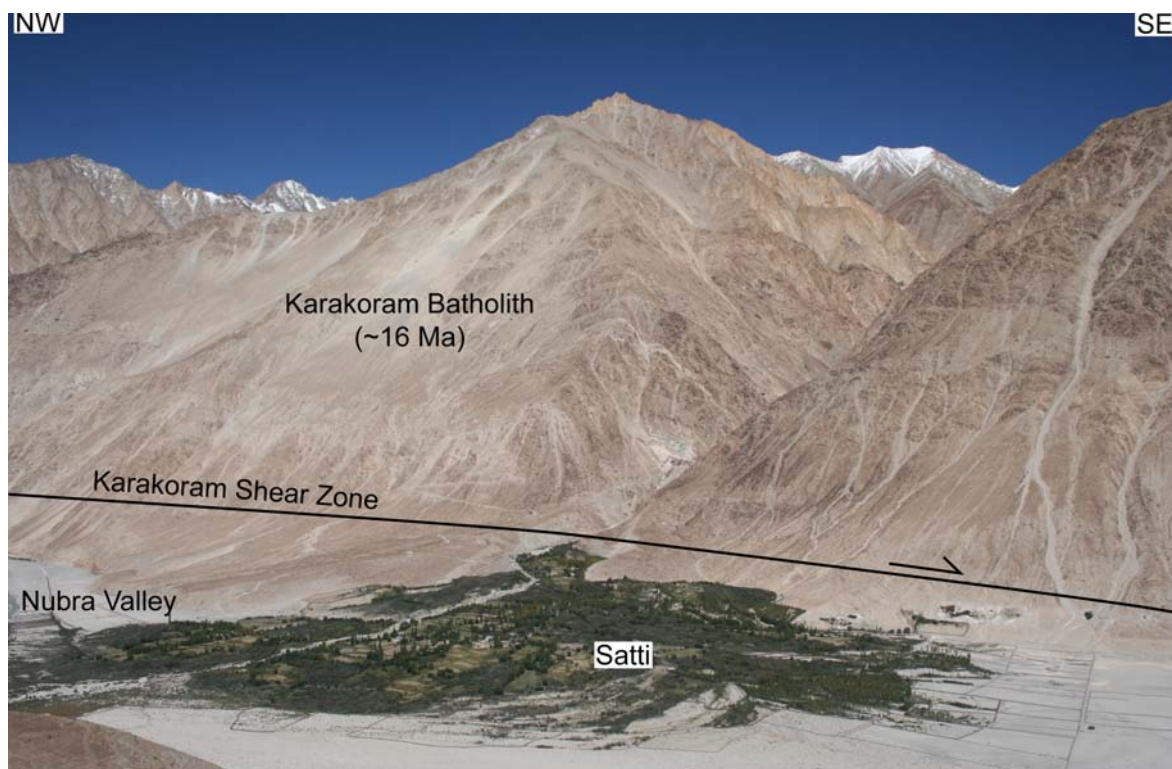


Fig. 4: The Karakoram Batholith at the NE slopes of the Nubra Valley ~ 70 km NW of the Tangtse region.

The leucogranites of the PMC have been used to limit the timing of initiation of movement along the Karakoram Shear Zone (Jain & Singh, 2008; Phillips *et al.*, 2004; Phillips & Searle, 2007; Rolland *et al.*, 2009; Searle *et al.*, 1998). Phillips *et al.* (2004) suggest that shearing along the Tangtse strand of the shear zone started after intrusion of mylonitic leucogranite dykes and finished before intrusion of undeformed pegmatitic leucogranite dykes. Thus they constrain shearing to have occurred zone initiation between ~ 15.7 and ~ 13.7 Ma (U-Pb zircon ages). Based on reconstructed cooling histories using Ar-Ar methods on micas and amphiboles and interpreted syn-magmatic deformation fabrics of the dated Tangtse granite (~ 18 Ma U-Pb zircon age; Searle *et al.* 1998), Rolland *et al.* (2009) suggested in contrast

that the Karakoram Shear must have been active at the time of granite formation, a view also supported by Weinberg & Mark (2008).

It has been suggested that the leucogranites of the PMC relate to leucogranites of the Karakoram Batholith (~15 Ma U-Pb zircon age) that crops out on the NE side of the Karakoram Shear Zone in the Shyok and Nubra River confluence area. This link was based on similar petrography and crystallization ages (Phillips & Searle, 2007; Searle, 1996; Searle *et al.*, 1998; Weinberg *et al.*, 2000). It was further inferred that the Karakoram Batholith in the Nubra Valley area is a SW continuation of the Baltoro granite (~ 21 Ma U-Pb zircon age) in Pakistan (Searle *et al.*, 1998).

1.4 Field laboratory Karakoram Shear Zone: addressing the research questions

The Pangong Metamorphic Complex in the Karakoram Shear Zone gives exceptional insight into metamorphic and magmatic processes in the middle crust. The study area lies above the tree line, even the valley floors are at 3800 m to 4000m above sea level, and vegetation is extremely sparse due to the semi-arid climate which also limits alteration of the rocks. These factors contribute to excellent outcrop conditions. Fast exhumation during dextral transpression in the Karakoram Shear Zone (Dunlap *et al.*, 1998) brought anatectic rocks to the surface that can now be studied in exposures of more than one kilometre relief. Cross-sections through all lithologies are easily accessible in two gorges cut by the Tangtse River almost perpendicular to strike of the Karakoram Shear Zone. On the down side, the high relief with peaks in the Pangong Range exceeding 6000 m and permanent snow cover, makes large areas inaccessible and leave them to reconnaissance studies through satellite images.

Migmatite outcrops offer the opportunity to study network formation from incipient melting on the centimetre-scale and the link to larger magma flow networks on the metric scale and thus give insight into the geometry of magma pathways. This is especially the case because no subsequent deformation phase under a different tectonic regime affected the migmatites and blurred the structures. Thus, some meta- and diatexite outcrops present spectacular ‘stop-motion’ images of melt migration.

Large networks of leucogranite dykes can be traced over distances of several kilometres, potentially linking leucogranite stocks and plutons ranging in width from tens of meters to kilometric size. Therefore, the Karakoram Shear Zone is ideal for studying and testing hypotheses on magma formation, its ascent and emplacement.

1.5 Structure of the thesis

This thesis is written as a coherent series of publications. It consists of this introductory chapter, followed by four main chapters, one of which has been published in *Lithos* (see Appendix I), the other three are in preparation for submission, and a concluding chapter that summarizes the results. This format makes some repetitions unavoidable. For example, the regional geology of the Karakoram Shear Zone will be introduced in every chapter, except the last one. Further, parts of the dataset will be used in more than one chapter, covering different research questions. The outline of the chapters is as follows.

- **Chapter I: Introduction**

An introduction to magma formation, segregation and subsequent ascent. Definition of the research questions and introduction to the study area.

- **Chapter II: Hybridization of granitic magmas in the source: The origin of the Karakoram Batholith, Ladakh, NW India**

This chapter investigates anatexis of distinct source rocks and hybridization of the resulting magmas very early in the migration history. By using Rb-Sr and Sm-Nd isotope systematics, source rocks are identified and the link of leucogranite magmas with identical isotopic signature from source to sink is shown. Timing of anatexis is determined by U-Pb SHRIMP dating on zircons and titanites on source rocks and magmatic products. Results indicate that magmas hybridize in the source by merging into shared magma channelways, and the hybrid magma is transported out of the anatectic source region via a large-scale dyke network that connects to the Karakoram Batholith.

- **Chapter III: Geochemistry of hornblende in meta- and diatexites and its fractionation in leucogranite magma**

Water-fluxed melting at upper amphibolite facies led to formation of hornblende-bearing leucosomes in meta- and diatexites. The geochemistry of hornblende grains was analysed using electron microprobe and Laser Ablation-ICP-MS methods. REE concentrations of hornblendes are highly variable and do not correspond to reported values in the literature. Systematic variations of the geochemical composition of protoliths, leucosomes and melanosomes are interpreted in view of these findings. Partition coefficients of hornblende are determined based on the data, and used to model fractionation and retainment of hornblende in the source. The results explain the high La_n/Yb_n and high Sr/Y values of some leucogranites of the Pangong Metamorphic Complex. It is proposed high La_n/Yb_n and high Sr/Y values, typical for adakites and TTGs, can be the result of water-fluxed melting in the mid-crust, without involvement of garnet in the residue.

- **Chapter IV: Leucogranite magma transport from source to sink: the dyke network in the Karakoram Shear Zone, NW India**

This chapter documents formation of continuous magma networks during dextral shearing from the source to the batholith. Network geometries are interpreted based on outcrop observations and analysis of dyke orientations and their intersections in stereographic projections. The results show that magma pathways in the PMC are parallel to the axial plane of folds, parallel to trend of the Karakoram Shear Zone, and define a common intersection parallel to the mineral elongation direction. Thus, magma pathways are perpendicular or at high angles to the axis of maximum shortening and not parallel to it as expected from melting and shearing experiments in the literature.

- **Chapter V: Are the Shyok Suture Zone and the Karakoram Shear Zone parallel in Ladakh?**

This chapter examines an important tectonic question. In the study area, two calc-alkaline batholiths are separated by the Tangtse Shear Zone. The SSZ, that separates the Ladakh arc from the Eurasian margin, is often interpreted to run parallel and to the south of the Tangtse

Shear Zone. Here I test the hypothesis that the calc-alkaline Muglib Batholith to the north of the supposed course of the SSZ, and the Ladakh Batholith to the south are genetically related. Geochemical, geochronological, and isotopic similarities, suggest a close genetic relationship of the batholiths. Especially the complete lack of older, inherited zircons and the isotopic signature, indicative of mantle sources with only minor crustal input, support the interpretation that both batholiths formed in the same island arc. The SSZ must thus follow a different course and does not separate the batholiths.

• Chapter VI: Summary and conclusions

A synthesis of the most important results in view of the research questions forms the last chapter of this thesis, and provides a final overview of the findings and their implications.

1.6 Methodology

Over 100 petrographic thin sections were made for studies of the mineral assemblages and textural relations. Geochemical data is used for classification of rocks, identification of melt compositions, interpretation of fractionation and accumulation processes and the identification of source rocks for leucogranite intrusions. XRF analyses of whole rock major element compositions were carried out at the facilities of James Cook University, QLD on 90 rock samples including trace element compositions of 54 of these. The trace element distribution including the group of REE of 52 whole rock powders was analyzed with a quadrupole ICP-MS at the School of Geosciences Monash University, Melbourne, in addition to 12 samples that were analyzed at the facilities of The University of Melbourne. Rb-Sr and Sm-Nd isotope geochemistry was analyzed for 20 whole rock powders at the School of Earth Sciences, Melbourne University using multi-collector ICP-MS. Age relationships between a leucogranite intrusion and its source rocks were examined by U-Pb geochronology. This method was applied on zircons and titanite grains of four specimens at the SHRIMP II at The Australian National University, in Canberra. Electron microprobe analysis on 15 polished thin sections was conducted in order to determine the composition of individual mineral phases and compositional changes within grains depending on their morphology. These analyses were carried out at the VIEPS facilities at The University of Melbourne. *In situ* Laser Ablation ICP-MS analysis of mineral grains in polished thin sections was performed on eight samples at the School of Geosciences, Monash University.

References

- Allègre, C. J., Courtillot, V., Tapponnier, P., Hirn, A., Mattauer, M., Coulon, C., Jaeger, J. J., Achache, J., Schärer, U., Marcoux, J., Burg, J. P., Girardeau, J., Armijo, R., Gariépy, C., Göpel, C., Tindong, L., Xuchang, X., Chenfa, C., Guangqin, L., Baoyu, L., Jiwen, T., Naiwen, W., Guoming, C., Tonglin, H., Xibin, W., Wanming, D., Huaibin, S., Yougong, C., Ji, Z., Hongrong, Q., Peisheng, B., Songchan, W., Bixiang, W., Yaoxiu, Z. & Xu, R. (1984). Structure and evolution of the Himalaya-tibet orogenic belt. *Nature* 307, 17-22.
- Arzi, A. A. (1978). Critical phenomena in the rheology of partially melted rocks. *Tectonophysics* 44, 173-184.
- Ashworth, J. R. (1985). Introduction. *Migmatites*, 1-35.
- Avouac, J. P. & Tapponnier, P. (1993). Kinematic model of active deformation in central Asia. *Geophysical Research Letters* 20, 895-898.

- Bateman, R. J. (1984). On the role of diapirism in the segregation, ascent and final emplacement of granitoid magmas. *Tectonophysics* 110, 211-231.
- Berger, A., Burri, T., Alt-Epping, P. & Engi, M. (2008). Tectonically controlled fluid flow and water-assisted melting in the middle crust: An example from the Central Alps. *Lithos* 102, 598-615.
- Brookfield, M. E. & Andrews-Speed, C. P. (1984). Sedimentology, petrography and tectonic significance of the shelf, flysch and molasse clastic deposits across the Indus Suture Zone, Ladakh, NW India. *Sedimentary Geology* 40, 249-286.
- Brown, E. T., Bendick, R., Bourles, D. L., Gaur, V., Molnar, P., Raisbeck, G. M. & Yiou, F. (2002). Slip rates of the Karakorum fault, Ladakh, India, determined using cosmic ray exposure dating of debris flows and moraines. *Journal of Geophysical Research* 107 Art. No. 2192.
- Brown, M. (1994). The generation, ascent and emplacement of granite magma: the migmatite-to-crustally-derived granite connection in thickened orogens. *Earth-Science Reviews* 36, 83-130.
- Brown, M. (2005). The mechanism of melt extraction from lower continental crust of orogens. *Transactions of the Royal Society of Edinburgh: Earth Sciences* 95, 35-48.
- Brown, M. (2007). Crustal melting and melt extraction, ascent and emplacement in orogens: mechanisms and consequences. *Journal of the Geological Society of London* 164, 709-730.
- Brown, M., Averkin, Y. A., McLellan, E. L., Sawyer, E. W. (1995). Melt segregation in migmatites. *Journal of Geophysical Research* 100, 15,655-615,679.
- Brown, M. & Rushmer, T. (1997). The role of deformation in the movement of granitic melt: views from the laboratory and the field. In: Holness, M. B. (ed.) *Deformation-enhanced Fluid Transport in the Earth's Crust and Mantle*: Chapman & Hall, 111-144.
- Brown, M. & Solar, G. S. (1998). Shear-zone systems and melts: feedback relations and self-organization in orogenic belts. *Journal of Structural Geology* 20, 211-227.
- Burri, T., Berger, A. & Engi, M. (2005). Tertiary migmatites in the Central Alps: Regional distribution, field relations, conditions of formation and tectonic implications. *Schweizerische Mineralogische und Petrographische Mitteilungen* 85, 215-232.
- Clemens, J. D. (2006). Melting of the continental crust; fluid regimes, melting reactions, and source rock fertility. In: Brown, M., Rushmer, T. (ed.) *Evolution and differentiation of the continental crust*. New York, NY, United States: Cambridge University Press, 296-330.
- Clemens, J. D. & Mawer, C. K. (1992). Granitic magma transport by fracture propagation. *Tectonophysics* 204, 339-360.
- Coward, M. P., Rex, D. C., Khan, M. A., Windley, B. F., Broughton, R. D., Luff, I. W., Petterson, M. G. & Pudsey, C. J. (1986). Collision tectonics in the NW Himalayas. *Geological Society, London, Special Publications* 19, 203-219.
- Crawford, M. B. & Searle, M. P. (1992). Field relationships and geochemistry of pre-collisional (India-Asia) granitoid magmatism in the central Karakoram, northern Pakistan. *Tectonophysics* 206, 171-192.
- Crawford, M. B. & Searle, M. P. (1993). Collision-related granitoid magmatism and crustal structure of the Hunza Karakoram, North Pakistan. *Geological Society of London Special Publications* 74, 53-68.
- Crawford, M. B. & Windley, B. F. (1990). Leucogranites of the Himalaya/Karakoram: implications for magmatic evolution within collisional belts and the study of collision-related leucogranite petrogenesis. *Journal of Volcanology and Geothermal Research* 44, 1-19.
- Cruciani, G., Franceschelli, M., Jung, S., Puxeddu, M. & Utzeri, D. (2008). Amphibole-bearing migmatites from the Variscan Belt of NE Sardinia, Italy: Partial melting of mid-Ordovician igneous sources. *Lithos* 105, 208-224.

- Cruden, A. R. (1998). On the emplacement of tabular granites. *Journal of the Geological Society* 155, 853-862.
- D'Lemos, R. S., Brown, M. & Strachan, R. A. (1992). Granite magma generation, ascent and emplacement within a transpressional orogen. *Journal of the Geological Society* 149, 487-490.
- Debon, F., Le Fort, P., Dautel, D., Sonet, J. & Zimmermann, J. L. (1987). Granites of western Karakorum and northern Kohistan (Pakistan): A composite mid-cretaceous to upper cenozoic magmatism. *Lithos* 20, 19-40.
- Debon, F., Zimmermann, J. L. & Bertrand, J. M. (1986). Le granite du Baltoro (batholite axial du Karakorum, nord Pakistan): une intrusion subalkaline d'âge Miocene Supérieur. *Comptes Rendus de l'Académie des Sciences, Paris, Série II* 303, 463-468.
- Dell'Angelo, L. N. & Tullis, J. (1988). Experimental deformation of partially melted granitic aggregates. *Journal of Metamorphic Geology* 6, 495-515.
- Desio, A. & Zanettin, B. (1970). Geology of the Baltoro Basin. Italian Expeditions to the Karakorum (K2) and Hindu Kush (leader A. Desio). *Scientific Reports* section II, vol. 2, Brill, Leiden, 308.
- Dietrich, V. J., Frank, W. & Honegger, K. (1983). A Jurassic-Cretaceous island arc in the Ladakh-Himalayas. *Journal of Volcanology and Geothermal Research* 18, 405-433.
- Dunlap, W. J., Weinberg, R. F. & Searle, M. P. (1998). Karakoram fault zone rocks cool in two phases. *Journal of the Geological Society of London* 155, 903-912.
- Emery, S. H., Marret, R. (1990). Why dikes? *Geology* 18, 231-233.
- Frank, W., Gansser, A. & Trommsdorff, V. (1977). Geological observations in the Ladakh area (Himalayas); a preliminary report. *Schweizerische Mineralogische und Petrographische Mitteilungen* 57, 89-113.
- Gansser, A. (1980). The significance of the Himalayan suture zone. *Tectonophysics* 62, 37-40, 43-52.
- Genier, F., Bussy, F., Epard, J. L. & Baumgartner, L. (2008). Water-assisted migmatization of metagraywackes in a Variscan shear zone, Aiguilles-Rouges massif, western Alps. *Lithos* 102, 575-597.
- Harris, N. B. W., Pearce, J. A. & Tindle, A. G. (1986). Geochemical characteristics of collision-zone magmatism. *Geological Society of London, Special Publication* 19, 67-81.
- Hawkesworth, C. J. & Vollmer, R. (1979). Crustal contamination versus enriched mantle: $^{143}\text{Nd}/^{144}\text{Nd}$ and $^{87}\text{Sr}/^{86}\text{Sr}$ evidence from the Italian volcanics. *Contributions to Mineralogy and Petrology* 69, 151-165.
- Holtzman, B. K. & Kohlstedt, D. L. (2007). Stress-driven melt segregation and strain partitioning in partially molten rocks; effects of stress and strain. *Journal of Petrology* 48, 2379-2406.
- Honegger, K., Dietrich, V., Frank, W., Gansser, A., Thöni, M. & Trommsdorff, V. (1982). Magmatism and metamorphism in the Ladakh Himalayas (the Indus-Tsangpo suture zone). *Earth and Planetary Science Letters* 60, 253-292.
- Hutton, D. H. W. (1982). A tectonic model for the emplacement of the Main Donegal Granite, NW Ireland. *Journal of the Geological Society of London* 139, 615-631.
- Jain, A. K. & Singh, S. (2008). Tectonics of the southern Asian Plate margin along the Karakoram Shear Zone: Constraints from field observations and U-Pb SHRIMP ages. *Tectonophysics* 451, 186-205.
- Ji, W.-Q., Wu, F.-Y., Chung, S.-L., Li, J.-X. & Liu, C.-Z. (2009). Zircon U-Pb geochronology and Hf isotopic constraints on petrogenesis of the Gangdese batholith, southern Tibet. *Chemical Geology* 262, 229-245.
- Katz, R. F., Spiegelman, M. & Holtzman, B. (2006). The dynamics of melt and shear localization in partially molten aggregates. *Nature* 442, 676-679.
- Kenah, C. & Hollister, L. S. (1983). Anatexis in the Central Gneiss Complex. In: Atherton, M. P., Gribble, C. D. (ed.) *Migmatites, Melting, and Metamorphism*. Nantwich:

- Shiva, 142-162.
- Khan, S. D., Walker, D. J., Hall, S. A., Burke, K. C., Shah, M. T. & Stockli, L. (2009). Did the Kohistan-Ladakh island arc collide first with India? *Geological Society of America Bulletin* 121, 366-384.
- Kohlstedt, D. L. & Holtzman, B. K. (2009). Shearing melt out of the earth: An experimentalist's perspective on the influence of deformation on melt extraction. *Annual Review of Earth and Planetary Sciences*, 561-593.
- Kretz, R. (1983). Symbols for rock-forming minerals. *American Mineralogist* 68, 277-279.
- Lacassin, R., Franck, V., Nicolas, A., Leloup, P. H., Paquette, J. L., Haibling, L., Tapponnier, P., Chevalier, M-L., Guillot, S., Mahéo, G., Zhiqin, X. (2004). Large-scale geometry, offset and kinematic evolution of the Karakorum fault, Tibet. *Earth and Planetary Science Letters* 219, 255-269.
- Lappin, A. R. & Hollister, L. S. (1980). Partial melting in the Central Gneiss Complex near Prince Rupert, British Columbia. *American Journal of Science* 280, 518-545.
- Mahéo, G., Blichert-Toft, J., Pin, C., Guillot, S. & Pêcher, A. (2009). Partial Melting of Mantle and Crustal Sources beneath South Karakorum, Pakistan: Implications for the Miocene Geodynamic Evolution of the India-Asia Convergence Zone. *Journal of Petrology*, 427-449.
- Mahéo, G., Guillot, S., Blichert-Toft, J., Rolland, Y. & Pêcher, A. (2002). A slab breakoff model for the Neogene thermal evolution of South Karakorum and South Tibet. *Earth and Planetary Science Letters* 195, 45-58.
- Marchildon, N. & Brown, M. (2003). Spatial distribution of melt-bearing structures in anatectic rocks from Southern Brittany, France: implications for melt transfer at grain- to orogen-scale. *Tectonophysics* 364, 215-235.
- Matte, P., Tapponnier, P., Arnaud, N., Bourjot, L., Avouac, J. P., Vidal, P., Qing, L., Yusheng, P. & Yi, W. (1996). Tectonics of western Tibet, between the Tarim and the Indus. *Earth and Planetary Science Letters* 142, 311-330.
- McCarthy, M. R. & Weinberg, R. F. (in press). Structural complexity resulting from pervasive ductile deformation in the Karakoram Shear Zone, Ladakh, NW India. *Tectonics*.
- Mehnert, K. R. (1968). *Migmatites and the origin of granitic rocks*.
- Milord, I., Sawyer, E. W. & Brown, M. (2001). Formation of diatexite migmatite and granite magma during anatexis of semi-pelitic metasedimentary rocks: An example from St. Malo, France. *Journal of Petrology* 42, 487-505.
- Mogk, D. W. (1992). Ductile shearing and migmatization at mid-crustal levels in an Archaean high-grade gneiss belt, northern Gallatin Range, Montana, USA. *Journal of Metamorphic Geology* 10, 427-438.
- Molnar, P. & Tapponnier, P. (1975). Cenozoic tectonics of Asia, effects of a continental collision. *Science* 189, 419-426.
- Parrish, R. R. & Tirrul, R. (1989). U-Pb age of the Baltoro granite, northwest Himalaya, and implications for monazite U-Pb systematics. *Geology* 17, 1076-1079.
- Paterson, S. R., Fowler, K. T. (1993). Re-examining pluton emplacement processes. *Journal of Structural Geology* 15, 191-206.
- Petford, N., Lister, J. R., Kerr, R. C. (1994). The ascent of felsic magmas in dykes. *Lithos* 32, 161-168.
- Petterson, M. G. & Windley, B. F. (1985). RbSr dating of the Kohistan arc-batholith in the Trans-Himalaya of north Pakistan, and tectonic implications. *Earth and Planetary Science Letters* 74, 45-57.
- Phillips, R. J., Parrish, R. R. & Searle, M. P. (2004). Age constraints on ductile deformation and long-term slip rates along the Karakoram fault zone, Ladakh. *Earth and Planetary Science Letters* 226, 305-319.
- Phillips, R. J. & Searle, M. P. (2007). Macrostructural and microstructural architecture of the Karakoram fault; relationship between magmatism and strike-slip faulting. *Tectonics* 26.

- Pitcher, W. S. (1979). The nature, ascent and emplacement of granitic magmas. *Journal of the Geological Society* 136, 627-662.
- Pognante, U. (1992). Migmatites and Leucogranites of tertiary age from the high Himalayan Crystallines of Zaskar (NW India): a case history of anatexis of Palaeozoic orthogneisses. *Mineralogy and Petrology* 46, 291-313.
- Rabinowicz, M. & Vigneresse, J. L. (2004). Melt segregation under compaction and shear channeling: Application to granitic magma segregation in a continental crust. *Journal of Geophysical Research* 109, B04407 04401-04420.
- Rai, H. (1997). Geology of the Shyok Tectonic Zone in eastern Ladakh, India. *Journal of the Geological Society of India* 49, 727-730.
- Ravikant, V., Wu, F.-Y. & Ji, W.-Q. (2009). Zircon U-Pb and Hf isotopic constraints on petrogenesis of the Cretaceous-Tertiary granites in eastern Karakoram and Ladakh, India. *Lithos* 110, 153-166.
- Rex, A. J., Searle, M. P., Tirrul, R., Crawford, M. B., Prior, D. J., Rex, D. C. & Barnicoat, A. C. (1988). The geochemical and tectonic evolution of the central Karakoram, North Pakistan. *Philosophical Transactions of the Royal Society of London, Series A: Mathematical and Physical Sciences* 326, 229-255.
- Robertson, A. H. F. & Collins, A. S. (2002). Shyok Suture Zone, N Pakistan: Late Mesozoic-Tertiary evolution of a critical suture separating the oceanic Ladakh Arc from the Asian continental margin. *Journal of Asian Earth Sciences* 20, 309-351.
- Robin, P. Y. F. (1979). Theory of metamorphic segregation and related processes. *Geochimica et Cosmochimica Acta* 43, 1587-1600.
- Rolland, Y., Mahéo, G., Pêcher, A. & Villa, I. M. (2009). Syn-kinematic emplacement of the Pangong metamorphic and magmatic complex along the Karakorum Fault (N Ladakh). *Journal of Asian Earth Sciences* 34, 10-25.
- Rolland, Y. & Pêcher, A. (2001). The Pangong granulites of the Karakoram Fault (western Tibet); vertical extrusion within a lithosphere-scale fault? *Comptes Rendus de l'Academie des Sciences, Serie II. Sciences de la Terre et des Planetes* 332, 363-370.
- Rolland, Y., Pêcher, A. & Picard, C. (2000). Middle Cretaceous back-arc formation and arc evolution along the Asian margin; the Shyok suture zone in northern Ladakh (NW Himalaya). *Tectonophysics* 325, 145-173.
- Rolland, Y., Picard, C., Pêcher, A., Lapierre, H., Bosch, D. & Keller, F. (2002). The Cretaceous Ladakh arc of NW Himalaya--slab melting and melt-mantle interaction during fast northward drift of Indian Plate. *Chemical Geology* 182, 139-178.
- Rosenberg, C. L. & Berger, A. (2001). Syntectonic melt pathways in granitic gneisses, and melt-induced transitions in deformation mechanisms. *Physics of the Chemical Earth* 26, 287-293.
- Rosenberg, C. L. & Handy, M. R. (2005). Experimental deformation of partially melted granite revisited: Implications for the continental crust. *Journal of Metamorphic Geology* 23, 19-28.
- Rutter, E. H., Faulkner, D. R., Brodie, K. H., Phillips, R. J. & Searle, M. P. (2007). Rock deformation processes in the Karakoram fault zone, Eastern Karakoram, Ladakh, NW India. *Journal of Structural Geology* 29, 1315-1326.
- Rutter, E. H. & Neumann, D. H. K. (1995). Experimental deformation of partially molten Western Granite under fluid-absent conditions, with implications for the extraction of granitic magmas. *Journal of Geophysical Research* 100, 15,697-615,715.
- Sawyer, E. W. (2001). Melt segregation in the continental crust: distribution and movement of melt in anatectic rocks. *Journal of Metamorphic Geology* 19, 291-309.
- Sawyer, E. W. (2008). *Atlas of migmatites*: Mineralogical Association of Canada, Ottawa, ON, Canada 9, pp. 371.
- Schärer, U., Hamet, J. & Allègre, C. J. (1984). The Transhimalaya (Gangdese) plutonism in the Ladakh region: a UPb and RbSr study. *Earth and Planetary Science Letters* 67,

327-339.

- Searle, M. P. (1996). Geological evidence against large-scale pre-Holocene offsets along the Karakoram Fault: Implications for the limited extrusion of the Tibetan plateau. *Tectonics* 15, 171-186.
- Searle, M. P., Crawford, M. B., Rex, A. J. (1992). Field relations, geochemistry, origin and emplacement of the Baltoro granite, Central Karakoram. *Transactions of the Royal Society of Edinburgh: Earth Sciences* 83, 519-538.
- Searle, M. P., Weinberg, R. F. & Dunlap, W. J. (1998). Transpressional tectonics along the Karakoram Fault Zone, northern Ladakh. In: Holdsworth, R. E. & Strachan, R. A. (eds.) *Continental Transpressional and Transtensional Tectonics*. London: Geological Society of London Special Publication, 307-326.
- Sederholm, J. J. (1907). *On granite and gneiss, their origin, relations and occurrence in the pre-Cambrian complex of Fenno-Scandia. Om granit och gneis deras uppkomst, uppträdande och utbredning inom urberget i Fennoskandia*: Societas Geographica Fenniae, Helsinki, Finland.
- Sederholm, J. J. (1913). Über die Entstehung der migmatitischen Gesteine - Einige kritische Bemerkungen. *Geologische Rundschau* 4, 174-185.
- Singh, S., Kumar, R., Barley, M. E. & Jain, A. K. (2007). SHRIMP U-Pb ages and depth of emplacement of Ladakh Batholith, Eastern Ladakh, India. *Journal of Asian Earth Sciences* 30, 490-503.
- Stevenson, D. J. (1989). Spontaneous small-scale melt segregation in partial melts undergoing deformation. *Geophysical Research Letters* 16, 1067-1070.
- Tapponnier, P., Peltzer, G. & Armijo, R. (1986). On the mechanics of the collision between India and Asia. *Collision Tectonics*, 115-157.
- Tapponnier, P., Peltzer, G., LeDain, A. Y., Armijo, R. & Cobbold, P. R. (1982). Propagating extrusion tectonics in Asia: new insights from simple experiments with plasticine. *Geology* 10, 611-616.
- Thakur, V. C., Viridi, N. S., Rai, H. & Gupta, K. R. (1981). A note on the geology of Nubra-Shyok area of Ladakh, Kashmir, Himalaya. *Journal of the Geological Society of India* 22, 46-50.
- Upadhyay, R. (2008). Implications of U-Pb zircon age of the Tirit granitoids on the closure of the Shyok suture zone, northern Ladakh, India. *Current Science* 94, 1635-1640.
- Upadhyay, R., Frisch, W. & Siebel, W. (2008). Tectonic implications of new U-Pb zircon ages of the Ladakh Batholith, Indus suture zone, northwest Himalaya, India. *Terra Nova* 20, 309-317.
- Upadhyay, R., Sinha, A. K., Chandra, R. & Rai, H. (1999). Tectonic and magmatic evolution of the eastern Karakoram, India. *Geodinamica Acta* 12, 341-358.
- Valli, F., Arnaud, N., Leloup, P. H., Sobel, E. R., Mahéo, G., Lacassin, R., Guillot, S., Li, H., Tapponnier, P. & Xu, Z. (2007). Twenty million years of continuous deformation along the Karakorum fault, western Tibet: A thermochronological analysis. *Tectonics* 26.
- van der Molen, I. & Paterson, M. S. (1979). Experimental deformation of partially-melted granite. *Contributions to Mineralogy and Petrology* 70, 299-318.
- Vanderhaeghe, O. (1999). Pervasive melt migration from migmatites to leucogranite in the Shuswap metamorphic core complex, Canada: Control of regional deformation. *Tectonophysics* 312, 35-55.
- Vigneresse, J. L. (1995). Control of granite emplacement by regional deformation. *Tectonophysics* 249, 173-186.
- Viruete, E. J. (1999). Hornblende-bearing leucosome development during syn-orogenic crustal extension in the Tormes gneiss dome, NW Iberian Massif, Spain. *Lithos* 46, 751-772.
- Wagner, R., Rosenberg, C. L., Handy, M. R., Moebus, C., Albers, M. (2006). Fracture-driven intrusion and upwelling of a mid-crustal pluton fed from a transpressive shear zone

- The Rieserferner Pluton (Eastern Alps). *Geological Society of America Bulletin* 118, 219-237.
- Weinberg, R. F. (1996). Ascent mechanism of felsic magmas: news and views. *Special Paper 315: The Third Hutton Symposium on the Origin of Granites and Related Rocks* 315, 95-103.
- Weinberg, R. F. (1999). Mesoscale pervasive melt migration: alternative to dyking. *Lithos* 46, 393-410.
- Weinberg, R. F. & Dunlap, W. J. (2000). Growth and deformation of the Ladakh Batholith, Northwest Himalayas; implications for timing of continental collision and origin of calc-alkaline batholiths. *Journal of Geology* 108, 303-320.
- Weinberg, R. F., Dunlap, W. J. & Whitehouse, M. (2000). New field, structural and geochronological data from the Shyok and Nubra valleys, northern Ladakh: linking Kohistan to Tibet. In: Khan, A., Treloar, P. J. & Searle, M. P. (eds.) *Tectonics of the Nanga Parbat Syntaxis and the Western Himalaya*. London: Geological Society of London Special Publication, 253-275.
- Weinberg, R. F. & Mark, G. (2008). Magma migration, folding, and disaggregation of migmatites in the Karakoram shear zone, Ladakh, NW India. *Geological Society of America Bulletin* 120, 994-1009.
- Weinberg, R. F., Mark, G. & Reichardt, H. (2009). Magma ponding in the Karakoram shear zone, Ladakh, NW India. *Geological Society of America Bulletin* 121, 278-285.
- Weinberg, R. F. & Regenauer-Lieb, K. (2010). Ductile fractures and magma migration from source. *Geology* 38, 363-366.
- Weinberg, R. F. & Searle, M. P. (1998). The Pangong Injection Complex, Indian Karakoram: a case of pervasive granite flow through hot viscous crust. *Journal of the Geological Society of London* 155, 883-891.
- Weinberg, R. F., Sial, A. N. & Mariano, G. (2004). Close spatial relationship between plutons and shear zones. *Geology* 32, 377-380.
- Wickham, S. M. (1987). The segregation and emplacement of granitic magmas. *Journal of the Geological Society* 144, 281-297.
- Wyllie, P. J. (1977). Crustal anatexis: An experimental review. *Tectonophysics* 43, 41-71.

Declaration for Thesis Chapter 2

Declaration by candidate

In the case of Chapter 2, the nature and extent of my contribution to the work was the following:

Nature of contribution	Extent of contribution (%)
Development of ideas, collection of data, writing up and interpretation of results.	70%

The following co-authors contributed to the work. Co-authors who are students at Monash University must also indicate the extent of their contribution in percentage terms:

Name	Nature of contribution	Extent of contribution (%) for student co-authors only
Roberto Weinberg	Development of ideas, intellectual input during revision process.	
Ulf Andersson	Data collection, intellectual input during revision process.	
Mark Fanning	Data collection, intellectual input during revision process.	

Candidate's
Signature

	Date
--	------

Declaration by co-authors

The undersigned hereby certify that:

- (1) the above declaration correctly reflects the nature and extent of the candidate's contribution to this work, and the nature of the contribution of each of the co-authors.
- (2) they meet the criteria for authorship in that they have participated in the conception, execution, or interpretation, of at least that part of the publication in their field of expertise;
- (3) they take public responsibility for their part of the publication, except for the responsible author who accepts overall responsibility for the publication;
- (4) there are no other authors of the publication according to these criteria;
- (5) potential conflicts of interest have been disclosed to (a) granting bodies, (b) the editor or publisher of journals or other publications, and (c) the head of the responsible academic unit; and
- (6) the original data are stored at the following location(s) and will be held for at least five years from the date indicated below:

Location(s) School of Geosciences, Monash University

Signature 1		Date
Signature 2		2010-04-07
Signature 3		23/4/2010

.....

Chapter II.

Hybridization of granitic magmas in the source:

The origin of the Karakoram Batholith, Ladakh, NW India

Reichardt, H.^a, Weinberg, R. F.^a, Andersson, U.B.^b, Fanning, M. C.^c

Article is published in Lithos

^aSchool of Geosciences, Monash University, Clayton, VIC 3800, Australia

^bLaboratory for Isotope Geology, Swedish Museum for Natural History, Box 50007, SE-104 05 Stockholm, Sweden

^cPRISE, Research School of Earth Sciences, The Australian National University, Mills Road, Canberra ACT 0200, Australia

Abstract

Many magmatic bodies have a hybrid isotopic signature suggesting that somewhere during genesis, transport and emplacement, magmas assimilated other rocks or mixed with other magmas. Where and how hybridization takes place is seldom documented. Here, we investigate a magmatic system in the Eastern Karakoram, Ladakh, NW India, comprising an anatectic zone, and a network of sheets, stocks and plutons exposed in the Pangong Metamorphic Complex within the Karakoram Shear Zone, as well as the Karakoram Batholith. These granitic rocks have an isotopic signature indicative of a mixture between mantle and crustal sources. In the anatectic region, calc-alkaline granitoids and their meta-sedimentary country rocks underwent water-fluxed partial melting at upper amphibolite facies between 20 and 14 Ma ago. Anatexis gave rise to leucosomes and intrusive rocks that have a range in composition from leucotonalite to leucogranite. Those related to the partial melting of calc-alkaline rocks contain hornblende, whereas those related to Bt-psammites contain two micas \pm garnet. Leucosomes rooting in different source rocks merge with each other and homogenize as they link up to form a hierarchy of magma channels, feeding into stocks, plutons and ultimately into the Karakoram Batholith. This interpretation is supported by Sr and Nd isotopes. Initial $^{87}\text{Sr}/^{86}\text{Sr}$ and ϵ_{Nd} values are distinct for each of the magma protoliths in the anatectic zone and for the magmatic products. Calc-alkaline granitoids have initial $^{87}\text{Sr}/^{86}\text{Sr} = 0.7042$ to 0.7077 and $\epsilon_{\text{Nd}} = +0.6$ to $+2.4$, indicative of a slightly depleted mantle source region. This is in contrast to the meta-sedimentary rocks that yield initial

$^{87}\text{Sr}/^{86}\text{Sr} = 0.7115$ to 0.7161 and $\epsilon_{\text{Nd}} = -10.0$ to -9.6 , suggesting a stronger crustal component. Leucogranitic rocks, including a variety of leucosomes in the anatectic zone and samples from the Karakoram Batholith, yield intermediate values of initial $^{87}\text{Sr}/^{86}\text{Sr} = 0.7076$ to 0.7121 and $\epsilon_{\text{Nd}} = -3.6$ to -7.1 that can be modeled by mixing of the two source rocks. The hybrid signature of leucosomes and their similarity to intrusive leucogranites indicate that magma hybridization must have taken place within the source region as a result of the confluence of magmas to form the escape channels. We conclude that the voluminous leucogranites of the Miocene Karakoram Batholith result from water-fluxed intracrustal melting of sources with crustal and mantle signatures, and that mixing occurred within the source.

Keywords: Karakoram Shear Zone; Karakoram Batholith; crustal anatexis; magma mixing; radiogenic isotopes.

1. Introduction

Granitic magma generation in continental collision zones can involve various source rocks and takes place under a range of conditions. Isotopic compositions of magmatic bodies are widely applied to trace their origin as the source rocks leave their isotopic fingerprint on the magmas (e.g. Beard *et al.*, 2005). Granitoids with isotopic signatures intermediate between those of crustal and mantle sources, indicate that mixing of different magmas may have been involved (e.g. Andersson, 1991; Guillot & Le Fort, 1995; Hawkesworth & Vollmer, 1979). Generally, Himalayan Miocene leucogranites are examples of crustal melting with clear crustal isotopic signature (Deniel *et al.*, 1987; Guillot & Le Fort, 1995; Le Fort *et al.*, 1987). Broadly contemporaneous leucogranites of the Karakoram Range in the western parts of the Himalayan orogen, however, have isotopic signatures intermediate between mantle and crust (Crawford & Searle, 1992; Mahéo *et al.*, 2009; Mahéo *et al.*, 2002; Schärer *et al.*, 1990; Searle *et al.*, 1992). The signature was explained by Mahéo *et al.*, (2002) as resulting from break-off of the subducted Indian lithosphere causing higher heat flow from the asthenosphere and melting of metasomatised mantle of the Asian lithosphere. These melts then mixed with crustal melts. Mixing of magmas derived from a mantle and a crustal source has also been suggested by Crawford & Searle (1992) and Rex *et al.* (1988) who concluded that mantle-derived lamprophyre dykes found in the Karakoram could have influenced crustal magmas.

In the Tangtse-Shyok region of the Pangong Range within the Karakoram Shear Zone, in Ladakh, NW India (Fig. 1), migmatites are associated with leucogranite intrusions (Weinberg & Mark, 2008; Weinberg *et al.*, 2009; Weinberg & Searle, 1998). Leucosomes are linked to leucogranites that form a complex intrusive sheet network linked to stocks and plutons that extend along the shear zone towards the Karakoram Batholith to the NW (Fig. 1a). In this paper, we present new geochemical, isotopic and geochronological data which support a link between magma migration and mixing processes that took place in the exposed migmatitic crustal source. This has led to the hybrid isotopic signature of the Karakoram Batholith. In the following, we introduce the Karakoram Shear Zone and describe the migmatites and their field relationships with leucogranite intrusions, including an overview of their geochemistry. Sr-Nd isotope and U-Pb SHRIMP results are then used to test field-based interpretations and to support regional-scale inferences.

2. Regional geology

The Karakoram Shear Zone lies in the central part of the Karakoram Fault and separates the Karakoram Terrane to the NE, from the Ladakh Terrane to the SW (Fig. 1a) (e.g. Raz and Honegger, 1989; Searle *et al.*, 1998; Weinberg and Dunlap, 2000). The Karakoram Shear Zone itself is part of a crustal-scale, possibly lithospheric-scale (Lacassin *et al.*, 2004; Rolland & Pecher, 2001) strike-slip fault system that accommodates the northward push of the Indian plate into Eurasia and is characterized by dextral strike-slip motion, trending NW-SE, traceable for at least 700 km. The Karakoram Shear Zone in the Pangong Range area, in NE Ladakh is bounded by two roughly parallel mylonitic shear strands (Fig. 1a, b). The Tangtse Shear Zone (SW strand) dips 70° NE and separates the Pangong Metamorphic Complex (PMC) to the NE from the Ladakh Batholith to the SW. The Pangong Shear Zone (NE strand) is sub-vertical to steeply dipping SW, and separates the PMC from rocks of the Karakoram Terrane and the Karakoram Metamorphic Complex (KMC). The Karakoram Batholith crops out alongside the Nubra Valley to the NE of the Karakoram Shear Zone.

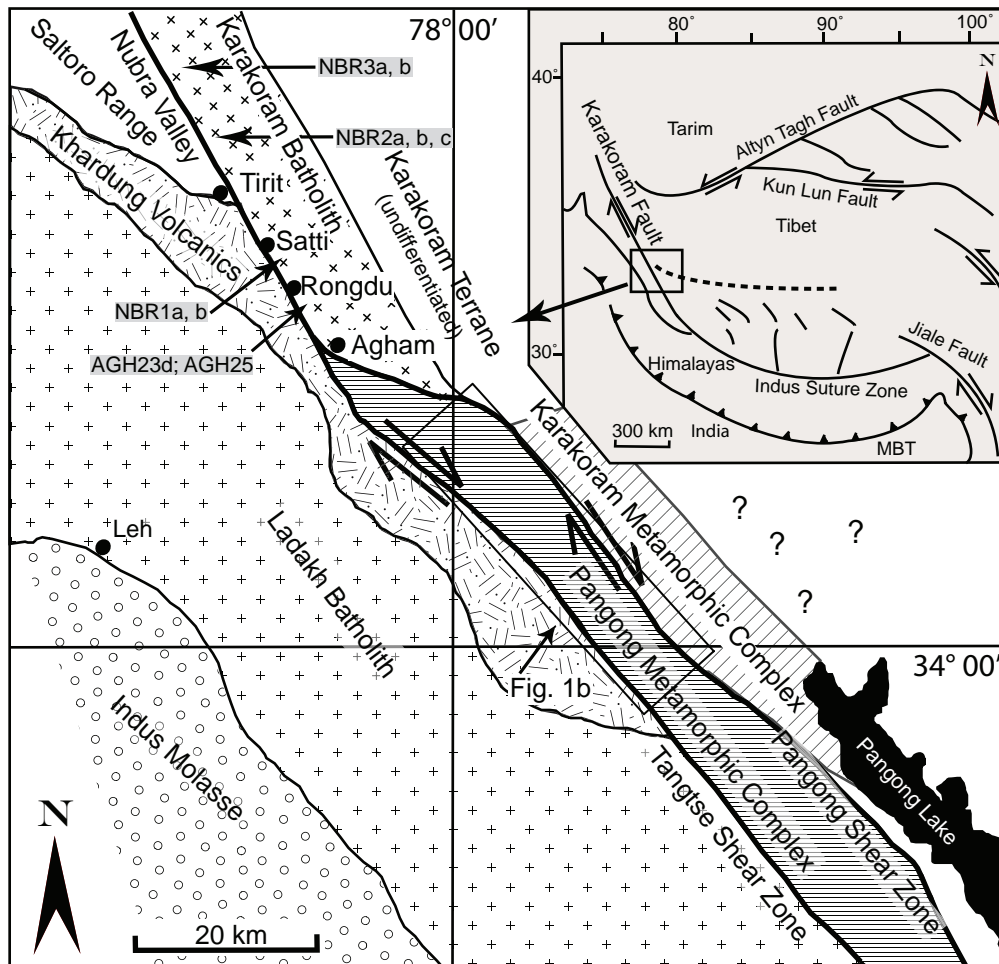


Fig. 1: (a) Geological sketch map of the Eastern Karakoram, based on Weinberg & Searle (1998). For explanations see text. Locations for samples from the Karakoram Batholith are shown.

South of the PMC, the Ladakh Batholith granitoids comprise mainly Bt-Hbl granodiorites, commonly with mafic magmatic enclaves. The overlying Kardhung Volcanics are extrusive equivalents of the granitoids. This batholith is part of the Ladakh-Kohistan arc system with crystallization ages between 49 and 103 Ma (Honegger *et al.*, 1982; Ravikant *et al.*, 2009; Upadhyay *et al.*, 2008; Weinberg & Dunlap, 2000). The PMC comprises a calc-alkaline

granitoid suite, a meta-sedimentary rock sequence and leucogranite intrusions.

The calc-alkaline suite is dominated by a large body that we refer to as the Muglib Batholith. It is comprised mainly of Hbl-Bt-granodiorite, Bt-granodiorite and diorite. It extends at least from the area close to the Pangong Lake northwestwards to the Shyok Valley and links up discontinuously to the Tirit granite at the northeastern flanks of the Saltoro Range in the Nubra Valley further NW (Weinberg *et al.*, 2000) through a number of dioritic-granodioritic bodies (Fig. 1a, b). The Muglib Batholith thus crops out for at least 85 km along strike of the Karakoram Shear Zone. The meta-sedimentary sequence comprises Bt-psammites, Bt-pelites, Bt-Hbl-gneisses ranging to amphibolites and calc-silicate rocks. Minor beds of marble crop out in the Tangtse Shear Zone (Dunlap *et al.*, 1998; Phillips *et al.*, 2004; Weinberg & Searle, 1998). The calc-alkaline granitoids and meta-sedimentary sequence are migmatized, giving rise to leucogranite intrusions (Weinberg *et al.*, 2009). Leucogranites, including pegmatitic dykes, are mostly two mica \pm garnet leucogranites and Bt-leucogranites, and have crystallization ages between 19.1 ± 1.1 Ma (Ravikant *et al.*, 2009) and 13.7 ± 0.2 Ma (Phillips *et al.*, 2004)

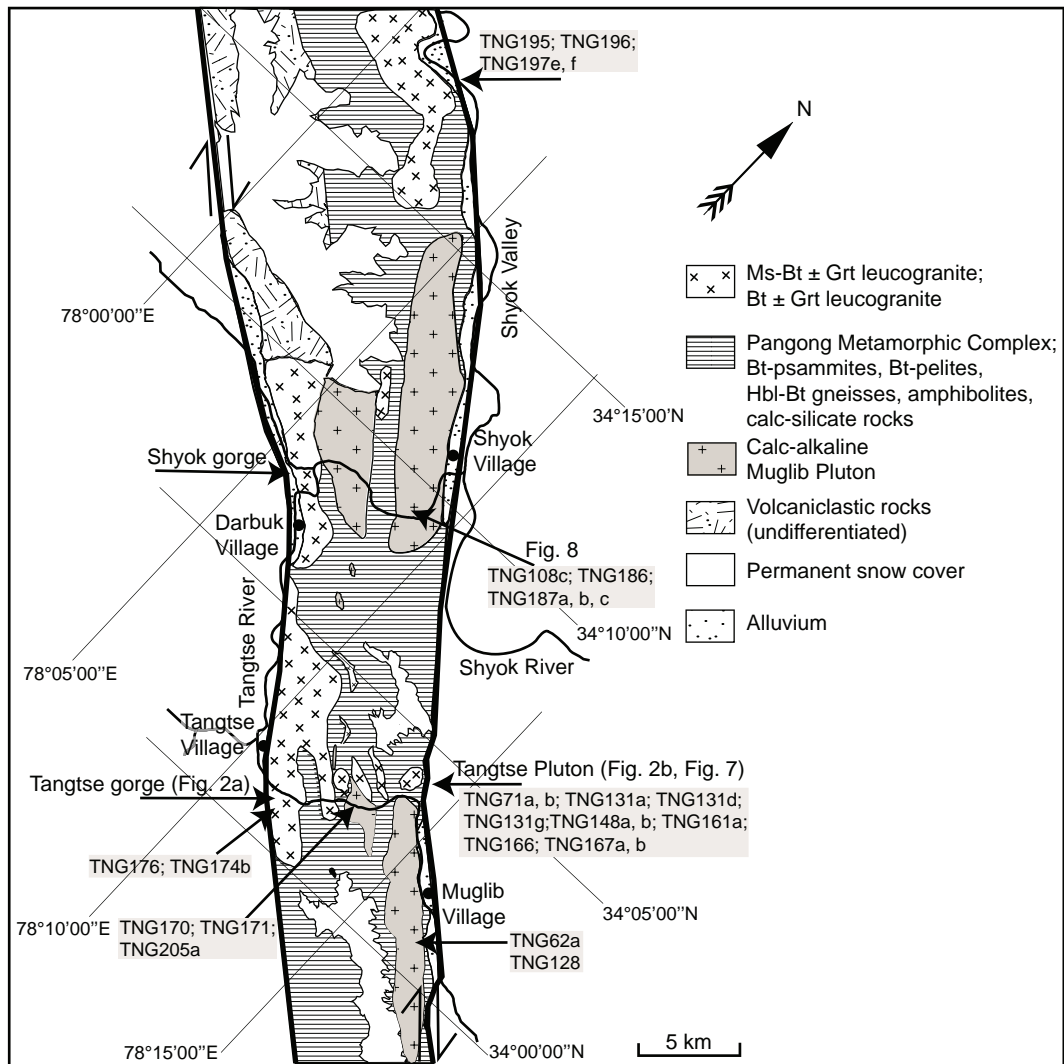


Fig. 1: (b) Geological overview map of the Karakoram Shear Zone and sample locations.

The Karakoram Metamorphic Complex (KMC), NE of the Pangong Range consists mainly of pelitic Grt-St-bearing Bt-schists, amphibolites and marbles (Dunlap *et al.*, 1998; Searle & Tirrul, 1991). The Karakoram Batholith crops out along strike of the Pangong Range and of the Karakoram Shear Zone further NW in the Nubra Valley as a 6 to 7 km wide

band (Fig. 1a; Searle *et al.*, 1998; Weinberg *et al.*, 2000).

Strain in the PMC is strongly partitioned into the main mylonitic shear strands and deformation intensity decreases away from these. Fold axes of isoclinal folds within the PMC plunge moderately (20-30°) towards NW (320-345°). A continuous schistosity is defined by aligned biotite and, when present, hornblende. It generally trends 320-330° and has a stretching lineation defined by biotite and stretched quartz grains plunging gently to moderately (generally 10-40°, rarely horizontal) towards NW in amphibolite facies rocks. Consistent dextral S-C-C' fabrics throughout the PMC indicate dextral transpressional shearing with a NE-side-up component (Searle *et al.*, 1998). A greenschist facies overprint is locally evident along the mylonitic Pangong Shear Zone where Ms, Ep and Chl (mineral abbreviations after Kretz, 1983) stretching lineations plunge moderately SE, indicating fault reactivation with a NE-side-down component. Evidence for present-day movements in the area has been reported only in one locality from the Pangong Shear Zone, whereas the Tangtse Shear Zone seems to be inactive (Brown *et al.*, 2002; Rutter *et al.*, 2007). There are wide variations in the estimation of total offset and the current slip rate along the Karakoram Shear Zone (see Valli *et al.* 2007 for discussion). Estimates of recent movements are in the range of 4 ± 1 mm/a (Brown *et al.*, 2002), 3.4 ± 5 mm/a (Jade *et al.*, 2004) or as low as 1 ± 3 mm/a (Wright, 2004).

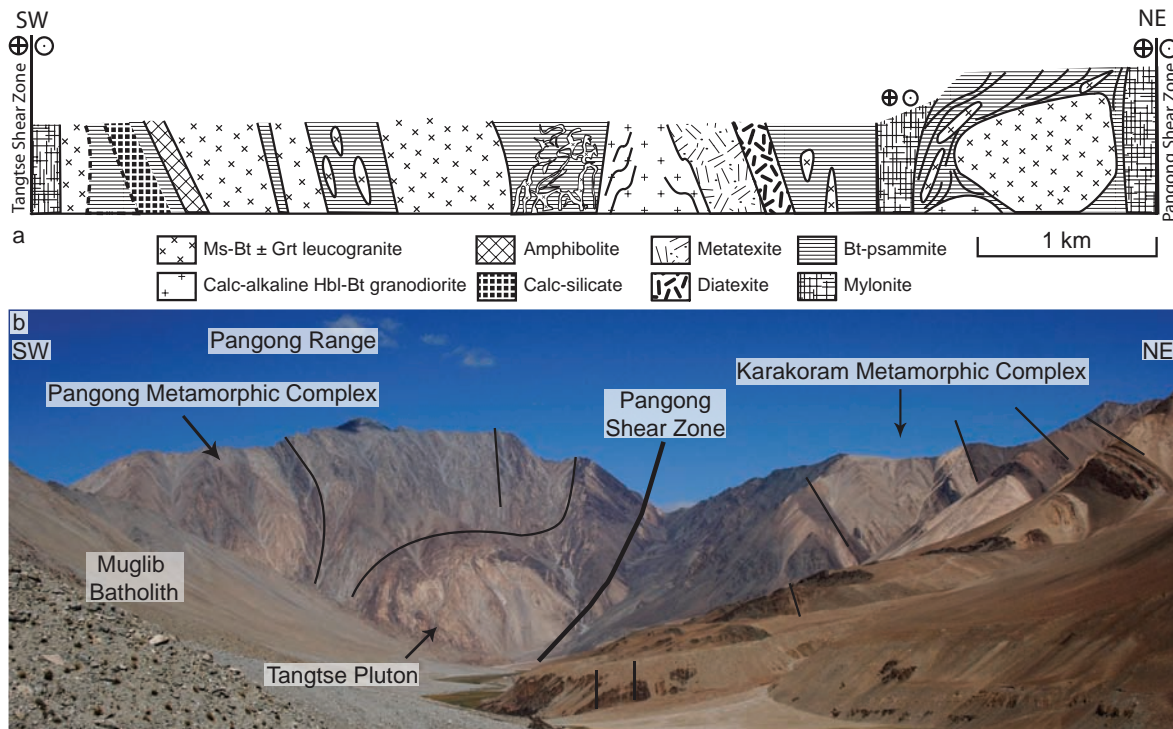


Fig. 2: (a) Schematic cross section through the Tangtse gorge roughly perpendicular to strike of the Karakoram Shear Zone. The Tangtse Shear Zone separates the Pangong Metamorphic Complex (PMC) from the Ladakh Batholith to the SW. The Pangong Shear Zone bounds the PMC from the Karakoram Metamorphic Complex to the NE. (b) Photograph of the NE end of the Tangtse gorge (looking NW). Calc-alkaline Muglib Batholith (lower left) and leucogranitic Tangtse Pluton (centre) in the Pangong Range. The Tangtse Pluton intrudes Bt-psammites of the PMC. Grt-St-Hbl-schists and marbles (bright colors) of the upper greenschist /lower amphibolite facies Karakoram Metamorphic Complex (KMC) were overthrust by the PMC during dextral transpressive movement.

3. Methodology

3.1 Geochemical analysis

For major element and trace element analysis, pulverized whole rock samples were analyzed after preparation of fused discs and pressed pellets, respectively, in a Bruker-AXS S4 Pioneer XRF Spectrometer at the Advanced Analytical Centre (AAC) of James Cook University. In Table 1 and Appendix A, only samples labeled with * were analyzed for trace elements by XRF. For all other samples, trace elements were analyzed using a Thermo Finnigan X series II, quadrupole ICP-MS. Sample solutions were produced from approximately 50 mg of sample powder using high pressure digestion methods. ICP-MS count rates were externally standardized by means of calibration curves based on the USGS standard reference material AGV-1 and RGM-1 following Eggins *et al.*, (1997) for their trace element contents. Drift corrections were applied by the combined use of In, Bi as internal standards. Reproducibility on replicate analyzes and accuracy was in the order of 5% for all elements.

3.2 Rb-Sr and Sm-Nd isotope geochemistry

Radiogenic isotope analytical work was carried out in the VIEPS facilities at the University of Melbourne, following procedures described in detail by Maas *et al.*, (2005). The isotopic data were obtained with a NU Plasma multi-collector ICP-MS coupled to a CETAC Aridus desolvating nebulizer operated at an uptake rate of 40 $\mu\text{l}/\text{min}$. Typical sensitivity in this set-up is in the range of 100-130 V/ppm Sr or Nd. Instrumental mass bias was corrected by normalizing to $^{88}\text{Sr}/^{86}\text{Sr}=8.37521$ and $^{146}\text{Nd}/^{145}\text{Nd}=2.0719425$ (equivalent to $^{146}\text{Nd}/^{144}\text{Nd} = 0.7219$, Vance and Thirlwall, 2002), using the exponential law as part of an on-line iterative spike-stripping/internal normalization procedure. Data are reported relative to the accepted values for the standards: La Jolla $^{143}\text{Nd}/^{144}\text{Nd} = 0.511860$ and SRM987 $^{86}\text{Sr}/^{87}\text{Sr} = 0.710230$. This secondary normalization yields the following results for international standards ($\pm 2\text{sd}$): BCR-1 $^{143}\text{Nd}/^{144}\text{Nd} = 0.512641 \pm 18$, BHVO-1 = 0.512998 ± 18 , JNdi-1 = 0.512113 ± 22 ; and for $^{86}\text{Sr}/^{87}\text{Sr}$ E&A Sr = 0.708005 ± 47 , BCR-1 = 0.705016 ± 46 , BHVO-1 = 0.703478 ± 36 . These results compare well with data based on TIMS from other laboratories (e.g. Maas and McCulloch, 1991; Raczek *et al.*, 2003; Tanaka *et al.*, 2000). Typical within-run precisions (2se) are ± 0.000010 ($^{143}\text{Nd}/^{144}\text{Nd}$) and $\leq \pm 0.000020$ ($^{86}\text{Sr}/^{87}\text{Sr}$), while external precision (reproducibility, 2sd) based on the results for secondary standards is ± 0.000020 (Nd) and ± 0.000040 (Sr). External precision for $^{87}\text{Rb}/^{86}\text{Sr}$ and $^{147}\text{Sm}/^{144}\text{Nd}$ obtained by isotope dilution is $\pm 0.5\%$ and $\pm 0.2\%$, respectively. Parent/daughter ratios obtained by Q-ICPMS (Monash University) for unspiked samples have uncertainties of $\pm 2\%$ to $\pm 3\%$ for $^{87}\text{Rb}/^{86}\text{Sr}$ and $\pm 3\%$ to $\pm 5\%$ for $^{147}\text{Sm}/^{144}\text{Nd}$, respectively.

The Sm–Nd and Rb–Sr analytical work of the samples from the Ladakh Batholith (marked with ** in Table 5) were performed at the Laboratory for Isotope Geology at the Swedish Museum of Natural History and followed the analytical procedure reported in Andersson *et al.* (2002). The average of measurements of the LaJolla Nd standard during the measurements of samples LEH40 and LEH52 was 0.511843 ± 13 (1s, $n=13$), and during measurements of

The decay constants used are: ^{87}Rb $1.42 \cdot 10^{-11}/\text{yr}$; ^{147}Sm $6.54 \cdot 10^{-12}/\text{yr}$.

Table 1; analysis of representative samples

Type	Leucogranite		Tangtse Pluton		<i>In situ</i> leucosome		Hbl-bearing leucosome		Leucogranite Dyke		Pegmatite Dyke		Leucogr. Shyok	
Sample	ING166	ING71a*	ING167a	ING161a	ING170	ING171	ING60d	AGH23a	ING174b	ING186	ING187a	ING187b	ING187c	ING195
Coordinates	34°04'10.5"N 78°13'39.4"E	34°03'42.6"N 78°13'37.2"E	34°03'57.7"N 78°13'37.2"E	34°02'35.6"N 78°13'16.0"E	34°02'35.6"N 78°13'16.0"E	34°02'50.1"N 78°13'02.7"E	34°03'25.3"N 78°14'13.3"E	34°25'10.6"N 77°49'23.5"E	34°01'26.7"N 78°12'12.9"E	34°08'41.8"N 78°08'17.8"E	34°08'48.6"N 78°08'26.9"E	34°08'48.6"N 78°08'26.9"E	34°18'06.8"N 78°00'46.2"E	
Major Elements wt%														
SiO ₂	70.83	73.40	74.10	73.55	72.09	75.53	62.3	58.1	72.11	71.16	75.12	74.35	75.41	70.79
TiO ₂	0.29	0.09	0.17	0.06	0.13	0.06	0.57	0.70	0.19	0.22	0.05	0.05	0.07	0.32
Al ₂ O ₃	15.55	14.90	15.33	14.89	15.96	14.72	16.3	12.5	16.24	15.41	14.14	14.01	14.21	15.40
Fe ₂ O ₃ †	1.57	0.63	0.93	0.59	0.71	0.39	2.30	4.61	1.15	1.37	0.74	1.04	0.72	1.70
MnO	0.03	0.02	0.01	0.02	0.01	0.01	0.06	0.13	0.01	0.02	0.05	0.06	0.03	0.04
MgO	0.33	bd	0.26	0.26	0.26	0.26	1.31	3.88	0.48	0.40	0.26	0.26	0.26	0.45
CaO	1.79	1.71	1.97	1.73	2.37	2.37	2.65	8.05	3.99	2.09	1.52	1.38	1.65	2.19
Na ₂ O	4.02	3.73	3.66	3.90	4.33	3.57	1.68	1.92	3.68	3.28	4.11	3.54	3.85	3.87
K ₂ O	4.50	4.76	4.15	3.76	2.98	2.94	10.1	6.53	1.69	4.56	3.30	4.36	3.73	3.77
P ₂ O ₅	0.09	0.02	0.03	0.01	0.03	0.02	0.40	2.06	0.07	0.09	bd	0.01	bd	0.10
LOI	0.46	0.77	0.39	0.33	0.47	0.34	0.46	0.59	0.41	0.44	0.21	0.22	0.49	0.47
Total	99.45	99.95	101.00	99.07	99.34	100.20	98.1	99.0	99.99	99.04	99.47	99.25	100.41	99.07
A/CNK	1.06	1.03	1.09	1.09	1.09	1.10	0.88	0.50	1.07	1.09	1.08	1.07	1.06	1.07
Mg/(Fe+Mg)	0.29	0.00	0.36	0.47	0.42	0.57	0.53	0.63	0.45	0.37	0.41	0.33	0.42	0.34
Trace Elements ppm														
Sc	1.3	bd	1.2	0.6	0.5	0.3	6.1	16.4	1.0	2.0	2.6	2.3	1.2	1.1
Ba	1963.1	849	641.2	80.4	1360.1	1320.4	8279.9	4136.1	533.3	1500.7	21.8	51.8	93.2	1404.6
Ti	973.8	593	687.9	112.5	553.2	185.8	2551.2	4068.8	830.5	966.2	182.7	151.4	206.1	990.9
V	14.0	7	6.9	bd	9.1	2.9	38.0	75.4	10.9	15.7	3.2	5.3	1.9	16.1
Cr	bd	23	bd	bd	1.7	0.3	36.6	60.9	0.9	0.7	bd	bd	bd	bd
Mn	153.4	69	97.5	52.1	41.4	39.4	348.7	928.0	67.4	125.2	382.0	387.0	170.3	188.8
Co	38.5	1	55.9	26.2	68.6	79.4	20.3	35.1	67.6	46.7	65.5	60.7	67.1	27.4
Ni	0.9	4	0.3	-0.6	3.1	1.0	28.2	39.2	1.4	1.3	0.1	0.0	0.6	1.6
Cu	7.6	14	0.4	0.2	39.7	7.8	31.6	66.0	2.6	3.4	6.0	2.4	1.8	2.1
Zn	29.5	24	27.1	18.5	8.4	6.1	38.7	86.1	28.8	26.9	12.3	13.4	9.5	29.6
Ga	23.2	16	13.2	4.0	20.0	21.8	165.3	13.9	12.3	21.5	4.7	4.3	4.6	17.8
Pb	86.6	55	55.5	62.2	15.7	14.2	85.4	30.2	24.7	34.1	50.9	49.5	40.7	69.7
Rb	321.0	156	172.8	176.4	52.1	57.4	440.9	151.4	80.4	140.6	145.8	162.1	131.2	140.6
Sr	741.1	398	433.1	162.1	1090.0	816.2	1083.2	903.4	542.5	438.8	66.3	78.4	121.2	546.2
Y	5.3	2	2.3	2.1	1.0	1.4	20.9	29.9	3.2	3.9	15.7	16.7	6.3	5.2
Zr	54.9	39	18.4	14.3	6.5	6.6	39.7	30.4	8.4	23.0	27.7	63.9	10.2	27.8
Nb	7.8	4	2.8	7.2	1.3	0.5	9.7	21.2	2.4	4.2	2.6	2.9	1.9	6.3
Th	58.6	bd	4.1	0.6	0.8	2.2	93.3	21.3	27.3	27.0	4.0	7.3	1.2	40.4
U	8.4	bd	1.0	0.6	0.1	0.2	6.5	3.7	0.8	1.0	2.0	1.9	0.5	4.0
Rb/Sr	0.43	0.39	0.40	1.09	0.05	0.07	0.41	0.17	0.15	0.32	2.20	2.07	1.08	0.26

Table 1 (continued): analysis of representative samples

Type	Leucor. Shyok Valley			Karakoram Batholith				Muglib Batholith				Pangong Metamorphic Complex			
Sample	Leucor. Shyok Valley			Karakoram Batholith				Muglib Batholith				Pangong Metamorphic Complex			
	TNG196	TNG197e	AGH25a	NBR1b	NBR2a	NBR3b	TNG131a*	TNG207	TNG169a	TNG205a	AGH5	TNG131d*	TNG167b	TNG108c*	TNG208
Coordinates	34°18'07.2"N 78°00'46.6"E	34°17'39.6"N 78°02'02.9"E	34°27'04.4"N 77°45'53.1"E	34°29'06.0"N 77°44'20.0"E	34°37'54.6"N 77°38'24.1"E	34°46'27.5"N 77°32'45.7"E	34°03'38.8"N 78°13'52.1"E	34°03'01.4"N 78°13'41.3"E	34°02'40.3"N 78°13'07.8"E	34°02'38.3"N 78°13'25.4"E	34°18'47.7"N 77°52'03.8"E	34°03'38.8"N 78°13'52.1"E	34°03'40.4"N 78°13'52.7"E	34°08'42.0"N 78°08'18.5"E	34°01'33.5"N 78°12'01.7"E
Major Elements wt%															
SiO ₂	73.31	71.91	72.3	73.40	72.92	73.83	67.50	68.23	61.95	54.91	52.4	61.60	60.99	52.82	52.49
TiO ₂	0.17	0.22	0.27	0.22	0.24	0.20	0.56	0.50	0.70	1.37	1.10	0.83	0.82	1.01	0.64
Al ₂ O ₃	14.92	15.61	14.9	14.89	14.92	14.07	16.30	15.26	14.29	17.56	19.8	17.00	16.97	15.55	14.69
Fe ₂ O ₃ t	0.98	1.17	1.88	1.42	1.51	1.39	3.49	3.05	5.18	8.04	7.91	6.56	6.85	8.94	5.77
MnO	0.02	0.02	0.03	0.02	0.04	0.03	0.09	0.07	0.15	0.13	0.15	0.11	0.10	0.15	0.11
MgO	0.26	0.27	0.43	0.29	0.28	0.26	1.57	1.22	4.55	3.01	2.93	2.84	3.27	7.18	3.74
CaO	1.65	2.17	2.61	1.60	1.77	1.68	3.16	2.85	6.46	5.90	7.89	5.23	3.77	10.03	15.00
Na ₂ O	3.91	4.15	4.03	3.79	3.80	3.18	4.37	3.17	3.01	3.81	3.22	1.82	2.00	3.47	0.98
K ₂ O	4.27	3.66	2.26	3.64	3.65	4.11	2.85	4.57	2.47	2.97	1.04	3.02	3.25	0.73	3.41
P ₂ O ₅	0.04	0.05	0.07	0.06	0.09	0.07	0.22	0.19	0.14	0.50	0.27	0.16	0.15	0.09	0.15
LOI	0.37	0.35	0.80	0.64	0.86	0.80	0.50	0.57	0.93	0.82	2.92	1.06	1.59	0.36	2.03
Total	99.88	99.58	99.6	99.95	100.07	99.60	100.62	99.65	99.83	99.00	99.6	100.17	99.74	100.30	98.99
A/CNK	1.06	1.06	1.08	1.14	1.11	1.10	1.02	0.99	0.74	0.87	0.95	1.08	1.24	0.63	0.45
Mg/(Fe+Mg)	0.34	0.31	0.31	0.29	0.27	0.27	0.47	0.44	0.64	0.43	0.42	0.46	0.49	0.61	0.56
Trace Elements ppm															
Sc	1.1	1.7	2.1	1.8	8.0	1.9	9	5.4	19.9	12.7	17.5	22	11.5	37	16.2
Ba	893.4	997.1	860.2	679.2	1000.5	789.8	337	379.7	586.5	540.1	154.0	448	255.1	19	396.5
Ti	665.7	903.2	688.3	742.8	3946.8	723.3	4103	2121.4	3833.4	7373.2	5423.7	7362	3270.7	5844	3419.7
V	11.7	14.6	4.5	10.9	76.2	6.5	87	49.7	103.7	123.5	193.0	186	95.1	235	119.0
Cr	bd	0.1	55.2	bd	9.9	bd	63	21.1	74.8	12.7	20.9	178	124.8	220	102.9
Mn	114.3	130.0	144.3	132.7	476.3	160.4	790	415.1	1053.4	859.2	910.1	909	497.3	1183	737.8
Co	44.0	37.5	69.3	0.9	8.1	0.9	7	36.2	45.1	27.6	18.5	20	43.4	47	22.7
Ni	1.0	1.3	1.0	bd	12.3	bd	32	13.4	53.5	16.7	7.2	62	76.5	57	48.9
Cu	6.0	9.1	2.7	0.9	36.1	bd	17	6.3	21.5	47.7	23.2	24	20.1	84	12.8
Zn	21.1	26.6	17.8	20.0	48.2	26.5	81	38.4	62.6	86.7	73.3	112	72.1	61	73.2
Ga	16.8	17.0	14.4	11.9	17.5	13.4	20	8.9	12.6	14.4	17.6	20	6.5	15	9.4
Pb	89.0	60.1	52.3	35.7	37.4	40.5	43	20.5	12.4	12.2	5.0	29	20.7	8	25.5
Rb	219.4	164.1	161.5	201.1	208.7	201.3	199	161.1	49.4	124.1	26.5	168	253.5	10	153.9
Sr	563.5	597.5	146.8	363.2	501.3	336.8	379	413.3	547.6	568.6	497.3	159	96.6	132	339.7
Y	2.2	3.5	8.6	6.2	13.8	10.1	19.00	17.6	18.8	24.3	20.2	28	20.7	25	22.4
Zr	29.5	48.6	31.5	30.8	95.2	41.6	164	18.8	11.5	58.6	7.9	185	6.7	86	11.2
Nb	3.2	4.7	8.5	6.4	12.5	8.5	27	15.0	18.2	25.5	5.7	25	12.8	9	11.1
Th	31.6	27.5	15.8	15.6	20.0	20.2	15	15.2	1.1	11.2	1.8	12	12.9	2	10.6
U	6.9	2.5	4.2	1.4	4.9	3.5	bd	2.2	2.1	1.1	0.3	bd	2.1	bd	1.8
Rb/Sr	0.39	0.27	1.1	0.55	0.42	0.60	0.53	0.39	0.09	0.22	0.05	1.06	2.62	0.08	0.45

the other samples 0.511844 ± 5 (1s, n=10). No correction was applied. Similarly, an average of the measurements of the SRM987 Sr standard during measurements of the samples was 0.710245 ± 32 (1s, n=16). No correction was applied.

Age corrections (18-100 Ma) for the samples analyzed here are generally small, amounting to <1 unit for ϵ_{Nd} and ~ 0.00100 (mostly much less) for $^{87}\text{Sr}/^{86}\text{Sr}$. The propagated error for initial ϵ_{Nd} is $\sim \pm 0.5$ unit and 0.00007 or less for initial $^{87}\text{Sr}/^{86}\text{Sr}$. Propagated errors for samples analyzed unspiked (i.e. with Rb/Sr and Sm/Nd by Q-ICPMS) are similar.

3.3 U-Pb SHRIMP analysis

Zircon and titanite grains were separated from whole rock samples using standard crushing, washing, heavy liquid (density 2.96 and 3.3), and paramagnetic procedures. The zircon and titanite concentrates were hand picked and placed onto double-sided tape, mounted in epoxy together with chips of the reference zircons (Temora, and SL13) and titanite (BLR-1), sectioned approximately in half, and polished. Sample TNG148b was analyzed in situ in a polished thin section. Reflected and transmitted light photomicrographs were obtained for all zircons. Cathodoluminescence (CL) and Scanning Electron Microscope (SEM) images were prepared for all zircon grains; back scattered SEM (BSE) images were prepared for the titanite grains. These CL and BSE images were used to decipher the internal structures of the sectioned grains and to ensure that the $\sim 20\mu\text{m}$ SHRIMP spot was wholly within a single age component within the sectioned grains.

The U-Th-Pb analyses were made using the SHRIMP II at the Research School of Earth Sciences, The Australian National University, Canberra, Australia, following procedures given in Williams (1998, and references therein). Each analysis consisted of 6 scans through the mass range, with a U-Pb reference grain analyzed for every three unknown analyses. The data have been reduced using the SQUID Excel Macro of Ludwig (2001).

For the zircon analyses, the U/Pb ratios have been normalized relative to a value of 0.0668 for the Temora reference zircon, equivalent to an age of 417 Ma (see Black *et al.*, 2003). Uncertainties in the U-Pb calibration were 0.40% for TNG62a and TNG131a analytical sessions, and 1.18% for in situ analysis of TNG148b. The U-Pb ratios for titanite were normalized relative to the BLR-1 standard (1051 Ma, Aleinikoff *et al.*, 2007). Uncertainties in the U-Pb calibrations were 0.43% for titanite SHRIMP sessions TNG131a and TNG148a.

Uncertainties given for individual analyses (ratios and ages) are at the one sigma level (Tables 2 to 4). Tera and Wasserburg (1972) concordia plots, probability density plots with stacked histograms and weighted mean $^{206}\text{Pb}/^{238}\text{U}$ age calculations were carried out using ISOPLOT/EX (Ludwig, 2003).

4. Field relations and anatexis in the Tangtse and Darbuk-Shyok areas

The Tangtse and Darbuk-Shyok gorges are cut by the Tangtse River roughly perpendicular to strike of the Karakoram Shear Zone, 20 km apart. Here, a mid-crustal section including the main lithologies of the PMC is exposed between the Tangtse Shear Zone and the Pangong Shear Zone (Fig. 2a). These migmatized rocks will be described here following the terminology suggested by Sawyer (2008).

4.1 Meta-sedimentary sequence

This sequence comprises Bt-psammmites, Bt-pelites, Bt-Hbl-gneisses ranging to amphibolites, and calc-silicate rocks. These rock types are interlayered at the scale of tens of meters to hundreds of meters. Bt-psammmites and Bt-pelites are generally characterized by the mineral assemblage $Bt + Pl + Qtz \pm Grt$, and muscovite occurs in retrograde shear zones. Common accessory phases are $Ap + Ttn + Mag + Mnz + Aln + Zrn$. We found sillimanite in only one sample of PMC meta-sedimentary rocks, but its occurrence has also been reported by Rolland & Pêcher (2001). Calc-silicate rocks generally contain $Cpx + Hbl + Pl + Qtz \pm Bt \pm Cc$.

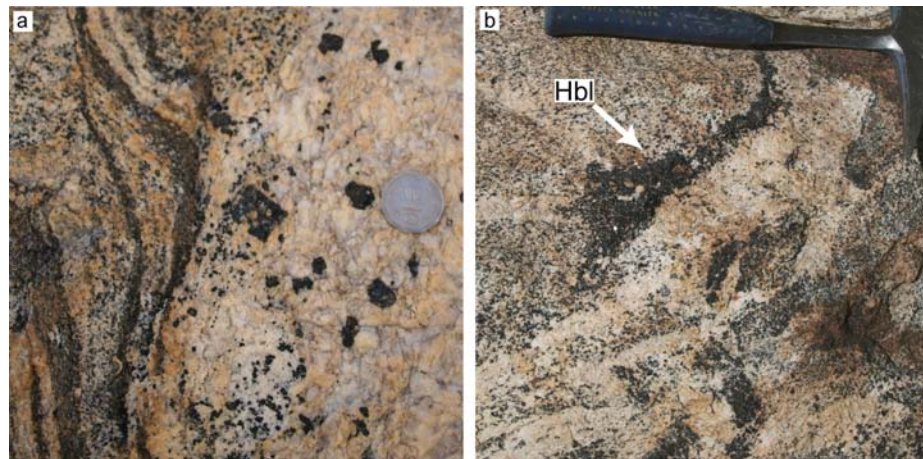


Fig. 3: (a) Up to ~1 cm poikilitic hornblende crystals in leucosome in metatexite. (b) Accumulation of hornblende crystals in leucosome network in calc-alkaline Hbl-Bt granodiorite of the Muglib Batholith.

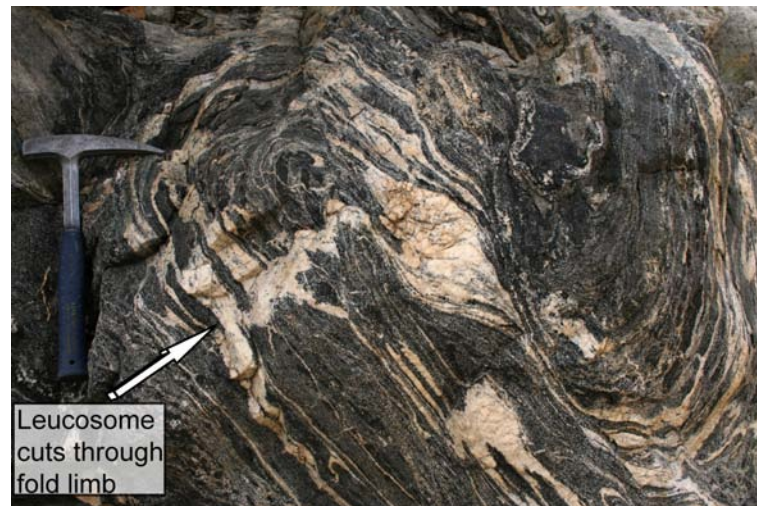


Fig. 4: Leucosomes in folded amphibolite. Melt must have been present at the time of deformation, because the folded layer-parallel leucosome cuts across the fold limb but stays in continuity with layer parallel leucosomes on the opposite limb.

Whilst calc-silicate rocks and mafic amphibolites ($SiO_2 < 50$ wt %) do not present evidence for anatexis, Bt-psammmites and Bt-bearing amphibolites have leucosomes that are interpreted to be the remainders of crystallized melt that segregated from the melanosome. Diffuse leucosome patches are common, and layer-parallel leucosomes in stromatic migmatites have melanosome rims that consist mostly of biotite. Leucosomes in migmatitic Bt-psammmites range in composition from leucotonalite to leucogranite and commonly contain garnet. Leucosomes in the Hbl-rich gneissic to amphibolitic rocks of this sequence commonly

contain large poikilitic hornblende crystals (Fig. 3a).

In the central part of the Tangtse gorge there are metatexites and diatexites (indicated in cross section, Fig. 2a) that have melanosomes ranging compositionally from Hbl-Bt-schists to amphibolitic gneisses. Leucosomes in these rocks are Bt-leucogranites, Hbl-Bt-leucogranites and leucotonalites. Interplay between folding, shearing and magma migration in these meta- and diatexites has been described by Weinberg & Mark (2008). Typically, layer-parallel leucosomes in metatexites are linked with leucosomes parallel to the axial plane in folds. Folded leucosomes also cut through fold limbs and connect to leucosomes of different layers (Fig. 4). Fold hinges are truncated by axial planar shearing which further facilitates leucosome interconnection. Disruption of melanosomes, especially in the diatexites leads to a large range of compositions and a heterogeneous rock where distinction between leucosome and melanosome is blurred. In either meta- or diatexite the exact nature of the protolith is obscured by compositional changes related to melt extraction.

4.2 Calc-alkaline granitoids

The main facies of the Muglib Batholith is a medium to coarse-grained titanite bearing Hbl-Bt-granodiorite, commonly with Ap + Aln + Zrn as accessory minerals and decimetric mafic magmatic enclaves. A continuous foliation is defined by aligned Hbl, Bt and Ttn grains. Within the main facies, there are up to 100m long lenses of Hbl-Cpx diorite. A Bt-granodiorite occurs at the margins of the batholith and forms a border facies which crops out close to the Pangong Shear Zone near Muglib Village (Fig. 1b), and also intrudes the meta-sedimentary country rocks as dykes.

Migmatization of the Muglib Batholith is evident in the Bt-granodiorite border facies, in patches of the main facies as well as in the Hbl-Cpx diorite lenses. Leucosomes parallel to the dominant foliation parallel to the Karakoram Shear Zone are continuous with crosscutting leucosomes, thus forming a network interpreted to represent a melt flow network during anatexis (Weinberg & Searle, 1998). Melanosome rims are generally present and consist of mostly biotite and hornblende around leucosomes. Up to 3 cm large euhedral poikilitic hornblende crystals in leucosomes are common especially in diorites but rare in the Hbl-free border facies. In these migmatitic diorites, leucosomes that dominantly consist of Hbl megacrysts and Kfs (Fig. 3b) are interpreted as a residual assemblage after the melt was extracted.

4.3 Leucogranites

Leucogranites are ubiquitous in the Karakoram Shear Zone either as dykes, stocks on the scale of tens to hundreds of meters or kilometer-sized plutons (Fig. 1b, 2) such as the Darbuk Pluton, a sheared Ms-Bt \pm Grt-leucogranite (Fig. 1b) or the Tangtse Pluton which is related to the Pangong Injection Complex that is depicted in Fig. 2b (Weinberg & Searle, 1998; Weinberg *et al.*, 2009). The Tangtse Pluton is approximately 1.3 km in length, has an outcrop height of ~600 m (Fig. 2b), and is a result of the amalgamation of multiple magma sheets that intruded Bt-psammities and which are still preserved as screens inside the pluton. Leucogranite sheets in the Pangong Injection Complex are most likely derived from

a combination of local and intrusive magma sheets (Weinberg & Searle 1998, Weinberg *et al.*, 2009). The pluton is petrographically heterogeneous consisting mainly of medium-grained Bt-leucogranite, Ms-Bt \pm Grt-leucogranite and coarse-grained Grt-Ms-leucogranite. Accessory minerals are commonly Ap, Zrn, Mnz, Aln and Grt. Only rarely, small and strongly corroded hornblende crystals are found.

The leucogranites are generally deformed and show S-C fabrics, and in some biotite-rich examples, Bt-foliae that wrap around feldspar crystals or form asymmetric tails thereby defining dextral S-C-C' fabrics. In some cases, deformation fabrics are not apparent in hand specimen, because micas are lacking, but are visible under the microscope. Microstructures, however, reveal dextral S-C fabrics.

4.4 Syndeformational melting

Leucosomes in shear bands suggest that these are either the loci of incipient partial melting or that melt migrated into and accumulated in these zones (Fig. 5). Like this structure, a number of field relationships between melt, faults, shear zones and folds have been interpreted to result from synkinematic melting (Weinberg & Mark, 2008). A common feature found in many of the least deformed leucogranite sheets is shown in Fig. 6 where a broad dextral S-C fabric is defined by the alignment of feldspar lozenges. The interstitial finer-grained Qtz and Pl are only weakly deformed and are interpreted as having crystallized directly from a melt, indicating synkinematic magma crystallization. We therefore take the view here that anatexis was contemporaneous with deformation. This was also the interpretation by Rolland *et al.* (2009) based on microstructural relationships, and contradicts the pre-kinematic view presented by Phillips *et al.* (2004).



Fig. 5: Shear band in stromatic migmatite developed in calc-alkaline diorite. A leucosome forms within the shear band that runs from the upper left to the lower right. Layer-parallel leucosomes have diffuse boundaries with the leucosome in the shear band in the central part. The dark layer (melanosome) in the upper part of the photograph (tip of hammer) is continuous across the shear zone. The thick coarse grained layer parallel-leucosome in the lower part of the photograph is nearly truncated by the shear zone, indicating that it formed earlier. However, the thinned out right part of the leucosomes almost connects to the counterpart on the left hand side.

Deformation outlasted magmatism, continuing as the rock mass cooled to temperatures below 250°C, as documented in microstructures in the Muglib area (Rutter *et al.*, 2007) and Shiquanhe area further SE in the Karakoram Shear Zone (Valli *et al.*, 2007). This low temperature deformation is reflected by porphyroclasts of K-feldspar and plagioclase in leucogranites with rims of fine-grained, sheared and recrystallized Kfs + Pl + Qtz (Fig. 6).

4.5 Water-fluxed melting

The presence of large, poikilitic hornblende crystals in leucosomes in calc-alkaline granodiorites and diorites (Fig. 3, 6) and the lack of other obvious peritectic minerals, suggests melting in the presence of a H_2O -rich fluid phase (Kenah & Hollister, 1983; Lappin & Hollister, 1980; Mogk, 1992). This interpretation is also supported by the lack of peritectic minerals in leucosomes in Bt-psammmites (Weinberg & Mark, 2008). Mogk (1992) stressed the importance of water infiltration in order to form Hbl-bearing leucosomes in migmatites and proposed that shear zones form pathways for H_2O -rich fluids. Accordingly, in the melting

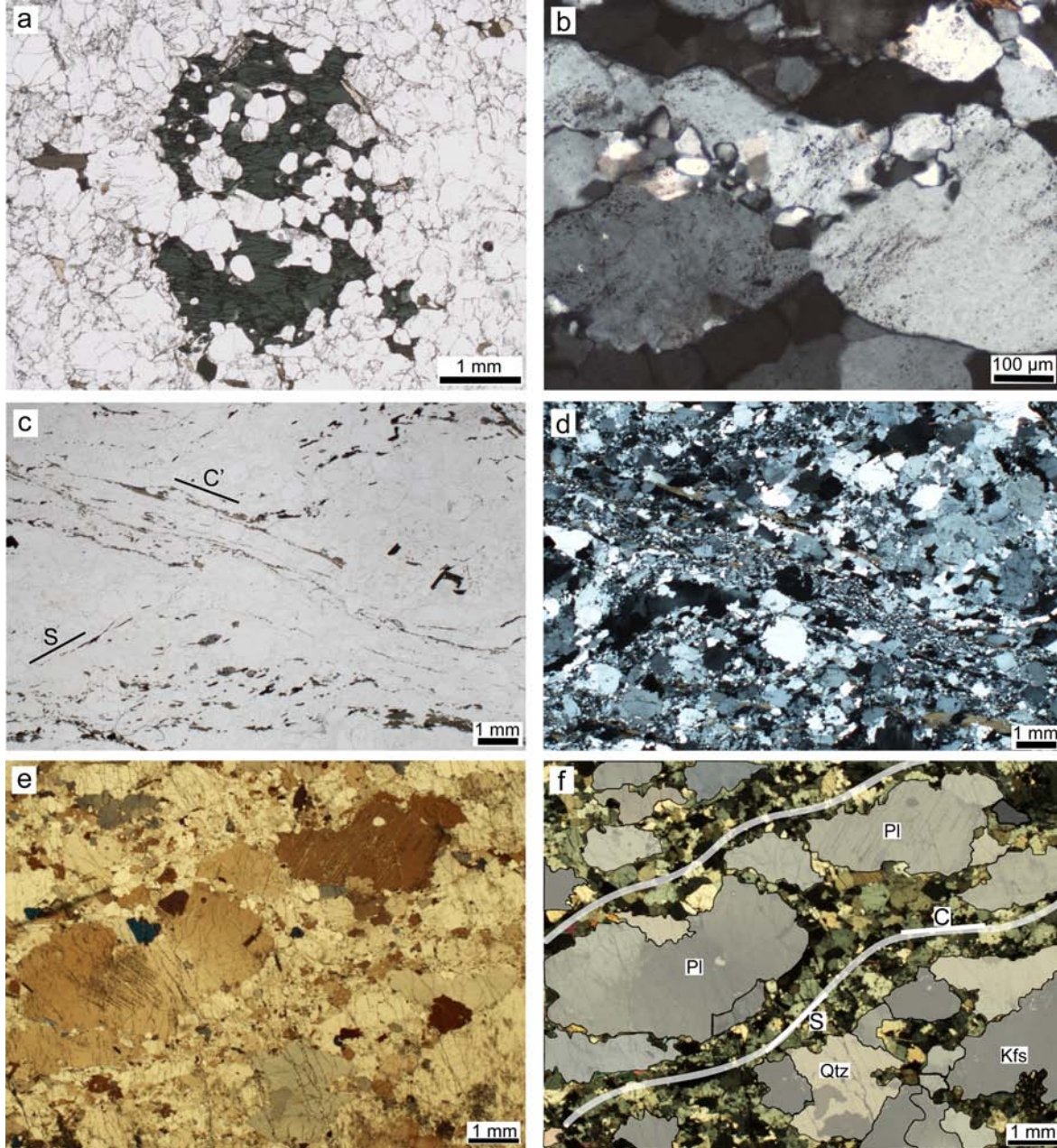
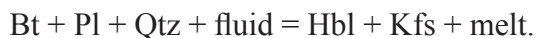


Fig. 6: Photomicrographs. (a) Hornblende crystal in tonalitic leucosome of a diatexite in the Tangtse gorge. The poikilitic texture suggests that the hornblende is peritectic. Plane-polarized light. (b) Recrystallization of deformed K-feldspar grains in a shear band in $Bt \pm Grt$ leucogranite. Cross-polarized light. (c) and (d) C'-type shear band in $Bt \pm Grt$ leucogranite indicating dextral shear sense. Plane-polarized light and cross-polarized light, respectively. (e) Plagioclase and K-feldspar phenocrysts and fine-grained Qtz, Pl and Kfs in Grt-Ms-Bt leucogranite. Polarizer is only half turned in. (f) Same as in (e) but with crossed polarizer and line drawing to illustrate that the fine grains define a dextral C-S fabric. This fabric is interpreted to have been developed before complete crystallization of the magma.

experiments of Gardien *et al.* (2000) hornblende was found as a crystallizing phase only when water was added. We suggest that the melting reactions proposed by McLellan (1988) and Lappin & Hollister (1980) account for hornblende bearing leucosomes at calculated temperatures between 675 and 750° C and 6 to 8 kbar,



or



Based on mineral paragenesis and thermobarometry, Rolland & Pêcher (2001) proposed that peak metamorphic temperatures in the Tangtse area reached 700 ± 20 °C at 7 ± 1 kbar, i.e. just below the onset of muscovite dehydration melting and well below biotite dehydration melting. Rolland *et al.* (2009) concluded that a small thermal increase initiated muscovite dehydration melting in the Tangtse area. However, this is unnecessary when considering external water influx. In this case, melting is expected to begin at the water saturated solidus for pelites and quartzofeldspathic rocks, which is essentially similar to that of the haplogranitic system $\text{Qtz} + \text{Ab} + \text{Or} + \text{H}_2\text{O}$ with temperatures as low as 650°C (Clemens & Vielzeuf, 1987; Holtz *et al.*, 1992). Water influx can create significant amounts of melt, depending on the size of the infiltrated (shear-) zone (Genier *et al.* 2008, Mogk, 1992). Possible sources for infiltrating water are hydrated, low-grade metamorphosed sedimentary rocks of the Karakoram Metamorphic Complex, overthrust by the Pangong Metamorphic Complex (Weinberg & Mark, 2008).

In summary, field relations suggest widespread partial melting of two major rock sequences, meta-sedimentary and calc-alkaline rocks, in the presence of a water rich fluid contemporaneous with deformation. In the process, a large network of magmatic bodies developed, linking nearly in situ leucosomes with a large network of magma sheets and bodies.

5. Evidence for magma hybridization in migmatites

In the PMC, different rock types that underwent anatexis are interlayered on the scale of meters to hundreds of meters (Figs. 2, 3). This provides an opportunity for magmas from different sources to interact early in their migration history as they travel through an expanding channel network. In the following, we describe two field examples where this might have happened.

5.1 Base of Tangtse Pluton

At the exposed base of the Tangtse Pluton, an irregular sheet of calc-alkaline Bt-granodiorite of the Muglib Batholith border facies intrudes Bt-psammities (Fig. 7). Both rock types have undergone partial melting. This is evidenced in the Bt-psammities by chaotically folded leucosomes and leucosome patches comprised of $\text{Ms-Bt} \pm \text{Grt-leucogranite}$ with melanosome rims consisting mostly of biotite and small amounts of $\text{Pl} + \text{Qtz} + \text{Grt}$ (Fig. 7f).

In the Bt-granodiorite sheet anatexis is evidenced by leucosome patches with diffuse boundaries with the melanosome that form an irregular network of $\text{Bt} \pm \text{Grt-leucogranite}$

pockets and veins, feeding into a larger leucosome with width varying up to one meter (Fig. 7b). Although sometimes difficult to distinguish, the neosome is coarser-grained and more felsic than the paleosome. Melanosome rims bordering the leucosome are absent. Isolated rafts of Bt-granodiorite with diffuse boundaries are found in the large leucosome (Fig. 7d).

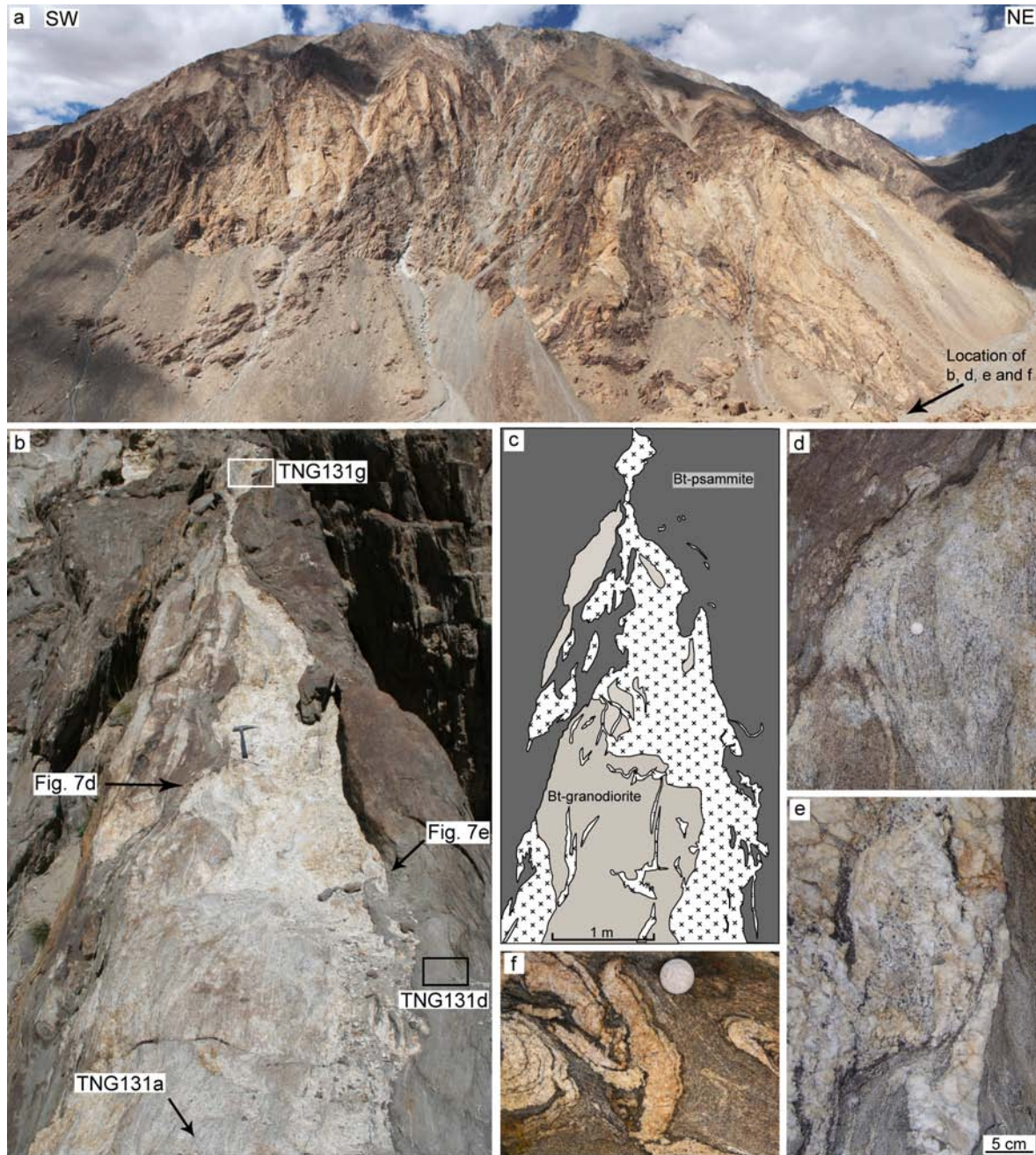


Fig. 7: Outcrops at the base of the Tangtse Pluton indicative of magma hybridization in the source. (a) Pangong Injection Complex and Tangtse Pluton looking NW. Dark rocks are Bt-psammites of the PMC, and light rocks are leucogranites. (b) Migmatite outcrop at the foot of the Tangtse Pluton. Leucosomes in a calc-alkaline Bt-granodiorite (lower centre; sample TNG131a; Zircon age = 70.5 ± 0.6 Ma) show diffuse boundaries with the leucosome (sample TNG131g, Table 2) in the centre of the photo which is connected to the leucogranite sheets that form the Tangtse Pluton. The surrounding Bt-psammite (sample TNG131d, Table 2) is also migmatitic. (c) Line drawing of (b). (d) Detail of (b); In situ leucosomes in Bt-granodiorite merge with the large pegmatitic leucosome. The Bt-granodiorite also forms rafts (towards right side of photograph). (e) Detail of (b); entrained wispy schlieren of Bt-psammite containing garnet. (f) Detail of folded leucosomes in Bt-psammite. Thin melanosome rims around leucosomes consist mostly of biotite.

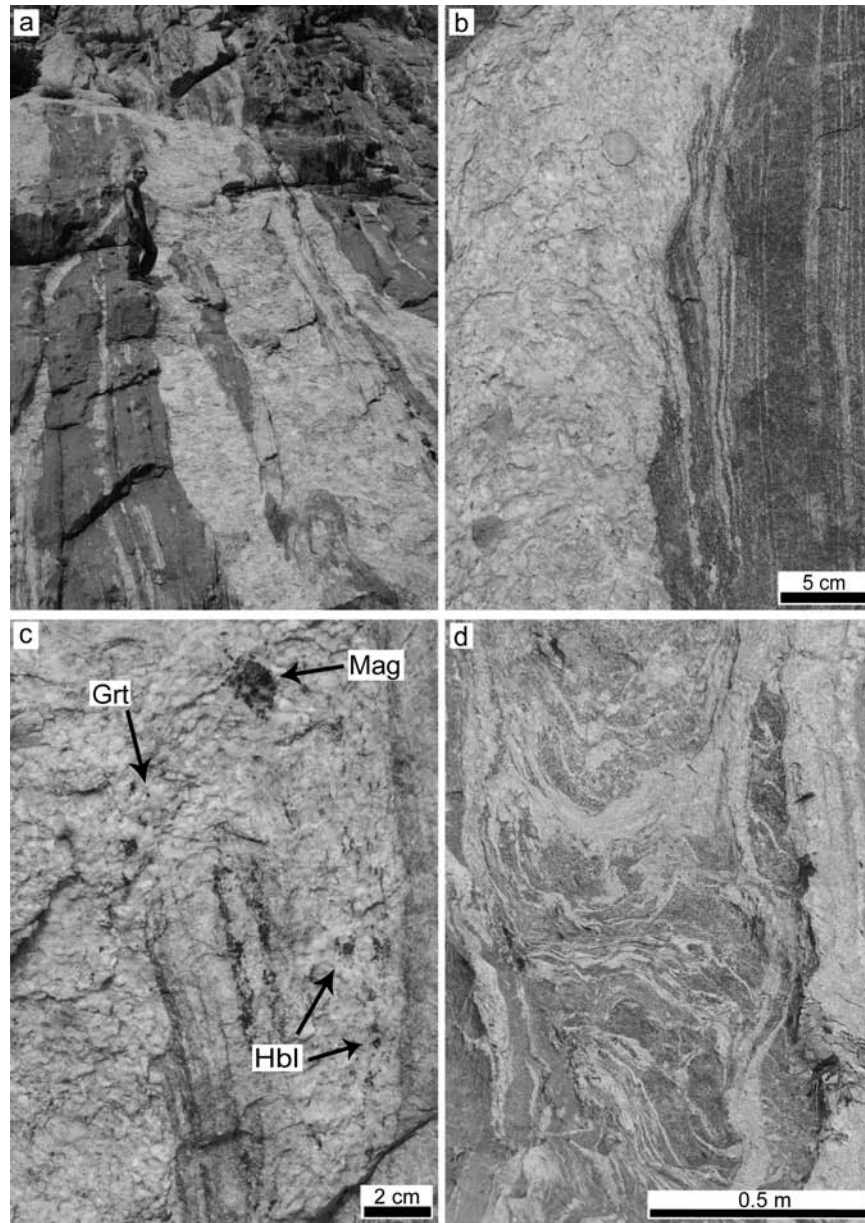


Fig. 8: (a) Pegmatitic leucogranite dykes intrude Hbl-Bt gneiss in the Darbuk-Shyok gorge (samples TNG187a and TNG187b in Table 5). (b) Continuity between layer-parallel in situ Hbl-bearing leucosomes and crosscutting large garnet-bearing leucogranite dyke. In situ leucosomes generally have thin melanosome rims and are sometimes connected to leucosomes patches that have diffuse boundaries to the melanosome. (c) Seamless merging between dyke and in situ Hbl-bearing leucosome. Garnet crystals and cluster of magnetite in pegmatitic Grt-Bt-leucogranite dyke. The dyke continues to the upper left side of the photograph. (d) Diatexite migmatite. The pegmatitic leucogranite dyke that borders the diatexite migmatite is continuous with leucosomes in migmatite.

Garnet is heterogeneously distributed in the leucosome and absent in the melanosome except for high concentrations on wispy schlieren of biotite dragged from the Bt-psammite at the contact with the partially molten Bt-granodiorite sheet. The presence of garnet and biotite-garnet schlieren from the Bt-psammite in the leucosome suggests it is a hybrid formed by merging of magma from the Bt-granodiorite with magma from the Bt-psammite. If this is so, then the pre-existing granodiorite gave rise to a magma channelway that was used by leucosomes from both rock types. In order to test this hypothesis, we sampled the different rock types in this and adjoining outcrops to study their isotopic composition.

5.2 Leucogranite dykes in the Darbuk-Shyok gorge

In the Darbuk-Shyok gorge (Fig. 1b), mainly pegmatitic $Bt \pm Ms \pm Grt$ leucogranite dykes cut across interlayered amphibolites and calc-silicate rocks, calc-alkaline diorites of the Muglib Batholith, but also merge continuously with in situ leucosomes in dioritic protoliths (Fig. 8). Diorite gneisses show leucosome patches with euhedral hornblende poikiloblasts and diffuse margins to the melanosome, interpreted to represent in situ leucosomes. These leucosomes are generally parallel to tectonic foliation and compositional layering and have melanosome rims consisting of mostly $Hbl + Bt$, forming a stromatic migmatite. These Hbl -bearing leucosomes are connected with the crosscutting $Bt \pm Ms \pm Grt$ -leucogranite dykes and, in the field and in thin section, the contact is seamless (Fig. 8b). In parts of this outcrop, large amounts of magma disrupt pre-existing layering in the calc-alkaline protolith and form a diatexite migmatite (Fig. 8c). Continuity between in situ leucosome in the dioritic protolith and intrusive dykes suggest contemporaneity of dyke intrusion and local anatexis.

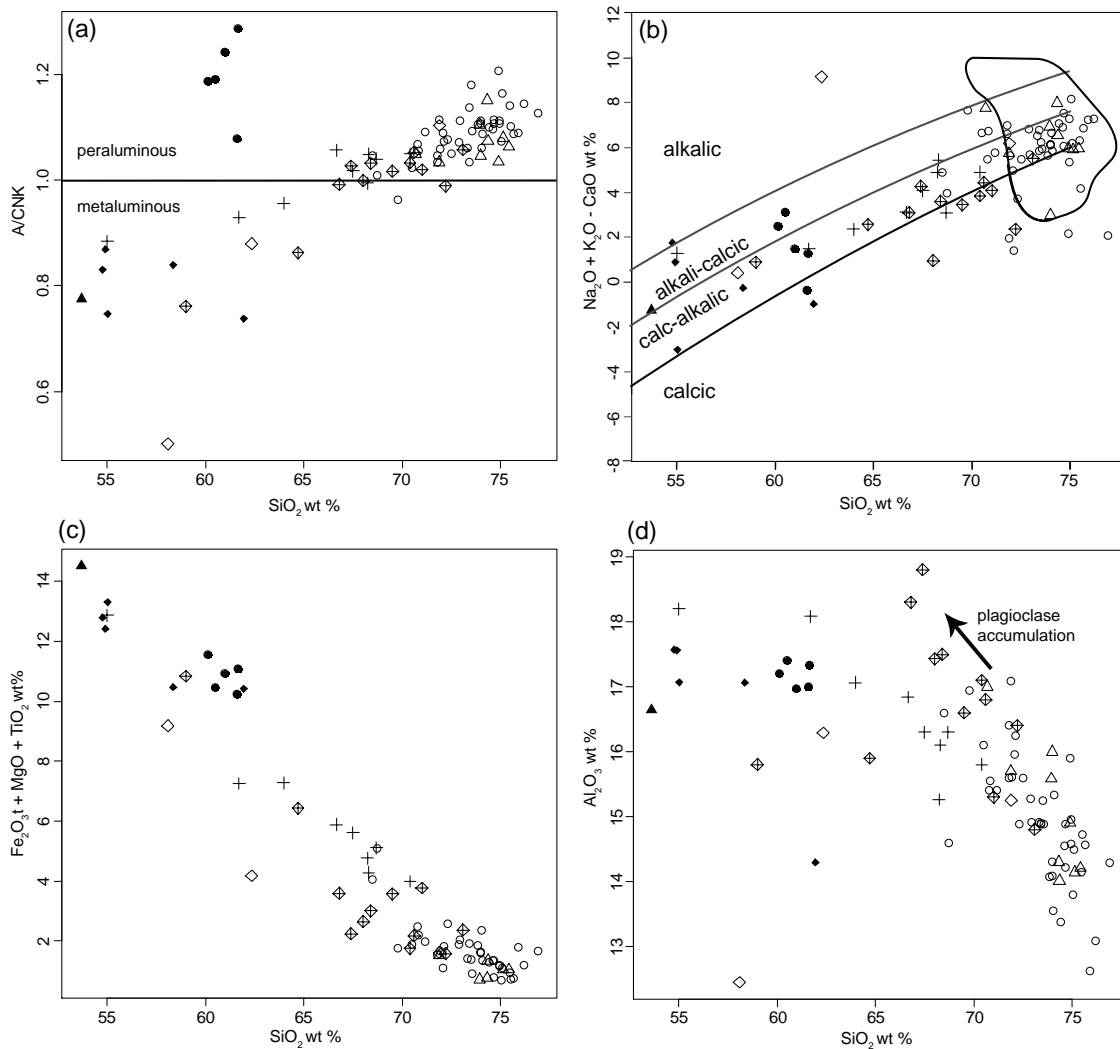


Fig. 9: Variations of major element concentrations of whole rock samples expressed as oxide weight percent. See explanations in text. (b) Alkali-lime vs. SiO_2 diagram after Frost et al. (2001). Rocks of the PMC that show no signs of anatexis are not included. Filled triangle: amphibolite gneiss (possibly andesitic protolith); Filled diamonds: calc-alkaline diorites; filled circles: Bt -psammmites and Bt -pelites; crosses: calc-alkaline granodiorites; open diamonds with crosses: diatexites; open triangles: pegmatitic leucogranite dykes; open diamonds: Hbl - Kfs leucosome; open circles: leucogranites. The arrow in (d) indicates plagioclase accumulation. $N = 87$.

6. Major and Trace Element Geochemistry

We carried out major and trace element analysis on 88 samples of the main lithologies of the PMC, including 58 leucogranitic samples from the Karakoram Shear Zone and Karakoram Batholith. In general, $\text{Fe}_2\text{O}_3\text{t}$, MgO , TiO_2 and CaO contents of source rocks and leucogranites in the Karakoram Shear Zone and Karakoram Batholith correlate negatively with SiO_2 . K_2O and SiO_2 show no clear trend. Leucogranites have SiO_2 contents between 64.0 wt% and 76.2 wt% and are dominantly mildly peraluminous (A/CNK 1.02 to 1.16; Fig. 9a). In the alkali-lime vs. SiO_2 diagram (Fig. 9b), the source rocks follow the calc-alkalic to alkali-calcic trend and almost all leucogranite samples lie in the field of peraluminous leucogranites as defined in Frost *et al.* (2001). The different rock types define different fields depending on their $\text{Fe}_2\text{O}_3\text{t} + \text{MgO} + \text{TiO}_2$ content (Fig. 9c). While the ferromagnesian and titaniferous phases are concentrated in the calc-alkaline diorites, Bt-psammities, Bt-pelites and melanosome samples, the calc-alkaline granodiorites and diatexites form an intermediate group. The leucogranites have the lowest $\text{Fe}_2\text{O}_3\text{t} + \text{MgO} + \text{TiO}_2$ contents (< 2.15 wt %). K_2O contents of leucogranites are usually high between 4 and 5 wt%, ranging from 0.94 wt% to 5.63 wt%. High, and variable, K_2O concentrations suggest K-feldspar accumulation trends in leucogranites. $\text{CaO} + \text{Na}_2\text{O}$ concentrations in leucogranites range from 3.41 wt % to 9.89 wt % (not shown in Fig. 9).

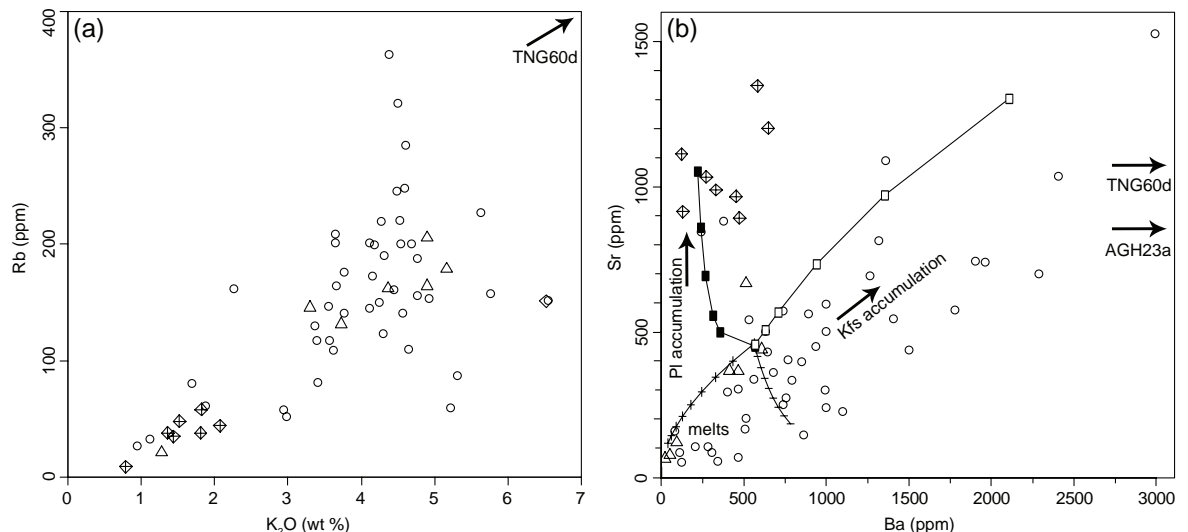


Fig. 10: (a) Rb contents correlate positively with K_2O in leucogranites, interpreted as the result of K-feldspar accumulation. Sample TNG60d (Hbl-Kfs leucosome) with extremely high K_2O (10.1 wt %) and Rb (441 pm) concentrations is not shown ($N=60$). (b) Ba vs. Sr in leucogranites. High Ba and Sr concentrations indicate feldspar cumulates. The Hbl-Kfs leucosome samples TNG60d ($\text{Ba} = 8280$ ppm and $\text{Sr} = 1083$ ppm) and AGH23a ($\text{Ba} = 4136$ ppm and $\text{Sr} = 903$ ppm) are not shown for scaling reasons. The curves represent model calculations for fractionation and accumulation. Starting composition is leucosome TNG71b ($\text{Ba} = 565$ ppm and $\text{Sr} = 448$ ppm). Plus and minus symbols represent modelled compositions of residual liquids after Raleigh fractionation of K-feldspar and plagioclase, respectively, in 5 % increments (5 %, 10 %, 15 %... fractionated minerals). Open and filled squares represent modelled compositions of cumulates after Raleigh fractionation of K-feldspar and plagioclase, respectively, for different degrees of accumulation $F = 0.1 \dots 0.8$. Partition coefficients (K_d) after Arth (1976). Calculation after Rollinson (1993). See Fig. 9 for symbols. $N = 59$.

The high K_2O content of 10.1 wt% in a leucosome sample of a Muglib Batholith migmatite (sample TNG60d in Table 1) is the result of K-feldspar accumulation in the Hbl-bearing

leucosomes in Hbl-Bt diorite (Fig. 3b) in accordance with petrographic observations. Rb correlates positively with K_2O (Fig. 10a), but not with Fe_2O_3 and TiO_2 , suggesting that Rb contents are mainly controlled by the amount of K-feldspar and not by muscovite or biotite in the leucogranites. High Ba and Sr concentrations suggest feldspar crystallization leading to relatively quartz-poor but feldspar-rich leucogranites with a cumulate character (Fig. 10b). Feldspar accumulation as a result of Rayleigh fractionation is shown in the calculated trace element contents in the added curves of Fig. 10b. Relatively low Rb contents result in low Rb/Sr ratios, generally below one. The Tangtse Pluton (Fig. 2) appears to be an example of this; a magma that has started to crystallize close to the source.

7. Geochronology

In order to constrain the relation between timing of protolith crystallization, anatexis and leucogranite intrusion, we dated zircon and titanite grains from two samples of potential source rocks and two leucogranite samples using U-Pb SHRIMP analysis. We selected a melanosome (sample TNG62a), rich in hornblende and biotite as well as titanite, apatite and zircon. This sample was taken from a migmatized part of the Muglib Batholith ~ 3 km along strike to the SE of the Tangtse Pluton. The second sample (TNG131a) is a Bt-granodiorite sheet, interpreted as Muglib Batholith border facies, from the outcrop at the base of the Tangtse Pluton in Fig. 7b. For age determination of leucogranites we chose two samples from the Tangtse Pluton, one for zircon and one for titanite analysis (sample TNG148a and TNG148b).

7. 1 Age of the Muglib Batholith

Zircons from samples TNG62a and TNG131a are prismatic, either translucent or pinkish in colour and between 150 μm and 500 μm in length, on average 200 μm . Cathodoluminescence (CL) imaging shows dominantly oscillatory zoning with little evidence for inherited cores, or overgrowths. These are interpreted to represent igneous zoning. A total of 23 areas have been analyzed on 17 zircon grains from sample TNG62a (melanosome), where 18 analyses form a dominant bell-shaped age probability distribution with a weighted mean $^{206}Pb/^{238}U$ age of 71.4 ± 0.6 Ma (MSWD = 1.14, Fig. 11a; Table 2). One analysis is slightly older whilst the remaining four analyses are younger and are interpreted to have lost radiogenic Pb; for example analysis 1.1 in Table 2. The mean age of 71.4 ± 0.6 Ma is interpreted to represent a single population indicating the magmatic crystallization age of the Hbl-Bt-granodiorite.

Sample TNG131a corresponds to the Bt-granodiorite border facies that intruded Bt-psammites (Fig. 7b). As for the previous sample, the zircon grains are dominated by relatively simple igneous oscillatory zoning as seen under CL, although some discordant central areas may reflect a more complicated igneous crystallization history. A total of 22 areas were analyzed from 17 zircon grains (Fig. 11b; Table 3). An analysis was also made on a zircon included within a titanite grains during the same SHRIMP session. It yielded a significantly younger $^{206}Pb/^{238}U$ date of ~63 Ma but the area has likely lost radiogenic Pb and hence was not included in the following discussion or age calculation. The zircon $^{206}Pb/^{238}U$ ages are slightly dispersed ranging between ~67 and ~74 Ma. The probability density distribution

appears bimodal with a more prominent peak at about 70 Ma and another at about 73 Ma, with some younger analyses considered to reflect radiogenic Pb loss. The older group at ~73 Ma may indicate that there was an early period of magmatic zircon crystallization, but with the dominant zircon having crystallized at 70.5 ± 0.6 Ma (mean weighted $^{206}\text{Pb}/^{238}\text{U}$ age of 14 analyses, MSWD = 1.03; Fig. 11b). This age is overlapping within error but slightly younger than the 71.4 ± 0.6 Ma for sample TNG62a, and confirms that both intrusions relate to the same magmatic event.

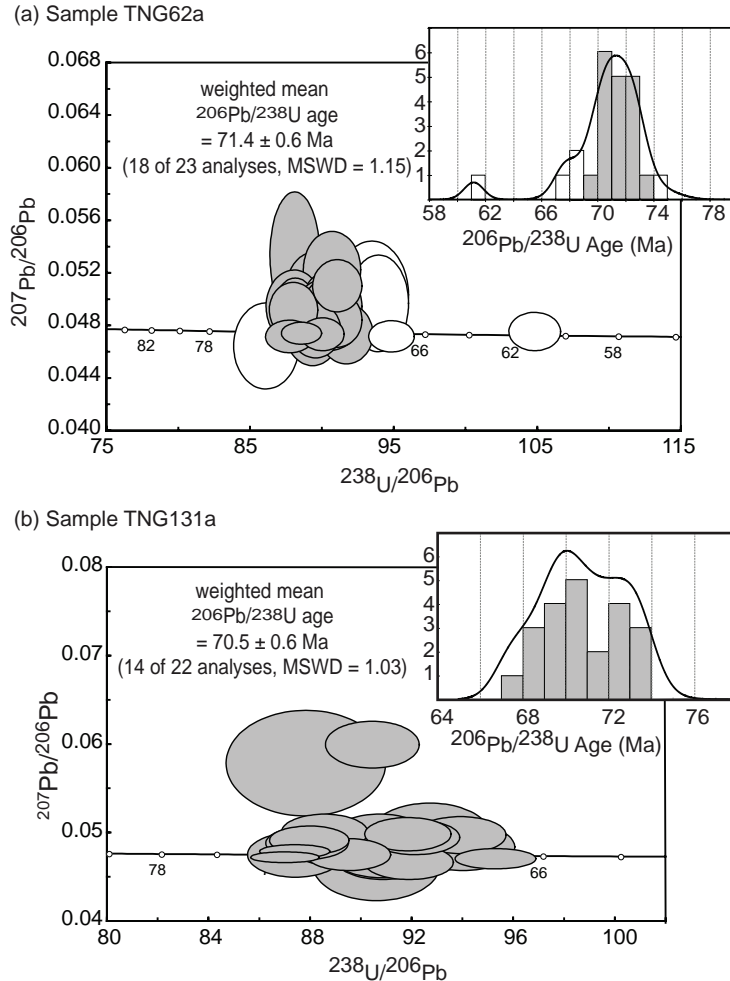


Fig. 11: Tera-Wasserburg concordia diagrams for sample TNG62a and sample TNG131a (Zrn). Inserts are histograms of relative age probability vs. number of spots in U-Pb SHRIMP analysis. Error ellipses are 68.3% confidence.. (a) Zircons form the melanosome of a Hbl-Bt granodiorite (sample TNG62a). (b) Zircons from a Bt-granodiorite (sample TNG131a).

The titanite grains have a light brown color, are mostly anhedral to subhedral and are between 100 and 250 μm in diameter. In some grains the BSE images show a faint oscillatory zoning, whereas most grains have irregular internal structures, often with a slightly darker, central phase, irregularly surrounded by a lighter BSE component (Fig. 12b). Twenty four areas have been analyzed on 14 titanite grains (Fig. 13c; Table 3). As is common in metamorphic titanite, there are high amounts of common Pb and so the calculated radiogenic ratios and ages have high uncertainties compared to the U-Pb zircon data. In the Tera-Wasserburg plot of Fig. 13a, discordia lines have been fitted to the common Pb uncorrected data. It can be seen that there is an older grouping that forms a linear array, intersecting the concordia at 65 ± 3 Ma. A second, sub-parallel group is slightly younger (~55 Ma), and then other analyses

Table 2: U-Pb SHRIMP data; sample TNG62a

Zircon analysis

Coordinates 34°02'16.8"N

78°14'57.7"E

Grain	Spot	U (ppm)		Th (ppm)	Th/U	²⁰⁶ Pb*			f ₂₀₆ %	²³⁸ U/ ²⁰⁶ Pb		²⁰⁷ Pb/ ²⁰⁶ Pb	²⁰⁶ Pb/ ²³⁸ U	Radiogenic age (Ma)	
		U (ppm)	Th (ppm)			²⁰⁶ Pb*	²⁰⁴ Pb/ ²⁰⁶ Pb	±		±	±	±	±	±	±
1.1	924	516	0.56	7.6	0.000084	-	0.05	104.82	1.19	0.0477	0.0009	0.0095	0.0001	61.2	0.7
1.2	358	277	0.78	3.5	-	-	0.23	88.01	1.12	0.0493	0.0014	0.0113	0.0001	72.7	0.9
2.1	2137	1398	0.65	20.9	0.000093	-	<0.01	87.73	1.11	0.0473	0.0008	0.0114	0.0001	73.1	0.9
2.2	421	317	0.75	4.0	-	-	0.14	91.00	1.16	0.0485	0.0014	0.0110	0.0001	70.4	0.9
3.1	136	100	0.74	1.2	0.001987	-	0.31	93.94	1.38	0.0498	0.0024	0.0106	0.0002	68.1	1.0
4.1	403	294	0.73	3.9	0.000515	-	0.04	89.54	1.15	0.0478	0.0014	0.0112	0.0001	71.6	0.9
5.1	185	118	0.64	1.8	0.000872	-	0.40	89.50	1.37	0.0506	0.0020	0.0111	0.0002	71.3	1.1
6.1	123	109	0.89	1.1	0.000938	-	0.39	93.46	1.68	0.0505	0.0027	0.0107	0.0002	68.3	1.2
7.1	227	159	0.70	2.2	0.000981	-	0.62	90.68	1.33	0.0523	0.0019	0.0110	0.0002	70.3	1.0
8.1	229	252	1.10	2.2	0.000518	-	0.26	88.05	1.29	0.0495	0.0018	0.0113	0.0002	72.6	1.1
9.1	385	273	0.71	3.8	-	-	0.75	88.10	1.14	0.0534	0.0032	0.0113	0.0002	72.2	1.0
10.1	171	163	0.95	1.7	0.001165	-	<0.01	86.10	1.50	0.0466	0.0021	0.0116	0.0002	74.5	1.3
11.1	239	163	0.68	2.3	0.000502	-	0.27	90.65	1.38	0.0495	0.0018	0.0110	0.0002	70.5	1.1
11.2	2525	1941	0.77	24.5	-	-	0.01	88.56	0.93	0.0475	0.0005	0.0113	0.0001	72.4	0.8
12.1	298	226	0.76	2.8	0.001338	-	0.22	90.01	1.23	0.0491	0.0016	0.0111	0.0002	71.1	1.0
12.2	1458	909	0.62	13.2	-	-	<0.01	94.82	1.04	0.0473	0.0008	0.0105	0.0001	67.6	0.7
13.1	365	355	0.97	3.4	-	-	0.01	91.69	1.22	0.0475	0.0015	0.0109	0.0001	69.9	0.9
13.2	1157	742	0.64	11.0	0.000018	-	0.01	90.01	1.00	0.0475	0.0008	0.0111	0.0001	71.2	0.8
14.1	278	421	1.52	2.7	-	-	0.03	89.34	1.26	0.0477	0.0017	0.0112	0.0002	71.7	1.0
15.1	470	331	0.70	4.4	0.000711	-	0.47	91.03	1.14	0.0511	0.0013	0.0109	0.0001	70.1	0.9
16.1	526	286	0.54	5.0	0.000199	-	0.08	90.25	1.52	0.0481	0.0012	0.0111	0.0002	71.0	1.2
16.2	390	324	0.83	3.7	-	-	0.27	90.49	1.17	0.0496	0.0014	0.0110	0.0001	70.7	0.9
17.1	677	612	0.90	6.6	0.000189	-	0.19	88.15	1.03	0.0490	0.0018	0.0113	0.0001	72.6	0.9

f206 % denotes the percentage of ²⁰⁶Pb that is common Pb.

Table 3: U-Pb SHRIMP data; sample TNG131a

Zircon analysis

Sample TNG131a

Coordinates 34°03'38.8"N

78°13'52.1"E

Grain	Spot	U (ppm)		Th (ppm)	Th/U	²⁰⁶ Pb*			f ₂₀₆ %	²³⁸ U/ ²⁰⁶ Pb		²⁰⁷ Pb/ ²⁰⁶ Pb	²⁰⁶ Pb/ ²³⁸ U	Radiogenic age (Ma)	
		U (ppm)	Th (ppm)			²⁰⁶ Pb*	²⁰⁴ Pb/ ²⁰⁶ Pb	±		±	±	±	±	±	±
1.1	1696	1160	0.68	15.3	0.000129	-	<0.01	95.31	1.06	0.0472	0.0007	0.0105	0.0001	67.3	0.7
1.2	465	349	0.75	4.3	0.000176	-	0.28	92.15	1.15	0.0496	0.0013	0.0108	0.0001	69.4	0.9
2.1	553	551	1.00	5.2	0.000033	-	<0.01	90.89	1.19	0.0469	0.0012	0.0110	0.0001	70.6	0.9
2.2	258	184	0.71	2.4	0.000764	-	0.01	90.87	1.28	0.0475	0.0017	0.0110	0.0002	70.6	1.0
3.1	412	333	0.81	4.0	0.000571	-	0.34	88.57	1.12	0.0502	0.0013	0.0113	0.0001	72.1	0.9
4.1	134	185	1.38	1.2	-	-	0.28	92.72	1.61	0.0496	0.0025	0.0108	0.0002	69.0	1.2
5.1	643	600	0.93	6.3	0.000494	-	0.23	87.96	1.04	0.0493	0.0011	0.0113	0.0001	72.7	0.9
6.1	4364	4115	0.94	43.1	-	-	<0.01	87.01	0.90	0.0474	0.0004	0.0115	0.0001	73.7	0.8
7.1	54	55	1.01	0.5	0.003931	-	1.32	87.83	2.08	0.0580	0.0039	0.0112	0.0003	72.0	1.7
8.1	554	425	0.77	5.2	0.000254	-	0.33	91.85	1.12	0.0500	0.0012	0.0109	0.0001	69.6	0.9
9.1	451	333	0.74	4.2	0.000383	-	<0.01	91.89	1.16	0.0468	0.0013	0.0109	0.0001	69.8	0.9
9.2	303	139	0.46	2.9	-	-	0.17	88.97	1.21	0.0488	0.0015	0.0112	0.0002	71.9	1.0
10.1	325	202	0.62	3.1	0.001032	-	1.59	90.45	1.22	0.0600	0.0017	0.0109	0.0001	69.8	1.0
10.2	516	301	0.58	5.0	0.000040	-	0.20	87.88	1.07	0.0490	0.0012	0.0114	0.0001	72.8	0.9
11.1	251	244	0.97	2.5	0.000403	-	0.02	87.42	1.24	0.0477	0.0017	0.0114	0.0002	73.3	1.0
12.1	262	166	0.63	2.5	0.000520	-	0.27	90.75	1.28	0.0496	0.0017	0.0110	0.0002	70.5	1.0
12.2	250	170	0.68	2.3	0.000106	-	0.15	94.03	1.35	0.0486	0.0018	0.0106	0.0002	68.1	1.0
13.1	418	227	0.54	3.8	0.000424	-	0.32	93.91	1.20	0.0499	0.0014	0.0106	0.0001	68.1	0.9
14.1	506	433	0.86	4.9	-	-	0.03	89.51	1.09	0.0477	0.0012	0.0112	0.0001	71.6	0.9
15.1	113	175	1.55	1.1	-	-	<0.01	90.61	1.66	0.0466	0.0027	0.0110	0.0002	70.8	1.3
16.1	3055	2050	0.67	30.0	0.000070	-	0.08	87.39	0.91	0.0481	0.0005	0.0114	0.0001	73.3	0.8
17.1	196	106	0.54	1.8	0.001090	-	0.14	91.30	1.40	0.0486	0.0020	0.0109	0.0002	70.1	1.1
zircon included in titanite															
2.1	593	273	0.46	6.8	0.013439	-	26.44	74.46	0.93	0.2569	0.0316	0.0099	0.0006	63.4	3.5

Table 3 continued

Titanite analysis															
Sample		TNG131a													
Grain	Spot	U (ppm)	Th (ppm)	Th/U	²⁰⁶ Pb* (ppm)	²⁰⁴ Pb/ ²⁰⁶ Pb	±	f ₂₀₆ %	²³⁸ U/ ²⁰⁶ Pb	±	²⁰⁷ Pb/ ²⁰⁶ Pb	±	²⁰⁶ Pb/ ²³⁸ U	±	
1.1	406	48	0.12	1.7	0.031001	0.002476	57.9	202.99	2.87	0.4805	0.0064	0.0021	0.0003	13.4	1.8
2.1	146	29	0.20	0.9	0.028931	0.002446	54.0	141.04	2.41	0.4690	0.0084	0.0033	0.0004	21.0	2.5
3.1	180	7	0.04	0.9	0.034459	0.002420	64.4	167.62	2.71	0.4928	0.0081	0.0021	0.0003	13.7	2.2
3.2	37	396	10.61	0.6	0.021536	0.002722	40.0	55.11	1.34	0.4282	0.0096	0.0109	0.0010	69.8	6.6
4.1	98	6	0.06	0.7	0.034500	0.002938	64.4	116.85	2.20	0.6005	0.0110	0.0030	0.0006	19.6	3.6
5.1	107	71	0.67	0.8	0.035582	0.002774	66.4	108.33	1.98	0.5921	0.0107	0.0031	0.0006	20.0	3.7
5.2	34	456	13.49	0.6	0.027273	0.002768	50.7	45.15	1.11	0.4566	0.0096	0.0109	0.0013	70.0	8.4
6.1	88	65	0.73	1.0	0.020407	0.001886	38.0	72.92	1.31	0.3152	0.0059	0.0085	0.0006	54.6	3.7
7.1	64	466	7.30	1.0	0.030482	0.002392	56.7	57.19	1.13	0.5689	0.0092	0.0076	0.0010	48.6	6.1
7.2	91	27	0.30	0.8	0.031392	0.002969	58.6	101.37	2.01	0.5523	0.0107	0.0041	0.0006	26.3	4.1
8.1	99	369	3.73	1.1	0.013155	0.001402	24.5	74.71	1.30	0.2358	0.0046	0.0101	0.0004	64.8	2.7
8.2	54	671	12.47	0.9	0.029445	0.002516	54.8	53.98	1.16	0.5018	0.0092	0.0084	0.0010	53.8	6.7
6.2	57	435	7.62	0.7	0.017611	0.002039	32.8	66.93	1.38	0.2997	0.0066	0.0100	0.0007	64.4	4.2
9.1	35	430	12.21	0.6	0.027630	0.002883	51.4	52.11	1.28	0.4160	0.0093	0.0093	0.0012	59.9	7.5
9.2	57	398	7.00	0.8	0.034492	0.002761	64.3	59.77	1.24	0.5771	0.0100	0.0060	0.0010	38.4	6.7
10.1	87	420	4.81	1.0	0.013854	0.001558	25.8	72.01	1.30	0.2584	0.0051	0.0103	0.0005	66.1	3.1
10.2	44	411	9.30	0.6	0.025447	0.002662	47.3	58.69	1.34	0.4184	0.0098	0.0090	0.0010	57.6	6.2
11.1	34	369	10.75	0.5	0.027740	0.002921	51.6	54.33	1.34	0.4124	0.0092	0.0089	0.0011	57.2	7.3
11.2	45	394	8.75	0.7	0.028876	0.002621	53.7	53.24	1.18	0.5294	0.0107	0.0087	0.0011	55.8	6.9
12.2	497	50	0.10	1.6	0.028322	0.001868	52.9	260.51	3.68	0.4760	0.0068	0.0018	0.0002	11.6	1.1
13.1	151	8	0.05	1.0	0.034971	0.002753	65.3	136.17	2.38	0.5833	0.0100	0.0025	0.0005	16.4	2.9
13.2	48	437	9.05	0.7	0.028979	0.002682	53.9	55.55	1.22	0.4381	0.0094	0.0083	0.0011	53.2	6.7
14.1	49	425	8.65	0.7	0.023750	0.002314	44.2	62.23	1.37	0.3423	0.0076	0.0090	0.0008	57.6	5.2
14.2	52	447	8.61	0.7	0.024840	0.002444	46.2	61.30	1.32	0.4416	0.0087	0.0088	0.0009	56.3	5.5

f₂₀₆ % denotes the percentage of ²⁰⁶Pb that is common P

Table 4; U-Pb SHRIMP data; sample TNG148a, TNG148b

Titanite analysis																
Sample TNG148a																
Coordinates		34°03'40.4"N 78°13'52.7"E														
Grain	Spot	U (ppm)	Th (ppm)	Th/U	²⁰⁶ Pb* (ppm)	²⁰⁴ Pb/ ²⁰⁶ Pb	±	f ₂₀₆ %	²³⁸ U/ ²⁰⁶ Pb	±	²⁰⁷ Pb/ ²⁰⁶ Pb	±	²⁰⁶ Pb/ ²³⁸ U	±	Radiogenic age (Ma)	
1.1	208	790	3.80		1.8	0.040139	0.002097	74.9	98.65	4.94	0.6528	0.0315	0.0025	0.0006	16.4	3.7
2.1	352	47	0.13		2.5	0.037675	0.002185	70.3	122.82	1.63	0.5935	0.0060	0.0024	0.0005	15.5	2.9
3.1	237	45	0.19		2.1	0.038220	0.002227	71.3	98.95	1.40	0.6388	0.0068	0.0029	0.0006	18.6	3.7
4.1	158	171	1.08		2.1	0.049082	0.002556	91.6	65.07	0.98	0.7046	0.0074	0.0013	0.0011	8.3	6.8
4.2	474	206	0.44		3.0	0.035915	0.001540	67.1	134.34	1.74	0.5603	0.0054	0.0025	0.0003	15.8	2.2
5.1	305	50	0.16		2.2	0.041903	0.002224	78.3	120.02	1.63	0.6085	0.0064	0.0018	0.0005	11.7	3.2
6.1	455	115	0.25		3.1	0.034043	0.001693	63.6	127.73	1.62	0.5746	0.0061	0.0029	0.0004	18.4	2.3
6.2	262	40	0.15		2.1	0.037824	0.001839	70.6	109.40	1.56	0.6410	0.0071	0.0027	0.0005	17.3	3.0
6.3	127	875	6.88		1.7	0.044925	0.002325	83.8	65.53	1.09	0.6986	0.0088	0.0025	0.0010	15.9	6.1
7.1	357	35	0.10		2.5	0.035071	0.001621	65.5	123.36	1.65	0.5812	0.0060	0.0028	0.0004	18.0	2.4
8.1	254	43	0.17		2.1	0.038986	0.001901	72.8	102.82	1.48	0.6308	0.0071	0.0026	0.0005	17.0	3.3
9.1	249	26	0.11		2.1	0.041786	0.001999	78.0	103.02	1.50	0.6532	0.0077	0.0021	0.0005	13.7	3.5
10.1	221	224	1.01		1.8	0.039211	0.002012	73.2	105.52	1.55	0.6406	0.0075	0.0025	0.0005	16.3	3.3
10.2	207	20	0.10		2.2	0.041973	0.002220	78.3	82.02	1.28	0.6695	0.0083	0.0026	0.0007	17.0	4.6
11.1	185	63	0.34		1.6	0.037226	0.002174	69.5	100.15	1.57	0.6379	0.0083	0.0030	0.0006	19.6	3.5
12.1	252	24	0.09		2.1	0.039991	0.003275	74.7	104.59	1.52	0.6200	0.0072	0.0024	0.0007	15.6	4.5
13.1	220	30	0.13		2.0	0.040177	0.001954	75.0	94.86	1.40	0.6460	0.0073	0.0026	0.0006	17.0	3.7
14.1	527	288	0.55		3.3	0.034685	0.001475	64.8	138.82	1.78	0.5499	0.0054	0.0025	0.0003	16.3	2.1
15.1	209	88	0.42		1.9	0.042656	0.002092	79.6	92.08	1.38	0.6374	0.0075	0.0022	0.0006	14.2	4.0

Titanite analysis

zircon included within titanite grains in sample TNG148a

1.1	3034	1861	0.61	11.6	0.020867	0.002902	35.17	224.30	2.95	0.3245	0.0299	0.0029	0.0002	18.6	1.1
2.1	5655	2607	0.46	14.9	0.001053	0.000248	0.92	326.41	3.52	0.0537	0.0008	0.0030	0.0000	19.5	0.2

Titanite analysis

zircon analyzed *in situ* in polished thin section

24-1	1425	4	0.003	3.7	0.004420	0.001228	5.5	329.6	6.0	0.0895	0.0051	0.0029	0.0001	18.5	0.4
24-2	5784	3703	0.64	35.2	0.026992	0.002627	49.8	141.2	2.2	0.4406	0.0144	0.0036	0.0002	22.9	1.0
29-1	2060	1304	0.63	148.2	0.051735	0.000951	96.4	11.941	0.136	0.8127	0.0091	0.0030	0.0018	19.6	11.6
29-2	1464	2858	1.95	5.7	0.020839	0.002127	37.0	222.1	6.8	0.3389	0.0198	0.0028	0.0001	18.3	0.9
29-3	1709	823	0.48	4.4	0.006514	0.001335	8.3	333.7	5.0	0.1121	0.0062	0.0027	0.0000	17.7	0.3
29-4	1251	1503	1.20	163.2	0.054529	0.000701	97.6	6.588	0.073	0.8266	0.0198	0.0036	0.0047	23.1	30.1
47-1	2006	1015	0.51	5.5	0.000608	0.000248	2.2	313.2	4.3	0.0640	0.0020	0.0031	0.0000	20.1	0.3
47-2	672	1095	1.63	1.6	0.001152	0.000628	1.0	362.5	7.4	0.0546	0.0042	0.0027	0.0001	17.6	0.4
47-3	1116	2284	2.05	3.5	0.012479	0.001932	23.2	271.6	4.5	0.2294	0.0075	0.0028	0.0001	18.2	0.4

f₂₀₆ % denotes the percentage of ²⁰⁶Pb that is common Pb.

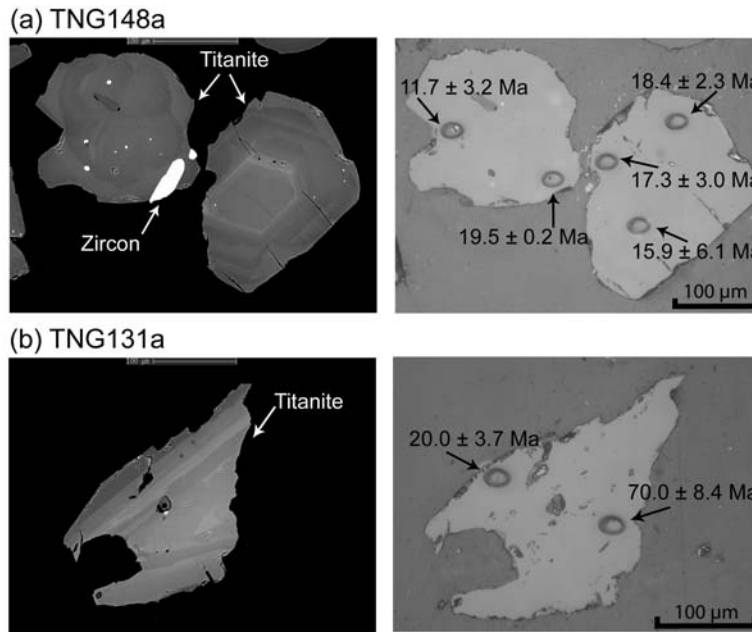


Fig. 12: (a) BSE image (left) and post analysis photograph (right) of titanite grains from sample TNG148a. Note that the zircon inclusion yielded an older age than that of the surrounding titanite (see also Table 4). (b) BSE image (left) and post-analysis photograph (right) of a titanite grain from sample TNG131a. Ages are indicated for each analyzed spot (see also Table 3).

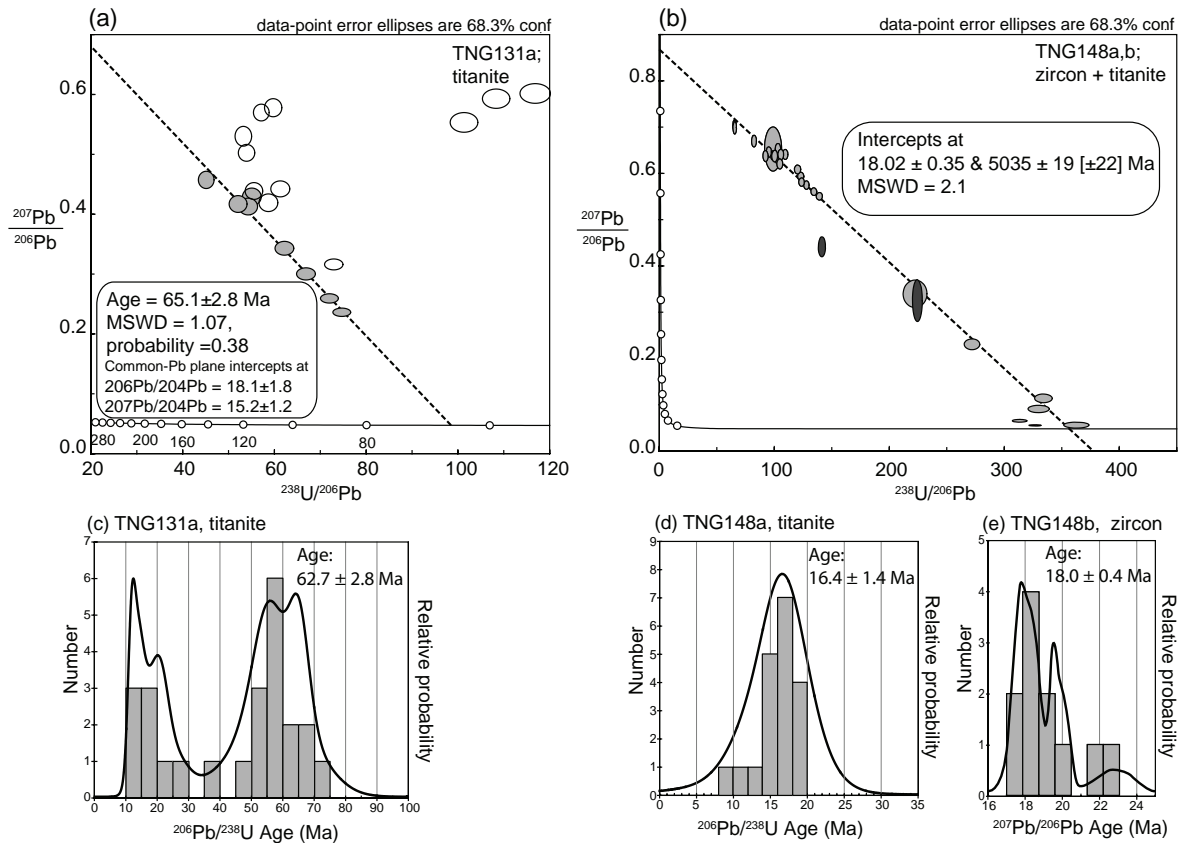


Fig. 13: (a) Concordia constrained linear 3-D isochron for sample TNG131a (Ttn). (b) Concordia diagram for samples TNG148a (Ttn) and TNG148b (Zrn) plotted together. (c) Histogram of titanite analyses of sample TNG131a. (d and e) Histogram of titanite and zircon analyses of samples TNG148a and TNG148b, respectively.

range down to ~11 Ma. The oldest calculated age is younger than that calculated from zircons of the same sample, the likely true magmatic age, and either is spurious or relates to a cooling event post initial magmatism. An early metamorphic event due to continued calc-alkaline intrusion is also possible. The relative probability plot of common Pb corrected $^{206}\text{Pb}/^{238}\text{U}$

ages highlights the two older age components with a scattered younger cluster peaking between ~11 and 21 Ma (Fig. 13c). It is not possible to calculate a meaningful age date for this younger, metamorphic titanite, but it is indicative of a metamorphic crystallization event broadly contemporaneous with anatexis (see below).

7.2 Age of the leucogranites from the Tangtse Pluton

Initially zircons were not recovered from the standard mineral separation applied to sample TNG148a. Titanites were separated similarly to the Bt-granodiorite sample. They have a light brown colour, are mostly anhedral to subhedral and are between 100 and 250 μm large. BSE images show weak oscillatory zoning, more common than in titanites from sample TNG131a, while irregular structures are not as prominent. We interpret the BSE internal structure to reflect compositional differences during magmatic growth as opposed to core and rim structures. Zircon inclusions are common. A total of 19 areas on 15 titanite grains from sample TNG148a have been analyzed (Fig. 13d; Table 4). The analyses are significantly enriched in common Pb with many measured $^{207}\text{Pb}/^{206}\text{Pb}$ ratios ≥ 0.55 , and ranging to ~0.70. Interpolation to a radiogenic end member is therefore tenuous. However, it is possible to calculate a 3-dimensional linear fit to this common Pb enriched data and this provides a lower intercept at 16.7 ± 1.0 Ma (MSWD = 1.4, 19 analyses). A weighted mean of common Pb corrected $^{206}\text{Pb}/^{238}\text{U}$ ages gives 16.4 ± 1.4 Ma (MSWD = 0.4, 19 analyses). Two zircon inclusions within the same titanite separate were also analyzed (Table 4), and have $^{206}\text{Pb}/^{238}\text{U}$ ages of 18.6 ± 1.1 Ma and 19.5 ± 0.2 Ma, respectively. These zircon grains have very high U concentrations ~3000 ppm and ~5650 ppm, respectively, and so the radiogenic $^{206}\text{Pb}/^{238}\text{U}$ ages are unreliable by SHRIMP (see Williams & Hergt, 2000).

From a second sample from the same outcrop (TNG148b), nine areas on 3 zircon grains were analyzed in situ in a polished thin section. As with the zircon included within the titanite, the U concentrations range to very high values (~5785 ppm). However, lower, more reasonable U concentrations are recorded, and 5 analyses with ≤ 1710 ppm U have a weighted mean $^{206}\text{Pb}/^{238}\text{U}$ age of 18.0 ± 0.4 Ma (MSWD = 1.09, Fig. 13e; Table 4). It should be noted that the zircon grain with ~3000 ppm U that is included in titanite has a $^{206}\text{Pb}/^{238}\text{U}$ age within uncertainty of the titanite age. Thus, overall the zircon records a slightly older age than that obtained from titanite with high common Pb.

8. Rb-Sr and Sm-Nd isotope geochemistry

In order to track the origin and mixing of magmas from different sources as inferred in the field, we analyzed Rb-Sr and Sm-Nd isotopes of rocks that we interpret to represent magma sources and those that represent melting products, i.e. the leucogranites. We used 18 Ma for recalculation of initial $^{87}\text{Sr}/^{86}\text{Sr}$ and $^{143}\text{Nd}/^{144}\text{Nd}$ ratios for leucogranites. This is the most likely crystallization age based on U-Pb SHRIMP data for such rocks (Searle *et al.*, 1998 and our new analyses). For direct comparison with the products of anatexis, we also calculated the isotope data of source rocks and those of the Ladakh Batholith to that time.

8.1 Results

Initial $^{87}\text{Sr}/^{86}\text{Sr}$ between 0.7042 and 0.7077 and initial ϵ_{Nd} values between 0.6 and 2.4 for calc-alkaline granitoids of the Muglib Batholith indicate a mantle origin with a slight crustal influence, or juvenile crustal sources (Table 5, Fig. 14). For comparison we analyzed six samples from the Ladakh Batholith close to Leh (Fig. 1a). These yielded essentially identical $^{87}\text{Sr}/^{86}\text{Sr}_i$ ranging between 0.7045 and 0.7066 and ϵ_{Nd_i} ranging between -0.1 and 2.1. The overlap with the values for the Muglib Batholith indicates a possible genetic relationship (see discussion below). In contrast, meta-sedimentary rocks of the PMC yielded $^{87}\text{Sr}/^{86}\text{Sr}_i$ between 0.7115 and 0.7161 that indicate longer crustal residence and ϵ_{Nd_i} that show limited variation between -10.0 and -9.6 (Table 5, Fig. 14). Thus, the protoliths recognized in the field have significantly different isotopic compositions.

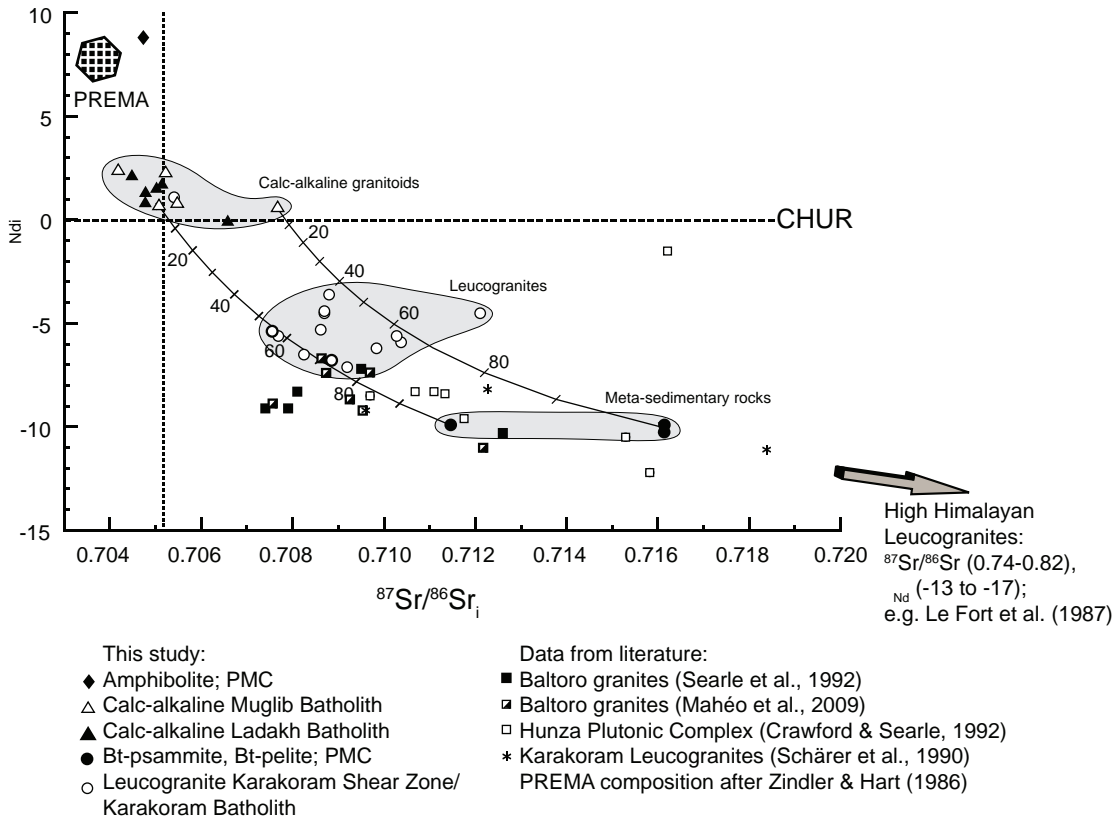


Fig. 14: $^{87}\text{Sr}/^{86}\text{Sr}_i$ vs. ϵ_{Nd_i} diagram calculated at 18 Ma. Curves are calculated mixing lines between end-member isotopic compositions of calc-alkaline granitoids and meta-sedimentary rocks. The grey fields mark the range of isotopic compositions for leucogranites (field I) and source rocks (fields II and III).

The leucogranites, including in situ leucosomes interpreted to represent melt products in the PMC have $^{87}\text{Sr}/^{86}\text{Sr}_i$ ranging from 0.7086 to 0.7121, and ϵ_{Nd_i} values between -3.6 and -6.2. Similar values were obtained for four Ms-Bt ± Grt-leucogranite samples from the Karakoram Batholith collected in the Shyok and Nubra River confluence area and in the Nubra Valley (Fig. 1a) at approximately 60 km, 65 km, 85 km and almost 100 km distance from the Tangtse gorge ($^{87}\text{Sr}/^{86}\text{Sr}_i$ = 0.7076 to 0.7092 and ϵ_{Nd_i} = -5.4 to -7.1). In the region of Rongdu (Fig. 1a) in the Shyok Valley, we have mapped a kilometer-wide Hbl-leucogranite

Table 5: Rb-Sr and Sm-Nd isotopes

Sample	Type / Location	Coordinates	Rb ppm	Sr ppm	$^{87}\text{Rb}/^{86}\text{Sr}$	$^{87}\text{Sr}/^{86}\text{Sr}$	Sm ppm	Nd ppm	$^{147}\text{Sm}/^{144}\text{Nd}$	$^{143}\text{Nd}/^{144}\text{Nd}$	Nd now	$^{87}\text{Sr}/^{86}\text{Sr}$ at 18 Ma	$^{143}\text{Nd}/^{144}\text{Nd}$ at 18 Ma	Nd _i at 18 Ma
TNG 71a	Grt-Ms-Bt leucogranite, Tangtse Pluton	34°03'42.6"N 78°13'52.2"E	157.72	406.39	1.123	0.71066	0.65	3.21	0.1224	0.51233	-6.05	0.7104	0.51231	-5.9
TNG 71b	Ms-Bt leucogranite, Tangtse Pluton	34°03'42.6"N 78°13'52.2"E	131.43	455.57	0.835	0.71048	1.20	6.92	0.1048	0.51234	-5.79	0.7103	0.51233	-5.6
TNG148a	Bt leucogranite, Tangtse Pluton	34°03'40.4"N 78°13'52.7"E	145.57	1046.06	0.403	0.70993	2.94	18.36	0.0966	0.51231	-6.42	0.7098	0.51230	-6.2
TNG148b	Bt leucogranite, Tangtse Pluton	34°03'40.4"N 78°13'52.7"E	149.88	1528.89	0.284	0.70868	4.45	29.30	0.0917	0.51235	-5.58	0.7086	0.51234	-5.3
TNG 131g	Pegmatitic leucosome, Tangtse Pluton	34°03'38.8"N 78°13'52.1"E	119.76	351.52	0.986	0.70904	0.50	2.51	0.1202	0.51244	-3.80	0.7088	0.51243	-3.6
TNG170*	Leucosome, Tangtse gorge	34°02'35.6"N 78°13'16.0"E	52.14	1089.96	0.138	0.70544	0.53	2.97	0.1071	0.51268	0.90	0.7054	0.51267	1.1
TNG186	Leucogranite dyke, Darbuk-Shyok gorge	34°08'41.8"N 78°08'17.8"E	140.62	438.78	0.926	0.71234	4.53	29.49	0.0929	0.51239	-4.76	0.7121	0.51238	-4.5
TNG187a	Pegmatite dyke, Darbuk-Shyok gorge	34°08'48.6"N 78°08'26.9"E	109.87	73.56	4.322	0.70979	0.42	0.93	0.2757	0.51242	-4.34	0.7087	0.51238	-4.5
TNG187b	Pegmatite dyke, Darbuk-Shyok gorge	34°08'48.6"N 78°08'26.9"E	131.98	98.23	3.888	0.70968	1.80	5.73	0.1902	0.51241	-4.37	0.7087	0.51239	-4.4
AGH23a*	Hbl bearing leucosome, Nubra Valley	34°25'10.6"N 77°49'23.5"E	151.40	903.40	0.485	0.70897	14.35	81.59	0.1064	0.51228	-7.02	0.7088	0.51227	-6.8
AGH25a	Grt-Ms-Bt leucogranite, Nubra Valley	34°27'04.4"N 77°45'53.1"E	158.44	155.61	2.946	0.70831	1.99	12.03	0.1003	0.51235	-5.60	0.7076	0.51234	-5.4
NBR1b*	Ms-Bt leucogranite, Nubra Valley	34°29'06.0"N 77°44'20.0"E	201.14	363.24	1.600	0.70809	2.86	16.05	0.1079	0.51234	-5.80	0.7077	0.51233	-5.6
NBR2a*	Ms-Bt leucogranite, Nubra Valley	34°37'54.6"N 77°38'24.1"E	208.66	501.35	1.203	0.70855	4.44	24.47	0.1097	0.51230	-6.66	0.7082	0.51228	-6.5
NBR3b*	Ms-Bt leucogranite, Nubra Valley	34°46'27.5"N 77°32'45.7"E	201.27	336.80	1.727	0.70963	3.55	20.27	0.1060	0.51226	-7.32	0.7092	0.51225	-7.1
TNG 62a	Melanosome, SW Muglib	34°02'16.8"N 78°14'57.7"E	122.37	538.39	0.658	0.70783	7.30	43.29	0.1019	0.51266	0.37	0.7077	0.51265	0.6
TNG128	Calc-alkaline Hbl-Bt-granodiorite, SW Muglib	33°59'08.3"N 78°18'37.8"E	120.43	575.26	0.605	0.70523	5.41	32.32	0.1011	0.51266	0.43	0.7051	0.51265	0.6
TNG169a*	Calc-alkaline diorite, Tangtse gorge	34°02'40.3"N 78°13'07.8"E	49.42	547.63	0.261	0.70528	3.18	13.46	0.1428	0.51275	2.17	0.7052	0.51273	2.3
TNG98a	Calc-alkaline Hbl-Bt-granodiorite, Darbuk-Shyok gorge	34°09'23.1"N 78°08'52.0"E	116.76	573.49	0.589	0.70562	5.48	35.28	0.0939	0.51267	0.53	0.7055	0.51265	0.8
AGH5*	Calc-alkaline gabbro, Pangong Range	34°18'47.7"N 77°52'03.8"E	26.52	497.28	0.154	0.70421	3.63	15.39	0.1427	0.51276	2.28	0.7042	0.51274	2.4
TNG 70a	Bt-psammite, Tangtse Pluton	34°03'41.6"N 78°13'53.2"E	255.15	250.40	2.949	0.71251	5.35	28.11	0.1150	0.51214	-9.81	0.7118	0.51212	-9.6
TNG 131d	Bt-psammite, Tangtse Pluton	34°03'38.8"N 78°13'52.1"E	183.68	155.69	3.416	0.71700	6.21	32.64	0.1148	0.51211	-10.22	0.7161	0.51210	-10.0
TNG112	Pelite, Shyok Valley	34°12'19.6"N 78°07'55.9"E	168.65	299.82	1.628	0.71188	6.45	32.52	0.1198	0.51212	-10.10	0.7115	0.51211	-9.9
PNG03b	Pelite, Tangtse Valley	33°57'53.5"N 78°23'46.0"E	168.22	147.66	3.299	0.71698	5.44	29.33	0.1120	0.51212	-10.12	0.7161	0.51211	-9.9
TNG108c	Amphibolite, Darbuk-Shyok gorge	34°08'42.0"N 78°08'18.5"E	4.04	125.56	0.093	0.70477	2.40	6.92	0.2098	0.51309	8.82	0.7047	0.51307	8.8
LEH40**	Ladakh Batholith, Leh	Leh region	not available		0.339	0.70485	3.13	14.21	0.1331	0.51267	0.66	0.7048	0.51266	0.8
LEH55**	Ladakh Batholith, Leh	Leh region	159.00	95.00	4.843	0.70782	1.10	5.86	0.1131	0.51262	-0.29	0.7066	0.51261	-0.1
LEH29**	Ladakh Batholith, Leh	Leh region	49.00	219.00	0.647	0.70465	1.87	9.81	0.1152	0.51274	1.93	0.7045	0.51272	2.1
LEH38a**	Ladakh Batholith, Gyamsa	Leh region	85.00	119.00	2.066	0.70555	1.69	11.51	0.0888	0.51270	1.27	0.7050	0.51269	1.5
LEH38b**	Ladakh Batholith, Gyamsa	Leh region	79.00	188.00	1.216	0.70545	5.30	22.64	0.1416	0.51272	1.54	0.7051	0.51270	1.7
LEH52**	Ladakh Batholith, Gyamsa	Leh region	30.40	350.00	0.251	0.70485	8.49	36.85	0.1392	0.51270	1.13	0.7048	0.51268	1.3

Samples marked with * were analyzed unspiked.

body within the Karakoram Batholith similar in field appearance to Hbl-bearing leucosomes of the Tangtse migmatites. An enclave of calc-alkaline diorite migmatite was collected from within this body. Analysis of the hornblende-bearing leucosome of this sample (AGH23a in Table 5), which is petrographically and geochemically comparable to leucosomes in Hbl-Cpx diorites of the Muglib Batholith close to Muglib (sample TNG60d in Table 1), yielded isotope values similar to those of the Karakoram Batholith.

In the ϵ_{Ndi} vs. $^{87}\text{Sr}/^{86}\text{Sr}_i$ diagram (Fig. 14), leucogranites from the PMC and the Karakoram Batholith define a field with intermediate values between those of the calc-alkaline granitoids and meta-sedimentary rocks. In a simple two end-member mixing calculation, this field lies within hyperbolic curves between samples we infer to be representative of source rocks (Fig. 14). While ϵ_{Ndi} values of leucogranites show only little variation, $^{87}\text{Sr}/^{86}\text{Sr}_i$ scatter over a wider range.

Like the majority of leucogranite samples analyzed, those collected from the two outcrops described above (Figs. 7 and 8) also yielded intermediate signatures between those of calc-alkaline granitoids and meta-sedimentary rocks. The pegmatitic leucosome in the outcrop in Fig. 7b (sample TNG 131g in Table 5) yielded a $^{87}\text{Sr}/^{86}\text{Sr}_i$ of 0.7088, and a ϵ_{Ndi} value of -3.6. These are similar to isotope values obtained from two Ms-Bt \pm Grt-leucogranite samples from leucogranite sheets such as in Fig. 7c (TNG71a and TNG71b in Table 5) and two other Bt-leucogranite samples from the Tangtse Pluton close to the outcrop in Fig. 7 (TNG148a and TNG148b in Table 5).

The isotope values of samples from two pegmatitic Grt-Ms-Bt-leucogranite dykes from the outcrop in Fig. 8 (TNG187a, TNG187b in Table 5) also show intermediate values ($^{87}\text{Sr}/^{86}\text{Sr}_i = 0.7087$ for both samples, $\epsilon_{\text{Ndi}} = -4.5$ and -4.4 , respectively). A Ms-Bt-leucogranite dyke (TNG186 in Table 5) that intrudes calc-silicate rocks close by, has a comparable ϵ_{Ndi} value of -4.5 , but a remarkably high $^{87}\text{Sr}/^{86}\text{Sr}_i$ of 0.7121.

Whilst the majority of leucosomes show this intermediate signature, a Ms-Bt-leucogranite sample (TNG170, Table 5) collected from within a metatexite in the centre of the Tangtse gorge has isotope values close to those for a patchy melanosome in diorite ($^{87}\text{Sr}/^{86}\text{Sr}_i = 0.7052$ and $\epsilon_{\text{Ndi}} = 2.3$) in the same outcrop (TNG169a in Table 5). These values are similar to those of the calc-alkaline source rocks ($^{87}\text{Sr}/^{86}\text{Sr}_i = 0.7054$ and $\epsilon_{\text{Ndi}} = 1.1$), and indicates that in this particular case the leucosome was not hybridized.

An exceptional amphibolite gneiss sample ($\text{SiO}_2 = 52.82$ wt %) of the PMC (TNG108c in Table 5) has an isotope signature ($^{87}\text{Sr}/^{86}\text{Sr}_i = 0.7047$, $\epsilon_{\text{Ndi}} = 8.8$) close to the field of present day prevalent mantle (Zindler & Hart, 1986). This sample is isotopically and geochemically comparable to Kohistan-Ladakh island arc lavas (Northern Group, type 2 lavas in Rolland *et al.* 2002).

9. Discussion

9.1 Geochemical characteristics: comparison to other Miocene Himalayan leucogranites

Leucogranites of the broader Karakoram region are remarkably different from the High

Himalayan leucogranites studied in Nepal (e.g. Deniel *et al.*, 1987, Le Fort *et al.*, 1987). High Himalayan leucogranites are generally strongly peraluminous, have high Rb/Sr ratios and high $^{87}\text{Sr}/^{86}\text{Sr}$ (0.74-0.82), whereas Karakoram leucogranites are mildly peraluminous, have low Rb/Sr ratios and $^{87}\text{Sr}/^{86}\text{Sr}$ (0.71 to 0.72; Crawford & Windley, 1990). The leucogranites we studied in the Karakoram Shear Zone are geochemically comparable to the latter with A/CNK between 1.02 and 1.16, Rb/Sr ratios on average below one, and $^{87}\text{Sr}/^{86}\text{Sr}_i$ (0.7086 to 0.7121). Muscovite dehydration melting leads to high Rb/Sr ratios in the melt (Inger and Harris, 1993), whereas the low Rb/Sr ratios of the Karakoram rocks are most likely the result of H_2O -fluxed melting because plagioclase will melt preferably over biotite or muscovite (Patiño Douce & Harris, 1998).

9.2 Significance of water-fluxed melting

The significance of water-fluxed melting synchronous with deformation for crustal differentiation has been discussed for the European Alps (e.g. Berger *et al.*, 2008; Burri *et al.*, 2005). Most experimental work in the literature has been undertaken for fluid absent conditions where the limiting factor for melt production is the abundance of water-bearing phases, e.g. muscovite, in the source rock (see discussion in Clemens, 2006). This is in contrast with water-fluxed melting, where the availability of free water is the main limiting factor and melting would continue as long as water is brought into the system, for example via a shear zone (e.g. Genier *et al.*, 2008; Mogk, 1992). In the Karakoram Shear Zone these processes operate on a large scale, potentially giving rise to magma volumes of batholith dimensions.

9.3 Age relations between leucogranites and the Muglib Batholith

Titanite and zircon grains from the two leucogranite samples dated yielded slightly different ages: 16.4 ± 1.4 Ma for titanite (sample TNG148a; Fig. 13d), compared to 18.0 ± 0.4 Ma for zircon (sample TNG148b; Fig. 13e). Because the titanite is strongly enriched in common Pb and hence less reliable, we consider the 18.0 ± 0.4 Ma zircon age as most closely reflecting the crystallization age of the Tangtse Pluton. Despite the slight differences, the two results overlap within error. However, ID-TIMS zircon age data of the Tangtse Pluton (the Muglib dome of Phillips and Searle, 2007) yielded 15.1 ± 0.6 Ma (Phillips & Searle, 2007). Other age results for leucogranite intrusions in the Tangtse area include 15.6 ± 0.1 Ma for a sample within the Tangtse Shear Zone (Phillips *et al.*, 2004), 18.0 ± 0.6 Ma for a Grt-Ms-Bt-leucogranite sampled close to Tangtse (Searle *et al.*, 1998), and between 16.6 ± 0.2 Ma and 19.1 ± 1.1 Ma from Ms-Bt-leucogranite samples collected close to Darbuk (Ravikant *et al.*, 2009). A similar Ar-Ar age of 18 Ma was obtained for amphibole in an amphibolite sample from the Tangtse area (Rolland *et al.*, 2009). Late-stage pegmatite dykes from the Tangtse Shear Zone yielded an even younger U-Pb zircon age of 13.7 ± 0.2 Ma (Phillips *et al.*, 2004), but it is not clear whether these younger intrusions result from in situ melting of the anatectic rocks exposed in that area or whether they are intrusive rocks generated elsewhere. Due to the general spread in ages, we conclude that magmatism in the region lasted at least between 20 and 13.5 Ma and that the difference in ages found for the Tangtse Pluton (18.0 ± 0.4 Ma

and 15.1 ± 0.6 Ma) indicates the duration of its growth.

The younger ages of leucogranites in the Karakoram Shear Zone are comparable to samples from the Karakoram Batholith. A leucogranite sample collected close to Satti in the Nubra Valley, NW of the Pangong Metamorphic Complex, yielded a zircon SHRIMP crystallization age of 15.0 ± 0.4 Ma (Weinberg *et al.*, 2000), similar to a mylonitic leucogranite also from Satti (ID-TIMS zircon age 15.9 ± 0.1 Ma; Phillips *et al.*, 2004). A late-stage leucogranite dyke from this batholith collected further NW along strike of the Nubra Valley yielded ID-TIMS zircon age of 13.7 ± 0.3 Ma (Phillips *et al.*, 2004).

The crystallization ages of the calc-alkaline Muglib Batholith obtained here, at 71.4 ± 0.6 Ma (sample TNG62a) and 70.5 ± 0.6 Ma (sample TNG131a), overlap with a Rb-Sr age of 72 ± 8 Ma (Ravikant, 2006) for a Hbl-Bt granodiorite sample close to Muglib village, while Ravikant (2006) obtained a Rb-Sr age of 118 ± 15 Ma for a migmatitic granodiorite in the Tangtse gorge. A U-Pb SHRIMP zircon age of 68 ± 1 Ma was determined for the calc-alkaline Tirit granite at the confluence of the Shyok and Nubra Rivers by Weinberg *et al.* (2000). This suggests that a series of calc-alkaline bodies, possibly forming a continuous batholith that runs from Muglib along the Pangong Range and at the feet of the Saltoro Range in the Nubra Valley were emplaced between 67 and 72 Ma, possibly extending back to c. 120 Ma.

Titanite analyses of the Bt-granodiorite at the base of the Tangtse Pluton (Fig. 7b; sample TNG131a) yielded two age populations (Fig. 13c). The older group, 60-65 Ma, may represent early metamorphism in the Muglib Batholith, related to the heat from intrusion of late phases of calc-alkaline magmatism or, to slow cooling through the blocking temperature of titanite. The fact that the younger age range of ~11 to 21 Ma overlaps with the crystallization ages of the anatectic leucogranites of the Tangtse Pluton supports our interpretation that magma derived from anatexis of the Muglib Batholith contributed to form the Miocene leucogranite intrusions in the area. This interpretation is further supported by the presence of 63.0 ± 0.8 Ma zircon cores in Miocene leucogranites from Tangtse (Searle *et al.*, 1998). In the same study, a migmatitic orthogneiss, probably related to the Muglib Batholith, showed two age groups. The older group with a mean weighted U-Pb age of 106.3 ± 2.3 Ma was interpreted as the crystallization age of the orthogneiss, and the younger group with ages ranging between 22 and 15 Ma as the result of metamorphic growth during migmatization (Searle *et al.*, 1998).

9.4 Origin of the Muglib Batholith

Considering the temporal and compositional similarities between the Tirit granite and the Muglib Batholith, and the extent of our mapping in the region (Fig. 1), we suggest that a Cretaceous calc-alkaline body crops out semi-continuously for at least 85 km along the Karakoram Shear Zone: from SE of Muglib and northwestwards along the Pangong Range to the Nubra-Shyok confluence where it links with the Tirit granite along the northeastern side of the Saltoro Range (Weinberg *et al.*, 2000). These magmatic rocks are also temporally, chemically and isotopically similar to the Ladakh Batholith which crops out immediately south of the Karakoram Shear Zone (Ravikant *et al.*, 2009; Upadhyay *et al.*, 2008; Weinberg & Dunlap, 2000).

The Ladakh Batholith resulted from subduction-related calc-alkaline magmatism which ceased as a result of the collision with India ca. 50 Ma (Schärer *et al.*, 1984; Upadhyay *et al.*,

2008; Weinberg & Dunlap, 2000). Crystallization ages range between 49 Ma and 103 Ma, broadly coincident with those determined for the the Muglib-Tirit bodies with ages centered around 70 Ma. Ravikant *et al.* (2009) concluded that the Ladakh Batholith formed in two magmatic stages, one between 83 and 103 Ma and the other between 50 and 67 Ma. The 67-72 Ma age of the Muglib Batholith and Tirit granite (Ravikant 2006, Weinberg *et al.*, 2000) thus represent the upper end of the younger group. Calc-alkaline intrusions around 70 Ma are at odds with the model of ‘flat subduction’ of Neotethyan lithosphere that resulted in a cessation of magmatic activity at the South Tibetan margin in the period between 60 and 70 Ma (Wen *et al.*, 2008). However, given the large distance to the study area in Ladakh, this discrepancy might indicative diachronous changes along the subduction zone.

Both the Ladakh and Muglib Batholiths have an identical isotopic signature indicative of mantle derivation with only minor crustal influence, or derivation from crustal rocks that themselves have short crustal pre-histories. Based on these similarities we suggest that the calc-alkaline Muglib Batholith, including the Tirit granite, and the Ladakh Batholith are effectively part of the same island arc, developed south of the Asian margin.

9.5 Linking source to sink

9.5.1 Field relations

In migmatites of the Tangtse gorge region, layer parallel leucosomes in folds merge with axial planar leucosomes thus forming an interconnected melt flow network and demonstrating contemporaneity of anatexis with folding and shearing (Weinberg & Mark 2008). The network that arises allows for contemporaneous migration and mixing of magmas from different sources as demonstrated by the features documented at the base of the Tangtse Pluton (Fig. 7) and the Darbuk-Shyok gorge (Fig. 8) and supported by the isotope systematics (Fig. 14).

Moving up from outcrop scale, an interconnected network of leucogranite sheets, each several meters wide, is well developed in interlayered amphibolites and calc-silicate rocks hundreds of meters wide at the SW end of the Tangtse gorge and in the Darbuk-Shyok gorge over 13 km along strike (Fig. 15a). A large scale network is also developed in the anatectic calc-alkaline and meta-sedimentary rocks, but is much more irregular in terms of sheet orientations and widths (see also the Pangong Injection Complex of Weinberg & Searle, 1998). We interpret these networks as large-scale magma pathways through both anatectic and non-anatectic rocks.

This system of intrusive sheets is related to a number of kilometer-sized leucogranite plutons in the Karakoram Shear Zone, such as the Tangtse and Darbuk Plutons (Fig. 1b, 2) and the ~600 m wide sheeted body through the centre of the Pangong Range in Fig. 15b. The anastomosing sheet network, plutons and sheeted bodies are together interpreted as the magma transfer zone between the source and the Karakoram Batholith that crops out to the NW of the Pangong Range (Fig. 15b). This interpretation is supported by our mapping closer to the Karakoram Batholith and by isotopic similarity from the source all the way to the Karakoram Batholith. At Agham, further NW of the Tangtse-Darbuk area and at the southern tip of the Karakoram Batholith, leucogranite dykes partly retrogressed to greenschist facies,

intrude strongly deformed chlorite and muscovite schists as well as gabbroic rocks of the Muglib Batholith. Leucogranites here have the same isotopic composition as in the source area (sample AGH25a, Table 5). Further NW, the exposed contact between the Karakoram Batholith and its footwall in Rongdu is characterized by a network of mylonitized leucogranite sheets. Thus, sheets of essentially similar leucogranites can be followed from their source in the Pangong Range to the Karakoram Batholith over 80 km along strike.

This link between the source zone and the batholith is further supported by the presence of a kilometer-wide zone of Hbl-bearing leucogranites, including partly disrupted decimetric to metric enclaves of migmatitic Hbl-Cpx-diorite inside the Karakoram Batholith near Rongdu.

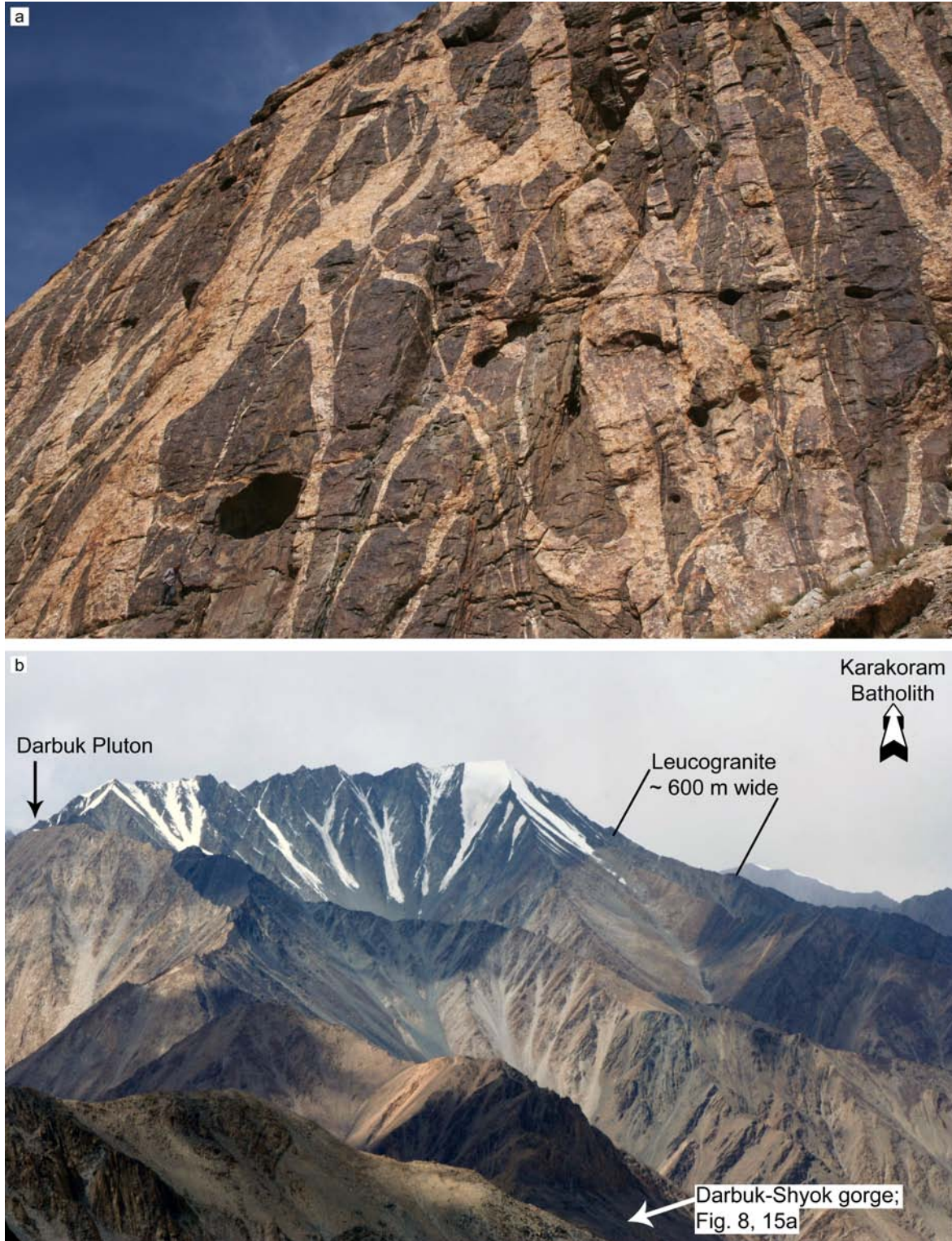


Fig. 15: Magma transport out of the source region. (a) Leucogranite dyke network in calc-silicate rocks the Darbuk-Shyok gorge. The dykes on this photo are up to ~5m wide and merge and split seamlessly. Person on lower left of photograph as scale (below and left of shadow). (b) Pangong Range looking NW, showing an elongated leucogranite body 600 m thick (light band) that can also be seen in satellite images. Viewpoint is Pangong Range close to the Tangtse Pluton. The band can be followed into the Darbuk-Shyok gorge, where the dyke network in (a) and Fig. 8 are exposed (closer to viewer). The leucogranite pluton on the left hand side is connected to the dyke network. The far ridge of the leucogranite band is 15 km along strike from viewpoint.

These Hbl-bearing leucogranites are similar to those documented in the source region near Muglib, and the migmatitic diorite enclaves are similar to the anatectic diorites of the Muglib Batholith and are interpreted to represent blocks of the migmatitic source. As seen above, the leucosomes in these dioritic enclaves yielded a hybrid signature similar to the rest of the Karakoram Batholith, rather than the pure signature of the Muglib Batholith (sample AGH23a, Table 5).

Along the NE side of the Nubra Valley, the Karakoram Batholith is emplaced in greenschist-facies meta-sedimentary rocks and meta-volcanic rocks (e.g Phillips *et al.*, 2004; Weinberg *et al.* 2000), and thus exposes a higher structural crustal level than the deeply exhumed upper amphibolite facies rocks of the PMC. Interestingly, the width of the Karakoram Batholith, as partly interpreted from satellite images, is similar to the width of the Pangong Range measured between the Tangtse and the Pangong shear zones (Fig. 1, 2). If the Karakoram Batholith intruded synkinematically (Mahéo *et al.*, 2004) as has also been demonstrated for the Tangtse Pluton and other leucogranites along the Karakoram Fault (Lacassin *et al.*, 2004; Rolland *et al.* 2009; Weinberg *et al.*, 2009), its measured displacement does not measure the full displacement on the Karakoram Shear Zone.

The southernmost tip of the Karakoram Batholith currently crops out ~40 km from the northernmost significant migmatite area in the Darbuk-Shyok gorge (Fig. 1a, b). Given the dextral movement on the shear zone, the Karakoram Batholith in Ladakh would have been further away from the migmatite area at the time of anatexis. The link between the anatectic rocks exposed in the PMC and the Karakoram Batholith demonstrated here does not necessarily imply that voluminous magma from this particular source found its way to the now exposed batholith, but rather suggests that the Karakoram Batholith was fed mostly from a source similar to the one exposed in the PMC.

9.5.2 Implications of the isotopic signatures

Initial $^{87}\text{Sr}/^{86}\text{Sr}$ and ϵ_{Ndi} values of the leucogranites and leucosomes from the Pangong Range are intermediate between those of the meta-sedimentary rocks of the Pangong Metamorphic Complex and the Muglib Batholith, the likely magma sources. In the $^{87}\text{Sr}/^{86}\text{Sr}_i$ vs. ϵ_{Ndi} diagram (Fig. 14), these intermediate values lie in a field defined by hyperbolic mixing curves between representative end member compositions. It is interesting to notice that leucosomes, interpreted to be roughly *in situ*, also have mixed signatures (samples TNG71a, TNG131g; Table 5). The only exception is a tonalitic leucosome sample (sample TNG170, Table 5) from a metatexite migmatite in the central part of the Tangtse gorge. It yields isotopic values similar to a patchy melanosome in diorite (sample TNG169a) in the

same outcrop and also to other samples of the Muglib Batholith. These findings suggest that in general, mixing occurred at an early stage in the migration history of the magmas.

These hybrid leucogranites exposed close to the source have similar values to those in intrusive sheets or plutons in the vicinity, as well as to those of the Karakoram Batholith (samples AGH25a, NBR1b, NBR2a and NBR3b in Table 5) supporting our field-based interpretation that the system is effectively connected from the source in the Pangong Range to the Karakoram Batholith. This is further supported by Hf isotope data, which suggest a similar origin for the leucogranites in the Karakoram Shear Zone and granitoids of similar ages of the Karakoram Batholith (Ravikant *et al.*, 2009). We therefore conclude that magmas derived from the meta-sedimentary sequence and the calc-alkaline Muglib Batholith mixed early in their migration, and that this mixed magma gave rise to the Karakoram Batholith.

9.6 Similar leucogranite intrusions elsewhere in the Karakoram?

The Hunza Plutonic Unit and the Baltoro Batholith in Pakistan mark the NW continuation of the Karakoram Batholith (Crawford & Windley, 1990; Searle *et al.*, 1992; Searle *et al.*, 1998; Srimal, 1986). The Baltoro Batholith is mostly composed of Bt \pm Ms \pm Grt-monzogranites and leucogranites that show mineralogical and geochemical similarities to the leucogranites of the Karakoram Shear Zone and the Karakoram Batholith (Searle *et al.*, 1992), and are only slightly older (U-Pb zircon age 21 ± 0.5 Ma; Parrish and Tirrul, 1989). Trace element concentrations of our granites compare well to those of the Baltoro granite (Fig. 16; Crawford

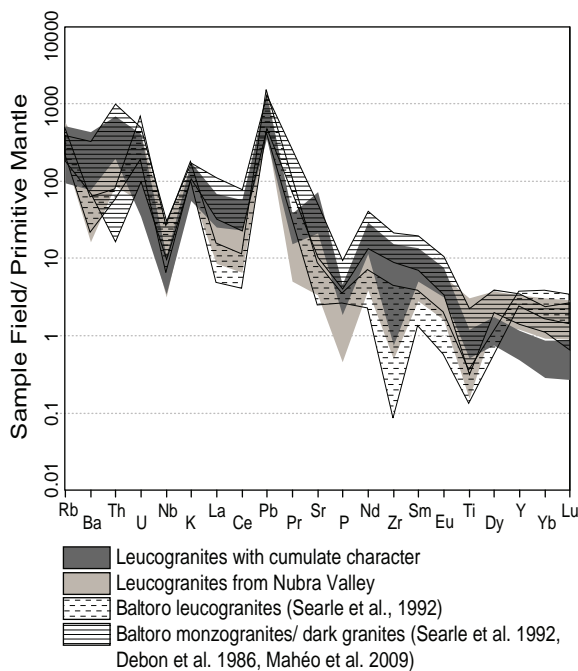


Fig. 16: Comparison of averaged subsets of leucogranite samples to available data for Baltoro granites. Samples are normalized to primitive mantle composition (Sun and McDonough, 1989). Leucogranites with cumulate character (high Sr and Ba): $N = 9$; leucogranites from Nubra Valley: $N = 9$; Baltoro leucogranites: $N = 5$; Baltoro monzogranites: $N = 4$; Baltoro dark granites: $N = 5$.

& Windley, 1990; Mahéo *et al.*, 2009), suggesting a genetic link across the Pakistan-India border and across the Karakoram Shear Zone. Comparison of isotopic data in Fig. 14 further supports this link. Here we have included isotope data for the Karakoram and Baltoro granites, and granites of the Hunza Plutonic Unit from previous studies. Some of the Baltoro and Hunza samples overlap with our data, but others tend to show lower ϵ_{Nd} and some samples show higher $^{87}\text{Sr}/^{86}\text{Sr}_i$ values.

The isotope data for the Hunza and Baltoro granitoids can be explained using the same two source rocks inferred to have produced the Karakoram Batholith, but require more input from the meta-sedimentary sequence carrying the crustal signature. Whilst the Karakoram Batholith requires 40-70 % input from magmas derived from the meta-sedimentary rocks, the Hunza and Baltoro granitoids require more than 70%. Exceptions are samples from Karakoram granites in

Pakistan that show an even stronger crustal signature. Schärer *et al.* (1990) proposed, based on zircon and monazite inheritance and Pb, Sr and Nd isotopes that likely sources of these granites are the meta-sedimentary rocks of the Karakoram Metamorphic Complex in that region.

Alternative sources for the origin of the isotopic signature of granites in the Hunza and Baltoro areas have been suggested by Mahéo *et al.* (2002) and Mahéo *et al.* (2009). These include melting of metasomatized mantle in which melting was induced by asthenospheric upwelling after an inferred slab break-off of the subducted Indian plate, at the time of magmatism in the Karakoram and South Tibet. This component is indicated by the presence of lamprophyres cropping out in the area and which would have provided the heat for crustal melting or mixed with other magma sources to produce the leucogranites (Mahéo *et al.*, 2009). Further, Mahéo *et al.* (2009) proposed partial melting of Cretaceous, calc-alkaline mafic to dioritic lower crust to account for the Baltoro granitic magmatism.

Multiple alternatives may be and have been proposed for interpreting essentially the same isotopic signatures. We argue that field relations allow us to directly document the process of magma generation and migration from the anatectic terrane exposed in the Pangong Metamorphic Complex, comprising a Late Cretaceous island arc batholith and its meta-sedimentary country rocks, to the Miocene leucogranites of the Karakoram Batholith.

10. Conclusions

In the Karakoram Shear Zone, anatexis of Late Cretaceous calc-alkaline granodiorites and diorites of the Muglib Batholith and of meta-sedimentary rocks of the Pangong Metamorphic Complex took place during deformation and as a result of water-fluxed melting. Magmas from this heterogeneous source formed an extensive network of channels, across a number of scales, which allowed for extraction. The initial $^{87}\text{Sr}/^{86}\text{Sr}$ and ϵ_{Nd} values of leucosomes, leucogranite sheets, stocks and plutons in the Karakoram Shear Zone are similar to those of the Karakoram Batholith and vary between 0.7086 to 0.7121 and -7.1 to -3.6, respectively. This is a hybrid signature between the two sources identified in the anatectic zone. We conclude therefore that the Karakoram Batholith is a result of melting of a heterogeneous source in the presence of a water-rich fluid, and that the mixing of these different magmas took place already within the source region.

Acknowledgements

We would like to thank Yann Rolland and Vadlamani Ravikant for constructive reviews and Olav Eklund for handling of the paper in the editing process. We also thank Bruce Schaefer for helpful discussions on isotope geochemistry, Roland Maas for carrying out isotope analysis, as well as Massimo Raveggi for help with ICP-MS analysis. This paper is part of the PhD thesis of the first author.

References

- Aleynikov, J. N., Wintsch, R. P., Tollo, R. P., Unruh, D. M., Fanning, C. M. & Schmitz, M. D. (2007). Ages and origins of rocks of the Killingworth Dome, south-central Connecticut; implications for the tectonic evolution of southern New England.

- American Journal of Science* 307, 63-118.
- Andersson, U. B. (1991). Granitoid episodes and mafic/felsic magma interaction in the Svecofennian of the Fennoscandian Shield, with main emphasis on the approximately 1.8 Ga plutonics. *Precambrian Research* 51, 127-149.
- Andersson, U. W., Neymark, L. A. & Billstrom, K. (2002). Petrogenesis of Mesoproterozoic (Subjotnian) rapakivi complexes of central Sweden; implications from U-Pb zircon ages, Nd, Sr and Pb isotopes. *Transactions of the Royal Society of Edinburgh: Earth Sciences* 92, Part 3-4, 201-228.
- Arth, J. G. (1976). Behavior of trace elements during magmatic processes; a summary of theoretical models and their applications. *Journal of Research of the U. S. Geological Survey* 4, 41-47.
- Beard, J. S., Ragland, P. C. & Crawford, M. L. (2005). Reactive bulk assimilation; a model for crust-mantle mixing in silicic magmas. *Geology* 33, 681-684.
- Berger, A., Burri, T., Alt-Epping, P. & Engi, M. (2008). Tectonically controlled fluid flow and water-assisted melting in the middle crust: An example from the Central Alps. *Lithos* 102, 598-615.
- Black, L. P., Kamo, S. L., Allen, C. M., Aleinikoff, J. N., Davis, D. W., Korsch, R. J. & Foudoulis, C. (2003). TEMORA 1; a new zircon standard for Phanerozoic U-Pb geochronology. *Chemical Geology* 200, 155-170.
- Brown, E. T., Bendick, R., Bourles, D. L., Gaur, V., Molnar, P., Raisbeck, G. M. & Yiou, F. (2002). Slip rates of the Karakorum fault, Ladakh, India, determined using cosmic ray exposure dating of debris flows and moraines. *Journal of Geophysical Research* 107 Art. No. 2192.
- Burri, T., Berger, A. & Engi, M. (2005). Tertiary migmatites in the Central Alps: Regional distribution, field relations, conditions of formation and tectonic implications. *Schweizerische Mineralogische und Petrographische Mitteilungen* 85, 215-232.
- Clemens, J. D. (2006). Melting of the continental crust; fluid regimes, melting reactions, and source rock fertility. In: Brown, M., Rushmer, T. (ed.) *Evolution and differentiation of the continental crust*. New York, NY, United States: Cambridge University Press, 296-330.
- Clemens, J. D. & Vielzeuf, D. (1987). Constraints on melting and magma production in the crust. *Earth and Planetary Science Letters* 86, 287-306.
- Crawford, M. B. & Searle, M. P. (1992). Field relationships and geochemistry of pre-collisional (India-Asia) granitoid magmatism in the central Karakoram, northern Pakistan. *Tectonophysics* 206, 171-192.
- Crawford, M. B. & Windley, B. F. (1990). Leucogranites of the Himalaya/Karakoram: implications for magmatic evolution within collisional belts and the study of collision-related leucogranite petrogenesis. *Journal of Volcanology and Geothermal Research* 44, 1-19.
- Debon, F., Zimmermann, J. L. & Bertrand, J. M. (1986). Le granite du Baltoro (batholite axial du Karakorum, nord Pakistan): une intrusion subalkaline d'âge Miocène Supérieur. *Comptes Rendus de l'Académie des Sciences, Paris, Série II* 303, 463-468.
- Deniel, C., Vidal, P., Fernandez, A., Le Fort, P. & Peucat, J. J. (1987). Isotopic study of the Manaslu granite (Himalaya, Nepal); inference on the age and source of Himalayan leucogranites. *Contributions to Mineralogy and Petrology* 96, 78-92.
- Dunlap, W. J., Weinberg, R. F. & Searle, M. P. (1998). Karakoram fault zone rocks cool in two phases. *Journal of the Geological Society of London* 155, 903-912.
- Eggins, S. M., Woodhead, J. D., Kinsley, L. P. J., Mortimer, G. E., Sylvester, P., McCulloch, M. T., Hergt, J. M. & Handler, M. R. (1997). A simple method for the precise determination of ≥ 40 trace elements in geological samples by ICPMS using enriched isotope internal standardisation. *Chemical Geology* 134, 311-326.
- Gardien, V., Thompson, A. B. & Ulmer, P. (2000). Melting of biotite + plagioclase + quartz gneisses; the role of H (sub 2) O in the stability of amphibole. *Journal of Petrology*

- 41, 651-666.
- Genier, F., Bussy, F., Epard, J.-L. & Baumgartner, L. (2008). Water-assisted migmatization of metagraywackes in a Variscan shear zone, Aiguilles-Rouges massif, western Alps. *Lithos* 102, 575-597.
- Guillot, S. & Le Fort, P. (1995). Geochemical constraints on the bimodal origin of High Himalayan leucogranites. *Lithos* 35, 221-234.
- Hawkesworth, C. J. & Vollmer, R. (1979). Crustal contamination versus enriched mantle: $^{143}\text{Nd}/^{144}\text{Nd}$ and $^{87}\text{Sr}/^{86}\text{Sr}$ evidence from the Italian volcanics. *Contributions to Mineralogy and Petrology* 69, 151-165.
- Holtz, F., Pichavant, M., Barbey, P. & Johannes, W. (1992). Effects of H_2O on liquidus phase relations in the haplogranite system at 2 and 5 kbar. *American Mineralogist* 77, 1223-1241.
- Honegger, K., Dietrich, V., Frank, W., Gansser, A., Thöni, M. & Trommsdorff, V. (1982). Magmatism and metamorphism in the Ladakh Himalayas (the Indus-Tsangpo suture zone). *Earth and Planetary Science Letters* 60, 253-292.
- Inger, S. & Harris, N. (1993). Geochemical constraints on leucogranite magmatism in the Langtang Valley, Nepal Himalaya. *Journal of Petrology* 34, 345-368.
- Jade, S., Bhatt, B. C., Yang, Z., Bendick, R., Gaur, V. K., Molnar, P., Anand, M. B. & Kumar, D. (2004). GPS measurements from the Ladakh Himalaya, India: Preliminary tests of plate-like or continuous deformation in Tibet *Geological Society of America Bulletin* 116, 1385-1391.
- Kenah, C. & Hollister, L. S. (1983). Anatexis in the Central Gneiss Complex. In: Atherton, M. P., Gribble, C. D. (ed.) *Migmatites, Melting, and Metamorphism*. Nantwich: Shiva, 142-162.
- Kretz, R. (1983). Symbols for rock-forming minerals. *American Mineralogist* 68, 277-279.
- Lappin, A. R. & Hollister, L. S. (1980). Partial melting in the Central Gneiss Complex near Prince Rupert, British Columbia. *American Journal of Science* 280, 518-545.
- Le Fort, P., Cuney, M., Deniel, C., France-Lanord, C., Sheppard, S. M. F., Upreti, B. N. & Vidal, P. (1987). Crustal generation of the Himalayan leucogranites. *Tectonophysics* 134, 39-57.
- Ludwig, K. R. (2001). SQUID 1.02, A user's manual. *Berkeley Geochronology Center Special Publication* 2.
- Ludwig, K. R. (2003). User's manual for Isoplot/Ex, Version 3.0, A geochronological toolkit for Microsoft Excel. *Berkeley Geochronology Center Special Publication* 4.
- Maas, R., Kamenetsky, M. B., Sobolev, A. V., Kamenetsky, V. S. & Sobolev, N. V. (2005). Sr, Nd, and Pb isotope evidence for a mantle origin of alkali chlorides and carbonates in the Udachnaya Kimberlite, Siberia. *Geology* 33, 549-552.
- Maas, R. & McCulloch, M. T. (1991). The provenance of Archean clastic metasediments in the Narryer Gneiss Complex, Western Australia; trace element geochemistry, Nd isotopes, and U-Pb ages for detrital zircons. *Geochimica et Cosmochimica Acta* 55, 1915-1932.
- Mahéo, G., Blichert-Toft, J., Pin, C., Guillot, S. & Pêcher, A. (2009). Partial Melting of Mantle and Crustal Sources beneath South Karakorum, Pakistan: Implications for the Miocene Geodynamic Evolution of the India-Asia Convergence Zone. *Journal of Petrology*, 427-449.
- Mahéo, G., Guillot, S., Blichert-Toft, J., Rolland, Y. & Pêcher, A. (2002). A slab breakoff model for the Neogene thermal evolution of South Karakorum and South Tibet. *Earth and Planetary Science Letters* 195, 45-58.
- Mahéo, G., Pêcher, A., Guillot, S., Rolland, Y. & Delacourt, C. (2004). Exhumation of Neogene gneiss domes between oblique crustal boundaries in south Karakorum, northwest Himalaya, Pakistan. *Special Paper - Geological Society of America* 380, 141-154.
- McLellan, E. L. (1988). Migmatite structures in the Central Gneiss Complex, Boca de

- Quadra, Alaska. *Journal of Metamorphic Geology* 6, 517-542.
- Mogk, D. W. (1992). Ductile shearing and migmatization at mid-crustal levels in an Archaean high-grade gneiss belt, northern Gallatin Range, Montana, USA. *Journal of Metamorphic Geology* 10, 427-438.
- Parrish, R. R. & Tirrul, R. (1989). U-Pb age of the Baltoro granite, northwest Himalaya, and implications for monazite U-Pb systematics. *Geology* 17, 1076-1079.
- Patiño Douce, A. E. & Harris, N. (1998). Experimental constraints on Himalayan anatexis. *Journal of Petrology* 39, 689-710.
- Phillips, R. J., Parrish, R. R. & Searle, M. P. (2004). Age constraints on ductile deformation and long-term slip rates along the Karakoram fault zone, Ladakh. *Earth and Planetary Science Letters* 226, 305-319.
- Phillips, R. J. & Searle, M. P. (2007). Macrostructural and microstructural architecture of the Karakoram fault; relationship between magmatism and strike-slip faulting. *Tectonics* 26.
- Raczek, I., Jochum, K. P. & Hofmann, A. W. (2003). Neodymium and strontium isotope data for USGS reference materials BCR-1, BCR-2, BHVO-1, BHVO-2, AGV-1, AGV-2, GSP-1, GSP-2 and eight MPI-DING reference glasses. *Geostandards Newsletter* 27, 173-179.
- Ravikant, V. (2006). Utility of Rb-Sr geochronology in constraining Miocene and Cretaceous events in the eastern Karakoram, Ladakh, India. *Journal of Asian Earth Sciences* 27, 534-543.
- Raz, U. & Honegger, K. (1989). Magmatic and tectonic evolution of the Ladakh Block from field studies. *Tectonophysics* 161, 107-118.
- Rex, A. J., Searle, M. P., Tirrul, R., Crawford, M. B., Prior, D. J., Rex, D. C. & Barnicoat, A. C. (1988). The geochemical and tectonic evolution of the central Karakoram, North Pakistan. *Philosophical Transactions of the Royal Society of London, Series A: Mathematical and Physical Sciences* 326, 229-255.
- Rolland, Y., Mahéo, G., Pêcher, A. & Villa, I. M. (2009). Syn-kinematic emplacement of the Pangong metamorphic and magmatic complex along the Karakorum Fault (N Ladakh). *Journal of Asian Earth Sciences* 34, 10-25.
- Rolland, Y. & Pêcher, A. (2001). The Pangong granulites of the Karakoram Fault (western Tibet); vertical extrusion within a lithosphere-scale fault? *Comptes Rendus de l'Academie des Sciences, Serie II. Sciences de la Terre et des Planetes* 332, 363-370.
- Rolland, Y., Picard, C., Pêcher, A., Lapierre, H., Bosch, D. & Keller, F. (2002). The cretaceous Ladakh arc of NW himalaya--slab melting and melt-mantle interaction during fast northward drift of Indian Plate. *Chemical Geology* 182, 139-178.
- Rollinson, H. R. (1993). *Using geochemical data; evaluation, presentation, interpretation*: Longman Scientific & Technical, Harlow, United Kingdom.
- Rutter, E. H., Faulkner, D. R., Brodie, K. H., Phillips, R. J. & Searle, M. P. (2007). Rock deformation processes in the Karakoram fault zone, Eastern Karakoram, Ladakh, NW India. *Journal of Structural Geology* 29, 1315-1326.
- Sawyer, E. W. (2008). *Atlas of migmatites*: Mineralogical Association of Canada, Ottawa, ON, Canada 9, pp. 371.
- Schärer, U., Copeland, P., Harrison, T. M., Searle, M. P. (1990). Age, cooling history, and origin of post-collisional leucogranites in the Karakoram Batholith; a multi-system isotope study. *Journal of Geology* 98, 233-251.
- Schärer, U., Hamet, J. & Allègre, C. J. (1984). The Transhimalaya (Gangdese) plutonism in the Ladakh region: a UPb and RbSr study. *Earth and Planetary Science Letters* 67, 327-339.
- Searle, M. P. (1996). Geological evidence against large-scale pre-Holocene offsets along the Karakoram Fault: Implications for the limited extrusion of the Tibetan plateau. *Tectonics* 15, 171-186.

- Searle, M. P., Crawford, M. B., Rex, A. J. (1992). Field relations, geochemistry, origin and emplacement of the Baltoro granite, Central Karakoram. *Transactions of the Royal Society of Edinburgh: Earth Sciences* 83, 519-538.
- Searle, M. P. & Tirrul, R. (1991). Structural and thermal evolution of the Karakoram crust. *Journal of the Geological Society* 148, 65-82.
- Searle, M. P., Weinberg, R. F. & Dunlap, W. J. (1998). Transpressional tectonics along the Karakoram Fault Zone, northern Ladakh. In: Holdsworth, R. E. & Strachan, R. A. (eds.) *Continental Transpressional and Transtensional Tectonics*. London: Geological Society of London Special Publication, 307-326.
- Srimal, N. (1986). India-Asia collision: implications from the geology of the eastern Karakoram. *Geology* 14, 523-527.
- Tanaka, T., Togashi, S., Kamioka, H., Amakawa, H., Kagami, H., Hamamoto, T., Yuhara, M., Orihashi, Y., Yoneda, S., Shimizu, H., Kunimaru, T., Takahashi, K., Yanagi, T., Nakano, T., Fujimaki, H., Shinjo, R., Asahara, Y., Tanimizu, M. & Dragusanu, C. (2000). JNdi-1; a neodymium isotopic reference in consistency with LaJolla neodymium. *Chemical Geology* 168, 279-281.
- Tera, F. & Wasserburg, G. J. (1972). U-Th-Pb systematics in three Apollo 14 basalts and the problem of initial Pb in lunar rocks. *Earth and Planetary Science Letters* 14, 281-304.
- Upadhyay, R., Frisch, W. & Siebel, W. (2008). Tectonic implications of new U-Pb zircon ages of the Ladakh Batholith, Indus suture zone, northwest Himalaya, India. *Terra Nova* 20, 309-317.
- Valli, F., Arnaud, N., Leloup, P. H., Sobel, E. R., Mahéo, G., Lacassin, R., Guillot, S., Li, H., Tapponnier, P. & Xu, Z. (2007). Twenty million years of continuous deformation along the Karakorum fault, western Tibet: A thermochronological analysis. *Tectonics* 26.
- Vance, D. & Thirlwall, M. (2002). An assessment of mass discrimination in MC-ICPMS using Nd isotopes. *Chemical Geology* 185, 227-240.
- Weinberg, R. F. & Dunlap, W. J. (2000). Growth and deformation of the Ladakh Batholith, Northwest Himalayas; implications for timing of continental collision and origin of calc-alkaline batholiths. *Journal of Geology* 108, 303-320.
- Weinberg, R. F., Dunlap, W. J. & Whitehouse, M. (2000). New field, structural and geochronological data from the Shyok and Nubra valleys, northern Ladakh: linking Kohistan to Tibet. In: Khan, A., Treloar, P. J. & Searle, M. P. (eds.) *Tectonics of the Nanga Parbat Syntaxis and the Western Himalaya*. London: Geological Society of London Special Publication, 253-275.
- Weinberg, R. F. & Mark, G. (2008). Magma migration, folding, and disaggregation of migmatites in the Karakoram shear zone, Ladakh, NW India. *Geological Society of America Bulletin* 120, 994-1009.
- Weinberg, R. F., Mark, G. & Reichardt, H. (2009). Magma ponding in the Karakoram shear zone, Ladakh, NW India. *Geological Society of America Bulletin* 121, 278-285.
- Weinberg, R. F. & Searle, M. P. (1998). The Pangong Injection Complex, Indian Karakoram: a case of pervasive granite flow through hot viscous crust. *Journal of the Geological Society of London* 155, 883-891.
- Wen, D.-R., Liu, D., Chung, S.-L., Chu, M.-F., Ji, J., Zhang, Q., Song, B., Lee, T.-Y., Yeh, M.-W. & Lo, C.-H. (2008). Zircon SHRIMP U-Pb ages of the Gangdese Batholith and implications for Neotethyan subduction in southern Tibet. *Chemical Geology* 252, 191-201.
- Williams, I. S. (1998). U-Th-Pb geochronology by ion microprobe. *Reviews in Economic Geology* 7, 1-35.
- Williams, I. S. & Hergt, J. M. (2000). U-Pb dating of Tasmanian dolerites: A cautionary tale of SHRIMP analysis of high-U zircon. *Beyond 2000: New Frontiers in Isotope Geoscience*, 185-188.

- Wright, T. J., Parsons, B., England, P.C., Fielding, E. J. (2004). InSAR observations of low slip rates on the major faults of western Tibet. *Science* 305, 236-239.
- Zindler, A. & Hart, S. R. (1986). Chemical geodynamics. *Annual Review of Earth and Planetary Sciences* 14, 493-571.

Declaration for Thesis Chapter 3

Declaration by candidate

In the case of Chapter 3, the nature and extent of my contribution to the work was the following:

Nature of contribution	Extent of contribution (%)
Development of ideas, collection of data, writing up and interpretation of results.	80%

The following co-authors contributed to the work. Co-authors who are students at Monash University must also indicate the extent of their contribution in percentage terms:

Name	Nature of contribution	Extent of contribution (%) for student co-authors only
Roberto Weinberg	Development of ideas, intellectual input during revision process.	

Candidate's
Signature

	Date
--	-------------

Declaration by co-authors

The undersigned hereby certify that:

- (1) the above declaration correctly reflects the nature and extent of the candidate's contribution to this work, and the nature of the contribution of each of the co-authors.
- (2) they meet the criteria for authorship in that they have participated in the conception, execution, or interpretation, of at least that part of the publication in their field of expertise;
- (3) they take public responsibility for their part of the publication, except for the responsible author who accepts overall responsibility for the publication;
- (4) there are no other authors of the publication according to these criteria;
- (5) potential conflicts of interest have been disclosed to (a) granting bodies, (b) the editor or publisher of journals or other publications, and (c) the head of the responsible academic unit; and
- (6) the original data are stored at the following location(s) and will be held for at least five years from the date indicated below:

Location(s) School of Geosciences, Monash University

Signature 1

	Date
--	-------------

Chapter III.

Hornblende chemistry in meta- and diatexites and its fractionation in leucogranite magma

Abstract

A suite of calc-alkaline arc rocks in the Pangong Metamorphic Complex in the Karakoram Shear Zone, Ladakh, NW India, was migmatized at upper amphibolite facies under water-fluxed conditions. Meta- and diatexites contain abundant hornblende in leucosome and melanosome. These form idiomorphic, poikilitic megacrysts in the leucosome or form melanosome rims around leucosomes. Hornblende chemistry, particularly its REE pattern, is highly variable in protoliths and neosomes, and in most cases the REE contents do not reflect hornblende partition coefficients reported in the literature. These variations are systematic and the result of complex crystallization histories of migmatites. REE variations in whole rock diatexites and leucogranites demonstrate the role of hornblende in controlling the REE budget. Fractionation of HREE-enriched hornblende and its accumulation in the source, results in leucogranitic magmas with high La_n/Yb_n and Sr/Y values typical of adakites. We thus show that leucogranitic magmas, depleted in HREE can be generated by water-fluxed partial melting of arc-related rocks in the mid-crust without involvement of garnet retention in the source.

1. Introduction

Fractionation of hornblende is a significant factor for crustal differentiation (Arth & Barker, 1976; Davidson *et al.*, 2007; Defant & Drummond, 1990; Foley *et al.*, 2002; Patiño Douce, 1999). The geochemical signatures of Archean tonalite-trondhjemite-gneisses (TTGs) and adakites with typical high La_n/Yb_n and Sr/Y values are generally thought to be largely the result of fractionation processes that lead to residual rocks rich in hornblende and garnet in the source (Defant & Drummond, 1990; Martin, 1987; Martin, 1999; Nehring *et al.*, 2009). Tiepolo & Tribuzio (2008) proposed that hornblende fractionation alone, without involvement of garnet can account for highly fractionated, HREE depleted magmas. Although many model calculations are well-constrained in terms of whole rock and mineral chemistry, field relations that confirm the modelled processes are relatively scarce because they involve mantle and lower crustal restitic rocks or melt sources that are rarely exposed.

The Pangong Metamorphic Complex in Ladakh, NW India, exposes migmatites that have hornblende as a peritectic phase. *In situ* leucosomes feed into a network of leucogranite magma sheets that locally coalesce to form stocks and plutons, and eventually feed into the Karakoram Batholith (Reichardt *et al.*, 2010). Building on field relations, we investigate hornblende chemistry and its link with the REE composition of source rocks, meta- and

diatexites, and leucogranites. We show that hornblende REE patterns vary amongst different samples and that their fractionation exerts a strong control on the REE budget of the magmatic rocks, explaining why some of these rocks have high La_n/Yb_n and Sr/Y values similar to Archean TTGs and adakites.

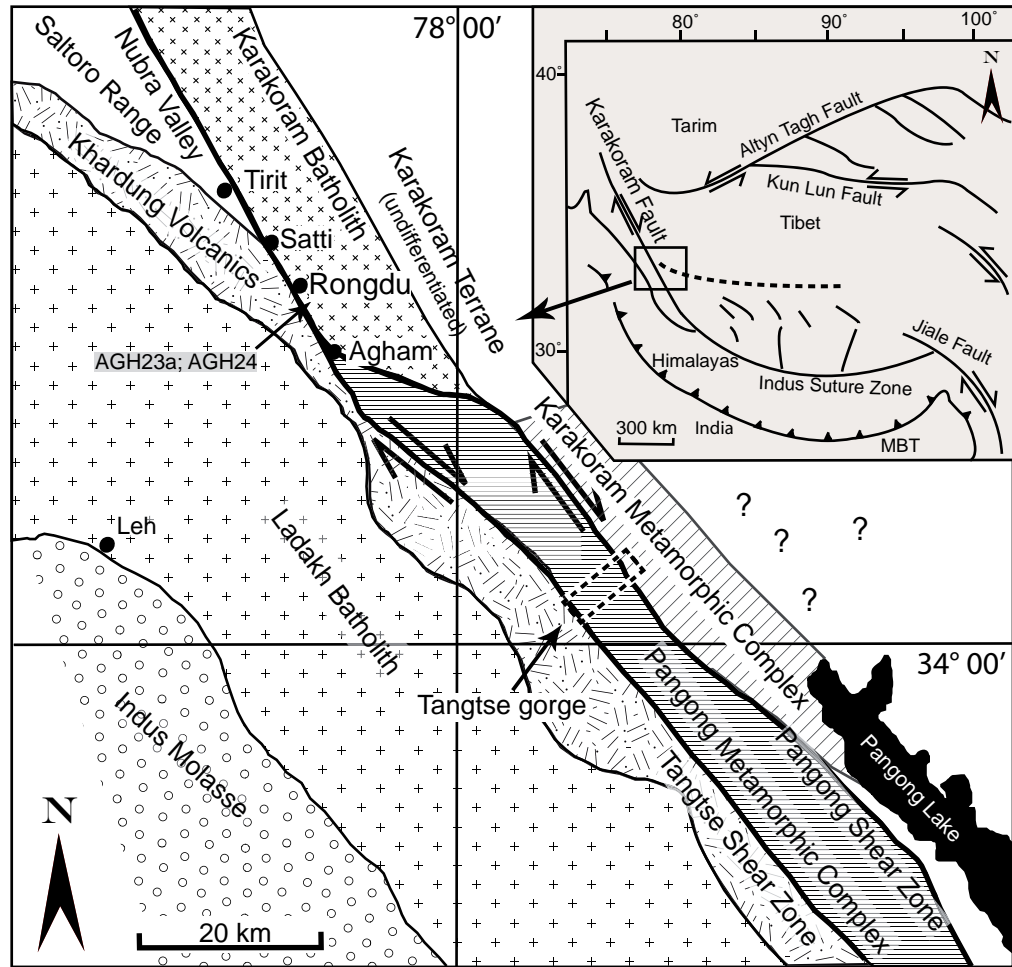


Fig. 1: Geological map of the Karakoram Shear Zone in Ladakh, NW India. Location of the Tangtse gorge in the Pangong Metamorphic Complex (PMC) is indicated by dashed frame. Sample location in Rongdu area is indicated by arrow.

2. Geological background

The Pangong Metamorphic Complex is exposed in the central part of the Karakoram Shear Zone (Fig. 1). Here, the shear zone that runs NW-SE for a least 700 km from the Pamir Mountains in Pakistan through the Eastern Karakoram to the Mt Kailas region in India, is divided into two parallel strands, the Tangtse and the Pangong Shear Zones (Fig. 1). The Tangtse Shear Zone bounds rocks of the Ladakh arc to the SW from those of the Pangong Metamorphic Complex (PMC). The Pangong Shear Zone bounds the PMC from rocks of the Karakoram Metamorphic Complex (KMC) to the NE. The Ladakh arc rocks are mainly calc-alkaline granitoids ranging from granites to gabbros that have crystallization ages ranging between 49 and 103 Ma (Schärer *et al.*, 1984; Singh *et al.*, 2007; Upadhyay *et al.*, 2008; Weinberg & Dunlap, 2000), and are associated with a volcanic sequence, known as the Khardung Volcanics. The KMC consists mainly of staurolite-garnet schists, amphibolites and marbles (McCarthy & Weinberg, in press). The PMC comprises a calc-alkaline granitoid suite of Hbl-Bt-granodiorites and diorites, consisting of varying proportions of plagioclase,

K-feldspar, quartz, hornblende and titanite, commonly with the accessory minerals allanite, apatite and zircon. Mafic varieties of diorites commonly contain clinopyroxene. Only Bt-granodiorites are hornblende-free. These rocks form the Muglib Batholith (Reichardt *et al.*, 2010; Weinberg *et al.*, 2009) and intruded amphibolites, calc-silicate rocks, Bt-psammites, Bt-pelites and minor marble beds. Rocks of the Muglib Batholith have crystallization ages centred around 70 Ma (see Chapter II; Ravikant, 2006; Reichardt *et al.*, 2010; Weinberg *et al.*, 2000) and isotopic compositions similar to the Ladakh arc (Ravikant, 2006; Reichardt *et al.*, 2010). Amphibolites in the PMC have been related to volcanic rocks of the Ladakh arc (Rolland *et al.*, 2009; Rolland *et al.*, 2002). Whole rock geochemistry of all major rock groups in the PMC was presented by Reichardt *et al.* (Chapter II), showing typical calc-alkaline trends for the arc-related rocks.

Rolland & Pêcher (2001) determined that peak metamorphic temperatures in the Tangtse area reached 700 ± 20 °C at 7 ± 1 kbar based on thermobarometric calculations using mineral chemistry. Rocks of the calc-alkaline granitoid suite and Bt-psammites were migmatized under water-fluxed conditions (Reichardt *et al.*, 2010), as inferred from the lack of anhydrous peritectic minerals such as garnet, pyroxene or sillimanite, and the presence of peritectic hornblende. Leucogranite dykes, stocks and plutons that span crystallization ages from ~13.5 to ~20 Ma (Phillips *et al.*, 2004; Ravikant *et al.*, 2009; Reichardt *et al.*, 2010; Searle *et al.*, 1998; Weinberg & Searle, 1998) have been related to anatexis of the PMC, based on field relations, geochronological and isotopic data (Reichardt *et al.*, 2010; Weinberg & Searle, 1998). These leucogranite dykes and sheets link the source region to the Karakoram Batholith, and are generally mildly peraluminous Bt \pm Ms \pm Grt-leucogranites to leucotonalites and commonly show feldspar cumulate signatures (high Sr, Ba; Reichardt *et al.*, 2010, Chapter II).

This study focuses on the exposures of the Tangtse gorge (Fig. 1) that transects the Karakoram Shear Zone and exposes a cross-section of all major lithologies in the PMC, including a several hundred meters wide layer of meta- and diatexites and the Pangong Injection Complex (Weinberg & Searle, 1998; Weinberg *et al.*, 2009).

3. Migmatite morphology and hornblende accumulation

In the Tangtse gorge area (Fig. 2) migmatized calc-alkaline arc rocks have abundant hornblende in the leucosome. There are also large areas where calc-alkaline rocks are not migmatized, presumably because of the lack of infiltrating water. Metatexites show alternating leucocratic, mesocratic and melanocratic layers. These are interpreted to represent melt-enriched parts (leucosome) and melt-depleted, residual parts (melanosome) as well as compositional differences in the unmelted protolith. Mesocratic layers (mesosome) in migmatized areas are also regarded as melanosome because they are inferred to have lost melt. Patchy leucosomes are also common. Leucosomes have varying modal contents of plagioclase, K-feldspar, quartz, hornblende, biotite and titanite giving rise to leucosomes ranging compositionally from leucogranite to trondhjemite. Leucosomes are mostly medium-grained, but plagioclase and K-feldspar megacrysts up to ~3 cm long are also common. Leucosomes often show dextral C-S fabrics defined by deformed feldspar and biotite foliae wrapping around feldspar grains. Tonalitic, K-feldspar-poor leucosomes are

generally related to the more mafic, dioritic protoliths. Leucosome with diffuse boundaries to melanosome in shear planes suggests syn-deformational melting (Fig. 4 in Chapter II). Tight to isoclinal folds show leucosomes parallel to the axial plane that are continuous with layer-parallel leucosomes and indicate that melting and deformation were coeval. Continuous folding and shearing of leucosome-bearing layers has led to disaggregation of metatexites to form diatexites (Fig. 2a, b; see also Weinberg & Mark, 2008). Disaggregation of layering also gives rise to schlieren, consisting of mostly hornblende, biotite and titanite (Fig. 2c). Amphibolite blocks that seem to be unaffected by anatexis, form schollen in the diatexite (Fig. 2d). Sometimes these blocks, up to ~1.5 m large, are internally fragmented but are still recognizable as one formerly coherent block (Fig. 2e).

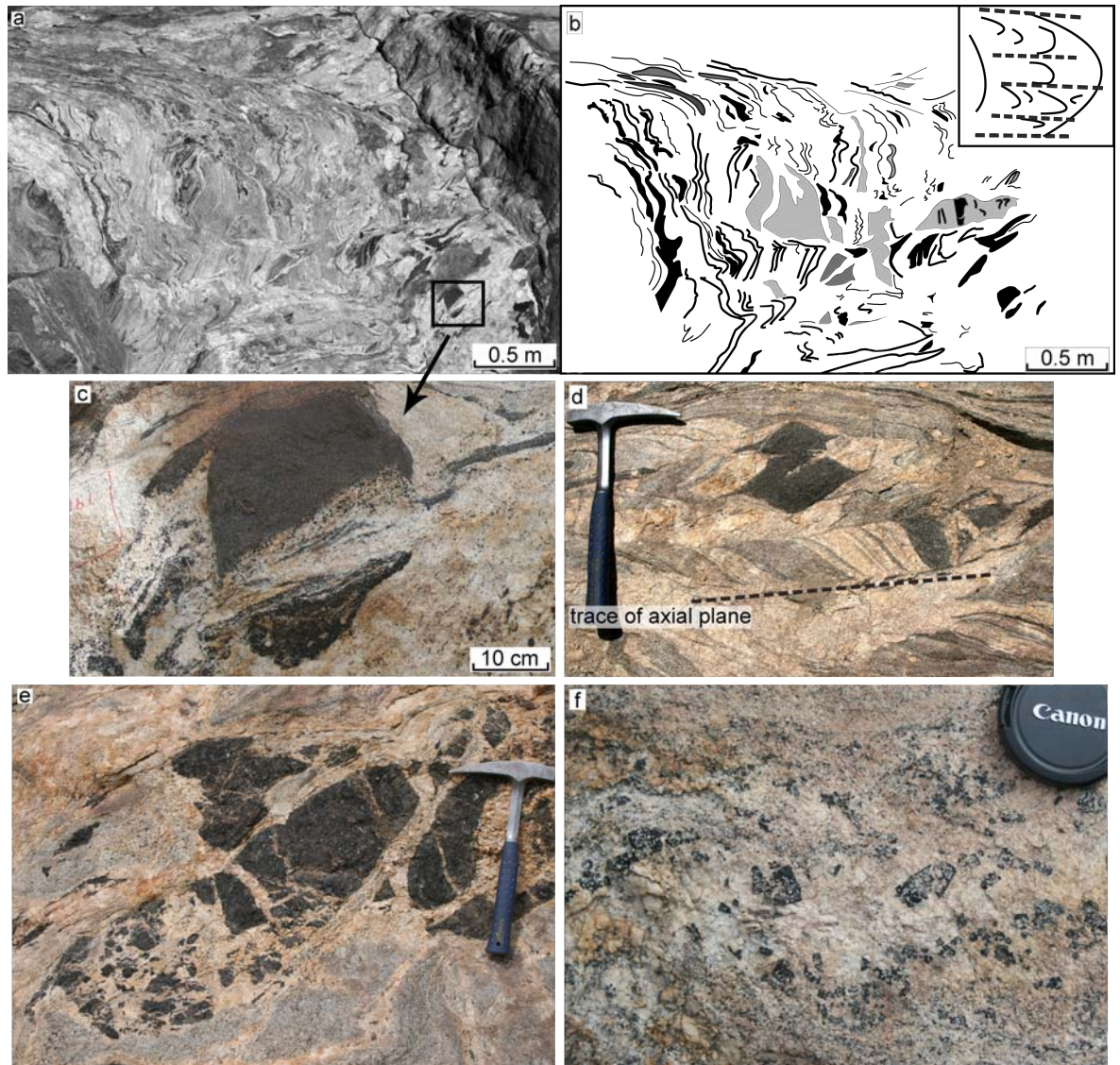


Fig. 2: General features of hornblende-bearing migmatites in the Tangtse gorge. (a) Disaggregation of metatexite to form diatexite. The outcrop is ~20° inclined towards viewer. (b) Line drawing of (a) showing folding of layers. Inset: interpretation of folding and axial planar leucosomes indicated as dashed line. (c) Disrupted amphibolite schollen and entrainment of schollen material to form schlieren in leucosome. (d) Rotation of layering in metatexite into parallelism with axial plane. (e) Fragmented amphibolite schollen in diatexite migmatite. Fragments are surrounded by leucosome but show jigsaw fit. (f) Large, euhedral poikilitic hornblende megacrysts in leucosome in Hbl-Bt-granodiorite.

Commonly, hornblende in leucosomes is large, poikilitic and euhedral, and is interpreted as peritectic (Fig. 2f). In many places, diatexites show a patchy texture characterized by

leucosome grading into melanosome (Fig. 3a). Locally, hornblende in patchy leucosomes forms accumulations (Fig. 3c). Leucosomes in the diorites also contain large hornblende forming aggregates (Fig. 3d). Isolated rafts of mafic diorite in the leucosome are commonly rimmed by hornblende megacrysts. In some cases, accumulation of hornblende gives rise to dark veins mostly consisting of hornblende (Fig. 3e). These ~5 to 10 cm thick veins are continuously linked to wider (~0.5 m) leucosomes and are interpreted as parts of the leucosome where interstitial melt has been extracted, leaving behind an accumulation of early formed crystals.

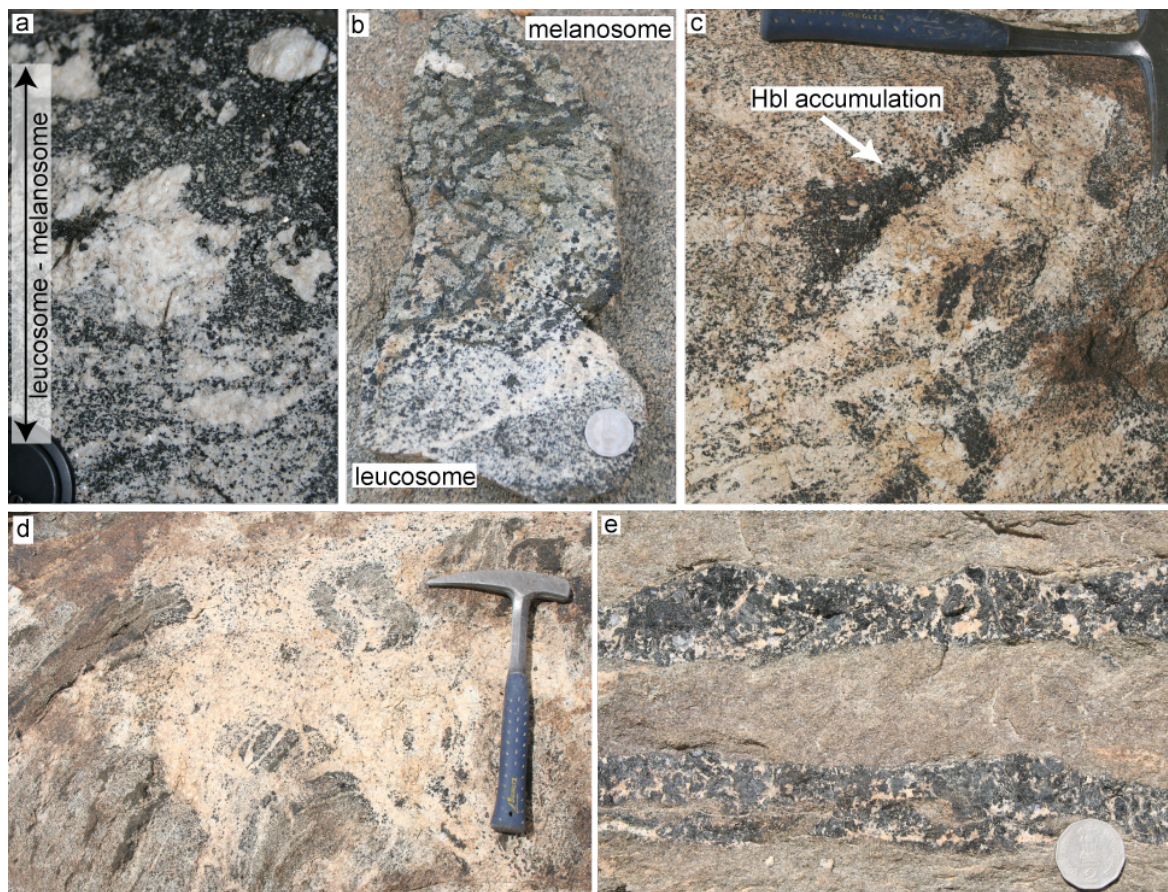


Fig. 3: (a) Diffuse, patchy grading from melanosome into leucosome in diatexite; diorite protolith. (b) Mottled texture formed by clinopyroxene clusters (pale green) surrounded by hornblende (dark green) and biotite in melanosome of metatexite. Diffuse, patchy leucosome consisting mostly of hornblende and K-feldspar. Protolith to this migmatite is diorite. (c) Hornblende accumulation in leucosome in Hbl-Bt-granodiorite. (d) Patchy, coarse-grained Hbl-bearing leucosome in diorite. Schollen of diorite, e.g. at tip of hammer, shows rims of hornblende megacrysts. (e) Hornblende and K-feldspar accumulation in veins in diorite, interpreted to be the result of melt extraction from a leucosome that now preserves a residual assemblage.

4. Petrography

Hornblende is petrographically distinct in protolith, melanosome and leucosome. In granodiorite and diorite protoliths, hornblende grains are subhedral to anhedral, rarely exceed 5 mm length, and are generally aligned with the regional tectonic fabric (Fig. 4a). In places, hornblende in these rocks is deformed and shows sigmoidal shapes.

Hornblende grains in leucosomes, and sometimes also in diffuse melanosomes, are significantly larger, ranging between a few millimetres to megacrysts up to ~3 cm long.

They are euhedral to subhedral, poikilitic and commonly show inclusions of plagioclase, K-feldspar, biotite, allanite and apatite (Fig. 4c). Locally developed patchy tonalitic leucosomes show a granoblastic texture with euhedral to subhedral hornblende megacrysts that have plagioclase inclusions (Fig. 4d). In this tonalite, plagioclase is in most cases euhedral with straight boundaries, whereas quartz crystallized in interstices (Fig. 4e).

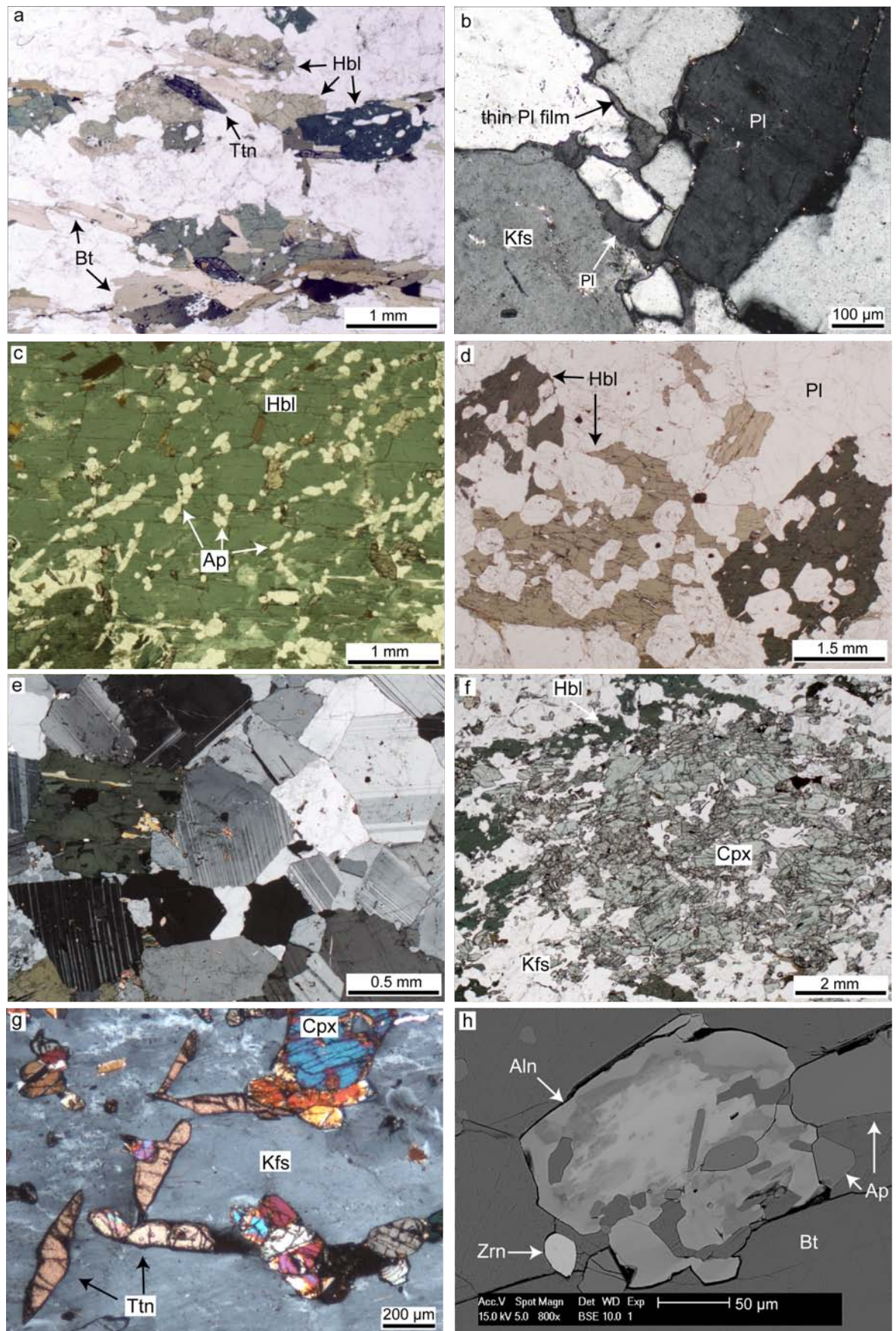


Fig. 4: Photomicrographs. (a) Example of hornblende texture in calc-alkaline Hbl-Bt-granodiorite protolith. Hornblende is mostly subhedral to anhedral and aligned together with biotite and titanite forming the foliation. Plane polarized light (PPL). (b) Thin plagioclase film, between plagioclase grains in Hbl-Bt-granodiorite. Small plagioclase grains in centre of image are interpreted to have undergone melting. This interpretation is based on embayment plagioclase grains, and good to see on the small Pl grain on the lower centre that is enclosed by the film. Cross polarized light (XPL). (c) Large amounts of euhedral apatite inclusions in hornblende megacrysts in Hbl-Kfs leucosome in rocks such as shown Fig. 3c. Plane polarized light (PPL). (d) Euhedral, poikilitic hornblende megacrysts with mainly plagioclase, but also quartz inclusions in tonalitic leucosome (PPL); diorite protolith. (e) Same leucosome as in (d), showing granoblastic texture and straight boundaries between plagioclase grains (XPL). (f) Cluster of subhedral and small (< 500 μm) anhedral clinopyroxene grains in a patchy melanosome of mottled diorite as shown in Fig. 3b (PPL). (g) Titanite and clinopyroxene in Hbl-Kfs leucosome. Most of the field of view is taken up by K-feldspar. Some of the titanite grains fill interstitial space between K-feldspar grains (e.g. in upper, central part of image); most clinopyroxene grains are small, anhedral and enclosed by K-feldspar (XPL); diorite protolith. (h) Scanning Electron Microscopy (SEM) image showing zoned allanite with apatite inclusions, apatite and zircon in biotite schlieren in migmatitic calc-alkaline Bt-granodiorite.

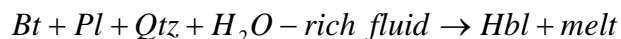
As opposed to grains in the paleosome, hornblende in leucosomes generally is not aligned. Under the microscope, hornblende in all studied rocks has a dark green colour and lack visible zonation. Samples from the Rongdo area (Fig. 1) are an exception and show grains with patchy zoning or with green-brown cores and green rims.

In diatexites, hornblende grains in leucocratic parts show two different textures, one is characterized by euhedral to subhedral poikilitic grains, the other is anhedral and generally smaller and have higher aspect ratios. Grains that show the latter texture also occur in schlieren together with biotite and titanite and are interpreted to be entrained from residual melanosome, to which the schlieren are commonly physically linked. In a Hbl-Bt-granodiorite where pre-migmatization texture is still preserved, thin rims of felsic material are found around plagioclase and K-feldspar grains. Sometimes, these films connect interstices between larger, framework building plagioclase and K-feldspar grains (Fig. 4b). Small embayed plagioclase grains are also common, and these are interpreted as partially melted relic grains. These features indicate either low degrees of partial melting or crystallisation of small amounts of residual melt after melt extraction (Fig. 4a, b; Sawyer 1999; Sawyer 2001).

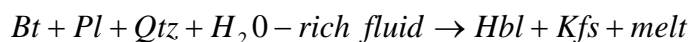
Some leucosomes in Hbl-Bt-granodiorites and diorites contain only K-feldspar, quartz and hornblende as major minerals. Plagioclase is only present in interstices, as thin rims around hornblende and K-feldspar or as inclusions in hornblende. Here, some hornblende grains contain exceptionally large amounts of euhedral apatite inclusions (Fig. 4c). These leucosomes also contain large amounts of apatite and titanite (Fig. 4g), small, often corroded clinopyroxene grains, and allanite. Allanite is also commonly contained in biotite schlieren in migmatitic Bt-granodiorites (Fig. 4h). Some of these Hbl-Kfs leucosomes grade into melanosomes in diorites that show dark green rims of hornblende \pm biotite surrounding pale green clusters of clinopyroxene giving rise to a mottled texture (Fig. 3b, 4f).

Petrographic evidence shows that biotite remained stable during partial melting, and an anhydrous assemblage (e.g. orthopyroxene + garnet) in residual rocks is absent. Based on the thermobarometric constraints ($T = 700 \pm 20$ °C, $P = 7 \pm 1$ kbar; Rolland & Pêcher, 2001),

the petrographic observations above and widespread occurrence of peritectic hornblende in the leucosome, we infer that migmatization took place under water-fluxed conditions. This is in agreement with melting experiments that have demonstrated that hornblende is only stable as a crystallizing phase in a magma when external water is added (Gardien *et al.*, 2000). We suggest the following reactions that have also been documented in migmatites with comparable mineralogies (Lappin & Hollister, 1980; McLellan, 1988) are responsible for melt production in the migmatites described above:



or



The high abundance of small, often euhedral titanite together with hornblende in the Hbl-Kfs leucosomes (Fig. 4g) suggests a third melt producing reaction (Lappin & Hollister, 1980):



We have analysed whole rock geochemistry of rocks of near protolith composition, various parts of migmatites ranging from leucosome to melanosome and also the leucogranite plutons in the PMC, to constrain petrogenetic relations. The results are presented below.

5. Geochemistry

5.1 Analytical procedures

5.1.1 Whole rock analysis

We analysed 34 whole rock samples for major and trace element geochemistry. Pulverized whole rock samples were analysed after preparation of fused discs and pressed pellets, respectively. Analyses were carried out in a Bruker-AXS S4 Pioneer XRF Spectrometer at the Advanced Analytical Centre (AAC) of James Cook University. Trace elements labelled with * in Table 1 were analyzed using a Thermo Finnigan X series II, quadrupole ICP-MS at Monash University. Sample solutions were produced from approximately 50 mg of sample powder using high pressure digestion methods. ICP-MS count rates were externally standardized by means of calibration curves based on the USGS standard reference material AGV-1 and RGM-1 following Eggins *et al.*, (1997) for their trace element contents. Drift corrections were applied by the combined use of In, Bi as internal standards and the repeated analysis of dummy standards during the analytical session. Reproducibility on replicate analyses and accuracy was in the order of 5% for all elements. Trace element values marked with ** in Table 1 are taken from Instrumental Neutron Activation Analysis (INAA) of pressed whole rock pellets, performed at Activation Laboratories Ltd., Ontario Canada. For methodology see www.actlabs.com.

5.1.2 Mineral analysis

Major element concentrations of minerals were determined using electron microprobe analyses, performed on 13 polished and carbon coated thin sections at The University of

Table 1. Whole rock major and trace element data

Sample	TNG98a	TNG131a	TNG131f	TNG205a	TNG205b	TNG207	TNG62a	TNG114a	TNG169a	TNG205c	TNG168	TNG113d1*	TNG113d2	TNG113a1*	TNG113a2*	TNG113b3	TNG113b4	TNG113e*
Rock type																		
Major Elements wt%																		
SiO ₂	66.65	67.50	68.70	54.91	55.02	68.23	55.00	53.70	61.95	47.62	47.20	46.90	46.50	66.80	68.40	72.20	67.40	70.60
TiO ₂	0.68	0.56	0.48	1.37	1.16	0.50	1.29	1.46	0.70	1.10	1.74	1.59	1.58	0.36	0.33	0.22	0.21	0.23
Al ₂ O ₃	16.84	16.30	16.30	17.56	17.07	15.26	18.20	16.90	14.29	15.53	12.02	17.40	17.50	18.30	17.50	16.40	18.80	16.80
Fe ₂ O ₃	3.58	3.49	3.35	8.04	7.51	3.05	7.75	8.80	5.18	10.25	11.93	11.80	11.50	2.18	1.77	0.97	1.40	1.39
MnO	0.09	0.09	0.09	0.13	0.13	0.07	0.15	0.16	0.15	0.18	0.12	0.18	0.18	0.03	0.02	0.02	0.02	0.02
MgO	1.63	1.57	1.28	3.01	4.64	1.22	3.83	4.26	4.55	8.58	10.95	6.52	6.22	1.05	0.91	0.39	0.63	0.56
CaO	3.44	3.16	3.37	5.90	8.22	2.85	5.79	7.18	6.46	11.78	10.07	10.00	10.00	4.08	3.44	3.77	3.60	2.80
Na ₂ O	4.62	4.37	4.56	3.81	4.08	3.17	4.28	4.17	3.01	2.36	1.97	3.48	3.56	5.81	5.51	5.52	5.79	5.42
K ₂ O	1.92	2.85	1.89	2.97	1.11	4.57	2.79	1.75	2.74	1.11	1.29	1.62	1.56	1.36	1.52	0.60	2.07	1.81
P ₂ O ₅	0.29	0.22	0.17	0.50	0.33	0.19	0.51	0.37	0.14	0.15	0.38	0.40	0.38	0.12	0.10	0.05	0.08	0.09
LOI	0.65	0.50	0.45	0.82	0.84	0.75	1.00	1.13	0.93	1.35	1.53	0.75	0.85	0.56	0.53	0.39	0.42	0.70
Total	100.37	100.62	100.62	99.00	100.08	99.65	100.59	99.85	99.83	100.12	99.18	100.60	99.83	100.65	100.02	100.52	100.45	100.45
A/CNK	1.06	1.02	1.04	0.87	0.75	0.99	0.88	0.77	0.74	0.59	0.52	0.68	0.68	0.99	1.03	0.99	1.03	1.05
Mg/(Fe+Mg)	0.47	0.47	0.43	0.43	0.55	0.44	0.49	0.49	0.64	0.62	0.65	0.52	0.52	0.49	0.50	0.44	0.47	0.44
Trace Elements ppm																		
Sc	5.58	8.479	5.514	12.69	16.67	5.44	15.70	26.57	19.86	30.73	26.76	32	31	4	bd	4.47	0.40	bd
Ti	4066.77	3953.19	3518.27	7373.16	6504.50	2121.40	7787.69	11688.61	3833.40	6513.84	8419.75	8900	8832	2183	2238	2040.31	389.38	1541
V	61.85	91.99	75.326	123.54	145.92	49.71	151.86	332.12	103.66	197.62	239.38	292	292	42	34	29.96	13.61	27
Cr	13.13	71.26	52.814	12.68	15.23	21.07	49.98	41.29	74.77	26.71	57.42	70	58	31	36	4.43	34.85	24
Mn	556.83	892.94	898.224	859.20	862.36	415.11	1068*	1793.96	1053.38	1106.96	816.66	1499	1446	247	165	196.35	201.14	112
Co	9.69	9.12	7.500	27.64	28.61	36.20	20.56	41.08	45.13	34.68	44.66	52	51	5	bd	3.07	5.61	4
Ni	15.81	65.56	61.958	16.72	26.31	13.38	40.61	92.49	53.55	30.85	92.20	35	31	8	7	11.39	27.44	4
Cu	6.27	12.99	3.033	47.67	84.12	6.29	62.85	73.66	21.45	52.58	191.27	104	46	45	20	291.47	135.55	38
Zn	63.22	81.83	93.259	86.66	76.38	38.42	111.94	119.16	62.57	79.35	114.29	101	98	43	41	18.03	27.83	44
Ga	19.16	13.31	13.814	14.41	9.73	8.87	22.06	13.72	12.58	8.95	11.98	20	19	19	18	10.80	17.50	20
Rb	116.94	206.37	48.53	124.10	25.63	161.13	122.31	70.70	49.42	22.95	39.40	40	35	38	48	0.70	7.30	38
Sr	543.01	438.70	354.46	568.57	550.93	413.29	541.97	627.94	547.63	418.10	353.80	650	724	1034	990	1392.02	884.77	1347
Y	15.80	20.11	8.48	24.30	20.46	17.56	27.30	16.85	18.77	20.83	21.28	23	25	8	4	4.62	1.77	4
Zr	10.92	4.29	3.63	58.57	60.52	18.82	166.82	10.89	11.54	71.17	67.69	108	104	127	98	6.04	3.01	99
Nb	18.00	21.36	23.68	25.52	15.09	15.05	27.40	21.59	18.25	8.85	10.39	16	15	1	bd	5.34	0.55	bd
Ba	279.61	286.124	83.970	540.12	118.69	379.67	334.05	212.90	586.51	118.18	196.58	203	227	273	332	92.50	458.02	584
La	55.87	75.25	11.68	58.46	26.21	40.87	55.98	27.57	7.05	14.25	18.93	17.6**	15.2**	9.8**	10.5**	1.00	1.89	14.4**
Ce	99.52	103.75	19.54	107.82	52.17	75.33	111.68	46.37	20.43	32.18	45.05	39**	32**	19**	21**	3.14	3.83	26**
Pr	10.54	9.47	2.28	10.58	5.84	7.59	12.29	5.30	2.86	3.93	5.78	bd	bd	bd	bd	0.59	0.52	bd
Nd	35.28	29.82	7.98	39.55	24.30	27.47	42.77	20.04	13.46	18.48	26.84	14**	15**	6	10**	2.80	2.20	8**
Sm	5.48	5.12	1.71	6.90	4.95	4.71	7.57	4.21	3.18	4.43	6.30	4.9**	4.4**	1.6**	1.3**	1.00	0.64	1.6**
Eu	1.32	1.08	0.39	1.67	1.36	1.08	2.03	1.27	1.03	1.24	1.63	1.6	1.4**	0.6**	0.5**	0.46	0.23	0.5**
Gd	4.27	4.14	1.40	5.76	4.03	3.88	6.35	3.53	2.89	3.63	4.91	88	bd	bd	bd	0.86	0.51	bd
Tb	0.54	0.62	0.24	0.86	0.67	0.58	0.91	0.56	0.50	0.63	0.80	bd	bd	bd	bd	0.17	0.08	bd
Dy	2.80	3.41	1.41	4.53	3.76	3.20	5.06	3.16	3.02	3.67	4.27	bd	bd	bd	bd	0.98	0.44	bd
Ho	0.51	0.71	0.33	0.84	0.74	0.59	1.00	0.88	0.61	0.75	0.79	bd	bd	bd	bd	0.22	0.09	bd
Er	1.36	1.80	0.95	2.32	1.96	1.63	2.69	1.68	1.76	1.95	1.97	bd	bd	bd	bd	0.56	0.20	bd
Tm	0.19	0.24	0.14	0.34	0.30	0.24	0.40	0.21	0.28	0.30	0.28	bd	bd	bd	bd	0.07	0.03	bd
Yb	1.15	1.62	1.14	2.06	1.88	1.57	2.55	1.39	1.90	1.87	1.65	2**	1.7**	0.5**	0.2**	0.49	0.15	bd
Lu	0.16	0.25	0.21	0.32	0.30	0.23	0.37	0.21	0.31	0.28	0.24	0.3**	0.32**	bd	0.09**	0.07	0.02	0.05**
Pb	10.86	42.98	37.13	12.16	11.45	20.46	11.55	11.00	12.42	5.27	3.85	23	23	13	12	12.15	17.06	10
Th	10.60	17.67	5.14	11.21	4.15	15.21	10.93	2.02	1.14	1.74	2.06	1.7**	1.4**	3**	3.1**	0.38	0.77	3.5**
U	2.32	3.84	2.76	1.08	1.26	2.22	2.84	1.23	2.11	1.20	0.80	bd	1.8**	1.7**	bd	0.46	0.28	2.6**
La _N /Y _{BN}	32.68	31.28	6.89	19.15	9.39	17.53	14.82	13.34	2.50	5.13	7.74	5.9	6.0	13.2	35.4	1.39	8.36	n.a.
Sum REE	218.99	237.28	49.41	242.01	128.47	168.98	251.65	116.19	59.26	87.61	119.43	n.a	n.a	n.a	n.a	12.41	10.84	n.a.

Table 1 continued
Sample
Rock Type

Major Elements wt%	TNG113f	TNG113g	TNG113h	TNG113i*	TNG114b1	TNG114b2	TNG62b	TNG169b	TNG170	TNG171	TNG172	AGH23d	AGH24	TNG60d	AGH23a
				Diatexite					Leucosome				Hbl-leucocr	Hbl-Kfs	leucosome
SiO ₂	64.70	69.50	59.00	70.40	73.10	71.00	71.80	68.02	72.09	75.53	76.93	68.74	74.42	62.34	58.08
TiO ₂	0.57	0.48	0.93	0.18	0.25	0.38	0.27	0.15	0.13	0.06	0.18	0.40	0.13	0.57	0.70
Al ₂ O ₃	15.90	16.60	15.80	17.10	14.80	15.30	16.40	17.43	15.96	14.72	14.29	14.59	13.37	16.29	12.45
Fe ₂ O ₃	3.65	2.06	6.53	1.09	1.51	2.39	0.43	1.91	0.71	0.39	1.13	3.34	0.89	2.30	4.61
MnO	0.06	0.02	0.12	bd	0.02	0.04	bd	0.06	0.01	0.01	0.01	0.06	0.02	0.06	0.13
MgO	2.21	1.03	3.38	0.48	0.61	1.00	bd	0.59	0.26	0.26	0.36	1.35	0.26	1.31	3.88
CaO	4.61	3.38	6.13	3.20	2.13	2.90	2.09	4.72	2.37	2.37	2.84	3.15	3.10	2.65	8.05
Na ₂ O	4.08	4.99	3.65	5.58	3.34	3.89	3.73	4.87	4.33	3.57	3.95	1.87	3.10	1.68	1.92
K ₂ O	3.09	1.82	3.35	1.44	4.28	3.08	5.31	0.79	2.98	2.94	0.94	5.22	4.92	10.11	6.53
P ₂ O ₅	0.21	0.14	0.31	0.05	0.07	0.10	0.02	0.11	0.03	0.02	0.04	0.08	0.02	0.40	2.06
LOI	0.75	0.67	0.58	0.48	0.47	0.51	0.35	0.56	0.47	0.34	0.45	0.47	1.10	0.46	0.59
Total	99.86	100.63	99.78	99.97	100.60	100.56	100.25	99.19	99.34	100.20	101.09	99.24	99.16	98.14	99.01
A/CNK	0.86	1.02	0.76	1.03	1.06	1.02	1.05	1.00	1.09	1.10	1.13	1.01	1.10	0.88	0.50
Mg/(Fe+Mg)	0.55	0.50	0.51	0.47	0.44	0.45	0.00	0.38	0.42	0.57	0.39	0.44	36.66	0.53	0.63
Trace Elements ppm															
Sc	15.98	0.14	44.08	bd	2.05	5.29	bd	9.63	0.52	0.33	0.75	2.34	9.85	6.05	16.36
Ti	5328.81	192.96	8952.75	1238	2205.53	3398.18	169.57	630.96	553.21	185.83	691.86	1496.57	2306.87	2551.15	4068.80
V	143.59	29.34	236.56	19	41.58	64.50	2.34	21.36	9.09	2.91	9.58	22.39	52.30	37.99	75.37
Cr	140.51	41.49	228.49	33	27.93	49.43	0.38	3.40	1.69	0.30	bd	58.34	43.83	36.63	60.92
Mn	800.65	251.86	1528.76	90	205.73	388.59	21.62	406.25	41.36	39.40	65.54	193.55	412.22	348.67	921.99
Co	15.93	7.99	21.68	1	4.52	7.61	0.30	50.36	68.63	79.41	80.80	34.36	38.89	20.29	35.08
Ni	86.64	40.43	120.27	5	17.61	35.87	1.39	3.56	3.08	0.98	2.23	1.45	3.05	28.17	39.16
Cu	4.81	193.23	25.21	5	60.22	31.95	1.06	9.13	39.72	7.75	15.79	2.25	5.01	31.58	65.95
Zn	68.61	37.52	109.28	30	24.17	40.63	0.12	23.40	8.39	6.08	13.83	40.22	37.73	38.74	86.07
Ga	20.28	13.45	26.20	18	22.69	18.21	7.27	6.35	19.99	21.78	6.85	16.02	13.24	165.33	13.90
Rb	43.08	9.04	41.32	35	47.89	61.82	15.10	9.01	52.14	57.43	26.72	59.22	153.25	440.88	151.37
Sr	1019.10	619.20	959.00	967	607.48	638.71	148.49	914.92	1089.96	816.18	843.64	572.20	228.80	1083.16	903.35
Y	13.44	3.16	34.74	3	4.27	10.18	0.61	14.64	0.97	1.40	0.94	3.12	23.14	20.85	29.90
Zr	15.42	21.84	19.25	93	4.83	8.70	0.92	16.59	6.51	6.57	1.87	23.63	14.18	39.72	30.38
Nb	7.67	0.19	18.82	bd	5.71	8.42	0.61	5.39	1.34	0.54	0.89	3.47	8.98	9.66	21.17
Ba	744.44	274.36	1290.87	453	1259.63	740.77	1906.00	130.76	1360.10	1320.40	239.04	735.97	1101.98	8279.89	4136.14
La	4.66	15.40	9.03	8.6**	13.90	24.40	2.04	30.85	3.80	7.01	19.59	28.99	52.18	98.30	68.37
Ce	14.11	24.15	26.66	13**	22.45	38.95	3.39	53.96	8.09	13.71	35.33	50.99	96.10	353.85	160.68
Pr	2.39	2.59	4.46	bd	2.39	4.11	0.40	4.95	0.78	1.27	3.34	5.27	9.65	31.67	20.59
Nd	11.62	9.22	21.86	bd	8.02	14.22	1.42	17.67	2.97	4.44	11.47	17.46	31.66	140.37	81.59
Sm	3.53	1.82	7.20	0.9**	1.43	2.71	0.29	3.05	0.53	0.73	1.54	2.53	5.27	26.54	14.35
Eu	1.16	0.55	2.21	0.4**	0.45	0.72	0.10	0.86	0.34	0.55	0.44	0.66	1.06	5.04	2.91
Gd	2.95	1.29	6.48	bd	1.09	2.13	0.19	2.74	0.40	0.55	0.98	1.59	4.50	15.06	9.53
Tb	0.48	0.17	1.12	bd	0.16	0.32	0.03	0.44	0.05	0.07	0.09	0.17	0.66	1.60	1.09
Dy	2.55	0.76	6.31	bd	0.87	1.79	0.13	2.58	0.25	0.32	0.31	0.72	3.77	6.00	5.24
Ho	0.51	0.13	1.30	bd	0.18	0.37	0.03	0.49	0.04	0.05	0.03	0.11	0.76	0.72	0.93
Er	1.18	0.30	3.05	bd	0.45	0.94	0.06	1.37	0.10	0.12	0.09	0.26	2.20	1.60	2.46
Tm	0.14	0.03	0.37	bd	0.06	0.12	0.01	0.20	0.01	0.01	0.01	0.03	0.32	0.16	0.34
Yb	0.90	0.21	2.27	bd	0.39	0.78	0.05	1.26	0.08	0.08	0.04	0.09	1.99	0.89	2.10
Lu	0.13	0.03	0.31	bd	0.06	0.11	0.01	0.18	0.01	0.01	0.01	0.03	0.29	0.11	0.30
Pb	18.63	13.18	18.30	10	19.80	16.59	4.72	10.17	15.67	14.23	9.65	26.26	28.15	85.37	30.21
Th	1.63	4.52	2.52	5.3**	7.15	9.16	2.62	11.08	0.80	2.23	6.59	16.67	22.44	93.30	21.32
U	1.46	0.53	2.33	2.3**	1.24	1.27	0.34	1.27	0.10	0.18	0.25	0.73	1.27	6.53	3.73
La _N /Yb _N	3.48	48.49	2.68	n.a	23.78	21.13	25.75	16.55	33.54	61.24	312.05	102.37	17.71	74.07	21.94
Sum REE	46.31	56.65	92.62	n.a	51.90	91.67	8.14	120.62	17.45	28.92	73.25	109.01	210.40	681.92	370.48

Melbourne, School of Earth Sciences using a Cameca SX-50 Electron Microprobe with four Vertical Wavelength Dispersive Spectrometers (WDS). Beam current = 35 nA, acceleration voltage = 15 kV, take off angle = 40. Detection limits: All elements better than 0.05 elemental weight percent except for Zn which is 0.09 elemental weight percent.

Trace element concentrations were determined via laser ablation ICP-MS on polished thick sections (~150 μm) of eight samples. The data were obtained using a New Wave UP 213 nm N:YAG laser ablation microprobe coupled with a Thermo Finnigan X series II, quadrupole ICP-MS at Monash University, School of Geosciences. Analyses employed a pulse rate of 4 Hz and beam energy of ~12 J/cm² at the sample. Laser spot size was ~110 μm diameter. For each analyses background readings were collected for 25 s followed by 60 s ablation time. The LA- ICP-MS raw data was reduced using the GLITTER 4.0 software package (van Achterbergh *et al.*, 2001). Quantitative results for the trace elements were obtained through calibration of relative element sensitivities using the NIST612 glass as an external standard. Electron microprobe data for Ca was used for internal standardisation. In order to improve accuracy the trace element concentrations were subsequently corrected to the difference between the measured and recommended values of the USGS glass standard BCR2. Analysis results of standards are given in an electronic appendix on a data CD.

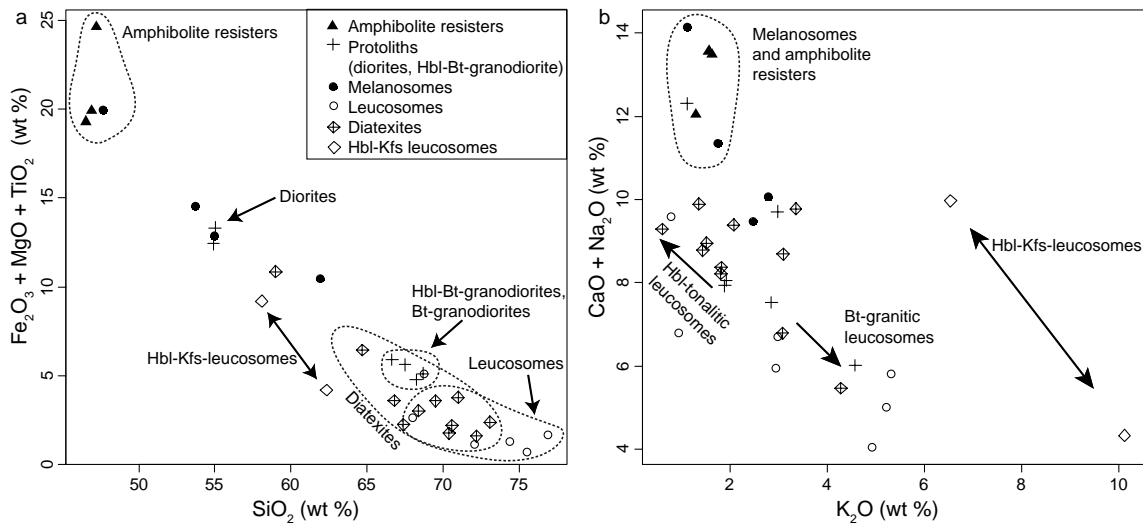


Fig. 5: (a) $\text{Fe}_2\text{O}_3 + \text{MgO} + \text{TiO}_2$ vs. SiO_2 diagram indicating decrease of ferromagnesian and titaniferous phases with increasing silica content. Symbols: see inset. (b) $\text{CaO} + \text{Na}_2\text{O}$ vs. K_2O diagram showing a central field of Hbl-Bt-granodiorite protoliths and melanosomes overlapping with diatexites. The arrow towards higher K_2O indicates accumulation of K-feldspar in leucosomes. Plagioclase accumulation in diatexites is indicated by arrow in opposite direction. High hornblende contents contribute to high $\text{CaO} + \text{Na}_2\text{O}$ contents in diorites and amphibolite resisters. The two samples of Hbl-Kfs leucosomes show extremely high K_2O , and variable $\text{CaO} + \text{Na}_2\text{O}$ concentrations reflecting variations in Kfs and Hbl contents. Symbols as in (a).

5.2 Whole rock geochemistry

5.2.1 Major elements

The calc-alkaline protoliths all have similar mineralogy, but with varying mineral proportions, except for clinopyroxene which is only present in diorites, and generally follow compositional trends characteristic for arc related magmatic and volcanic rocks (e.g. Debon

et al., 1987; Frost *et al.*, 2001). Calc-alkaline protoliths, leucosomes and melanosomes lie in distinct fields in a number of diagrams, whereas diatexites are intermediate between leuco- and melanosome. In a $\text{Fe}_2\text{O}_3 + \text{MgO} + \text{TiO}_2$ vs. SiO_2 diagram (Fig. 5a), calc-alkaline granitoids define a field of intermediate values, while melanosomes show higher ferromagnesian and titanium contents and lower silica values than leucosomes. Lowest SiO_2 contents (46.2 and 46.9 wt %) are recorded by two amphibolite resisters found as schollen in diatexite, whereas the highest values are found in leucosomes. The leucogranitic melting products are generally mildly peraluminous, whereas the protoliths are metaluminous (Reichardt *et al.*, 2010). A $\text{CaO} + \text{Na}_2\text{O}$ vs. K_2O diagram (Fig. 5b) shows trends indicating K-feldspar accumulation in Hbl-Kfs leucosomes, and plagioclase accumulation in tonalitic, Hbl-free leucosomes as well as Hbl-bearing diatexites. Relative to protoliths, the granitic leucosomes are depleted in $\text{CaO} + \text{Na}_2\text{O}$ but strongly enriched in K_2O . Conversely, tonalitic leucosomes are depleted in K_2O and enriched in $\text{CaO} + \text{Na}_2\text{O}$. Amphibolites and diorites, rich in hornblende, titanite and sometimes clinopyroxene-bearing, have the highest $\text{CaO} + \text{Na}_2\text{O}$ values.

5.2.2 Trace elements

Protoliths and products of partial melting also vary systematically in terms of their trace element concentrations. Figure 6 compares La_n/Yb_n and Sr/Y values of source rocks with all leucogranites interpreted to be derived from partial melting that were sampled in the Karakoram Shear Zone and the Karakoram Batholith. The protoliths and Karakoram Batholith leucogranites plot in the field of arc-related rocks whereas the leucocratic magmatic products plot in the field of Archean TTGs and adakites.

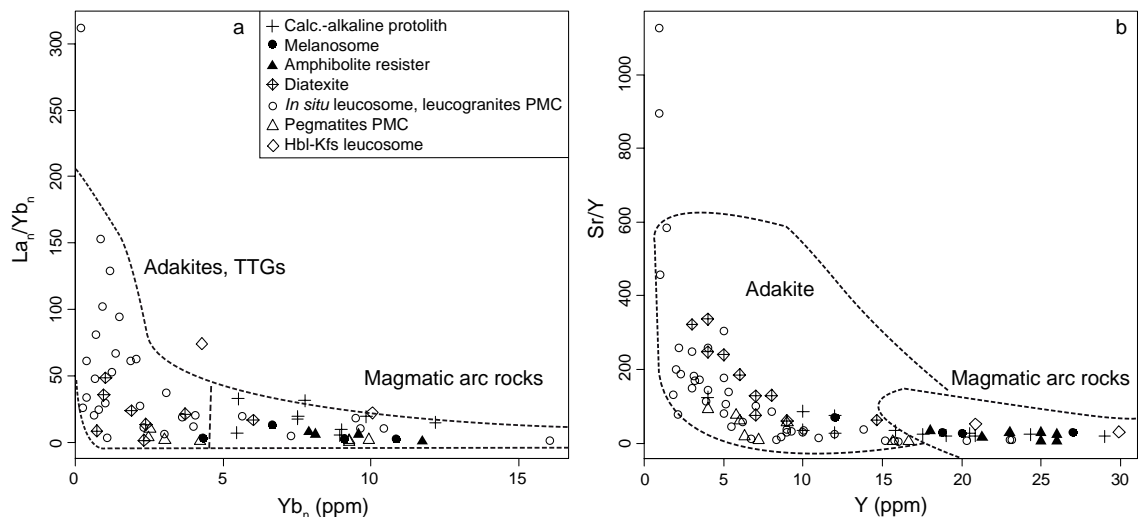


Fig. 6: (a) La_n/Yb_n vs. Yb_n diagram of calc-alkaline arc rocks and leucogranites of the PMC. Leucogranites from the Karakoram Batholith are also included. For geochemical data of leucogranites of PMC and Karakoram Batholith see Appendix A. Symbols as in Fig. 5 except for open triangles = pegmatite dykes. Fields for arc magmatic rocks and for adakites and TTGs are taken from Defant *et al.* (2002). (b) Sr/Y vs. Y diagram.

Diorite, Hbl-Bt-granodiorite and Bt-granodiorite protoliths show roughly sub-parallel and moderately fractionated REE patterns (Fig. 6a; $\text{La}_n/\text{Yb}_n = 17.53$ to 32.68) with slightly concave upward MREE to HREE shapes and negative Eu anomalies ($\text{Eu}/\text{Eu}^* = 0.72$ to 0.83) (Fig. 7a). Hbl-Bt gneisses and amphibolite resisters (Fig. 7b) show comparable compositions to andesites and basalts, respectively, of the Ladakh arc (Rolland *et al.*, 2002). The amphibolite

resisters are the least fractionated rocks ($La_N/Yb_N = 5.13$ to 7.74).

Melanocratic, Hbl-rich parts of diatexites show slight LREE depletions relative to MREE with a concave downward REE shape, and leading to low La_N/Yb_N values (Fig. 7c; $La_N/Yb_N = 2.50$ to 3.48). Interestingly, this is a typical REE shape for hornblende (see below), suggesting the importance of hornblende for the REE budget these rocks (Hilyard *et al.*, 2000).

Hornblende-free, tonalitic leucosomes have steep, strongly fractionated REE patterns with La_N/Yb_N ranging from 33 to 312 (Fig. 7d) in contrast to La_N/Yb_N (1.39 to 74.07 ; Table 1) values in hornblende-bearing leucosomes. Tonalitic Hbl-free leucosomes also have pronounced positive Eu anomalies (Fig. 7d), indicative of plagioclase accumulation, in agreement with Sr enrichment. Combined with Y depletion compared to protoliths, this gives rise to the highest Sr/Y ratios in the region ($Sr/Y = 583.5$ to 1127.5 in Fig. 6).

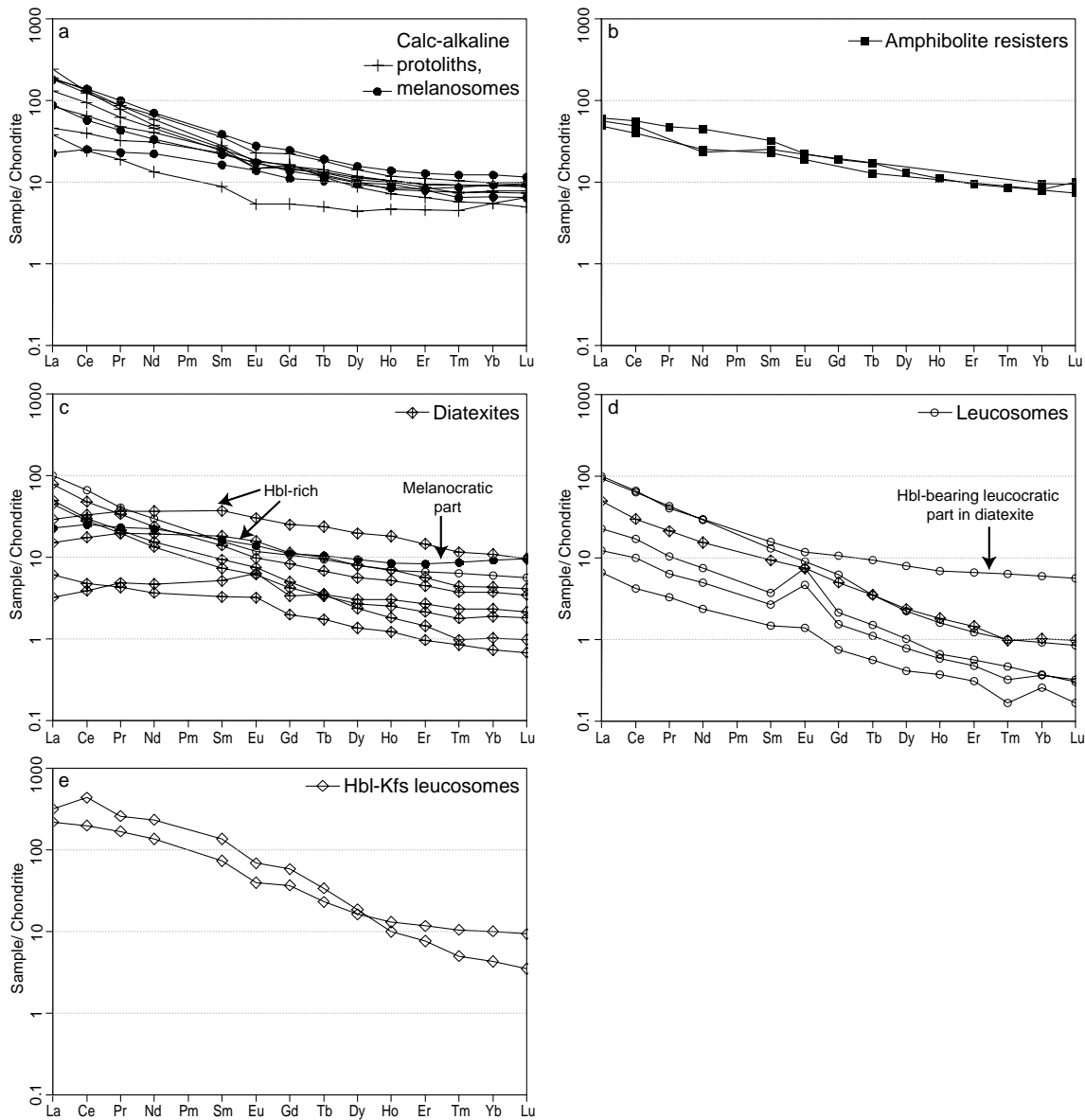


Fig. 7: (a) REE patterns of protoliths and melanosomes, (b) amphibolite resisters, (c) diatexites, and (d) leucosomes. Note lower HREE values for Hbl-free leucosomes compared to Hbl-bearing leucosomes. (e) Hbl-Kfs leucosomes. These rocks contain unusually high amounts of Ap, Aln and Ttn. Chondrite normalization after Boynton (1984).

The Hbl-Kfs leucosomes (Fig. 7e) are very rich in accessory phases such as apatite and titanite (see Petrography above), and show anomalous trace element contents, particularly

enriched in LREE (Fig. 7e). These rocks are also strongly enriched in Ba, Rb, Sr and P_2O_5 (see Table1).

Lowest values for LILE are shown for the amphibolite resisters (Fig. 8a). Diatexites and leucosomes are generally enriched in Ba and Sr, but depleted in Rb compared to protoliths, in agreement with water-fluxed melting which leads to high Sr/Rb values because of prevalence of feldspars over micas in the melting reaction (Patiño Douce & Harris, 1998). Strong Ba and Rb enrichments, however, are shown for the Hbl-Kfs leucosomes (Fig. 8b). High Ba and Sr values correlate with high values for $CaO+Na_2O$ and Al_2O_3 , and modelling for leucogranites in the PMC has shown that these values are indicative of plagioclase accumulation (Reichardt *et al.* 2010, Chapter II).

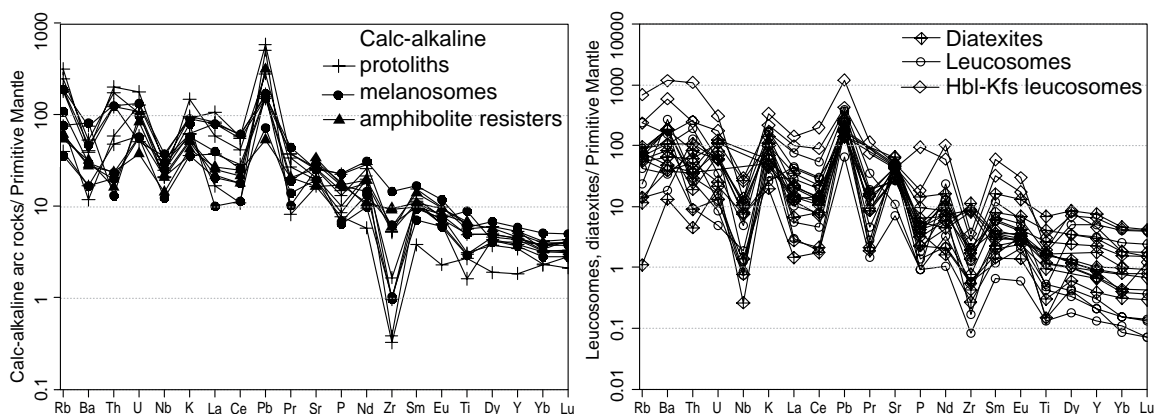


Fig. 8: Multielement diagrams normalized to primitive mantle after Sun & McDonough (1989). (a) Amphibolite resisters, protoliths and melanosomes. (b) Diatexites and leucosomes. Note extreme LILE enrichments in the Hbl-Kfs leucosomes. Lowest Nb, Ti and Zr values are recorded for leucosomes that show feldspar accumulations in their petrography.

Fractionation trends are also apparent for compatible elements, with the highest concentrations of V, Cr and Ni in amphibolite resisters (Fig. 8a). The HFSE Ti and Zr are generally enriched in melanosomes compared to protoliths. Concentrations of Nb are variable in protoliths and melanosomes, showing no trend. Leucosomes show the lowest concentrations of HFSE. Diatexites show variable HFSE contents (Fig. 8b) that can be attributed to different contents of residuum in the sample, so that residuum-rich samples show HFSE contents overlapping with those of protoliths. In the following section we investigate mineral chemistry and the contribution of different minerals to the whole rock trace element contents.

5.3 Mineral Geochemistry

5.3.1 Major element geochemistry

Hornblende

All analysed amphiboles are calcic ($CaO = 10.91$ to 12.10 wt %, Table 2), and according to the classification scheme after Leake *et al.* (1997), most amphiboles lie in the field of ferropargasites ($Ca > 1$, $Na + K > 0.5$, $XMg < 0.5$, and $5.5 > Si < 6.5$ atoms per formula unit) or straddle the boundary to the field of pargasites ($XMg > 0.51$) (Fig. 9). They show

Table 2. Major element concentrations of hornblende

Sample	TNG59	TNG169a	TNG169b	TNG203	TNG165	TNG204c	TNG60c	TNG60d	AGH23a	AGH24
Average of N analyses	N = 7	N = 5	N = 7	N = 8	N = 12	N = 10	N = 4	N = 18	N = 6	N = 8
Oxides										
SiO ₂	41.62 ± 0.69	43.87 ± 1.31	40.06 ± 0.32	42.73 ± 0.65	44.80 ± 2.39	40.71 ± 0.55	40.11 ± 0.39	42.33 ± 1.23	46.89 ± 1.52	45.36 ± 1.43
TiO ₂	0.93 ± 0.08	1.03 ± 0.14	1.43 ± 0.02	0.78 ± 0.03	0.68 ± 0.16	1.10 ± 0.12	0.81 ± 0.03	0.61 ± 0.06	0.71 ± 0.15	1.43 ± 0.54
Al ₂ O ₃	10.97 ± 0.54	10.60 ± 1.04	12.48 ± 0.29	10.27 ± 0.61	9.42 ± 1.97	11.79 ± 0.51	11.54 ± 0.10	10.24 ± 0.29	6.92 ± 1.05	7.40 ± 1.08
V ₂ O ₃	0.05 ± 0.01	0.05 ± 0.02	0.04 ± 0.03	0.06 ± 0.02	0.03 ± 0.02	0.08 ± 0.03	0.05 ± 0.01	0.05 ± 0.02	0.02 ± 0.02	0.05 ± 0.02
Cr ₂ O ₃	0.02 ± 0.03	0.04 ± 0.02	0.00 ± 0.01	0.09 ± 0.05	0.12 ± 0.06	0.03 ± 0.02	0.01 ± 0.02	0.05 ± 0.03	0.03 ± 0.01	0.01 ± 0.01
FeO	19.56 ± 0.19	15.34 ± 1.02	20.14 ± 0.11	17.15 ± 0.83	15.07 ± 1.10	19.09 ± 0.28	21.01 ± 0.18	15.67 ± 1.31	15.38 ± 0.77	19.26 ± 0.51
MnO	0.51 ± 0.05	0.53 ± 0.05	0.74 ± 0.06	0.33 ± 0.08	0.38 ± 0.03	0.35 ± 0.03	0.34 ± 0.02	0.41 ± 0.05	0.40 ± 0.03	0.49 ± 0.08
MgO	9.51 ± 0.29	11.83 ± 0.91	8.01 ± 0.13	11.02 ± 0.62	12.55 ± 1.28	8.90 ± 0.33	8.31 ± 0.09	11.45 ± 0.17	13.38 ± 0.78	10.68 ± 0.68
CaO	11.68 ± 0.08	11.81 ± 0.16	11.33 ± 0.11	11.59 ± 0.10	11.83 ± 0.15	11.61 ± 0.16	11.33 ± 0.05	11.47 ± 0.59	11.83 ± 0.12	11.30 ± 0.30
Na ₂ O	1.50 ± 0.08	1.39 ± 0.12	1.45 ± 0.04	1.77 ± 0.06	1.69 ± 0.20	1.31 ± 0.07	1.82 ± 0.02	1.76 ± 0.05	1.66 ± 0.14	1.23 ± 0.28
K ₂ O	1.54 ± 0.19	1.28 ± 0.18	1.79 ± 0.10	1.50 ± 0.13	1.27 ± 0.33	1.63 ± 0.13	1.80 ± 0.05	1.50 ± 0.09	0.93 ± 0.17	0.87 ± 0.20
NiO	0.01 ± 0.01	0.03 ± 0.02	0.01 ± 0.01	0.05 ± 0.02	0.08 ± 0.01	0.02 ± 0.01	0.02 ± 0.02	0.05 ± 0.03	0.02 ± 0.02	0.01 ± 0.01
ZnO	0.04 ± 0.04	0.05 ± 0.04	0.03 ± 0.03	0.02 ± 0.02	0.05 ± 0.05	0.04 ± 0.04	0.05 ± 0.04	0.05 ± 0.03	0.05 ± 0.06	0.03 ± 0.03
Nb ₂ O ₅	0.00 ± 0.01	0.01 ± 0.01	0.02 ± 0.02	0.03 ± 0.04	0.02 ± 0.02	0.01 ± 0.02	0.03 ± 0.02	0.01 ± 0.02	0.05 ± 0.06	0.01 ± 0.01
Kations										
Si	6.27 ± 0.08	6.47 ± 0.14	6.11 ± 0.04	6.42 ± 0.07	6.60 ± 0.28	6.23 ± 0.06	6.17 ± 0.03	6.44 ± 0.05	6.87 ± 0.17	6.73 ± 0.16
Ti	0.11 ± 0.01	0.11 ± 0.02	0.16 ± 0.00	0.09 ± 0.00	0.07 ± 0.02	0.13 ± 0.01	0.09 ± 0.00	0.07 ± 0.01	0.08 ± 0.02	0.16 ± 0.06
Al tot	1.95 ± 0.10	1.84 ± 0.20	2.24 ± 0.05	1.82 ± 0.11	1.64 ± 0.36	2.13 ± 0.10	2.09 ± 0.02	1.84 ± 0.04	1.20 ± 0.19	1.30 ± 0.20
Cr	0.00 ± 0.00	0.01 ± 0.00	0.00 ± 0.00	0.01 ± 0.01	0.01 ± 0.01	0.00 ± 0.00	0.00 ± 0.00	0.01 ± 0.00	0.00 ± 0.00	0.00 ± 0.00
Fe tot	3.25 ± 0.07	2.50 ± 0.17	3.30 ± 0.05	2.79 ± 0.11	2.39 ± 0.20	3.09 ± 0.07	3.46 ± 0.03	2.58 ± 0.14	2.43 ± 0.15	3.20 ± 0.16
Mn	0.07 ± 0.01	0.07 ± 0.01	0.10 ± 0.01	0.04 ± 0.01	0.05 ± 0.00	0.05 ± 0.00	0.04 ± 0.00	0.05 ± 0.01	0.05 ± 0.00	0.06 ± 0.01
Mg	2.14 ± 0.05	2.60 ± 0.18	1.82 ± 0.03	2.47 ± 0.14	2.75 ± 0.25	2.03 ± 0.07	1.90 ± 0.02	2.60 ± 0.07	2.92 ± 0.15	2.36 ± 0.13
Ca	1.89 ± 0.02	1.87 ± 0.02	1.85 ± 0.02	1.86 ± 0.01	1.87 ± 0.01	1.90 ± 0.02	1.87 ± 0.01	1.87 ± 0.04	1.86 ± 0.01	1.80 ± 0.05
Na	0.44 ± 0.03	0.40 ± 0.04	0.43 ± 0.01	0.51 ± 0.02	0.48 ± 0.06	0.39 ± 0.02	0.54 ± 0.01	0.52 ± 0.02	0.47 ± 0.04	0.35 ± 0.08
K	0.30 ± 0.04	0.24 ± 0.04	0.35 ± 0.02	0.29 ± 0.02	0.24 ± 0.06	0.32 ± 0.03	0.35 ± 0.01	0.29 ± 0.01	0.17 ± 0.03	0.17 ± 0.04
Ni	0.00 ± 0.00	0.00 ± 0.00	0.00 ± 0.00	0.01 ± 0.00	0.01 ± 0.00	0.00 ± 0.00	0.00 ± 0.00	0.01 ± 0.00	0.00 ± 0.00	0.00 ± 0.00
XMg	0.40 ± 0.01	0.51 ± 0.03	0.36 ± 0.00	0.47 ± 0.02	0.53 ± 0.04	0.40 ± 0.01	0.35 ± 0.00	0.50 ± 0.02	0.55 ± 0.03	0.42 ± 0.02

Kations recalculated on the basis of 23 oxygen atoms; ± is one standard deviation. For complete analysis see Appendix C.

a linear trend from ferropargasites over pargasite to edenite with increasing Si and XMg, except for amphiboles from a Hbl-leucogranite from the Rongdo location (sample AGH24) that have lower XMg and lie in the field of ferro-edenite. Generally, hornblendes from the Rongdo location (Fig. 1; samples AGH23a, AGH24) show a wide spread of Si contents. Hornblendes of one Hbl-Kfs leucosome from the Tangtse area (sample TNG165) also show widely scattering Si contents. High Si is generally coupled with low Al tot contents, a trend that is generally related to equilibration at lower pressures (Hammarstrom & Zen, 1986). Conversely, lower XMg indicate higher pressures (Hammarstrom & Zen, 1986). Alkali (Na+K) contents range between 0.54 and 0.91 for samples from the Tangtse gorge area and correlate positively with aluminium contents, but negatively with silica contents (Fig. 10a), reflecting a trend common for calcic amphiboles in calc-alkaline magmas (Femenias *et al.*, 2006). A similar trend is observed for Ti contents (Fig. 10b). For simplicity we refer to all amphibole varieties as hornblende.

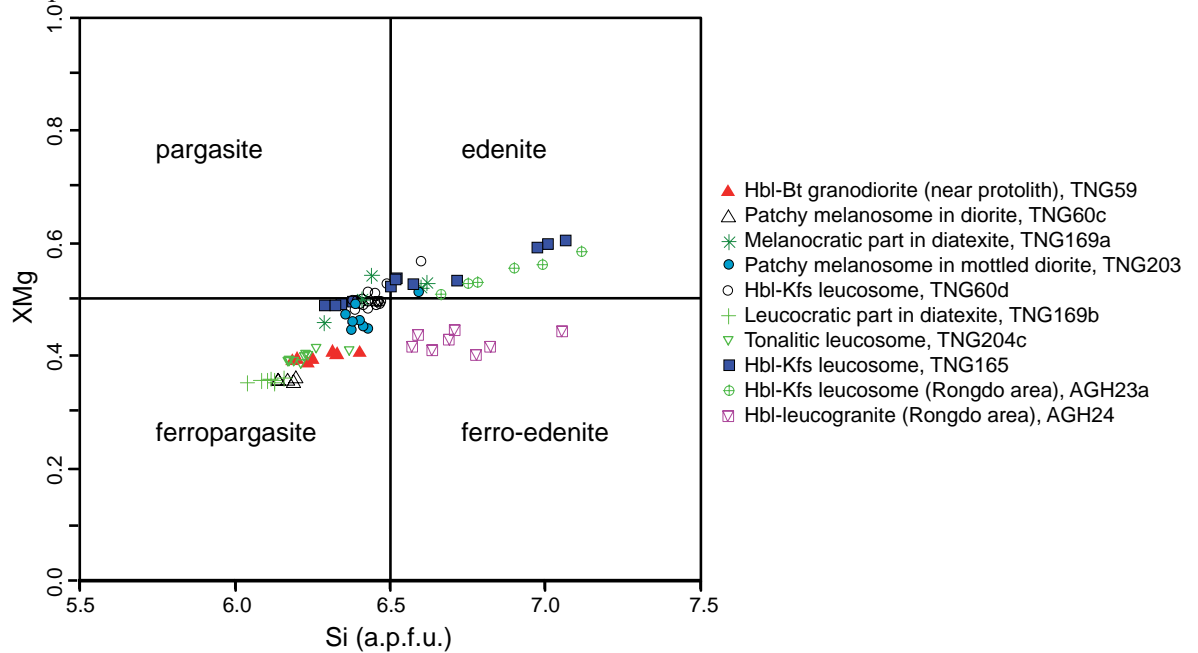


Fig. 9: Hornblende classification after Leake *et al.* (1997). Fe in XMg is Fe tot. Values given in atoms per formula unit (a.p.f.u.) calculated for 23 oxygen atoms.

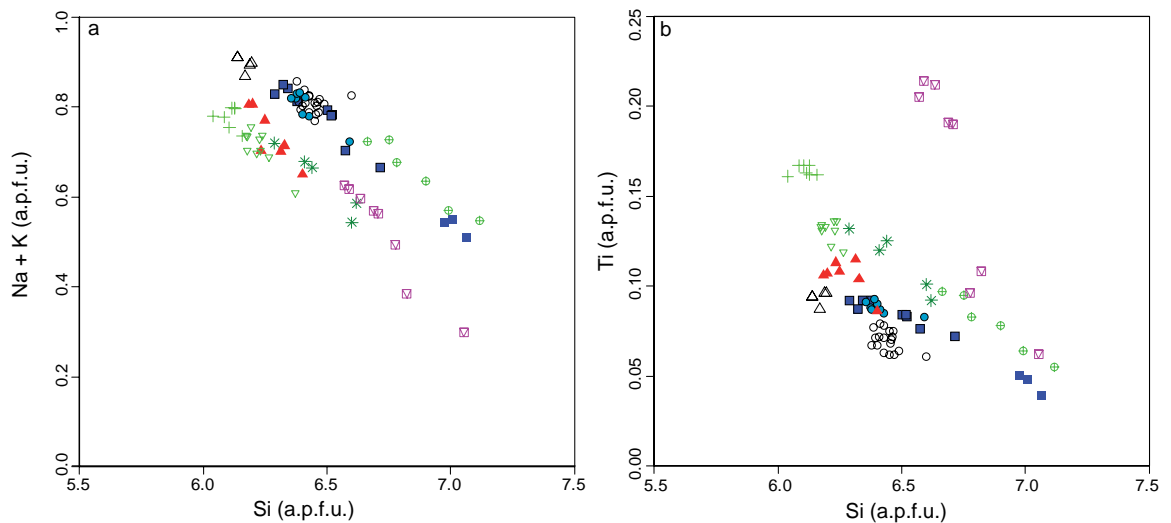


Fig. 10: (a) Na + K vs. Si and (b) Ti vs. Si showing similar negative correlation. Note high Ti values for hornblendes from one sample from the Karakoram Batholith in the Rongdo area and their scatter to lower Ti values, but higher Si, indicating alteration. Symbols as in Fig. 9.

Total aluminium contents (Al tot) vary between 1.07 and 2.28 atoms per formula unit (a.p.f.u.) in samples from the Tangtse gorge area, and between 0.87 and 1.5 a.p.f.u. at the Rongdo location. Highest variations, especially in Al tot and Si contents are shown for hornblendes from the Rongdo area. In a sample of ~2 cm wide leucosome in a mafic diorite, hornblende grains show a trend towards higher Al contents and lower XMg from the centre towards the melanosome rims (Fig. 9, sample TNG165). A significant difference between hornblende composition in melanosome and leucosome is apparent in a diatexite that has diorite as its most probable protolith (samples TNG169a, TNG169b, respectively). Here, grains in the leucosome have higher Fe and lower Mg contents.

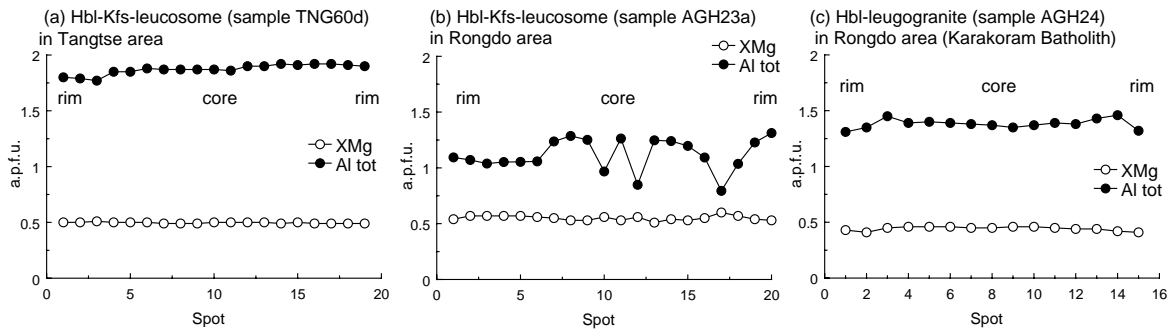


Fig. 11: Examples of line analysis of hornblende grains. (a) Large, poikilitic hornblende in Hbl-Kfs leucosome in Tangtse area. (b) Hornblende grain with slight patchy irregular zoning in Hbl-Kfs leucosome in Rongdo area. (c) Brown-green hornblende with green rims in Hbl-leucogranite of Karakoram Batholith, Rongdo area. Note lower Al tot contents in hornblende from Rongdo area (b and c) compared to the Tangtse area (a). Hornblende in (a) has even Al tot and XMg concentration throughout the whole grain, indicating equilibrium during growth. This is in contrast to hornblende in (b), which has high variations in Al tot. Hornblende in (c) shows slightly lower Al tot on rims, compared to centre of grain. For analysis details see Appendix C.

The Al tot values analysed were used to estimate crystallization pressure using Al-in-Hornblende (Hammarstrom & Zen, 1986, Schmidt, 1992). The required mineral paragenesis for use of this equation, Hbl + Bt + Pl + Qtz + Ttn + Mgt (or Ilm) is present in all studied thin sections. For these estimates, the rim of a growing crystal that is in equilibrium contact with the last phase to crystallize, usually quartz, is most likely to record the pressure of solidification of the rock (Johnson & Rutherford, 1989). Pressure determinations were carried out using (Schmidt, 1992),

$$P \text{ (kbar)} = 4.76 \text{ Al tot} - 3.01.$$

These yielded pressures for rocks in the Tangtse area that are consistently higher than those obtained for samples from the Rongdo region. In samples from the Tangtse area with which we undertook line analyses or probed specifically the rims of hornblende grains (sample TNG60d, Appendix C) hornblendes show constant major element concentrations throughout the grains, and no variation when comparing rims in contact with different minerals. This homogeneity is considered as indicative of equilibrium during crystal growth (Spear, 1981). Hence, we use average values from the line scans of sample TNG60d for pressure estimation, and these yield 5.73 ± 0.23 kbar ($N = 43$). In contrast, line analyses of hornblendes from the Rongdo area show relatively large variations without obvious trends from core to rim (Fig. 11b). We therefore cannot reliably quantify the pressure difference between the

Tangtse and Rongdo regions. However, zonation from core to rim with systematic changes of major element concentrations is apparent in one line analysis (Fig. 11c). For this grain, calculation of the equilibration pressure at the rims yielded 3.22 and 3.26 kbar, respectively. (sample AGH24, Appendix C). These results suggest hornblende in the Karakoram Batholith crystallized at ~2 kbar lower pressures than those in the Tangtse area and are in agreement with the interpretation that the Tangtse area exposes part of the anatectic source region of the leucogranites that were emplaced in the upper crust in the Rongdo area (Reichardt *et al.*, 2010).

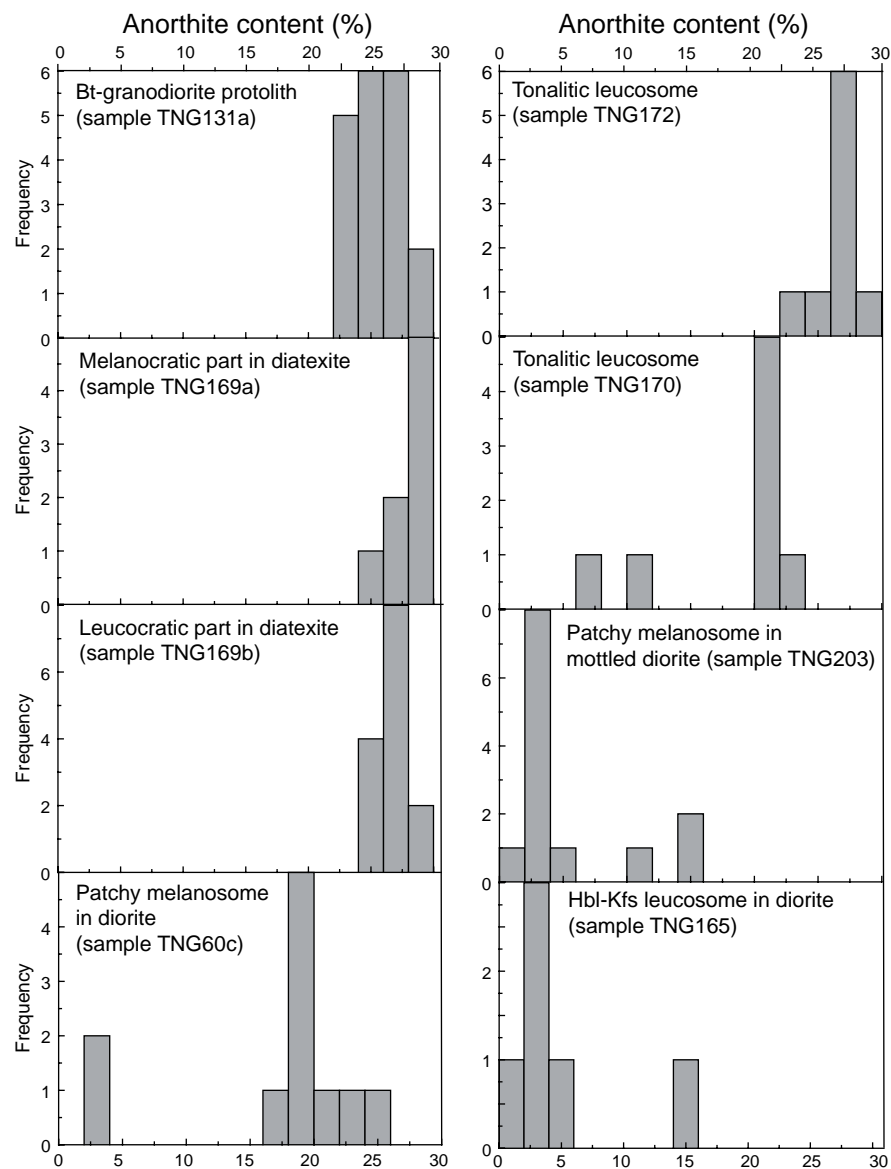


Fig. 12: Anorthite contents of plagioclase. Note overlap in protolith, melanosome and leucosome. For plagioclase electron microprobe data see Appendix D.

Plagioclase

We analysed plagioclase grains from ten samples. Anorthite contents of plagioclase are higher in melanosomes in diorites compared to more silica-rich Bt-granodiorites (Fig. 12). Plagioclase grains in a Bt-granodiorite protolith (whole rock $\text{SiO}_2 = 67.5$ wt %) show compositional ranges ($\text{An} = 22.7$ to 29.1) expected for plutonic rocks of a calc-alkaline differentiation series (Bowen, 1919). Plagioclase in a melanocratic part of diatexite has only slightly higher anorthite contents ($\text{An} = 25.2$ to 29.4) than in its leucocratic counterpart (An

= 24.3 to 28.9). Such small differences between melanosome and leucosome have been reported from migmatites in both water-present and water-absent partial melting (Gupta & Johannes, 1982; Johannes *et al.*, 2003; Kenah & Hollister, 1983), suggesting that plagioclase in the melanosome equilibrated with percolating melt (Marchildon & Brown, 2001). It is also possible that plagioclase in the patchy melanosome is not residual, but a melting product that did not segregate. Leucosome in a diffuse, patch migmatite diorite, has plagioclase with An = 17.4 to 24.5. A Hbl-Kfs leucosome in mafic diorite that has only small plagioclase grains in interstices or as thin overgrowths on K-feldspar, and these have the most sodic composition (An = 1.4 to 19.7) of all analysed samples. Some of these grains are almost pure albite (An = 1.4 to 5.1). Such thin albite rims are also present in Hbl-Kfs leucosome patches in the diorite with mottled texture in Fig. 3b. A tonalitic leucosome shows less calcic plagioclase (An = 20.7 to 22.7) with rims reaching An = 11.9. This data indicates that in general, plagioclase in leucosomes is less calcic than in protoliths and melanosomes, and that albite is only found as small grains in some unusual leucosome types.

5.5.2 Trace element geochemistry

Trace elements are useful indicators of partial melting processes. In order to better understand these processes, we undertook mineral analysis using LA-ICP-MS. We report trace element concentrations of the main mineral phases in the migmatites of the PMC with particular emphasis on hornblende (Table 3). Abnormal analyses where the laser hit an inclusion leading to extreme values for certain trace elements, e.g. Zr for zircon, La, Ce and Th for allanite and Ba for K-feldspar, have been omitted from the results.

Hornblende

Hornblendes from eight samples were analysed and show large variation in trace element contents, and substantially distinct patterns in chondrite normalized REE and multi-element profiles (Fig. 13, 14). This is rather surprising and in sharp contrast to values in the literature where hornblende has a well-defined bell-shaped, concave downward REE pattern dependent on the silica content of the host magma, with a maximum value around the MREE (e.g. Hilyard *et al.*, 2000; Tiepolo *et al.*, 2007).

In terms of REE patterns it is possible to group together hornblendes of a Hbl-Bt-granodiorite, a melanocratic part of a diatexite and a patchy, tonalitic leucosome in diatexite (first three samples in Table 3). These hornblendes show rising concentrations from LREE to MREE in a concave downward shape, remarkably followed by a relatively flat trend from MREE to HREE without defining the common peak in values around Gd to Dy. The averages from analyses of these three samples show La_n/Yb_n values of 0.42 ± 0.22 , 0.55 ± 0.34 and 0.30 ± 0.08 (Fig. 13a, b and c. Table 3). Despite these similarities, the Hbl-Bt-granodiorite is the only sample that show hornblendes with positive Eu anomalies (average $Eu/Eu^* = 1.53 \pm 0.38$). Concentrations of LILE (Rb, Ba and Sr) are comparable in these samples. However, the melanocratic diatexite (sample TNG169a) shows much higher Nb and Ta contents, but lower Th contents.

Hornblendes from Hbl-Kfs leucosomes and a patchy melanosome bordering a Hbl-Kfs

leucosome form another distinct group of wave-shaped REE patterns (Fig. 13 d, e, f). They have concave downward LREE to MREE shape and concave upward MREE to HREE shape. While the REE patterns of the Hbl-Kfs leucosome and the bordering patchy melanosome in a dioritic protolith in the Tangtse area are essentially similar (Fig. 13 d, e), the Hbl-Kfs leucosome from the Rongdo location (Fig. 13f) shows enrichment in LREE and a decrease toward MREE.

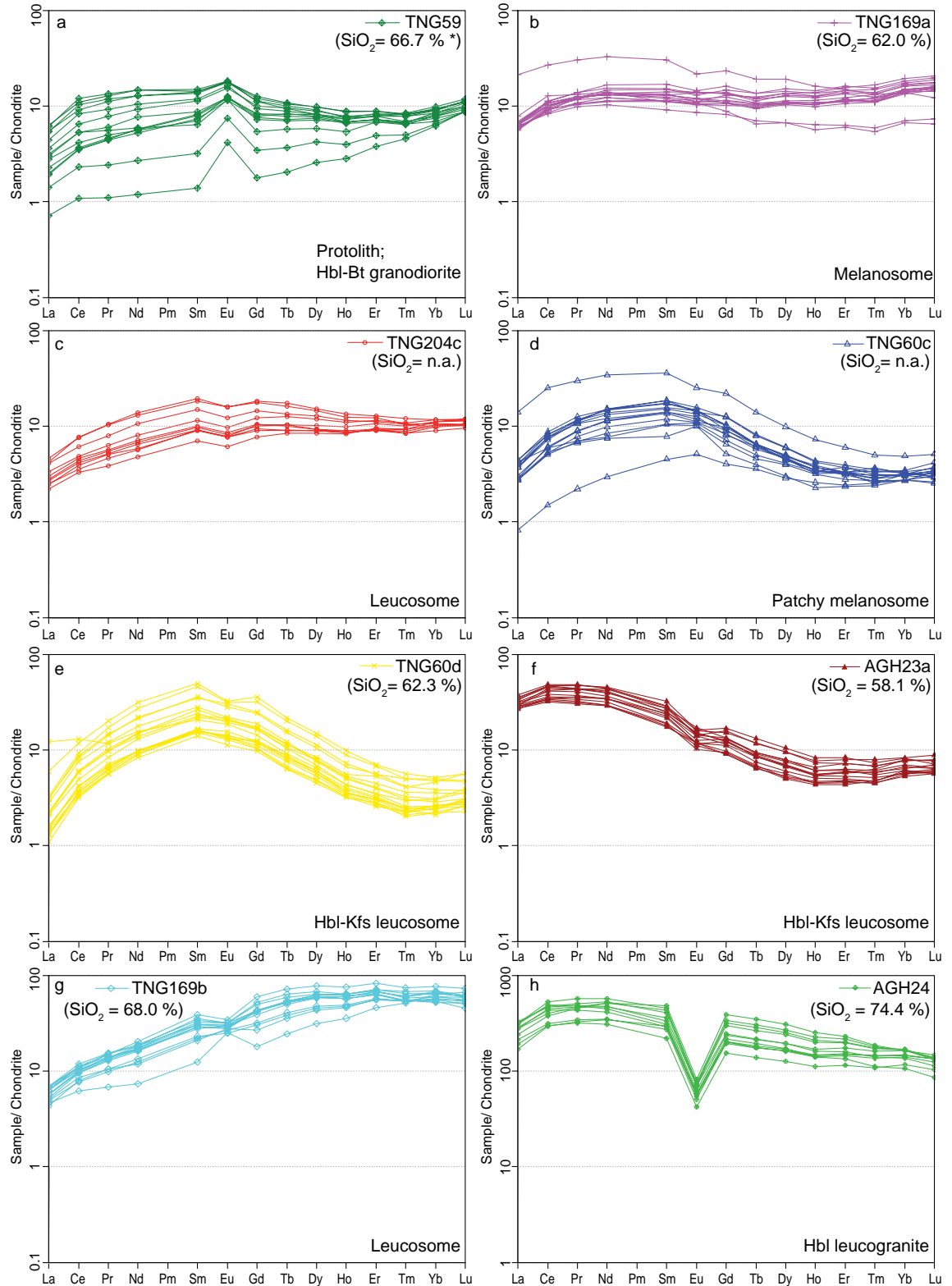


Fig. 13: REE patterns for hornblende. Chondrite normalization in all REE plots after Boynton (1984). SiO_2 content of whole rock of the respective samples are indicated where available. The SiO_2 content for sample TNG59 is estimated from a comparable Hbl-Bt-granodiorite (sample TNG98a, Table 1). Note different scale on y-axis in (h).

Table 3. Trace elements concentrations (ppm) of hornblende

Sample Rock type Average of N analyses	TNG59 N=14		TNG169a N=17		TNG169b N=13		TNG204c N=10		TNG60c N=15		TNG60d N=18		AGH23a N=15		AGH24 N=11	
	Hbl-Bt-granodiorite	melanosome in diorite	leucosome in diorite	leucosome in diorite	leucosome in diorite	melanosome in diorite	leucosome in diorite	melanosome in diorite	Hbl-Kfs leucosome	Hbl-Kfs leucosome	Hbl-Kfs leucosome	Hbl-Bt-leucogranite				
Sc	72.21 ± 6.78	n.a	114.85 ± 12.50	72.72 ± 8.65	30.88 ± 5.35	45.50 ± 6.48	42.95 ± 3.88	154.25 ± 41.79								
Ti	5785.20 ± 256.00	n.a	8224.30 ± 494.16	7041.94 ± 239.18	4997.07 ± 175.25	3742.07 ± 235.52	4046.88 ± 665.01	10297.36 ± 2108.61								
V	442.67 ± 34.36	n.a	273.66 ± 15.24	511.19 ± 76.03	357.26 ± 22.83	289.72 ± 22.26	261.91 ± 32.08	578.03 ± 149.70								
Cr	132.75 ± 107.46	n.a	31.88 ± 6.54	138.18 ± 25.07	27.62 ± 38.67	256.52 ± 182.58	81.63 ± 27.29	49.85 ± 11.82								
Mn	4215.62 ± 130.99	3447.43 ± 380.49	5300.46 ± 210.94	2887.69 ± 64.38	2596.91 ± 147.84	3033.59 ± 168.87	3295.95 ± 151.32	4008.03 ± 792.72								
Co	49.68 ± 1.86	n.a	32.74 ± 1.02	52.71 ± 1.54	56.54 ± 3.99	60.68 ± 3.82	58.37 ± 4.49	46.88 ± 4.51								
Ni	41.85 ± 5.06	n.a	18.06 ± 0.84	115.67 ± 12.55	13.27 ± 2.29	151.74 ± 18.23	83.95 ± 17.18	10.68 ± 2.55								
Cu	4.84 ± 4.53	n.a	b.d	2.25 ± 0.76	11.19 ± 17.54	13.53 ± 17.26	5.57 ± 6.49	1.25 ± 0.68								
Zn	365.86 ± 36.56	n.a	459.92 ± 40.52	399.96 ± 20.24	570.11 ± 47.08	500.67 ± 25.92	501.75 ± 29.54	297.11 ± 28.99								
Ga	37.34 ± 2.24	n.a	39.64 ± 1.07	39.20 ± 2.13	39.31 ± 2.47	42.49 ± 1.56	25.89 ± 3.95	25.33 ± 2.64								
Rb	13.59 ± 4.63	4.53 ± 0.89	9.98 ± 0.82	12.48 ± 1.30	20.31 ± 2.34	14.99 ± 1.34	8.01 ± 5.00	3.81 ± 0.57								
Sr	37.99 ± 8.20	41.32 ± 6.23	72.92 ± 6.91	69.42 ± 4.62	144.90 ± 13.35	74.81 ± 5.65	77.30 ± 8.74	57.42 ± 14.14								
Y	15.27 ± 3.48	24.23 ± 5.58	118.16 ± 19.17	21.28 ± 3.71	8.47 ± 2.32	11.31 ± 4.49	13.38 ± 2.77	350.02 ± 78.81								
Zr	17.53 ± 1.88	n.a	25.91 ± 3.47	30.39 ± 3.83	52.25 ± 91.49	16.27 ± 1.31	27.46 ± 4.35	79.71 ± 14.62								
Nb	7.60 ± 1.29	15.83 ± 5.16	58.89 ± 6.84	7.69 ± 1.84	5.26 ± 0.81	4.28 ± 0.52	7.45 ± 1.96	43.10 ± 9.45								
Ba	26.49 ± 49.13	24.15 ± 10.76	73.81 ± 11.20	113.85 ± 23.00	107.62 ± 11.67	50.34 ± 5.38	39.63 ± 13.44	139.18 ± 67.97								
La	1.08 ± 0.56	2.26 ± 1.15	1.81 ± 0.29	0.99 ± 0.26	1.27 ± 0.90	0.87 ± 0.82	0.97 ± 1.03	82.80 ± 16.92								
Ce	5.00 ± 2.81	8.96 ± 3.42	7.82 ± 1.31	4.07 ± 1.29	6.24 ± 4.20	5.00 ± 2.44	32.70 ± 4.84	333.78 ± 65.51								
Pr	0.87 ± 0.48	1.61 ± 0.57	1.55 ± 0.31	0.80 ± 0.29	1.29 ± 0.73	1.21 ± 0.53	4.87 ± 0.76	54.06 ± 9.78								
Nd	4.93 ± 2.63	8.69 ± 2.99	9.52 ± 2.14	4.95 ± 1.91	7.73 ± 4.17	8.94 ± 4.11	22.43 ± 3.52	269.73 ± 51.15								
Sm	1.82 ± 0.83	2.70 ± 0.92	5.51 ± 1.38	2.31 ± 0.83	2.94 ± 1.38	4.74 ± 2.12	4.71 ± 0.87	68.73 ± 16.53								
Eu	0.99 ± 0.31	0.91 ± 0.21	2.16 ± 0.21	0.74 ± 0.26	0.96 ± 0.32	1.45 ± 0.51	1.00 ± 0.16	4.67 ± 0.87								
Gd	2.16 ± 0.82	3.26 ± 0.90	10.44 ± 2.90	3.11 ± 0.95	2.51 ± 1.09	4.44 ± 1.97	3.21 ± 0.63	66.13 ± 18.80								
Tb	0.37 ± 0.12	0.53 ± 0.14	2.38 ± 0.60	0.55 ± 0.15	0.31 ± 0.12	0.53 ± 0.21	0.42 ± 0.10	10.81 ± 3.05								
Dy	2.42 ± 0.66	3.82 ± 0.95	18.39 ± 3.92	3.54 ± 0.81	1.58 ± 0.53	2.49 ± 0.99	2.32 ± 0.55	66.20 ± 17.89								
Ho	0.49 ± 0.12	0.82 ± 0.19	4.12 ± 0.74	0.73 ± 0.13	0.27 ± 0.08	0.36 ± 0.14	0.42 ± 0.09	12.50 ± 3.11								
Er	1.53 ± 0.30	2.57 ± 0.60	13.56 ± 1.95	2.21 ± 0.31	0.71 ± 0.18	0.86 ± 0.30	1.26 ± 0.27	35.88 ± 7.58								
Tm	0.23 ± 0.04	0.39 ± 0.09	1.91 ± 0.22	0.32 ± 0.04	0.10 ± 0.02	0.10 ± 0.04	0.19 ± 0.04	4.91 ± 0.86								
Yb	1.72 ± 0.23	3.05 ± 0.71	12.96 ± 1.43	2.21 ± 0.18	0.67 ± 0.11	0.67 ± 0.22	1.40 ± 0.22	30.89 ± 4.43								
Lu	0.33 ± 0.04	0.49 ± 0.12	1.87 ± 0.24	0.35 ± 0.03	0.11 ± 0.02	0.11 ± 0.03	0.22 ± 0.03	4.06 ± 0.59								
Hf	1.12 ± 0.13	1.09 ± 0.10	1.59 ± 0.27	1.53 ± 0.17	1.71 ± 1.84	1.04 ± 0.14	1.82 ± 0.52	4.91 ± 0.85								
Ta	0.07 ± 0.02	0.29 ± 0.14	1.84 ± 0.53	0.10 ± 0.04	0.05 ± 0.02	0.03 ± 0.01	0.10 ± 0.04	1.71 ± 0.49								
Pb	5.49 ± 1.35	1.65 ± 0.54	3.24 ± 0.19	5.74 ± 0.37	28.09 ± 64.47	6.70 ± 1.45	4.21 ± 1.03	4.32 ± 0.55								
Th	0.34 ± 0.54	0.03 ± 0.09	0.02 ± 0.01	0.07 ± 0.02	1.71 ± 5.53	0.18 ± 0.23	0.11 ± 0.03	1.02 ± 0.24								
U	0.13 ± 0.06	0.11 ± 0.16	0.09 ± 0.05	0.08 ± 0.02	0.47 ± 0.95	0.10 ± 0.03	0.06 ± 0.02	0.19 ± 0.05								
La _N /Yb _N	0.42 ± 0.22	0.55 ± 0.34	0.09 ± 0.01	0.30 ± 0.08	1.23 ± 0.57	0.87 ± 0.80	4.72 ± 0.64	1.80 ± 0.24								
La _N /Sm _N	0.37 ± 0.08	0.52 ± 0.10	0.22 ± 0.05	0.28 ± 0.03	0.26 ± 0.07	0.12 ± 0.12	1.32 ± 0.18	0.78 ± 0.17								
Gd _N /Yb _N	1.01 ± 0.37	0.90 ± 0.26	0.65 ± 0.18	1.13 ± 0.32	2.97 ± 0.87	5.26 ± 0.98	1.84 ± 0.23	1.72 ± 0.35								
Eu/Eu*	1.53 ± 0.38	0.96 ± 0.08	0.93 ± 0.26	0.84 ± 0.02	1.13 ± 0.17	0.99 ± 0.09	0.80 ± 0.08	0.22 ± 0.02								
Sum REE	23.94 ± 9.45	40.06 ± 11.32	94.00 ± 16.12	26.87 ± 7.18	26.69 ± 13.60	31.79 ± 13.45	84.82 ± 12.34	1045.16 ± 189.68								

± indicates 1 standard deviation. For complete analysis see Appendix E.

A leucocratic part of a diatexite contains hornblendes that show extreme enrichments in HREE (Fig. 13g). The hornblendes show concave downwards shapes from LREE to MREE and relatively flat shapes from MREE to HREE. However, REE concentrations are overall rising towards HREE reaching up to ~ 70 times enrichment compared to chondrite values. This leads to extremely low La_n/Yb_n values with an average of 0.09 ± 0.01 . These hornblendes also show extremely high Nb and Ta concentrations (Fig. 14b).

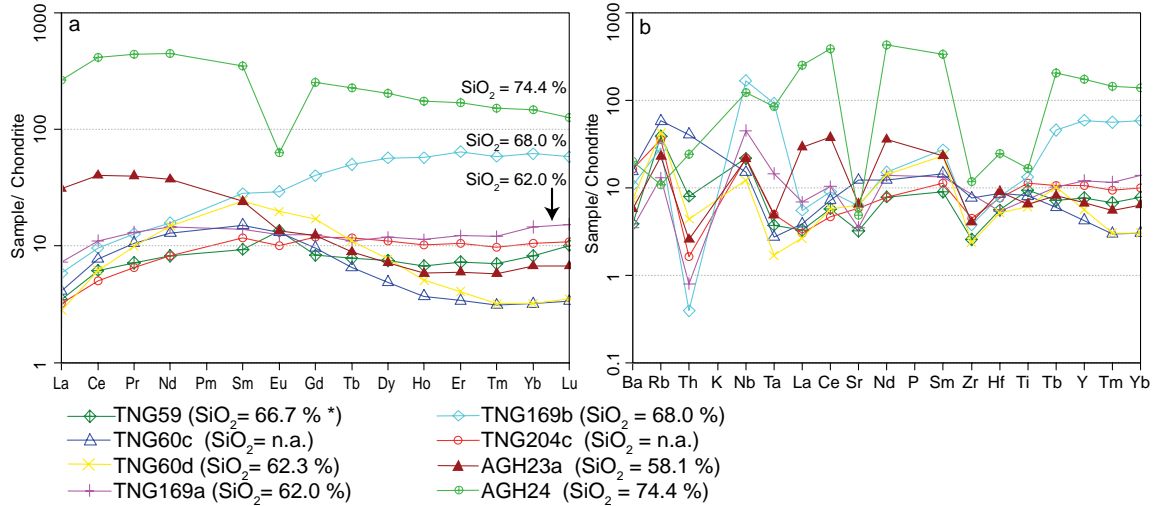


Fig. 14: REE patterns of averages of hornblende for all samples shown in Fig. 13. (b) Multi-element patterns of hornblende normalized to values of Sun & McDonough (1989).

Finally, a Hbl-Bt-leucogranite from the Karakoram Batholith from the Rongdo location (Fig. 13g; sample AGH24, $SiO_2 = 74.4$ wt %) shows hornblendes entirely different to all other analysed samples. These are extremely enriched in REE (sum REE = 1045 ± 190 ppm) in comparison with the highest total REE concentration reached in the other samples of 94.00 ± 16.12 ppm (sample TNG169b). The overall shape is moderately concave downward. Eu anomalies are strong and negative ($Eu/Eu^* = 0.19$ to 0.24). La_n/Yb_n values are above unity, on average 1.80 ± 0.24 . Nb and Ta concentrations are high, and only slightly lower than those from hornblendes in the leucosome sample TNG169b. Interestingly, not all trace elements show similar severe enrichments, with Ba and Sr values comparable to the values from the samples above, and the lowest Rb contents of all samples (Fig. 14b).

In summary, trace element concentrations in hornblende are consistent between grains within each sample, but highly variable across all samples.

REE patterns of other minerals

Here we detail REE patterns of clinopyroxene, biotite, plagioclase, titanite and allanite (Fig. 15). Plagioclase from a patchy leucosome and a patchy melanosome in diorite show low REE concentrations except for Eu. Clinopyroxene shows wave-like REE shapes with concave upward LREE to MREE and concave downward MREE to HREE patterns. REE contents in biotite were generally too low to yield reliable results except for two analyses. One from a Hbl-Bt-granodiorite protolith that shows a flat REE pattern, the other from a Hbl-leucogranite from the Karakoram Batholith, Rongdo area (sample AGH24). The latter shows a relatively flat REE pattern with slight enrichment of LREE over HREE ($La_n/Yb_n = 2.2$), a positive Eu anomaly ($Eu/Eu^* = 2.18$) and REE concentrations on average more than

100 times chondrite values. Overall REE enrichment is unusual for biotite (e.g. Gromet & Silver, 1983), and we note that severe REE enrichment was also found for hornblendes of the same sample (AGH24). Despite these REE-rich hornblende and biotite, the whole rock REE pattern of this sample shows only higher values of HREE compared to leucogranites of the PMC (Table 1).

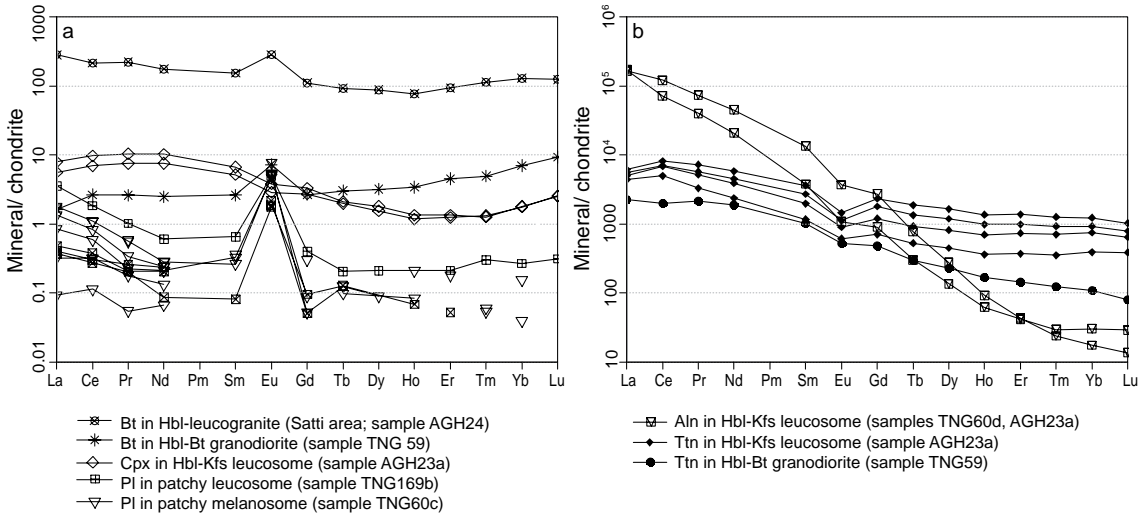


Fig. 15: (a) REE patterns of biotite, clinopyroxene and plagioclase. (b) REE patterns for allanite in Hbl-Kfs leucosome and titanite in Hbl-Bt-granodiorite and in Hbl-Kfs leucosome. For LA-ICP-MS data see Appendix F.

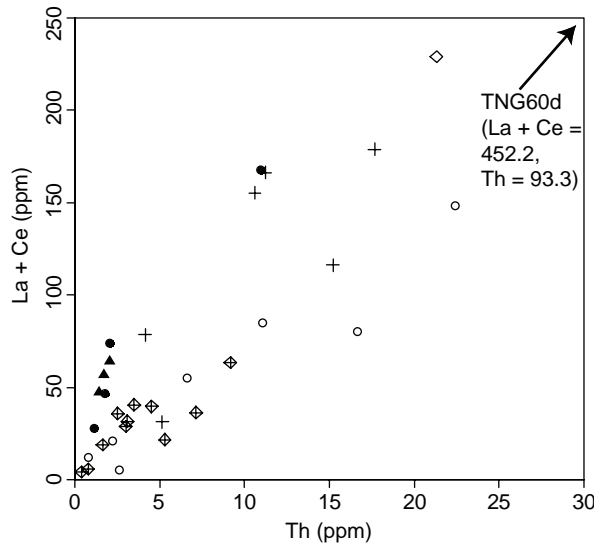


Fig. 16: La + Ce vs. Th diagram. The positive correlation of these elements indicates control of allanite in the whole rock geochemistry (e.g. Hermann, 2002). The extreme enrichments of these elements in the Hbl-Kfs leucosome are not shown for scaling reasons.

Our results for titanite and allanite (Fig. 15 b) compare well with the results of Gromet & Silver (1983). Titanite shows an overall REE enrichment of more than 1000 times chondrite values, slightly convex upward LREE to MREE pattern, negative Eu anomalies ($\text{Eu}/\text{Eu}^* = 0.50$ to 0.74). We obtained two analyses of allanite grains from Hbl-Kfs leucosomes (samples TNG60d, AGH23a). These show extreme enrichment in LREE, reaching around 10^5 chondrite values for La and Ce, and strong fractionation of LREE over HREE ($\text{La}_n/\text{Yb}_n = 5603.69$). The allanite grains also show extremely high Th concentrations (see Appendix F), indicating its potential control on the whole rock Th budget (Hermann, 2002). High La and Ce concentrations are not surprising as these elements are part of allanite's stoichiometry.

The coupling of La and Ce with Th concentrations of the whole rock (Fig. 16) confirms large contributions of allanite to the trace element budget of whole rocks.

The influence of titanite and allanite on whole rock REE contents is particularly evident in the Hbl-Kfs leucosomes that are rich in these accessory phases, and that show LREE enrichment, the highest total REE and highest Th contents of all analysed whole rocks (Fig. 7e; Table 1). Interestingly, the only hornblendes that show LREE enrichment over MREE and HREE were found in one of allanite-bearing Hbl-Kfs leucosomes (sample AGH23a). In the following we use geochemical model calculations to evaluate the significance of different mineral modal contents in the migmatites by using data from the literature as well as our own analyses.

5.6 Geochemical modelling

Models to calculate element concentrations are commonly applied to simulate partial melting of known source rocks, the melt products or to identify unknown sources hidden at depth. In the PMC, field relations allow for good control on choosing appropriate samples that exemplify source rocks, *in situ* melt products (leucosome) and residual rocks (melanosome). However, approaches to model the complicated processes involved in partial melting have the intrinsic risk of oversimplification. Despite these limitations, relatively simple model calculations can be used to test assumptions drawn from field observations and the interpretation of geochemical data. We therefore apply numerical models to test if we can reproduce the geochemical signatures of melts stemming from the migmatites in the PMC under special consideration of the role of hornblende.

5.6.1 Batch melting

For modelling of partial melting we used a two step approach. The first step is equilibrium batch melting after the equations of Shaw (1970):

$$C_L^i = \frac{C_0^i}{D_{(bulk)} + F(1 - D_{(bulk)})}$$

In this simple model, the mineral proportions in the protolith and in the partial melt are constant, and it follows that the results are only sensitive to the initial mineral proportions and to the partition coefficients $D_{(bulk)}$ for each element and not to the melting reaction. Further, any fractionation and accumulation processes are not accounted for. Here, C_L represents the concentration of mineral i in the liquid in relation to its concentration in the initial solid C_0 . The amount of partial melting is given as the percentage F , where all mineral contribute to the melt equally. The partition coefficient $D_{(bulk)}$ is the sum of D of mineral i , multiplied by its weight proportion in the initial solid ($D_{(bulk)} = \sum D_i X_i$).

We modelled partial melting of the average of two Hbl-Bt-granodiorites and two diorites that were chosen as representative protoliths based on their petrography. Estimated initial modal mineral proportions were also based on petrographic observations on thin sections. However, measuring the correct amount of accessory phases is difficult, and small variations can have large effects on the REE pattern. To avoid bias in the model calculations, we chose

equal amounts (0.5 % modal content) of allanite, apatite and zircon for the batch melting model. The used partition coefficients are given in Table 4. Petrographic observations have shown that the Hbl-Kfs leucosomes contain unusually high amounts of accessory phases. This makes modelling of these rocks extremely difficult and hence these leucosomes are not considered in our models.

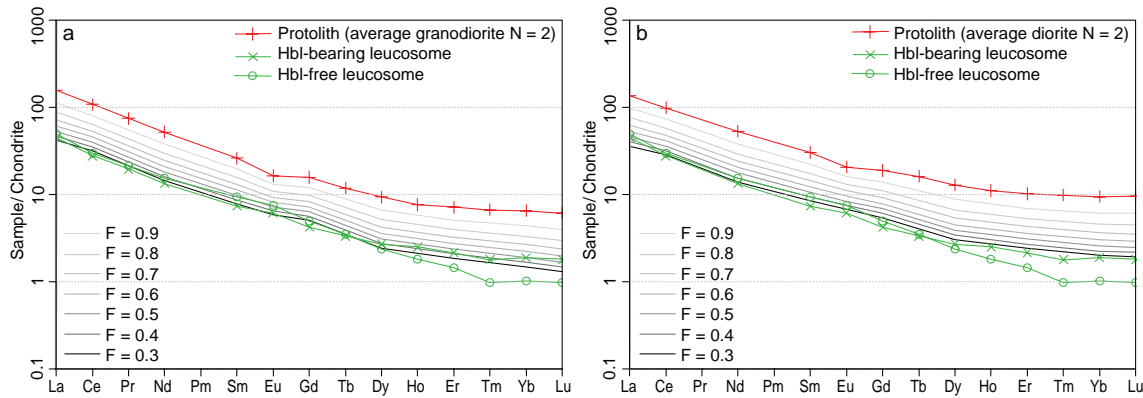


Fig. 17: Equilibrium batch melting models after Shaw (1970). The set of used partition coefficients is given in Table 4. Results show melt composition for 10 % increments of partial melting. Representative Hbl-bearing leucosome is sample TNG114b1 (Table 1). Representative Hbl-free leucosome is sample TNG113g (Table 1). (a) Partial melting of average Hbl-Bt-granodiorite protolith $N = 2$ (samples TNG98a, TNG207; Table 1). Mineral proportions of protoliths are roughly estimated from petrography in thin sections and are expressed as fractions. $Pl = 0.2$, $Kfs = 0.1$, $Qtz = 0.22$, $Hbl = 0.2$, $Bt = 0.255$, $Ttn = 0.01$, $Aln = 0.005$, $Ap = 0.005$, $Zrn = 0.005$. (b) Partial melting of average (Qtz)-diorite protolith $N = 2$ (samples TNG205a, TNG205b; Table 1); Mineral proportions of protolith estimated from petrography in thin sections are $Pl = 0.225$, $Kfs = 0.1$, $Qtz = 0.15$, $Hbl = 0.3$, $Bt = 0.2$, $Ttn = 0.01$, $Aln = 0.005$, $Ap = 0.005$, $Zrn = 0.005$. Note that these values are estimates only despite the precise numerical values given here.

Table 4. Partition coefficients used in batch melt model

Mineral	K_D La	K_D Ce	K_D Nd	K_D Sm	K_D Eu	K_D Gd	K_D Dy	K_D Er	K_D Yb	K_D Lu	Author(s)
Plagioclase	0.26*	0.24	0.17	0.13	2.11	0.9	0.086	0.084	0.077	0.062	Schnetzer & Philpotts (1970)
K-feldspar		0.044	0.025	0.018	1.13	0.011	0.006	0.06	0.001	0.006*	Schnetzer & Philpotts (1970)
Quartz	0.015	0.014	0.016	0.015	0.056	0.01	0.015	0.01	0.017	0.014	Nash & Crecraft (1985)
Amphibole	0.7	0.89	2.89	3.99	3.44	5.48	6.2	5.94	4.89	4.53	Arth & Barker (1976), dacite
Biotite		0.037	0.044	0.058	0.145	0.082	0.097	0.162	0.179		Schnetzer & Philpotts (1970)
Titanite	46	87	152	204	181	200	206	180*	104	92	Luhr & Carmichael (1980)
Zircon	1.14	1.17	1.38	2.03	0.85	6.01	44.9	107	516	689	Fujimaki (1986)
Apatite	28.2	29.6	57.1	84.8	9.22		246	275	232	199	Nagasawa (1970)
Allanite	820	635	463	205	81	130	50	20	8.9	7.7	Brooks (1980)

*interpolated values

The results in Fig. 17a and b show that for melt fractions of ~30%, there is good agreement between the calculated melt compositions and representative leucosomes (samples TNG114b1, TNG113g) for LREE to MREE. In contrast, this model can only produce melts with HREE contents that agree with those in Hbl-bearing leucosomes, whereas Hbl-free leucosomes have significantly lower HREE. Only few commonly occurring minerals are enriched in, and can fractionate HREE. These are cordierite, zircon, garnet and hornblende (Arth & Barker, 1976; Ayres & Harris, 1997; Bea *et al.*, 1994; Gromet & Silver, 1983). Cordierite and garnet were not found in our samples and zircon was only found in small amounts, and these minerals are thus not further considered in the model. On the contrary, hornblende is an important rock forming mineral in both leucosomes and protoliths and therefore we detail further the effects

of hornblende fractionation and accumulation. Because we inferred from field observations that leucosomes with and without hornblende are linked on outcrop scale, we model in a second step, the effect of hornblende fractionation in migmatites (Fig. 19). For these models, we use hornblende data from our own analysis.

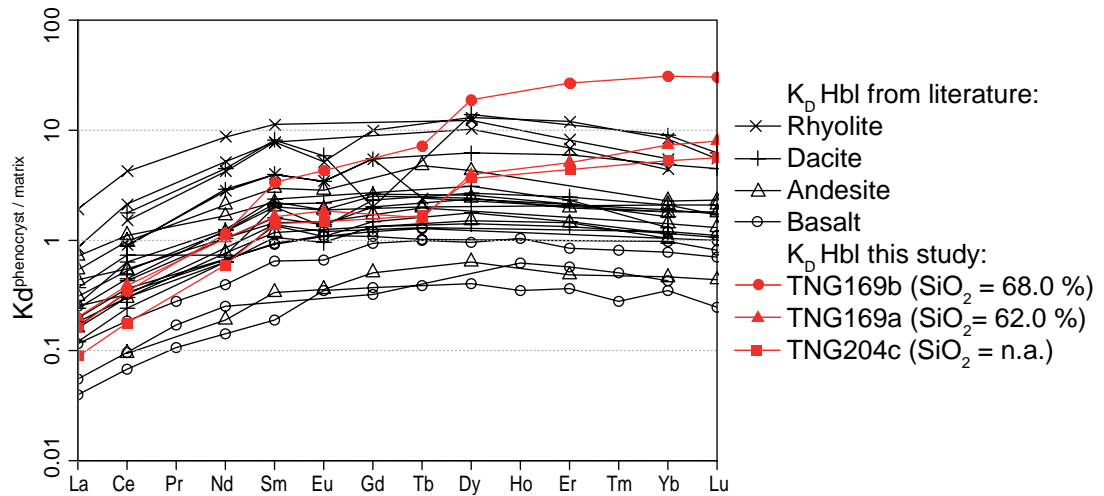


Fig. 18: Comparison of published partition coefficients for hornblende and calculated values from our own data. Note that from our experience, Hbl K_D values in our migmatites vary from sample to sample, and can thus not be applied to different rocks. Also note large variations ranging from incompatibility to highly compatible in the data from the literature with rising values from basaltic to rhyolitic rocks. Data taken from Arth (dacite; 1976), Arth & Barker (dacite; 1976), Bacon & Druitt (andesite, rhyolite; 1988), Botazzi et al. (basalt; 1999), Dalpe & Baker (basanite-basalt; 1994), Dostal et al. (basalt-andesite; 1983), Fujimaki et al. (andesite; 1984), Higuchi & Nagasawa (basalt; 1969), Klein et al. (dacite; 1997), Latourette et al. (basanite; 1995), Luhr et al. (trachyandesite; 1984), Matsui et al. (basalt, andesite; 1977), Nagasawa & Schnetzler (dacite; 1971), Sisson (basalt-andesite, dacite, rhyolite; 1994), Tiepolo et al. (dacite; 2000).

Table 5. Calculated partition coefficients of hornblende

	melt*	TNG169a	TNG169b	TNG204c	TNG169a	TNG169b	TNG204c
	Hbl ppm	Hbl ppm	Hbl ppm	Hbl ppm	K_D Hbl	K_D Hbl	K_D Hbl
La	11.19	2.26	1.81	0.99	0.20	0.16	0.09
Ce	23.03	8.96	7.82	4.07	0.39	0.34	0.18
Nd	8.33	8.69	9.52	4.95	1.04	1.14	0.59
Sm	1.64	2.70	5.51	2.31	1.65	3.37	1.41
Eu	0.50	0.91	2.16	0.74	1.84	4.35	1.48
Gd	1.41	3.26	10.44	3.11	2.32	7.42	2.21
Tb	0.33	0.53	2.38	0.55	1.59	7.18	1.68
Dy	0.97	3.82	18.39	3.54	3.93	18.93	3.64
Er	0.50	2.57	13.56	2.21	5.11	26.96	4.39
Yb	0.42	3.05	12.96	2.21	7.35	31.21	5.32
Lu	0.06	0.49	1.87	0.35	8.05	30.47	5.66

*estimated melt composition taken from calculated 30% partial melting of diorite.

5.6.2 Fractional crystallization

For the fractional crystallization model, we use the equation for Rayleigh fractionation, in which the crystallizing phase is removed from the melt without equilibration with melt (Shaw, 1970).

$$C_L^i = C_0^i \cdot F^{(D_i-1)}$$

Choosing the correct partition coefficients is difficult because our La-ICP-MS data shows large variations for trace element concentrations of hornblende within our dataset and these

also contrast to the hornblende data in the literature. Our hornblende REE patterns cannot be achieved using available K_D s. We therefore applied hornblende partition coefficients derived from our own data (Fig. 18, Table 5). To calculate crystal/ melt partition coefficients $^{S/L}D$ for hornblende, we used the following equation:

$$^{S/L}D_i = \frac{{}^SC_i}{{}^LC_i},$$

where SC_i is the concentration of element i in the solid (= crystal), and LC_i its concentration in the liquid (= melt). However, the results are only valid if equilibrium between melt and crystal has been attained. Although we assume based on the texture in thin section and the consistency of the hornblende compositions within each sample, that the hornblende grains were in equilibrium with the melt, the results have to be interpreted with some caution. For this model, we used the hornblende data from three samples from the meta- and diatexite outcrops in the Tangtse gorge (samples TNG169a, TNG169b, TNG204c; Fig. 14 b, c, g) because these are directly related to the leucosomes we aim to model. We can only estimate approximate values for melt compositions based on the batch melting calculations above. As approximate melt compositions, we used the values of partial melt for $F = 0.3$ from the diorite batch melting model in Fig. 17b. The calculated partition coefficients of hornblende are given in Table 5.

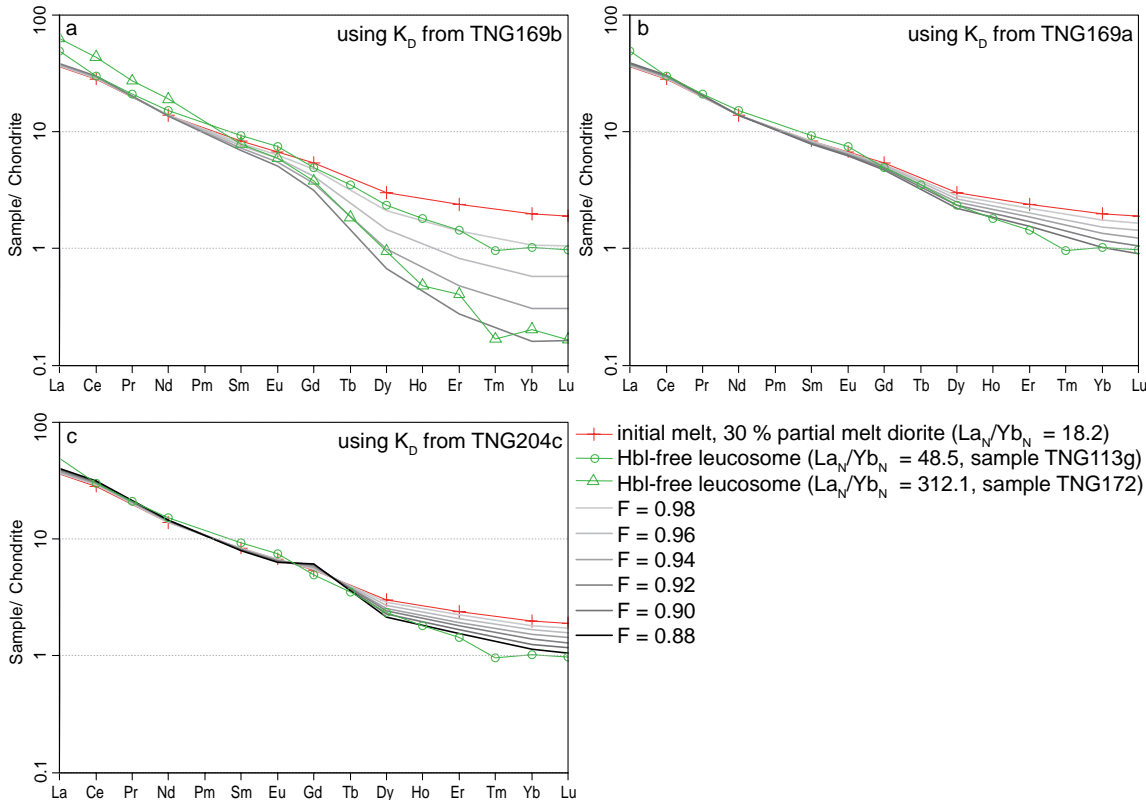


Fig. 19: Models of melt compositions after Rayleigh mineral fractionation from an initial melt. Initial melt composition taken from 30 % partial melting ($F = 0.3$) of average diorite in Fig. 17b. Partition coefficients K_D for hornblende are shown in Table 5. (a) Fractionation of hornblende with calculated K_D from sample TNG169b. Note extreme HREE depletions for small values of fractionation. (b) Fractionation of hornblende with K_D from sample TNG169a. (c) Fractionation of hornblende with calculated K_D from sample TNG204c.

Our results in Fig. 19 show that <10 % hornblende fractionation from a calculated initial melt can reproduce the relative HREE depletion and thus high La_N/Yb_N values of Hbl-free leucosomes. In case of the hornblendes with extremely high partition coefficients for HREE (sample TNG169b), only ~2% fractionation ($F = 0.98$) is enough to reproduce the MREE to HREE shape of the Hbl-free leucosome (sample TNG113g, Table 1), and fractionation of these hornblendes can also model the extreme HREE depletions found in one particular leucosome ($\text{La}_N/\text{Yb}_N = 312$, sample TNG172, Table 1).

5.6.3 Accumulation model

Some diatexites represent accumulations of hornblende, and these are reflected in their REE patterns. In particular, two melanocratic diatexite samples (TNG113f, h) show REE patterns that do not compare well with protolith, melanosome or leucosome (Fig. 7a, 20). Field observations showed high amounts of hornblende in these parts of the sampled diatexites, and we model their origin by calculating the effects of adding hornblende through a process of hornblende accumulation. We used the equation for Rayleigh crystal accumulation, assuming that the cumulate crystals are effectively taken out of the melt without further equilibration as follows:

$$C_s^i = C_0^i \frac{1 - F^{D_i}}{1 - F}$$

The partition coefficients for hornblende were taken from our hornblende analyses as calculated above (Table 5). In Fig. 20 we show an example of hornblende accumulation, modelling 20 % accumulation ($F = 0.2$) in a Hbl-bearing leucosome sample that has an REE shape sub-parallel to leucosomes from the batch melting model, but with higher overall REE concentrations. The results indicate that hornblende accumulation reproduces the REE shapes of diatexites with high amounts of hornblende.

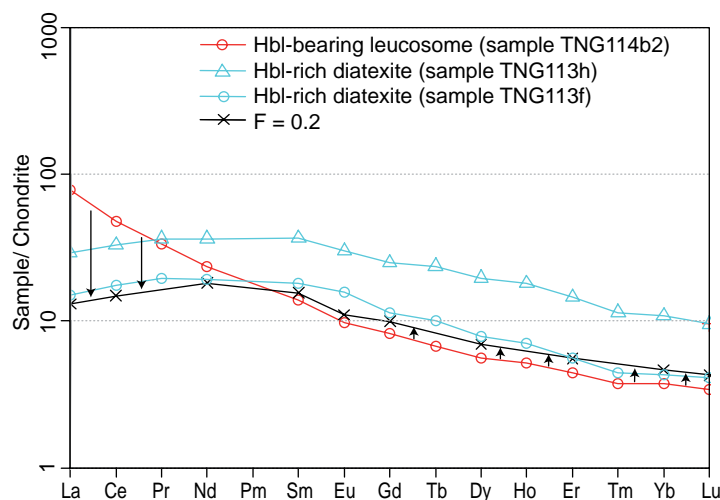


Fig. 20: Model of hornblende accumulation in diatexites using partition coefficients for hornblende from sample TNG204c (Table 5). In this case, accumulation of ~20 modal % hornblende to sample TNG114b2 (Table 1) reproduces the REE shape of Hbl-rich diatexite TNG113f (Table 1). Higher or lower overall REE values of the initial rock would shift the resulting REE shape of the Hbl-cumulate rock up or down, respectively.

Other leucosomes show low overall REE contents and positive Eu anomalies (Figs. 7d, 21; samples TNG170, TNG171). These leucosomes also have high Sr and Ba concentrations, and the petrography suggests that they are largely feldspar cumulates. Because of comparable K_D s for plagioclase and K-feldspar (Table 4), changes of the cumulate proportions only have minor effect on the modelling result. For simplicity we thus calculated plagioclase and K-feldspar accumulation in equal proportions. In this case, we assumed equilibration with the melt, thus considering changing compositions of the melt. This modification replaces C_0 with C_L that is calculated from the fractional crystallization model. This calculation thus uses mass balancing of the results of the fractional crystallization model as follows:

$$C_S^i = C_L^i \frac{1 - F^{D_i}}{1 - F}$$

The results in Fig. 21 confirm that some of the leucosomes are likely to be the product of accumulation of feldspars (~15 to 25 % modal content) in the initial partial melt. We emphasize that these models are by no means unique solutions and combinations of crystallization of a primary partial melt, fractionation of some minerals and accumulation of other minerals might very well occur. In summary, the numerical models explain the REE patterns of diatexites that have lost hornblende and diatexites that gained hornblende (Fig. 7c), and they also explain high La_n/Yb_n values in Hbl-free, granitic leucosomes.

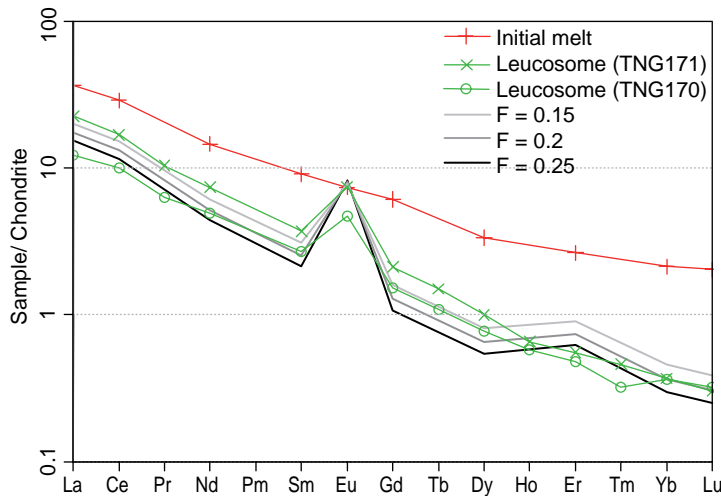


Fig. 21: Model of feldspar accumulation in leucosomes. Accumulating crystals are plagioclase and K-feldspar in equal proportions. Partition coefficients are taken from Table 4. Initial melt composition is taken from 30 % batch melting of average diorite (Fig. 17b).

6. Discussion

6.1 REE patterns of hornblende and partition coefficients

Our trace element data for hornblende show large variations. These cannot be explained with mineral/ melt partition coefficients from the literature. Despite a plethora of partition coefficients for hornblende being available, these are unlikely to be applicable to the migmatites we investigated. In general, the partition coefficients of hornblende increase with decreasing ionic radius of REE from LREE to MREE, reaching a maximum at Dy

or Ho and slightly decreasing towards HREE, giving rise to an overall concave downward bell-shape (e.g. Bottazzi *et al.*, 1999; Klein *et al.*, 1997). The data compilation in Fig. 18 shows that although the REE patterns are sub-parallel, the partition coefficients change an order of magnitude as a function of silica content of the melt, from depletion for basaltic melts, to ~10 times enrichment above chondrite values for granitic melts (e.g. Adam *et al.*, 1993; Hilyard *et al.*, 2000; Nagasawa & Schnetzler, 1971). Sisson (1994) showed increasing curvature of the REE shapes and a strong increase in HREE partitioning into hornblende when a magma approaches rhyolitic compositions. In accordance, Tiepolo *et al.* (2007) concluded that REE partition coefficients of hornblende increase with polymerisation of a magma, which correlates with silica contents. The K_D s for Hbl in our migmatites have a significantly different from those previously described in the literature (Fig. 18), show a continued increase of values from MREE to HREE, and have significantly lower ratios between K_D for La and K_D for Yb or Lu. This implies that our interpretations of hornblende REE patterns are somewhat speculative.

Despite their uncommon REE shapes we interpret the hornblende in rocks from the Tangtse and Rongdo areas are interpreted as follows. The hornblendes of the Hbl-Bt-granodiorite protolith (sample TNG59, Fig 13a) are interpreted as crystals that equilibrated with a calc-alkaline magma with ~65 wt % SiO_2 . The REE patterns are relatively flat in comparison with analyses from melanosomes and leucosomes, and show conspicuous positive Eu anomalies that are not observed in other samples of our dataset and were also not found in the literature.

Reported partition coefficients for Eu range from slight incompatibility to slight compatibility, but are always lower than those for the neighbouring Gd (see data compilation in Tiepolo *et al.*, 2007). Negative Eu anomalies in hornblende have been attributed to co-crystallization of plagioclase (Marks *et al.*, 2004). If this relationship holds true, negative Eu anomalies for hornblende would be expected to coincide with negative Sr anomalies because high partition coefficients for Sr in plagioclase. Slight negative Eu and Sr anomalies were found for hornblende in a patchy tonalitic leucosome (sample TNG204c), where a granoblastic mineral texture is interpreted to represent equilibrium crystallization of hornblende and plagioclase (Fig. 4c, d). The same feature is pronounced in one sample from the Rongdo location (AGH24) that shows both strong negative Eu and Sr anomalies and this sample is also plagioclase-rich.

Hornblendes in the patchy tonalitic leucosome above (Fig. 13f, sample TNG204c) show REE patterns comparable to the ones of hornblendes of the Hbl-Bt-granodiorite (sample TNG59) protolith in LREE to MREE (Fig. 13a), but slight enrichment from Gd to Yb, whilst Lu concentrations are similar. This enrichment is interpreted to be the result of equilibration with a magma that has higher silica contents than that of the protolith (Hilyard *et al.*, 2000; Klein *et al.*, 1997; Sisson, 1994).

The most pronounced difference between hornblende in different parts of a diatexite is shown in Fig 13b and g. Here, hornblende in the leucocratic part (Fig. 13g) shows strong enrichment in MREE to HREE compared to the melanocratic part (Fig. 13b). In agreement with the results of Sisson (1994), this enrichment can be explained with the higher silica contents of the leucosome. Whole analysis yielded SiO_2 contents of 61.95 wt % and 68.02

wt% for melanocratic part and leucocratic part, respectively. Although the hornblendes in both leucocratic and melanocratic part are also strongly enriched in Nb, Ta and Ti, the ones in the former are much more enriched compared to the latter.

It has also been shown that the Ti content of hornblende increases with increasing SiO_2 and decreasing TiO_2 content of the magma (Sisson, 1994). Here, a sharp increase in Ti contents of hornblende was observed when the SiO_2 contents of the magma overstep ~ 70 wt %. Accordingly, the whole rock analysis of the patchy melanosome and leucosome (samples TNG169a, TNG169b) show high Ti contents in the melanocratic part ($\text{Ti} = 3833.40$ ppm) and low Ti contents in the leucocratic part ($\text{Ti} = 630.96$ ppm), and an inverse correlation of Ti contents for the hornblendes. Because of the diffuse gradation from leucosome to melanosome (Fig. 3a), the hornblendes in both parts are likely to be affected by migmatization. Compared to hornblende in the Hbl-Bt-granodiorite, the hornblendes in the melanosome show overall enrichment in REE.

The REE patterns of hornblendes in Hbl-Kfs leucosomes (Fig. 13e, sample TNG60d) and in the diffuse melanosome (Fig. 13d, sample TNG60c) must have equilibrated under different conditions. The Hbl-Kfs leucosome only contains quartz in relatively small amounts compared to other leucosomes in our study, and whole rock analysis yielded a low SiO_2 content of 62.3 wt %. Whole rock data for the diffuse melanosome is not available. The REE patterns of hornblende grains from both rocks show similar shapes, but hornblendes in the leucosomes show a more pronounced curvature and a slight overall REE enrichment compared to the melanosome. As for the leucocratic/ melanocratic sample pair discussed above (samples TNG169b, TNG169a), we assume that hornblendes in leucosome and melanosome have been affected by migmatization, but in this case equilibrated with magma of a different composition.

From petrographic observations we interpret that the Hbl-Kfs leucosomes (Fig 3c, d) are unlikely to represent crystallized melts, but are interpreted to be residual mineral assemblages that were not extracted in the melt escape networks. It is thus likely that these hornblendes equilibrated with an already highly fractionated magma. A comparable interpretation was reached by Tiepolo *et al.* (2008) for hornblendes of differing REE contents in rocks that have been infiltrated by melts of different compositions. However, in microprobe line analyses of large, poikilitic hornblende grains in the Hbl-Kfs leucosome, we found no indication for equilibration with different magmas.

The Hbl-Kfs leucosome from the Rongdo location shows hornblendes with similar MREE to HREE patterns compared to the Hbl-Kfs leucosome from the Tangtse area, but with remarkably different LREE concentrations (Fig. 13g). LREE compatibility in hornblende was not found in published partition coefficient data. However, LA-ICP-MS line scans (Appendix E) indicate that the extremely LREE enriched mineral allanite is common as inclusions in these hornblendes. We thus speculate that diffusion of allanite into the melt could have enriched the melt in LREE and that these elements were subsequently incorporated into the hornblendes. In any case, the high amounts of the minerals allanite, apatite and titanite in the Hbl-Kfs leucosomes from the Tangtse area and the Rongdo location, give rise to abnormal trace element contents (Table 1), and we speculate that the trace element compositions of the hornblendes in these leucosomes is strongly influenced by these unusual chemistries.

Hornblende in the Hbl-leucogranite from the Karakoram Batholith at the Rongdo location shows the highest total REE concentrations and REE patterns that do not relate to the ones discussed above (Fig. 13h). However, the REE patterns compare to the ones described by Marks *et al.* (2004) for calcic-ferropargasites. Although the trace element concentrations, including REE, are almost identical for the LA-ICP-MS spot analyses, major element concentrations show large variations ranging from pargasite to edenite compositions. Further, the petrography of these grains shows extensive alterations to biotite and white mica, irregular patchy zoning and in some grains brown cores and green rims. Microprobe line analysis (Fig. 11) showed that the green rims have lower Al tot contents compared to the core, indicating equilibration at lower pressures. For these reasons hornblende from this rock is not included in our petrogenetic model. In the following we discuss the significance of hornblende for crustal differentiation in view of fractionation processes as shown in our geochemical models.

6.2 The role of hornblende in magma formation

We have documented partial melting of hornblende-bearing calc-alkaline arc rocks under water-fluxed conditions giving rise to migmatites with peritectic hornblende. In the source region, hornblende-rich, restitic rocks form melanosomes in meta- and diatexites. In contrast, other *in situ* leucosomes are Hbl-free and are petrographically leucotonalites to leucogranites consisting of plagioclase + K-feldspar + quartz + biotite. Leucosomes feed into a network of magma escape pathways, linking to stocks and plutons (Reichardt *et al.*, 2010; Weinberg *et al.*, 2009). The leucogranite plutons in the PMC are remarkably free of xenoliths and generally do not contain hornblende. We thus infer that a filter process must have taken place that leaves hornblende in the source.

Geochemical analysis showed gradational changes, especially in the REE patterns, between protoliths, migmatites and the magmatic products. Field observations showed that the most striking feature of various parts of meta- and diatexites are different amounts of hornblende, and we investigated how these relate to the different REE patterns of the rocks.

Restitic schlieren are composed of mostly hornblende, biotite and titanite. Biotite has a negligible effect on the REE patterns as it has low partition coefficients for REE (e.g. Gromet & Silver, 1983). In contrast, titanite has very large REE concentrations and fractionates LREE over HREE. Although enriched in melanosome (~3 to 5 % modal content) and in restitic schlieren that finger into leucosome, we did not further consider the role of titanite in this study. Here, we focus on hornblende, because it constitutes up to ~50 % modal content in melanosomes. Hbl-Bt-granodiorites and diorites show a large compositional range between less than ten and up to ~40 % modal hornblende content. Our trace element analysis has shown that hornblende contains significant amount of REE and is thus a major contributor to the whole rock REE concentrations. Because of the large variations in trace element contents that cannot be explained with partition coefficients from the literature, we applied our own calculated partition coefficients (Table 5) for hornblende to the batch melting and fractionation models.

In our petrogenetic considerations, we only included anatexis of the calc-alkaline rocks, while melt stemming from anatexis of the meta-sedimentary sequence (see Chapter II) was

not included. Garnet is not included in the models since it is lacking in the migmatites derived from calc-alkaline rocks. However, small amounts of garnet are contained in Bt-psammmites and pelites. Yet, restites in the migmatitic meta-sedimentary rocks lack garnet accumulations.

We demonstrate that retainment of hornblende in the source systematically increases La_n/Yb_n values, (Fig. 19). We emphasize that the results of the models are not to be taken as absolute quantitative values, but explain qualitatively the geochemical signatures. The resulting high La_n/Yb_n ratios of the melts is in agreement to the experiments of Tiepolo *et al.* (2000) who modelled hornblende fractionation for magmas ranging compositionally between mafic (<45 wt % SiO_2) and felsic (>60 wt % SiO_2). Tiepolo & Tribuzio (2008) studied the relations between hornblende-melt equilibration and fractionation of hornblende and proposed that hornblende fractionation and accumulation in the source is capable of creating magmas with geochemical signatures typical for Archean TTGs.

6.3 Adakite and TTG signatures

High La_n/Yb_n and Sr/Y as those shown for leucogranites in the PMC (Fig. 6) are the most prominent features of adakites (Defant & Drummond, 1990; Martin, 1987; Martin, 1999; Martin *et al.*, 2005; Moyen, 2009). However, not every rock with high La_n/Yb_n and Sr/Y is an adakite. Adakites also have to be andesitic to dacitic, have $\text{K}_2\text{O}/\text{Na}_2\text{O} \leq 0.42$ and generally show $\text{Al}_2\text{O}_3 > 15$ wt %, mg# ~50, Cr and Ni concentrations lower than 18 ppm, and Y and Yb concentrations lower than 1.9 ppm (see Moyen, 2009). The leucogranites and diatexites in the PMC are not adakites as per definition of Martin *et al.* (2005), because they are too silica-rich, have lower mg# and $\text{K}_2\text{O}/\text{Na}_2\text{O} > 0.42$, except for diatexites that have $\text{K}_2\text{O}/\text{Na}_2\text{O}$ values ~0.4.

The high La_n/Yb_n and Sr/Y signatures of rocks in the PMC compare to values that were reported for granites of the Karakoram Batholith by Mahéo *et al.* (2009) and also to rocks from the Late Cretaceous Gangdese Batholith in South Tibet (Wen *et al.*, 2008) and to Miocene granites in South Tibet (Xu *et al.*, in press). However, like our leucogranites, these rocks also have lower mg# and lower Cr and Ni concentrations than adakites. Rocks with such signatures are therefore sometimes referred to as pseudo-adakites (e.g. Kamei *et al.*, 2009; Wen *et al.*, 2008). In the interpretation of Wen *et al.* (2008), the most likely source rocks are older, calc-alkaline granitoids of the Gangdese Batholith which is part of the same Transhimalayan Batholith that includes the Ladakh arc (Honegger *et al.*, 1982; Schärer *et al.*, 1984; Weinberg & Dunlap, 2000). In case of the Miocene granites in South Tibet, high La_n/Yb_n and Sr/Y values have been inferred to be the result of melting of Indian crust with minor contamination from other sources (Xu *et al.*, in press). All these rocks have in common that they have been interpreted to be the results of partial melting in the lower crust that leaves hornblende and garnet in the residuum (Mahéo *et al.*, 2009; Wen *et al.*, 2008; Xu *et al.*, in press). We suggest that these ‘pseudo-adakitic’ signatures can also be produced by water-fluxed melting in the mid-crust.

TTGs are generally regarded as products of partial melting of basaltic source rocks under high pressures in the stability field of garnet, probably during subduction of oceanic crust or at the base of the crust that leaves garnet-amphibolites or eclogites in the source (Drummond

& Defant, 1990; Martin, 1994). Nehring *et al.* (2009) modelled melting of amphibolite to generate magmas with Archean Tonalite-Trondhjemite-Gneiss (TTG) signature. Similar to adakites, these rocks require amphibole and garnet in the residue. Tiepolo & Tribuzio (2008) suggested that hornblende fractionation may lead to cumulates in the source and gives rise to magmas with low HREE and the concave upward MREE to HREE pattern typical of TTGs. Kamei *et al.* (2009) modelled partial melting of arc-related tonalites and granodiorites with retainment of residual amphibole and reproduced the high La_n/Yb_n and Sr/Y signature of granites in their study area.

Although a number of petrogenetic processes and geodynamic regimes are possible to generate rocks with high La_n/Yb_n and Sr/Y, Moyen (2009) concluded that, in most general terms, melting of mafic rocks in great depths leaving residual amphibole and garnet in the source is responsible for the origin of the adakites and TTG signature. In the exposures of anatectic middle crust in the PMC, the relations between protoliths, their migmatized equivalents and magmatic products can be directly studied, and here fractionation of hornblende that has been produced due to water-fluxed melting generates high La_n/Yb_n and Sr/Y signatures.

7. Conclusions

Meta- and diatexites in the Pangong Metamorphic Complex resulted from water-fluxed partial melting of calc-alkaline arc rocks giving rise to hornblende-bearing leucosomes. These connect to a network of dykes that form magma escape pathways and link to Hbl-free leucogranite stocks and plutons (Reichardt *et al.* 2010; Weinberg *et al.* 2009). Hornblende forms residual cumulates that remain in the migmatite source. Most significantly, the REE pattern of hornblende is highly variable and yields partition coefficients that vary from sample to sample and are considerably different from those available in the literature. We interpret these as apparent K_D s resulting from a complex history of crystallization and equilibration during migmatite evolution. Despite these difficulties, our results demonstrate that fractionation of hornblende in the source leads to leucogranites with high La_n/Yb_n and Sr/Y values, and that retainment of garnet in the source need not be invoked to generate these geochemical characteristics.

References

- Adam, J., Green, T. H. & Sie, S. H. (1993). Proton microprobe determined partitioning of Rb, Sr, Ba, Y, Zr, Nb and Ta between experimentally produced amphiboles and silicate melts with variable F content. *Chemical Geology* 109, 29-49.
- Arth, J. G. (1976). Behavior of trace elements during magmatic processes; a summary of theoretical models and their applications. *Journal of Research of the U. S. Geological Survey* 4, 41-47.
- Arth, J. G. & Barker, F. (1976). Rare-earth partitioning between hornblende and dacitic liquid and implications for the genesis of trondhjemitic-tonalitic magmas. *Geology* 4, 534-536.
- Ayres, M. & Harris, N. (1997). REE fractionation and Nd-isotope disequilibrium during crustal anatexis: constraints from Himalayan leucogranites. *Chemical Geology* 139, 249-269.

- Bacon, C. R. & Druitt, T. H. (1988). Compositional evolution of the zoned calcalkaline magma chamber of Mount Mazama, Crater Lake, Oregon. *Contributions to Mineralogy and Petrology* 98, 224-256.
- Bea, F., Pereira, M. D. & Stroh, A. (1994). Mineral/leucosome trace-element partitioning in a peraluminous migmatite (a laser ablation-ICP-MS study). *Chemical Geology* 117, 291-312.
- Bottazzi, P., Tiepolo, M., Vannucci, R., Zanetti, A., Brumm, R., Foley, S. F. & Oberti, R. (1999). Distinct site preferences for heavy and light REE in amphibole and the prediction of (super Amph/L) D (sub REE) partition coefficients for rare earth elements between amphibole and liquid. *Contributions to Mineralogy and Petrology* 137, 36-45.
- Bowen, N. L. (1919). Crystallization differentiation in igneous magmas. *Journal of Geology* 27, 393-430.
- Boynton, W. V. (1984). Cosmochemistry of the rare earth elements; meteorite studies. In: Henderson, P. (ed.) *Rare earth element geochemistry. Developments in Geochemistry*, 63-114.
- Dalpe, C. & Baker, D. R. (2000). Experimental investigation of large-ion-lithophile-element-, high-field-strength-element- and rare-earth-element-partitioning between calcic amphibole and basaltic melt; the effects of pressure and oxygen fugacity. *Contributions to Mineralogy and Petrology* 140, 233-250.
- Davidson, J., Turner, S., Handley, H., Macpherson, C. & Dosseto, A. (2007). Amphibole “sponge” in arc crust? *Geology* 35, 787-790.
- Debon, F., Le Fort, P., Dautel, D., Sonet, J. & Zimmermann, J. L. (1987). Granites of western Karakorum and northern Kohistan (Pakistan): A composite mid-cretaceous to upper cenozoic magmatism. *Lithos* 20, 19-40.
- Defant, M. J. & Drummond, M. S. (1990). Derivation of some modern arc magmas by melting of young subducted lithosphere. *Nature* 347, 662-665.
- Defant, M. J., Xu, J. F., Kepezhinskis, P., Wang, Q., Zhang, Q. & Xiao, L. (2002). Adakites: Some variations on a theme. *Acta Petrologica Sinica* 18, 129-142.
- Dostal, J., Dupuy, C., Carron, J. P., Le Guen de Kerneizon, M. & Maury, R. C. (1983). Partition coefficients of trace elements; application to volcanic rocks of St. Vincent, West Indies. *Geochimica et Cosmochimica Acta* 47, 525-533.
- Drummond, M. S. & Defant, M. J. (1990). A model for trondhjemite-tonalite-dacite genesis and crustal growth via slab melting: Archean to modern comparisons. *Journal of Geophysical Research* 95, 21,503-521,521.
- Femenias, O., Mercier, J.-C. C., Nkono, C., Diot, H., Berza, T., Tatu, M. & Demaiffe, D. (2006). Calcic amphibole growth and compositions in calc-alkaline magmas; evidence from the Motru dike swarm (Southern Carpathians, Romania). *American Mineralogist* 91, 73-81.
- Foley, S., Tiepolo, M. & Vannucci, R. (2002). Growth of early continental crust controlled by melting of amphibolite in subduction zones. *Nature*, 417, 837-840.
- Frost, B. R., Barnes, C. G., Collins, W. J., Arculus, R. J., Ellis, D. J. & Frost, C. D. (2001). A geochemical classification for granitic rocks. *Journal of Petrology* 42, 2033-2048.
- Fujimaki, H. (1986). Partition coefficients of Hf, Zr, and REE between zircon, apatite, and liquid. *Contributions to Mineralogy and Petrology* 94, 42-45.
- Fujimaki, H., Tatsumoto, M. & Aoki, K. (1984). Partition coefficients of Hf, Zr, and REE between phenocrysts and groundmasses. *Journal of Geophysical Research* 89, 662-672.
- Gardien, V., Thompson, A. B. & Ulmer, P. (2000). Melting of biotite + plagioclase + quartz gneisses; the role of H (sub 2) O in the stability of amphibole. *Journal of Petrology* 41, 651-666.
- Gromet, L. P. & Silver, L. T. (1983). Rare earth element distributions among minerals in a granodiorite and their petrogenetic implications. *Geochimica et Cosmochimica Acta* 47, 925-939.

- Gupta, L. N. & Johannes, W. (1982). Petrogenesis of a stromatic migmatite (Nelaug, southern Norway). *Journal of Petrology* 23, 548-567.
- Hammarstrom, J. M. & Zen, E. (1986). Aluminum in hornblende: an empirical igneous geobarometer. *American Mineralogist* 71, 1297-1313.
- Hermann, J. (2002). Allanite: thorium and light rare earth element carrier in subducted crust. *Chemical Geology* 192, 289-306.
- Higuchi, H. & Nagasawa, H. (1969). Partition of trace elements between rock-forming minerals and the host volcanic rocks. *Earth and Planetary Science Letters* 7, 281-287.
- Hilyard, M., Nielsen, R. L., Beard, J. S., Patiño-Douce, A. & Blencoe, J. (2000). Experimental determination of the partitioning behavior of rare earth and high field strength elements between pargasitic amphibole and natural silicate melts. *Geochimica et Cosmochimica Acta* 64, 1103-1120.
- Honegger, K., Dietrich, V., Frank, W., Gansser, A., Thöni, M. & Trommsdorff, V. (1982). Magmatism and metamorphism in the Ladakh Himalayas (the Indus-Tsangpo suture zone). *Earth and Planetary Science Letters* 60, 253-292.
- Johannes, W., Ehlers, C., Kriegsman, L. M. & Mengel, K. (2003). The link between migmatites and S-type granites in the Turku area, southern Finland. *Lithos* 68, 69-90.
- Johnson, M. C. & Rutherford, M. J. (1989). Experimental calibration of the aluminum-in-hornblende geobarometer with application of Long Valley caldera (California) volcanic rocks. *Geology* 17, 837-841.
- Kamei, A., Miyake, Y., Owada, M. & Kimura, J. I. (2009). A pseudo adakite derived from partial melting of tonalitic to granodioritic crust, Kyushu, southwest Japan arc. *Lithos* 112, 615-625.
- Kenah, C. & Hollister, L. S. (1983). Anatexis in the Central Gneiss Complex. In: Atherton, M. P., Gribble, C. D. (ed.) *Migmatites, Melting, and Metamorphism*. Nantwich: Shiva, 142-162.
- Klein, M., Stosch, H. G. & Seck, H. A. (1997). Partitioning of high field-strength and rare-earth elements between amphibole and quartz-dioritic to tonalitic melts: an experimental study. *Chemical Geology* 138, 257-271.
- Lappin, A. R. & Hollister, L. S. (1980). Partial melting in the Central Gneiss Complex near Prince Rupert, British Columbia. *American Journal of Science* 280, 518-545.
- LaTourrette, T., Hervig, R. L. & Holloway, J. R. (1995). Trace element partitioning between amphibole, phlogopite, and basanite melt. *Earth and Planetary Science Letters* 135, 13-30.
- Leake, B. E., Woolley, A. R., Arps, C. E. S., Birch, W. D., Gilbert, M. C., Grice, J. D., Hawthorne, F. C., Kato, A., Kisch, H. J., Krivovichev, V. G., Linthout, K., Laird, J., Mandarino, J. A., Maresch, W. V., Nickel, E. H., Rock, N. M. S., Schumacher, J. C., Smith, D. C., Stephenson, N. C. N., Ungaretti, L., Whittaker, E. J. W. & Guo, Y. (1997). Nomenclature of amphiboles; Report of the Subcommittee on Amphiboles of the International Mineralogical Association, Commission on New Minerals and Mineral Names. *American Mineralogist* 82, 1019-1037.
- Luhr, J. F. & Carmichael, I. S. E. (1980). The Colima Volcanic complex, Mexico - I. Post-caldera andesites from Volcan Colima. *Contributions to Mineralogy and Petrology* 71, 343-372.
- Mahéo, G., Blichert-Toft, J., Pin, C., Guillot, S. & Pêcher, A. (2009). Partial Melting of Mantle and Crustal Sources beneath South Karakorum, Pakistan: Implications for the Miocene Geodynamic Evolution of the India-Asia Convergence Zone. *Journal of Petrology*, 427-449.
- Marchildon, N. & Brown, M. (2001). Melt segregation in late syn-tectonic anatectic migmatites: An example from the Onawa Contact Aureole, Maine, USA. *Physics and Chemistry of the Earth* 26, 25-229.
- Marks, M., Halama, R., Wenzel, T. & Markl, G. (2004). Trace element variations in

- clinopyroxene and amphibole from alkaline to peralkaline syenites and granites: implications for mineral-melt trace-element partitioning. *Chemical Geology* 211, 185-215.
- Martin, H. (1987). Petrogenesis of Archaean Trondhjemites, Tonalites, and Granodiorites from Eastern Finland: Major and Trace Element Geochemistry. *J. Petrology* 28, 921-953.
- Martin, H. (1994). The Archean grey gneisses and the genesis of continental crust. *Developments in Precambrian Geology* 11, 205-259.
- Martin, H. (1999). Adakitic magmas; modern analogues of Archaean granitoids. *Lithos* 46, 411-429.
- Martin, H., Smithies, R. H., Rapp, R., Moyen, J.-F. & Champion, D. (2005). An overview of adakite, tonalite-trondhjemite-granodiorite (TTG), and sanukitoid; relationships and some implications for crustal evolution. *Lithos* 79, 1-24.
- Matsui, Y., Onuma, N., Nagasawa, H., Higuchi, H. & Banno, S. (1977). Crystal structure control in trace element partition between crystal and magma. *Bulletin de la Societe Francaise de Mineralogie et de Cristallographie* 100, 315-324.
- McCarthy, M. R. & Weinberg, R. F. (in press). Structural complexity resulting from pervasive ductile deformation in the Karakoram Shear Zone, Ladakh, NW India. *Tectonics*.
- McLellan, E. L. (1988). Migmatite structures in the Central Gneiss Complex, Boca de Quadra, Alaska. *Journal of Metamorphic Geology* 6, 517-542.
- Moyen, J.-F. (2009). High Sr/Y and La/Yb ratios: The meaning of the “adakitic signature”. *Lithos* 112, 556-574.
- Nagasawa, H. (1970). Rare earth concentrations in zircons and apatites and their host dacites and granites. *Earth and Planetary Science Letters* 9, 359-364.
- Nagasawa, H. & Schnetzler, C. C. (1971). Partitioning of rare earth, alkali and alkaline earth elements between phenocrysts and acidic igneous magma. *Geochimica et Cosmochimica Acta* 35, 953-968.
- Nash, W. P. & Crecraft, H. R. (1985). Partition coefficients for trace elements in silicic magmas. *Geochimica et Cosmochimica Acta* 49, 2309-2322.
- Nehring, F., Foley, S. F., Holtta, P. & Van Den Kerkhof, A. M. (2009). Internal Differentiation of the Archean Continental Crust: Fluid-Controlled Partial Melting of Granulites and TTG-Amphibolite Associations in Central Finland. *Journal of Petrology* 50, 3-35.
- Patiño Douce, A. E. (1999). What do experiments tell us about the relative contributions of crust and mantle to the origin of granitic magmas? *Geological Society of London Special Publications* 168, 55-75.
- Patiño Douce, A. E. & Harris, N. (1998). Experimental constraints on Himalayan anatexis. *Journal of Petrology* 39, 689-710.
- Phillips, R. J., Parrish, R. R. & Searle, M. P. (2004). Age constraints on ductile deformation and long-term slip rates along the Karakoram fault zone, Ladakh. *Earth and Planetary Science Letters* 226, 305-319.
- Ravikant, V. (2006). Utility of Rb-Sr geochronology in constraining Miocene and Cretaceous events in the eastern Karakoram, Ladakh, India. *Journal of Asian Earth Sciences* 27, 534-543.
- Ravikant, V., Wu, F.-Y. & Ji, W.-Q. (2009). Zircon U-Pb and Hf isotopic constraints on petrogenesis of the Cretaceous-Tertiary granites in eastern Karakoram and Ladakh, India. *Lithos* 110, 153-166.
- Reichardt, H., Weinberg, R. F., Andersson, U. B. & Fanning, C. M. (2010). Hybridization of granitic magmas in the source: The origin of the Karakoram Batholith, Ladakh, NW India. *Lithos* 116, 249-272.
- Rolland, Y., Mahéo, G., Pêcher, A. & Villa, I. M. (2009). Syn-kinematic emplacement of the Pangong metamorphic and magmatic complex along the Karakorum Fault (N Ladakh). *Journal of Asian Earth Sciences* 34, 10-25.
- Rolland, Y. & Pêcher, A. (2001). The Pangong granulites of the Karakoram Fault (western

- Tibet); vertical extrusion within a lithosphere-scale fault? *Comptes Rendus de l'Academie des Sciences, Serie II. Sciences de la Terre et des Planetes* 332, 363-370.
- Rolland, Y., Picard, C., Pêcher, A., Lapierre, H., Bosch, D. & Keller, F. (2002). The cretaceous Ladakh arc of NW himalaya--slab melting and melt-mantle interaction during fast northward drift of Indian Plate. *Chemical Geology* 182, 139-178.
- Schärer, U., Hamet, J. & Allègre, C. J. (1984). The Transhimalaya (Gangdese) plutonism in the Ladakh region: a UPb and RbSr study. *Earth and Planetary Science Letters* 67, 327-339.
- Schmidt, M. W. (1992). Amphibole composition in tonalite as a function of pressure; an experimental calibration of the Al-in-hornblende barometer. *Contributions to Mineralogy and Petrology* 110, 304-310.
- Schnetzler, C. C. & Philpotts, J. A. (1970). Partition coefficients of rare-earth elements between igneous matrix material and rock-forming mineral phenocrysts-II. *Geochimica et Cosmochimica Acta* 34, 331-340.
- Searle, M. P., Weinberg, R. F. & Dunlap, W. J. (1998). Transpressional tectonics along the Karakoram Fault Zone, northern Ladakh. In: Holdsworth, R. E. & Strachan, R. A. (eds.) *Continental Transpressional and Transtensional Tectonics*. London: Geological Society of London Special Publication, 307-326.
- Shaw, D. M. (1970). Trace element fractionation during anatexis. *Geochimica et Cosmochimica Acta* 34, 237-243.
- Singh, S., Kumar, R., Barley, M. E. & Jain, A. K. (2007). SHRIMP U-Pb ages and depth of emplacement of Ladakh Batholith, Eastern Ladakh, India. *Journal of Asian Earth Sciences* 30, 490-503.
- Sisson, T. W. (1994). Hornblende-melt trace-element partitioning measured by ion microprobe. *Chemical Geology* 117, 331-344.
- Spear, F. S. (1981). An experimental study of hornblende stability and compositional variability in amphibolite. *American Journal of Science* 281, 697-734.
- Sun, S. S. & McDonough, W. F. (1989). Chemical and isotopic systematics of oceanic basalts; implications for mantle composition and processes. *Geological Society of London Special Publications* 42, 313-345.
- Tiepolo, M., Oberti, R., Zanetti, A., Vannucci, R. & Foley, S. F. (2007). Trace-element partitioning between amphibole and silicate melt. *Reviews in Mineralogy and Geochemistry*, 417-452.
- Tiepolo, M. & Tribuzio, R. (2008). Petrology and U-Pb zircon geochronology of amphibole-rich cumulates with sanukitic affinity from Husky Ridge (northern Victoria Land, Antarctica); insights into the role of amphibole in the petrogenesis of subduction-related magmas. *Journal of Petrology* 49, 937-970.
- Tiepolo, M., Vanucci, R., Bottazzi, P., Oberti, R., Zanetti, A., Foley, S. (2000). Partitioning of rare earth elements, Y, Th, U, and Pb between pargasite, kaersutite, and basanite to trachyte melts; implications for percolated and veined mantle. *Geochemistry, Geosystems, Geophysics* 1, 2000GC00064.
- Upadhyay, R., Frisch, W. & Siebel, W. (2008). Tectonic implications of new U-Pb zircon ages of the Ladakh Batholith, Indus suture zone, northwest Himalaya, India. *Terra Nova* 20, 309-317.
- van Achterbergh, E., Ryan, C. G., Jackson, S. E. & Griffin, W. L. (2001). Data reduction software for LA-ICP-MS. In: Sylvester, P. J. (ed.) *Short Course Handbook: Mineralogical Association of Canada*, Ottawa, ON, Canada 29, 239-243.
- Weinberg, R. F. & Dunlap, W. J. (2000). Growth and deformation of the Ladakh Batholith, Northwest Himalayas; implications for timing of continental collision and origin of calc-alkaline batholiths. *Journal of Geology* 108, 303-320.
- Weinberg, R. F., Dunlap, W. J. & Whitehouse, M. (2000). New field, structural and geochronological data from the Shyok and Nubra valleys, northern Ladakh: linking

- Kohistan to Tibet. In: Khan, A., Treloar, P. J. & Searle, M. P. (eds.) *Tectonics of the Nanga Parbat Syntaxis and the Western Himalaya*. London: Geological Society of London Special Publication, 253-275.
- Weinberg, R. F. & Mark, G. (2008). Magma migration, folding, and disaggregation of migmatites in the Karakoram shear zone, Ladakh, NW India. *Geological Society of America Bulletin* 120, 994-1009.
- Weinberg, R. F., Mark, G. & Reichardt, H. (2009). Magma ponding in the Karakoram shear zone, Ladakh, NW India. *Geological Society of America Bulletin* 121, 278-285.
- Weinberg, R. F. & Searle, M. P. (1998). The Pangong Injection Complex, Indian Karakoram: a case of pervasive granite flow through hot viscous crust. *Journal of the Geological Society of London* 155, 883-891.
- Wen, D.-R., Chung, S.-L., Song, B., Iizuka, Y., Yang, H.-J., Ji, J., Liu, D. & Gallet, S. (2008). Late Cretaceous Gangdese intrusions of adakitic geochemical characteristics, SE Tibet: Petrogenesis and tectonic implications. *Lithos* 105, 1-11.
- Xu, W.-C., Zhang, H.-F., Guo, L. & Yuan, H.-L. (in press). Miocene high Sr/Y magmatism, south Tibet: Product of partial melting of subducted Indian continental crust and its tectonic implication. *Lithos* 114, 293-306.

Declaration for Thesis Chapter 4

Declaration by candidate

In the case of Chapter 4, the nature and extent of my contribution to the work was the following:

Nature of contribution	Extent of contribution (%)
Development of ideas, collection of data, writing up and interpretation of results.	75%

The following co-authors contributed to the work. Co-authors who are students at Monash University must also indicate the extent of their contribution in percentage terms:

Name	Nature of contribution	Extent of contribution (%) for student co-authors only
Roberto Weinberg	Development of ideas, intellectual input during revision process.	

Candidate's
Signature

	Date
--	------

Declaration by co-authors

The undersigned hereby certify that:

- (1) the above declaration correctly reflects the nature and extent of the candidate's contribution to this work, and the nature of the contribution of each of the co-authors.
- (2) they meet the criteria for authorship in that they have participated in the conception, execution, or interpretation, of at least that part of the publication in their field of expertise;
- (3) they take public responsibility for their part of the publication, except for the responsible author who accepts overall responsibility for the publication;
- (4) there are no other authors of the publication according to these criteria;
- (5) potential conflicts of interest have been disclosed to (a) granting bodies, (b) the editor or publisher of journals or other publications, and (c) the head of the responsible academic unit; and
- (6) the original data are stored at the following location(s) and will be held for at least five years from the date indicated below:

Location(s) School of Geosciences, Monash University

Signature 1

	Date
--	------

Chapter IV.

Leucogranite magma transport from source to sink:

the dyke network in the Karakoram Shear Zone, NW India

Abstract

The link between leucosomes in migmatites with magma channels (dykes) that eventually connect to a pluton or batholith is rarely documented. In the Karakoram Shear Zone, Ladakh, NW India, the syn-kinematic transfer of magma in an interconnected magma flow network can be traced from the anatectic source region in the Pangong Metamorphic Complex (PMC) along strike to the Karakoram Batholith through a complex network of dykes. In the PMC, water-fluxing at upper amphibolite facies led to migmatization of calc-alkaline magmatic rocks and of a meta-sedimentary sequence. The anatectic zone is characterized by syn-magmatic folding and shearing of meta- and diatexite migmatites and by pervasive and irregular magma migration paths forming injection complexes. Transitioning from anatectic to sub-solidus zones, a number of dyke network styles are documented. The most prominent are: (a) dykes conformable to the regional foliation plane, (b) magma sheets in ductile fractures, and (c) chaotic networks. The geometries are controlled by the regional stress field, strain localization, pre-existing anisotropies and rheology contrasts. Typically all geometries are characterized by the merging and diverging of dykes, with relatively rare cross-cutting and/or displacement relationships. They are also characterized by intersections preferentially oriented parallel to the regional main mineral stretching lineation. This suggests interconnectivity of magma in the dyke system and is supported by petrographic continuity between merging dykes. We propose that magma transport from source to sink in a continuous deformation-driven crustal-scale magma system was achieved by an interconnected swarm of dykes. Unlike theoretical and laboratory predictions dykes are not oriented perpendicular to the maximum extensional axis, but form a variety of complex interlinked networks exploiting shear planes and axial planes at low angles or parallel to the maximum extension axis.

1. Introduction

Whether or not dykes represent viable and efficient means of magma transport to generate granitoid plutons in the upper crust has been the subject of many discussions (Clemens & Mawer, 1992; Emmerman, 1990; Petford *et al.*, 2000; Petford, 1994; Rubin, 1993; Weinberg, 1996; Weinberg, 1999). Although dykes seem to compete with other ascent mechanisms such as diapirism, pervasive flow and shear channeling, more than one of these might operate at the same time and gradational changes from one to the other might occur (Brown, 1994; Brown & Solar, 1998; Rubin, 1993; Weinberg & Podladchikov, 1994). While pervasive flow may

prevail in the partially molten lower to middle crust (Weinberg, 1996; Weinberg & Searle, 1998) dyking is widely accepted as an efficient mechanism for magma transport in the colder upper crust (Clemens & Mawer, 1992; Petford, 1994; Weinberg & Regenauer-Lieb, 2010). The processes of melt segregation in the source region and magma (melt + crystals) ascent through the crust to final emplacement sites are inextricably linked (Bons *et al.*, 2004; Brown & Solar, 1998; Marchildon & Brown, 2003; Vanderhaeghe, 1999). An important question that arises when studying magma transport is whether a continuous network in which the different parts communicate with each other, was active at any given point in time.

Deformation controls the sites of melt formation, its segregation, subsequent transport and accumulation (Brown, 1994; Collins & Sawyer, 1996; Hand & Dirks, 1992; Vanderhaeghe, 1999). Build up of melt pressure in conjunction with deformation facilitates interconnection of melt pockets at grain scale and leads to development of connected networks (e.g. Brown & Solar, 1998; Weinberg & Searle, 1998). Marchildon & Brown (2003) showed deformation band networks of layer conformable and cross-cutting leucosomes in petrographic continuity in anatectic rocks. Here, folding and shearing in the presence of melt gave rise to channelways elongated parallel to the direction of maximum stretching. Concurrently, elongation of melt-bearing structures normal to the axis of maximum compression has been documented in tight to isoclinal folds in migmatites (Hand & Dirks, 1992), and magma pumping along the foliation plane, parallel to the maximum elongation direction has been proposed as the preferential flow direction in shear zones (Brown & Solar, 1998; Marchildon & Brown, 2003). Alternating phases of transpression and transtension in shear zones may lead to magma accumulation in low pressure sites and subsequent magma expulsion into a transport network (Weinberg *et al.*, 2009). At crustal scale, magma may be pumped in transcurrent shear zones into dilational jogs (Brown, 1994; D'Lemos *et al.*, 1992). Dykes that may transport magma out of the anatectic source region are thought to propagate by fracturing of the country rock at the dyke tip in a direction perpendicular to minimum compressive stress (Clemens & Mawer, 1992; Petford *et al.*, 1993). Under high compressive stresses that inhibit brittle fracturing of country rocks in the middle crust, dykes may intrude into ductile fractures (Brown, 2006; Weinberg & Regenauer-Lieb, 2010).

These ideas are fundamentally based on field observations in migmatite regions such as the metamorphic belt of South Brittany, France, the Central Main Belt, U.S.A, the Shuswap metamorphic core complex in Canada and the Karakoram Shear Zone in India. However, these observations contrast with experimental work on orientations of melt pathways in shearing media (Holtzman & Kohlstedt, 2007; Kohlstedt & Holtzman, 2009). Katz *et al.* (2006) showed accumulation of melt in bands at an angle of about 20° to shear planes, essentially parallel to the axis of maximum compressive stress in simple shear experiments, rather than perpendicular to it as commonly reported in nature (Vernon & Paterson, 2001; Weinberg & Mark, 2008). Similarly, simple shear experiments by Rosenberg & Handy (2001), demonstrated melt migration into dilational sites that develop subparallel to the maximum compression direction. ‘Squeezing’ of melt from initial films between grains parallel to maximum compression into cracks perpendicular to this axis under progressive deformation was observed in partial melting experiments of granitic rocks (Dell’Angelo & Tullis, 1988). In the models of Rabinowicz & Vigneresse (2004), melt first segregates into

veins parallel to the maximum shortening direction, but is subsequently channelized in the direction of maximum stretching. Thus it seems that model experiments in many cases can not predict the melt flow network geometries observed in nature.

The widely differing models indicate that magma ascent from the source to final emplacement sites, which may be the level of neutral buoyancy or a structural boundary, is still not fully understood. The Karakoram Shear Zone provides examples of magma flow networks linking the anatectic crust to the Karakoram Batholith (Reichardt *et al.*, 2010, Chapter II). We describe a variety of network styles comprising *in situ* leucosome networks in migmatites, pervasive injection complexes and dyke networks, then discuss the role of deformation in their formation, and demonstrate interconnectivity from source to sink.

2. Regional Geology

The Karakoram Shear Zone in Ladakh, NW India, lies in the central part of the Karakoram Fault and separates the Karakoram Terrane to the NE, from the Ladakh Terrane to the SW (Dunlap *et al.*, 1998; Searle *et al.*, 1998). The Karakoram Fault is part of a crustal-scale strike-slip fault system that accommodates the northward push of the Indian plate into Eurasia and is characterized by dextral strike-slip motion, trending NW-SE, and is at least 750 km long.

In Ladakh, the shear zone splits into two parallel mylonitic strands (Fig. 1). The Tangtse Shear Zone (SW strand) dips 70° NE and separates rocks of the Pangong Metamorphic Complex (PMC) from rocks of the Ladakh Batholith and its extrusive equivalents, the Kardhung Volcanics to the SW. The Pangong Shear Zone (NE strand) dips steeply SW to vertical and separates the PMC from the Karakoram Metamorphic Complex to the NE. The PMC comprises a ~70 Ma calc-alkaline suite consisting of mostly diorites, Hbl-Bt granodiorites and Bt-granodiorites known as the Muglib Batholith (Ravikant, 2006; Ravikant *et al.*, 2009; Reichardt *et al.*, 2010), a meta-volcanic rock sequence of Hbl-Bt gneisses ranging to amphibolites, and meta-sedimentary rock sequence comprising Bt-psammites, Bt-pelites, and calc-silicate rocks. Minor beds of marble out-crop in the Tangtse Shear Zone (Dunlap *et al.*, 1998; Phillips *et al.*, 2004; Weinberg & Searle, 1998).

The Tangtse and Darbuk-Shyok gorges, cutting perpendicular to the strike of the Karakoram Shear Zone through the Pangong Range (Fig. 1.b), exposes rocks of the Muglib Batholith and of the meta-sedimentary/ volcanic sequence that were migmatized at upper-amphibolite facies (Reichardt *et al.*, 2010; Weinberg & Mark, 2008). Anatexis in that region gave rise to leucogranite injection complexes, local stocks and plutons (Weinberg & Searle, 1998; Weinberg *et al.* 2009). All lithologies are intruded by Bt-leucogranites, and Bt-Ms ± Grt leucogranites derived from this anatectic event. Irregular leucosomes and intrusive sheets and planar dykes can be traced into plutons such as the Tangtse Pluton at the NE end of the Tangtse gorge (Weinberg & Searle 1998, Weinberg *et al.* 2009) or the Darbuk Pluton at the SW end of the Darbuk-Shyok gorge (Fig. 2).

These leucogranites are petrographically and isotopically similar to the Karakoram Batholith that crops out alongside the Nubra Valley ~75 km NW of the Tangtse gorge region, and a genetic relationship between these rocks is inferred (Reichardt *et al.*, 2010). This relationship is also supported by comparable crystallization ages based on zircon dating (Weinberg *et al.*, 2000). Leucogranite crystallization age determinations based on U-Pb ages

of zircons and titanites indicate that magmatic activity in the Karakoram Shear Zone lasted at least between 20 and 13.5 Ma (Phillips *et al.* 2004, Reichardt *et al.*, 2010; Weinberg & Searle 1998, Ravikant *et al.* 2009). The Tangtse Pluton is related to the Pangong Injection Complex (Weinberg & Searle 1998, Weinberg *et al.* 2009), and has ages ranging between ~18

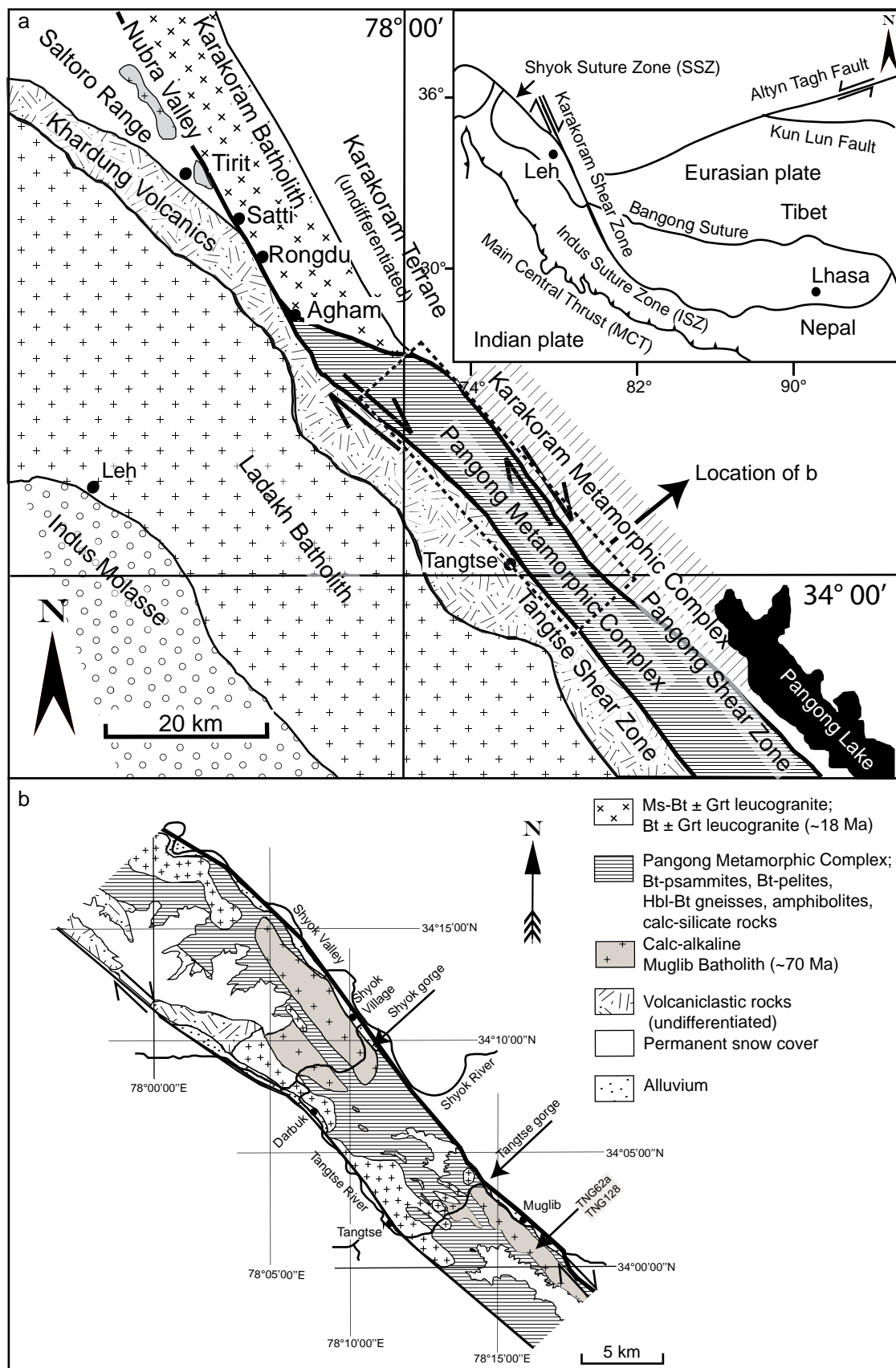


Fig. 1a, b: Geological overview map of the Karakoram Shear Zone and bordering units. Locations of important outcrops, the Tangtse gorge and the Darbuk-Shyok gorge, are indicated on (b).

and 15 Ma indicating that the intrusion formed through amalgamation of multiple magma pulses (Phillips *et al.* 2004, Reichardt *et al.*, 2010). The Darbuk Pluton (Fig. 1.b) also yields a similar age range between ~20 and ~15 Ma (Ravikant *et al.*, 2009).

The main tectonic foliation within the PMC trends generally 130° to 140° and dips steeply parallel to the trend of the Karakoram Shear Zone. An ubiquitous mineral stretching lineation generally plunges gently to moderately (20-45°, rarely horizontal) NW to NNW (Dunlap *et al.*, 1998; McCarthy & Weinberg, in press; Weinberg *et al.*, 2009). Tight to isoclinal folds also trend 130° to 140° and plunge parallel to the mineral stretching lineation. The PMC rocks were uplifted in a pop-up structure in relation to the surrounding rocks (Dunlap *et al.* 1998, McCarthy & Weinberg, in press). This resulted in exposure of upper amphibolite facies rocks in contrast to lower grade rocks to the NE and SW. In the following section we discuss the melting conditions that gave rise to migmatites and magmatic bodies.

3. Water-fluxed melting and magma ascent

Anatexis in the PMC was triggered by water influx (Weinberg & Mark 2008; Reichardt *et al.*, 2010), as indicated by the presence of large, poikilitic and often euhedral hornblende megacrysts in leucosomes of migmatites (Fig. 2; Gardien *et al.*, 2000; Kenah & Hollister, 1983; Lappin & Hollister, 1980; Mogk, 1992) and the lack of any other, anhydrous peritectic mineral such as sillimanite, cordierite, garnet or orthopyroxene. This interpretation is in agreement with thermobarometry by Rolland & Pecher (2001) who determined peak metamorphic temperatures in the Tangtse area to be 700 ± 20 °C at 7 ± 1 kbar, just below the onset of muscovite dehydration melting and well below biotite dehydration melting.

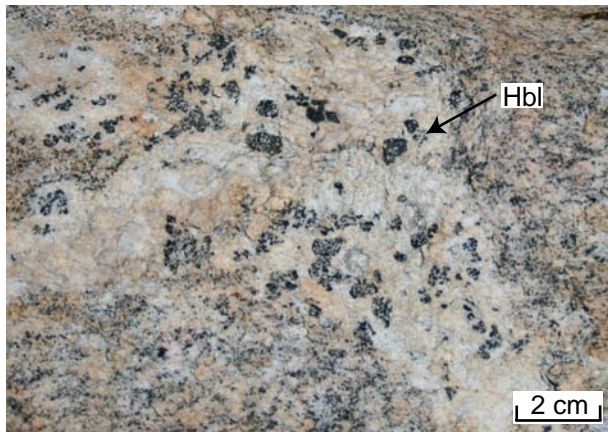


Fig. 2: Idiomorphic, poikilitic hornblende megacrysts in a patchy leucosome in calc-alkaline Hbl-Bt granodiorite. Peritectic hornblende is indicative of water-fluxed melting (e.g. Lappin & Hollister, 1980; Mogk, 1992). Note diffuse boundaries to melanosome.

Ascent of magma resulting from water-fluxed melting is problematic because of crystallization of the relatively cool magma during decompression due to the negative slope of the wet granite solidus (Clemens & Vielzeuf, 1987). However, ascent is possible if the magma is heated either above its solidus temperature (e.g. Weinberg, 1999) or if it is effectively segregated from restitic phases (Leitch & Weinberg, 2002). If water is brought into the system externally, the onset of the melting reaction could take place above the wet solidus temperature, but still below temperatures required for dehydration melting. As a consequence of

segregation, the magma solidus may be decreased because it can not re-equilibrate with the restite and the melt may ascend until it reaches its new wet solidus (Clemens & Droop, 1998). This implies that once segregated, magma can ascend into sub-solidus rocks without freezing (e.g. Clemens & Droop, 1998). In doing so, magma may progressively heat up the surroundings, allowing new batches to ascend higher and expand the zone in which it is

freed from freezing (Leitch & Weinberg, 2002). Over time, this isotherm shallows as latent heat of newly arriving magma pulses heats the country rocks, thus expanding the free-ride layer and moving the magma front upwards (Brown, 2007; Leitch & Weinberg, 2002).

In summary, magma migration from the source, combined with super-solidus water-fluxed melting and the gradual heating up of the magma pathway may allow for significant upward magma migration. In the PMC, remnants of different types of magma flow networks of potentially water-saturated magma are exposed on the way from source to batholith. These networks vary from place to place depending on partial melting distribution, strain localization and the nature and orientation of lithological contacts.

4. Magma networks from source to batholith

Melting and melt migration have been interpreted to be syn-kinematic with folding and shearing during transpressive movement (Reichardt *et al.*, 2010; Rolland *et al.*, 2009; Weinberg & Mark, 2008). This is reinforced by the magma networks described here. Starting at the centimeter to metric scale in the anatectic region, we describe the network styles of *in situ* leucosomes that relate to melt extraction in partially molten rocks and mark the root of the magma transport network in the anatectic zone. Then we proceed to the kilometric scale, where dykes define complex transport zones, and zones of accumulation, finally linking to intrusions of batholith dimensions.

4. 1 Magma extraction networks in the anatectic zone

This network is interpreted as the roots of the system, where magma is formed and extracted from the source rocks. Leucosomes in migmatites are interpreted to represent regions of melt extraction from pores of partially molten rock (Sawyer, 2008). Leucosomes are regarded as a combination of material directly crystallized from the melt phase and solid reaction products (Johannes & Gupta, 1982; Mehnert, 1968). *In situ* leucosomes form channelways that feed the larger scale transport dykes and ultimately plutons and batholiths. The meta- and diatexites in the Tangtse area record the development of a magma network during folding and shearing

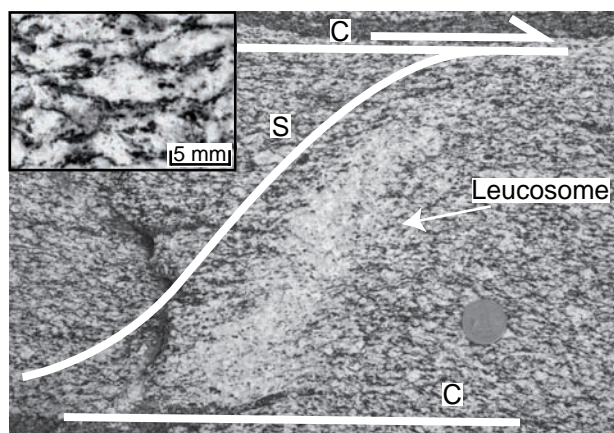


Fig. 3: Leucosome in S-plane orientation in sheared calc-alkaline Hbl-Bt-granodiorite of the Muglib Batholith. Coin for scale has ~2 cm diameter. Inset shows dextral C-S fabric in the Hbl-Bt-granodiorite.

(Weinberg & Mark, 2008). Migmatitic Hbl-Bt-granodiorites, Bt-granodiorites and diorites show leucosomes with diffuse boundaries with mesocratic and melanocratic rock, interpreted to represent the melanosome (migmatite nomenclature after Sawyer, 2008). Bt-psammities may either give rise to patchy migmatites, with diffuse boundaries, or stromatic migmatites rimmed by thin melanosomes.

The migmatites in the PMC show an abundance of evidence for syn-deformational melting, such as magma-filled shear zones or continuous leucosomes

in folded layers and axial-planar leucosomes (Reichardt *et al.*, 2010; Weinberg & Mark, 2008). These features contrast the view that migmatization and metamorphism took place before dextral shearing along the Karakoram Shear Zone (Phillips *et al.*, 2004; Searle & Phillips, 2007). An example of a sy-kinematic patchy leucosome in Hbl-Bt-granodiorite is shown in Fig. 3. The leucosome is parallel to the S-plane in the surrounding sheared melanosome, with diffuse contact. In this case the melanosome is difficult to distinguish from the protolith. The C-S fabric in this outcrop indicates dextral shearing similar to the deformation fabric throughout the PMC (e.g. McCarthy & Weinberg, in press; Weinberg & Searle, 1998). It is interpreted that melt accumulated parallel to the S-plane during deformation.



Fig. 4: Fold in metatexite migmatite in the central part of the Tangtse gorge. Leucosomes in axial planar orientation are continuous with layer parallel leucosomes. Axial planar leucosomes cut through fold hinge. Layering close to the axial planar leucosomes rotates towards the axial plane.

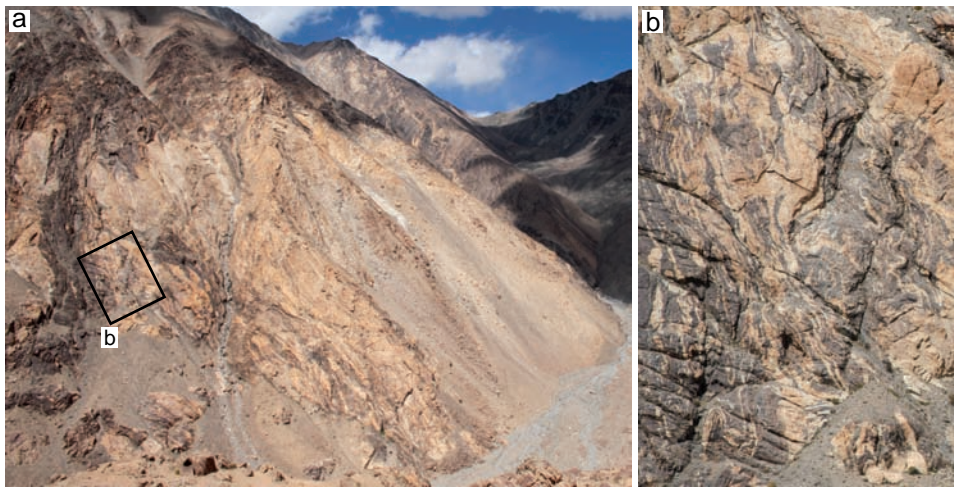


Fig. 5: (a) Leucogranitic Tangtse Pluton at NE end of Tangtse gorge (U-Pb age: ~18 Ma; Reichardt *et al.*, 2010). (b) Irregular magma sheets of the Pangong Injection Complex on the SW-side of the Tangtse Pluton. Pervasive intrusion into migmatized Bt-psammites gives rise to chaotic folds.

Evidence for synchronous melting and folding is given by leucosomes parallel to layering in folded rocks that are continuously linked to leucosomes parallel to the axial plane (Fig. 4; see also Weinberg & Mark, 2008). Magma filled shear zones trend 120° to 130° , parallel to the axial plane of folds. Weinberg & Mark (2008) showed that interplay between folding and melting facilitates connectivity between leucosomes giving rise to magma escape pathways from folding sequences. In the transition stages from metatexite to diatexite, layering is broken up and transposed into axial planar orientation. Further, it was argued that magma transfer and stretching along the axial plane allows for shortening parallel to the maximum compression axis (Weinberg & Mark, 2008). Kinematic and geometric compatibility

supports the interpretation that folding and shearing along the Karakoram Shear Zone were contemporaneous (Dunlap *et al.*, 1998; Weinberg *et al.*, 2009).

In the anatexic region, leucogranite networks at the decimeter to metric scale are linked with an irregular pervasive injection complex (Weinberg & Searle, 1998). At the NE-end of the Tangtse gorge, magmas intruded the meta-sedimentary sequence, forming the Pangong Injection Complex, where leucogranites form more than 30% of the exposure (Fig. 5) (Reichardt *et al.*, 2010; Weinberg *et al.*, 2009; Weinberg & Searle, 1998). The intruded Bt-psammities are migmatitic as evidenced by patchy leucosomes with diffuse boundaries and leucosomes with thin melanosome rims (Fig. 7 in Chapter II). These migmatites were deformed viscously, resulting in irregular intrusive magma sheets and also chaotically folded *in situ* leucosomes (Weinberg & Searle, 1998). This irregular network of magmas seems to be limited to regions that were evidently undergoing partial melting during injection.

4.2 Organized network geometries

The leucosome network at m-scale related to *in situ* melting links continuously with, and almost imperceptibly, to these disorganized injection complexes and to a much larger scale intrusive network of dykes that follow a number of possible patterns, presumably reflecting different mechanisms of dyking, and interaction of rocks with different rheologies, under different stresses, and with internal anisotropies. Collectively, these networks transfer magma from the source to larger accumulations. All different geometries have in common that the networks are formed by anastomosing dykes that merge, diverge and remerge continuously, only rarely cross-cutting each other. Petrographically it is impossible to discern the merging dykes or define a boundary between them. The dykes range in width from a few centimeters to more than one meter. Pegmatitic dykes are not visibly foliated, but finer-grained leucogranite dykes, commonly linked continuously with pegmatitic regions, are foliated parallel to the foliation in the country rocks.

Most commonly dykes in the PMC follow the orientation of the dominant anisotropy defined by the main foliation trending 130-150°, parallel to the main shear zones. These foliation-parallel dykes are found in all rock types. Intersection with dykes at other orientations produces the interconnected networks. We measured 190 attitudes of dykes in exposures at the SW end of the Tangtse gorge, where an interlayered sequence of Bt-psammities, amphibolites and calc-silicate rocks is extensively intruded. The mean strike of these dykes is 140.5° and their mean dip is 68.5° NE (Fig. 6a, b). In a rose diagram the correlation of strike of the dykes with the general strike of the Karakoram Shear Zone (140°) is shown (Fig. 6a). The close correlation of dyke orientation with the regional foliation is illustrated by comparing stereographic projections (Fig. 6b, c).

Dyke intersections typically plunge moderately to steeply NW (Fig. 6d). The mean value of all intersections trends 326° and plunges 39°. An almost identical value (324/35°) results from calculation of the centre of the intersection cluster in the NW quadrant of the stereographic projection in Fig. 6d, excluding the more scattered intersections. These values are similar to the mean value and main cluster centre (327/29° and 322/33°, respectively) of the mineral stretching lineations of biotite and quartz on foliation surfaces in the PMC (Fig. 6e). The mineral stretching lineation is in turn parallel to the fold axis of open to isoclinal

folds (Fig. 6e; Weinberg *et al.*, 2009; Weinberg & Mark, 2008). Dyke intersections (Fig. 6d) also reveal a more subtle spread along a great circle that coincides with the dominant foliation in the PMC. This includes another, more scattered cluster of intersections that plunge moderately towards SE ($109/35^\circ$), roughly perpendicular to the main cluster.

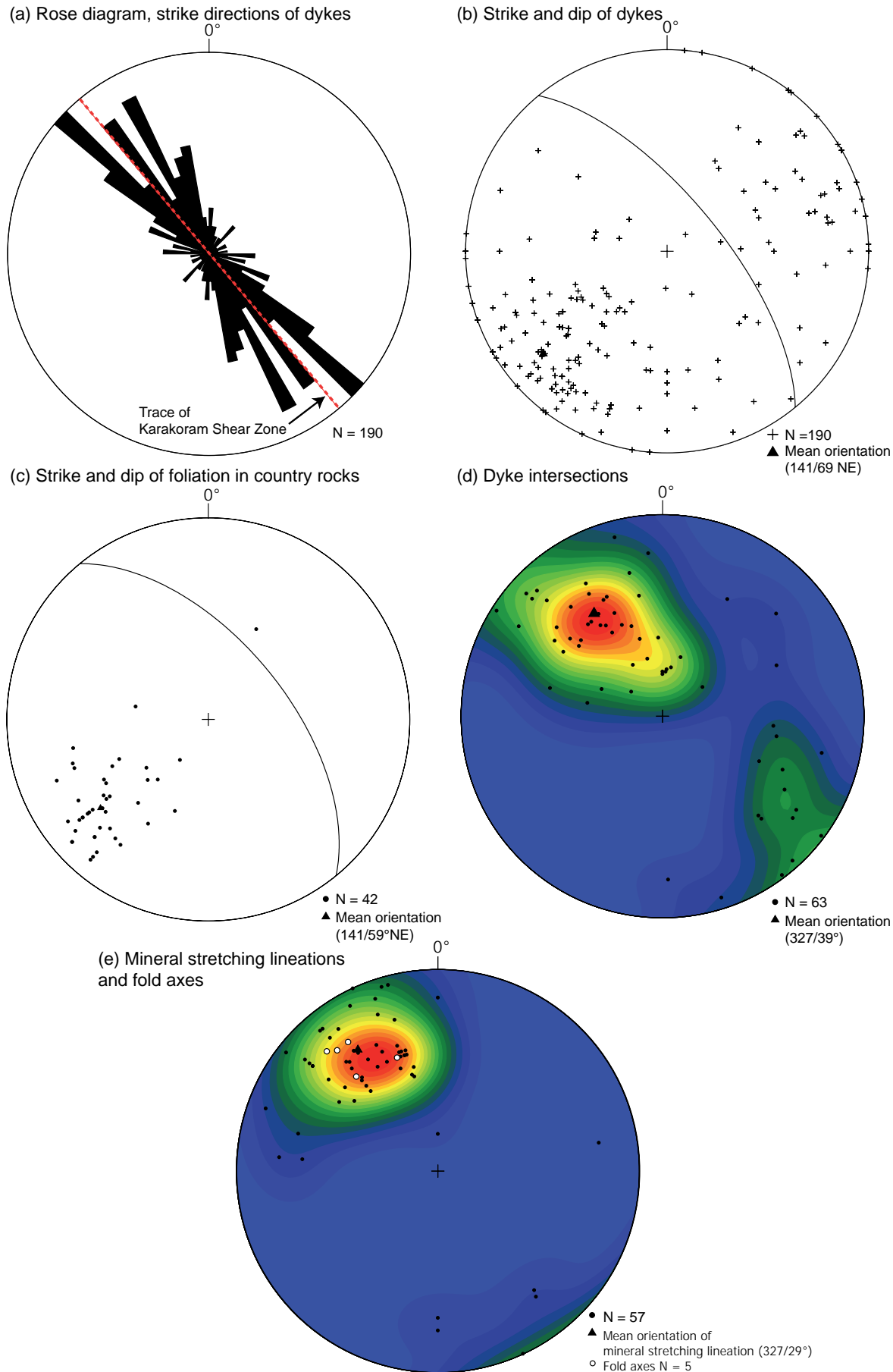


Fig. 6: (a) Rose diagram of strike directions of 190 leucogranite dykes in 5° classes. The dashed red line indicates the mean strike of the Karakoram Shear Zone at 140°. (b) Stereographic equal area, lower hemisphere projection of the poles to the dykes in (a). Great circle indicates mean vector orientation of all measurements (141/69°). (c) Foliation planes in intruded country rocks to the dykes in (a), an interlayered sequence of calc-silicate rocks, amphibolites and Bt-psammmites. (d) Density distribution of dyke intersections with a mean value of 327/39°. (e) Density distribution of mineral stretching lineations in the PMC. Mean orientation is 327/29°. Only amphibolite facies lineations are plotted. Note that fold axes are parallel to the mineral stretching lineations.

In places, two or more dykes come together from different angles (Fig. 7), and we refer to these structures as spider dykes after Brown (2006). In every documented case, the merging point, or junction, has a larger diameter than the width of the merging dykes, and defines a common intersection, in general parallel with the regional lineation. In spider dykes, like in the networks above, the merging dykes are in petrographic continuity and do not cross cut each other. Brown (2006) argued that the intersection between these dykes could provide a high permeability channel for magma flow.



Fig. 7: (a) Spider dykes in calc-alkaline Hbl-Bt-granodiorite in the Pangong Range close to Shyok. Dykes show no crosscutting relationships. (b) Spider dykes in interlayered calc-silicate rocks and amphibolites at the SW-end of Tangtse gorge. Dykes are in petrographic continuity.

These typical network characteristics are common to all lithologies of the PMC. However, in proximity to local shear zones, in areas in calc-silicate rocks and at some lithological contacts, dykes show network geometries differing from these general patterns. We now detail the different types of dyke networks documented.

Shear fabric dyke network

Another network style is developed where dykes intrude both the C- and S-foliations associated with oblique dextral shear fabrics. An example of this geometry is exposed in a several hundred meters high outcrop wall (Fig. 8). Here leucogranite dykes intruded granodiorites and diorites of the Muglib Batholith mainly along the dominant foliation plane parallel to the shear plane (C-plane, ~140°/subvertical) but also along an oblique set of dykes (~100°/ steep and varied SW dips). These oblique dykes commonly have an asymmetric wave shape characterized by steepening dips as they merge with vertical dykes parallel to the regional C-plane (Fig. 8). Pinch and swell structures and boudins in some of the dykes are indicative of continued deformation after crystallization. Note that attitudes were not measured directly but were estimated from 3D protrusion on the surface and estimates were

checked against orientation of dykes that could be measured directly on exposures nearby. Their attitudes are plotted in the stereonet inset in Fig. 8 and define a common intersection plunging SE (minor group of intersections in Fig. 6d). We interpret this to be the S-plane of a shear fabric characterized by a transport direction to the SE along a stretching lineation plunging NW, at right angles to the intersection between C-S planes, such as observed at small scale in mylonitic outcrops elsewhere.

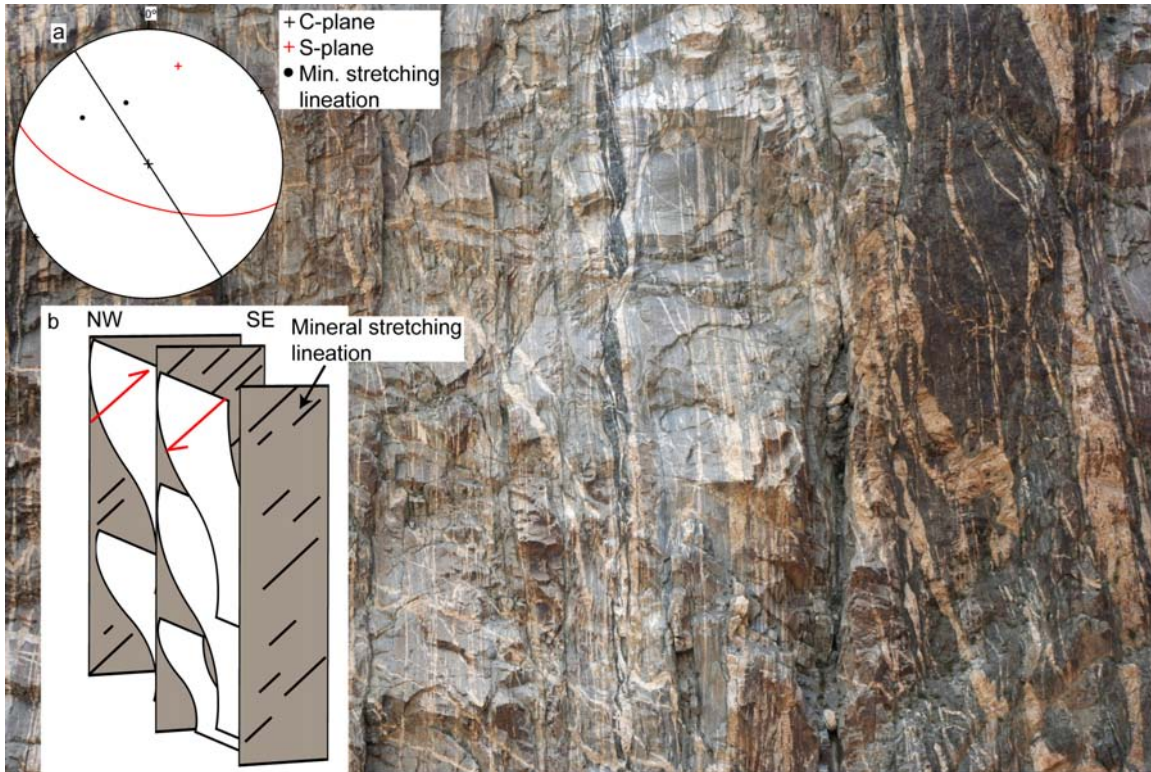


Fig. 8: Leucogranite dykes in Hbl-Bt-granodiorites ranging to diorites in Darbuk-Shyok gorge. Outcrop wall is estimated to be 200 m high and 400 m wide, inaccessible for measurements. The majority of dykes are subvertical. Note second main orientation of dykes running diagonally to near horizontal from upper left to lower right of photograph. Dykes on upper right side of photograph form a dextral C-S fabric. Inset (a): Representative stereographic projections, equal area, lower hemisphere of typical C-plane (147/90) and S-plane (107/65SW) in Hbl-Bt-granodiorite in outcrops in the area. Inset (b): 3D interpretation of shear fabric in outcrop wall. Note that mineral stretching lineation plunges NW and the intersection of C-plane and S-plane plunge SE almost perpendicular to it. Red arrows indicate oblique (dextral and NE-side up) shear movement.

Ductile fracture and chaotic dyke networks

There are two types of networks in calc-silicate layers: (a) dykes that form conjugate sets and zigzagging and interconnected networks, or (b) chaotic networks. These dykes form a continuous network characterized by a zigzagging pattern cutting with sharp contacts through bedding and foliation (Fig. 9). This network was described in detail in Weinberg & Regenauer-Lieb (2010) who argued they are a result of magma intrusion into ductile fractures resulting from deformation of the calc-silicate rocks. Here we will only summarize its main features. In contrast to the dykes in foliation-parallel networks, the zigzagging dykes generally have blunt tips. Similar zigzag cracks have been observed in experiments modeling strain localization in extensional shear zones that simulate ductile fracturing of

rocks (Weinberg & Regenauer-Lieb, 2010). In contrast to brittle dykes that characteristically propagate by overcoming the tensile strength of the country rock at the dyke tip (Clemens & Mawer, 1992; Petford *et al.*, 1993), ductile fractures nucleate in regions of negative pore pressure (Weinberg & Regenauer-Lieb, 2010). Coalescence of pores in these dilational regions initiates the ductile fracture, and the arising negative pressure gradient drives magma into it. Furthermore, ductile fractures show no mutual offsets.



Fig. 9: Conjugate sets of dykes formed by ductile fracture in calc-silicate rocks. Dykes in this outcrop are up to seven meters wide. person as scale.



Fig. 10: Interconnected dyke network dissecting fold in calc-silicate rocks, and forming lozenge shaped calc-silicate blocks in between Y-shaped fractures. Fold axis: $325/20^\circ$. Inset: sketch..

In examples of ductile fractures in the PMC, extension is evident in Y-shaped structures where the dykes diverge and remerge thereby fracturing the country rocks in conjugate sets with acute angles of roughly 60° (Fig. 10). Commonly, these dykes isolate rotated blocks of calc-silicate rock. Interestingly, the common intersection of zigzagging dykes is parallel to the regional mineral stretching lineation as observed in the networks of foliation parallel dykes.

There are also large lenses of calc-silicate rocks in which a more chaotic style of dyke network developed. Here, dykes do not follow any obvious systematic pattern (Fig. 11) apart from sharing a common intersection parallel to the stretching lineation (Fig. 12).

4.3 Lithological contacts

In places, lithological contacts influence the dyke network. This rather rare feature is documented at contacts between anatectic and sub-solidus rocks. This is exemplified in Fig. 13, where a sub-vertical dyke in calc-silicate rocks intrudes unconformable to bedding and

and cuts across calc-silicate rocks until it reaches the contact to metatexite migmatite in Bt-psammites. The dyke meets the migmatite at a high angle and is deflected into parallelism with stromatic layering in the internally folded migmatite, thus forming a sill. Here, a rheological contrast between neighboring rock types imprints on dyke orientations. The inability of the dyke to intrude the migmatite reflects a rheological contrast. The change from dyke to sill is marked by schlieren in the leucogranite.

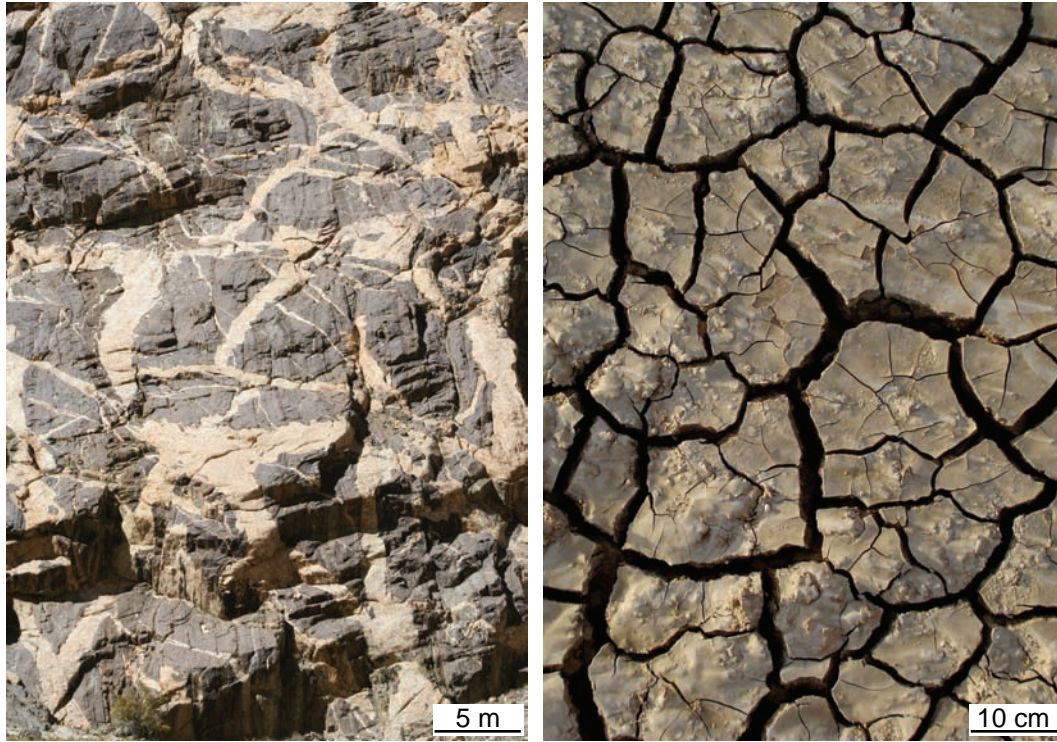


Fig. 11: (a) Chaotic leucogranite dykes in calc-silicate rocks in Tangtse gorge. Dykes merge at apparently random angles and form spider dykes. (b) Mud cracks for comparison, suggesting that this pattern could be related to general extension on the exposed plane.

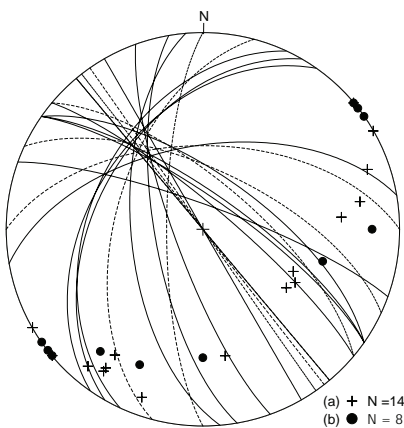


Fig.12: Stereographic projection (equal area, lower hemisphere) of dykes with apparent chaotic orientations in calc-silicate rocks forming spider dykes. Note common intersections plunging NW. Different symbols represent measurements in two different regions of the same outcrop partly shown in Fig. 12a.

5. Pluton growth

In amongst the various networks described above, there are kilometric size magma accumulations such as the Tangtse Pluton (Weinberg *et al.*, 2009) and the Darbuk Pluton (Fig. 1b). Magma sheets in the pervasive injection complex (Fig. 5) amalgamated giving rise to the Tangtse Pluton by wedging apart the country rock under continuous deformation. The ~18 Ma Tangtse Pluton (Reichardt *et al.*, 2010, Chapter II) formed in the pressure shadow of the older more competent rocks of the ~71 Ma calc-alkaline Muglib Batholith (Weinberg *et al.*, 2009). The foliation of the meta-sedimentary country rocks is deflected around the

NW tip of the calc-alkaline pluton in a manner akin to strain shadows around porphyroblasts in sheared rocks at the microscopic scale. The foliation is also deflected at the margins of the Tangtse Pluton, indicative of continued deformation after the leucogranites solidified (Weinberg *et al.*, 2009). Build up of a local leucogranite pluton by coalescence of dykes, is shown in Fig. 14. Here, a network of dykes parallel to the main foliation and cross-cutting dykes merges to feed into the leucogranite Darbuk Pluton. Magma accumulations as plutons within the source or along the transport zone have been interpreted as frozen-in magma accumulations in the anatectic zone that could have been tapped to feed transport networks that connect to final emplacement sites at upper crustal levels (Weinberg *et al.*, 2009).

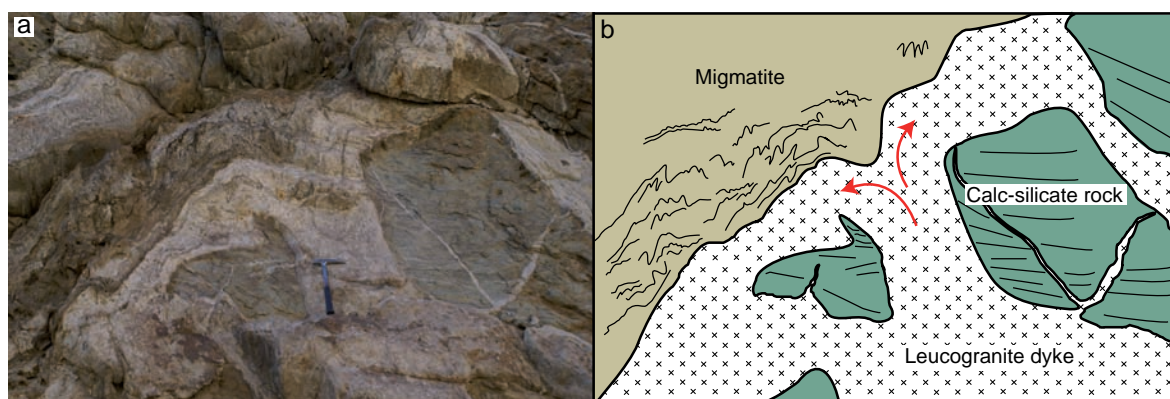


Fig. 13: (a) Subvertical leucogranite dyke in calc-silicate rocks is deflected at contact with migmatite. (b) Line drawing of (a). Arrows indicate interpreted magma flow direction.

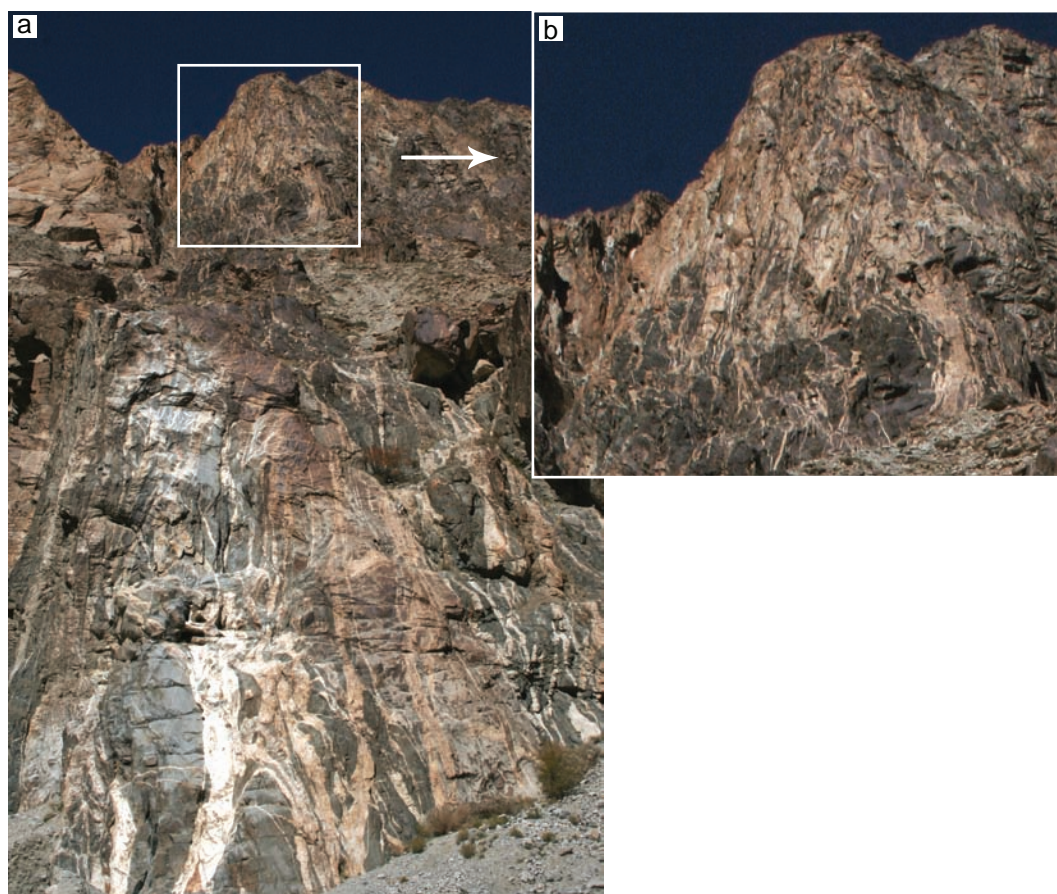


Fig. 14: (a) Leucogranite dykes intruding calc-alkaline diorites of the Muglib Batholith at the SW end of the Darbuk-Shyok gorge. (b) Enlargement of inset in (a) showing merging of dykes upwards and connection to the leucogranitic Darbuk Pluton at the top of the ~100 m high exposure.

6. Regional connections: feeding the batholith

The Karakoram Shear Zone was mapped, where accessible, from a region where mid-crustal anatectic rocks are exposed, to colder, upper-crustal regions where the Karakoram Batholith was emplaced. Using a hierarchy of magma channels, *in situ* leucosomes connect to the dyke networks exposed in the Tangtse gorge and feed magma sheets related to the Pangong Injection Complex (Reichardt *et al.*, 2010; Weinberg *et al.*, 2009; Weinberg & Searle, 1998). In other outcrops close by in the Tangtse gorge, disruption of folds and layers leads to formation of diatexites that link continuously to local magma stocks in the Pangong Range. The dyke networks in the Tangtse gorge can be traced northwestwards along strike to the Darbuk-Shyok gorge ~13 km NW. The leucogranites of the dyke network characterized by ductile fracture and the dykes characterized by shear fabric orientation in the Darbuk-Shyok gorge are inferred to be connected to the dyke networks in the Tangtse gorge, as they both are isotopically identical (Reichardt *et al.*, 2010, Chapter II). The networks in the Darbuk-Shyok gorge such as shown in Figs. 8, 9 and 14 extend further NW by linking to a ~600 m wide leucogranite band that trends NW-SE in the Pangong Range (Fig. 15), which is flanked to the NE by a band of migmatitic calc-alkaline rocks exposed along the Shyok river.

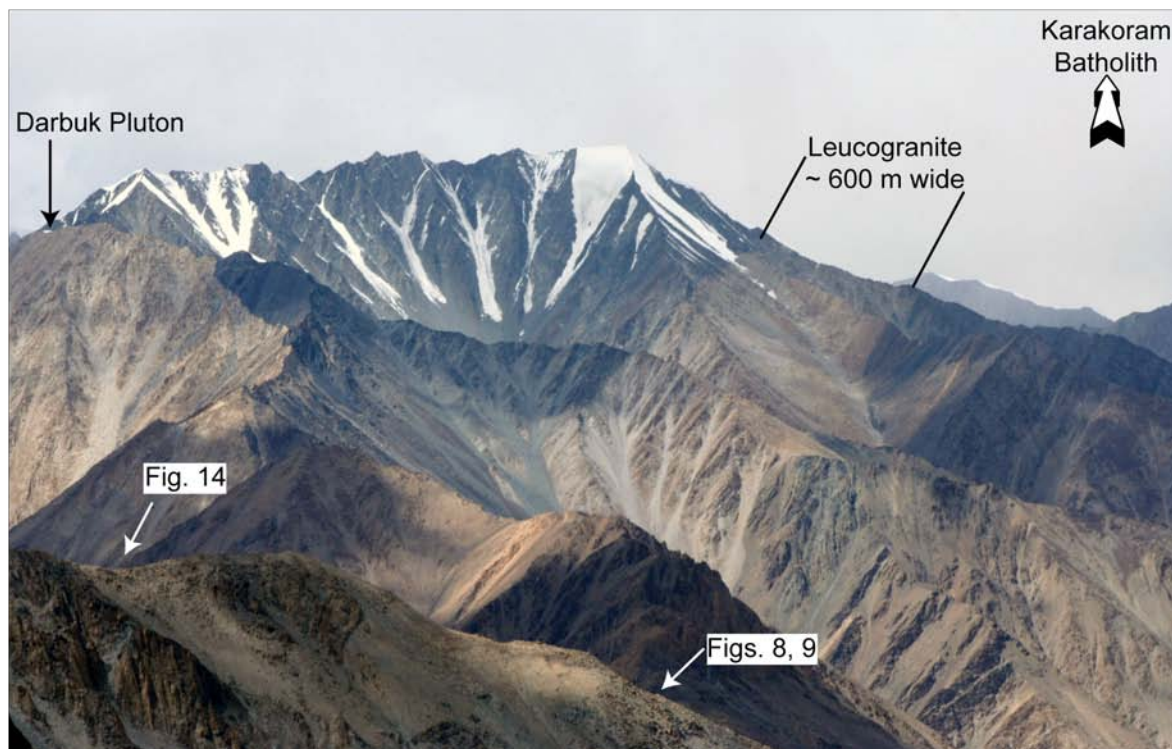


Fig. 15: Pangong Range looking NW, showing an elongated leucogranite body ~600 m wide (light band). Viewpoint is Pangong Range close to the Tangtse Pluton. The band can be followed into the Darbuk-Shyok gorge, where the dyke networks in Fig. 8 and 9 are exposed (closer to viewer). The far ridge of the leucogranite band is 15 km along strike from the viewpoint.

At a regional map scale, the two lineaments bounding the Pangong Range merge at Agham to form a single shear zone immediately SW of the Karakoram Batholith (Fig. 1a). At the point where the two strands merge, the Karakoram Shear Zone changes trend abruptly from 140° to approximately 110°. Geologically this change is accompanied by a switch from migmatitic rocks and extensive leucogranite network and minor stock and plutons of the PMC,

to the continuous, at least 50 km long, leucogranite body of the Karakoram Batholith. Here, in the Nubra and Shyok Rivers confluence area, the Karakoram Batholith crops out NE of a band of greenschist to lower amphibolite facies meta-sedimentary and meta-igneous rocks intensely intruded by leucogranite dykes and mylonitized by the Karakoram Shear Zone. Interestingly, the outcrop width of the Karakoram Batholith is approximately similar to the width of the Pangong Range. Thus, leucogranite networks of essentially similar composition and age (Phillips *et al.*, 2004; Ravikant *et al.*, 2009; Reichardt *et al.*, 2010) can be followed along strike from the anatectic root zone in the PMC, through an intermediate network of dykes and plutons to the Karakoram Batholith. The Karakoram Shear Zone comprises the source and the pathway as well as the sink for Miocene-age magmas.

7. Discussion

7. 1 Filtering processes

In situ melting products in migmatites in the source region contrast with leucogranites in dykes and plutons. Leucosomes in meta- and diatexites in the PMC commonly contain peritectic hornblende megacrysts, and entrained schlieren, consisting of mostly hornblende and biotite (Reichardt *et al.*, 2010; Weinberg & Mark, 2008). In places, peritectic hornblende forms accumulations, remaining close to the source on outcrop scale (see also Chapter III). Diatexites also contain isolated schollen of amphibolite resisters as well as fragments of metatexite, forming a heterogeneous rock mass.

An extreme process of filtering is represented by leucosomes consisting of mostly hornblende and K-feldspar megacrysts and high amounts of the accessory phases titanite, apatite and allanite. These are interpreted to be a combination of early formed magmatic minerals and residual assemblages of minerals that have not been extracted in the melt flow network (Reichardt *et al.*, 2010). These rocks in the source region contrast with clean homogeneous leucogranites in the transport zone where restite is generally missing. Also leucogranite plutons such as the Darbuk Pluton (Fig. 14) are mostly free from peritectic minerals or residuum. Thus, there seems to be an efficient mechanism of filtering of melt from solid residue.

7. 2 Magma transfer in axial planar orientation and shear fabrics

In ductily deforming anatectic rocks, melt migration along anisotropic planes such as the foliation planes occurs because the tensile strength normal to the fabric is presumably low (Brown & Solar, 1998; Davidson *et al.*, 1994). In the meta- and diatexite migmatites of the PMC, magma channels in axial planar orientation of open to isoclinal folds, trend 120-130°. Similarly, most dykes are parallel to the axial plane of folds and to strike of the Karakoram Shear Zone (Fig. 6a). This implies that they intruded perpendicular to the maximum shortening axis or parallel to the main shear plane of the Karakoram Shear Zone and not parallel to the maximum shortening axis as expected from analogue and numerical modeling (Holtzman & Kohlstedt, 2007; Katz *et al.*, 2006; Kohlstedt & Holtzman, 2009). The possibility that dykes intruded at some other orientation and then rotated toward the dominant shear plane is not

entirely excluded, but the delicate features recording magma extraction along axial planar orientations (Weinberg & Mark, 2008) and the well-defined patterns described above on dykes that are at least tens of meters long, suggest that the majority must have intruded along these dominant anisotropies.

Weinberg & Mark (2008) used examples from the meta- and diatexite migmatites in the Tangtse gorge to argue that magma migration parallel to the axial plane, together with block rotations and transposition of layering, allows for enhanced mass transfer and shortening parallel to the axis of maximum compressional stress, perpendicular to the axial plane. The main trend recorded by magma sheets and schlieren in diatexites and foliation-parallel dykes in non-anatectic rocks therefore suggest that a significant component of magma transfer in the Karakoram Shear Zone was in axial planar orientation, perpendicular to the axis of maximum compression.

The leucogranite dyke network characterized by C-S fabric dyke patterns exemplifies how leucogranite dykes exploit the axial planar foliation and shear fabrics (Fig. 8). These orientations are in stark contrast to magma migration into antithetic shear zone found in shear experiments (Holtzman & Kohlstedt, 2007; Kohlstedt & Holtzman, 2009). The C-S-fabric in Hbl-Bt-granodiorites in this region defines planes parallel to those of dykes (Fig. 13). We interpret this network as evidence that magma also migrated parallel to shear zone orientation and synthetic rotation of dykes.

7.3 Intersections increasing permeability

The intersection between two planar sheets is a zone of high permeability (Petford & Koenders, 1998). The resulting cylindrical structure, however, only has an impact on magma transfer if its orientation coincides with a significant pressure gradient that drives magma transfer in that direction. We demonstrated that dyke intersections typically plunge NW, parallel to fold axes and the main mineral stretching lineation (Fig. 6d, e). The potential for efficient magma transfer along the cylindrical intersections such as in spider dykes has been inferred by Brown (2005, 2006). Marchildon & Brown (2003) documented that lineations in a shear zone also partly dictate the orientations of melt-bearing structures in migmatites and argued for high magma permeability parallel to the lineation. Further, Collins & Sawyer (1996) argued for magma migration into pre-existing anisotropies such as the foliation plane, followed by focusing of magma into channelways parallel to the maximum elongation direction that developed during contractional deformation. We infer that dyke intersections parallel to the mineral and stretching lineations and fold axes could potentially channelize magma effectively in the orientation of maximum elongation.

7.4 Ductile fractures and apparent chaotic networks

Ductile fractures can be an efficient way of magma transport through ductile rocks, and we suggest that the dyke networks in the calc-silicate layer in the Darbuk-Shyok gorge (Fig. 9) are an example of this mechanism (Weinberg & Regenauer-Lieb, 2010). We only found this type of network in calc-silicate layers, while migmatized Hbl-Bt-granodiorites and diorites show conformable, shear zone related dyke networks. The zigzag pattern of the dyke

network in calc-silicate rocks in the Darbuk-Shyok gorge does not follow the main regional foliation. In contrast to other networks, anisotropies in the host rock appear to be irrelevant as the dykes cut across both bedding and axial planar foliation. Here, dykes bifurcate at high angles, commonly $\sim 60^\circ$, forming conjugate sets. The exposed network does not show signs of cross-cutting relationships, and the branches are in petrographic continuity. The formation of zigzagging paths with blunt fracture tips, into which magma would be able to move, was interpreted as the result of ductile fracturing (Eichhubl & Aydin, 2003) during extensional shearing by coalescence of pores in regions of negative pore pressures (Weinberg & Regenauer-Lieb, 2010). These extensional shear zones are exploited by magma, eventually forming magma sheets in conjugate sets.

Clinopyroxene is generally regarded as a relatively competent mineral (e.g. Kirby, 1980) and we assume that clinopyroxene-rich calc-silicate rocks are more competent than granites and diorites (Carter & Tsenn, 1987; Kirby, 1985). This contrast is amplified by anatexis of the granitoids which are thus significantly weakened (Arzi, 1978; Dell'Angelo & Tullis, 1988; van der Molen & Paterson, 1979). We infer that the several hundred meters wide calc-silicate layers formed a relatively competent block within the anatectic rocks of the PMC, where ductile fractures developed.

7.5 Implications for magma transfer

The dyke network in the PMC is interconnected at all scales. We have described a variety of magma network styles, all of which are controlled by tectonic stresses related to dextral transpressional deformation (Weinberg *et al.*, 2009). Connectivity between melt-bearing domains in migmatites and shear zones and thus build-up of the magma network was achieved by syn-magmatic folding and shearing. Transpressional movements of the Karakoram Shear Zone are interpreted to have expelled the accumulations that formed the Tangtse Pluton (Weinberg *et al.*, 2009). Such magma accumulation could have been tapped and pumped through the network. This mechanism establishes a connection between local stocks in the anatectic zone and the axial planar oriented dyke networks. On their passage out of the source, the leucogranite dyke networks cover anatectic and sub-solidus rocks in different structural levels of the crust.

Water-fluxed melting is generally considered to play only a minor role in crustal differentiation (Clemens, 2006; Clemens & Vielzeuf, 1987). Furthermore, ascent of magma derived from water-fluxed melting is thought to be limited because of the shape of the solidus curve that dictates magma freezing under decompression (Clemens & Droop, 1998). We argue that the crustal-scale Karakoram Shear Zone provided the conditions for both water-fluxed melting and magma ascent based on the following grounds. Water-rich fluids could have infiltrated the PMC from the underthrust meta-sedimentary rocks of the Karakoram Metamorphic Complex (McCarthy & Weinberg, in press). Melt segregation was controlled by deformation providing conditions for magma separation from its source, thus preventing it from back-reacting and thus freezing (Leitch & Weinberg, 2002). Magma migration may warm up its surroundings thus progressively pushing the magma solidus isotherm to shallower crustal levels. Because the networks are continuous at the scale of kilometers, we interpret that the transport zone was in permanent or intermittent communication with

the source region. Therefore, a crustal-scale shear zone such as the dextral transcurrent and transpressive Karakoram Shear Zone can initiate water-fluxed melting, and simultaneously form networks of magma channelways in the source, that feed into transport channelways and ultimately to a batholith.

8. Conclusions

The Pangong Metamorphic Complex hosts a complex network of leucogranites from the roots of the system in the anatectic source, through a transport zone of dykes to the Karakoram Batholith. Syn-deformational water-fluxed melting at upper amphibolite conditions gave rise to migmatites with a growing magma network characterized by axial planar magma pathways and transposition of pre-existing layering. Drainage of *in situ* leucosomes into channelways led to development of a transport zone dominated by a number of network styles, characterized by axial planar dykes and shear zone-parallel dykes. The key defining features of the magma network are continuity with rare cross-cutting relationships and intersection parallel to the mineral elongation lineation. The axial planar- or shear-parallel dyke orientation at high angle to the axis of maximum compression in nature, contrast to model predictions that channelways form preferentially parallel to the maximum compression axis. The mechanisms of felsic magma transport have long been discussed, here we show a complete system from source to batholith where magma migrates through dykes at high angles to the maximum elongation, this contrasts with predictions based on elastic-brittle mechanisms of dyke propagation.

References

- Arzi, A. A. (1978). Critical phenomena in the rheology of partially melted rocks. *Tectonophysics* 44, 173-184.
- Bons, P. D., Arnold, J., Elburg, M. A., Kalda, J., Soesoo, A. & van Milligen, B. P. (2004). Melt extraction and accumulation from partially molten rocks. *Lithos* 78, 25-42.
- Brown, M. (1994). The generation, ascent and emplacement of granite magma: the migmatite-to-crustally-derived granite connection in thickened orogens. *Earth-Science Reviews* 36, 83-130.
- Brown, M. (2005). The mechanism of melt extraction from lower continental crust of orogens. *Transactions of the Royal Society of Edinburgh: Earth Sciences* 95, 35-48.
- Brown, M. (2006). Melt extraction from the lower continental crust of orogens; the field evidence. In: Brown, M., Rushmer, T. (ed.) *Evolution and differentiation of the continental crust*. New York, NY, United States: Cambridge University Press, 331-383.
- Brown, M. (2007). Crustal melting and melt extraction, ascent and emplacement in orogens: mechanisms and consequences. *Journal of the Geological Society* 164, 709-730.
- Brown, M. & Solar, G. S. (1998). Shear-zone systems and melts: feedback relations and self-organization in orogenic belts. *Journal of Structural Geology* 20, 211-227.
- Carter, N. L. & Tsenn, M. C. (1987). Flow properties of continental lithosphere. *Tectonophysics* 136, 27-63.
- Clemens, J. D. (2006). Melting of the continental crust; fluid regimes, melting reactions, and source rock fertility. In: Brown, M., Rushmer, T. (ed.) *Evolution and differentiation of the continental crust*. New York, NY, United States: Cambridge University Press, 296-330.
- Clemens, J. D. & Droop, G. T. R. (1998). Fluids, P-T paths and the fates of anatectic melts

- in the Earth's crust. *Lithos* 44, 21-36.
- Clemens, J. D. & Mawer, C. K. (1992). Granitic magma transport by fracture propagation. *Tectonophysics* 204, 339-360.
- Clemens, J. D. & Vielzeuf, D. (1987). Constraints on melting and magma production in the crust. *Earth and Planetary Science Letters* 86, 287-306.
- Collins, W. J. & Sawyer, E. W. (1996). Pervasive granitoid magma transfer through the lower-middle crust during non-coaxial compressional deformation. *Journal of Metamorphic Geology* 14, 565-579.
- D'Lemos, R. S., Brown, M. & Strachan, R. A. (1992). Granite magma generation, ascent and emplacement within a transpressional orogen. *Journal of the Geological Society of London* 149, 487-490.
- Davidson, C., Schmid, S. M. & Hollister, L. S. (1994). Role of melt during deformation in the deep crust. *Terra Nova* 6, 133-142.
- Dell'Angelo, L. N. & Tullis, J. (1988). Experimental deformation of partially melted granitic aggregates. *Journal of Metamorphic Geology* 6, 495-515.
- Dunlap, W. J., Weinberg, R. F. & Searle, M. P. (1998). Karakoram fault zone rocks cool in two phases. *Journal of the Geological Society of London* 155, 903-912.
- Eichhubl, P. & Aydin, A. (2003). Ductile opening-mode fracture by pore growth and coalescence during combustion alteration of siliceous mudstone. *Journal of Structural Geology* 25, 121-134.
- Emerman, S. H., Marret, R. (1990). Why dikes? *Geology* 18, 231-233.
- Gardien, V., Thompson, A. B. & Ulmer, P. (2000). Melting of biotite + plagioclase + quartz gneisses; the role of H (sub 2) O in the stability of amphibole. *Journal of Petrology* 41, 651-666.
- Hand, M. & Dirks, P. H. G. M. (1992). The influence of deformation on the formation of axial-planar leucosomes and the segregation of small melt bodies within the migmatitic Napperby Gneiss, central Australia. *Journal of Structural Geology* 14, 591-604.
- Holtzman, B. K. & Kohlstedt, D. L. (2007). Stress-driven melt segregation and strain partitioning in partially molten rocks; effects of stress and strain. *Journal of Petrology* 48, 2379-2406.
- Johannes, W. & Gupta, L. N. (1982). Origin and evolution of a migmatite. *Contributions to Mineralogy and Petrology* 79, 114-123.
- Katz, R. F., Spiegelman, M. & Holtzman, B. (2006). The dynamics of melt and shear localization in partially molten aggregates. *Nature* 442, 676-679.
- Kenah, C. & Hollister, L. S. (1983). Anatexis in the Central Gneiss Complex. In: Atherton, M. P., Gribble, C. D. (ed.) *Migmatites, Melting, and Metamorphism*. Nantwich: Shiva, 142-162.
- Kirby, S. H. (1980). Tectonic stresses in the lithosphere: constraints provided by the experimental deformation of rocks. *Journal of Geophysical Research* 85, 6353-6363.
- Kirby, S. H. (1985). Rock mechanics observations pertinent to the rheology of the continental lithosphere and the localization of strain along shear zones. *Tectonophysics* 119, 1-27.
- Kohlstedt, D. L. & Holtzman, B. K. (2009). Shearing melt out of the earth: An experimentalist's perspective on the influence of deformation on melt extraction. *Annual Review of Earth and Planetary Sciences*, 561-593.
- Lappin, A. R. & Hollister, L. S. (1980). Partial melting in the Central Gneiss Complex near Prince Rupert, British Columbia. *American Journal of Science* 280, 518-545.
- Leitch, A. M. & Weinberg, R. F. (2002). Modelling granite migration by mesoscale pervasive flow. *Earth and Planetary Science Letters* 200, 131-146.
- Marchildon, N. & Brown, M. (2003). Spatial distribution of melt-bearing structures in anatectic rocks from Southern Brittany, France: implications for melt transfer at grain- to orogen-scale. *Tectonophysics* 364, 215-235.

- McCarthy, M. R. & Weinberg, R. F. (in press). Structural complexity resulting from pervasive ductile deformation in the Karakoram Shear Zone, Ladakh, NW India. *Tectonics*.
- Mehnert, K. R. (1968). *Migmatites and the origin of granitic rocks*. Elsevier Publishing Corporation, pp. 393.
- Mogk, D. W. (1992). Ductile shearing and migmatization at mid-crustal levels in an Archaean high-grade gneiss belt, northern Gallatin Range, Montana, USA. *Journal of Metamorphic Geology* 10, 427-438.
- Petford, N., Cruden, A. R., McCaffrey, K. J. W. & Vigneresse, J. L. (2000). Granite magma formation, transport and emplacement in the Earth's crust. *Nature* 408, 669-673.
- Petford, N., Kerr, R. C. & Lister, J. R. (1993). Dike transport of granitoid magmas. *Geology* 21, 845-848.
- Petford, N. & Koenders, M. A. (1998). Self-organisation and fracture connectivity in rapidly heated continental crust. *Journal of Structural Geology* 20, 1425-1434.
- Petford, N., Lister, J. R., Kerr, R. C. (1994). The ascent of felsic magmas in dykes. *Lithos* 32, 161-168.
- Phillips, R. J., Parrish, R. R. & Searle, M. P. (2004). Age constraints on ductile deformation and long-term slip rates along the Karakoram fault zone, Ladakh. *Earth and Planetary Science Letters* 226, 305-319.
- Rabinowicz, M. & Vigneresse, J. L. (2004). Melt segregation under compaction and shear channeling: Application to granitic magma segregation in a continental crust. *Journal of Geophysical Research B: Solid Earth* 109, B04407 04401-04420.
- Ravikant, V. (2006). Utility of Rb-Sr geochronology in constraining Miocene and Cretaceous events in the eastern Karakoram, Ladakh, India. *Journal of Asian Earth Sciences* 27, 534-543.
- Ravikant, V., Wu, F.-Y. & Ji, W.-Q. (2009). Zircon U-Pb and Hf isotopic constraints on petrogenesis of the Cretaceous-Tertiary granites in eastern Karakoram and Ladakh, India. *Lithos* 110, 153-166.
- Reichardt, H., Weinberg, R. F., Andersson, U. B. & Fanning, C. M. (2010). Hybridization of granitic magmas in the source: The origin of the Karakoram Batholith, Ladakh, NW India. *Lithos* 116, 249-272.
- Robin, P. Y. F. & Cruden, A. R. (1994). Strain and vorticity patterns in ideally ductile transpression zones. *Journal of Structural Geology* 16, 447-466.
- Rolland, Y., Mahéo, G., Pêcher, A. & Villa, I. M. (2009). Syn-kinematic emplacement of the Pangong metamorphic and magmatic complex along the Karakoram Fault (N Ladakh). *Journal of Asian Earth Sciences* 34, 10-25.
- Rolland, Y. & Pêcher, A. (2001). The Pangong granulites of the Karakoram Fault (western Tibet); vertical extrusion within a lithosphere-scale fault? *Comptes Rendus de l'Académie des Sciences, Serie II. Sciences de la Terre et des Planètes* 332, 363-370.
- Rosenberg, C. L. & Berger, A. (2001). Syntectonic melt pathways in granitic gneisses, and melt-induced transitions in deformation mechanisms. *Physics of the Chemical Earth* 26, 287-293.
- Rubin, A. M. (1993). Dikes vs. diapirs in viscoelastic rock. *Earth and Planetary Science Letters* 119, 641-659.
- Sawyer, E. W. (2008). *Atlas of migmatites*: Mineralogical Association of Canada, Ottawa, ON, Canada 9, pp. 371.
- Searle, M. P. & Phillips, R. J. (2007). Relationships between right-lateral shear along the Karakoram fault and metamorphism, magmatism, exhumation and uplift: evidence from the K2-Gasherbrum-Pangong ranges, north Pakistan and Ladakh. *Journal of the Geological Society* 164, 439-450.
- Searle, M. P., Weinberg, R. F. & Dunlap, W. J. (1998). Transpressional tectonics along the Karakoram Fault Zone, northern Ladakh. In: Holdsworth, R. E. & Strachan, R. A. (eds.) *Continental Transpressional and Transtensional Tectonics*. London: Geological

- Society of London Special Publication, 307-326.
- van der Molen, I. & Paterson, M. S. (1979). Experimental deformation of partially-melted granite. *Contributions to Mineralogy and Petrology* 70, 299-318.
- Vanderhaeghe, O. (1999). Pervasive melt migration from migmatites to leucogranite in the Shuswap metamorphic core complex, Canada: Control of regional deformation. *Tectonophysics* 312, 35-55.
- Vernon, R. H. & Paterson, S. R. (2001). Axial-surface leucosomes in anatectic migmatites. *Tectonophysics* 335, 183-192.
- Weinberg, R. F. (1996). Ascent mechanism of felsic magmas: news and views. *Special Paper - Geological Society of America, 315: The Third Hutton Symposium on the Origin of Granites and Related Rocks* 315, 95-103.
- Weinberg, R. F. (1999). Mesoscale pervasive melt migration: alternative to dyking. *Lithos* 46, 393-410.
- Weinberg, R. F., Dunlap, W. J. & Whitehouse, M. (2000). New field, structural and geochronological data from the Shyok and Nubra valleys, northern Ladakh: Linking Kohistan to Tibet. In: Khan, A., Treloar, P. J. & Searle, M. P. (eds.) *Tectonics of the Nanga Parbat Syntaxis and the Western Himalaya*. London: Geological Society of London Special Publication, 253-275.
- Weinberg, R. F. & Mark, G. (2008). Magma migration, folding, and disaggregation of migmatites in the Karakoram shear zone, Ladakh, NW India. *Geological Society of America Bulletin* 120, 994-1009.
- Weinberg, R. F., Mark, G. & Reichardt, H. (2009). Magma ponding in the Karakoram shear zone, Ladakh, NW India. *Geological Society of America Bulletin* 121, 278-285.
- Weinberg, R. F. & Podladchikov, Y. (1994). Diapiric ascent of magmas through power law crust and mantle. *Journal of Geophysical Research* 99, 9543-9559.
- Weinberg, R. F. & Regenauer-Lieb, K. (2010). Ductile fractures and magma migration from source. *Geology* 38, 363-366.
- Weinberg, R. F. & Searle, M. P. (1998). The Pangong Injection Complex, Indian Karakoram: a case of pervasive granite flow through hot viscous crust. *Journal of the Geological Society of London* 155, 883-891.

Declaration for Thesis Chapter 5

Declaration by candidate

In the case of Chapter 5, the nature and extent of my contribution to the work was the following:

Nature of contribution	Extent of contribution (%)
Development of ideas, collection of data, writing up and interpretation of results.	80%

The following co-authors contributed to the work. Co-authors who are students at Monash University must also indicate the extent of their contribution in percentage terms:

Name	Nature of contribution	Extent of contribution (%) for student co-authors only
Roberto Weinberg	Development of ideas, intellectual input during revision process.	
Ulf Andersson	Data collection, intellectual input during revision process.	

Candidate's
Signature


	Date
--	------

Declaration by co-authors

The undersigned hereby certify that:

- (1) the above declaration correctly reflects the nature and extent of the candidate's contribution to this work, and the nature of the contribution of each of the co-authors.
- (2) they meet the criteria for authorship in that they have participated in the conception, execution, or interpretation, of at least that part of the publication in their field of expertise;
- (3) they take public responsibility for their part of the publication, except for the responsible author who accepts overall responsibility for the publication;
- (4) there are no other authors of the publication according to these criteria;
- (5) potential conflicts of interest have been disclosed to (a) granting bodies, (b) the editor or publisher of journals or other publications, and (c) the head of the responsible academic unit; and
- (6) the original data are stored at the following location(s) and will be held for at least five years from the date indicated below:

Location(s) School of Geosciences, Monash University

Signature 1		Date
Signature 2		2010-09-07

.....

Chapter V.

Are the Shyok Suture Zone and the Karakoram Shear Zone parallel in Ladakh?

Abstract

The Ladakh island arc, in NW India, is separated from the Eurasian plate to the north by the Shyok Suture Zone (SSZ) and from the Indian plate to the south by the Indus Suture Zone (ISZ). In Ladakh, the SSZ has been interpreted to run between the Ladakh and the Muglib Batholiths along with the Karakoram Shear Zone (KSZ). However, evidence of a suture zone, mostly in the form of ultramafic rocks, is sparse. Both batholiths form typical calc-alkaline magmatic differentiation series ranging from gabbros to Bt-granites but if they are separated by a suture zone, one would expect the southern Ladakh Batholith to have an island arc signature, and the northern Muglib Batholith to have a continental signature, having formed at the southern margin of Eurasia. The Ladakh Batholith forms part of the >2500 km long arcuate body of the Trans-Himalayan Plutonic Belt. It has zircon crystallization ages between ~45 and ~103 Ma, lack older inherited zircons, and zircons have juvenile Hf-isotopes. Whole rock isotope systematics indicate a mantle source with minor crustal influence (initial $^{87}\text{Sr}/^{86}\text{Sr} = 0.7030$ to 0.7046 ; initial $\epsilon_{\text{Nd}} = 0.5$ to 2.7). The calc-alkaline Muglib Batholith outcrops in the Pangong Metamorphic Complex in the Pangong Range, which is bound by two parallel strands of the dextral transpressive Karakoram Shear Zone. Plutons of the Muglib Batholith shows crystallization ages between 115 ± 18 Ma (Rb-Sr whole rock age) and 56.0 ± 0.5 Ma (U-Pb zircon age), also lacks older inherited zircons, and also has zircons with juvenile Hf-isotopes. The whole rock isotopic signature of the Muglib Batholith is essentially identical (initial $^{87}\text{Sr}/^{86}\text{Sr} = 0.7041$ to 0.7072 ; initial $\epsilon_{\text{Nd}} = 1.2$ to 2.7) to the one of the Ladakh Batholith, and indicates a similar origin. We postulate that the Ladakh and Muglib Batholiths originated in the same island arc, and consequently are unlikely to lie on opposite sides of a suture zone. Therefore, the SSZ probably does not run parallel and to the south of the Pangong Range.

1. Introduction

South of the Tibetan block, Mid-Cretaceous to Eocene calc-alkaline granitic intrusions, commonly referred to as the Trans-Himalayan Plutonic Belt, form a semicontinuous arcuate body over 2500 km (Fig. 1; e.g. Allègre *et al.*, 1984, Coward *et al.*, 1986, Petterson & Windley, 1985). In the western Karakoram in Afghanistan and Pakistan, these calc-alkaline plutons form the Kohistan Batholith (Jagoutz *et al.*, 2009; Petterson & Windley, 1985), followed to the east from Pakistan into NW India by the Ladakh Batholith (e.g. Honegger *et al.*, 1982; Raz & Honegger, 1989; Schärer *et al.*, 1984) and further SE by the Gangdese

Batholith, in southern Tibet (e.g. Wen *et al.*, 2008). It is generally accepted that the calc-alkaline magmatism that gave rise to the Trans-Himalaya batholiths resulted from northward subduction of Indian oceanic crust beneath the Eurasian plate in the course of closure of the Neo-Tethyan Ocean (Allègre *et al.*, 1984; Dietrich *et al.*, 1983; Honegger *et al.*, 1982; Ji *et al.*, 2009).

In Ladakh, NW India, magmatic activity lasted from mid-Cretaceous to Eocene times ceased closely after the collision of India with Eurasia at ~50 Ma, as a consequence of hindered further subduction (Honegger *et al.*, 1982; Khan *et al.*, 2009; Schärer *et al.*, 1984; Weinberg & Dunlap, 2000). The Ladakh arc and Kohistan arc are in most studies considered as a single Kohistan-Ladakh arc, only divided by the Nanga Parbat syntaxis that developed by a combination of indentation and block rotation after collision of the Indian and Eurasian continents (Coward *et al.*, 1986). The Ladakh terrane is separated from the Indian plate to the south by the Indus Suture Zone (ISZ) and from the Asian shield (Karakoram terrane) to the north by the Shyok Suture Zone (SSZ), and thus is sandwiched between two continents (Coward *et al.*, 1986; Frank *et al.*, 1977; Gansser, 1980; Honegger *et al.*, 1982; Robertson & Collins, 2002; Thakur & Misra, 1984; Thakur *et al.*, 1981). The timing of closure of the SSZ is debated and took place as early as ~100 to ~75 Ma (Pettersen & Windley, 1985; Upadhyay *et al.*, 1999) and before closure of the ISZ, or around ~50 Ma and after closure of the ISZ (Khan *et al.*, 2009). The SSZ has been related to the Bangong- and Shiquanhe sutures (Lacassin, 2004; Matte *et al.*, 1996; Robinson, 2009; Srinial, 1986), or alternatively Rolland *et al.*, (2002) suggested that the SSZ terminates in Eastern Ladakh.

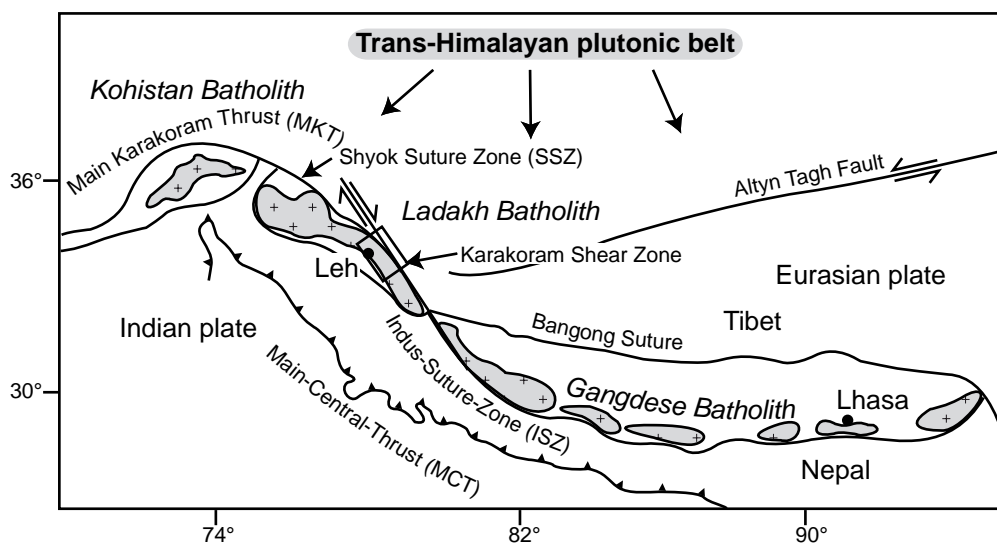


Fig. 1 Sketch map showing major geological boundaries and the Trans-Himalayan plutonic belt. Frame indicates location of study area, Fig 2.

The course of the SSZ as the southward continuation of the Northern Suture Zone (Fig. 1a), is well documented in Kohistan (Pakistan) by the contact between obducted lower crustal sections of the mafic Jial and Chilas Complexes, granitic rocks of the Kohistan Batholith and volcanic sequences, all with consistent isotopic evidence for an island arc origin (Heuberger *et al.*, 2007; Khan *et al.*, 2009; Pettersen & Windley, 1985; Robertson & Collins, 2002), and the Karakoram Batholith to the north with a stronger crustally influenced isotopic signature indicative of intrusion into the Asian margin (Crawford & Searle, 1992; Mahéo *et al.*, 2009; Mahéo *et al.*, 2002). In contrast, the position of the SSZ in Ladakh is debated (Rai, 1982;

Rai, 1997; Rolland *et al.*, 2000; Upadhyay *et al.*, 1999; Weinberg *et al.*, 2000). This difficulty is mostly because no rock sequence has been demonstrably related to a suture zone and because continued tectonic activity in the region gave rise to reworking of the SSZ by the younger, Miocene KSZ, which complicates interpretation and correlation of juxtaposed geological units.

In our study area in Ladakh, two broadly contemporaneous calc-alkaline batholiths run parallel to each other on either side of the postulated course of the SSZ. These are the Ladakh Batholith to the south, and the Muglib Batholith to the north. If these calc-alkaline bodies are separated by the SSZ, the Muglib Batholith would have intruded the Eurasian margin similar to the Karakoram terrane granitoids in Pakistan and thus would have presumably formed under stronger continental influence (Crawford & Searle, 1992; Debon *et al.*, 1987) in contrast to the island arc Ladakh Batholith. In this study, we compare geochemical, geochronological and isotopic data of the Ladakh and the Muglib Batholiths to determine whether the two batholiths record their different origins on either side of a suture zone.

2. Regional geology

2.1 Shyok Suture Zone (SSZ)

In early papers, the SSZ was inferred to run parallel to the Shyok Valley in Ladakh (Fig. 2), because of occurrences of disrupted lenses of sheared mafic- and ultramafic rocks that were interpreted as ophiolites, or an ophiolitic melange (Gansser, 1980; Rai, 1982; Srimal, 1986; Thakur *et al.*, 1981). These disconnected blocks supposedly comprise peridotites, pyroxenites, gabbros and serpentinites, but the exposures are scattered and field relations are much less clear than for the SSZ to the NW in Pakistan (Robertson & Collins, 2002).

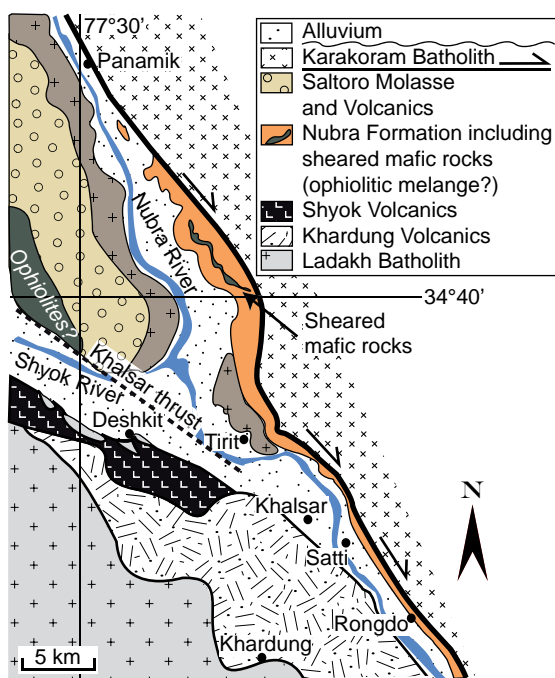


Fig. 2: Geological map of the Nubra and Shyok River confluence area. Redrawn after Weinberg *et al.* (2000).

Where other described a ophiolitic melange, Weinberg *et al.* (2000) mapped interlayered sheared volcanic rocks and sedimentary phyllites and marbles and sheared gabbros and granodiorites metamorphosed under greenschist facies conditions and mylonitized by the KSZ. They are either grouped as the Shyok ophiolitic melange (Upadhyay *et al.*, 1999) or the Nubra Formation (Weinberg *et al.*, 2000). The volcanic Shyok formation in the Shyok and Nubra River confluence area (Fig. 2), is interlayered with meta-sedimentary beds in which fossil fauna suggests Cretaceous ages (Upadhyay *et al.*, 1999). It is overlain by the Khardung Volcanics, and both Shyok and Khardung Volcanics are related to the Ladakh arc (Dunlap & Wysoczanski, 2002). A younger sequence of volcanic rocks is interlayered with

the Tertiary Saltoro molasses (Rai, 1982). Rolland *et al.* (2000) interpreted mafic rocks in the Shyok and Nubra rivers confluence area as evidence for a back-arc basin or oceanic floor, confirming the presence of the SSZ in that region. This interpretation was questioned because occurrences of sheared mafic rocks can also be related to differentiation series of calc-alkaline magmatic rocks cropping out in that area (Weinberg *et al.*, 2000). These calc-alkaline rocks are associated with the Tirit Batholith (Fig. 2; U-Pb zircon age = 68.0 ± 1 Ma; Weinberg *et al.* 2000), which in turn has been related to the Ladakh Batholith (Uphadhyay *et al.*, 2009).

More recently, gabbroic rocks north of Chang La (la = pass; Fig. 3a), to the south of the KSZ have been related to the ophiolites because their chemistry shows ocean floor affinities (Rolland *et al.*, 2002). Findings of Jurassic ammonoids in a sedimentary sequence with continental affinities that was intruded by their ultramafic unit, was interpreted as evidence for a continental base of the island arc (Ehiro *et al.*, 2007). In these interpretations, the SSZ runs parallel to the KSZ south of the Pangong Range.

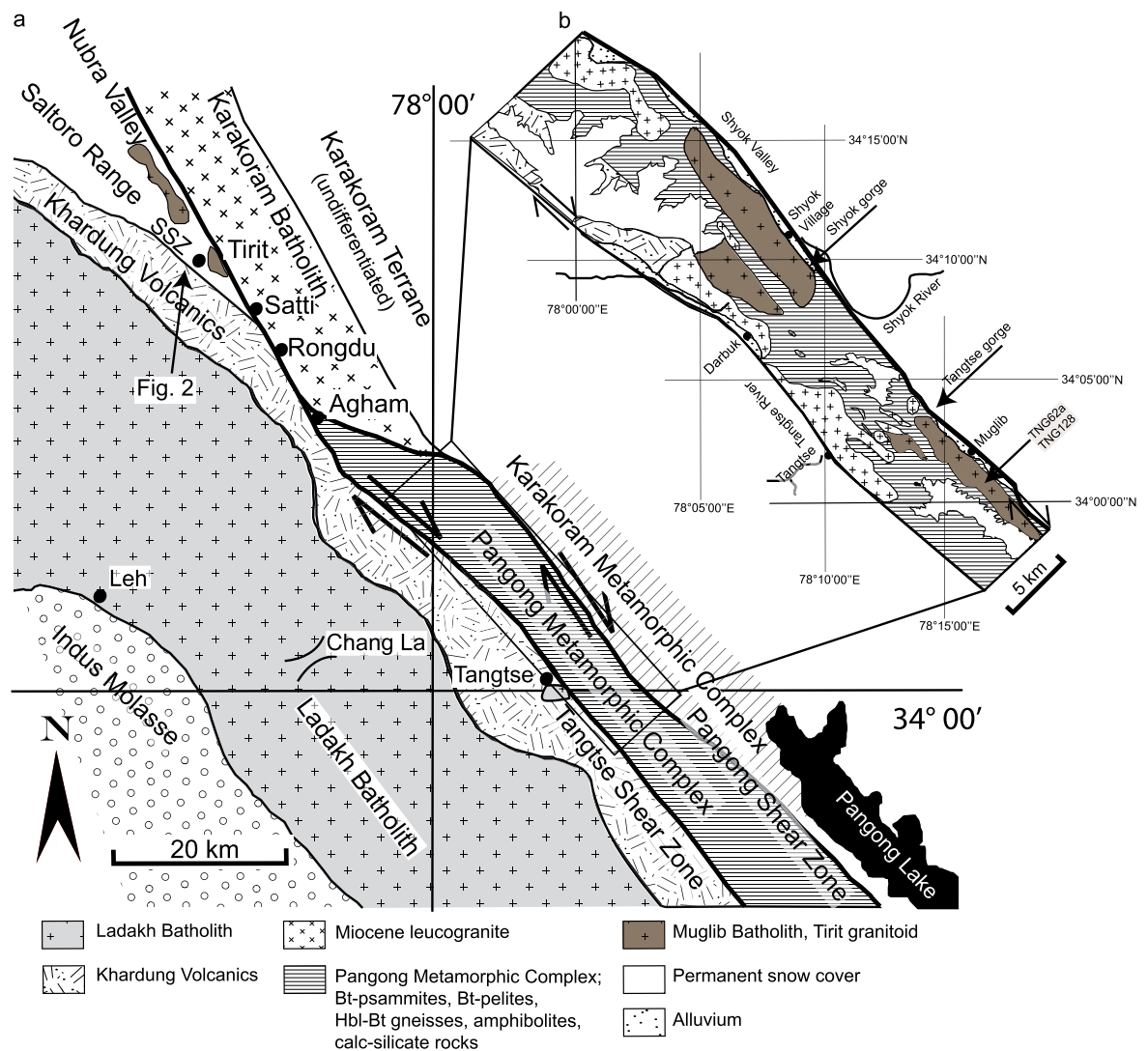


Fig. 3: (a) Overview map of the central part of the Ladakh Batholith and Karakoram Shear Zone. (b) Geological map of the Pangong Metamorphic Complex.

2.2 Karakoram Shear Zone and Pangong Metamorphic Complex

In response to the ongoing northward movement of the Indian plate after closure of the

ISZ and SSZ, a crustal-scale strike-slip shear zone system developed, forming the right-lateral KSZ north of the Ladakh Batholith (Fig. 3a, b). It trends NW-SE, is traceable for at least 700 km, and in the Shyok-Tangtse region, the shear zone is split into two parallel mylonitic main strands that bound the Pangong Range that comprises the deeply exhumed rocks of the Pangong Metamorphic Complex (PMC; Fig. 1c). The Tangtse Shear Zone (SW strand) dips vertical and bounds the PMC to the NE from the Ladakh Batholith, and its overlying extrusive equivalents, the Khardung Volcanics, to the SW. The Pangong Shear Zone (NE strand) dips steeply SE to sub-vertical and bounds the PMC from the Karakoram Metamorphic Complex to the NE. Transpressional movements thrust upper amphibolite facies rocks of the PMC over colder, greenschist facies to lower amphibolite facies rocks of the Karakoram Metamorphic Complex (McCarthy & Weinberg, in press). Mineral stretching lineations of biotite and quartz plunge consistently NW to NNW generally 20° - 40°, rarely horizontal. In the Pangong Shear Zone only, reactivation of the shear zone under greenschist facies produced a SW trending, moderately plunging (~40°) stretching lineation of chlorite. The Hbl-Bt-granodiorites of the Ladakh Batholith and the Khardung Volcanics immediately to the south of the Tangtse Shear Zone have not been metamorphosed.

The PMC consists of a calc-alkaline granitoid suite, a sequence of meta-volcanic rocks ranging from amphibolites to Hbl-Bt-schists, a meta-sedimentary sequence of Bt-psammities and Bt-pelites, calc-silicate rocks and rare marbles (mineral abbreviations after Kretz, 1983). The calc-alkaline granitoids are collectively referred to as the Muglib Batholith (Reichardt *et al.*, 2010), and are described below. The PMC is intensely intruded by Ms-Bt \pm Grt-leucogranites and Bt-leucogranites that form dykes, stocks and plutons (Phillips *et al.*, 2004; Searle *et al.*, 1998; Weinberg & Searle, 1998). The leucogranites span crystallization ages between ~20 and ~13.5 Ma (Phillips *et al.*, 2004; Ravikant *et al.*, 2009; Reichardt *et al.*, 2010; Searle *et al.*, 1998) and have been related to anatexis of PMC rocks (Weinberg & Searle, 1998; Weinberg & Mark, 2008; Reichardt *et al.*, 2010). In the following section, we summarize the rocks of the Ladakh Batholith with particular focus on the Leh region, and the Muglib Batholith in the PMC, and then investigate their genetic relationships.

2.3 Ladakh Batholith

The products of calc-alkaline magmatism in the Ladakh arc comprise volcanic successions ranging from basalts to rhyolites and plutonic suites ranging from Ol-norites to Bt-granites (Dietrich *et al.*, 1983; Dunlap & Wysoczanski, 2002; Frank *et al.*, 1977; Honegger *et al.*, 1982; Raz & Honegger, 1989; Rolland *et al.*, 2002). A number of plutons of the Ladakh Batholith have been dated indicating magmatic activity between ~45 Ma and ~102 Ma (Table 1; Honegger *et al.*, 1982; Schärer *et al.*, 1984; Singh *et al.*, 2007; Upadhyay *et al.*, 2008; Weinberg & Dunlap, 2000). These ages are broadly contemporaneous with other calc-alkaline intrusions of the Trans-Himalayan plutonic belt that mark magmatic activity from the mid-Cretaceous to Eocene times (Jagoutz *et al.*, 2009; Ji *et al.*, 2009; Petterson & Windley, 1985; Wen *et al.*, 2008).

The volcanic rocks of the Dras group of the Ladakh arc that outcrop in Western Ladakh on the southern side of the Ladakh Batholith close to the Indus Suture Zone, are inferred to be related to the Chalt Volcanics of the Kohistan arc (Dietrich *et al.*, 1983; Honegger *et al.*,

1982). Gabbros and norites of the Ladakh arc have been correlated with the mafic intrusives of the Chilas complex in Kohistan (Jagoutz *et al.*, 2009; Raz & Honegger, 1989).

Volcanic sequences of the Ladakh arc were described in other studies (Dietrich *et al.*, 1983; Dunlap & Wysoczanski, 2002; Honegger *et al.*, 1982; Rolland *et al.*, 2002), here we focus on intrusive calc-alkaline granitoid suites. In the Leh region (Fig. 2a), Weinberg & Dunlap (2000) mapped two calc-alkaline plutons, the Leh Pluton and the Gyamsa Pluton. In both plutons, the least evolved granitoids are gabbros. The main body of the Leh pluton grades from diorites rich in microdioritic enclaves to enclave-free, more felsic Hbl-Bt-granites (Weinberg, 1997). The enclaves are interpreted as being of magmatic origin. Cumulate sequences that form layers consisting mostly of hornblende and biotite indicate that modal changes are related to continuous crystal fractionation, but also to sinking of enclaves. Similarly to the Leh Pluton, the main body of the Gyamsa Pluton grades from diorites to Hbl-Bt-granites, but here, mafic fragments are interpreted as restites of an amphibolitic source rock which is also exposed. Porphyritic varieties commonly show plagioclase phenocrysts in a quartz-rich matrix. The granitoids generally have the mineral assemblage Qtz + Pl + Kfs + Bt + Hbl + Ttn \pm Cpx. Common accessory phases are Ap + Ep + Zr + Aln. Broken plagioclase phenocrysts, and quartz filling these fractures indicate deformation during crystallization of the pluton.

Based on intrusion relationships and zircon inheritance between calc-alkaline granitoids in the Leh region, Weinberg & Dunlap (2000) suggested that remelting of slightly earlier intrusions of the Ladakh Batholith gave rise to more evolved felsic granites, as indicated by zircon inheritance. Here, a migmatitic quartz-diorite of the Leh Pluton showed two U-Pb zircon age populations, one at 49.8 ± 0.8 Ma, the other at 58.1 ± 1.6 Ma. A dated sample of source rock fragments in the Gyamsa Pluton yielded the older zircon age group ($61.5 \text{ Ma} \pm 2$ Ma) in the study of Weinberg & Dunlap (2000). The overall age spread of the analysed from the Leh and Gyamsa Plutons indicates addition of magma pulses between 50 and 70 Ma, but no older, inherited zircons were found (Weinberg & Dunlap, 2000).

2.4 Muglib Batholith

It has been suggested that calc-alkaline granitoids in the Pangong Range are associated with the Karakoram Terrane (Rai, 1982; Ravikant, 2006; Srimal, 1986). The calc-alkaline granitoid suite in the PMC ranges from diorites, Hbl-Bt-granodiorites to Bt-granodiorites. Major outcrops of the Muglib Batholith are shown in Fig. 2b. It forms a semicontinuous body that runs along strike of the KSZ from SE of Muglib in the Pangong Range to the NW tip of the Pangong Range in the Shyok and Nubra River confluence area where they are inferred to link up with the calc-alkaline Tirit Batholith. The main body of the Muglib Batholith comprises Hbl-Bt-granodiorites and diorites with the general mineral assemblage Hbl + Bt + Ttn + Pl + Kfs + Qtz. Common accessory phases are Aln, Ap, Ep and Zr. More mafic varieties ($\text{SiO}_2 < 60$ wt %) sometimes also contain clinopyroxene. Mafic enclaves are common in Hbl-Bt-granodiorites. In areas that have not been migmatized, these granodiorites appear in terms of mineral content, grain size and occurrences of mafic enclaves, identical to those of the Ladakh Batholith that crop out to the south of the Tangtse Shear Zone. Within the main body of Hbl-Bt-granodiorite at Muglib, there are lenses of Hbl-Cpx-diorite, tens of meters wide. At the margins of this body close to the Pangong Shear Zone, there is a ~200 m wide

Table 1. Crystallization ages of Ladakh and Muglib Batholith

Ladakh Batholith				Muglib Batholith			
Region	Age (Ma)	Method	Author(s)	Region	Age (Ma)	Method	Author(s)
Leh	61.5 ± 2.0	U-Pb SHRIMP on zircons	Weinberg & Dunlap (2000)	Tangtse gorge	70.5 ± 0.6	U-Pb SHRIMP on zircons	Reichardt <i>et al.</i> (2010)
	58.4 ± 1.0			Pangong Range	71.4 ± 0.6		
	58.1 ± 1.6			SE Muglib			
Karhu-La/Chang-La	49.8 ± 0.8			Tangtse Shear Zone	75.7 ± 1.0	U-Pb SHRIMP on zircons	Jain & Singh (2008)
	60.1 ± 0.9	U-Pb SHRIMP on zircons	Singh <i>et al.</i> (2007)	Tangtse gorge	60.4 ± 1.1		
Kargil	58.4 ± 1.0			Road from Chang-La to Tangtse	~45 to ~52		
	101 ± 2	U-Pb SHRIMP on zircons	Schärer <i>et al.</i> (1984)	SE Muglib	118 ± 15	Rb-Sr whole rock	Ravikant (2006)
Leh	103 ± 3			Tangtse gorge	72 ± 8		
	60.7 ± 0.4	U-Pb SHRIMP on monazite/allanite		Tangtse gorge	72.8 ± 0.9	U-Pb SHRIMP on zircons	Ravikant <i>et al.</i> (2009)
Hundar (near Shyok River)	73.4 ± 2.4	Rb-Sr whole rock		Tangtse gorge	72.6 ± 1.4		
	60.8 ± 1.3 to 65.8 ± 1.4	K-Ar on biotite	Thanh <i>et al.</i> (2010)	SE Muglib	63.0 ± 1.0		
Khardung La	49.3 ± 1.1 to 51.2 ± 1.1			SE Muglib	56.0 ± 0.5		
	50.9 ± 1.1	U-Pb SHRIMP on zircons	Ravikant <i>et al.</i> (2009)	Tangtse gorge	106.3 ± 2.3	U-Pb SHRIMP on zircons	Searle <i>et al.</i> (1998)
Leh	50.9 ± 1.1	U-Pb SHRIMP on zircons	Ravikant <i>et al.</i> (2009)	Shyok-Nubra rivers confluence (Tirit Batholith)	68 ± 1	U-Pb SHRIMP on zircons	Weinberg <i>et al.</i> (2000)
Darbuk	51.0 ± 0.5			Shyok-Nubra rivers confluence (Tirit Batholith)	71.4 ± 0.36	U-Pb TIMS on zircons	Upadhyay (2008)
Darbuk	50.4 ± 0.4			Skyanpoche (NE slopes of Nubra Valley)	103 ± 1.8	U-Pb SHRIMP on zircons	Ravikant <i>et al.</i> (2009)
Chang La	64.0 ± 0.7			(enclaves in Karakoram Batholith)	103 ± 1.0		
Confluence Hanle and Indus Rivers	67.9 ± 1.3				100.6 ± 1.5		
Daah-Hanu region (~30 km NW Leh)	45.3 ± 0.6	U-Pb TIMS on zircons	Upadhyay (2008)				
Chang La	52.5 ± 0.5						
	53.4 ± 1.8						
	57.6 ± 1.4						
Hundar (near Shyok River)	66.6 ± 1						

zone of Bt-granodiorites that forms a border facies. Samples of the main facies and border facies were chosen for U-Pb dating (see below). A penetrative foliation trending 120° - 150° is defined by aligned biotite, hornblende and titanite, and C'-C-S fabrics indicate dextral shear. In the Tangtse gorge area, in the Pangong Range SW of Muglib and in some outcrops in the Darbuk-Shyok gorge (Fig. 1c), the Muglib Batholith is migmatized, giving rise to leucosome networks, leucogranite injection complexes and leucogranite plutons (Reichardt *et al.*, 2010; Weinberg *et al.*, 2009; Weinberg & Searle, 1998).

Crystallization ages of the Muglib Batholith span an age range between ~ 70 Ma (U-Pb zircon age, Reichardt *et al.*, 2010) and ~ 115 Ma (Rb-Sr age, Ravikant 2006; see also Table 1). Based on age similarities and mapping, it was inferred that the Tirit Batholith forms a semi-continuous body with the Muglib Batholith (Reichardt *et al.*, 2010). The Tirit batholith has also been related to the ~ 74 Ma Rutok granite in Tibet (Srimal, 1986; Ravikant, 2006). In the following section we will compare both rock suites by using geochemical analysis, geochronology and isotope systematics from our own data as well as selected published data.

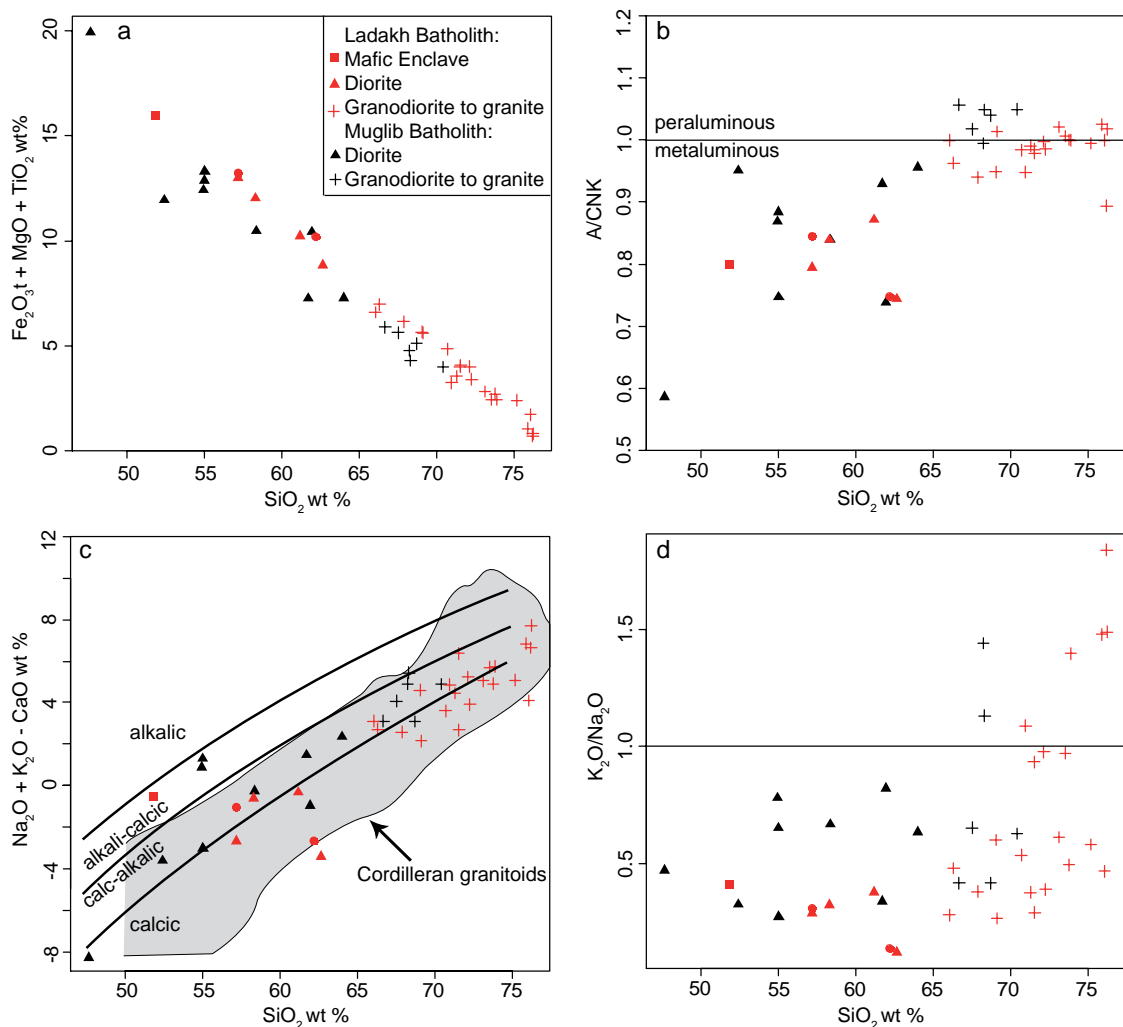


Fig. 4: Major element concentrations of Ladakh Batholith and Muglib Batholith. Symbols are identical for a, b, c and d. Explanations in text.

3. Major and Trace Element Geochemistry

A suite of samples from both batholiths were analysed, including 28 samples from the Ladakh Batholith, 15 of which from the Gyamsa Pluton, 11 from the Leh Pluton and two mafic

Table 2. Representative geochemical analyses

Sample	Muglib Batholith										Ladakh Batholith									
Major Elements wt%	TNG62a	TNG131a	TNG169a	TNG205a	TNG205b	TNG205c	TNG98a2	AGH5	96-03	96-06	96-15	96-21	96-29	96-38A	96-38B	96-41	96-42	96-52	96-53	95-55
SiO ₂	55	67.5	62	54.9	55	47.6	66.7	52.4	70.95	61.16	51.87	57.15	75.17	75.88	66.04	66.3	76.2	57.17	73.11	76.19
TiO ₂	1.29	0.56	0.7	1.37	1.16	1.1	0.68	1.1	0.25	0.76	1.1	0.93	0.27	0.11	0.62	0.56	0.09	0.88	0.27	0.07
Al ₂ O ₃	18.2	16.3	14.3	17.6	17.1	15.5	16.8	19.8	14.34	16.8	18.3	17.11	13.23	13.11	16.7	16.34	13.54	17.15	13.74	12.89
Fe ₂ O ₃	7.75	3.49	5.18	8.04	7.51	10.3	3.58	7.91	2.31	6.81	10.2	8.42	1.74	0.82	4.52	4.68	0.66	8.85	2.06	0.55
MnO	0.15	0.09	0.15	0.13	0.13	0.18	0.09	0.15	0.05	0.13	0.3	0.18	0.05	0.03	0.14	0.14	0.03	0.18	0.06	0.02
MgO	3.83	1.57	4.55	3.01	4.64	8.58	1.63	2.93	0.68	2.66	4.66	3.66	0.38	0.12	1.45	1.73	0.05	3.5	0.49	0.08
CaO	5.79	3.16	6.46	5.9	8.22	11.8	3.44	7.89	2.7	5.97	7.18	7.68	1.84	1.23	3.59	3.97	1.03	6.56	1.92	1.91
Na ₂ O	4.28	4.37	3.01	3.81	4.08	2.36	4.62	3.22	3.62	4.1	4.69	3.87	4.38	3.25	5.23	4.51	3.51	4.23	4.32	3.01
K ₂ O	2.79	2.85	2.47	2.97	1.11	1.11	1.92	1.04	3.94	1.54	1.93	1.11	2.54	4.81	1.46	2.16	5.23	1.3	2.64	5.54
P ₂ O ₅	0.51	0.22	0.14	0.5	0.33	0.15	0.29	0.27	0.04	0.17	0.25	0.09	0.04	0	0.18	0.14	-0.01	0.18	0.04	0.02
LOI	1.00	0.50	0.93	0.82	0.84	1.35	0.65	2.92												
Total	100.59	100.62	99.83	99.00	100.08	100.12	100.37	99.6	98.88	100.10	100.48	100.20	99.64	99.36	99.93	100.53	100.33	100	98.65	99.16
A/CNK	0.88	1.02	0.74	0.87	0.75	0.59	1.06	0.95	0.95	0.87	0.80	0.79	0.99	1.03	1.00	0.96	1.02	0.85	1.02	0.89
Mq/(Fe+Mg)	0.49	0.47	0.64	0.43	0.55	0.62	0.47	0.42	0.37	0.44	0.48	0.46	0.30	0.22	0.39	0.42	0.13	0.44	0.32	0.22
Trace Elements ppm																				
Sc	15.70	8.48	19.86	12.69	16.67	30.73	5.58	17.47	4.2	15.9	31.8	28.8	4.3	0.8	5.2	19.4	2.3	27	6.2	2.1
Ti	7787.69	3953.19	3833.40	7373.16	6504.50	6513.84	4066.77	5423.67	1389	4353	6465	5399	1558	383	3297	3439	344	5329	1475	321
V	151.86	91.99	103.66	123.54	145.92	197.62	61.85	193.01	41	155	270	235	17	7	53	72	5	170	24	6.7
Cr	49.98	71.26	74.77	12.68	15.23	26.71	13.13	20.93	4.1	11.1	43.3	55	-0.2	4.8	5.1	6.8	2.7	6.5	3.1	1
Mn	1068.00	892.94	1053.38	859.20	862.36	1106.96	556.83	910.08	n.a.	n.a.	n.a.	n.a.	n.a.	n.a.	n.a.	n.a.	n.a.	n.a.	n.a.	n.a.
Co	20.56	9.12	45.13	27.64	28.61	34.68	9.69	18.52	2.5	16.5	24.5	22.2	0	1	5.2	9	0.6	24.4	2.7	46
Ni	40.61	65.56	53.55	16.72	26.31	30.85	15.81	7.19	2.5	7.2	15.2	9.6	1.4	0.9	3.3	5.4	1.5	9.1	1.9	3
Cu	62.85	12.99	21.45	47.67	84.12	52.58	6.27	23.21	3.5	25.2	75.7	38.3	4.1	4.1	3.6	2.4	3.5	25.4	2.5	1
Zn	111.94	81.83	62.57	86.66	76.38	79.35	63.22	7.33	25.9	68.7	119.6	110.2	25.5	14.3	67.7	61.9	12.1	76.2	39.4	8
Ga	22.06	13.31	12.58	14.41	9.73	8.95	19.16	17.58	13.3	17.9	20.7	17.4	11.9	8.9	20.4	15.6	11.4	15	11.8	14
Rb	122.31	206.37	49.42	124.10	25.63	22.95	116.94	26.52	90	51	70.3	34.5	48.6	85.2	79	66.3	122.8	30.4	78.3	159
Sr	541.97	438.70	547.63	568.57	550.93	418.10	543.01	497.28	226	440	388	321	219	119	188	271	70	350	163	95
Y	27.30	20.11	18.77	24.30	20.46	20.83	15.8	20.2	10.3	21.82	50.66	25.66	7.82	3.57	26.94	40.5	16.4	31.3	12.8	7
Zr	166.82	4.29	11.54	58.57	60.52	71.17	10.92	7.95	88	155	77	42	168	37	216	138	40	160	148	53
Nb	27.40	21.36	18.25	25.52	15.09	8.85	18	5.74	3.6	4.3	9.3	4.4	3.4	1.3	8.4	8.4	5.8	4.9	5.1	3
Ba	334.05	286.12	586.51	540.12	118.69	118.18	279.61	154.01	414	281	416	173	1088	420	72	133	147	243	537	243
La	55.98	75.25	7.05	58.46	26.21	14.25	55.87	12.48	10.6	15.3	25	12.2	32.9	12.4	22.7	16.6	15.2	15.2	21.4	16
Ce	111.68	103.75	20.43	107.82	52.17	32.18	99.52	27.59	23.8	33.7	58.1	26.4	62.3	25.5	51.1	35	34.1	31.7	41.1	18.5
Pr	12.29	9.47	2.86	10.58	5.84	3.93	10.54	3.34	2.59	4.01	8.04	3.32	5.93	2.4	5.71	4.58	3.42	4.23	4.07	1.9
Nd	42.77	29.82	13.46	39.55	24.30	18.48	35.28	15.39	9.64	17.01	36.81	14.75	20.29	6.67	21.9	20.21	10.97	19.88	14.19	6.6
Sm	7.57	5.12	3.18	6.90	4.95	4.43	5.48	3.63	1.8	3.72	8.77	3.69	2.79	1.03	4.88	4.95	2.24	4.83	2.52	1.3
Eu	2.03	1.08	1.03	1.67	1.36	1.24	1.32	1.19	0.49	0.99	1.44	1.16	0.98	0.52	0.73	0.75	0.54	1.26	0.58	0.36
Gd	6.35	4.14	2.89	5.76	4.03	3.63	4.27	3.5	1.55	3.66	8.42	3.88	1.84	0.93	4.77	5.14	1.85	4.94	2.25	1.09
Tb	0.91	0.62	0.50	0.86	0.67	0.63	0.54	0.59	0.24	0.58	1.36	0.68	0.23	0.15	0.74	0.94	0.34	0.79	0.34	0.161
Dy	5.06	3.41	3.02	4.53	3.76	3.67	2.8	3.57	1.47	3.72	8.62	4.21	1.21	0.66	4.23	6.19	2.2	5.15	2.12	1.07
Ho	1.00	0.71	0.61	0.84	0.74	0.75	0.51	0.72	0.33	0.73	1.72	0.89	0.26	0.15	0.83	1.28	0.6	1.08	0.43	0.23
Er	2.69	1.80	1.76	2.32	1.96	1.95	1.36	2.02	0.95	2.1	4.96	2.55	0.74	0.41	2.3	3.76	1.83	3.2	1.28	0.76
Tm	0.40	0.24	0.28	0.34	0.30	0.30	0.19	0.29	0.17	0.33	0.75	0.39	0.12	0.09	0.36	0.58	0.33	0.5	0.2	0.128
Yb	2.55	1.62	1.90	2.06	1.88	1.87	1.15	1.85	1.17	2.24	5.05	2.67	0.88	0.7	2.45	4.02	2.73	3.43	1.52	0.939
Lu	0.37	0.25	0.31	0.32	0.30	0.28	0.16	0.28	0.19	0.35	0.74	0.43	0.15	0.2	0.42	0.6	0.55	0.53	0.26	0.176
Pb	11.55	42.98	12.42	12.16	11.45	5.27	10.86	5	12.7	9.1	7.4	8.2	12.9	18.2	11.7	9.5	23.2	5.9	17.3	39
Th	10.93	17.67	1.14	11.21	4.15	1.74	10.6	1.84	5.62	5.03	2.43	7.07	10.28	12.51	4.73	9.06	18.7	2.84	13.84	21.5
U	2.84	3.84	2.11	1.08	1.26	1.20	2.32	0.3	1.06	1.02	1.08	1.64	0.4	2.34	0.92	1.74	6.72	0.52	1.04	2.9
La _w /Sm _w	4.65	9.25	1.40	5.33	3.33	2.02	6.41	2.16	3.70	2.59	1.79	2.08	7.42	7.57	2.93	2.11	4.27	1.98	5.34	4.37
La _w /Yb _w	14.82	31.28	2.50	19.15	9.39	5.13	32.75	4.55	6.11	4.60	3.34	3.08	25.21	11.94	6.25	2.78	3.75	2.99	9.49	11.27
Sum REE	251.65	237.28	59.26	242.01	128.47	87.61	218.99	76.44	54.99	88.44	169.78	77.22	130.62	51.81	123.12	104.60	76.90	96.72	92.26	60.39

For analysis details of Muglib Batholith samples see Chapter II, section 3. For full dataset of Muglib Batholith see Appendix A. For full dataset of Ladakh Batholith see electronic Appendix 1 on data CD.

granitoid dykes that could not be ascribed with certainty to either pluton. Compositionally, the Leh and Gyamsa Plutons overlap in all analysed elements, and we thus refer to both sample suites as Ladakh Batholith for simplicity. These are compared to analyses of 16 samples from plutons of the Muglib Batholith (Table 2).

As is characteristic for magmatic differentiation series, SiO_2 contents are negatively coupled to Fe_2O_3 , MgO and TiO_2 contents (Fig. 4a), and correlate with decreasing modal amounts of ferromagnesian and titaniferous phases in hand-specimen. Our sample series of the Ladakh Batholith shows SiO_2 contents ranging between 51.9 wt % for a microdiorite enclave from the Leh Pluton, and 76.2 wt % for a leucogranite from the Gyamsa Pluton. The Muglib rocks have SiO_2 contents between 47.6 wt % for diorites and 70.4 wt % for Bt-granodiorites. For both batholiths most samples are metaluminous, only a few Bt-granites are slightly peraluminous (Fig. 4b; $\text{A}/\text{CNK} = 0.74$ to 1.03). In an alkali-lime vs. SiO_2 diagram (Fig. 4c), most samples from both batholiths follow calc-alkaline to calcic trends and mostly fall into the field of cordilleran granitoids (Frost *et al.*, 2001). Generally granitoids from both batholiths show $\text{Na}_2\text{O} > \text{K}_2\text{O}$ (Fig. 4d), indicating preponderance of plagioclase over K-feldspar. However, the most evolved (SiO_2 -rich) granites of the Ladakh Batholith show $\text{Na}_2\text{O} < \text{K}_2\text{O}$, suggesting K-feldspar accumulation in those rocks. This is supported by high Ba concentrations for the K_2O -enriched granitoids.

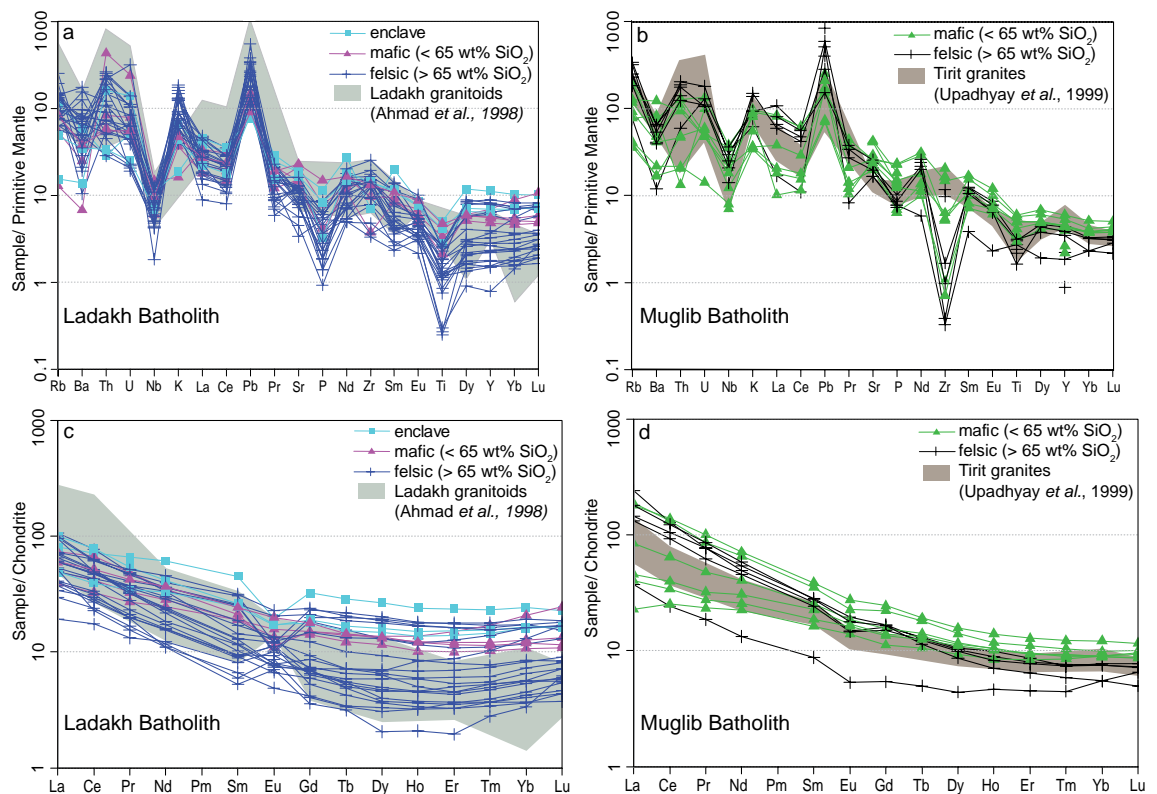


Fig. 5: Multi element diagrams of Ladakh Batholith (a) and Muglib Batholith (b). Normalized to primitive mantle after Sun & McDonough (1989). (c), (d) REE patterns of Ladakh Batholith and Muglib Batholith, respectively. Fields added for comparison with data from previous studies of the Ladakh Batholith (Ahmad *et al.*, 1998) in (c), and Tirit granite (Upadhyay *et al.*, 1999) in (d). Normalized to chondrite after Boynton (1984).

Multi trace element patterns show a general overlap of Ladakh and Muglib Batholith samples (Fig. 5a, b). The least differentiated patterns are shown for mafic enclaves. Compared to primitive mantle values, the rocks from both batholiths show LILE enrichments and HFSE

depletions typical for island arc magmas. Felsic granitoids of the Ladakh Batholith show the most evolved trace element patterns with strong depletions in Nb, P and Ti. The most evolved granites of the Muglib Batholith show the strongest Zr depletions. In contrast to the Ladakh rocks, these low values indicate zircon fractionation or its retainment in the source.

REE patterns from both calc-alkaline suites indicate fractionation trends. For the Ladakh Batholith samples, the least evolved, mafic rocks show slight LREE enrichment over HREE, with an overall almost straight REE shape (Fig. 5c). Fractionation trends are indicated for the diorites of the Muglib Batholith, however with more strongly curved REE shapes compared to the Ladakh Batholith samples, suggesting that these particular rocks crystallized from slightly more evolved magmas. Some of the mafic diorites show negative Eu anomalies, indicative of plagioclase removal from the magma. The more evolved granites of the Ladakh Batholith show complementary positive Eu anomalies, and feldspar accumulation in these rocks is confirmed by their petrography. Concave upward patterns (U-shapes) from MREE to HREE are strongly developed in evolved granodiorites and granites from the Ladakh Batholith, but only in one sample of a Bt-granodiorite from the Muglib Batholith. HREE enrichments are commonly due to the presence of either garnet which has high partition coefficients for HREE (e.g. Gromet & Silver, 1983) or hornblende which fractionates HREE over LREE, but with a maximum around MREE (Arth & Barker, 1976). However, garnet was not observed in any of our samples, whereas hornblende cumulates are common in the Ladakh Batholith (Weinberg & Dunlap, 2000) and the curved REE shapes may record hornblende removal from the felsic magmas (Arth & Barker, 1976). U-shaped MREE to HREE patterns coupled with decreasing hornblende contents suggests that these patterns are the result of hornblende fractionation. Similar trends have also been observed for volcanic rocks of the Ladakh arc (Dietrich *et al.*, 1983). Fractionation trends are also reflected by an increase in La_n/Sm_n values generally towards higher silica contents (Fig. 6a, b). This trend, however, is less obvious when comparing LREE and HREE, expressed as La_n/Yb_n .

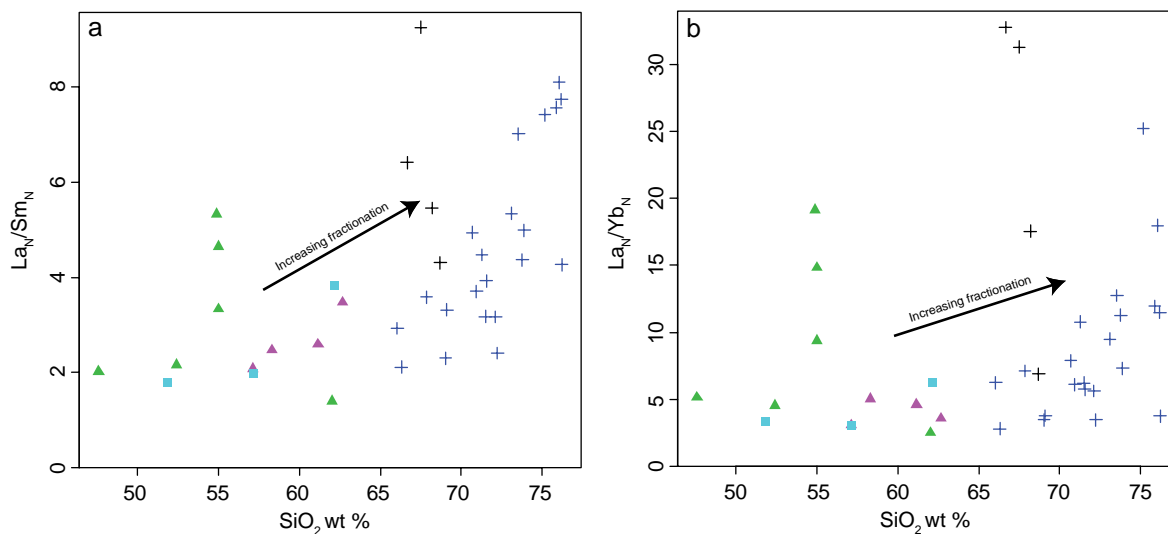


Fig. 6: (a) La_n/Sm_n vs. SiO_2 contents showing fractionation trends. (b) La_n/Yb_n vs. SiO_2 .

4. Geochronology

The crystallization ages of the Ladakh Batholith are broadly contemporaneous with

Table 3. Rb-Sr and Sm-Nd isotopes

SAMPLE	Batholith	Rock type	Rb ppm	Sr ppm	⁸⁷ Rb/ ⁸⁶ Sr	⁸⁷ Sr/ ⁸⁶ Sr	Sm ppm	Nd ppm	¹⁴⁷ Sm/ ¹⁴⁴ Nd	¹⁴³ Nd/ ¹⁴⁴ Nd	Nd now	⁸⁷ Sr/ ⁸⁶ Sr	¹⁴³ Nd/ ¹⁴⁴ Nd	Nd _i
TNG 62a	Muglib	Migmatitic granodiorite	122.37	538.39	0.658	0.70783	7.30	43.29	0.1019	0.51266	0.37063	0.7072	0.51261	1.2
TNG98a	Muglib	Hbl-Bt-granodiorite	116.76	573.49	0.589	0.70562	5.48	35.28	0.0939	0.51267	0.52669	0.7050	0.51262	1.4
TNG108c	Muglib	Amphibolite	4.04	125.56	0.093	0.70477	2.40	6.92	0.2098	0.51309	8.81714	0.7047	0.51299	8.7
TNG128	Muglib	Hbl-Bt-granodiorite	120.43	575.26	0.605	0.70523	5.41	32.32	0.1011	0.51266	0.42915	0.7046	0.51261	1.3
TNG169a	Muglib	Migmatitic diorite	49.42	547.63	0.261	0.70528	3.18	13.46	0.1428	0.51275	2.17066	0.7050	0.51268	2.7
AGH5	Muglib	Gabbro	26.52	497.28	0.154	0.70421	3.63	15.39	0.1427	0.51276	2.28231	0.7041	0.51269	2.8
LEH29	Ladakh	Leh granite	49.00	219.00	0.647	0.70465	1.87	9.81	0.1152	0.51274	1.93119	0.7040	0.51268	2.7
LEH55	Ladakh	Leh leucogranite	159.00	95.00	4.843	0.70782	1.1	5.86	0.1131	0.51262	-0.29260	0.7030	0.51257	0.5
LEH38a	Ladakh	Gyamsa Bt-granite	85.00	119.00	2.066	0.70555	1.69	11.51	0.0888	0.51270	1.26795	0.7035	0.51266	2.2
LEH38b	Ladakh	Gyamsa Bt-granodiorite	79.00	188.00	1.216	0.70545	5.3	22.64	0.1416	0.51272	1.54105	0.7042	0.51265	2.0
LEH40	Ladakh	Gyamsa diorite gneiss	not available		0.339	0.70485	3.13	14.21	0.1331	0.51267	0.66324	0.7045	0.51261	1.2
LEH52	Ladakh	Gyamsa diorite gneiss	30.40	350.00	0.251	0.70485	8.49	36.85	0.1392	0.51270	1.13140	0.7046	0.51263	1.6

Initial values calculated to 70 Ma

For analysis details see Chapter II, section 3.

crystallization ages obtained for samples of the Muglib Batholith and other calc-alkaline granitoids from within the PMC (Table 1). A migmatitic orthogneiss in the Tangtse gorge was dated at 106.3 ± 2.3 Ma using U-Pb SHRIMP on zircons (Searle *et al.*, 1998). Hbl-Bt-granodiorite samples from the Tangtse gorge and from the vicinity of Muglib (Fig. 2b), yielded ages of 115 ± 18 Ma and 72 ± 8 Ma, respectively, using Rb-Sr isotope systematics on whole rocks (Ravikant, 2006). U-Pb dating of zircons by Ravikant *et al.* (2009), yielded crystallization ages of 72.8 ± 0.9 Ma and 72.6 ± 1.4 Ma for two samples of Hbl-Bt-granodiorite from the Tangtse gorge, and 63.0 ± 1.0 and 56.0 ± 0.5 for two Hbl-Bt-granodiorites from the Muglib area (Fig. 3b). Further, three tonalitic diorite and tonalite enclaves inside the Karakoram Batholith on the NE side of the KSZ in the Nubra Valley have crystallization ages of ~ 103 Ma (Ravikant *et al.*, 2009). Jain & Singh (2008) dated a mylonitized granitoid from the Tangtse Shear Zone and a Bt-granite from the Tangtse gorge, and found U-Pb crystallization ages of zircon of 75.7 ± 1.0 Ma and 60.4 ± 1.0 Ma, respectively.

We dated two samples of Muglib granitoids, a Bt-granodiorite from the NE-end of the Tangtse gorge and a melanosome in Hbl-Bt-granodiorite from the Pangong Range ~ 4 km SE from the previous sample (sample TNG131a, coordinates $34^{\circ}03'38.8''$ N, $78^{\circ}13'52.1''$ E; sample TNG62a, coordinates $34^{\circ}02'16.8''$ N, $78^{\circ}14'57.7''$ E, respectively). U-Pb SHRIMP analyses of zircons from both samples yielded ages of 70.5 ± 0.6 Ma and 71.4 ± 0.6 Ma, respectively, and were interpreted as the crystallization ages of related magmatic pulses (Reichardt *et al.*, 2010). For analysis details see Table 2 and 3 in Chapter II. Analyses of titanites from the Bt-granodiorite sample yielded two age populations, one that has a mean age of 65 ± 3 Ma, and a younger grouping between ~ 11 and 21 Ma. The older age group is significantly younger than the calculated zircon age and relates to a cooling event or to an early metamorphic event, or is spurious. The younger age group was interpreted to reflect the age of migmatization, relating to leucogranite intrusions in the PMC (Reichardt *et al.*, 2010, Chapter II).

These ages are contemporaneous with crystallization ages obtained from the Tirit Batholith in the Nubra and Shyok River confluence area (Fig. 2). For these calc-alkaline granitoids, two ages are available, 68.0 ± 1.0 Ma (Weinberg *et al.*, 2000) and 71.4 ± 0.36 Ma (Upadhyay, 2008). In summary, the calc-alkaline plutons in the PMC have crystallization ages that centre around 70 Ma, overlapping with those of plutons of the Ladakh Batholith and the Tirit Batholith, and also here, no inherited zircons have been found.

5. Rb-Sr and Sm-Nd isotope systematics

Isotope systematics helps to trace sources of magmatic rocks and to establish relationships or discern between individual plutons or magmatic provinces. We obtained Rb-Sr and Sm-Nd isotope data from six samples of the Ladakh Batholith from the Leh region and five samples from granitoids from the Muglib Batholith, four of which from within the PMC, and one from a gabbro on the NW tip of the Pangong Range close to Agham (Fig. 3a). We also analysed an amphibolite gneiss sample from the Darbuk-Shyok gorge, interpreted to be of volcanic origin (Reichardt *et al.*, 2010). Initial isotope ratios were calculated for 70 Ma, based on the probable crystallization ages of the granitoids (see above).

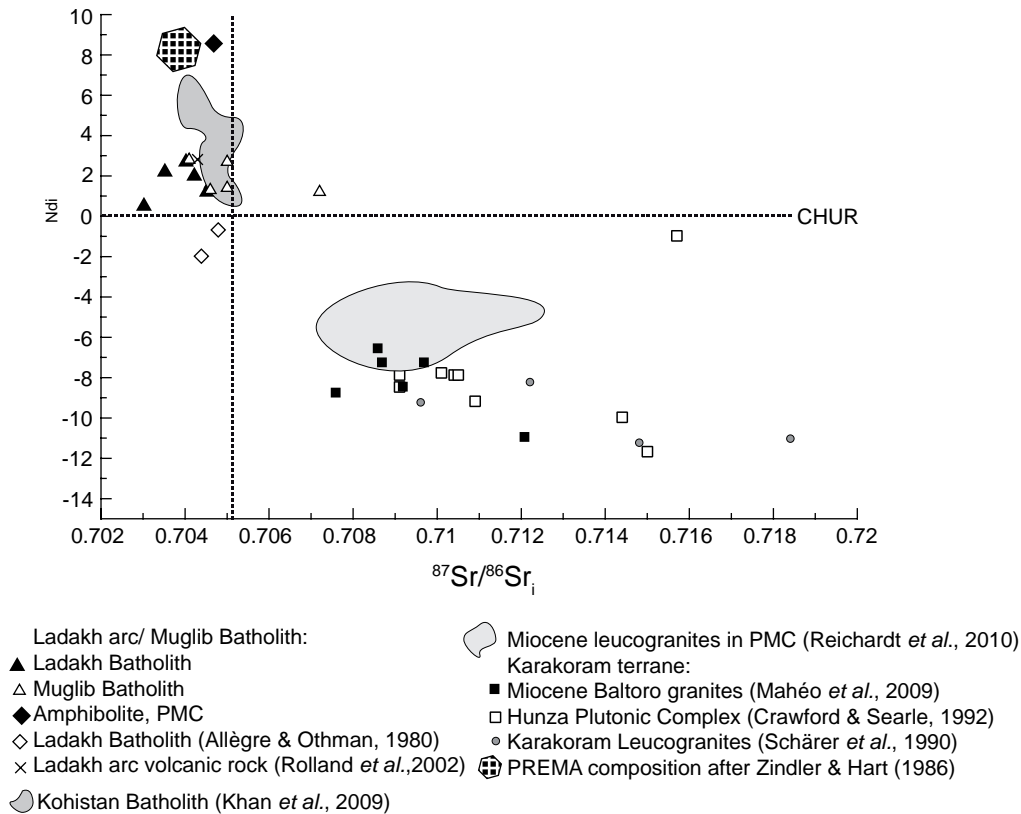


Fig. 7: $^{87}\text{Sr}/^{86}\text{Sr}_i$ vs. ϵ_{Nd_i} diagram, showing overlap between Ladakh and Muglib Batholiths. Note also overlap with the field for Kohistan arc rocks. Miocene leucogranites of the PMC and Karakoram terrane granitoids show significantly stronger crustal influences. Initial values calculated for 70 Ma except for Miocene granitoids, which were calculated for 20 Ma.

All samples from the Ladakh Batholith, taken from the Gyamsa and Leh Pluton show little variation in isotope ratios. Initial $^{87}\text{Sr}/^{86}\text{Sr}$ values range between 0.7030 and 0.7046, and initial ϵ_{Nd} values range between 0.5 and 2.7 (Fig. 7; Table 3). Based on field relations, a migmatitic diorite gneiss sample from the Gyamsa Pluton is interpreted to represent a restitic

source rock of the Gyamsa granitoids. Interestingly, it has similar isotope values ($^{87}\text{Sr}/^{86}\text{Sr}_i = 0.7046$, $\epsilon_{\text{Nd}} = 1.6$) as all other Gyamsa and Leh Pluton samples, supporting the hypothesis of remelting of older calc-alkaline granitoids (Weinberg & Dunlap, 2000).

The values above compare well to those of the samples from the Muglib Batholith that show initial $^{87}\text{Sr}/^{86}\text{Sr}$ ranging between 0.7041 and 0.7050, except for one value at 0.7072, and initial ϵ_{Nd} between 1.2 and 2.7. Thus, these samples are only slightly more radiogenic with regards to $^{87}\text{Sr}/^{86}\text{Sr}_i$, and have the same range of ϵ_{Nd} values (Fig. 7, Table 3) as rocks from the Ladakh Batholith. An anomalous value was found for the amphibolite gneiss from the PMC with initial $^{87}\text{Sr}/^{86}\text{Sr} = 0.7047$ and initial $\epsilon_{\text{Nd}} = 8.7$. These values are comparable to the present day prevalent mantle (Zindler & Hart, 1986). Volcanic rocks with similar isotopic compositions have been reported from the Ladakh arc in Western Ladakh, Pakistan (Rolland *et al.*, 2002). The isotope signatures of the Ladakh and Muglib Batholiths have been interpreted as indicative for mantle origin, with slight crustal influence (Reichardt *et al.*, 2010; Weinberg & Dunlap, 2000).

6. Discussion

6.1 Ladakh and Muglib Batholith similarities

In general, a suture zone separates terranes of entirely different origins and histories. Our results show that despite some differences in trace element chemistry that suggest slightly different crystallization histories, the Ladakh and Muglib Batholith form typical calc-alkaline differentiation series. The Muglib Batholith is also geochemically comparable to the calc-alkaline Tirit Batholith (Fig. 5b, d).

Further SE of our study area, in the Pangong Range and to the south of Pangong Lake, Thakur & Misra (1984) mapped a granitoid complex, referred to as the Chusul granitoid. The Chusul granitoids correspond to the Kakstet and Rutok granites in the map of Srimal (1986), and were together with the Tirit Batholith in the Shyok and Nubra River confluence region, interpreted to be related to Karakoram (terrane) granites. Upadhyay *et al.* (1999) on the other hand grouped the Tirit Batholiths in the Nubra and Shyok river confluence area to the Ladakh Batholith (Upadhyay *et al.*, 1999). Our mapping in the PMC and in the Nubra and Shyok Rivers confluence area suggests that a series of calc-alkaline granitoids, including the Tirit Batholith, all similar to the Ladakh Batholith, extends for at least 85 km along strike of the KSZ. We further speculate that these Ladakh-Muglib type granitoids link to the Rutok granite (Ravikant, 2006).

Based on U-Pb ages of zircons from several plutons in the Leh area, Chang-La and Shyok region, Upadhyay *et al.* (2008) suggested the Ladakh Batholith grew in four major pulses, between ~45 and ~67 Ma. These crystallization ages essentially correspond to the U-Pb zircon ages between ~50 and ~70 Ma from the Leh area (Weinberg & Dunlap, 2000). Here, batholith growth by addition of magma pulses over several million years was also shown by intrusion relationships between the dated (older) Gyamsa pluton and the (younger) Leh pluton. Crystallization ages of the Muglib Batholith and Tirit Batholith centre at ~70 Ma and are thus slightly older than most of the dated Ladakh Batholith samples (see also Table

1). Importantly, all dated Ladakh and Muglib granitoids lack inherited zircons that would indicate recycling of older crust, thus supporting magma derivation from juvenile sources.

Most significantly, the two batholiths have similar initial $^{87}\text{Sr}/^{86}\text{Sr}$ and ϵ_{Nd} values that indicate only small involvement of crustal material, supporting a similar source for both (Fig. 7; Reichardt *et al.*, 2010). Further, Hf isotope analysis of zircons of four calc-alkaline Hbl-Bt-granodiorites from the Muglib Batholith ($\epsilon_{\text{Hf}} = 5.4 \pm 0.3$ to 6.8 ± 0.7), yielded values similar to those of samples from the Ladakh Batholith that were collected south of the Tangtse Shear Zone ($\epsilon_{\text{Hf}} = 10.3 \pm 0.9$ to 6.4 ± 0.5). These values indicate a juvenile source for both magmatic rock sequences (Ravikant *et al.*, 2009), and support a genetic link across the shear zone. These isotope values are also consistent with data from the Kohistan and Gangdese Batholiths (Ji *et al.*, 2009). We therefore conclude based on: (a) the lack of older inherited zircons of these contemporaneous magmatic bodies, (b) the similarities in Sr and Nd isotopic composition indicative of modest input from continental crust, and (c) the values of Hf isotopes in zircons indicative of a juvenile source for both, that the Ladakh and Muglib Batholith formed in the same island arc setting. This conclusion requires broader investigations and comparison with other batholiths in the broader region.

6.2 Comparison to other batholiths

Younger, Miocene leucogranites in the PMC have a distinct isotopic signature ($^{87}\text{Sr}/^{86}\text{Sr}_i = 0.7086$ to 0.7121 , $\epsilon_{\text{Nd}} = -3.6$ to -6.2 ; Reichardt *et al.*, 2010) from the Ladakh and Muglib Batholiths (Fig. 7). These Miocene rocks compare to leucogranites of similar age from the Karakoram Batholith ($^{87}\text{Sr}/^{86}\text{Sr}_i = 0.7076$ to 0.7092 and $\epsilon_{\text{Nd}} = -5.4$ to -7.1 ; Reichardt *et al.*, 2010) including rocks from the Baltoro Batholith in Pakistan. It has been interpreted that the leucogranites in the PMC are the product of partial melting of the Muglib Batholith and a meta-sedimentary sequence, and that hybridized magma stemming from these sources was feeding into the Karakoram Batholith (Reichardt *et al.*, 2010, Chapter II). A different conclusion was reached by Ravikant *et al.*, (2009), who explained the stronger crustal influence in the (ϵ_{Hf}) isotopic signature of the Miocene leucogranites to be indicative of continued magmatism in the PMC after, or shortly before accretion of the Ladakh arc to Eurasia.

Cretaceous granitoids of the Karakoram Terrane (Hunza Plutonic Complex) have an isotopic signature distinct from the Ladakh and Muglib granitoids. Higher $^{87}\text{Sr}/^{86}\text{Sr}_i$ and lower ϵ_{Nd} values for these granitoids (Fig. 7) indicate a stronger crustal component in agreement with Andean-style intrusion at the Eurasian margin (Crawford & Searle, 1992; Mahéo *et al.*, 2009; Mahéo *et al.*, 2002). In contrast, our isotope data compares well to Rb-Sr isotope data from the Ladakh Batholith and the Kohistan Batholith that is available from previous studies (Fig. 8). Unfortunately, no Sm-Nd isotope data is available from the Kohistan Batholith, which forms the westernmost part of the Trans-Himalayan plutonic belt in Pakistan (Pettersson & Windley, 1985). All samples in Fig. 8 share essentially the same isotope signature. Pettersson & Windley (1985) interpreted the isotope signature of the Kohistan Batholith ($^{87}\text{Sr}/^{86}\text{Sr} = 0.7039$ to 0.7052) as indicative for upper mantle sources or crustal sources with short residence time in the crust.

Sm-Nd isotope data of two analyses from the Ladakh Batholith, a granodiorite and a

diorite (Allègre & Othman, 1980), were interpreted as indicative for a mantle source with near chondritic values (Weinberg & Dunlap, 2000). However, when recalculated to 70 Ma for comparison with our data, the ϵ_{Nd} values are significantly lower ($\epsilon_{\text{Nd}} = -0.7$ and -2.0), suggesting some crustal component in the source. Analysis of a sample from the Ladakh Batholith between Chang La and the Tangtse Shear Zone (Fig. 1), yielded ϵ_{Nd} values lower than all other Ladakh Batholith samples ($\epsilon_{\text{Nd}} = -7.5$), and was interpreted by Rolland *et al.* (2002) as indication of some crustal influence during magma ascent at a time when the Ladakh island arc was already close to the Karakoram (= Eurasian) margin. Concurrently, for the Kohistan Batholith in Pakistan, Heuberg *et al.* (2007) demonstrated increasing crustal contamination in the Hf isotope signature in successively younger intrusions, thus indicating the development from island arc to continental arc. In contrast, our isotope data from the Leh Pluton (Table 3), one of the youngest Ladakh arc plutons (Weinberg & Dunlap, 2000) shows no significant differences in Sr or Nd isotopes to the older plutons of the batholith.

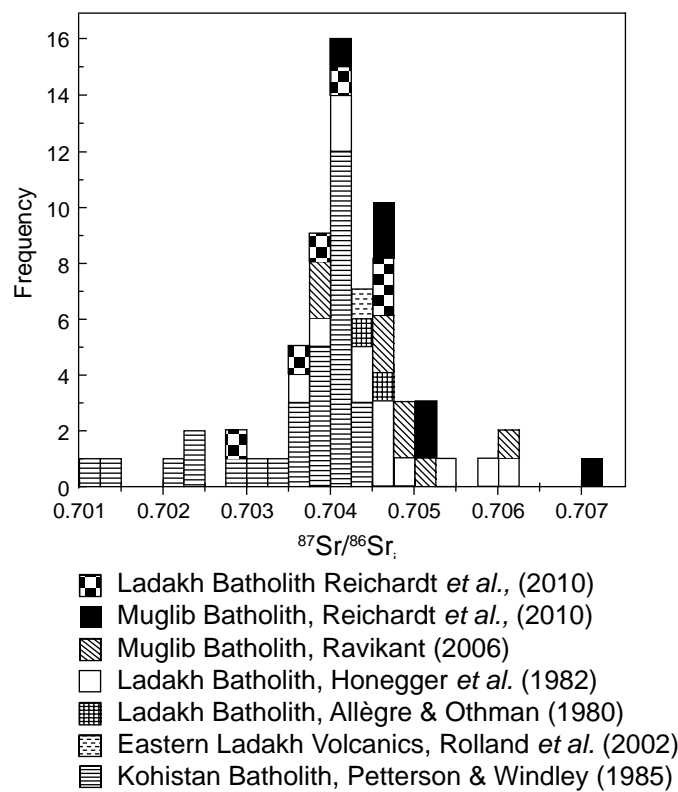


Fig. 8: Histogram of $^{87}\text{Sr}/^{86}\text{Sr}_i$ for Ladakh Batholith, Kohistan Batholith and Muglib Batholith. Initial values calculated for 70 Ma.

In summary, our data of Ladakh and Muglib Batholiths show similarities to other published data from the Ladakh Batholith and the Kohistan Batholith, that demonstrate island arc characteristics, but are distinct from granitoids that intruded the Eurasian margin with a continental affinity.

6.3 Position of the Shyok Suture Zone

The SSZ has been correlated with the Shiquanhe Suture Zone (Matte, 1996), and with the Bangong Suture Zone (Robinson, 2009), and it has been interpreted that they are now displaced by dextral movement of the KSZ. In contrast, Jain & Singh (2008), argued for continuity of the SSZ from the Nubra Valley (Fig. 2), further SE parallel to the Tangtse Shear Zone (Fig. 3b), to link continuously to the Shiquanhe Suture. Parallelism of the SSZ to the

Tangtse Shear Zone in the region was also proposed by Ehiro *et al.*, (2007), who interpreted a sedimentary sequence SW of the Tangtse Shear Zone as indication for continental basement of the Ladakh island arc, based on occurrences of Jurassic ammonoids. These sediments would then link to comparable Jurassic sediments in the Shiquanhe area (Matte *et al.*, 1996).

Ultra-mafic and mafic rocks in the Saltoro Range (Fig. 2) are interpreted as indication for obducted oceanic seafloor (e.g. Ravikant 2006, Ravikant *et al.*, 2009, Rai, 1982). These rocks were grouped as an ophiolite sequence that marks the position of the suture between the Ladakh and Karakoram terranes. In this interpretation, the SSZ runs either along the Shyok Valley or somewhere in the Saltoro Range (Fig. 2). In the map of Uphadhyay *et al.* (1999), the suture is reworked by the Karakoram Shear Zone and now runs parallel to it along the Nubra Valley, as evidenced by fragments of disconnected mafic rocks (ophiolites?) in sheared sedimentary rocks. However, some of these mafic rocks described in the literature as ophiolites were found to be more likely related to calc-alkaline differentiation series, and possibly related to the Tirit Batholith (Weinberg *et al.*, 2000). These are most likely (Fig. 2). Mylonitic rocks that crop out in a thin band along the KSZ on the NE side of the Nubra Valley, contain a variety of sedimentary and volcanic rocks as well as blocks of mafic rocks, all metamorphosed under greenschist facies. Because of the difficulty of unambiguous identification of the sheared mafic fragments, we feel that more evidence needs to be gathered before ascribing these rocks to an ophiolite sequence.

7. Conclusions

The position of the Shyok Suture Zone in Ladakh is defined by disconnected occurrences of sheared mafic/ ultramafic rocks between two calc-alkaline batholiths. We tested if the Ladakh Batholith on the southern side of the postulated course of the SSZ shows island arc characteristics, and conversely if the Muglib Batholith on the northern side shows evidence for intrusion into the Eurasian margin. Geochemically both batholiths form typical differentiation series of calc-alkaline magmas. U-Pb SHRIMP dating of zircons (Reichardt *et al.*, 2010; Weinberg & Dunlap, 2000) yielded broadly contemporaneous crystallization ages, and the lack of much older inherited zircons combined with juvenile zircon Hf isotopes, precludes recycling of continental crust. Rb-Sr and Sm-Nd isotope analysis yielded almost identical values for both batholiths, further indicating juvenile mantle source with minor crustal influence. We therefore propose that the Ladakh and Muglib Batholiths together with its continuation as Tirit Batholith in the Nubra Valley are part of the same island arc. Consequently, the Pangong Metamorphic Complex in the Pangong Range that hosts the Muglib Batholith is more likely to be part of the island arc crust than Eurasian continental crust. We suggest that the SSZ, marking the boundary between arc and continent, is probably located to the north of all calc-alkaline batholiths with island arc characteristics. Therefore the SSZ is unlikely to run parallel and to the south of the Karakoram Shear Zone in our study area in Ladakh.

References

Ahmad, T., Thakur, V. C., Islam, R., Khanna, P. P. & Mukherjee, P. K. (1998). Geochemistry

- and geodynamic implications of magmatic rocks from the Trans-Himalayan arc. *Geochemical Journal* 32, 383-404.
- Allègre, C. J., Courtillot, V., Tapponnier, P., Hirn, A., Mattauer, M., Coulon, C., Jaeger, J. J., Achache, J., Schärer, U., Marcoux, J., Burg, J. P., Girardeau, J., Armijo, R., Gariépy, C., Göpel, C., Tindong, L., Xuchang, X., Chenfa, C., Guangqin, L., Baoyu, L., Jiwen, T., Naiwen, W., Guoming, C., Tonglin, H., Xibin, W., Wanming, D., Huaibin, S., Yougong, C., Ji, Z., Hongrong, Q., Peisheng, B., Songchan, W., Bixiang, W., Yaoxiu, Z. & Xu, R. (1984). Structure and evolution of the Himalaya-tibet orogenic belt. *Nature* 307, 17-22.
- Allègre, C. J. & Othman, D. B. (1980). Nd-Sr isotopic relationship in granitoid rocks and continental crust development: A chemical approach to orogenesis. *Nature* 286, 335-342.
- Arth, J. G. & Barker, F. (1976). Rare-earth partitioning between hornblende and dacitic liquid and implications for the genesis of trondhjemitic-tonalitic magmas. *Geology* 4, 534-536.
- Boynton, W. V. (1984). Cosmochemistry of the rare earth elements; meteorite studies. In: Henderson, P. (ed.) *Rare earth element geochemistry. Developments in Geochemistry*, 63-114.
- Coward, M. P., Rex, D. C., Khan, M. A., Windley, B. F., Broughton, R. D., Luff, I. W., Pettersson, M. G. & Pudsey, C. J. (1986). Collision tectonics in the NW Himalayas. *Geological Society, London, Special Publications* 19, 203-219.
- Crawford, M. B. & Searle, M. P. (1992). Field relationships and geochemistry of pre-collisional (India-Asia) granitoid magmatism in the central Karakoram, northern Pakistan. *Tectonophysics* 206, 171-192.
- Debon, F., Le Fort, P., Dautel, D., Sonet, J. & Zimmermann, J. L. (1987). Granites of western Karakorum and northern Kohistan (Pakistan): A composite mid-Cretaceous to upper Cenozoic magmatism. *Lithos* 20, 19-40.
- Dietrich, V. J., Frank, W. & Honegger, K. (1983). A Jurassic-Cretaceous island arc in the Ladakh-Himalayas. *Journal of Volcanology and Geothermal Research* 18, 405-433.
- Dunlap, W. J. & Wysoczanski, R. (2002). Thermal evidence for early Cretaceous metamorphism in the Shyok suture zone and age of the Khardung volcanic rocks, Ladakh, India. *Journal of Asian Earth Sciences* 20, 481-490.
- Ehro, M., Kojima, S., Sato, T., Ahmad, T. & Ohtani, T. (2007). Discovery of Jurassic ammonoids from the Shyok suture zone to the northeast of Chang La Pass, Ladakh, northwest India and its tectonic significance. *Island Arc* 16, 124-132.
- Frank, W., Gansser, A. & Trommsdorff, V. (1977). Geological observations in the Ladakh area (Himalayas); a preliminary report. *Schweizerische Mineralogische und Petrographische Mitteilungen* 57, 89-113.
- Gansser, A. (1980). The significance of the Himalayan suture zone. *Tectonophysics* 62, 37-40, 43-52.
- Gromet, L. P. & Silver, L. T. (1983). Rare earth element distributions among minerals in a granodiorite and their petrogenetic implications. *Geochimica et Cosmochimica Acta* 47, 925-939.
- Heuberger, S., Schaltegger, U., Burg, J.-P., Villa, I. M., Frank, M., Dawood, H., Hussain, S. & Zanchi, A. (2007). Age and isotopic constraints on magmatism along the Karakoram-Kohistan suture zone, NW Pakistan; evidence for subduction and continued convergence after India-Asia collision. *Swiss Journal of Geosciences* 100, 85-107.
- Honegger, K., Dietrich, V., Frank, W., Gansser, A., Thöni, M. & Trommsdorff, V. (1982). Magmatism and metamorphism in the Ladakh Himalayas (the Indus-Tsangpo suture zone). *Earth and Planetary Science Letters* 60, 253-292.
- Jagoutz, O. E., Burg, J. P., Hussain, S., Dawood, H., Pettke, T., Iizuka, T. & Maruyama, S. (2009). Construction of the granitoid crust of an island arc part I: Geochronological

- and geochemical constraints from the plutonic Kohistan (NW Pakistan). *Contributions to Mineralogy and Petrology* 158, 739-755.
- Jain, A. K. & Singh, S. (2008). Tectonics of the southern Asian Plate margin along the Karakoram Shear Zone: Constraints from field observations and U-Pb SHRIMP ages. *Tectonophysics* 451, 186-205.
- Ji, W.-Q., Wu, F.-Y., Chung, S.-L., Li, J.-X. & Liu, C.-Z. (2009). Zircon U-Pb geochronology and Hf isotopic constraints on petrogenesis of the Gangdese batholith, southern Tibet. *Chemical Geology* 262, 229-245.
- Khan, S. D., Walker, D. J., Hall, S. A., Burke, K. C., Shah, M. T. & Stockli, L. (2009). Did the Kohistan-Ladakh island arc collide first with India? *Geological Society of America Bulletin* 121, 366-384.
- Kretz, R. (1983). Symbols for rock-forming minerals. *American Mineralogist* 68, 277-279.
- Lacassin, R., Franck, V., Nicolas, A., Leloup, P. H., Paquette, J. L., Haibling, L., Tapponnier, P., Chevalier, M.-L., Guillot, S., Mahéo, G., Zhiqin, X. (2004). Large-scale geometry, offset and kinematic evolution of the Karakorum fault, Tibet. *Earth and Planetary Science Letters* 219, 255-269.
- Mahéo, G., Blichert-Toft, J., Pin, C., Guillot, S. & Pêcher, A. (2009). Partial Melting of Mantle and Crustal Sources beneath South Karakorum, Pakistan: Implications for the Miocene Geodynamic Evolution of the India-Asia Convergence Zone. *Journal of Petrology*, 427-449.
- Mahéo, G., Guillot, S., Blichert-Toft, J., Rolland, Y. & Pêcher, A. (2002). A slab breakoff model for the Neogene thermal evolution of South Karakorum and South Tibet. *Earth and Planetary Science Letters* 195, 45-58.
- Matte, P., Tapponnier, P., Arnaud, N., Bourjot, L., Avouac, J. P., Vidal, P., Qing, L., Yusheng, P. & Yi, W. (1996). Tectonics of western Tibet, between the Tarim and the Indus. *Earth and Planetary Science Letters* 142, 311-330.
- McCarthy, M. R. & Weinberg, R. F. (in press). Structural complexity resulting from pervasive ductile deformation in the Karakoram Shear Zone, Ladakh, NW India. *Tectonics*.
- Petterson, M. G. & Windley, B. F. (1985). RbSr dating of the Kohistan arc-batholith in the Trans-Himalaya of north Pakistan, and tectonic implications. *Earth and Planetary Science Letters* 74, 45-57.
- Phillips, R. J., Parrish, R. R. & Searle, M. P. (2004). Age constraints on ductile deformation and long-term slip rates along the Karakoram fault zone, Ladakh. *Earth and Planetary Science Letters* 226, 305-319.
- Rai, H. (1982). Geological evidence against the Shyok palaeo-suture, Ladakh Himalaya. *Nature* 297, 142-144.
- Rai, H. (1997). Geology of the Shyok Tectonic Zone in eastern Ladakh, India. *Journal of the Geological Society of India* 49, 727-730.
- Ravikant, V. (2006). Utility of Rb-Sr geochronology in constraining Miocene and Cretaceous events in the eastern Karakoram, Ladakh, India. *Journal of Asian Earth Sciences* 27, 534-543.
- Ravikant, V., Wu, F.-Y. & Ji, W.-Q. (2009). Zircon U-Pb and Hf isotopic constraints on petrogenesis of the Cretaceous-Tertiary granites in eastern Karakoram and Ladakh, India. *Lithos* 110, 153-166.
- Raz, U. & Honegger, K. (1989). Magmatic and tectonic evolution of the Ladakh Block from field studies. *Tectonophysics* 161, 107-118.
- Reichardt, H., Weinberg, R. F., Andersson, U. B. & Fanning, C. M. (2010). Hybridization of granitic magmas in the source: The origin of the Karakoram Batholith, Ladakh, NW India. *Lithos* 116, 249-272.
- Robertson, A. H. F. & Collins, A. S. (2002). Shyok Suture Zone, N Pakistan: Late Mesozoic-Tertiary evolution of a critical suture separating the oceanic Ladakh Arc from the Asian continental margin. *Journal of Asian Earth Sciences* 20, 309-351.
- Robinson, A. C. (2009). Geologic offsets across the northern Karakorum fault: Implications

- for its role and terrane correlations in the western Himalayan-Tibetan orogen. *Earth and Planetary Science Letters* 279, 123-130.
- Rolland, Y., Pecher, A. & Picard, C. (2000). Middle Cretaceous back-arc formation and arc evolution along the Asian margin; the Shyok suture zone in northern Ladakh (NW Himalaya). *Tectonophysics* 325, 145-173.
- Rolland, Y., Picard, C., Pêcher, A., Lapierre, H., Bosch, D. & Keller, F. (2002). The cretaceous Ladakh arc of NW himalaya--slab melting and melt-mantle interaction during fast northward drift of Indian Plate. *Chemical Geology* 182, 139-178.
- Schärer, U., Copeland, P., Harrison, T. M., Searle, M. P. (1990). Age, cooling history, and origin of post-collisional leucogranites in the Karakoram Batholith; a multi-system isotope study. *Journal of Geology* 98, 233-251.
- Schärer, U., Hamet, J. & Allègre, C. J. (1984). The Transhimalaya (Gangdese) plutonism in the Ladakh region: a UPb and RbSr study. *Earth and Planetary Science Letters* 67, 327-339.
- Searle, M. P., Weinberg, R. F. & Dunlap, W. J. (1998). Transpressional tectonics along the Karakoram Fault Zone, northern Ladakh. In: Holdsworth, R. E. & Strachan, R. A. (eds.) *Continental Transpressional and Transtensional Tectonics*. London: Geological Society of London Special Publication, 307-326.
- Singh, S., Kumar, R., Barley, M. E. & Jain, A. K. (2007). SHRIMP U-Pb ages and depth of emplacement of Ladakh Batholith, Eastern Ladakh, India. *Journal of Asian Earth Sciences* 30, 490-503.
- Srimal, N. (1986). India-Asia collision: implications from the geology of the eastern Karakoram. *Geology* 14, 523-527.
- Sun, S. S. & McDonough, W. F. (1989). Chemical and isotopic systematics of oceanic basalts; implications for mantle composition and processes. *Geological Society of London Special Publications* 42, 313-345.
- Thakur, V. C. & Misra, D. K. (1984). Tectonic framework of the Indus and Shyok suture zones in eastern Ladakh, Northwest Himalaya. *Tectonophysics* 101, 207-220.
- Thakur, V. C., Viridi, N. S., Rai, H. & Gupta, K. R. (1981). A note on the geology of Nubra-Shyok area of Ladakh, Kashmir, Himalaya. *Journal of the Geological Society of India* 22, 46-50.
- Thanh, N. X., Itaya, T., Ahmad, T., Kojima, S., Ohtani, T. & Ehiro, M. (2010). Mineral chemistry and K-Ar ages of plutons across the Karakoram fault in the Shyok-Nubra confluence of northern Ladakh Himalaya, India. *Gondwana Research* 17, 180-188.
- Upadhyay, R. (2008). Implications of U-Pb zircon age of the Tirit granitoids on the closure of the Shyok suture zone, northern Ladakh, India. *Current Science* 94, 1635-1640.
- Upadhyay, R., Frisch, W. & Siebel, W. (2008). Tectonic implications of new U-Pb zircon ages of the Ladakh Batholith, Indus suture zone, northwest Himalaya, India. *Terra Nova* 20, 309-317.
- Upadhyay, R., Sinha, A. K., Chandra, R. & Rai, H. (1999). Tectonic and magmatic evolution of the eastern Karakoram, India. *Geodinamica Acta* 12, 341-358.
- Weinberg, R. F. (1997). The Disruption of a Diorite Magma Pool by Intruding Granite: The Sobu Body, Ladakh Batholith, Indian Himalayas. *The Journal of Geology* 105, 87-98.
- Weinberg, R. F. & Dunlap, W. J. (2000). Growth and deformation of the Ladakh Batholith, Northwest Himalayas; implications for timing of continental collision and origin of calc-alkaline batholiths. *Journal of Geology* 108, 303-320.
- Weinberg, R. F., Dunlap, W. J. & Whitehouse, M. (2000). New field, structural and geochronological data from the Shyok and Nubra valleys, northern Ladakh: linking Kohistan to Tibet. In: Khan, A., Treloar, P. J. & Searle, M. P. (eds.) *Tectonics of the Nanga Parbat Syntaxis and the Western Himalaya*. London: Geological Society of London Special Publication, 253-275.
- Weinberg, R. F. & Mark, G. (2008). Magma migration, folding, and disaggregation of

- migmatites in the Karakoram shear zone, Ladakh, NW India. *Geological Society of America Bulletin* 120, 994-1009.
- Weinberg, R. F., Mark, G. & Reichardt, H. (2009). Magma ponding in the Karakoram shear zone, Ladakh, NW India. *Geological Society of America Bulletin* 121, 278-285.
- Weinberg, R. F. & Searle, M. P. (1998). The Pangong Injection Complex, Indian Karakoram: a case of pervasive granite flow through hot viscous crust. *Journal of the Geological Society of London* 155, 883-891.
- Wen, D.-R., Liu, D., Chung, S.-L., Chu, M.-F., Ji, J., Zhang, Q., Song, B., Lee, T.-Y., Yeh, M.-W. & Lo, C.-H. (2008). Zircon SHRIMP U-Pb ages of the Gangdese Batholith and implications for Neotethyan subduction in southern Tibet. *Chemical Geology* 252, 191-201.

Chapter VI.

Summary and conclusions

1. Introduction to research outcomes

This research project investigated crustal differentiation from incipient partial melting to emplacement of large granitic bodies. The Pangong Metamorphic Complex (PMC), bound by strands of the Karakoram Shear Zone (KSZ), is an exceptional field area to undertake these studies. The meta- and diatexites in the and Darbuk-Shyok and Tangtse gorges cutting across the PMC provide spectacular examples of syn-deformational melting and the development of magma escape pathways parallel to the axial plane of folds and perpendicular to the axis of maximum compression (Weinberg & Mark, 2008). The Pangong Injection Complex demonstrates pervasive magma migration in an anatectic region (Weinberg & Searle, 1998), and the related Tangtse Pluton provides an example of magma accumulation in structurally controlled sites (Weinberg *et al.*, 2009). Regarding the timing of anatexis in the PMC, Rolland *et al.* (2009) argued for syn-kinematic intrusion of leucogranites, thus opposing the interpretation of leucogranite formation before dextral shearing along the KSZ (Phillips *et al.*, 2004; Searle & Phillips, 2007). These leucogranites that span crystallization ages between ~20 and ~13.5 Ma (Phillips *et al.*, 2004; Ravikant *et al.*, 2009; Reichardt *et al.*, 2010; Searle *et al.*, 1998) are inferred to be related to the Miocene Karakoram Batholith in the Shyok and Nubra River confluence area (Searle *et al.*, 1998; Weinberg *et al.*, 2000).

These observations and inferences provided the starting point to the research in this thesis. In the course of the research project, field relations were established by mapping in the KSZ. Rock samples were collected for geochemical, isotopic and geochronological analysis to test hypothesis drawn in the field. A summary of the main results and conclusions are presented below in an order from beginning of melt formation in the anatectic source to the final emplacement of the melt products.

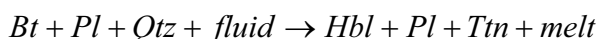
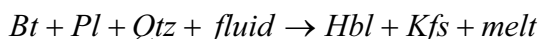
2. Synthesis of results

2.1 Water-fluxed melting

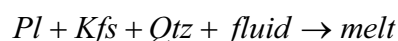
In the PMC, a suite of calc-alkaline magmatic and volcanic arc rocks and a meta-sedimentary sequence, were metamorphosed at upper amphibolite facies conditions, as indicated by thermobarometric calculations (700 ± 20 °C and 7 ± 1 kbar; Rolland & Pêcher (2001)). These conditions are just below the onset of muscovite dehydration melting and well below biotite dehydration melting. Migmatites, however, are present, and it has been inferred that melting took place under water-fluxing (Weinberg & Mark, 2008). This interpretation was based on the presence of euhedral, poikilitic hornblende porphyroblasts in leucosomes in meta- and diatexites (e.g. Fig. 3, Chapter II), and the lack of anhydrous peritectic minerals such as garnet, orthopyroxene, cordierite or sillimanite (Kenah & Hollister, 1983; Lappin

& Hollister, 1980; Mogk, 1992). Water-fluxed conditions are also supported by melting experiments demonstrating that hornblende is only stable as a crystallizing phase in magma when > 4 % water is added (Gardien *et al.*, 2000).

Study of the migmatites in the Tangtse area brought more evidence for water-fluxed melting. In places leucosomes in migmatitic calc-alkaline granodiorites and diorites consist mostly of K-feldspar, quartz and hornblende, and they also contain significant amounts of titanite, apatite and allanite. The mineralogy in hornblende-bearing leucosomes is indicative of the following melting reactions after Lappin & Hollister (1980):



In contrast, leucosomes in migmatitic Bt-psammities of the meta-sedimentary sequence lack any peritectic minerals and suggest the general water-fluxed melting reaction at the wet-granite solidus (e.g. Holtz *et al.*, 1992):



Evidence that the leucogranites of the PMC are not the result of muscovite dehydration melting, which was inferred for some local plutons including the Tangtse Pluton (Rolland *et al.*, 2009), is given indirectly by the low Rb/Sr ratios of leucogranites (generally below one), because muscovite (and biotite) dehydration melting would release Rb into the melt, thus increasing the Rb/Sr ratios (Inger & Harris, 1993; Patiño Douce & Harris, 1998). The water necessary to drive the melting reactions above was probably brought into the rocks via shear zones as suggested by Mogk (1992), and it is inferred that the meta-sedimentary rocks of the underthrust Karakoram Metamorphic Complex could be the water sources (McCarthy & Weinberg, in press). To further investigate the relationships between hornblende in protolith, melanosome and leucosome, detailed mineral analysis was carried out. These results are presented below.

2.2 Hornblende geochemistry

In crustal differentiation processes, hornblende plays an important role in fractionating magmas because it carries significant amounts of REE, and in particular, because it fractionates MREE to HREE from the magma (Arth & Barker, 1976; Davidson *et al.*, 2007). Melt products in the PMC are commonly associated with peritectic hornblende, and have high La_n/Yb_n and high Sr/Y so that they plot in the adakite-TTG field. In order to understand this chemical signature, hornblende grains were analysed using electron microprobe for major element concentrations and Laser Ablation-ICP-MS methods for trace element contents. In terms of major element contents, most hornblendes from the anatectic zone in the PMC vary from pargasite to edenite, defining a linear trend (Fig. 9, Chapter III).

Unexpectedly, hornblendes in meta- and diatexites in the PMC show unusual REE patterns that do not match the characteristic REE patterns reported in the literature (e.g. Arth & Barker,

1976; Bottazzi *et al.*, 1999; Tiepolo, 2000). In particular, hornblende with very low LREE and high HREE contents that reach a maximum at Yb to Lu differ from the expected overall concave downward shape and a maximum at Dy. In view of the mineral fractionation and accumulation documented in Chapter III, these hornblendes can have significant influence on the geochemistry of melanosomes, *in situ* leucosomes and also magmas that have segregated from the source. Therefore partition coefficients for hornblende have been determined using the LA-ICP-MS results. Geochemical modelling using my own determined $K_{D,s}$ (Table 5, Chapter III) confirmed that fractionation of hornblende and its retainment in the source systematically increases the La_n/Yb_n values of the magma (Fig. 19, Chapter III).

Thus, this thesis demonstrates that, in contrast to the deep-origin of adakites and TTGs, it is possible to explain extreme HREE depletion in Hbl-free leucosomes, and explain the origin of high La_n/Yb_n (and high Sr/Y) values in leucogranites in the Karakoram by water-present melting and retention of hornblende in the mid-crustal anatectic source region.

2.3 Formation and orientation of magma flow networks

Synchronous melting, folding and shearing enhance interconnection of leucosomes in growing leucosome networks (e.g. Brown, 1995). Despite arguments in the literature, we demonstrate that melting is generally syn-kinematic. A number of features in leucosome networks indicate their syn-kinematic origin detailed in Chapter IV, such as layer-parallel leucosomes in folds are continuous with leucosomes in the axial planar orientation forming complex networks that provide magma pathways parallel to the axial plane (Fig. 4, Chapter II; Fig. 3, Chapter IV), or leucosomes with diffuse boundaries to the melanosome parallel to the S-plane in C-S fabric in deformed migmatites (Fig. 3, Chapter IV).

Patchy leucosomes in metatexites connect to foliation parallel leucosomes and these come together to form hierarchies of magma escape pathways. Continuity between *in situ* leucosomes in migmatites and intrusive dykes demonstrates general connectivity (Fig. 8, Chapter II). In meta- and diatexites, transposition of layers into parallelism with the axial plane and stretching of folds along the axial plane allows for efficient magma transport and concomitant shortening parallel to maximum compression direction (Weinberg & Mark, 2008). These magma networks are thus parallel to the maximum elongation direction and not perpendicular to it as suggested by shear experiments (Holtzman & Kohlstedt, 2007; Katz *et al.*, 2006; Kohlstedt & Holtzman, 2009).

Similarly, dyke networks show dominantly axial planar parallel orientations, or are parallel to strike of the KSZ. Dykes rarely cross-cut and offset each other, on the contrary, in most cases intersecting dykes merge seamlessly. The mean value of dyke intersections coincides with the general mineral stretching lineation, and trend of the common fold axis, plunging moderately NW (Fig. 6, Chapter IV). Moreover, intersections of apparent chaotic dykes in sub-solidus calc-silicate rocks show this common orientation. In some places, dykes in calc-silicate rocks form networks as if intruded in conjugate sets indicative of opening via ductile fracturing under extensional shearing (Fig. 10, Chapter IV; Weinberg & Regenauer-Lieb, 2010). Dykes in shear fabric orientations resemble the relationships in sheared migmatites that show leucosomes in S-planes and are compatible with dextral transpression in ductile shear zones. All these various network styles are interconnected and form a continuous

magma network from migmatites in the source region to larger dykes in the transport zone that eventually link to the Karakoram Batholith.

In summary, Chapter IV describes a network of magma pathways that create an efficient, interconnected dyke swarm communicating the magma source with the batholith. This region provides a rare opportunity to document magma transport from source to batholith, and demonstrates that dykes do feed granitic batholiths, but that unlike previous work and experimental predictions, dykes in the KSZ are at high angles or even perpendicular to the maximum compression axis rather than parallel to it.

2.4 Timing of anatexis

In order to establish age relationships between source rocks and magmatic products, zircons and titanite grains were analysed using U-Pb SHRIMP methods. Two samples from the calc-alkaline Muglib Batholith, a Bt-granodiorite and a melanosome in Hbl-Bt-granodiorite were selected for analysis.

Analyses of zircon grains from the Hbl-Bt-granodiorite yielded a dominant bell shaped age probability distribution with a weighted mean $^{206}\text{Pb}/^{238}\text{U}$ age of 71.4 ± 0.6 Ma (18 analyses, MSWD = 1.14) (Fig. 11a, Chapter II). The zircon $^{206}\text{Pb}/^{238}\text{U}$ ages of the Bt-granodiorite yielded slightly scattered ages between ~67 and ~74 Ma, but the dominant zircon age indicates crystallization at 70.5 ± 0.6 Ma (mean weighted $^{206}\text{Pb}/^{238}\text{U}$ age of 14 analyses, MSWD = 1.03) (Fig. 11b, Chapter II). The crystallization ages of both samples are thus within error and confirm that both intrusions relate to the same magmatic event.

Analysis of titanite grains from the Bt-granodiorite sample yielded several age groupings. The oldest group shows a mean age of 65 ± 3 Ma, a second group is slightly younger (~55 Ma), and other analyses yielded ages ranging to ~11 Ma (Fig. 13c, Chapter II). The oldest calculated age is thus younger than that calculated from zircons analyses. It reflects either the true magmatic age, relates to a cooling event post initial magmatism or an early metamorphism event due to continued calc-alkaline intrusion, but could also be spurious. However, the younger analyses form a cluster peaking between ~11 and ~21 Ma, and this is indicative of a metamorphic crystallization event.

The Tangtse Pluton was dated using titanites on one sample of Bt-leucogranite and *in situ* zircons in a polished thin section from a second sample of Bt-leucogranite. Analysis of 15 titanite grains yielded a weighted mean of common Pb corrected $^{206}\text{Pb}/^{238}\text{U}$ ages of 16.4 ± 1.4 Ma (MSWD = 0.4, 19 analyses) (Fig. 13d, Chapter II). Two zircon inclusions in the titanite grains show $^{206}\text{Pb}/^{238}\text{U}$ ages of 18.6 ± 1.1 Ma and 19.5 ± 0.2 Ma, respectively, though reasonable these ages are regarded as unreliable because of very high U concentrations (~3000 ppm and ~5650 ppm). *In situ* analysis was carried out on nine areas on three zircons in the polished thin section. Some areas also showed very high U concentrations, but five analyses show lower U concentrations (≤ 1710 ppm U), and these have a weighted mean $^{206}\text{Pb}/^{238}\text{U}$ age of 18.0 ± 0.4 Ma (MSWD = 1.09) (Fig. 13e, Chapter II).

The results of the U-Pb SHRIMP dating indicate that the calc-alkaline Muglib Batholith crystallized at ~71 Ma similar to other calc-alkaline granitoids in the region such as the Ladakh and Tirit Batholiths (Chapter V), and was metamorphosed between ~21 and ~11 Ma contemporaneous with anatexis and leucogranite production. Leucogranite from the Tangtse

Pluton shows two likely crystallization ages, overlapping within error, ~16 Ma and ~18 Ma, interpreted to date a protracted pluton growth. Here, titanite analysis yielded a slightly younger age than that obtained from zircon.

The results support and expand previous ones, and indicate that the magmatic event that gave rise to the leucogranites in the PMC lasted from ~20 to ~13 Ma (Phillips *et al.*, 2004; Ravikant *et al.*, 2009; Reichardt *et al.*, 2010; Searle *et al.*, 1998). Furthermore, the results presented in this thesis confirm that anatexis was coeval with dextral shearing as also inferred by Rolland *et al.*, (2009), thus opposing the interpretation that the leucogranites in the PMC crystallized pre-kinematic. Furthermore, the relationships between the migmatized calc-alkaline rocks and the leucogranites, demonstrate that the sources of the leucogranite magmas lie within the PMC.

2.5 Magma hybridization in the source

In the PMC magmas sourced from different protoliths merge in early stages of migration. Two main rock types have undergone contemporaneous anatexis, calc-alkaline granitoids and Bt-psammite/ pelites of a meta-sedimentary sequence. This is indicated by similar timing of anatexis and deformation, and by field evidence indicative of melts from different sources migrating into the same pathways and merging in the process.

One example of this is documented by *in situ* leucosomes in calc-alkaline Bt-granodiorite feeding into a larger, intrusive leucogranite dyke, and leucosomes sourced in a neighbouring migmatitic Bt-psammite that merge with the same dyke (Fig. 7, Chapter II). This leucogranite dyke shows schollen of Bt-granodiorite and schlieren entrained from the Bt-psammite, and forms part of the magma sheets of the Pangong Injection Complex, that coalesce to form the Tangtse Pluton (Weinberg & Searle, 1998).

Field observations indicative of mingling of magmas in the source were tested by using isotope systematics. The different source rocks have distinct isotope signatures. For comparison of the isotopes at the time of anatexis, we chose 18 Ma for recalculation of initial values. Initial $^{87}\text{Sr}/^{86}\text{Sr}$ between 0.7042 and 0.7077 and initial ϵ_{Nd} values between 0.6 and 2.4 for calc-alkaline granitoids of the Muglib Batholith indicate a mantle origin with a slight crustal influence, or juvenile crustal sources. Meta-sedimentary rocks in contrast yielded $^{87}\text{Sr}/^{86}\text{Sr}_i$ between 0.7118 and 0.7161 and ϵ_{Nd_i} between -10.0 and -9.6 that indicate longer crustal residence. Thus the two protoliths have significantly different isotopic compositions.

Leucogranites derived from these rocks, including leucosomes inferred to be *in situ*, leucogranite dykes from the transport network and rocks from the Tangtse Pluton, all have $^{87}\text{Sr}/^{86}\text{Sr}_i$ ranging from 0.7086 to 0.7121, and ϵ_{Nd_i} values between -3.6 and -6.2. Leucogranites from the Karakoram Batholith in the Shyok and Nubra River confluence area show an identical isotope signature ($^{87}\text{Sr}/^{86}\text{Sr}_i = 0.7076$ to 0.7092 and $\epsilon_{\text{Nd}_i} = -5.4$ to -7.1). Most significantly, these values are intermediate between the values of the two sources and define a field within hyperbolic curves in a two end-member mixing calculation (Fig. 14, Chapter II).

It is therefore concluded that anatexis of two different source rocks in the PMC gave rise to a hybrid magma by migration into and intermingling along magma channelways already within the source region. These magmas are interpreted to be the source equivalent of the leucogranite Karakoram Batholith.

2.6 Similarities between Ladakh and Muglib Batholith

The Ladakh and the Muglib Batholith form calc-alkaline magmatic bodies on opposite sides of the inferred course of the Shyok Suture Zone (SSZ), which separates the Ladakh island arc from the Eurasian continental margin (e.g. Coward *et al.*, 1986; Gansser, 1980). In this thesis, the Muglib Batholith is defined as a semi-continuous body that runs in the Pangong Range parallel to strike and sheared by the KSZ. It links to the calc-alkaline Tirit granite in the Shyok and Nubra River confluence area, thus forming a batholith of at least 85 km length. If the current interpretation of the course of the SSZ is correct, then the Muglib Batholith formed at a continental margin, in contrast to the island arc rocks of the Ladakh Batholith. Conspicuous similarities observed in the field were the incentive to investigate a possible genetic relationship between the two calc-alkaline batholiths. This has an important tectonic implication: if they are related, then SSZ is most likely to follow a different course.

The two batholiths show major element distributions typical for calc-alkaline magmatic differentiation series (Frost *et al.*, 2001). Multi trace-element patterns show overlapping geochemical signatures. However, the most evolved, silica-rich ($\text{SiO}_2 > 70 \text{ wt } \%$) granites of the Ladakh Batholith show depletions in Nb, P and Ti that were not observed in the Muglib Batholith.

Comparison of crystallization ages also shows that both batholiths were broadly contemporaneous (see Table 1, Chapter V). Available age data for the Ladakh Batholith indicates magmatic activity between $\sim 45 \text{ Ma}$ and $\sim 102 \text{ Ma}$ (Honegger *et al.*, 1982; Schärer *et al.*, 1984; Singh *et al.*, 2007; Upadhyay *et al.*, 2008; Weinberg & Dunlap, 2000). Plutons of the Muglib Batholith show crystallization ages between $115 \pm 18 \text{ Ma}$ (Rb-Sr whole rock age; Ravikant, 2006) and $56.0 \pm 0.5 \text{ Ma}$ (U-Pb zircon age Ravikant *et al.*, 2009). My own U-Pb SHRIMP analyses of zircons from two samples of the Muglib Batholith yielded ages of $70.5 \pm 0.6 \text{ Ma}$ and $71.4 \pm 0.6 \text{ Ma}$, respectively. Importantly, inherited zircons that would indicate reworking of older (continental) crust are lacking in both batholiths.

For isotopic comparison, six samples from the Ladakh Batholith and five sample from the Muglib Batholith were analysed for Rb-Sr and Sm-Nd isotope values. Initial values were calculated to 70 Ma (Fig. 7, Chapter V). Samples from the Ladakh Batholith show little variation, with initial $^{87}\text{Sr}/^{86}\text{Sr}$ values ranging between 0.7030 and 0.7046, and initial ϵ_{Nd} values ranging between 0.5 and 2.7. The isotopic signature of the Muglib Batholith is essentially similar with initial $^{87}\text{Sr}/^{86}\text{Sr}$ values ranging between 0.7041 and 0.7072, and initial ϵ_{Nd} ranging between 1.2 and 2.7. These values, particularly the more robust Nd signature, indicate that both had mantle sources with only minor crustal influence in agreement with island arc origin. It is therefore unlikely that the Muglib Batholith represents a section of a continental Andean-type arc.

In summary, the Ladakh Batholith and the Muglib Batholith are comparable in terms of geochemistry, geochronology and isotope systematics. It is postulated that both have formed in the same island arc and that the Muglib Batholith is a slice of the arc transported along the side of the main Ladakh Batholith by the KSZ. Thus most probably, the SSZ, bounding the southern margin of Asia, follows a different course.

3. Conclusions

The thesis has investigated a magmatic system developed within a major active shear zone bounding the southern margin of the Tibetan Plateau. Here, the exposures provide a rare opportunity to follow magma from its source through to its sink. The results of my studies in the KSZ demonstrate that partial melting took place during deformation related to dextral shearing in the KSZ under water-fluxed conditions. As opposed to hornblende-bearing leucosomes in migmatites in the source region, leucogranites in transport channels and in local stocks and plutons are almost completely hornblende-free. It has been shown that hornblende fractionation and accumulation in the source, without involvement of garnet, gives rise to granitic magmas with high La_n/Yb_n and high Sr/Y values. Significantly, these processes take place in the mid-crust in contrast to common models for the origin of this geochemical signature, that require great depths for stabilization of residual garnet.

The formation of leucosome networks is strongly controlled by the tectonic regime of the KSZ. Leucosomes in axial planar orientation form melt channels that connect to dyke networks parallel to the regional (axial planar) foliation and parallel to trend of the shear zone. Intersections of continuous dykes give rise to magma channels parallel to the general mineral stretching lineation and parallel to the general fold axis in the KSZ.

Geochronological relationships confirm that timing of anatexis of the calc-alkaline Muglib Batholith coincides with crystallization of the Tangtse Pluton. Hybridization of magmas from different sources is commonly observed, but there are physical difficulties in explaining where and how hybridization takes place. Isotope systematics indicates that the leucogranite intrusions of the PMC, including the Tangtse Pluton, are most likely derived from hybridization of magmas from the two distinct anatectic sources exposed in the PMC. Hybridization occurred already within the source and resulted from the development of a common migration network.

The Karakoram Batholith that outcrops ~75 km along strike of the migmatites in the source zone has an isotope signature identical to the leucogranites in the PMC. It is proposed that the KSZ provides the source and the pathway for leucogranite magma that is transported parallel to the axis of maximum elongation from the mid-crust to upper crustal levels via a continuous magma network to eventually feed into the batholith.

The SSZ is purported to run parallel and to the south of the KSZ, separating the Ladakh arc from the Karakoram Terrane at the Eurasian margin. We tested the hypothesis that the Muglib Batholith represented a magmatic arc at the margin of the Asian continent, contemporaneous to the fully oceanic Ladakh island arc. This study has shown that the two have comparable geochemical compositions, overlapping crystallization ages and essentially identical isotopic signatures indicative of a mantle origin with minor crustal influence. I suggest that the Muglib Batholith formed in the same island arc as the Ladakh Batholith and that it represents an allochthonous slice transported by the KSZ. Thus the SSZ, marking the southern boundary of Eurasia, most likely does not run parallel to the Tangtse Shear Zone, as it is found in maps in the literature.

References

- Arth, J. G. & Barker, F. (1976). Rare-earth partitioning between hornblende and dacitic liquid and implications for the genesis of trondhjemitic-tonalitic magmas. *Geology* 4, 534-536.
- Bottazzi, P., Tiepolo, M., Vannucci, R., Zanetti, A., Brumm, R., Foley, S. F. & Oberti, R. (1999). Distinct site preferences for heavy and light REE in amphibole and the prediction of (super Amph/L) D (sub REE) partition coefficients for rare earth elements between amphibole and liquid. *Contributions to Mineralogy and Petrology* 137, 36-45.
- Brown, M., Averkin, Y. A., McLellan, E. L., Sawyer, E. W. (1995). Melt segregation in migmatites. *Journal of Geophysical Research* 100, 15,655-615,679.
- Coward, M. P., Rex, D. C., Khan, M. A., Windley, B. F., Broughton, R. D., Luff, I. W., Petterson, M. G. & Pudsey, C. J. (1986). Collision tectonics in the NW Himalayas. *Geological Society, London, Special Publications* 19, 203-219.
- Davidson, J., Turner, S., Handley, H., Macpherson, C. & Dosseto, A. (2007). Amphibole “sponge” in arc crust? *Geology* 35, 787-790.
- Frost, B. R., Barnes, C. G., Collins, W. J., Arculus, R. J., Ellis, D. J. & Frost, C. D. (2001). A geochemical classification for granitic rocks. *Journal of Petrology* 42, 2033-2048.
- Gansser, A. (1980). The significance of the Himalayan suture zone. *Tectonophysics* 62, 37-40,43-52.
- Gardien, V., Thompson, A. B. & Ulmer, P. (2000). Melting of biotite + plagioclase + quartz gneisses; the role of H (sub 2) O in the stability of amphibole. *Journal of Petrology* 41, 651-666.
- Holtz, F., Pichavant, M., Barbey, P. & Johannes, W. (1992). Effects of H (sub 2) O on liquidus phase relations in the haplogranite system at 2 and 5 kbar. *American Mineralogist* 77, 1223-1241.
- Holtzman, B. K. & Kohlstedt, D. L. (2007). Stress-driven melt segregation and strain partitioning in partially molten rocks; effects of stress and strain. *Journal of Petrology* 48, 2379-2406.
- Honegger, K., Dietrich, V., Frank, W., Gansser, A., Thöni, M. & Trommsdorff, V. (1982). Magmatism and metamorphism in the Ladakh Himalayas (the Indus-Tsangpo suture zone). *Earth and Planetary Science Letters* 60, 253-292.
- Inger, S. & Harris, N. (1993). Geochemical constraints on leucogranite magmatism in the Langtang Valley, Nepal Himalaya. *Journal of Petrology* 34, 345-368.
- Katz, R. F., Spiegelman, M. & Holtzman, B. (2006). The dynamics of melt and shear localization in partially molten aggregates. *Nature* 442, 676-679.
- Kenah, C. & Hollister, L. S. (1983). Anatexis in the Central Gneiss Complex. In: Atherton, M. P., Gribble, C. D. (ed.) *Migmatites, Melting, and Metamorphism*. Nantwich: Shiva, 142-162.
- Kohlstedt, D. L. & Holtzman, B. K. (2009). Shearing melt out of the earth: An experimentalist's perspective on the influence of deformation on melt extraction. *Annual Review of Earth and Planetary Sciences*, 561-593.
- Lappin, A. R. & Hollister, L. S. (1980). Partial melting in the Central Gneiss Complex near Prince Rupert, British Columbia. *American Journal of Science* 280, 518-545.
- McCarthy, M. R. & Weinberg, R. F. (in press). Structural complexity resulting from pervasive ductile deformation in the Karakoram Shear Zone, Ladakh, NW India. *Tectonics*.
- Mogk, D. W. (1992). Ductile shearing and migmatization at mid-crustal levels in an Archaean high-grade gneiss belt, northern Gallatin Range, Montana, USA. *Journal of Metamorphic Geology* 10, 427-438.
- Patiño Douce, A. E. & Harris, N. (1998). Experimental constraints on Himalayan anatexis. *Journal of Petrology* 39, 689-710.
- Phillips, R. J., Parrish, R. R. & Searle, M. P. (2004). Age constraints on ductile deformation and long-term slip rates along the Karakoram fault zone, Ladakh. *Earth and Planetary*

- Science Letters* 226, 305-319.
- Ravikant, V. (2006). Utility of Rb-Sr geochronology in constraining Miocene and Cretaceous events in the eastern Karakoram, Ladakh, India. *Journal of Asian Earth Sciences* 27, 534-543.
- Ravikant, V., Wu, F.-Y. & Ji, W.-Q. (2009). Zircon U-Pb and Hf isotopic constraints on petrogenesis of the Cretaceous-Tertiary granites in eastern Karakoram and Ladakh, India. *Lithos* 110, 153-166.
- Reichardt, H., Weinberg, R. F., Andersson, U. B. & Fanning, C. M. (2010). Hybridization of granitic magmas in the source: The origin of the Karakoram Batholith, Ladakh, NW India. *Lithos* 116, 249-272.
- Rolland, Y., Mahéo, G., Pêcher, A. & Villa, I. M. (2009). Syn-kinematic emplacement of the Pangong metamorphic and magmatic complex along the Karakorum Fault (N Ladakh). *Journal of Asian Earth Sciences* 34, 10-25.
- Rolland, Y. & Pêcher, A. (2001). The Pangong granulites of the Karakoram Fault (western Tibet); vertical extrusion within a lithosphere-scale fault? *Comptes Rendus de l'Académie des Sciences, Serie II. Sciences de la Terre et des Planètes* 332, 363-370.
- Schärer, U., Hamet, J. & Allègre, C. J. (1984). The Transhimalaya (Gangdese) plutonism in the Ladakh region: a UPb and RbSr study. *Earth and Planetary Science Letters* 67, 327-339.
- Searle, M. P. & Phillips, R. J. (2007). Relationships between right-lateral shear along the Karakoram fault and metamorphism, magmatism, exhumation and uplift: evidence from the K2-Gasherbrum-Pangong ranges, north Pakistan and Ladakh. *Journal of the Geological Society* 164, 439-450.
- Searle, M. P., Weinberg, R. F. & Dunlap, W. J. (1998). Transpressional tectonics along the Karakoram Fault Zone, northern Ladakh. In: Holdsworth, R. E. & Strachan, R. A. (eds.) *Continental Transpressional and Transtensional Tectonics*. London: Geological Society of London Special Publication, 307-326.
- Singh, S., Kumar, R., Barley, M. E. & Jain, A. K. (2007). SHRIMP U-Pb ages and depth of emplacement of Ladakh Batholith, Eastern Ladakh, India. *Journal of Asian Earth Sciences* 30, 490-503.
- Tiepolo, M., Vanucci, R., Bottazzi, P., Oberti, R., Zanetti, A., Foley, S. (2000). *Partitioning of rare earth elements, Y, Th, U, and Pb between pargasite, kaersutite, and basanite to trachyte melts; implications for percolated and veined mantle*: American Geophysical Union and The Geochemical Society.
- Upadhyay, R., Frisch, W. & Siebel, W. (2008). Tectonic implications of new U-Pb zircon ages of the Ladakh Batholith, Indus suture zone, northwest Himalaya, India. *Terra Nova* 20, 309-317.
- Weinberg, R. F. & Dunlap, W. J. (2000). Growth and deformation of the Ladakh Batholith, Northwest Himalayas; implications for timing of continental collision and origin of calc-alkaline batholiths. *Journal of Geology* 108, 303-320.
- Weinberg, R. F., Dunlap, W. J. & Whitehouse, M. (2000). New field, structural and geochronological data from the Shyok and Nubra valleys, northern Ladakh: linking Kohistan to Tibet. In: Khan, A., Treloar, P. J. & Searle, M. P. (eds.) *Tectonics of the Nanga Parbat Syntaxis and the Western Himalaya*. London: Geological Society of London Special Publication, 253-275.
- Weinberg, R. F. & Mark, G. (2008). Magma migration, folding, and disaggregation of migmatites in the Karakoram shear zone, Ladakh, NW India. *Geological Society of America Bulletin* 120, 994-1009.
- Weinberg, R. F., Mark, G. & Reichardt, H. (2009). Magma ponding in the Karakoram shear zone, Ladakh, NW India. *Geological Society of America Bulletin* 121, 278-285.
- Weinberg, R. F. & Regenauer-Lieb, K. (2010). Ductile fractures and magma migration from source. *Geology* 38, 363-366.

Weinberg, R. F. & Searle, M. P. (1998). The Pangong Injection Complex, Indian Karakoram: a case of pervasive granite flow through hot viscous crust. *Journal of the Geological Society of London* 155, 883-891.

Appendix A. Major and trace element chemistry of whole rocks

Sample	TNG62b	TNG63b	TNG69a	TNG70b	TNG71a	TNG71b	TNG84	TNG85b	TNG98b	TNG99c	TNG99d	TNG144	TNG148a	TNG148b	TNG153	TNG161a	TNG166
Type	Leucogranites in Pangong Metamorphic Complex																
Latitude	34°02'16"N 34°02'06.1"N 34°03'39.9"N 34°03'41.6"N 34°03'42.6"N 34°07'34.5"N 34°07'47.1"N 34°09'23.1"N 34°09'11.9"N 34°09'54.1"N 34°02'18.3"N 34°03'57.7"N 34°04'10.5"N																
Longitude	78°14'57.7"E 78°14'57.2"E 78°13'52.7"E 78°13'53.2"E 78°13'52.2"E 78°06'28.4"E 78°06'35.0"E 78°08'53.0"E 78°08'53.4"E 78°08'53.4"E 78°08'53.4"E 78°08'53.4"E 78°13'52.7"E 78°13'52.7"E 78°13'52.7"E 78°12'53.8"E 78°13'37.2"E 78°13'39.4"E																
Major Elements wt%																	
SiO ₂	71.80	71.86	71.90	74.90	73.40	72.50	73.53	75.07	74.94	75.05	68.50	74.65	72.88	71.80	70.50	69.80	73.55
TiO ₂	0.27	bd	0.19	0.12	0.09	0.19	0.11	0.10	0.10	0.06	0.54	0.15	0.25	0.21	0.29	0.16	0.06
Al ₂ O ₃	16.40	17.08	15.25	15.90	14.90	15.60	15.24	14.49	14.95	13.79	16.59	14.89	15.28	15.60	16.10	16.94	14.89
Fe ₂ O ₃	0.43	1.19	1.10	0.58	0.63	1.28	1.02	0.73	0.82	0.38	2.70	0.94	1.37	0.99	1.24	1.35	0.59
MnO	bd	0.01	0.03	bd	0.02	0.02	0.03	0.02	0.03	0.04	0.03	0.02	0.03	0.02	0.02	0.03	0.02
MgO	bd	0.54	0.32	bd	bd	bd	0.26	0.26	0.26	0.26	0.83	0.26	0.26	0.34	0.37	0.26	0.26
CaO	2.09	3.68	2.00	3.10	1.71	2.25	1.52	1.37	1.93	2.85	1.77	1.62	1.62	1.89	2.09	2.01	1.73
Na ₂ O	3.73	4.51	2.40	3.35	3.73	4.33	3.18	3.22	3.70	2.50	4.11	3.16	3.92	4.38	4.47	6.23	3.90
K ₂ O	5.31	1.12	5.76	1.88	4.76	3.37	4.54	4.31	3.55	6.55	3.62	4.65	4.49	4.11	4.24	3.41	3.76
P ₂ O ₅	0.02	0.05	0.06	0.04	0.02	0.04	0.16	0.06	0.02	0.19	0.19	0.02	0.12	0.07	0.09	0.02	0.09
LOI	0.35	0.38	0.30	0.84	0.77	0.31	0.45	0.39	0.20	0.24	0.34	0.35	0.17	0.43	0.37	0.56	0.33
Total	100.25	100.65	99.29	100.69	99.95	99.89	100.02	100.01	100.49	99.75	100.28	100.84	100.37	99.78	99.85	100.75	99.45
A/CNK	1.05	1.11	1.10	1.21	1.03	1.05	1.18	1.16	1.11	1.07	1.05	1.11	1.07	1.03	1.02	0.96	1.09
Mg/(Fe+Mg)	0.00	0.47	0.37	0.00	0.00	0.00	0.34	0.41	0.39	0.58	0.38	0.35	0.27	0.40	0.37	0.28	0.47
Trace Elements ppm																	
Sc	bd	1	bd	3	1.12	3.63	1	1	1	bd	4	bd	1	1.32	1.03	bd	0.61
Ti	169.57	1856	1387	859	476.79	1098.97	795	603	582	284	3518	983	1699	1258.31	1784.07	667	112.53
V	2.34	23	19	28	3.19	9.99	10	6	5	bd	57	12	30	14.83	18.07	7	bd
Cr	0.38	54	17	39	0.56	0.27	52	41	42	28	27	14	23	0.91	0.43	28	bd
Mn	21.62	115	169	62	n.a.	n.a.	215	143	174	225	259	93	212	n.a.	n.a.	141	52.12
Co	0.30	11	13	bd	0.39	0.89	12	13	10	bd	15	11	22	1.42	2.32	22	38.48
Ni	1.39	bd	11	5	0.52	0.48	1	bd	bd	bd	5	bd	2	1.21	2.55	bd	0.87
Cu	1.06	bd	7	26	1.44	0.24	3	4	2	45	37	3	11	28.41	11.96	5	0.20
Zn	0.12	12	14	21	8.82	38.51	34	13	15	17	58	12	12	23.25	28.04	bd	18.54
Ga	7.27	15	16	16	16.66	19.60	20	20	14	17	20	14	21	16.60	17.40	9	4.01
Rb	15.10	33	158	61	155.21	131.78	200	190	147	152	109	110	246	144.70	149.77	81	176.42
Sr	148.49	883	702	407	401.33	459.21	168	205	274	295	693	577	340	1001.40	1470.05	305	162.10
Y	0.61	5	7	5	1.29	2.31	11	23	9	12	8	4	9	4.13	4.82	10	2.09
Zr	0.92	213	131	49	40.68	110.53	85	84	72	63	214	120	129	121.20	149.54	128	54.92
Nb	0.61	bd	bd	7	2.36	7.44	15	21	13	6	5	2	7	4.44	5.49	7	7.16
Ba	1906.00	380	2288	770	792.67	569.42	510	512	755	403	1265	1782	564	2329.31	2997.75	466	1963.12
La	2.04	na	na	na	3.95	9.21	na	na	na	na	na	na	na	27.81	43.55	na	1.12
Ce	3.39	na	na	na	7.90	17.67	na	na	na	na	na	na	na	51.85	81.66	na	2.23
Pr	0.40	na	na	na	0.91	1.94	na	na	na	na	na	na	na	5.82	9.18	na	0.24
Nd	1.42	na	na	na	3.36	6.92	na	na	na	na	na	na	na	20.10	31.65	na	0.98
Sm	0.29	na	na	na	0.70	1.21	na	na	na	na	na	na	na	3.18	4.79	na	0.31
Eu	0.10	na	na	na	0.33	0.40	na	na	na	na	na	na	na	0.70	1.09	na	0.13
Gd	0.19	na	na	na	0.46	0.79	na	na	na	na	na	na	na	1.81	2.49	na	0.32
Tb	0.03	na	na	na	0.05	0.09	na	na	na	na	na	na	na	0.20	0.26	na	0.07
Dy	0.13	na	na	na	0.25	0.46	na	na	na	na	na	na	na	0.89	1.09	na	0.37
Ho	0.03	na	na	na	0.05	0.08	na	na	na	na	na	na	na	0.14	0.17	na	0.19
Er	0.06	na	na	na	0.13	0.21	na	na	na	na	na	na	na	0.34	0.40	na	0.20
Tm	0.01	na	na	na	0.02	0.03	na	na	na	na	na	na	na	0.05	0.05	na	0.03
Yb	0.05	na	na	na	0.13	0.21	na	na	na	na	na	na	na	0.28	0.31	na	0.22
Lu	0.01	na	na	na	0.02	0.03	na	na	na	na	na	na	na	0.04	0.04	na	0.05
Pb	4.72	9	102	44	55	57	46	45	37	20	21	25	51	77.76	82.96	12	62.21
Th	2.62	6	44	14	bd	bd	8	15	7	18	36	9	20	40.42	48.86	16	0.64
U	0.34	1.00	7.00	bd	bd	bd	bd	6	1	6	6	bd	1	4.63	5.61	2	0.57
Rb/Sr	0.10	0.04	0.23	0.15	0.39	0.29	1.19	0.93	0.54	0.52	0.16	0.19	0.72	0.14	0.10	0.27	1.09

All major elements analyzed by XRF. Trace elements analyzed by quadrupole ICP-MS. Trace elements of samples marked with * analyzed by XRF.

Trace elements of samples marked with ** analyzed by multi-collector ICP-MS. Trace elements marked with ** analyzed by INAA.

Appendix A. Major and trace element chemistry of whole rocks

Sample	ING167a	ING170	ING171	ING172	ING176	ING186	ING195	ING196	ING197e	ING197f	ING201	ING131c	ING131h	ING148d*	ING167c	ING174a	ING184a	ING187a
Type	Leucogranites in Panguoq Metamorphic Complex																	
Latitude	34°03'40.4"N	34°02'35.6"N	34°02'50.1"N	34°02'48.1"N	34°00'14.5"N	34°08'41.8"N	34°18'06.8"N	34°18'07.2"N	34°17'39.6"N	34°15'18.0"N	34°03'38.8"N	34°03'38.8"N	34°03'38.8"N	34°03'40.4"N	34°01'26.7"N	34°06'56.4"N	34°08'48.6"N	
Longitude	78°13'52.7"E	78°13'16.0"E	78°13'02.7"E	78°13'09.3"E	78°12'55.9"E	78°08'17.8"E	78°00'46.2"E	78°00'46.6"E	78°02'02.9"E	78°02'02.9"E	78°05'21.5"E	78°13'52.1"E	78°13'52.1"E	78°13'52.7"E	78°12'12.9"E	78°07'46.3"E	78°08'26.9"E	
Major Elements wt%																		
SiO ₂	74.10	72.09	75.53	76.93	75.89	71.16	70.79	73.31	71.91	74.04	74.95	71.90	70.70	74.90	73.93	74.31	74.59	75.12
TiO ₂	0.17	0.13	0.06	0.18	0.15	0.22	0.32	0.17	0.22	0.23	0.12	0.14	0.04	0.08	0.06	0.07	0.11	0.05
Al ₂ O ₃	15.33	15.96	14.72	14.29	12.62	15.41	15.40	14.92	15.61	13.55	14.58	15.70	17.00	14.90	15.58	14.30	14.55	14.14
Fe ₂ O ₃	0.93	0.71	0.39	1.13	1.38	1.37	1.70	0.98	1.17	1.87	0.82	1.02	0.44	0.96	0.39	0.43	0.98	0.74
MnO	0.01	0.01	0.01	0.01	0.09	0.02	0.04	0.02	0.02	0.06	0.06	0.05	bd	bd	0.03	0.01	0.07	0.05
MgO	0.26	0.26	0.26	0.36	0.26	0.40	0.45	0.26	0.27	0.26	0.26	0.26	0.36	bd	0.26	0.26	0.26	0.26
CaO	1.97	2.37	2.37	2.84	0.66	2.09	2.19	1.65	2.17	1.30	1.27	2.46	1.84	1.88	1.58	0.58	1.29	1.52
Na ₂ O	3.66	4.33	3.57	3.95	3.29	3.28	3.87	3.91	4.15	3.25	2.90	3.29	4.42	4.45	3.60	3.78	3.71	4.11
K ₂ O	4.15	2.98	2.94	0.94	4.59	4.56	3.77	4.27	3.66	4.68	5.63	4.90	5.16	3.39	4.90	4.76	4.45	3.30
P ₂ O ₅	0.03	0.03	0.02	0.04	0.02	0.09	0.10	0.04	0.05	0.06	0.02	0.04	0.01	0.02	bd	0.03	0.02	bd
LOI	0.39	0.47	0.34	0.45	0.25	0.44	0.47	0.37	0.35	0.30	0.49	0.50	0.42	0.42	0.31	0.61	0.41	0.21
Total	101.00	99.34	100.20	101.09	99.18	99.04	99.07	99.88	99.58	99.59	101.05	100.30	99.98	101.01	100.62	99.12	100.41	99.47
A/CNK	1.09	1.09	1.10	1.13	1.09	1.09	1.07	1.06	1.06	1.06	1.11	1.03	1.05	1.03	1.11	1.15	1.10	1.08
Mol/(Fe+Mg)	0.36	0.42	0.57	0.39	0.27	0.37	0.34	0.34	0.31	0.22	0.39	0.41	0.00	0.00	0.57	0.55	0.34	0.41
Trace Elements ppm																		
Sc	1.19	0.52	0.83	0.75	1.73	1.97	1.14	1.07	1.73	2.08	1.31	2.40	bd	bd	0.87	1.88	1.45	2.56
Ti	687.92	553.21	185.83	691.86	534.31	966.23	990.88	665.73	903.17	858.16	445.65	472.70	283	482	138.10	190.91	112.54	182.73
V	6.89	9.09	2.91	9.58	2.61	15.67	16.07	11.72	14.64	8.10	2.78	10.87	4	5	1.30	2.95	1.23	3.16
Cr	bd	1.69	0.30	bd	0.68	bd	bd	bd	bd	bd	bd	bd	35	23	bd	bd	bd	bd
Mn	97.46	41.36	39.40	65.54	519.18	125.15	188.81	114.33	130.01	345.91	81.97	n.a.	65	45	212.34	32.59	404.59	382.02
Co	55.95	68.63	79.41	80.80	57.82	46.72	27.43	44.01	37.45	40.91	57.55	1.22	bd	3	72.12	77.27	42.57	65.50
Ni	0.34	3.08	0.98	2.23	bd	1.29	1.62	0.97	1.32	bd	bd	4.57	2	bd	1.14	0.46	0.11	0.10
Cu	0.40	39.72	7.75	15.79	2.30	3.41	2.09	5.96	9.14	1.25	1.39	1.89	26	47	6.65	6.82	1.29	6.00
Zn	27.14	8.39	6.08	13.83	42.12	26.85	29.61	21.15	26.56	28.66	13.58	12.39	19	22	36.95	4.30	21.31	12.26
Ga	13.19	19.99	21.78	6.85	4.31	21.45	17.77	16.77	17.00	5.92	15.72	20.01	19	16	13.95	8.41	8.05	4.71
Rb	172.81	52.14	57.43	26.72	248.59	140.62	140.56	219.40	164.10	200.22	227.40	125.89	179	117	205.61	187.96	160.76	145.82
Sr	433.12	1089.96	816.18	843.64	53.47	438.78	546.23	563.52	597.51	107.58	242.04	376.68	368	503	442.10	57.64	86.20	66.32
Y	2.30	0.97	1.40	0.94	16.01	3.88	5.16	2.18	3.49	20.30	1.83	13.45	4	9	5.78	7.20	15.74	15.66
Zr	18.43	6.51	6.57	1.87	11.23	23.05	27.85	29.47	48.64	21.90	34.30	93.37	38	13	33.17	4.32	19.55	27.66
Nb	2.81	1.34	0.54	0.89	15.17	4.18	6.26	3.19	4.66	13.73	3.40	4.34	2	7	1.35	4.04	4.89	2.64
Ba	641.23	1360.10	1320.40	239.04	121.83	1500.71	1404.63	893.37	997.13	208.48	1000.83	395.46	415	634	606.19	340.88	305.63	21.76
La	6.01	3.80	7.01	19.59	29.78	46.42	40.20	17.14	20.21	34.01	10.00	3.36	2.74	na	1.43	7.60	4.59	0.61
Ce	14.29	8.09	13.71	35.33	56.44	79.11	61.31	40.67	48.07	78.07	19.80	5.69	4.95	na	7.09	16.78	10.11	1.62
Pr	1.51	0.78	1.27	3.34	5.14	7.96	6.26	4.22	4.99	7.57	1.84	0.64	0.60	na	0.38	1.87	1.15	0.20
Nd	5.78	2.97	4.44	11.47	17.17	29.49	22.93	15.28	18.48	26.62	6.21	2.26	2.30	na	1.50	7.48	4.59	0.93
Sm	1.07	0.53	0.73	1.54	3.02	4.53	3.51	2.22	2.84	4.83	1.01	0.48	0.64	na	0.34	1.68	1.24	0.42
Eu	0.41	0.34	0.55	0.44	0.24	0.89	0.81	0.53	0.69	0.60	0.44	0.35	0.26	na	0.36	0.19	0.28	0.23
Gd	0.73	0.40	0.55	0.98	0.58	2.81	2.20	1.31	1.75	3.96	0.71	0.48	0.48	na	0.35	1.41	1.20	0.71
Tb	0.09	0.05	0.07	0.09	0.43	0.28	0.25	0.14	0.20	0.64	0.09	0.13	0.08	na	0.08	0.23	0.26	0.22
Dy	0.46	0.25	0.32	0.31	2.58	1.11	1.16	0.55	0.83	3.62	0.40	1.25	0.52	na	0.68	1.31	2.06	1.84
Ho	0.08	0.04	0.05	0.03	0.53	0.14	0.18	0.07	0.12	0.70	0.06	0.42	0.13	na	0.16	0.23	0.56	0.46
Er	0.20	0.10	0.12	0.09	1.63	0.35	0.49	0.19	0.33	2.02	0.17	1.41	0.37	na	0.53	0.60	2.16	1.53
Tm	0.03	0.01	0.01	0.01	0.28	0.04	0.07	0.03	0.04	0.32	0.03	0.24	0.06	na	0.09	0.08	0.43	0.28
Yb	0.17	0.08	0.08	0.04	2.02	0.24	0.43	0.14	0.26	2.18	0.14	1.94	0.52	na	0.63	0.53	3.36	1.94
Lu	0.02	0.01	0.01	0.01	0.32	0.04	0.07	0.02	0.04	0.33	0.02	0.34	0.09	na	0.10	0.07	0.58	0.31
Pb	55.45	15.67	14.23	9.65	27.25	34.13	69.69	89.04	60.05	20.38	48.76	68.33	76	56.00	84.18	52.38	42.34	50.93
Th	4.10	0.80	2.23	6.59	18.07	27.03	40.38	31.57	27.47	17.94	8.11	1.76	bd	bd	2.39	7.31	3.98	
U	1.00	0.10	0.18	0.25	1.77	0.99	4.01	6.90	2.52	3.47	0.67	2.97	bd	bd	1.68	0.71	2.42	1.96
Rb/Sr	0.40	0.05	0.07	0.03	4.65	0.32	0.26	0.39	0.27	1.86	0.94	0.33	0.49	0.23	0.47	3.26	1.86	2.20

All major elements analyzed by XRF. Trace elements analyzed by quadrupole ICP-MS. Trace elements of samples marked with *, analyzed by XRF.

Appendix A. Major and trace element chemistry of whole rocks

Sample	TNG187b	TNG187c	TNG113a1*	TNG113a2*	TNG113b3	TNG113b4	TNG113a3*	TNG113f	TNG113a	TNG113b	TNG113i*	TNG114a	TNG114b1	TNG114b2	TNG169b	TNG60d	AGH23a	AGH18b
Type	Pegmatites in PMC																	
Latitude	34°08'48.6"N	34°08'48.6"N	34°02'35.0"N	34°02'35.0"N	34°02'35.0"N	34°02'35.0"N	34°02'35.0"N	34°02'35.0"N	34°02'35.0"N	34°02'35.0"N	34°02'35.0"N	34°02'35.2"N	34°02'35.2"N	34°02'35.2"N	34°02'40.3"N	34°03'25.3"N	34°25'10.6"N	34°24'47.8"N
Longitude	78°08'26.9"E	78°08'26.9"E	78°13'23.0"E	78°13'23.0"E	78°13'23.0"E	78°13'23.0"E	78°13'23.0"E	78°13'23.0"E	78°13'23.0"E	78°13'23.0"E	78°13'23.0"E	78°13'22.5"E	78°13'22.5"E	78°13'22.5"E	78°13'07.8"E	78°14'13.3"E	77°49'23.5"E	77°48'19.9"E
Major Elements wt%																		
SiO ₂	74.35	75.41	66.80	68.40	72.20	67.40	70.60	64.70	69.50	59.00	70.40	53.70	73.10	71.00	68.02	62.3	58.1	74.7
TiO ₂	0.05	0.07	0.36	0.33	0.22	0.21	0.23	0.57	0.48	0.93	0.18	1.46	0.25	0.38	0.15	0.57	0.70	0.06
Al ₂ O ₃	14.01	14.21	18.30	17.50	16.40	18.80	16.80	15.90	16.60	15.80	17.10	16.90	14.80	15.30	17.43	16.3	12.5	0.48
Fe ₂ O ₃	1.04	0.72	2.18	1.77	0.97	1.40	1.39	3.65	2.06	6.53	1.09	8.80	4.61	2.39	1.91	2.30	1.51	0.01
MnO	0.06	0.03	0.03	0.02	0.02	0.02	0.02	0.06	0.02	0.12	bd	0.16	0.02	0.04	0.06	0.06	0.13	0.01
MgO	0.26	0.26	1.05	0.91	0.39	0.63	0.56	2.21	1.03	3.38	0.48	4.26	0.61	1.00	0.59	1.31	3.88	0.26
CaO	1.38	1.65	4.08	3.44	3.77	3.60	2.80	4.61	3.38	6.13	3.20	7.18	2.13	2.90	4.72	2.65	8.05	3.78
Na ₂ O	3.54	3.85	5.81	5.51	5.52	5.79	5.42	4.08	4.99	3.65	5.58	4.17	3.34	3.89	4.87	1.68	1.92	4.61
K ₂ O	4.36	3.73	1.36	1.52	0.60	2.07	1.81	3.09	1.82	3.35	1.44	1.75	4.28	3.08	0.79	10.1	6.53	4.61
P ₂ O ₅	0.01	bd	0.12	0.10	0.05	0.08	0.09	0.21	0.14	0.31	0.05	0.37	0.07	0.10	0.11	0.40	2.06	0.35
LOI	0.22	0.49	0.56	0.53	0.39	0.42	0.70	0.75	0.67	0.58	0.48	1.13	0.47	0.51	0.59	0.46	0.59	99.3
Total	99.25	100.41	100.65	100.02	100.52	100.45	100.45	99.86	100.63	99.78	99.97	99.85	100.66	100.56	99.19	98.1	99.0	99.3
A/CNK	1.07	1.06	0.99	1.03	0.99	1.03	1.05	0.86	1.02	0.76	1.03	0.77	1.06	1.02	1.00	0.88	0.50	1.11
Mg/(Fe+Mn)	0.33	0.42	0.49	0.50	0.44	0.47	0.44	0.55	0.50	0.51	0.47	0.49	0.44	0.45	0.38	0.53	0.63	0.52
Trace Elements ppm																		
Sc	2.33	1.18	4	bd	4.47	0.40	bd	15.98	0.14	44.08	bd	26.57	2.05	5.29	9.63	6.05	16.36	1.02
Ti	151.35	206.11	2183	2238	2040.31	389.38	1541	5328.81	192.96	8952.75	1238	11688.61	2205.53	3398.18	630.96	2551.15	4068.80	201.61
V	5.34	1.92	42	34	29.96	13.61	27	143.59	29.34	236.56	19	332.12	41.58	64.50	21.36	37.99	75.37	1.61
Cr	bd	bd	31	36	4.43	34.85	24	140.51	41.49	228.49	33	41.29	27.93	49.43	3.40	36.63	60.92	21.95
Mn	386.98	170.28	247	165	196.35	201.14	112	800.65	251.86	1528.76	90	1793.96	205.73	388.59	406.25	348.67	927.99	53.66
Co	60.67	67.06	5	bd	3.07	5.61	4	15.93	7.99	21.68	1	41.08	4.52	7.61	50.36	20.29	35.08	43.89
Ni	0.02	0.56	8	7	11.39	27.44	4	86.64	40.43	120.27	5	92.49	17.61	35.87	3.56	28.17	39.16	0.46
Cu	2.44	1.77	45	20	291.47	135.55	38	4.81	193.23	25.21	5	73.66	60.22	31.95	9.13	31.58	65.95	1.07
Zn	13.37	9.49	43	41	18.03	27.83	44	68.61	37.52	109.28	30	119.16	24.17	11.73	23.40	38.74	86.07	11.73
Ga	4.33	4.56	19	18	10.80	17.50	20	20.28	13.45	26.20	18	13.72	22.69	18.21	6.35	165.33	13.90	20.03
Rb	162.10	131.21	38	48	0.70	7.30	38	43.08	9.04	41.32	35	70.70	47.89	61.82	9.01	440.88	151.37	285.40
Sr	78.44	121.20	1034	990	1392.02	884.77	1347	1019.10	619.20	959.00	967	627.94	607.48	638.71	914.92	1083.16	903.35	85.93
Y	16.65	6.31	8	4	4.62	1.77	4	13.44	3.16	34.74	3	16.85	4.27	10.18	14.64	20.85	29.90	6.74
Zr	63.93	10.19	127	98	6.04	3.01	99	15.42	21.84	19.25	93	10.89	4.83	8.70	16.59	39.72	30.38	19.10
Nb	2.87	1.94	1	bd	5.34	0.55	bd	7.67	0.19	18.82	bd	21.59	5.71	8.42	5.39	9.66	21.17	20.02
Ba	51.76	93.15	273	332	92.50	458.02	584	744.44	274.36	1290.87	453	212.90	1259.63	740.77	130.76	8279.89	4136.14	111.98
La	4.56	0.64	9.8**	10.5**	1.00	1.89	14.4**	4.66	15.40	9.03	8.6**	27.57	13.90	24.40	30.85	98.30	68.37	5.93
Ce	10.55	1.41	19**	21**	3.14	3.83	26**	14.11	24.15	26.66	13**	46.37	22.45	38.95	53.96	353.85	160.68	11.56
Pr	1.31	0.18	bd	bd	0.59	0.52	bd	2.39	2.59	4.46	bd	5.30	2.39	4.11	4.95	31.67	20.59	5.20
Nd	5.73	0.83	6	10**	2.80	2.20	8**	11.62	9.22	21.86	bd	20.04	8.02	14.22	17.67	140.37	81.59	5.20
Sm	1.80	0.35	1.6**	1.3**	1.00	0.64	1.6**	3.53	1.82	7.20	0.9**	4.21	1.43	2.71	3.05	26.54	14.35	1.55
Eu	0.30	0.24	0.6**	0.5**	0.46	0.23	0.5**	1.16	0.55	2.21	0.4**	1.27	0.45	0.72	0.86	5.04	2.91	0.31
Gd	1.63	0.43	bd	bd	0.86	0.51	bd	2.95	1.29	6.48	bd	3.53	1.09	2.13	2.74	15.06	9.53	1.45
Tb	0.31	0.10	bd	bd	0.17	0.08	bd	0.48	0.17	1.12	bd	0.56	0.16	0.32	0.44	1.60	1.09	0.25
Dy	2.20	0.80	bd	bd	0.98	0.44	bd	2.55	0.76	6.31	bd	3.16	0.87	1.79	2.58	6.00	5.24	1.40
Ho	0.52	0.21	bd	bd	0.22	0.09	bd	0.51	0.13	1.30	bd	0.68	0.18	0.37	0.93	0.72	0.49	0.26
Er	1.67	0.71	bd	bd	0.56	0.20	bd	1.18	0.30	3.05	bd	1.68	0.45	0.94	1.37	1.60	2.46	0.71
Tm	0.29	0.13	bd	bd	0.07	0.03	bd	0.14	0.03	0.37	bd	0.21	0.06	0.12	0.20	0.16	0.34	0.10
Yb	2.07	0.88	0.5**	0.2**	0.49	0.15	bd	0.90	0.21	2.27	bd	1.39	0.39	0.78	1.26	0.89	2.10	0.63
Lu	0.34	0.14	bd	0.09**	0.07	0.02	0.05**	0.13	0.03	0.31	bd	0.21	0.06	0.11	0.18	0.11	0.30	0.09
Pb	49.45	40.74	13	12	12.15	17.06	10	18.63	13.18	18.30	10	11.00	19.80	16.59	10.17	85.37	30.21	108.75
Th	7.35	1.21	3**	3.1**	0.38	0.77	3.5**	1.63	4.52	2.52	5.3**	2.02	7.15	9.16	11.08	93.30	21.32	23.10
U	1.95	0.46	1.7**	bd	0.46	0.28	2.6**	1.46	0.53	2.33	2.3**	1.23	1.24	1.27	1.27	6.53	3.73	8.33
Rb/Sr	2.07	1.08	0.04	0.05	0.00	0.01	0.03	0.04	0.01	0.04	0.04	0.11	0.08	0.10	0.01	0.41	0.17	3.32

All major elements analyzed by XRF. Trace elements analyzed by quadrupole ICP-MS. Trace elements of samples marked with *; analyzed by XRF.

Trace elements of samples marked with ** analyzed by multi-collector ICP-MS. Trace elements marked with ** analyzed by INAA.

Appendix A. Major and trace element chemistry of whole rocks

Sample Type	AGH23d	AGH25a	NBR1a	NBR1b	NBR2a	NBR2b	NBR2c	NBR3a	NBR3b	TNG62a	TNG68a*	TNG68b*	TNG131a	TNG207	TNG98a	TNG99a*	TNG99b*	TNG128*
Latitude	34°25'10.6"N	34°27'04.4"N	34°29'06.0"N	34°29'06.0"N	34°37'54.6"N	34°37'54.6"N	34°37'54.6"N	34°46'27.5"N	34°46'27.5"N	34°02'16.8"N	34°03'38.8"N	34°03'38.8"N	34°03'01.4"N	34°03'01.4"N	34°09'23.1"N	34°09'11.9"N	34°09'11.9"N	33°59'08.3"N
Longitude	77°49'23.5"E	77°45'53.1"E	77°44'20.0"E	77°44'20.0"E	77°38'24.1"E	77°38'24.1"E	77°38'24.1"E	77°32'45.7"E	77°32'45.7"E	78°14'57.7"E	78°13'52.1"E	78°13'52.1"E	78°13'52.1"E	78°13'41.3"E	78°08'53.4"E	78°08'53.4"E	78°08'53.4"E	78°18'37.8"E
Major Elements wt%																		
SiO ₂	68.7	72.3	76.19	73.40	72.92	73.97	74.01	75.49	73.83	55.00	68.30	70.40	67.50	68.23	66.65	63.98	61.70	na
TiO ₂	0.40	0.27	0.11	0.22	0.24	0.13	0.14	0.08	0.20	1.29	0.40	0.37	0.56	0.50	0.68	0.82	0.79	na
Al ₂ O ₃	14.6	14.9	13.09	14.89	14.92	14.09	14.31	14.14	14.07	18.20	16.10	15.80	16.30	15.26	16.84	17.06	18.08	na
Fe ₂ O ₃	3.34	1.88	0.84	1.42	1.51	1.22	1.23	0.59	1.39	7.75	2.81	2.61	3.49	3.05	3.58	4.20	4.25	na
MnO	0.06	0.03	0.03	0.02	0.04	0.03	0.04	0.03	0.03	0.15	0.07	0.05	0.09	0.07	0.09	0.07	0.07	na
MgO	1.35	0.43	0.26	0.29	0.28	0.26	0.26	0.26	0.26	3.83	1.08	1.01	1.57	1.22	1.63	2.26	2.22	na
CaO	3.15	2.61	0.59	1.60	1.77	1.46	1.51	1.29	1.68	5.79	2.54	2.49	3.16	2.85	3.44	4.47	5.19	na
Na ₂ O	1.87	4.03	3.33	3.79	3.65	3.29	3.40	3.22	3.18	4.28	3.74	4.53	4.37	4.17	4.62	4.17	4.98	na
K ₂ O	5.22	2.26	4.52	3.64	3.65	4.30	4.18	4.38	4.11	2.79	4.23	2.84	2.85	4.57	1.92	2.64	1.68	na
P ₂ O ₅	0.08	0.07	0.02	0.06	0.09	0.04	0.05	0.03	0.07	0.51	0.17	0.16	0.22	0.19	0.29	0.40	0.29	na
LOI	0.47	0.80	0.49	0.64	0.86	0.63	0.75	0.69	0.80	1.00	0.71	0.64	0.50	0.57	0.65	0.44	0.40	na
Total	99.2	99.6	99.44	99.95	100.07	99.41	99.86	100.18	99.60	100.59	100.17	100.90	100.62	99.65	100.37	100.48	99.64	na
A/CNK	1.01	1.08	1.14	1.14	1.11	1.11	1.11	1.14	1.10	0.88	1.05	1.05	1.02	0.99	1.06	0.96	0.93	na
Mol/(Fe+Mg)	0.44	0.31	0.38	0.29	0.27	0.30	0.30	0.47	0.27	0.49	0.43	0.43	0.47	0.44	0.47	0.52	0.51	na
Trace Elements ppm																		
Sc	2.34	2.11	1.73	1.79	7.97	1.42	1.72	1.71	1.94	15.70	3	7	8.48	5.44	5.58	8	8	8.73
Ti	1496.57	688.30	345.63	742.79	3946.81	214.93	490.62	204.61	723.29	7787.69	2854	3133	3953.19	2121.40	4066.77	4567	4513	4404.74
V	22.39	4.47	1.55	10.95	76.20	5.45	5.99	1.19	6.52	151.86	49	58	91.99	49.71	61.85	90	98	86.82
Cr	58.34	55.22	bd	9.93	9.93	bd	bd	bd	bd	49.98	49	54	71.26	21.07	13.13	56	58	27.29
Mn	193.55	144.33	124.31	132.68	476.31	172.84	207.06	155.18	160.37	1068*	372	609	892.94	415.11	556.83	513	511	n.a.
Co	34.36	69.34	0.20	0.87	8.13	0.85	0.89	0.66	0.92	20.56	5	2	9.12	36.20	9.69	23	20	11.72
Ni	1.45	0.98	bd	12.30	0.36	0.33	0.33	bd	0.22	40.61	11	12	65.56	13.38	15.81	26	23	21.07
Cu	2.25	2.74	0.36	0.87	36.15	1.73	0.45	0.41	0.35	62.85	37	19	12.99	6.29	6.27	bd	323	25.50
Zn	40.22	17.81	20.20	20.03	48.21	25.31	27.79	13.76	26.55	111.94	63	81	81.83	38.42	63.22	49	53	51.83
Ga	16.02	14.39	9.03	11.86	17.47	13.14	14.42	6.92	13.43	22.06	17	22	13.31	8.87	19.16	20	17	16.94
Rb	59.22	161.53	220.76	201.14	208.66	123.13	199.19	363.11	201.27	122.31	147	218	206.37	161.13	116.94	81	59	124.82
Sr	572.20	146.79	70.01	363.24	501.35	249.95	302.82	106.10	336.80	541.97	498	353	438.70	413.29	543.01	903	867	580.59
Y	3.12	8.62	8.34	6.22	13.81	5.47	9.29	15.17	10.06	27.30	4	10	20.11	17.56	15.80	12	10	17.09
Zr	23.63	31.49	5.53	30.75	95.17	9.14	26.70	13.76	41.62	166.82	110	131	4.29	18.82	10.92	232	185	131.91
Nb	3.47	8.51	7.26	6.36	12.52	2.27	7.76	9.82	8.48	27.40	10	26	21.36	15.05	18.00	13	5	17.07
Ba	735.97	860.16	464.03	679.23	1000.46	739.14	994.37	283.34	789.80	334.05	459	444	286.12	379.67	279.61	867	290	526.67
La	28.99	20.69	35.17	18.58	33.65	7.65	14.94	9.70	25.01	55.98	na	na	75.25	40.87	55.87	na	na	45.11
Ce	50.99	36.65	67.66	43.73	62.58	18.17	34.68	20.11	58.37	111.68	na	na	103.75	75.33	99.52	na	na	85.46
Pr	5.27	3.70	6.59	4.40	6.46	1.89	3.52	2.13	5.72	12.29	na	na	9.47	7.59	10.54	na	na	9.42
Nd	17.46	12.03	22.71	16.05	24.47	6.79	13.02	7.81	20.27	42.77	na	na	29.82	27.47	35.28	na	na	32.74
Sm	2.53	1.99	3.89	2.86	4.44	1.24	2.43	2.01	3.55	7.57	na	na	5.12	4.71	5.48	na	na	5.56
Eu	0.66	0.36	0.33	0.56	0.98	0.34	0.49	0.27	0.66	2.03	na	na	1.08	1.08	1.32	na	na	1.45
Gd	1.59	1.60	2.86	2.06	3.39	0.98	1.93	1.87	2.62	6.35	na	na	4.14	3.88	4.27	na	na	4.37
Tb	0.17	0.23	0.38	0.29	0.52	0.18	0.31	0.41	0.39	0.91	na	na	0.62	0.58	0.54	na	na	0.61
Dy	0.72	1.32	1.88	1.44	2.76	1.04	1.73	2.64	2.07	5.06	na	na	3.41	3.20	2.80	na	na	3.29
Ho	0.11	0.26	0.31	0.23	0.49	0.20	0.32	0.51	0.36	1.00	na	na	0.71	0.59	0.51	na	na	0.64
Er	0.26	0.75	0.80	0.58	1.36	0.55	0.90	1.46	0.96	2.69	na	na	1.80	1.63	1.36	na	na	1.68
Tm	0.03	0.11	0.11	0.08	0.18	0.08	0.13	0.24	0.14	0.40	na	na	0.24	0.24	0.19	na	na	0.25
Yb	0.19	0.75	0.64	0.46	1.18	0.49	0.84	1.52	0.85	2.55	na	na	1.62	1.57	1.15	na	na	1.57
Lu	0.03	0.11	0.09	0.07	0.17	0.07	0.12	0.21	0.13	0.37	na	na	0.25	0.23	0.16	na	na	0.23
Pb	26.26	52.26	44.23	35.67	37.44	40.53	45.57	29.56	40.46	11.55	29	61	42.98	20.46	10.86	15	11	na
Th	16.67	15.80	32.65	15.59	19.99	9.41	15.57	7.22	20.24	10.93	12	16	17.67	15.21	10.60	8	4	na
U	0.73	4.24	2.36	1.37	4.92	1.13	2.23	2.91	3.55	2.84	bd	bd	3.84	2.22	2.32	1	bd	na
Rb/Sr	0.10	1.10	3.15	0.55	0.42	0.49	0.66	3.42	0.60	0.23	0.30	0.62	0.47	0.39	0.22	0.09	0.07	0.21

All major elements analyzed by XRF. Trace elements analyzed by quadrupole ICP-MS. Trace elements of samples marked with *, analyzed by XRF.

Trace elements of samples marked with **, analyzed by INAA.

Appendix A. Major and trace element chemistry of whole rocks

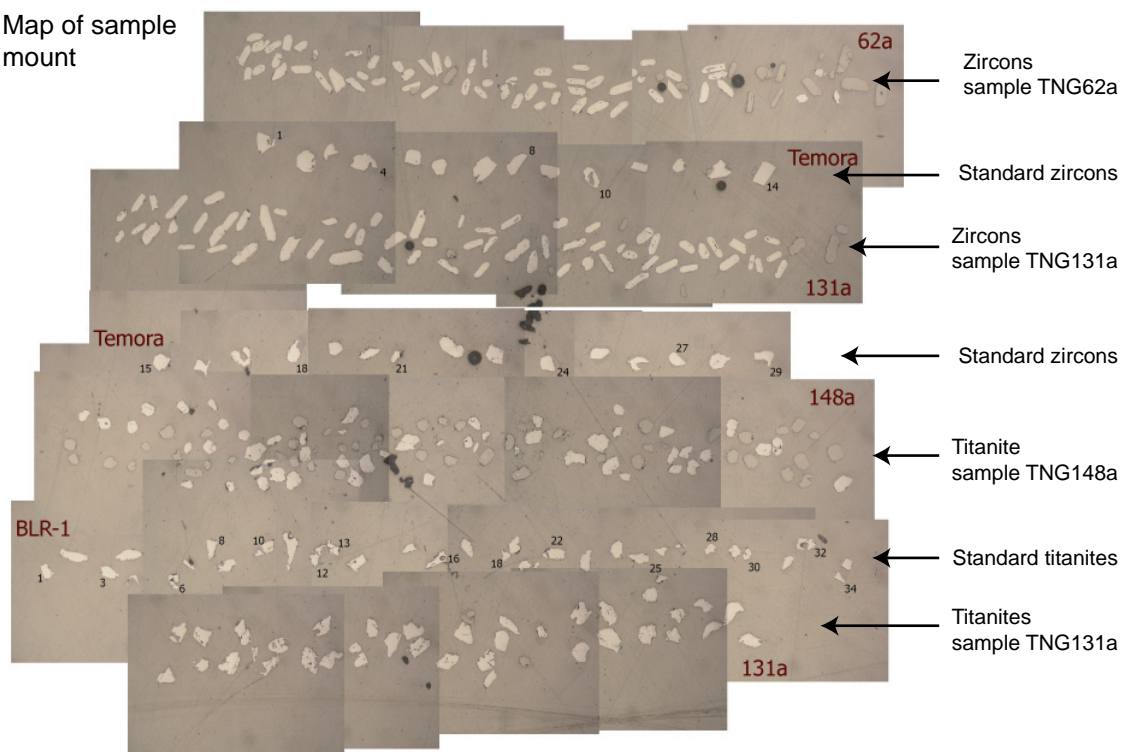
Sample	TNG169a	TNG104b	TNG205a	TNG205b	TNG205c	TNG105*	TNG108a*	TNG108b*	TNG108c*	TNG113d1*	TNG113d2*	TNG168	TNG208	TNG49d*	TNG70a*	TNG131d*	TNG167b	TNG112*	PNG03b*
Type	(Diatexile)		Diorite Mugilic Batholith						Amphibolite				Calc-silicate		Bit-psammitic			Bit-pelite	
Latitude	34°02'40.3"N	34°10'39.2"N	34°02'38.3"N	34°02'38.3"N	34°02'38.3"N	34°08'42.0"N	34°08'42.0"N	34°08'42.0"N	34°08'42.0"N	34°02'35.0"N	34°02'35.0"N	34°02'46.2"N	34°01'33.5"N	34°03'39.9"N	34°03'41.6"N	34°03'38.8"N	34°03'40.4"N	34°12'19.6"N	33°57'53.5"N
Longitude	78°13'07.8"E	78°07'07.0"E	78°13'25.4"E	78°13'25.4"E	78°13'25.4"E	78°08'18.5"E	78°08'18.5"E	78°08'18.5"E	78°08'18.5"E	78°13'23.0"E	78°13'23.0"E	78°13'33.6"E	78°12'01.7"E	78°13'52.7"E	78°13'53.2"E	78°13'53.1"E	78°13'52.7"E	78°07'55.9"E	78°23'46.0"E
Major Elements wt%																			
SiO ₂	61.95	75.64	54.91	55.02	47.62	58.35	54.77	55.38	52.82	46.90	46.50	47.20	52.49	61.65	60.50	61.60	60.99	na	na
TiO ₂	0.70	0.06	1.37	1.16	1.10	0.91	1.30	1.31	1.01	1.59	1.58	1.74	0.64	0.85	0.79	0.83	0.82	na	na
Al ₂ O ₃	14.29	14.57	17.56	17.07	15.53	17.06	17.57	13.87	15.55	17.40	17.50	12.02	14.69	17.34	17.40	17.00	16.97	na	na
FeO _{tot}	5.18	0.43	8.04	7.51	10.25	6.25	8.14	10.70	8.94	11.80	11.50	11.93	5.77	6.96	6.33	6.56	6.85	na	na
MnO	0.15	0.01	0.13	0.13	0.18	0.12	0.14	0.34	0.15	0.18	0.18	0.12	0.11	0.09	0.07	0.11	0.10	na	na
MgO	4.55	0.26	3.01	4.64	8.58	3.31	3.35	6.46	7.18	6.52	6.22	10.95	3.74	3.28	3.34	2.84	3.27	na	na
CaO	6.46	1.43	5.90	8.22	11.78	6.40	5.97	7.13	10.03	10.00	10.00	10.07	15.00	3.82	3.26	5.23	3.77	na	na
Na ₂ O	3.01	3.30	3.81	4.08	2.36	3.67	3.48	2.45	3.47	3.48	3.56	1.97	0.98	1.78	3.18	1.82	2.00	na	na
K ₂ O	2.47	4.97	2.97	1.11	1.11	2.45	4.23	1.98	0.73	1.62	1.56	1.29	3.41	3.32	3.19	3.02	3.25	na	na
P ₂ O ₅	0.14	0.01	0.50	0.33	0.15	0.31	0.45	0.12	0.09	0.40	0.38	0.38	0.15	0.16	0.14	0.16	0.15	na	na
LOI	0.93	0.14	0.82	0.84	1.35	0.70	0.43	0.51	0.36	0.75	0.85	1.53	2.03	0.99	1.57	1.06	1.59	na	na
Total	99.83	100.81	99.00	100.08	100.12	99.52	99.82	100.24	100.30	100.60	99.83	99.18	98.99	100.22	99.79	100.17	99.74	na	na
A/CNK	0.74	1.09	0.87	0.75	0.59	0.84	0.83	0.72	0.63	0.68	0.68	0.52	0.45	1.29	1.19	1.08	1.24	na	na
Ma/(Fe+Mg)	0.64	0.55	0.43	0.55	0.62	0.51	0.45	0.54	0.61	0.52	0.52	0.65	0.56	0.48	0.51	0.46	0.49	na	na
Trace Elements ppm																			
Sc	19.86	bd	12.69	16.67	30.73	16	17	34	38.12	32	31	26.76	16.19	22	17.58	16.04	11.52	16.24	15.11
Ti	3833.40	411	7373.16	6504.50	6513.84	4615	7148	7834	6140.48	8900	8832	8419.75	3419.69	6723	4873.06	5173.56	3270.71	4215.26	4648.56
V	103.66	5	123.54	145.92	197.62	152	180	291	229.59	292	292	239.38	119.04	185	142.49	137.54	95.12	113.00	132.92
Cr	74.77	39	12.68	15.23	26.71	71	50	274	204.76	70	58	57.42	102.91	203	118.20	117.99	124.80	79.83	99.52
Mn	1053.38	45	859.20	862.36	1106.96	949	1145	2706	n.a.	1499	1446	816.66	737.85	794	n.a.	n.a.	497.25	n.a.	n.a.
Co	45.13	12	27.64	28.61	34.68	24	27	49	43.09	52	51	44.66	22.71	27	17.97	17.78	43.35	16.15	21.35
Ni	53.55	bd	16.72	26.31	30.85	19	15	66	64.59	35	31	92.20	48.87	83	66.32	64.79	76.52	42.31	62.80
Cu	21.45	14	47.67	84.12	52.58	28	2	47	69.50	104	46	191.27	12.76	14	4.78	12.87	20.11	33.52	59.59
Zn	62.57	bd	86.66	76.38	79.35	61	84	91	62.54	101	98	114.29	73.22	94	93.89	101.70	72.10	93.03	95.66
Ga	12.58	13	14.41	9.73	8.95	17	18	16	14.97	20	19	11.98	9.41	20	21.93	20.73	6.55	20.39	19.95
Rb	49.42	100	124.10	25.63	22.95	76	125	79	4.12	40	35	39.40	153.89	179	263.10	179.34	253.51	169.92	171.90
Sr	547.63	456	568.57	550.93	418.10	618	604	165	129.57	650	724	353.80	339.72	159	256.25	159.14	96.63	301.19	150.15
Y	18.77	1	24.30	20.46	20.83	18	26	26	22.76	23	25	21.28	22.35	27	27.02	28.59	20.66	29.14	25.31
Zr	11.54	57	58.57	60.52	71.17	184	270	106	66.92	108	104	67.69	11.17	177	147.34	181.17	6.73	172.46	168.37
Nb	18.25	3	25.52	15.09	8.85	15	19	13	1.11	16	15	10.39	11.12	23	16.12	17.40	12.80	13.24	15.80
Ba	586.51	932	540.12	118.69	118.18	342	519	147	18.45	203	227	196.58	396.55	432	428.96	404.91	255.08	343.38	466.04
La	7.05	na	58.46	26.21	14.25	na	na	na	2.37	17.6**	15.2**	18.93	26.81	na	35.27	42.43	30.84	38.18	35.47
Ce	20.43	na	107.82	52.17	32.18	na	na	na	7.55	39**	32**	45.05	57.55	na	70.82	86.60	67.48	78.10	75.33
Pr	2.86	na	10.58	5.84	3.93	na	na	na	1.31	bd	bd	5.78	6.11	na	8.17	10.07	7.15	8.99	8.22
Nd	13.46	na	39.55	24.30	18.48	na	na	na	7.04	14**	15**	26.84	24.35	na	30.16	36.87	28.03	33.21	29.89
Sm	3.18	na	6.90	4.95	4.43	na	na	na	2.48	4.9**	4.4**	6.30	4.83	na	5.99	7.11	5.45	6.65	5.59
Eu	1.03	na	1.67	1.36	1.24	na	na	na	0.95	1.6	1.4**	1.63	0.92	na	1.30	1.39	1.19	1.34	1.03
Gd	2.89	na	5.76	4.03	3.63	na	na	na	3.48	88	bd	4.91	4.15	na	4.99	6.05	4.63	5.89	4.67
Tb	0.50	na	0.86	0.67	0.63	na	na	na	0.63	bd	bd	0.80	0.67	na	0.79	0.93	0.75	0.91	0.73
Dy	3.02	na	4.53	3.76	3.67	na	na	na	4.09	bd	bd	4.27	3.97	na	4.85	5.47	4.36	5.33	4.39
Ho	0.61	na	0.84	0.74	0.75	na	na	na	0.90	bd	bd	0.79	0.78	na	1.03	1.12	0.83	1.11	0.95
Er	1.76	na	2.32	1.96	1.95	na	na	na	2.56	bd	bd	1.97	2.23	na	2.96	3.04	2.29	3.10	2.76
Tm	0.28	na	0.34	0.30	0.30	na	na	na	0.38	bd	bd	0.28	0.34	na	0.45	0.44	0.34	0.47	0.43
Yb	1.90	na	2.06	1.88	1.87	na	na	na	2.45	2**	1.7**	1.65	2.20	na	2.89	2.80	2.11	3.08	2.78
Lu	0.31	na	0.32	0.30	0.28	na	na	na	0.36	0.3**	0.32**	0.24	0.33	na	0.42	0.41	0.31	0.46	0.42
Pb	12.42	25	12.16	11.45	5.27	18	32	20	2.25	23	23	3.85	25.47	33	25.53	24.53	20.71	16.58	12.58
Th	1.14	bd	11.21	4.15	1.74	9	3	bd	0.10	1.7**	1.4**	2.06	10.59	13	13.36	15.73	12.92	15.77	12.46
U	2.11	bd	1.08	1.26	1.20	1	1	2	0.11	bd	1.8**	0.80	1.84	3.00	3.40	4.07	2.06	2.73	2.53
Rb/Sr	0.09	0.22	0.22	0.05	0.05	0.12	0.21	0.48	0.03	0.06	0.05	0.11	0.45	1.13	1.03	1.13	2.62	0.56	1.14

All major elements analyzed by XRF. Trace elements analyzed by quadrupole ICP-MS. Trace elements of samples marked with *, analyzed by XRF.

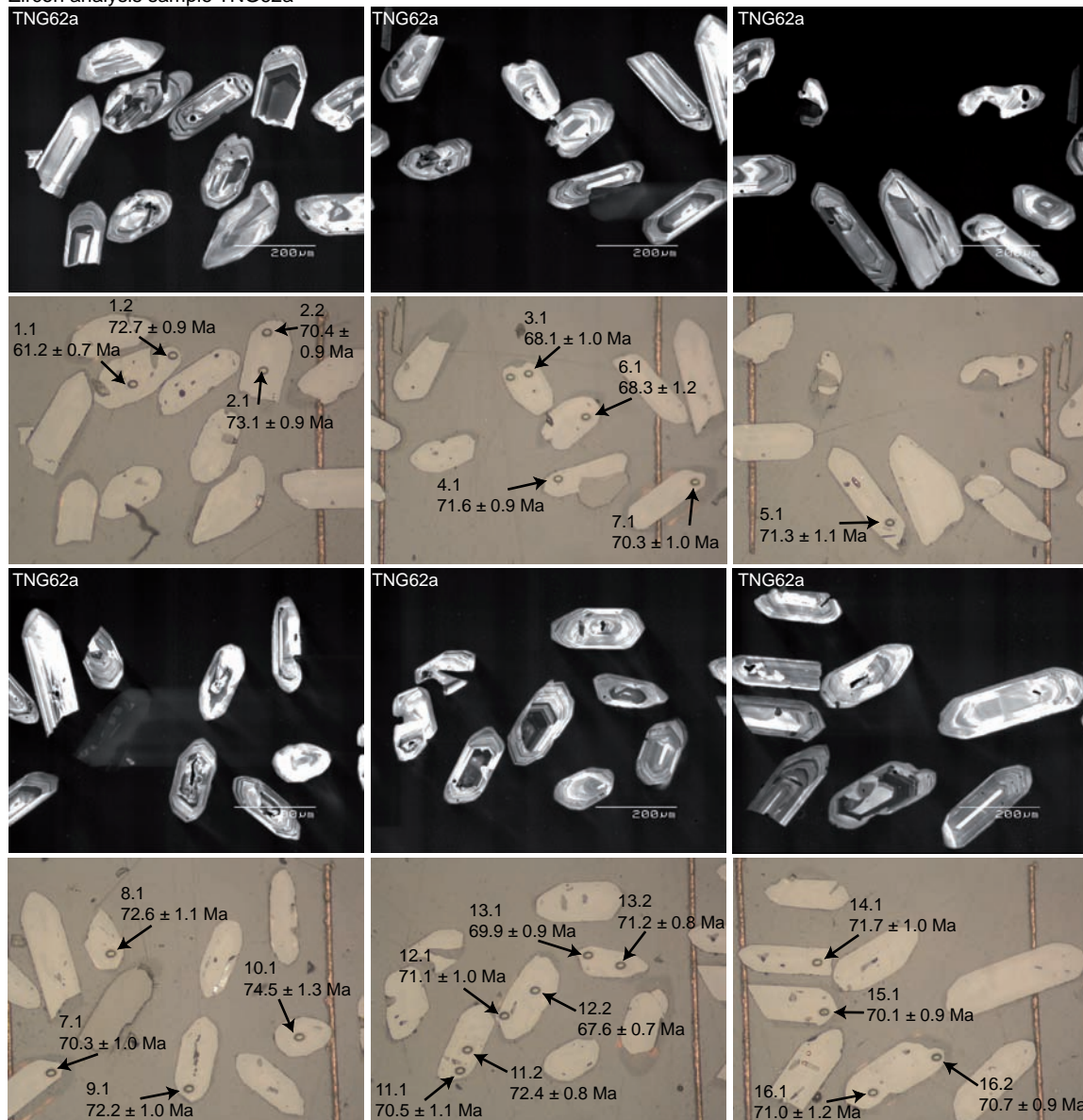
Trace elements of samples marked with **, analyzed by INAA.

B: U-Pb SHRIMP dating of zircons and titanites. Each analyzed spot is shown with its number and age as shown in Tables 2, 3 and 4 in Chapter II.

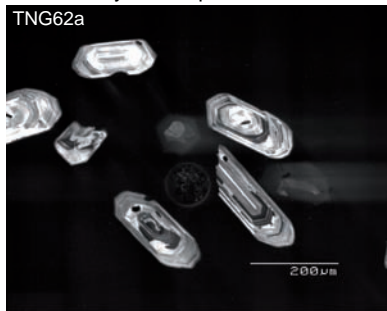
Map of sample mount



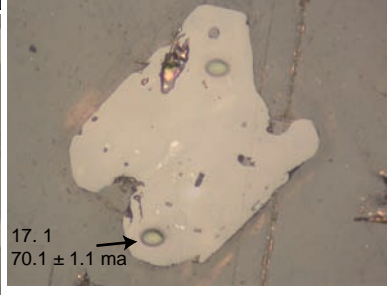
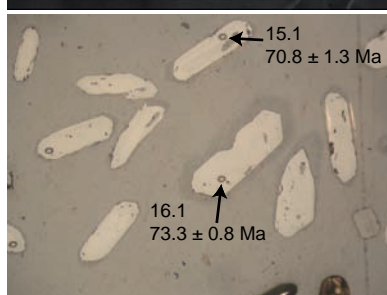
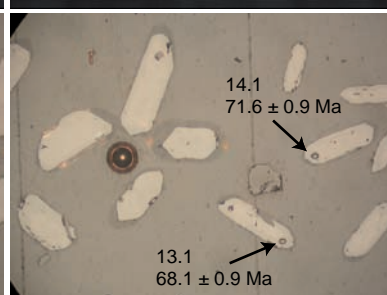
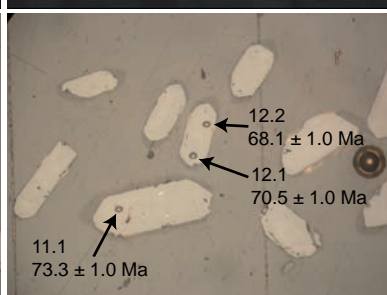
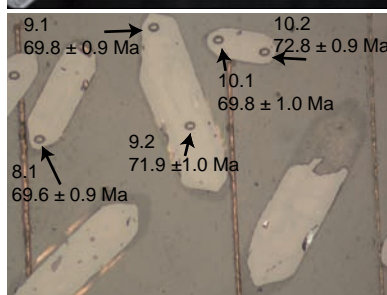
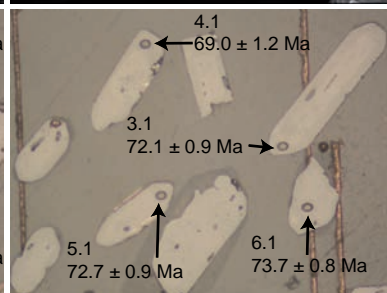
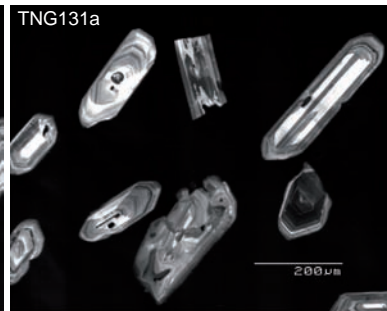
Zircon analysis sample TNG62a



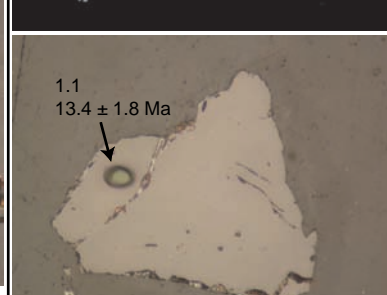
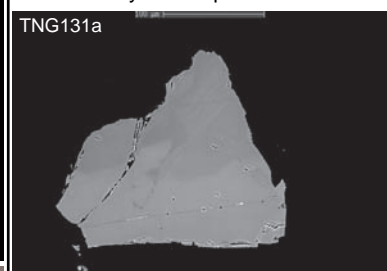
Zircon analysis sample TNG62a cont.

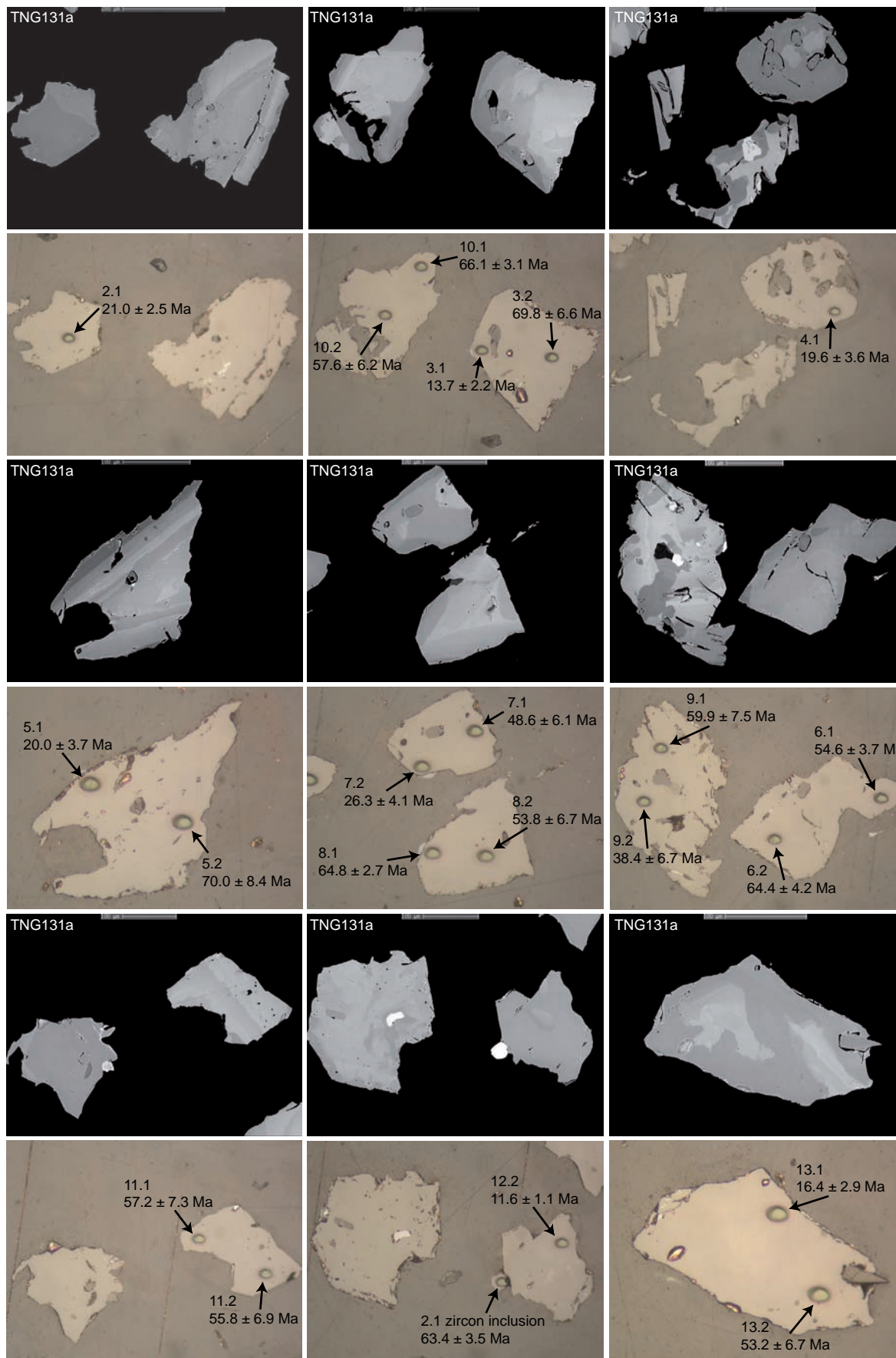


Zircon analysis sample TNG131a

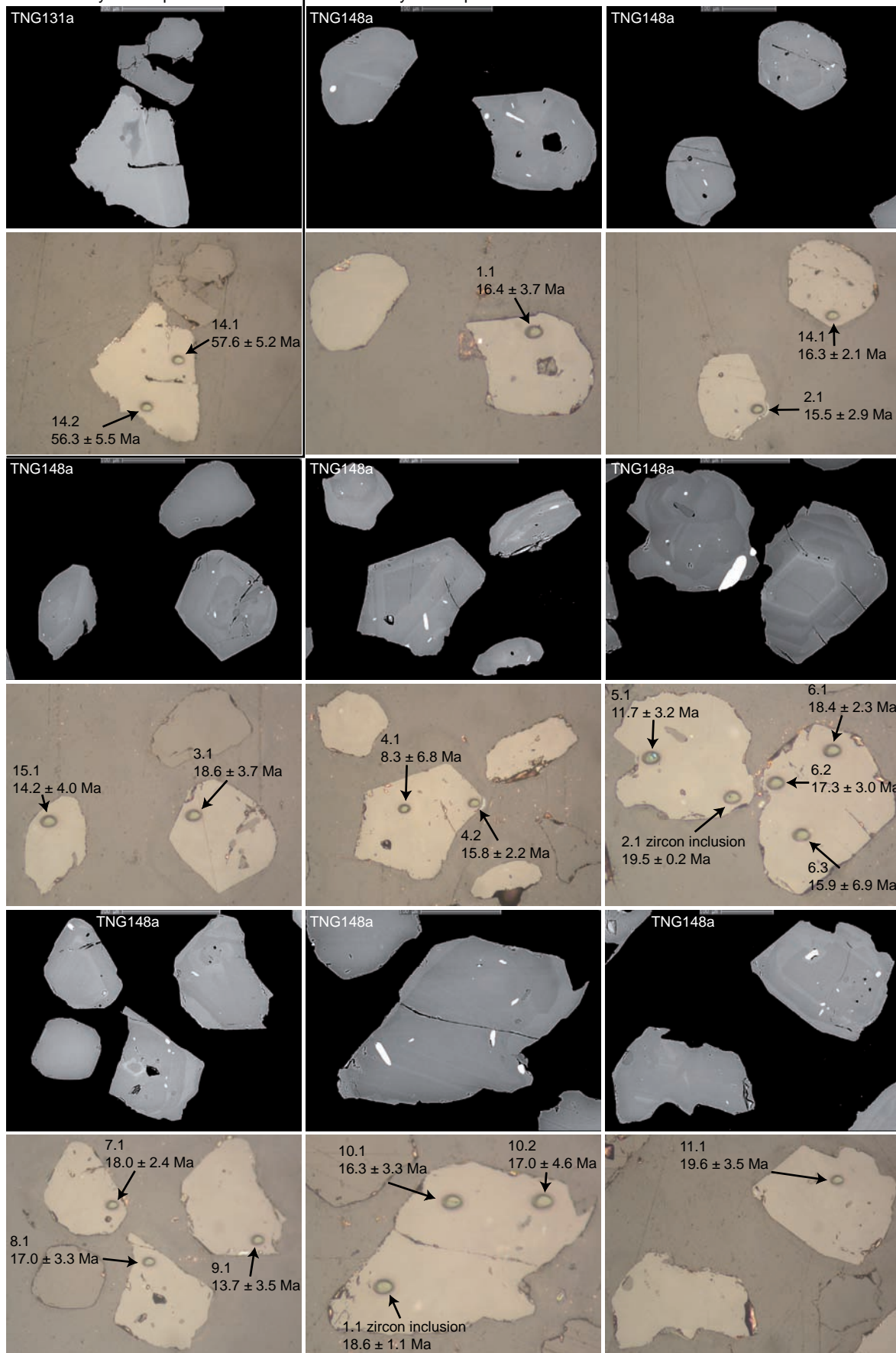


Titanite analysis sample TNG131a

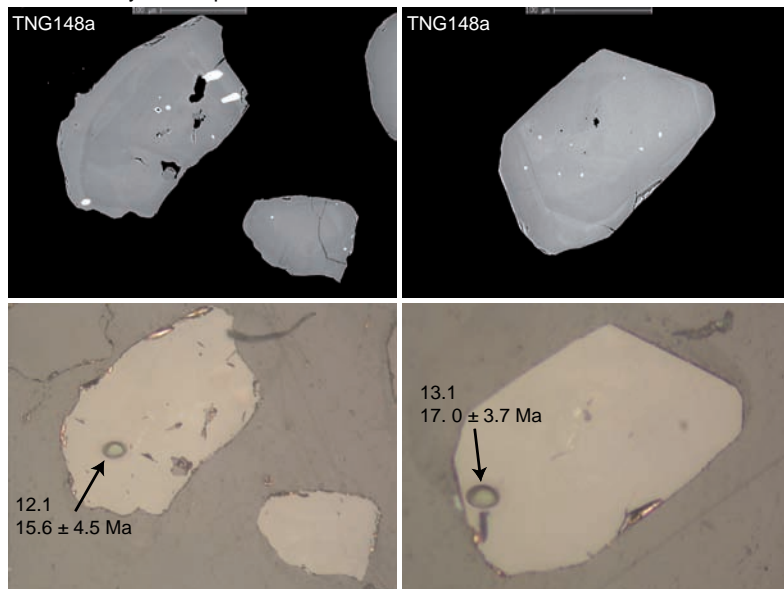




Titanite analysis sample TNG131a cont. Titanite analysis sample TNG148a



Titanite analysis sample TNG148a continued



Appendix C. Pressure estimates using Al in hornblende from electron microprobe analysis.

$$P \text{ (kbar)} = 4.76 \text{ Al tot} - 3.01$$

Tangtse area			Agham location		
Line analysis of 2 grains	Al tot	P(Kbar)	Line analysis of 1 grain	Al tot	P(Kbar)
TNG60D-hbl-L1--1	1.80	5.56	AGH24-HBL-L2-1-1	1.31	3.22 pressure estimate at rim
TNG60D-hbl-L1--2	1.79	5.52	AGH24-HBL-L2-2-1	1.35	3.41
TNG60D-hbl-L1--3	1.77	5.40	AGH24-HBL-L2-3-1	1.45	3.90
TNG60D-hbl-L1--4	1.85	5.81	AGH24-HBL-L2-4-1	1.39	3.58
TNG60D-hbl-L1--6	1.85	5.82	AGH24-HBL-L2-5-1	1.40	3.63
TNG60D-hbl-L1--7	1.88	5.93	AGH24-HBL-L2-6-1	1.39	3.62
TNG60D-hbl-L1--8	1.87	5.91	AGH24-HBL-L2-7-1	1.38	3.54
TNG60D-hbl-L1--9	1.87	5.88	AGH24-HBL-L2-8-1	1.37	3.53
TNG60D-hbl-L1--10	1.87	5.89	AGH24-HBL-L2-9-1	1.35	3.42
TNG60D-hbl-L1--11	1.87	5.88	AGH24-HBL-L2-10-1	1.37	3.50
TNG60D-hbl-L1--12	1.86	5.85	AGH24-HBL-L2-11-1	1.39	3.61
TNG60D-hbl-L1--13	1.90	6.02	AGH24-HBL-L2-12-1	1.38	3.55
TNG60D-hbl-L1--14	1.90	6.03	AGH24-HBL-L2-13-1	1.43	3.80
TNG60D-hbl-L1--15	1.92	6.11	AGH24-HBL-L2-14-1	1.46	3.95
TNG60D-hbl-L1--16	1.91	6.10	AGH24-HBL-L2-15-1	1.32	3.26 pressure estimate at rim
TNG60D-hbl-L1--17	1.92	6.12			
TNG60D-hbl-L1--18	1.92	6.12			
TNG60D-hbl-L1--19	1.91	6.06			
TNG60D-hbl-L1--20	1.90	6.04			
TNG60D-hbl-L2--2	1.78	5.46			
TNG60D-hbl-L2--3	1.82	5.64			
TNG60D-hbl-L2--4	1.78	5.47			
TNG60D-hbl-L2--5	1.78	5.46			
TNG60D-hbl-L2--6	1.85	5.77			
TNG60D-hbl-L2--7	1.84	5.75			
TNG60D-hbl-L2--8	1.85	5.81			
TNG60D-hbl-L2--9	1.86	5.84			
TNG60D-hbl-L2--10	1.82	5.67			
TNG60D-hbl-L2--11	1.82	5.65			
TNG60D-hbl-L2--12	1.80	5.53			
TNG60D-hbl-L2--13	1.80	5.57			
TNG60D-hbl-L2--14	1.83	5.70			
TNG60D-hbl-L2--15	1.84	5.75			
TNG60D-hbl-L2--16	1.80	5.53			
TNG60D-hbl-L2--17	1.83	5.70			
TNG60D-hbl-L2--18	1.82	5.63			
TNG60D-hbl-L2--19	1.81	5.60			
TNG60D-hbl-L2--20	1.81	5.60			
TNG60D-hbl-L2--21	1.81	5.60			
TNG60D-hbl-L2--22	1.76	5.38			
TNG60D-hbl-L2--23	1.77	5.40			
TNG60D-hbl-L2--24	1.74	5.26			
TNG60D-hbl-L2--25	1.77	5.42			

5.73 Average pressure

For complete data of all line analyses see electronic appendix on data CD.

Sample	TNG60C	TNG60C	TNG60C	TNG60D	TNG60D	TNG60D	TNG60D	TNG60D	TNG60D	TNG60D	TNG60D	TNG60D	TNG60D	TNG60D	TNG60D	TNG60D	TNG60D	TNG60D	TNG60D	TNG60D	TNG60D	TNG60D
Spot	HBL-1-1	HBL-10-1	HBL-11-1	HBL-14-1	HBL-3-1	HBL-3-1b	HBL-4-1	HBL-5-1	HBL-6-1	HBL-7-1	HBL-8-1	HBL-9-1	HBL-10-1	HBL-11-1	HBL-12-1	HBL-13-1	HBL-16-1	HBL-17-1	HBL-18-1	HBL-19-1	HBL-20-1	
Oxides																						
SiO ₂	40.59	40.39	40.12	39.72	43.17	42.98	43.20	42.65	43.50	42.71	42.73	43.35	43.23	43.59	38.59	41.59	41.15	41.67	41.85	42.25	42.79	
TiO ₂	0.84	0.83	0.76	0.81	0.69	0.67	0.55	0.63	0.61	0.69	0.70	0.64	0.67	0.63	0.47	0.54	0.53	0.58	0.63	0.63	0.60	
Al ₂ O ₃	11.58	11.40	11.47	11.63	10.23	10.16	10.09	10.50	10.33	10.43	10.45	10.41	10.19	10.62	9.40	10.23	9.72	10.49	10.29	10.23	10.42	
V ₂ O ₃	0.06	0.06	0.04	0.04	0.04	0.06	0.02	0.06	0.03	0.05	0.06	0.03	0.02	0.05	0.03	0.03	0.02	0.06	0.07	0.07	0.05	
Cr ₂ O ₃	0.00	0.00	0.00	0.03	0.05	0.00	0.07	0.07	0.04	0.03	0.03	0.01	0.04	0.03	0.05	0.10	0.02	0.05	0.03	0.12	0.04	
FeO	21.27	20.93	20.90	20.94	16.53	16.22	16.07	16.17	16.49	16.74	16.38	16.19	16.53	16.10	11.30	14.25	14.83	15.54	15.69	16.08	16.49	
MnO	0.31	0.35	0.34	0.34	0.44	0.42	0.44	0.41	0.40	0.44	0.44	0.48	0.36	0.46	0.25	0.38	0.38	0.43	0.39	0.39	0.40	
MgO	8.27	8.39	8.42	8.23	11.61	11.58	11.67	11.29	11.61	11.41	11.38	11.49	11.42	11.56	10.94	11.33	11.51	11.45	11.36	11.56	11.50	
CaO	11.35	11.29	11.27	11.37	11.62	11.84	11.56	11.70	11.80	11.81	11.75	11.67	11.77	11.63	9.42	11.07	11.16	11.37	11.50	11.91	12.00	
Na ₂ O	1.83	1.80	1.79	1.84	1.78	1.75	1.80	1.75	1.70	1.76	1.79	1.79	1.71	1.73	1.62	1.74	1.73	1.87	1.81	1.71	1.77	
K ₂ O	1.82	1.85	1.71	1.82	1.45	1.36	1.55	1.63	1.56	1.59	1.51	1.56	1.52	1.63	1.32	1.41	1.42	1.55	1.55	1.51	1.51	
NiO	0.03	0.00	0.05	0.00	0.05	0.00	0.09	0.01	0.05	0.03	0.04	0.07	0.01	0.07	0.00	0.05	0.07	0.00	0.07	0.03	0.07	
ZnO	0.08	0.00	0.08	0.02	0.02	0.06	0.00	0.04	0.02	0.08	0.07	0.06	0.01	0.08	0.03	0.06	0.08	0.01	0.07	0.10	0.06	
Nb ₂ O ₅	0.04	0.05	0.00	0.04	0.01	0.01	0.01	0.04	0.06	0.00	0.00	0.03	0.01	0.00	0.00	0.01	0.00	0.04	0.00	0.00	0.01	
Total	98.06	97.35	96.96	96.84	97.70	97.10	97.09	96.95	98.21	97.77	97.34	97.78	97.50	98.18	83.44	92.81	92.61	95.11	95.32	96.61	97.72	
Cations																						
Si	6.19	6.20	6.17	6.14	6.43	6.45	6.47	6.43	6.45	6.39	6.41	6.46	6.46	6.46	6.60	6.49	6.45	6.38	6.41	6.39	6.40	
Ti	0.10	0.10	0.09	0.09	0.08	0.08	0.06	0.07	0.07	0.08	0.08	0.07	0.08	0.07	0.06	0.06	0.06	0.07	0.07	0.07	0.07	
Al tot	2.08	2.06	2.08	2.12	1.79	1.80	1.78	1.87	1.81	1.84	1.85	1.83	1.80	1.85	1.89	1.88	1.80	1.89	1.86	1.83	1.84	
Fe tot	3.46	3.43	3.52	3.45	2.76	2.61	2.64	2.56	2.66	2.73	2.64	2.58	2.63	2.58	2.12	2.35	2.57	2.61	2.58	2.61	2.63	
Mn2+	0.04	0.05	0.04	0.05	0.06	0.05	0.06	0.05	0.05	0.06	0.06	0.06	0.05	0.06	0.04	0.05	0.05	0.06	0.05	0.05	0.05	
Mg	1.88	1.92	1.93	1.90	2.58	2.59	2.60	2.54	2.57	2.54	2.54	2.55	2.55	2.55	2.79	2.64	2.69	2.61	2.59	2.61	2.57	
Ca	1.85	1.86	1.86	1.88	1.85	1.90	1.85	1.89	1.88	1.89	1.89	1.86	1.89	1.85	1.73	1.85	1.87	1.87	1.89	1.93	1.92	
Na	0.54	0.54	0.53	0.55	0.51	0.51	0.52	0.51	0.49	0.51	0.52	0.52	0.50	0.50	0.54	0.53	0.53	0.55	0.54	0.50	0.51	
K	0.35	0.36	0.34	0.36	0.28	0.26	0.30	0.31	0.30	0.30	0.29	0.30	0.29	0.31	0.29	0.28	0.29	0.30	0.30	0.29	0.29	
Ni	0.00	0.00	0.01	0.00	0.01	0.00	0.01	0.00	0.01	0.00	0.01	0.01	0.00	0.01	0.00	0.01	0.01	0.00	0.01	0.00	0.01	
xMg	0.35	0.36	0.35	0.35	0.48	0.50	0.50	0.50	0.49	0.48	0.49	0.50	0.49	0.50	0.57	0.53	0.51	0.50	0.50	0.50	0.49	

Oxides in weight %. Kations in atoms per formula unit (a.p.f.u.) recalculated on the basis of 23 oxygen atoms.

Appendix C. Electron microprobe data of hornblende

Sample	TNG60D	TNG169B	TNG169B	TNG169B	TNG169B	TNG169A	TNG169A	TNG169A	TNG169A	TNG203b	TNG203b	TNG203b	TNG203b	TNG203b	TNG203a2	TNG203a2	TNG203a2
Spot	HL-23-1	HL-2-1	HL-4-1	HL-5-1	HL-9-1	HL-15-1	HL-16-1	HL-26-1	HL-5-1	HL-9-1	HL-10-1	HL-17-1	HL-19-1	HL-3-1	HL-9-1	HL-12-1	HL-15-1
Oxides																	
SiO ₂	40.95	39.58	40.17	39.68	40.17	40.37	40.03	40.41	43.24	45.02	42.01	45.18	43.88	42.94	42.80	42.58	42.84
TiO ₂	0.54	1.41	1.45	1.45	1.42	1.42	1.46	1.41	1.07	0.92	1.18	0.84	1.13	0.76	0.77	0.78	0.80
Al ₂ O ₃	10.05	12.70	12.49	12.55	12.63	12.52	12.61	11.85	11.10	9.61	11.69	9.36	11.24	10.32	10.45	10.61	10.70
V ₂ O ₃	0.07	0.01	0.08	0.05	0.07	0.01	0.04	0.03	0.05	0.04	0.06	0.03	0.08	0.08	0.05	0.04	0.08
Cr ₂ O ₃	0.06	0.00	0.00	0.01	0.00	0.00	0.01	0.01	0.06	0.03	0.03	0.03	0.07	0.03	0.03	0.05	0.13
FeO	14.40	20.13	20.06	20.07	19.98	20.31	20.17	20.23	15.42	15.19	16.97	14.89	14.23	18.07	17.75	18.01	17.23
MnO	0.41	0.80	0.82	0.69	0.68	0.74	0.70	0.77	0.52	0.58	0.57	0.52	0.45	0.38	0.42	0.37	0.41
MgO	11.48	8.10	7.90	7.95	8.03	7.92	7.91	8.24	11.50	12.34	10.40	12.70	12.23	10.53	10.63	10.55	10.76
CaO	10.91	11.33	11.23	11.39	11.24	11.20	11.48	11.45	11.58	12.00	11.72	11.88	11.89	11.68	11.47	11.63	11.60
Na ₂ O	1.78	1.42	1.47	1.44	1.48	1.51	1.40	1.45	1.47	1.20	1.49	1.33	1.45	1.76	1.83	1.76	1.68
K ₂ O	1.42	1.84	1.87	1.79	1.86	1.83	1.76	1.58	1.36	1.08	1.50	1.12	1.35	1.42	1.52	1.62	1.58
NiO	0.10	0.00	0.00	0.00	0.03	0.01	0.00	0.00	0.04	0.03	0.00	0.06	0.03	0.04	0.04	0.07	0.03
ZnO	0.11	0.00	0.00	0.03	0.08	0.05	0.03	0.04	0.06	0.00	0.00	0.07	0.10	0.01	0.00	0.07	0.01
Nb ₂ O ₅	0.00	0.06	0.01	0.00	0.00	0.00	0.01	0.03	0.02	0.00	0.00	0.03	0.00	0.01	0.09	0.04	0.04
Total	92.29	97.39	97.57	97.10	97.66	97.90	97.61	97.50	97.51	98.05	97.63	98.05	98.12	98.02	97.85	98.17	97.89
Kations																	
Si	6.43	6.04	6.13	6.08	6.12	6.13	6.11	6.16	6.41	6.60	6.29	6.62	6.44	6.43	6.41	6.37	6.40
Ti	0.06	0.16	0.17	0.17	0.16	0.16	0.17	0.16	0.12	0.10	0.13	0.09	0.13	0.09	0.09	0.09	0.09
Al tot	1.86	2.28	2.25	2.27	2.27	2.24	2.27	2.13	1.94	1.66	2.06	1.62	1.94	1.82	1.84	1.87	1.88
Fe tot	2.55	3.40	3.26	3.29	3.26	3.31	3.26	3.33	2.55	2.48	2.74	2.47	2.26	2.89	2.88	2.91	2.77
Mn2+	0.06	0.10	0.11	0.09	0.09	0.10	0.09	0.10	0.07	0.07	0.07	0.07	0.06	0.05	0.05	0.05	0.05
Mg	2.69	1.84	1.80	1.82	1.82	1.79	1.80	1.87	2.54	2.70	2.32	2.77	2.68	2.35	2.37	2.35	2.40
Ca	1.84	1.85	1.84	1.87	1.83	1.82	1.88	1.87	1.84	1.89	1.88	1.86	1.87	1.87	1.84	1.86	1.86
Na	0.54	0.42	0.44	0.43	0.44	0.44	0.41	0.43	0.42	0.34	0.43	0.38	0.41	0.51	0.53	0.51	0.49
K	0.28	0.36	0.36	0.35	0.36	0.35	0.34	0.31	0.26	0.20	0.29	0.21	0.25	0.27	0.29	0.31	0.30
Ni	0.01	0.00	0.00	0.00	0.00	0.00	0.00	0.00	0.01	0.00	0.00	0.01	0.00	0.01	0.01	0.01	0.00
xMg	0.51	0.35	0.36	0.36	0.36	0.35	0.36	0.36	0.50	0.52	0.46	0.53	0.54	0.45	0.45	0.45	0.46

Oxides in weight %. Kations in atoms per formula unit (a.p.f.u.) recalculated on the basis of 23 oxygen atoms.

Sample	TNG165																			
	TNG165 HBL-1-1	TNG165 HBL-2-1	TNG165 HBL-3-1	TNG165 HBL-4-1	TNG165 HBL-5-1	TNG165 HBL-6-1	TNG165 HBL-7-1	TNG165 HBL-14-1	TNG165 HBL-16-1	TNG165 HBL-17-1	TNG165 HBL-29-1	TNG165 HBL-34-1	HBL1-3-1	HBL2-4-1	HBL3-5-1	HBL4-6-1	HBL5-9-1	AGH23A1	AGH23A1	AGH24
Spot	HBL-1-1	HBL-2-1	HBL-3-1	HBL-4-1	HBL-5-1	HBL-6-1	HBL-7-1	HBL-14-1	HBL-16-1	HBL-17-1	HBL-29-1	HBL-34-1	HBL1-3-1	HBL2-4-1	HBL3-5-1	HBL4-6-1	HBL5-9-1	AGH23A1	AGH23A1	AGH24
Oxides																				
SiO ₂	42.12	42.65	42.51	45.78	43.79	48.90	44.02	42.72	48.13	44.67	48.09	44.18	45.68	48.14	46.26	49.06	47.12	45.05	45.31	46.02
TiO ₂	0.82	0.82	0.78	0.66	0.76	0.35	0.75	0.81	0.44	0.69	0.46	0.76	0.86	0.58	0.75	0.51	0.71	0.87	1.71	0.86
Al ₂ O ₃	11.58	11.44	11.72	8.46	9.96	6.27	10.10	10.73	6.65	9.34	6.74	10.06	7.69	6.08	7.48	5.40	6.68	8.17	7.76	7.16
V ₂ O ₃	0.01	0.05	0.01	0.04	0.05	0.02	0.02	0.04	0.03	0.02	0.00	0.05	0.05	0.02	0.02	0.01	0.01	0.01	0.05	0.06
Cr ₂ O ₃	0.27	0.06	0.06	0.11	0.05	0.17	0.09	0.06	0.14	0.13	0.14	0.13	0.02	0.03	0.03	0.05	0.03	0.04	0.00	0.01
FeO	15.97	16.21	16.27	15.29	15.37	13.23	14.77	16.18	13.67	15.40	13.41	15.07	15.81	14.81	15.79	14.29	15.16	16.40	18.55	19.90
MnO	0.36	0.43	0.42	0.39	0.39	0.38	0.38	0.35	0.32	0.36	0.40	0.33	0.41	0.43	0.36	0.37	0.43	0.37	0.37	0.57
MgO	11.25	11.18	11.02	12.83	12.18	14.65	12.38	11.48	14.17	12.60	14.44	12.37	12.75	14.09	13.06	14.43	13.55	12.41	10.90	10.76
CaO	11.63	11.71	11.76	11.79	11.75	12.04	11.69	11.74	12.10	11.96	11.96	11.84	11.65	11.93	11.81	11.91	11.96	11.73	11.33	10.93
Na ₂ O	1.83	1.84	1.90	1.61	1.82	1.37	1.81	1.81	1.42	1.64	1.39	1.82	1.81	1.49	1.70	1.50	1.67	1.81	1.33	1.20
K ₂ O	1.57	1.63	1.60	1.10	1.43	0.70	1.40	1.51	0.81	1.25	0.82	1.38	1.11	0.82	1.04	0.67	0.87	1.08	0.96	0.81
NiO	0.08	0.07	0.06	0.09	0.07	0.07	0.10	0.08	0.07	0.07	0.08	0.08	0.02	0.05	0.02	0.00	0.01	0.00	0.02	0.00
ZnO	0.00	0.01	0.16	0.06	0.10	0.09	0.03	0.02	0.04	0.03	0.00	0.08	0.02	0.16	0.05	0.01	0.03	0.03	0.00	0.06
Nb ₂ O ₅	0.02	0.00	0.00	0.01	0.06	0.00	0.05	0.06	0.01	0.04	0.00	0.00	0.13	0.09	0.07	0.00	0.00	0.00	0.00	0.00
Total	97.51	98.10	98.28	98.22	97.76	98.24	97.60	97.61	97.99	98.20	97.94	98.15	98.00	98.71	98.45	98.21	98.22	97.99	98.30	98.33
Kations																				
Si	6.29	6.34	6.32	6.71	6.50	7.07	6.52	6.38	7.01	6.58	6.98	6.52	6.75	6.99	6.78	7.12	6.90	6.66	6.71	6.78
Ti	0.09	0.09	0.09	0.07	0.08	0.04	0.08	0.09	0.05	0.08	0.05	0.08	0.10	0.06	0.08	0.06	0.08	0.10	0.19	0.10
Al tot	2.04	2.01	2.06	1.46	1.74	1.07	1.76	1.89	1.14	1.62	1.15	1.75	1.34	1.04	1.29	0.92	1.15	1.43	1.35	1.24
Fe tot	2.61	2.57	2.54	2.46	2.45	2.06	2.36	2.61	2.07	2.48	2.15	2.36	2.51	2.37	2.52	2.21	2.36	2.64	3.00	3.52
Mn2+	0.05	0.05	0.05	0.05	0.05	0.05	0.05	0.05	0.04	0.05	0.05	0.04	0.05	0.05	0.05	0.05	0.05	0.05	0.05	0.07
Mg	2.50	2.48	2.44	2.81	2.70	3.16	2.73	2.56	3.07	2.76	3.12	2.72	2.81	3.05	2.86	3.12	2.96	2.74	2.40	2.36
Ca	1.86	1.87	1.87	1.85	1.87	1.86	1.86	1.88	1.89	1.89	1.86	1.87	1.85	1.86	1.86	1.85	1.88	1.86	1.80	1.73
Na	0.53	0.53	0.55	0.46	0.52	0.38	0.52	0.53	0.40	0.47	0.39	0.52	0.52	0.42	0.48	0.42	0.47	0.52	0.38	0.34
K	0.30	0.31	0.30	0.21	0.27	0.13	0.27	0.29	0.15	0.24	0.15	0.26	0.21	0.15	0.20	0.13	0.16	0.21	0.18	0.15
Ni	0.01	0.01	0.01	0.01	0.01	0.01	0.01	0.01	0.01	0.01	0.01	0.01	0.00	0.01	0.00	0.00	0.00	0.00	0.00	0.00
xMg	0.49	0.49	0.49	0.53	0.52	0.60	0.54	0.49	0.60	0.53	0.59	0.54	0.53	0.56	0.53	0.59	0.56	0.51	0.45	0.40

Oxides in weight %. Kations in atoms per formula unit (a.p.f.u.) recalculated on the basis of 23 oxygen atoms.

[illegible]

Oxides in weight %. Kations in atoms per formula unit (a.p.f.u.) recalculated on the basis of 23 oxygen atoms.

[illegible]
$$\text{Other} = \text{Cr}_2\text{O}_3 + \text{V}_2\text{O}_3 + \text{ZnO} + \text{NiO} + \text{Nb}_2\text{O}_5$$

Appendix E. Hornblende trace element analysis by Laser Ablation ICP-MS

Sample Rock type	Hbl-Bt-granodiorite															Melanocratic part in diatexite				
	TNG591	TNG592	TNG593	TNG594	TNG595	TNG598	TNG599	TNG5911	TNG5912	TNG5914	TNG5915	TNG5916	TNG5917	TNG5918	TNG169A13	TNG169A14	TNG169A15	TNG169A16		
Sc	74.99	74.18	62.91	70.96	75.50	71.32	67.03	87.80	69.15	82.04	73.87	63.36	66.93	70.93	na	na	na	na		
Ti	5441.79	5823.17	5700.57	5621.36	5843.92	5821.79	5799.04	5255.17	5829.09	6245.60	5603.06	6121.83	5977.50	5908.84	na	na	na	na		
V	383.82	428.64	419.09	425.99	419.45	418.50	421.06	494.88	504.75	466.36	424.92	446.48	478.94	464.47	na	na	na	na		
Cr	426.03	143.15	41.01	158.36	113.04	48.04	56.70	130.77	89.10	103.71	93.82	52.52	304.89	97.39	na	na	na	na		
Mn	3963.11	4211.26	4332.49	4144.21	4118.09	4030.89	4382.44	4353.70	4291.90	4166.68	4157.32	4339.61	4359.46	4167.46	4169.49	3802.76	3810.87	3829.85		
Co	46.54	49.29	50.41	50.24	47.54	47.94	50.28	52.80	52.70	48.70	49.45	50.21	51.40	47.96	na	na	na	na		
Ni	36.62	40.90	41.75	42.48	38.11	39.61	58.06	43.73	43.30	39.25	40.08	41.23	41.56	39.27	na	na	na	na		
Cu	2.66	bd	1.53	4.15	bd	1.20	3.36	4.17	9.56	bd	15.91	2.51	bd	3.34	na	na	na	na		
Zn	262.85	350.72	381.98	362.14	346.20	358.99	390.52	403.79	393.63	348.48	346.76	394.05	403.10	378.77	na	na	na	na		
Ga	34.03	35.79	37.86	36.27	34.85	35.17	37.26	38.45	41.59	36.71	36.29	40.26	40.53	37.68	na	na	na	na		
Rb	11.82	12.00	12.93	12.07	12.20	10.09	13.24	13.81	11.88	12.75	29.38	13.38	12.02	12.73	6.09	4.78	4.78	4.31		
Sr	33.17	33.25	36.58	34.11	37.37	34.37	36.66	32.94	36.41	38.29	65.61	39.37	37.39	36.30	51.68	45.19	45.72	36.92		
Y	14.65	6.99	15.00	9.53	16.93	18.90	14.47	16.05	17.48	16.23	19.67	18.12	16.48	13.35	27.59	31.60	26.23	23.25		
Zr	16.71	14.92	16.93	14.53	19.40	20.66	16.75	15.83	18.22	18.64	20.14	18.96	17.46	16.21	na	na	na	na		
Nb	6.66	4.82	7.20	5.62	7.42	8.25	7.38	8.30	9.06	8.12	8.47	9.51	8.49	7.13	22.10	20.68	16.69	16.75		
Ba	12.31	10.97	13.07	11.24	13.20	13.07	13.84	11.92	17.21	14.37	197.07	15.97	13.82	12.79	32.25	22.81	23.42	14.39		
La	0.87	0.22	0.62	0.44	0.71	1.70	0.60	1.91	1.69	0.97	1.95	1.12	1.38	0.94	2.08	2.07	2.16	1.98		
Ce	3.35	0.88	2.87	1.88	2.97	7.40	2.83	9.79	8.40	4.31	8.97	5.27	6.73	4.34	8.78	9.17	9.08	8.80		
Pr	0.61	0.13	0.55	0.29	0.57	1.36	0.54	1.65	1.45	0.74	1.57	0.96	1.13	0.69	1.54	1.71	1.69	1.49		
Nd	3.37	0.72	3.45	1.63	3.42	7.76	3.15	8.87	7.76	4.65	8.85	5.59	6.31	3.55	7.90	9.98	9.36	7.98		
Sm	1.37	0.27	1.60	0.63	1.56	2.77	1.44	2.94	2.66	1.70	2.81	2.21	2.32	1.25	2.57	3.32	2.96	2.44		
Eu	0.93	0.31	0.91	0.55	0.88	1.33	0.85	1.36	1.30	0.91	1.34	1.14	1.21	0.86	1.03	1.07	1.00	0.82		
Gd	1.88	0.46	2.13	0.90	2.15	3.14	1.97	2.89	2.92	2.04	3.26	2.59	2.45	1.41	3.54	4.18	3.60	2.87		
Tb	0.34	0.10	0.37	0.18	0.39	0.50	0.34	0.45	0.48	0.40	0.51	0.45	0.42	0.27	0.54	0.65	0.56	0.45		
Dy	2.32	0.83	2.48	1.36	2.66	3.17	2.41	2.63	2.94	2.52	3.16	2.85	2.66	1.89	4.20	4.90	4.10	3.44		
Ho	0.49	0.20	0.49	0.29	0.55	0.63	0.47	0.49	0.55	0.53	0.64	0.56	0.52	0.39	0.91	1.05	0.88	0.74		
Er	1.52	0.80	1.53	1.04	1.77	1.86	1.43	1.51	1.66	1.68	1.87	1.72	1.65	1.44	2.92	3.42	2.82	2.47		
Tm	0.22	0.15	0.22	0.16	0.27	0.27	0.21	0.21	0.23	0.28	0.26	0.25	0.25	0.22	0.43	0.50	0.41	0.36		
Yb	1.71	1.31	1.57	1.37	1.99	1.92	1.67	1.46	1.63	2.06	1.92	1.89	1.77	1.81	3.39	3.85	3.14	3.14		
Lu	0.32	0.29	0.28	0.28	0.36	0.37	0.31	0.28	0.30	0.38	0.36	0.36	0.35	0.32	0.54	0.64	0.51	0.51		
Hf	1.12	0.99	1.16	0.97	1.19	1.42	1.18	1.02	1.03	1.10	1.15	1.30	1.04	0.99	1.18	1.22	1.23	1.11		
Ta	0.08	0.03	0.07	0.05	0.07	0.09	0.08	0.08	0.09	0.10	0.08	0.10	0.07	0.06	0.32	0.33	0.30	0.25		
Pb	4.51	4.72	5.17	4.92	4.92	4.34	5.49	4.90	5.80	5.41	9.89	5.84	5.55	5.38	1.39	1.03	1.07	0.96		
Th	0.06	0.00	0.01	0.76	0.01	0.08	0.32	0.16	0.68	0.03	2.03	0.20	0.18	0.19	0.01	0.01	0.01	0.01		
U	0.06	0.08	0.16	0.16	0.09	0.04	0.16	0.15	0.12	0.13	0.27	0.18	0.13	0.14	0.15	0.06	0.09	0.07		
La _N /Y _N	0.34	0.11	0.26	0.21	0.24	0.60	0.24	0.88	0.70	0.32	0.69	0.40	0.53	0.35	0.41	0.36	0.46	0.42		
La _N /Sm _N	0.40	0.51	0.24	0.44	0.29	0.39	0.26	0.41	0.40	0.36	0.44	0.32	0.37	0.47	0.51	0.39	0.46	0.51		
Gd _N /Y _N	0.89	0.28	1.09	0.53	0.87	1.32	0.95	1.60	1.45	0.80	1.37	1.11	1.12	0.63	0.84	0.87	0.93	0.74		
Eu/Eu*	1.78	2.67	1.51	2.26	1.48	1.38	1.55	1.42	1.43	1.49	1.35	1.46	1.56	1.97	1.04	0.88	0.94	0.95		
Sum REE	19.30	6.66	19.07	11.00	20.24	34.18	18.23	36.43	33.97	23.17	37.47	26.97	29.16	19.37	40.38	46.52	42.28	37.49		

Appendix E. Hornblende trace element analysis by Laser Ablation ICP-MS

Sample	Melanocratic part in diatexite										Leucocratic part in diatexite									
Rock type	TNG169A17	TNG169A18	TNG169A21	TNG169A1	TNG169A2	TNG169A3	TNG169A4	TNG169A5	TNG169A6	TNG169A7	TNG169A8	TNG169A9	TNG169A10	TNG169B1	TNG169B2	TNG169B3	TNG169B4	TNG169B5		
Sc	na	na	na	na	na	na	na	na	na	na	na	na	na	130.54	126.46	127.48	122.71	105.00		
Ti	na	na	na	na	na	na	na	na	na	na	na	na	na	8651.66	8824.42	7299.19	8607.20	8466.00		
V	na	na	na	na	na	na	na	na	na	na	na	na	na	283.31	278.03	300.79	266.02	264.26		
Cr	na	na	na	na	na	na	na	na	na	na	na	na	na	42.79	29.11	33.33	30.62	27.19		
Mn	3702.92	3795.70	3620.97	2686.27	3357.84	3133.74	3450.80	3407.95	3312.82	2960.03	3314.17	3175.63	3074.57	5695.66	5211.49	5700.92	5387.45	5203.01		
Co	na	na	na	na	na	na	na	na	na	na	na	na	na	34.32	32.96	35.03	32.49	33.14		
Ni	na	na	na	na	na	na	na	na	na	na	na	na	na	19.44	17.90	19.13	18.56	19.03		
Cu	na	na	na	na	na	na	na	na	na	na	na	na	na	na	na	na	na	na		
Zn	na	na	na	na	na	na	na	na	na	na	na	na	na	346.20	423.96	482.89	452.24	475.72		
Ga	na	na	na	na	na	na	na	na	na	na	na	na	na	40.93	39.77	41.00	40.27	39.62		
Rb	4.13	4.41	6.78	5.85	3.81	4.36	3.86	3.91	3.80	3.95	4.48	3.95	3.74	11.23	9.32	9.25	11.04	9.20		
Sr	33.22	43.41	47.29	55.66	36.05	34.97	40.31	35.40	35.19	39.13	41.78	39.68	40.86	79.23	82.74	64.07	76.90	72.53		
Y	23.15	29.55	11.49	27.78	22.66	12.20	23.71	22.15	30.80	22.93	22.52	25.30	28.99	156.21	78.58	115.78	122.21	102.32		
Zr	na	na	na	na	na	na	na	na	na	na	na	na	na	31.91	31.72	24.48	28.72	24.28		
Nb	15.79	20.08	3.60	11.87	16.46	3.36	18.28	16.39	18.13	15.96	17.90	16.96	18.10	64.70	44.00	50.09	57.73	53.91		
Ba	17.74	22.39	48.07	44.66	13.75	39.72	19.63	13.20	13.11	21.28	23.38	20.23	20.44	63.31	96.04	63.00	64.05	74.48		
La	1.95	1.80	2.44	6.67	2.02	1.93	1.74	2.01	2.01	1.85	2.01	1.90	1.80	2.15	1.44	1.77	2.10	1.53		
Ce	8.39	7.89	10.37	21.77	8.27	6.80	7.69	8.23	7.94	7.35	7.68	6.92	7.27	8.67	5.04	7.88	8.30	6.22		
Pr	1.50	1.49	1.63	3.75	1.51	1.21	1.44	1.43	1.52	1.33	1.26	1.31	1.50	1.83	0.84	1.62	1.71	1.20		
Nd	8.30	8.27	8.47	19.71	7.94	6.25	8.18	7.33	8.21	7.35	6.75	6.87	8.90	12.20	4.45	10.02	10.60	7.54		
Sm	2.56	2.74	2.16	5.97	2.37	1.78	2.55	2.23	2.64	2.21	2.19	2.25	2.92	7.61	2.43	5.68	6.35	4.30		
Eu	0.87	1.03	0.80	1.60	0.77	0.63	0.89	0.77	0.83	0.87	0.76	0.81	0.96	2.55	1.87	2.11	2.35	1.99		
Gd	3.23	3.47	2.31	6.07	2.76	2.13	2.94	2.75	3.36	2.80	2.64	2.98	3.81	15.64	4.70	10.92	12.87	8.33		
Tb	0.51	0.57	0.31	0.91	0.48	0.34	0.49	0.45	0.59	0.47	0.47	0.51	0.65	3.44	1.16	2.48	2.82	1.96		
Dy	3.51	4.38	2.15	6.15	3.46	2.16	3.53	3.33	4.38	3.57	3.40	3.68	4.59	25.34	10.15	19.08	20.76	15.51		
Ho	0.75	0.93	0.41	1.16	0.76	0.46	0.79	0.71	1.00	0.75	0.77	0.83	0.98	5.48	2.58	4.12	4.45	3.57		
Er	2.49	3.08	1.27	3.13	2.35	1.33	2.37	2.23	3.32	2.42	2.44	2.57	3.08	17.61	9.72	13.27	13.43	12.13		
Tm	0.36	0.45	0.18	0.43	0.37	0.19	0.40	0.36	0.54	0.39	0.38	0.43	0.48	2.42	1.67	1.77	1.79	1.75		
Yb	2.84	3.55	1.40	2.92	2.95	1.47	3.02	2.90	4.11	2.96	3.07	3.47	3.67	16.11	13.31	11.99	11.04	11.91		
Lu	0.48	0.58	0.21	0.40	0.49	0.24	0.53	0.50	0.67	0.46	0.50	0.56	0.61	2.38	2.16	1.73	1.66	1.78		
Hf	1.15	1.08	1.12	1.10	1.03	0.94	0.95	1.02	1.15	0.89	1.03	1.05	1.22	2.24	1.62	1.70	1.92	1.43		
Ta	0.26	0.35	0.07	0.72	0.27	0.04	0.29	0.26	0.37	0.27	0.26	0.27	0.30	1.90	0.83	1.66	1.69	1.62		
Pb	0.92	0.99	1.13	1.91	1.97	2.01	2.07	1.93	1.93	2.07	2.64	2.16	1.94	3.40	3.21	3.07	3.58	3.27		
Th	0.01	0.01	0.01	0.38	0.01	0.01	0.01	0.01	0.02	0.01	0.02	0.01	0.01	0.03	0.01	0.01	0.03	0.01		
U	0.04	0.07	0.04	0.72	0.06	0.02	0.08	0.06	0.06	0.08	0.10	0.08	0.08	0.12	0.12	0.06	0.18	0.07		
La _N /Yb _N	0.46	0.34	1.17	1.54	0.46	0.89	0.39	0.47	0.33	0.42	0.44	0.37	0.33	0.09	0.07	0.10	0.13	0.09		
La _N /Sm _N	0.48	0.41	0.71	0.70	0.54	0.68	0.43	0.57	0.48	0.53	0.58	0.53	0.39	0.18	0.37	0.20	0.21	0.22		
Gd _N /Yb _N	0.92	0.79	1.33	1.68	0.75	1.17	0.79	0.77	0.66	0.76	0.69	0.69	0.84	0.78	0.28	0.73	0.94	0.56		
Eu/Eu*	0.93	1.03	1.10	0.81	0.93	0.99	1.00	0.95	0.85	1.07	0.96	0.96	0.88	0.71	1.69	0.82	0.80	1.02		
Sum REE	37.72	40.23	34.11	80.65	36.50	26.91	36.56	35.22	41.13	34.79	34.31	35.08	41.21	123.44	61.52	94.43	100.23	79.71		

Appendix E. Hornblende trace element analysis by Laser Ablation ICP-MS

Sample	TNG16986	TNG169B7	TNG169B8	TNG169B9	TNG169B10	TNG169B12	TNG169B14	TNG169B15	TNG204c1	TNG204c2	TNG204c3	TNG204c4	TNG204c5	TNG204c6	TNG204c7	TNG204c8	TNG204c9	TNG204c10
Rock type	Leucocratic part in diatexite								Patchy leucosome in diorite									
Sc	120.06	106.96	104.42	107.68	101.02	135.60	103.37	101.74	61.98	75.72	81.19	81.62	58.81	64.31	80.43	76.48	67.90	78.78
Ti	8508.08	7879.11	8427.26	7752.23	8239.02	7354.73	8480.98	8426.04	6941.55	7337.03	7112.92	7039.02	7031.01	6687.94	6850.43	6782.30	7441.20	7195.97
V	260.65	266.76	277.29	262.22	261.36	307.16	263.79	265.97	596.26	520.39	495.99	426.38	611.92	554.62	470.10	391.92	454.72	589.58
Cr	32.30	28.56	29.41	30.85	32.20	47.43	28.12	22.57	134.86	82.19	142.94	144.30	157.41	135.37	134.95	120.85	178.23	150.65
Mn	5193.57	5086.71	5459.02	5232.21	5125.03	5167.00	5072.62	5371.22	2956.62	2960.86	2899.94	2906.17	2951.13	2902.47	2772.28	2802.26	2845.43	2879.72
Co	31.77	31.48	32.71	31.87	31.80	32.45	32.48	33.09	54.60	53.60	53.05	52.10	52.77	52.87	51.16	49.38	54.31	53.25
Ni	17.53	17.82	18.82	17.02	17.20	17.00	17.63	17.77	122.83	114.18	119.77	91.54	130.98	112.84	102.35	107.44	126.13	128.63
Cu	na	na	na	na	na	na	na	na	2.68	1.48	2.65	1.70	1.76	2.54	1.40	1.97	3.94	2.34
Zn	444.43	454.60	498.84	464.15	476.68	503.70	477.60	478.03	374.15	408.58	385.57	426.22	405.97	420.65	379.89	372.68	420.12	405.76
Ga	39.05	37.98	39.80	38.03	38.05	40.73	40.24	39.89	42.76	40.75	39.11	38.65	40.73	39.97	37.36	34.93	38.25	39.51
Rb	10.96	8.80	10.51	10.10	9.16	10.51	9.59	10.10	12.52	10.85	13.00	11.00	11.16	13.17	14.15	14.59	11.73	12.60
Sr	74.74	58.61	77.42	78.06	68.34	72.82	65.67	76.77	77.54	76.42	70.23	64.46	68.01	67.24	64.43	67.18	72.14	66.56
Y	127.66	102.29	121.07	131.20	130.34	121.44	99.35	127.62	17.48	28.12	21.20	25.50	19.27	18.03	23.42	23.61	17.93	18.23
Zr	29.27	21.64	23.58	25.78	24.74	21.37	23.63	25.77	28.36	32.45	31.69	27.27	27.03	26.95	36.26	37.20	28.63	28.12
Nb	57.92	57.39	64.92	65.88	63.61	60.30	56.95	68.13	5.26	8.35	8.84	10.02	5.06	8.92	9.58	8.03	7.37	5.42
Ba	64.98	90.71	70.86	72.96	65.94	73.48	89.37	70.34	164.70	128.15	93.53	98.32	128.81	92.64	94.04	123.81	112.95	101.52
La	1.97	1.34	1.96	2.17	1.80	1.62	1.58	2.16	0.69	1.43	0.78	1.30	0.87	0.76	1.04	1.27	0.84	0.94
Ce	8.34	6.47	9.04	9.11	8.17	7.76	6.99	9.60	2.65	6.20	2.88	6.21	3.52	3.19	3.94	4.92	3.39	3.77
Pr	1.70	1.28	1.73	1.86	1.67	1.56	1.29	1.89	0.47	1.28	0.56	1.27	0.67	0.62	0.78	0.98	0.63	0.69
Nd	11.02	8.13	10.01	11.07	10.41	9.71	7.18	11.39	2.87	8.33	3.41	7.82	4.13	3.49	4.89	6.37	3.91	4.27
Sm	6.93	4.55	5.44	6.03	5.98	5.68	4.09	6.60	1.37	3.78	1.78	3.56	1.91	1.75	2.27	2.93	1.78	1.95
Eu	2.37	1.83	2.22	2.24	2.17	2.03	2.03	2.34	0.45	1.17	0.58	1.18	0.61	0.57	0.72	0.90	0.57	0.63
Gd	13.57	7.88	10.18	11.35	10.97	11.05	7.05	11.20	2.01	4.75	2.69	4.58	2.59	2.33	3.18	3.78	2.44	2.71
Tb	3.05	1.83	2.37	2.55	2.56	2.49	1.69	2.51	0.40	0.83	0.49	0.76	0.49	0.43	0.60	0.64	0.43	0.48
Dy	22.09	14.60	18.68	19.89	20.21	19.10	14.12	19.55	2.72	4.92	3.31	4.72	3.01	2.89	3.81	4.13	2.89	3.01
Ho	4.64	3.43	4.34	4.59	4.57	4.16	3.32	4.33	0.60	0.96	0.71	0.89	0.65	0.62	0.79	0.83	0.61	0.63
Er	14.45	11.69	14.00	15.10	15.02	13.45	11.96	14.39	2.00	2.72	2.26	2.59	1.96	1.94	2.44	2.36	1.92	1.89
Tm	1.90	1.76	1.99	2.19	2.10	1.79	1.77	1.94	0.30	0.39	0.32	0.34	0.30	0.27	0.35	0.34	0.29	0.27
Yb	12.68	11.61	14.16	14.38	13.46	11.36	12.68	13.75	2.33	2.47	2.32	2.24	2.15	2.08	2.43	2.08	2.12	1.89
Hf	1.82	1.24	1.91	2.00	2.01	1.48	1.79	1.93	0.38	0.37	0.37	0.34	0.33	0.34	0.38	0.33	0.33	0.31
Ta	1.68	1.48	2.44	2.52	2.54	1.87	1.24	2.49	0.04	0.12	0.13	0.15	0.04	0.12	0.15	0.13	0.07	0.06
Pb	3.36	2.81	3.30	3.27	3.25	3.24	3.04	3.27	6.30	5.62	5.59	5.27	5.36	5.80	5.78	6.44	5.67	5.56
Th	0.02	0.01	0.01	0.02	0.02	0.01	0.01	0.02	bd	bd	0.06	0.05	0.05	0.06	0.08	0.12	0.07	0.06
U	0.13	0.02	0.10	0.12	0.09	0.06	0.02	0.11	bd	bd	0.08	0.05	0.07	0.05	0.09	0.11	0.07	0.07
La _N /Yb _N	0.10	0.08	0.09	0.10	0.09	0.10	0.08	0.11	0.20	0.39	0.23	0.39	0.27	0.25	0.29	0.41	0.27	0.34
La _N /Sm _N	0.18	0.19	0.23	0.23	0.19	0.18	0.24	0.21	0.32	0.24	0.28	0.23	0.29	0.27	0.29	0.27	0.30	0.30
Gd _N /Yb _N	0.86	0.55	0.58	0.64	0.66	0.78	0.45	0.66	0.70	1.56	0.93	1.65	0.97	0.91	1.05	1.47	0.93	1.16
Eu/Eu*	0.75	0.94	0.91	0.83	0.82	0.78	1.16	0.83	0.83	0.84	0.81	0.89	0.83	0.86	0.82	0.83	0.84	0.84
Sum REE	106.60	78.03	98.04	104.53	101.09	93.25	77.54	103.59	19.26	39.61	22.45	37.81	23.20	21.28	27.62	31.86	22.14	23.44

Appendix E: Hornblende trace element analysis by Laser Ablation ICP-MS

Sample	Patchy melanosome in diorite																Hbl-Kfs leucosome		
	Rock type	TNG60C1	TNG60C4	TNG60C5	TNG60C6	TNG60C7	TNG60C8	TNG60C10	TNG60C11	TNG60C12	TNG60C13	TNG60C15	TNG60C16	TNG60C17	TNG60C19	TNG60C20	TNG60D1	TNG60D2	TNG60D3
Sc		27.59	26.72	26.32	36.34	38.87	40.85	28.81	26.59	25.21	23.94	37.66	29.91	29.74	31.20	33.47	45.08	49.56	52.96
Ti		5065.97	4796.05	4694.93	4857.43	5087.24	5078.80	4860.96	5021.77	4971.18	5114.76	4923.10	5411.49	5193.06	4898.89	4980.46	3468.74	3769.70	3965.63
V		362.85	348.04	345.77	367.04	393.56	381.42	370.28	340.04	335.78	354.50	370.11	296.59	370.38	367.17	355.34	298.98	311.97	321.53
Cr		54.33	11.00	10.16	11.58	11.60	10.35	10.05	8.63	10.24	8.69	126.64	110.03	8.83	9.30	12.84	184.10	129.94	116.17
Mn		2756.73	2574.68	2660.24	2619.83	2637.44	2578.58	2674.48	2732.92	2642.95	2658.75	2506.75	2113.74	2570.05	2604.04	2622.40	3443.10	3283.55	3325.76
Co		61.16	58.38	58.71	56.15	58.00	54.72	58.18	60.10	58.81	60.32	54.02	44.90	56.28	54.77	53.64	66.16	62.72	64.14
Ni		19.73	13.95	14.06	11.28	12.00	11.10	13.96	14.57	13.80	14.72	12.06	9.66	13.10	12.87	12.17	184.77	120.63	122.99
Cu		65.05	2.95	23.06	0.78	1.69	0.63	0.52	2.76	0.60	16.95	1.23	9.97	29.90	0.94	10.86	19.50	0.68	5.83
Zn		629.66	540.44	553.63	526.26	546.31	519.08	555.89	563.40	611.05	639.43	569.76	470.70	603.97	619.00	603.07	539.39	498.21	522.65
Ga		43.59	38.70	40.41	40.33	41.40	39.15	40.07	40.15	38.10	40.74	39.10	32.04	39.39	38.22	38.30	42.30	44.12	44.01
Rb		22.47	20.61	20.44	21.52	21.49	21.45	22.83	22.02	19.71	22.19	16.57	14.04	19.84	19.48	20.00	15.70	16.40	16.18
Sr		146.31	136.88	140.18	152.23	151.40	146.02	146.99	148.39	129.19	140.21	131.20	186.52	140.92	140.38	136.66	83.20	81.26	79.66
Y		8.31	8.05	8.63	9.51	7.91	5.81	8.41	6.96	7.63	7.90	9.81	15.83	8.15	5.77	8.45	9.44	8.11	7.64
Zr		22.07	21.29	20.95	23.13	22.07	21.24	21.12	45.56	18.04	19.69	21.43	121.51	19.68	17.04	368.99	17.75	15.32	16.26
Nb		5.35	5.13	5.29	5.63	5.12	4.01	5.57	5.21	5.03	5.44	5.24	7.62	5.38	4.09	4.80	3.68	4.59	4.83
Ba		104.09	98.49	97.50	97.36	139.89	98.05	104.57	104.16	117.12	102.55	121.38	117.22	106.88	102.26	102.80	56.60	55.31	55.55
La		0.89	0.85	1.37	1.15	0.85	0.25	0.94	1.32	1.26	1.38	1.16	4.35	1.16	0.87	1.23	0.70	0.50	0.41
Ce		4.95	4.26	6.66	5.84	4.09	1.21	4.81	4.81	1.64	7.07	6.26	20.47	6.14	4.29	6.16	4.93	3.11	2.94
Pr		1.10	0.96	1.42	1.37	0.84	0.27	1.09	0.86	1.40	1.54	1.41	3.66	1.32	0.82	1.30	1.26	0.80	0.77
Nd		6.95	5.92	8.94	9.17	5.09	1.77	6.83	4.60	8.28	8.95	9.06	20.69	7.95	4.49	7.27	8.95	5.92	5.95
Sm		2.76	2.32	3.39	3.62	2.06	0.88	2.68	2.03	3.06	3.40	3.65	7.04	2.98	1.53	2.73	4.72	3.23	3.14
Eu		0.88	0.81	1.07	1.04	0.80	0.38	0.83	0.75	1.07	1.08	1.15	1.87	0.99	0.74	0.94	1.43	0.96	1.01
Gd		2.32	2.15	2.69	3.29	1.86	1.05	2.52	1.69	2.36	2.64	3.24	5.73	2.62	1.33	2.10	4.28	3.26	2.91
Tb		0.31	0.27	0.31	0.39	0.24	0.17	0.31	0.22	0.29	0.30	0.38	0.66	0.31	0.19	0.29	0.49	0.41	0.36
Dy		1.57	1.49	1.62	1.95	1.31	0.93	1.56	1.28	1.48	1.47	1.92	3.19	1.43	0.97	1.53	2.22	1.83	1.71
Ho		0.27	0.25	0.27	0.31	0.24	0.19	0.28	0.23	0.23	0.25	0.30	0.53	0.25	0.16	0.25	0.31	0.28	0.25
Er		0.69	0.70	0.70	0.83	0.68	0.51	0.70	0.58	0.68	0.65	0.77	1.26	0.67	0.49	0.78	0.73	0.67	0.64
Tm		0.10	0.11	0.10	0.11	0.09	0.08	0.12	0.09	0.08	0.09	0.10	0.16	0.09	0.08	0.11	0.08	0.08	0.08
Yb		0.66	0.68	0.64	0.70	0.67	0.66	0.67	0.57	0.58	0.58	0.64	1.02	0.64	0.57	0.72	0.54	0.44	0.50
Lu		0.10	0.10	0.09	0.12	0.09	0.12	0.11	0.11	0.10	0.08	0.11	0.16	0.11	0.08	0.14	0.10	0.09	0.09
Hf		1.04	1.09	1.08	1.24	1.14	1.04	1.09	1.43	0.97	1.05	1.21	3.25	1.06	0.99	8.05	1.20	1.10	1.12
Ta		0.06	0.05	0.04	0.06	0.05	0.04	0.06	0.07	0.05	0.05	0.05	0.13	0.05	0.03	0.04	0.04	0.04	0.04
Pb		260.91	10.09	16.50	10.62	11.59	11.32	10.81	10.78	8.91	13.56	8.73	19.13	9.83	9.24	9.32	6.37	7.32	11.52
Th		0.12	0.07	0.39	0.03	0.09	0.02	0.03	1.42	0.07	0.61	0.08	21.65	0.10	0.04	0.91	0.42	0.03	0.36
U		0.15	0.09	0.14	0.17	0.10	0.17	0.13	0.35	0.12	0.09	0.04	3.47	0.10	0.08	1.91	0.11	0.14	0.14
La _N /Yb _N		0.92	0.84	1.45	1.10	0.86	0.26	0.94	1.57	1.47	1.61	1.21	2.87	1.22	1.03	1.14	0.87	0.77	0.56
La _N /Sm _N		0.20	0.23	0.25	0.20	0.26	0.18	0.22	0.41	0.26	0.25	0.20	0.39	0.25	0.36	0.28	0.09	0.10	0.08
Gd _N /Yb _N		2.85	2.53	3.39	3.77	2.24	1.29	3.02	2.41	3.30	3.68	4.06	4.53	3.30	1.88	2.35	6.40	5.95	4.71
Eu/Eu*		1.06	1.11	1.08	0.92	1.24	1.20	0.97	1.24	1.21	1.10	1.02	0.90	1.08	1.59	1.19	0.98	0.90	1.02
Sum REE		23.55	20.88	29.28	29.88	18.94	8.47	23.45	19.13	27.51	29.47	30.16	70.81	26.66	16.64	25.54	30.75	21.56	20.79

Appendix E. Hornblende trace element analysis by Laser Ablation ICP-MS

Sample	TNG60D4	TNG60D5	TNG60D6	TNG60D7	TNG60D8	TNG60D9	TNG60D10	TNG60D11	TNG60D14	TNG60D15	TNG60D16	TNG60D17	TNG60D18	TNG60D19	TNG60D20	AGH23a1	AGH23a2	AGH23a3
Rock type								Hbl-Kfs leucosome								Hbl-Kfs leucosome		
Sc	49.45	50.16	47.73	44.43	45.42	55.10	45.15	43.02	40.72	54.58	47.73	45.39	32.81	35.56	34.10	47.72	48.02	47.82
Ti	3679.87	4346.20	4150.30	3804.75	3738.99	3831.22	3617.77	3630.48	3393.67	3752.60	3630.91	3758.59	3772.16	3597.01	3448.59	4469.53	4487.08	3205.35
V	311.47	302.36	307.11	302.65	307.83	275.54	279.61	285.84	287.55	307.16	282.48	280.66	249.52	245.36	257.24	291.84	303.25	315.71
Cr	177.98	144.48	124.15	162.38	128.99	810.01	105.56	140.20	252.84	269.84	396.76	247.10	265.76	455.70	505.47	65.65	99.92	102.80
Mn	3173.72	3171.15	3213.94	3148.41	3332.16	3047.62	2946.35	3029.76	3151.24	3299.89	3067.93	3032.89	2913.26	2801.26	2972.52	3348.94	3462.43	3252.90
Co	64.31	63.47	61.50	64.07	65.85	57.24	56.96	54.08	61.45	62.05	60.16	59.85	57.28	54.15	56.79	58.13	61.71	55.18
Ni	149.66	166.64	155.22	148.80	143.48	193.59	156.47	153.58	146.09	143.97	152.15	136.24	158.77	137.34	160.94	75.42	83.96	89.90
Cu	1.71	5.34	3.35		48.40	6.06	1.08	9.42	44.81			4.26		38.50	0.45	0.39	14.52	0.68
Zn	518.67	521.08	509.49	516.15	539.49	456.70	486.44	492.53	497.32	502.47	502.63	510.72	477.53	440.93	479.72	486.75	523.95	508.84
Ga	43.22	43.42	43.75	42.96	43.61	40.19	41.65	40.12	42.46	44.12	41.40	44.58	42.75	39.91	40.23	27.72	30.63	21.48
Rb	15.25	15.19	16.58	17.06	16.09	14.33	14.78	12.82	15.22	15.09	13.27	15.80	13.92	12.35	13.82	5.65	5.48	5.75
Sr	77.09	73.12	78.92	77.58	75.69	73.22	73.00	64.84	77.86	76.41	70.94	79.36	67.76	61.73	74.85	80.83	93.83	76.06
Y	8.29	15.18	11.55	10.90	6.99	13.84	11.71	19.11	8.01	7.28	7.16	8.68	17.71	21.87	10.08	17.43	18.50	10.10
Zr	14.50	17.50	16.74	17.52	14.52	18.27	15.35	15.82	14.92	16.53	15.38	15.16	16.31	19.03	15.95	26.86	22.10	24.25
Nb	4.08	5.07	4.68	3.92	4.85	4.73	4.24	3.59	4.73	4.95	4.74	3.86	4.13	3.69	3.66	10.15	10.53	6.79
Ba	48.87	50.96	59.26	61.85	50.70	45.92	48.03	48.80	47.58	48.01	43.39	51.03	43.99	45.94	44.30	32.79	31.90	24.51
La	0.40	0.96	0.67	0.86	0.49	0.65	0.69	1.02	0.41	0.34	0.47	0.45	0.98	1.87	3.81	10.94	10.34	8.86
Ce	2.96	7.03	4.74	6.16	3.44	4.02	4.78	7.57	2.68	2.59	3.39	2.81	6.72	9.58	10.55	37.86	38.26	27.62
Pr	0.75	1.81	1.19	1.48	0.87	1.03	1.20	2.11	0.70	0.88	0.83	0.70	1.74	2.46	1.42	5.80	5.84	3.96
Nd	5.58	12.94	8.96	10.73	5.89	7.88	8.37	16.47	5.38	5.04	5.83	5.40	13.32	19.01	9.39	27.10	27.22	17.75
Sm	3.24	7.11	5.19	5.48	3.11	4.30	4.44	8.98	3.04	2.75	2.97	3.14	6.81	9.70	4.04	5.71	6.34	3.67
Eu	1.15	2.08	1.53	1.63	1.00	1.51	1.59	2.33	1.05	0.83	0.94	1.04	2.24	2.41	1.37	1.18	1.20	0.76
Gd	3.19	6.29	4.51	4.87	2.72	4.38	4.24	8.32	3.07	2.54	2.69	3.15	6.48	9.32	3.73	3.95	4.39	2.47
Tb	0.39	0.72	0.55	0.58	0.32	0.54	0.51	0.96	0.38	0.30	0.30	0.41	0.77	1.03	0.43	0.57	0.63	0.32
Dy	1.98	3.40	2.59	2.45	1.58	2.71	2.54	4.49	1.83	1.46	1.55	1.96	3.65	4.81	2.12	3.09	3.40	1.82
Ho	0.26	0.49	0.38	0.36	0.24	0.40	0.37	0.64	0.26	0.23	0.23	0.29	0.53	0.71	0.31	0.56	0.60	0.32
Er	0.64	1.19	0.94	0.83	0.57	1.11	0.85	1.43	0.59	0.59	0.54	0.68	1.18	1.48	0.74	1.68	1.77	0.96
Tm	0.07	0.13	0.12	0.10	0.07	0.13	0.11	0.16	0.07	0.07	0.07	0.08	0.16	0.18	0.10	0.26	0.24	0.15
Yb	0.51	0.81	0.74	0.60	0.47	0.97	0.65	1.04	0.46	0.52	0.55	0.54	1.00	1.08	0.64	1.74	1.71	1.12
Lu	0.10	0.12	0.11	0.10	0.08	0.18	0.13	0.15	0.07	0.08	0.09	0.09	0.15	0.18	0.12	0.29	0.23	0.18
Hf	0.90	1.01	1.07	1.21	0.92	1.31	0.87	0.97	0.96	1.18	1.12	0.83	0.90	1.09	0.96	1.56	1.30	1.62
Ta	0.03	0.04	0.04	0.03	0.03	0.04	0.03	0.03	0.03	0.04	0.03	0.03	0.03	0.03	0.03	0.15	0.16	0.12
Pb	6.61	6.31	6.39	5.73	6.54	5.76	5.44	5.62	7.67	8.28	7.08	7.06	5.69	5.27	6.01	3.99	5.38	3.08
Th	0.06	0.08	0.04	0.03	0.20	0.05	0.03	0.05	0.56	0.01	0.02	0.04	0.03	0.60	0.69	0.13	0.11	0.06
U	0.13	0.09	0.13	0.11	0.13	0.09	0.10	0.05	0.09	0.08	0.07	0.12	0.06	0.06	0.06	0.06	0.08	0.05
La _N /Yb _N	0.53	0.80	0.61	0.97	0.70	0.45	0.72	0.66	0.59	0.44	0.58	0.56	0.66	1.17	3.99	4.24	4.08	5.33
La _N /Sm _N	0.08	0.08	0.08	0.10	0.10	0.09	0.10	0.07	0.08	0.08	0.10	0.09	0.09	0.12	0.59	1.21	1.03	1.52
Gd _N /Yb _N	5.04	6.31	4.91	6.51	4.69	3.64	5.28	6.44	5.33	3.93	3.93	4.68	5.25	6.97	4.68	1.84	2.07	1.78
Eu/Eu*	1.09	0.95	0.97	0.96	1.05	1.07	1.12	0.82	1.05	0.96	1.02	1.01	1.03	0.77	1.08	0.76	0.70	0.77
Sum REE	21.23	45.08	32.22	36.24	20.86	29.82	30.47	55.66	20.00	18.02	20.46	20.75	45.72	63.83	38.76	100.71	102.16	69.94

Appendix E. Hornblende trace element analysis by Laser Ablation ICP-MS

Sample	AGH23a4	AGH23a5	AGH23a6	AGH23a7	AGH23a8	AGH23a9	Hbl-Kfs leucosome		AGH23a10	AGH23a13	AGH23a14	AGH23a15	AGH23a17	AGH23a20	AGH241	AGH242	Hbl-Bt leucogranite		AGH243	AGH244	AGH245	AGH246
Rock type																						
Sc	38.44	45.73	47.16	36.10	45.42	42.13	39.21	38.81	42.74	41.13	40.89	42.95	142.47	256.98	166.04	99.60	144.66	125.18				
Ti	3249.26	4149.59	3867.65	5551.51	3339.68	3740.13	3484.73	4900.47	4215.97	3524.22	3996.86	4521.12	12618.46	12289.47	12627.29	6383.96	9915.81	9494.45				
V	221.24	250.46	243.10	296.41	273.85	266.07	213.03	261.78	248.46	209.60	261.21	272.58	694.22	801.27	625.52	341.60	739.11	493.94				
Cr	57.50	74.67	84.06	132.83	134.22	69.32	56.70	92.98	58.61	40.36	87.40	67.47	72.44	28.14	51.32	47.20	35.19	60.55				
Mn	3194.13	3146.79	3118.79	3387.27	3236.41	3205.13	3082.11	3327.60	3437.26	3163.86	3575.75	3499.95	4698.71	2786.01	2832.60	5367.11	3313.79	4611.47				
Co	53.63	53.88	57.26	60.16	56.61	55.76	59.17	59.53	59.22	55.38	57.72	72.20	44.38	51.97	51.06	47.09	52.56	51.39				
Ni	73.39	70.79	80.21	94.79	79.52	68.21	92.11	75.67	95.36	70.59	72.74	136.60	9.54	15.32	12.60	10.06	14.98	10.20				
Cu	2.07	1.25	4.40	15.52	1.19	0.96	5.59	1.61	20.56	1.18	10.26	3.32	1.85	1.75	1.26	1.68	2.70	0.86				
Zn	486.25	479.16	466.23	538.38	522.39	505.20	445.74	488.35	519.90	473.48	549.99	531.56	308.25	259.13	268.48	353.76	280.83	336.60				
Ga	20.42	26.55	25.05	32.88	23.67	22.41	20.80	27.97	29.14	21.90	27.92	29.83	28.23	25.48	25.60	19.50	26.17	28.65				
Rb	6.38	8.56	7.24	25.72	5.73	6.15	6.97	7.75	7.64	6.32	6.48	8.29	4.43	4.09	3.94	2.55	4.21	4.19				
Sr	62.72	69.36	73.74	89.62	79.07	73.31	67.93	91.95	76.29	73.97	75.14	75.62	69.97	75.16	68.08	28.71	57.86	52.12				
Y	13.30	17.18	15.63	13.10	10.24	11.12	10.71	14.08	12.43	10.07	13.01	13.87	328.93	482.36	408.54	231.03	273.65	296.63				
Zr	34.70	32.91	26.74	24.90	21.83	32.44	34.80	29.61	25.38	25.00	24.44	26.02	76.06	106.33	85.95	56.69	60.09	76.58				
Nb	6.89	9.60	7.40	7.65	6.70	6.96	3.40	8.69	6.36	4.28	7.66	8.72	44.11	35.31	47.31	32.21	26.86	53.08				
Ba	30.27	44.73	39.78	76.04	25.83	31.70	40.04	55.63	45.11	32.01	33.58	50.51	193.37	234.22	169.11	23.24	185.37	86.67				
La	9.12	9.95	8.33	10.99	8.89	9.72	8.75	11.77	10.52	8.56	9.24	9.13	85.78	74.98	99.56	59.87	52.96	96.08				
Ce	29.24	33.95	27.74	37.86	28.43	31.12	26.54	39.49	37.16	26.04	33.45	35.79	360.81	306.86	383.42	244.39	238.63	398.96				
Pr	4.35	5.31	4.43	5.40	4.15	4.58	3.86	5.93	5.36	3.74	4.96	5.32	57.57	55.33	62.24	38.96	40.02	58.94				
Nd	20.76	26.05	20.87	24.92	19.26	20.90	17.65	26.50	24.14	17.39	22.11	23.85	280.63	310.15	317.25	185.01	207.98	268.79				
Sm	4.42	5.57	4.73	4.87	3.74	4.26	3.54	5.37	4.99	3.43	4.66	5.33	70.38	94.14	80.36	42.83	58.04	60.17				
Eu	0.86	1.06	0.93	1.12	0.88	0.88	0.82	1.26	1.11	0.87	1.03	1.05	5.15	6.00	5.22	3.13	4.24	4.34				
Gd	3.20	4.12	3.38	3.17	2.53	2.90	2.39	3.47	3.28	2.35	3.00	3.48	64.14	100.95	77.87	40.02	56.62	51.90				
Tb	0.42	0.55	0.45	0.41	0.33	0.36	0.30	0.43	0.41	0.31	0.40	0.45	10.33	16.54	12.61	6.60	9.23	8.46				
Dy	2.25	3.10	2.54	2.22	1.66	1.94	1.71	2.46	2.16	1.62	2.24	2.55	63.03	99.23	77.87	41.03	55.19	52.18				
Ho	0.40	0.53	0.47	0.39	0.33	0.36	0.34	0.44	0.39	0.31	0.40	0.44	11.71	18.16	14.50	8.03	10.19	10.15				
Er	1.22	1.53	1.52	1.24	0.99	1.06	1.01	1.34	1.11	0.92	1.25	1.29	33.64	48.38	41.41	24.43	28.23	30.55				
Tm	0.19	0.22	0.22	0.21	0.15	0.15	0.16	0.20	0.17	0.16	0.19	0.18	4.55	6.02	5.61	3.52	3.63	4.42				
Yb	1.34	1.61	1.65	1.65	1.17	1.28	1.23	1.47	1.18	1.23	1.40	1.27	28.43	34.42	34.76	24.35	22.50	29.42				
Lu	0.23	0.26	0.25	0.25	0.20	0.18	0.21	0.21	0.19	0.19	0.21	0.19	3.64	4.26	4.46	3.33	2.78	3.99				
Hf	3.14	2.18	1.62	1.45	1.60	2.62	2.39	1.52	1.60	1.62	1.56	1.49	4.48	5.65	5.06	3.53	3.37	4.84				
Ta	0.10	0.15	0.12	0.05	0.08	0.08	0.02	0.10	0.06	0.03	0.12	0.12	1.48	1.23	1.70	1.43	0.84	2.17				
Pb	3.06	4.16	4.94	4.35	2.93	3.08	3.87	4.75	5.93	3.20	4.53	5.88	5.06	4.73	4.33	3.75	4.90	4.99				
Th	0.10	0.12	0.11	0.14	0.08	0.09	0.09	0.13	0.18	0.08	0.11	0.08	0.94	0.86	1.38	0.66	0.70	1.12				
U	0.05	0.06	0.06	0.05	0.05	0.04	0.06	0.07	0.08	0.03	0.10	0.05	0.18	0.13	0.25	0.17	0.13	0.24				
La _N /Yb _N	4.59	4.17	3.40	4.48	5.13	5.12	4.82	5.41	6.00	4.68	4.46	4.05	2.03	1.47	1.93	1.66	1.59	2.20				
La _N /Sm _N	1.30	1.12	1.11	1.42	1.50	1.44	1.55	1.38	1.33	1.57	1.25	1.08	0.77	0.50	0.78	0.88	0.57	1.00				
Gd _N /Yb _N	1.93	2.06	1.65	1.55	1.75	1.83	1.57	1.91	2.24	1.54	1.73	2.20	1.82	2.37	1.81	1.33	2.03	1.42				
Eu/Eu*	0.70	0.68	0.71	0.87	0.87	0.77	0.86	0.89	0.84	0.94	0.84	0.74	0.23	0.19	0.20	0.23	0.23	0.24				
Sum REE	78.00	93.80	77.52	94.70	72.70	79.68	68.50	100.35	92.18	67.12	84.54	90.32	1079.77	1175.43	1217.16	725.50	790.22	1078.36				

Appendix E. Hornblende trace element analysis by Laser Ablation ICP-MS

Sample	Rock type	AGH247	AGH248	AGH249	AGH2411	AGH2412
Sc	143.74	134.92	125.00	187.26	170.86	
Ti	10008.22	8532.18	8009.35	12479.00	10912.73	
V	480.44	455.41	414.81	700.16	605.81	
Cr	53.36	45.36	46.75	54.52	53.50	
Mn	4096.41	4438.37	4141.01	3953.76	3849.06	
Co	43.86	39.98	46.21	40.26	46.94	
Ni	9.50	7.84	8.81	8.16	10.52	
Cu	0.59	0.59	0.76	0.57	1.16	
Zn	290.08	288.12	304.65	270.83	307.45	
Ga	26.03	22.22	24.98	24.41	27.41	
Rb	3.76	3.27	4.33	3.27	3.84	
Sr	58.62	43.77	44.98	71.87	60.43	
Y	355.67	305.61	304.51	447.12	416.18	
Zr	88.69	75.87	78.39	97.78	74.35	
Nb	53.90	38.58	49.75	38.58	54.45	
Ba	106.11	103.71	64.93	223.64	140.59	
La	101.81	66.29	89.33	86.19	97.95	
Ce	378.39	253.64	350.92	327.21	428.39	
Pr	59.35	42.05	53.49	57.03	69.73	
Nd	284.78	210.77	249.21	308.20	344.26	
Sm	65.83	53.39	56.47	84.84	89.62	
Eu	4.58	3.75	4.02	5.61	5.38	
Gd	61.59	52.83	50.42	87.68	83.36	
Tb	10.11	8.72	8.34	14.41	13.54	
Dy	62.76	54.83	52.83	87.32	81.88	
Ho	12.21	10.69	10.41	16.31	15.14	
Er	36.97	31.79	31.75	45.35	42.20	
Tm	5.29	4.68	4.72	5.89	5.68	
Yb	34.47	30.35	31.05	34.48	35.57	
Lu	4.76	4.34	4.32	4.48	4.37	
Hf	5.88	5.32	5.39	5.80	4.68	
Ta	2.37	1.94	2.35	1.42	1.96	
Pb	3.91	3.62	4.32	3.58	4.38	
Th	1.28	0.97	1.33	0.95	1.04	
U	0.20	0.19	0.30	0.13	0.18	
La _N /Yb _N	1.99	1.47	1.94	1.69	1.86	
La _N /Sm _N	0.97	0.78	1.00	0.64	0.69	
Gd _N /Yb _N	1.44	1.40	1.31	2.05	1.89	
Eu/Eu*	0.22	0.22	0.23	0.20	0.19	
Sum REE	1122.90	828.13	997.28	1164.99	1317.08	

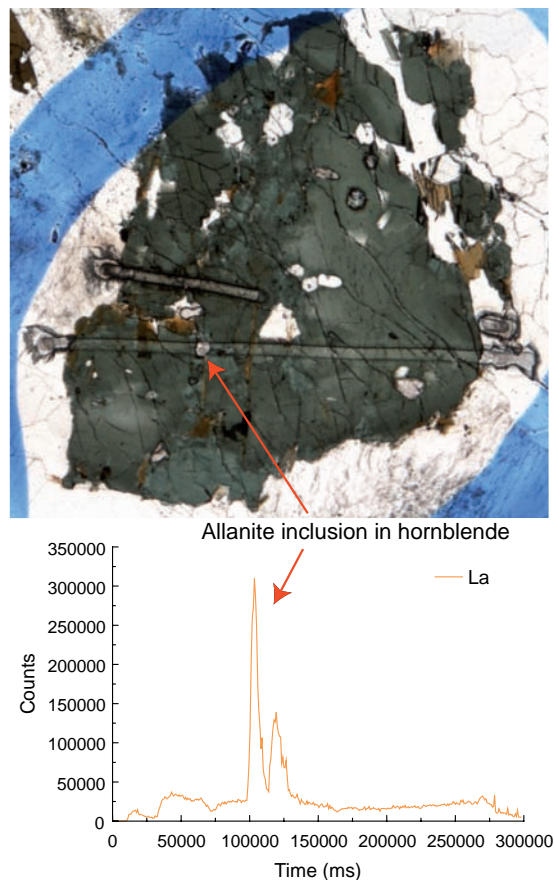
Appendix F. Laser Ablation ICP-MS analysis of other minerals

Sample	Mineral	TNG60C3	TNG60C14	TNG169A20	TNG169B19	TNG169B17	TNG169B16	TNG169B18	TNG169B20
Sc	3.07	3.01	3.64	bd	2.52	2.89	2.94	5.05	2.81
Ti	6.96	24.62	40.12	bd	14.24	21.18	14.58	57.86	17.89
V	bd	bd	2.01	bd	0.22	bd	bd	1.67	bd
Cr	bd	bd	bd	bd	bd	bd	bd	bd	bd
Mn	2.48	3.49	19.27	131.48	16.89	15.10	14.67	46.08	15.80
Co	bd	0.07	0.46	bd	bd	bd	bd	bd	bd
Ni	bd	bd	0.45	bd	bd	bd	bd	bd	bd
Cu	0.88	bd	9.42	bd	bd	bd	bd	bd	bd
Zn	5.84	6.52	10.96	bd	5.25	6.07	5.90	13.15	5.74
Ga	29.19	30.39	34.55	bd	31.17	36.52	30.07	57.88	36.94
Rb	3.62	1.58	2.54	35.09	1.24	0.86	0.75	1.33	1.14
Sr	2969.50	2986.52	2908.67	2203.51	bd	bd	bd	bd	bd
Y	0.10	0.02	0.06	0.44	0.04	0.08	0.04	0.25	0.12
Zr	0.09	0.05	0.11	bd	bd	0.04	bd	bd	bd
Nb	bd	bd	0.03	bd	bd	bd	bd	0.16	0.02
Ba	268.37	247.32	251.10	176.92	200.16	176.42	182.98	220.25	181.32
La	0.13	0.12	0.15	1.10	0.03	0.26	0.10	0.53	0.41
Ce	0.24	0.22	0.30	1.49	0.09	0.48	0.26	0.88	0.66
Pr	0.03	0.02	0.03	0.12	0.01	0.03	0.02	0.07	0.04
Nd	0.14	0.05	0.12	0.36	0.04	0.13	0.08	0.17	0.14
Sm	bd	0.02	0.13	0.13	bd	0.06	bd	0.07	0.05
Eu	0.14	0.13	0.16	0.36	0.40	0.35	0.40	0.56	0.37
Gd	0.02	bd	0.01	0.10	0.01	0.02	bd	0.08	bd
Tb	0.01	bd	bd	0.01	0.01	bd	0.00	bd	bd
Dy	bd	bd	bd	0.07	0.03	bd	bd	bd	bd
Ho	0.00	bd	bd	bd	bd	bd	0.01	0.02	bd
Er	bd	bd	0.01	0.04	bd	bd	bd	0.04	bd
Tm	bd	bd	bd	0.01	0.00	bd	0.00	bd	bd
Yb	bd	bd	bd	0.06	bd	0.01	bd	0.03	bd
Lu	bd	bd	bd	0.01	bd	bd	bd	bd	bd
Hf	bd	bd	bd	bd	bd	bd	bd	bd	bd
Ta	0.00	bd	0.00	0.01	bd	bd	0.01	bd	bd
Pb	57.15	53.82	61.11	18.87	19.20	18.62	18.40	31.49	19.06
Th	0.03	bd	0.02	0.01	bd	0.00	0.00	0.00	bd
U	0.09	bd	0.01	0.01	0.00	bd	bd	bd	bd
La _N /Yb _N				13.29	bd	21.59	11.10		
La _N /Sm _N		4.57		5.46		2.61	4.76		6.86
Gd _N /Yb _N				9.76		27.94	23.49		
Eu/Eu*	0.72	0.56	0.78	3.86	0.61	1.34	0.87	2.45	1.64
Sum REE									2.10

Appendix F. Laser Ablation ICP-MS analysis of other minerals

Sample	AGH23a11	AGH23a12	TNG5920	AGH2410	TNG5921	TNG5922	TNG5923	TNG5924	AGH23a16	AGH23a19	TNG60D12
Mineral	Ilmenopyroxene		Biotite		Titanite		Allanite				
Sc	36.64	32.57	60.07	2,426.12	12.04	12.82	6.73	9.40	5.55	18.25	13.56
Ti	207.96	678.00	bd	5,980,038.00	742.36	724.37	746.72	151,129.27	97,858.27	3,757.37	6,803.02
V	88.27	76.19	452.68	77,569.33	34.70	59.32	44.53	48.23	282.57	290.81	1,028.72
Cr	20.33	20.34	86.18	13,970.55	795.63	740.08	962.75	698.22	10.33	234.45	38.21
Mn	1,958.64	2,084.89	bd	575,589.80	0.12	0.35	4.83	0.14	162.38	1,783.15	2,961.99
Co	15.64	16.93	52.04	13,768.09	0.16	0.17	4.90	0.15	0.05	11.49	23.51
Ni	19.66	23.93	41.33	3,162.34	4.42	3.30	4.08	4.09	0.20	13.93	38.56
Cu	3.22	8.93	bd	454.13	7.07	5.95	40.34	7.92	2.95	0.28	19.92
Zn	125.57	135.33	403.47	94,205.89	112.76	125.32	61.39	86.21	2.91	152.68	285.78
Ga	2.99	3.60	39.88	8,184.51	0.21	0.32	43.60	2.06	11.92	326.44	633.74
Rb	0.26	0.35	13.84	153,425.03	18.72	26.35	22.16	21.40	0.35	0.04	0.27
Sr	73.58	181.65	35.55	327.28	528.55	593.13	378.60	403.03	275.17	450.03	2,643.43
Y	2.74	2.91	8.34	228.27	bd	bd	821.73	1,604.69	330.72	120.26	187.62
Zr	14.61	14.47	15.19	163.44	1,705.49	1,912.15	1,349.14	1,547.01	1,282.13	3.82	1.68
Nb	0.17	0.05	5.67	14,510.69	bd	bd	bd	1,902.64	578.35	0.03	0.04
Ba	1.62	2.12	12.59	1,343,852.89	bd	0.23	26.83	1.55	3.11	2.56	16.43
La	1.73	2.46	0.50	87.93	5,654.68	6,523.39	4,020.74	5,509.71	706.62	53,204.68	51,281.20
Ce	5.60	7.86	2.13	173.71	701.85	887.93	402.89	632.12	1,614.54	57,977.30	98,114.48
Pr	0.91	1.27	0.32	27.19	2,681.81	3,470.25	1,408.97	2,332.94	259.94	4,865.34	8,946.44
Nd	4.53	6.16	1.49	105.20	525.80	703.06	226.10	383.59	1,132.85	12,463.57	27,142.41
Sm	1.01	1.30	0.51	30.01	82.82	106.33	44.89	66.34	198.04	736.74	2,619.80
Eu	0.21	0.28	0.53	20.92	464.11	599.23	182.78	310.00	38.10	79.28	270.59
Gd	0.71	0.86	0.69	28.75	63.76	88.74	24.74	43.67	124.68	233.36	708.36
Tb	0.09	0.10	0.14	4.39	382.24	530.53	143.88	262.91	14.14	14.26	36.29
Dy	0.50	0.58	1.03	28.30	70.24	98.10	25.87	49.82	73.59	43.42	88.77
Ho	0.08	0.10	0.25	5.53	207.32	289.11	77.64	154.11	12.15	4.43	6.60
Er	0.26	0.28	0.95	19.70	29.81	40.79	11.36	22.80	30.14	8.75	9.09
Tm	0.04	0.04	0.16	3.68	29.81	40.79	11.36	22.80	4.00	0.96	0.77
Yb	0.37	0.38	1.47	26.90	194.12	255.11	81.71	156.38	22.89	6.30	3.64
Lu	0.08	0.08	0.30	4.00	25.30	33.03	12.43	20.84	2.57	0.93	0.44
Hf	0.96	0.89	0.86	26.32	42.65	47.41	31.99	30.71	63.98	0.24	0.10
Ta	0.01	0.01	0.03	595.07	244.88	343.38	104.43	181.59	36.02	0.00	0.00
Pb	1.12	2.50	5.73	864.70	4.00	4.56	4.07	3.69	1.68	28.22	120.22
Th	0.14	0.18	0.05	15.49	530.45	560.79	413.99	446.47	144.13	18,691.83	13,053.65
U	0.05	0.11	0.10	7.85	73.84	78.60	100.80	74.32	6.39	175.78	89.59
La _N /Yb _N	3.19	4.40	0.23	2.20	5.92	5.05	11.13	6.67	20.81	5,693.69	9,500.30
La _N /Sm _N	1.08	1.19	0.62	1.84	2.04	1.71	3.75	2.54	2.24	45.43	12.31
Gd _N /Yb _N	1.55	1.83	0.37	0.86	1.93	1.90	1.81	1.60	1.40	29.89	157.07
Eu/Eu*	0.76	0.81	2.75	2.18	0.51	0.50	0.68	0.59	0.74	0.58	0.61
Sum REE	16.13	21.74	10.45	566.21	12,789.35	15,537.75	8,013.16	11,492.24	4,234.25	129,639.32	189,228.88

Appendix G: Laser line-scan of hornblende in a Hbl-Kfs leucosome from the Agham location. Note peak where the laser hit an allanite inclusion. X-axis on diagram shows the time profile as the laser moves over the hornblende grain from left to right. Y-axis on diagram shows count rates per second.




THE
GEOLOGICAL
SOCIETY
OF AMERICA®

BULLETIN

ISSN 0016-7606

VOL. 120 NO. 7/8 JULY/AUGUST 2008



Photo of dyke networks in the Pangong Metamorphic Complex that was used as the cover image of The Geological Society of America Bulletin. Photo taken by Roberto Weinberg.

Magma ponding in the Karakoram shear zone, Ladakh, NW India

Roberto F. Weinberg[†]

Geordie Mark^{*}

Henning Reichardt

School of Geosciences, Monash University, Clayton, VIC 3800, Australia

ABSTRACT

Granitic melt migration and pluton emplacement are commonly closely associated with transcurent shear zones. The processes that link granites to shear zones are not yet fully understood. The dextral-transpressive Karakoram shear zone in Ladakh, NW India, exposes anatectic rocks where synkinematic melt migration and ponding at kilometer scale were controlled by competency contrasts. Metasedimentary rocks and a dominantly granodioritic calc-alkaline intrusion underwent fluid-present partial melting at upper-amphibolite facies to produce leucogranite sheets and irregular intrusive masses dated at 21–14 Ma. Leucogranitic magmas ponded in the low-pressure strain shadow of the competent granodioritic calc-alkaline pluton, giving rise to (a) migmatitic rocks that are pervaded by irregular leucogranite intrusions at a scale of meters or tens of meters, and (b) the growth of the Tangtse pluton, a kilometer-scale sheeted complex. Thus, magmas accumulated during shearing and anatexis in a low-pressure strain shadow within the Karakoram shear zone. This magma provided a readily available magma source that could have been tapped to feed larger plutons at shallower levels by modifications in the pressure distribution accompanying changes in shear zone geometry and kinematics. We conclude that shear zones tapping anatectic regions act as magma pumps, creating and destroying magma traps at depth as they evolve, and leading to incremental magma addition to upper-crustal plutons.

Keywords: shear zone, magma emplacement, magma transport, strain shadow, sheeted complex, leucogranite, Karakoram.

[†]E-mail: Roberto.Weinberg@sci.monash.edu.au

^{*}Present address: Haywood Securities Inc., 400 Burrard Street, Vancouver, British Columbia V6C 3A6, Canada.

INTRODUCTION

Plutons are commonly associated with transcurent shear zones, where they display a number of characteristic three-dimensional (3-D) shapes (Brown and Solar, 1999; D'Lemos et al., 1992; Elias-Herrera and Ortega-Gutiérrez, 2002; Lacroix et al., 1998; McCaffrey, 1992; Roman-Berdiel et al., 1997; Tikoff and Teyssier, 1992; Vigneresse, 1995; Weinberg et al., 2004). The close temporal and spatial association between synkinematic granitic plutons and crustal-scale transcurent shear zones suggests a causative link between the two (Hutton and Reavy, 1992). Either shear zones control ascent and emplacement of granitic magmas (Brown and Solar, 1998b; Weinberg et al., 2004), or magma emplacement triggers nucleation of shear zones (e.g., Neves et al., 1996). The hypothesis that shear zones control the ascent and emplacement of granitic plutons is supported by mesoscale structures in migmatites (e.g., Brown and Solar, 1999; Sawyer, 1999) and is generally ascribed to the ability of shear zones to accommodate magma influx in extensional jogs, as well as higher permeability, temperature, and strain rate in shear zones (e.g., Brown and Solar, 1998a; D'Lemos et al., 1992; Leloup et al., 1999; Pe-Piper et al., 1998).

Weinberg et al. (2004) suggested that low mean pressure zones that develop at the shoulders of shear zones close to regional rheological contacts control the emplacement of magma bodies. Mancktelow (2006) argued for brittle behavior in ductile shear zones to account for the low mean pressure implied by widespread evidence that shear zones act as fluid or magma channels. Most studies of pluton–shear zone relationships explore the system at emplacement levels, away from the magma source. This is partly because significant magma accumulations are rare in regions of crustal anatexis (Brown, 2004). The lack of such accumulations implies that there is either an efficient mechanism to drain diffuse magma in the source (Rabinowicz and Vigneresse, 2004), or that magma accumulations in the source are only transient features.

This paper explores a rare magma accumulation within anatectic rocks presumed to be a part of the magma source region for the leucogranitic, 20–15 Ma Karakoram batholith (Weinberg et al., 2000). These anatectic rocks are exposed within the 7-km-wide, dextral-transpressive Karakoram shear zone, in Ladakh, NW India (Weinberg and Mark, 2008). These magma accumulations provide an opportunity to explore simultaneously the controls on magma migration and accumulation within source regions, and the ways in which shear zones control magma migration.

KARAKORAM SHEAR ZONE AND THE PANGONG METAMORPHIC COMPLEX

The ~800-km-long Karakoram shear zone is part of a set of faults that accommodate the northward movement of India (e.g., Avouac and Tapponnier, 1993). The Tangtse gorge in Ladakh (Fig. 1) cuts transversally across the shear zone and the Pangong Range, both of which trend on average N40W, and ~7 km wide, exposing upper-amphibolite-facies rocks of the Pangong metamorphic complex (Table 1) (Rolland and Pêcher, 2001). The shear zone in this area is divided into a number of high-strain, mylonitic strands. The Tangtse strand (Fig. 1) dips 70°NE, with lineations plunging 20–40°N, defining a dextral thrust, separating the overriding Pangong metamorphic complex to the NE from the down-thrusted Cretaceous Ladakh batholith and contemporaneous Khardung volcanics to the SW (Weinberg et al., 2000). The Pangong strand is a subvertical dextral shear zone, at least 2 km wide that separates the Pangong metamorphic complex from the Karakoram metamorphic complex to the NE (Fig. 1; Table 1). The Pangong Range, bounded by these two strands, is dominated by pure shear deformation characterized by NW-plunging, upright folds, trending N40W to N60W (Weinberg and Mark, 2008). This range is traversed by simple shear bands defined by intense dextral mylonitic foliation (Figs. 2 and 3) and well-defined stretching lineation plunging 30–40°NW (Weinberg et al., 2000).

GSA Bulletin, January/February 2009; v. 121; no. 1/2; p. 278–285; doi: 10.1130/B26358.1; 5 figures; 1 table.

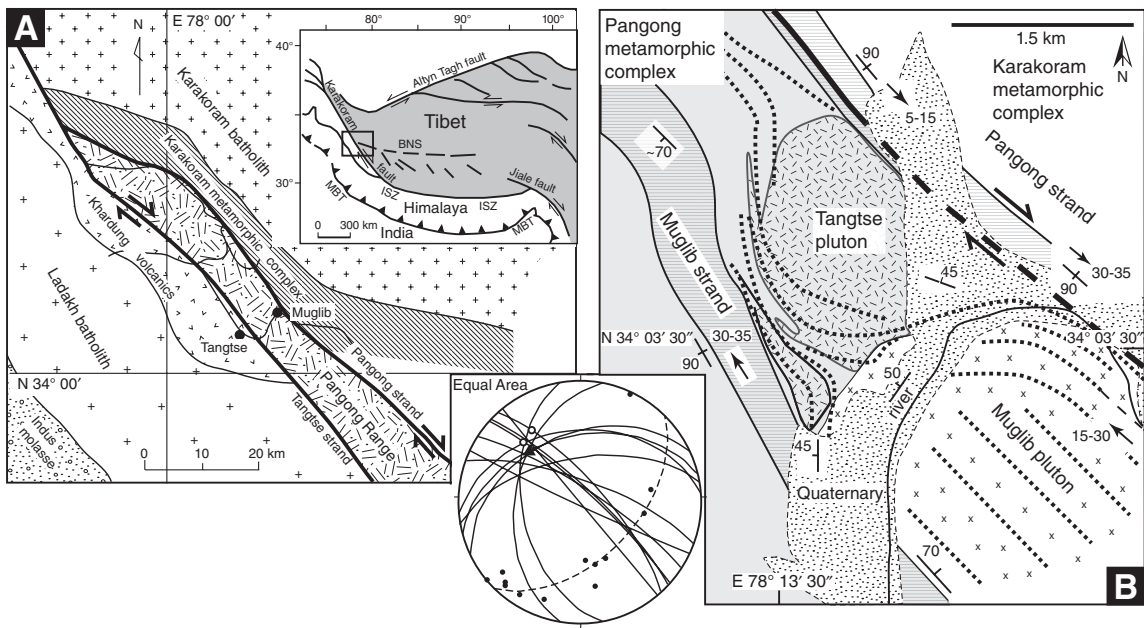


Figure 1. (A) Regional geological map of the Pangong Range where the Pangong metamorphic complex is exposed in Ladakh, NW India. The filled circle marked Muglib indicates the area covered in (B). (B) Geological map of the NE end of Tangtse gorge, where the Pangong strand of the Karakoram shear zone bounds the leucogranite Tangtse pluton and the older, calc-alkaline Muglib pluton. The Tangtse pluton is part of a sheet injection complex emplaced where the regional foliation (thick dashed lines) drapes around the NW-plunging nose of the competent Muglib pluton, defining a pressure shadow. The Muglib strand is not shown in (A). Leucogranites result from crustal anatexis as evidenced by migmatites exposed in the Tangtse gorge. Inset: Lower-hemisphere stereonet projection of foliation attitude (great circles) around the Muglib nose. Poles to foliation planes define a great circle (dashed line) and a fold axis plunging moderately NW (filled triangle), parallel to regional stretching lineations and outcrop-scale fold axes (white circles). MBT—Main Boundary thrust; ISZ—Indus suture zone; BNS—Bangong-Nujiang suture.

TABLE 1. SUMMARY OF ROCK SEQUENCES	
Field Name	Lithologies
Tangtse pluton and leucogranite sheets	21–14 Ma sheeted leucogranite pluton (Fig. 3A). Leucogranites grade to leucotonalites and are composed of varying proportions of K-feldspar, plagioclase, quartz, garnet, muscovite, biotite, hornblende, and tourmaline. Inherited zircon cores have been dated at ca. 63 Ma and ca. 106 Ma (Searle et al., 1998; Weinberg et al., 2000; Weinberg and Searle, 1998).
Muglib pluton	118 ± 15 Ma (Ravikant, 2006) calc-alkaline batholith composed primarily of medium- to coarse-grained granodiorite (Figs. 4A and 4B), and minor quartz diorite and fine-grained biotite granite (border facies).
Pangong metamorphic complex	Upper-amphibolite facies (Rolland and Pêcher, 2001), anatectic sequence of biotite schist, psammites (Fig. 4C), and amphibolites interlayered with calc-silicate bands up to several hundred meters wide. All are intruded by granodiorites and granites interpreted to be related to the Muglib pluton (Weinberg and Mark, 2008).
Biotite-hornblende metaclastic sequence	Part of the Pangong metamorphic complex. Sequence ranges from biotite schists and psammites to amphibolites, depending on the modal contents of biotite, hornblende, quartz and plagioclase.
Karakoram metamorphic complex	Crops out to the northeast of the Karakoram shear zone; composed of biotite schists, amphibolites, and marbles. Lower-amphibolite facies, minor leucogranite intrusions and no evidence for migmatization. It differs from the Pangong metamorphic complex by the presence of marble layers, rarity of leucogranites, and lower metamorphic facies (Weinberg and Mark, 2008).
Karakoram batholith	Ca. 20–15 Ma, two-mica, tourmaline, garnet-bearing leucogranite body cropping out along the Shyok and Nubra valleys, N-NNW from the study area (Weinberg et al., 2000).
Ladakh batholith and Khardung volcanics	70–50 Ma calc-alkaline batholith and its volcanoclastic overburden, part of the Transhimalayan batholith (Dunlap and Wysoczanski, 2002; Weinberg and Dunlap, 2000), composed of gabbros through to granites. Crops out parallel to and south of the Karakoram shear zone.

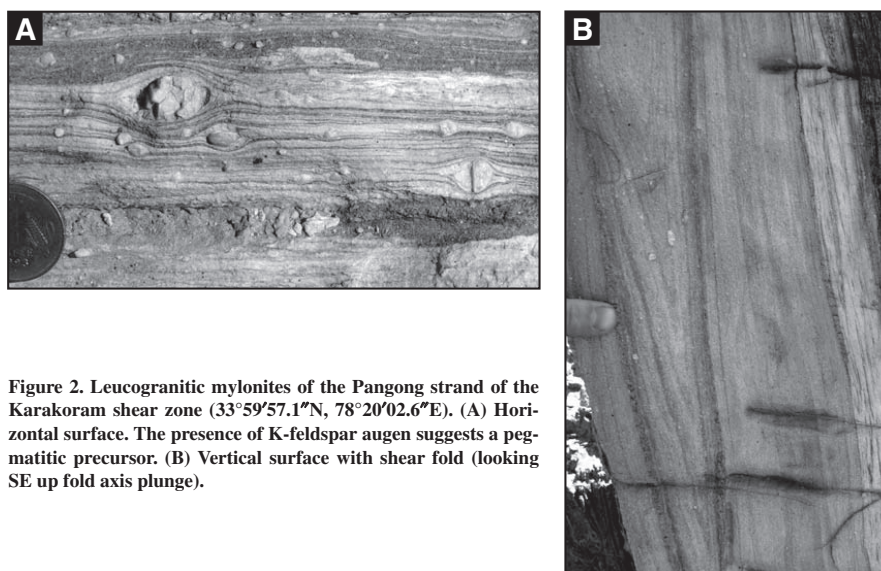


Figure 2. Leucogranitic mylonites of the Pangong strand of the Karakoram shear zone ($33^{\circ}59'57.1''\text{N}$, $78^{\circ}20'02.6''\text{E}$). (A) Horizontal surface. The presence of K-feldspar augen suggests a pegmatitic precursor. (B) Vertical surface with shear fold (looking SE up fold axis plunge).

The sequence of rocks comprising the Pangong metamorphic complex is described in Table 1. Rolland and Pêcher (2001) estimated upper-amphibolite conditions for rocks from this part of the complex, with peak temperatures around 700–750 °C and pressures of 4–5 kbar. During metamorphism, the biotite-rich end member of its metaclastic sequence is interpreted to have melted in situ without obvious peritectic minerals. Hornblende-bearing rocks are interpreted to have undergone similar melting and produced euhedral, poikilitic hornblende. Melting is inferred to have occurred at the wet solidus for these rocks, involving H_2O as a free phase, where biotite was stable, and new hornblende was either a peritectic product (Berger et al., 2008; Lappin and Hollister, 1980) or a result of magmatic crystallization. Layer-parallel leucosomes are linked continuously to axial-planar leucosomes, giving rise to leucogranite and pegmatite dikes, sheets, and plutons, which intrude all major rock types (Weinberg, 1999; Weinberg and Searle, 1998). Because of the continuous link from leucosomes to larger dikes and plutons, we interpret that, at least in part, leucogranites are locally derived magmas (Weinberg and Mark, 2008).

The Tangtse strand is generally characterized by amphibolite-facies mylonites with a strong, gently NW-plunging lineation. The Pangong strand has an early amphibolite facies stretching lineation that plunges from horizontal to moderately NW, indicative of dextral movement with a NE-side-up component. Locally it is over-

printed by narrow zones of greenschist-facies retrogression with stretching lineation plunging SE, also indicative of dextral movement but with a NE-side-down component. A kinematic change from amphibolite- to greenschist-facies deformation was also documented further SE in Tibet along the shear zone (Valli et al., 2007, 2008), where greenschist-facies shearing also was accompanied by a NE-side-down component (Lacassin et al., 2004).

Amphibolite-facies mylonites are characterized by: (1) sheared leucogranites and pegmatites (Fig. 2), (2) biotite-plagioclase-quartz schists and psammites, with minor muscovite, or (3) competent boudins of hornblende-biotite-plagioclase-quartz amphibolites. Greenschist-facies retrogression is characterized by sheared (1) muscovite-biotite-plagioclase-quartz schists, where the muscovite makes up 50% of micas, and (2) mafic rocks composed of tremolite-actinolite, chlorite, biotite, plagioclase, quartz, plus minor muscovite and calcite. Detailed studies of deformation mechanisms of rocks from this shear zone have concluded that there is a range of fault rocks from ductile to brittle, including cataclastic rocks and clay-bearing fault gouges (Phillips and Searle, 2007; Rutter et al., 2007).

K-Ar dating reveals that the Ladakh batholith, SW of the Pangong Range, had cooled significantly by ca. 36 Ma and was locally reheated in the vicinity of the Karakoram shear zone as a result of overthrusting of the Pangong metamorphic complex (see Dunlap et al. [1998] for a full dis-

cussion). The Karakoram metamorphic complex, NE of the Pangong Range, is composed of marbles, calc-silicate rocks interlayered with amphibolites, schists, and fine-grained slates (Dunlap et al., 1998). Their mineral parageneses are indicative of lower-amphibolite facies, where schists lack evidence for partial melting and are composed of muscovite, biotite, plagioclase, quartz, cordierite, and garnet.

Leucogranite samples from within the Tangtse gorge yielded U-Pb zircon crystallization ages between 21 and 14 Ma (Phillips et al., 2004; Searle et al., 1998). Two leucogranite samples yielded two inherited zircon age groups: ca. 63 Ma and ca. 106 Ma, consistent with low-temperature remelting of rocks related temporally to the calc-alkaline Ladakh batholith (e.g., Weinberg and Dunlap, 2000; Weinberg et al., 2000). The calc-alkaline rocks that are exposed in the gorge forming the Muglib pluton, which is interpreted to have undergone partial melting (see following) are the most likely source of these inherited zircons, as indicated by our unpublished zircon and sphene, U-Pb sensitive high-resolution ion microprobe (SHRIMP) ages, and by Rb-Sr geochronology (Ravikant, 2006).

CALC-ALKALINE MUGLIB PLUTON AND LEUCOGRANITE TANGTSE PLUTON

In the NE corner of the Tangtse gorge, leucogranitic rocks form an injection complex, which includes a sheeted pluton at the contact

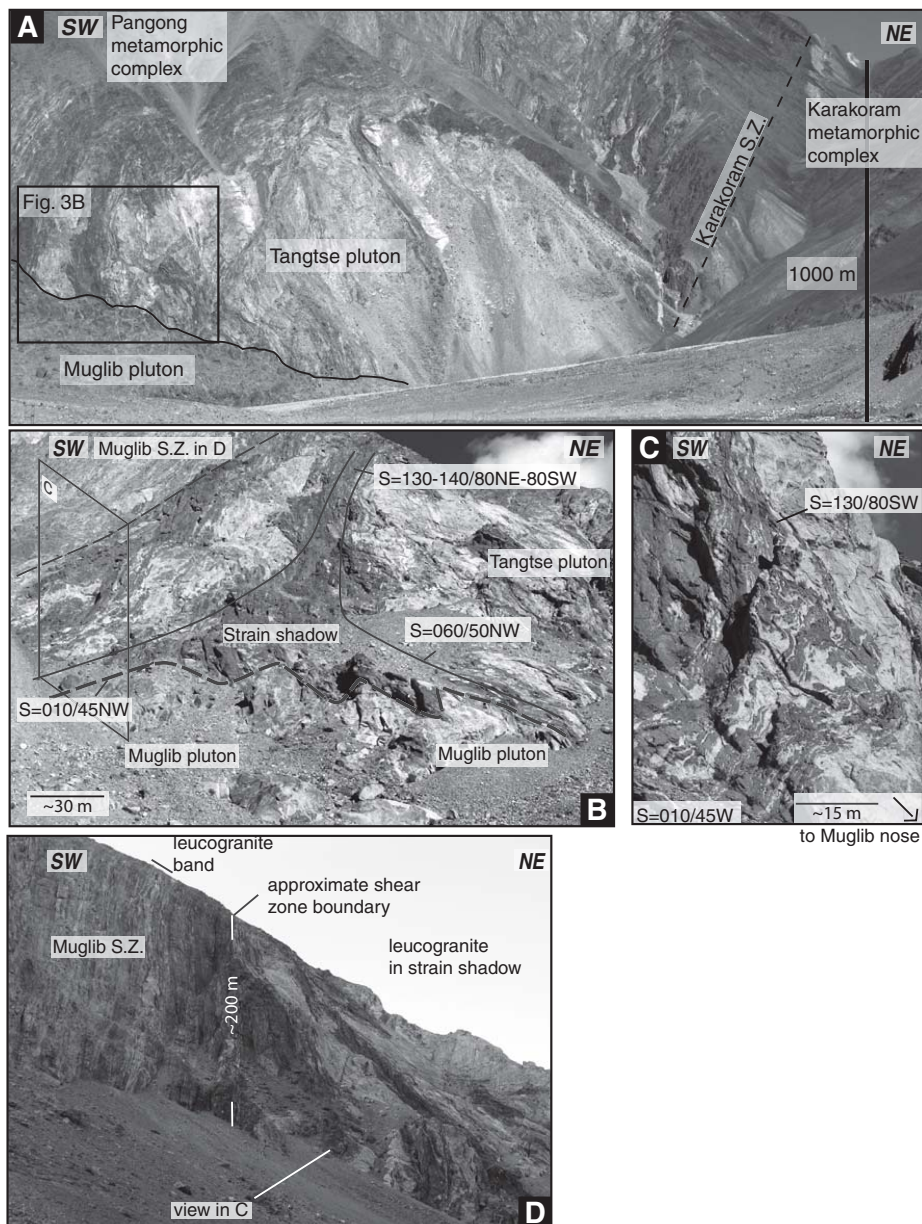


Figure 3. (A) Tangtse pluton NW of the Muglib pluton ($34^{\circ}03'30''\text{N}$, $78^{\circ}14'00''\text{E}$) showing dark screens of country rock within the pluton, and boudinaged leucogranite dikes in the distance, NW of the pluton and parallel to the dextral Pangong strand of the Karakoram shear zone, on the right-hand-side. All rocks are strongly sheared. The plane identified as the shear zone marks the contact between a mylonitic marble to the NE and strained migmatitic metasedimentary rocks intruded by leucogranite dikes to the SW. S.Z.—shear zone. Box on the left represents approximate position of B. (B) Foliation triple point resulting from the bifurcation of the regional trend around the NW termination of the Muglib pluton. (C) Irregular leucogranite sheets and pods on the SW of B where the regional foliation curves around the Muglib pluton. Photograph is looking NE. (D) Muglib strand characterized by intensely foliated rocks marking the SE boundary of the pressure shadow. The boundary of the shear zone is marked by two short white lines; a narrow band of leucogranite within the shear zone is also marked.

of the calc-alkaline Muglib pluton (Fig. 1B; Table 1). This area is bounded by the Pangong strand to the NE and the Muglib strand to the SE (Fig. 3D). The Muglib pluton is an elongate body trending parallel to the Pangong strand for at least 15 km. Close to the Muglib village, the northern contact is exposed where this pluton plunges under metasedimentary rocks and leucogranites, and defines a closure referred to here as the Muglib nose (Fig. 1B). The main facies of the Muglib pluton is a sheared medium- to coarse-grained biotite-hornblende

granodiorite that grades locally toward quartz-diorite and is intruded by leucogranitic dikes (Fig. 4A). Close to the NE margin, a medium-grained biotite-granite with local microdioritic enclaves defines a sheared, ~200-m-wide border facies. This facies forms dikes that intrude the country rocks and has narrow, foliation-parallel leucosomes with diffuse margins that lack melanosome rims. Leucosomes merge along the strike to form irregular coarse-grained leucogranitic patches, 10–30 cm wide, also with diffuse margins, such as in the boudin neck in

Figure 4B. This suggests that the leucosomes and leucogranitic patches are a result of in situ partial melting of the biotite-granite. By contrast, the main facies, although intruded by leucogranites (Fig. 4A), lacks widespread evidence for in situ melting. This anatexis is likely related to the regional 21–14 Ma anatexis that gave rise to leucogranites elsewhere, caused by the influx of a water-rich volatile phase (e.g., Fig. 4C; Weinberg and Mark, 2008).

Rocks of the Muglib pluton and country rocks have a strong penetrative solid-state foliation

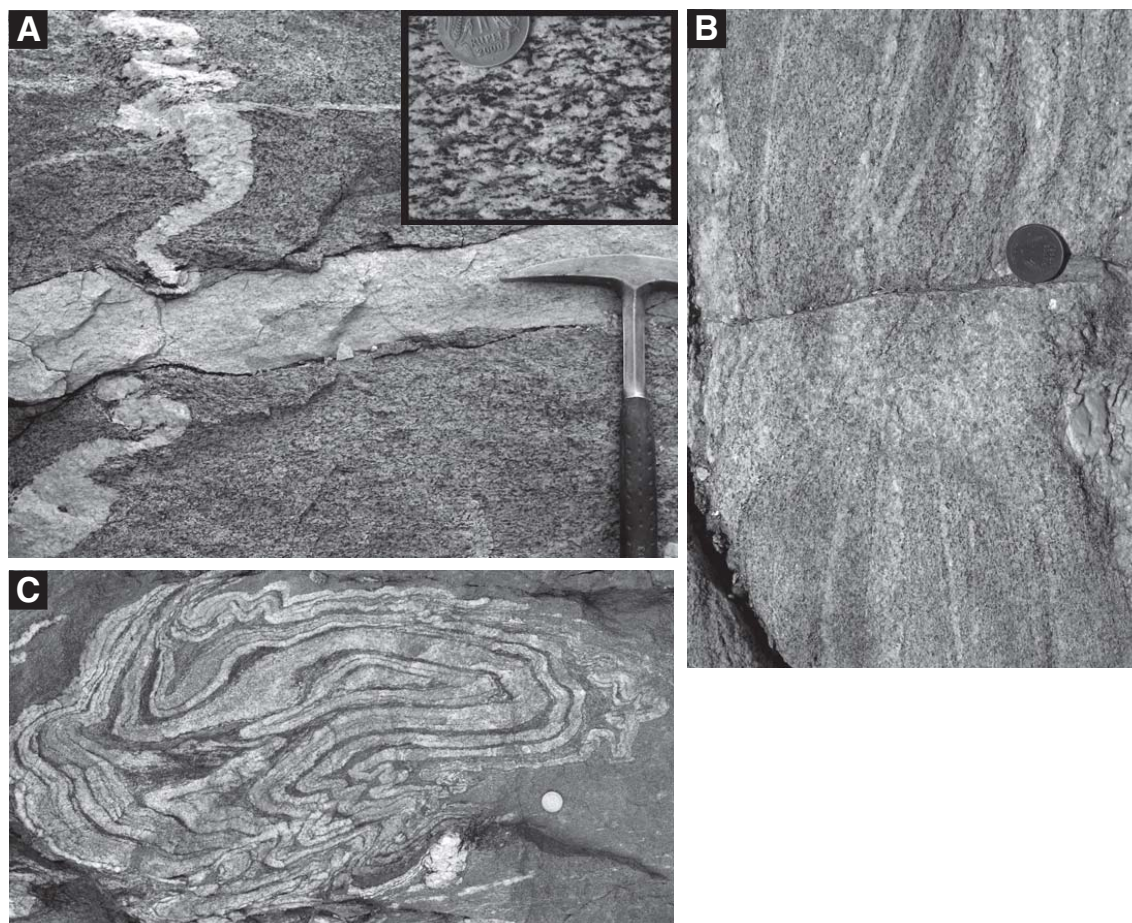


Figure 4. (A) Deformed granodiorite of the Muglib pluton intruded by pegmatitic leucogranite dikes, folded, and stretched. Inset: dextral shearing of granodiorite indicated by S-C-C' foliations. Both images are from nearly horizontal planes, and NW is to the right (33°59'05.0"N, 78°18'37.8"E). (B) Medium-grained biotite-granite and leucosome layers with indistinct boundaries linked to a pod in the boudin neck. This is interpreted to indicate in situ melting during deformation. Horizontal exposure, NW is toward the top of the photograph. (C) Migmatitic biotite-psammite with chaotically folded layered leucosomes in steep exposure within the Tangtse pluton. Looking WNW, up is to the left (34°03'42.6"N, 78°13'52.2"E).

(Fig. 4A) that strikes generally N40W, with variably steep dips, and lineation plunging moderately NW. Dextral shear deformation is indicated by S-C-C' fabric (Fig. 4A, inset), asymmetric folds, and asymmetric boudinage. Bedding in country rocks NE of the pluton is parallel to penetrative foliation and to the Pangong strand of the shear zone, but both deviate from that trend to drape around the Muglib nose, where they have moderate northerly dips (Figs. 1B, 3B, and 3C). Poles to foliation (Fig. 1, inset) in the Muglib nose define a great circle, from which a fold axis plunging moderately NW can be inferred. This is roughly parallel to both local and regional lineation (Weinberg et al., 2000) and to hinge lines of metric open folds mapped in the area.

Leucogranitic sheets and irregular pods crop out in the region of deflected foliation (Figs. 1 and 3) and occupy more than 50% of the surface area where they form an injection migmatite (Weinberg and Searle, 1998). The Tangtse pluton (Fig. 3A) was formed in this zone by the amalgamation of numerous leucogranite sheets. The pluton is 1.5 km long and is bounded by the Pangong strand to the NE. Its vertical exposure is ~600 m, and it is 200–300 m wide. The leucogranite sheets intrude older, fine- to medium-grained biotite-granite sheets, possibly related to the calc-alkaline Muglib pluton, and migmatitic biotite-hornblende metaclastic rocks that are preserved as screens inside the pluton (Figs. 3A and 3B). The regional foliation trend deflects not only around the Muglib pluton, but also around the northwestern end of the Tangtse pluton (Fig. 1B), implying that after solidification, it also behaved as a competent body during continued deformation. In the shear zones that surround the Muglib nose area, the volume of leucogranites is reduced to 10%–30% of the total. This is clear in the Muglib strand (Fig. 3D), where narrow, irregular bands of leucogranite are recognizable but less voluminous than away from the shear zone.

DISCUSSION

Contemporaneous Magmatism, Folding, and Dextral Shearing

Folds generally have steep axial-planar foliation striking between N60W to N40W, with NW-plunging fold axes (e.g., Fig. 4A; Weinberg and Mark, 2008). This fold geometry is compatible with the dominantly dextral shearing in the two NW-striking bounding strands of the Karakoram shear zone. Together, they account for transpression, which explains the large scale pop-up structure that characterizes the Pangong Range (Weinberg et al., 2000).

There is considerable discussion regarding the relative timing of melting and deformation

in the Karakoram shear zone. The geometries of leucosomes, representing what were once melt-rich parts of partially molten rocks, and folds demonstrate that melting took place during folding. For example, leucosomes parallel with migmatite layering merge continuously with leucosomes parallel to axial-planar foliation. Magma transfer through this leucosome network assisted folding (Weinberg and Mark, 2008). Evidence of contemporaneity between melting and dextral shearing can be found, but is obscured by subsequent subsolidus shearing (Dunlap et al., 1998; Rutter et al., 2007). Subsidiary deformation is reflected in variable strain intensities recorded by leucogranites as a function of grain size and as a function of their location in relation to high-strain zones. Leucogranites vary from virtually undeformed in coarse-grained pegmatitic portions, to weakly foliated in areas of folding, to fully recrystallized mylonites within shear zones (Figs. 2A and 2B). These foliations generally strike NW and dip steeply, and lineations in mylonitic leucogranites plunge NW, all of which are parallel to the shear zone fabric.

The outcrop at Tangtse Gompa, on the Tangtse strand of the shear zone (described in Phillips et al., 2004; Rutter et al., 2007), preserves evidence for the synkinematic intrusion of leucogranites. Here, the dominant strike of mylonitic foliation and lithologic layering is N70W, with a nearly vertical dip. A 20-cm-wide leucogranite dike intrudes a dextral brittle fault that strikes N-S, and displaces layering and mylonitic shear planes. This N-S-trending fault is kinematically compatible with the dextral shearing on the Tangtse strand, and the leucogranite that intrudes it records also a faint N70W-striking and steeply dipping foliation parallel to mylonitic foliation in surrounding rocks. These features suggest that dextral brittle faulting formed during shearing on the Tangtse strand and was exploited by a synkinematic leucogranite dike. Once solidified, the dike was overprinted by continued shearing.

In the same outcrop there are also layer-parallel leucogranite mylonitic bands, as well as leucogranitic dikes cutting across the main fabric at a variety of angles. When hosted by competent rocks, such as amphibolites, crosscutting dikes tend to be continuous and of regular width. However, when these dikes enter a less-competent rock type, such as marble, their trends deviate towards that of the shear zone orientation, in a manner consistent with increased straining. In the process, the dikes become strongly boudinaged, while, internally, they record varying bulk strain, from strongly deformed mylonites to apparently undeformed pegmatites. Strain in these magmatic rocks seems to decrease with decreasing age (Phil-

lips et al., 2004) but also decreases with increasing grain size. There are examples of folded dikes with apparently undeformed pegmatites coexisting in the same dike with strongly foliated medium-grained leucogranite. All the evidence in this outcrop is strongly suggestive of continued magma intrusion during shearing. This is at odds with conclusions by Phillips et al. (2004), but confirms a similar conclusion reached farther south along the shear zone in Tibet in rocks with a broadly similar history (Lacassin et al., 2004; Valli et al., 2007).

Thus, we conclude, based on: (1) the strain compatibility arguments, (2) the large-scale pop-up structure that exhumed the Pangong metamorphic complex (Weinberg et al., 2000), and (3) the evidence for synkinematic 21–14 Ma in situ melting and leucogranite intrusion, that all three events—folding, dextral shearing, and melting—were contemporaneous and related.

Pressure Shadow and Magma Accumulation

The large accumulation of younger leucogranitic rocks mapped immediately northwest and physically above the Muglib nose (Figs. 1 and 3) contrasts with the less voluminous leucogranite bands in the shear zones (Fig. 3D) including those that border the Muglib pluton. The irregular shape of leucogranite sheets and pods in the nose area, leading to the pervasive breakup of country rocks (Fig. 3C), suggests that this region was at temperatures above or close to magma solidus at the time of intrusion (Weinberg and Mark, 2008; Weinberg and Searle, 1998).

The deflection of the regional foliation trend around the Muglib pluton to drape around the Muglib nose (Fig. 1) is interpreted to result from the Muglib pluton behaving as a competent body during deformation. The deflection defines what is known as a foliation triple point (Johnson et al., 2003; Pons et al., 1995) and is associated with a low pressure strain shadow, like those developed around porphyroblasts. We argue that the magma accumulation resulted from migration and ponding driven by a negative pressure gradient into this zone. In this way, the older, competent Muglib pluton not only contributed with magma to the new pluton, as inferred from its partial melting and presence of inherited zircons in the leucogranites, but also created the conditions for growth of the younger pluton.

Magma Traps and Magma Pumping in Shear Zones

Shear zones can give rise to a number of low-pressure sites, not only in pressure shadows around competent rocks, but also in dilational

jogs (Fig. 5), pull-apart regions, shear zone terminations (Brown and Solar, 1998a; D'Lemos et al., 1992; Davies, 1982), or dilational areas resulting from active, crosscutting shear zones. These low-pressure sites form effective magma traps, and the volume of magma accumulated depends on: (1) the scale of the heterogeneity leading to low pressures, (2) pressure gradients driving melt into the low-pressure sites, which are a function of regional stresses, (3) the degree of partial melting and permeability of the system, and (4) the time available before the system is modified.

If the nature of strain and the distribution of stress in dilatant sites in shear zones are modified before magma solidification, traps can be destroyed, and magma accumulations can be pumped out, becoming available for pluton growth elsewhere in the system. Considering the evolving dynamic, kinematic, and geometric nature of large-scale tectonic systems, any particular shear zone in the system is likely to evolve through time. For example, changes in plate geometry, movement direction, or velocity will impact on the movement sense and stress distribution in shear zones. Shear zones are also sensitive to local block rearrangements. Furthermore, as the system evolves, the thermal profile and rock rheology around and within a shear zone will also change, triggering fluctuations in stress intensity and direction, changes in competency contrasts between rock types, and thus the nature of deformation and stress in and around the shear zones. All of these changes affect the stability of magma traps.

We postulate that magma traps are most likely transitory features that provide a temporary residence for magmas along their general upward migration. This is shown schematically in Figure 5, where a change from transtension to transpression is depicted. Tortuous shear zones that act to deform complex anatectic rock packages and undergo varied kinematic histories are likely to develop a number of such traps that can be created and destroyed during the history of the system. During periods of steady straining, magmas accumulate in traps with only minor leakage out of the anatectic zone (Fig. 5A). During periods of transition in the nature of straining, large volumes of melt are expelled from the anatectic shear zone (period between Figs. 5A and 5B) (e.g., Glazner, 1991). Each trap, and consequently each major magma batch being expelled, may have a distinct chemical signature that represents different proportions of magmas from different sources, degrees of partial melting and residuum separation.

In conclusion, shear zones may act as pumps by locally trapping magma in anatectic terranes until local or regional changes force the

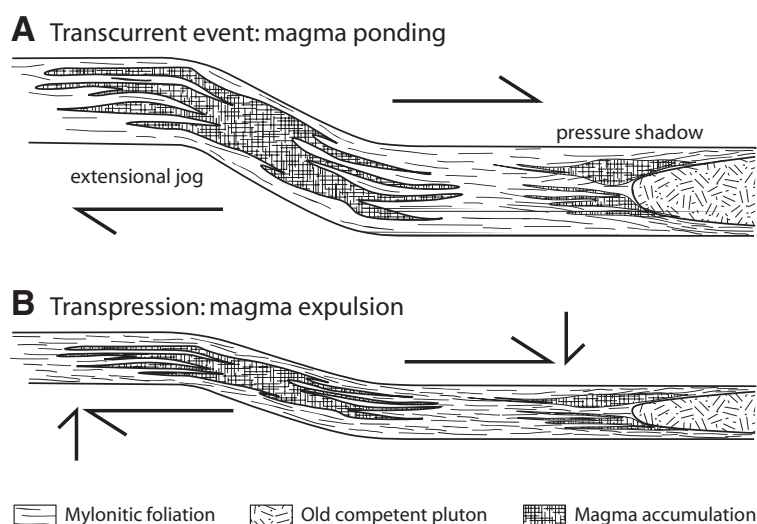


Figure 5. Magma accumulations in a shear zone. (A) During a transcurrent event, magma accumulates in dilational jogs or in strain shadows around competent bodies within an anatectic region. During this stage, minor volumes of magma leak out to the upper crust. (B) A change to transpression expels magma from these regions. The switch from a transcurrent to a transpressive regime leads to a magma pumping event. The change in regime exemplified here is one of a number of possibilities. Magma pumping will take place in any system, or part of a system, that changes from dilation to contraction. Repetitive pumping results from temporal fluctuation between these two states.

magma out, feeding batch growth of batholiths elsewhere. Major periods of magma pumping should accompany periods of changes in shear zone kinematics (D'Lemos et al., 1992). Thus, magma trapping in anatectic shear zones and shear pumping events during periods of change could explain incremental growth of complex plutons over millions of years (Coleman et al., 2004; Deniel et al., 1987; Mahan et al., 2003) punctuated by short periods of high magma flux (Matzel et al., 2006).

ACKNOWLEDGMENTS

We thank Andy Tomkins, Gary Solar, and Scott Patterson for reviews of an early version of this paper. We thank also Mike Brown, Jean-Louis Vigneresse, and Associate Editor Luca Ferrari for their detailed and constructive reviews.

REFERENCES CITED

- Avouac, J.-P., and Tapponnier, P., 1993, Kinematic model of active deformation in central Asia: *Geophysical Research Letters*, v. 20, no. 10, p. 895–898, doi: 10.1029/93GL00128.
- Berger, A., Burri, T., Alt-Epping, P., and Engi, M., 2008, Tectonically controlled fluid flow and water-assisted melting in the middle crust: An example from the Central Alps: *Lithos*, v. 102, 3/4, 598–615, doi:10.1016/j.lithos.2007.07.027.

- Brown, M., 2004, The mechanisms of melt extraction from lower continental crust of orogens: Is it a self-organized critical phenomenon?: *Transactions of the Royal Society of Edinburgh: Earth Sciences*, v. 95, p. 35–48, doi: 10.1017/S0263593300000900.
- Brown, M., and Solar, G.S., 1998a, Granite ascent and emplacement during contractional deformation in convergent orogens: *Journal of Structural Geology*, v. 20, no. 9–10, p. 1365–1393, doi: 10.1016/S0191-8141(98)00074-1.
- Brown, M., and Solar, G.S., 1998b, Shear-zone systems and melts: Feedback relations and self-organization in orogenic belts: *Journal of Structural Geology*, v. 20, no. 2–3, p. 211–227, doi: 10.1016/S0191-8141(97)00068-0.
- Brown, M., and Solar, G.S., 1999, The mechanism of ascent and emplacement of granite magma during transpression: A syntectonic granite paradigm: *Tectonophysics*, v. 312, p. 1–33, doi: 10.1016/S0040-1951(99)00169-9.
- Coleman, D.S., Gray, W., and Glazner, A.F., 2004, Rethinking the emplacement and evolution of zoned plutons: geochronologic evidence for incremental assembly of the Tuolumne Intrusive Suite, California: *Geology*, v. 32, no. 5, p. 433–436, doi: 10.1130/G20220.1.
- Davies, F.B., 1982, Pan-African granite intrusion in response to tectonic volume changes in a ductile shear zone from northern Saudi Arabia: *The Journal of Geology*, v. 90, no. 5, p. 467–483.
- Deniel, C., Vidal, P., Fernandez, A., LeFort, P., and Peucat, J.-J., 1987, Isotopic study of the Manaslu granite (Himalaya, Nepal): Inferences on the age and source of Himalayan leucogranites: *Contributions to Mineralogy and Petrology*, v. 96, p. 78–92, doi: 10.1007/BF00375529.
- D'Lemos, R.S., Brown, M., and Strachan, R.A., 1992, Granite magma generation, ascent and emplacement within a transpressional orogen: *Journal of the Geological Society of London*, v. 149, p. 487–490, doi: 10.1144/gsjgs.149.4.0487.

- Dunlap, W.J., and Wysoczanski, R., 2002, Thermal evidence for Early Cretaceous metamorphism in the Shyok suture zone and age of the Khardung volcanic rocks, Ladakh, India: *Journal of Asian Earth Sciences*, v. 20, p. 481–490.
- Dunlap, W.J., Weinberg, R.F., and Searle, M.P., 1998, Karakoram fault zone rocks cool in two phases: *Journal of the Geological Society of London*, v. 155, p. 903–912, doi: 10.1144/gsjgs.155.6.0903.
- Elias-Herrera, M., and Ortega-Gutiérrez, F., 2002, Caltepec fault zone: An Early Permian dextral transpressional boundary between the Proterozoic Oaxacan and Paleozoic Acatlán complexes, southern Mexico, and regional tectonic implications: *Tectonics*, v. 21, doi: 10.1029/2000TC001278.
- Glazner, A.F., 1991, Plutonism, oblique subduction, and continental growth: an example from the Mesozoic of California: *Geology*, v. 19, no. 8, p. 784–786, doi: 10.1130/0091-7613(1991)019<0784:POSACG>2.3.CO;2.
- Hutton, D.H.W., and Reavy, R.J., 1992, Strike-slip tectonics and granite petrogenesis: *Tectonics*, v. 11, no. 5, p. 960–967, doi: 10.1029/92TC00336.
- Johnson, S.E., Fletcher, J.M., Fanning, C.M., Vernon, R.H., Paterson, S.R., and Tate, M.C., 2003, Structure, emplacement and lateral expansion of the San Jose tonalite pluton, Peninsular Ranges Batholith, Baja California, Mexico: *Journal of Structural Geology*, v. 25, p. 1933–1957, doi: 10.1016/S0191-8141(03)00015-4.
- Lacassin, R., Valli, F., Arnaud, N., Leloup, P.H., Paquette, J.L., Haibing, L., Tapponnier, P., Chevalier, M.-L., Guillot, S., Maheo, G., and Zhiqin, X., 2004, Large-scale geometry, offset and kinematic evolution of the Karakoram fault, Tibet: *Earth and Planetary Science Letters*, v. 219, p. 255–269, doi: 10.1016/S0012-821X(04)00006-8.
- Lacroix, S., Sawyer, E.W., and Chown, E.H., 1998, Pluton emplacement within an extensional transfer zone during dextral strike-slip faulting: An example from the late Archaean Abitibi Greenstone Belt: *Journal of Structural Geology*, v. 20, no. 1, p. 43–59, doi: 10.1016/S0191-8141(97)00071-0.
- Lappin, A.R., and Hollister, L.S., 1980, Partial melting in the Central gneiss complex near Prince Rupert, British Columbia: *American Journal of Science*, v. 280, p. 518–545.
- Leloup, P.H., Ricard, Y., Battaglia, J., and Lacassin, R., 1999, Shear heating in continental strike-slip shear zones: Model and field examples: *Geophysical Journal International*, v. 136, p. 19–40, doi: 10.1046/j.1365-246X.1999.00683.x.
- Mahan, K.H., Bartley, J.M., Coleman, D.S., Glazner, A.F., and Carl, B.S., 2003, Sheeted intrusion of the synkinematic McDoyle pluton, Sierra Nevada, California: *Geological Society of America Bulletin*, v. 115, no. 12, p. 1570–1582, doi: 10.1130/B22083.1.
- Mancktelow, N.S., 2006, How ductile are ductile shear zones? *Geology*, v. 34, no. 5, p. 345–348, doi: 10.1130/G22260.1.
- Matzel, J.E.P., Bowring, S.A., and Miller, R.B., 2006, Time scales of pluton construction at differing crustal levels: Examples from the Mount Stuart and Tenpeak intrusions; North Cascades, Washington: *Geological Society of America Bulletin*, v. 118, p. 1412–1430, doi: 10.1130/B25923.1.
- McCaffrey, K.J.W., 1992, Igneous emplacement in a transpressive shear zone: Ox Mountains igneous complex: *Journal of the Geological Society of London*, v. 149, p. 221–235, doi: 10.1144/gsjgs.149.2.0221.
- Neves, S.P., Vauchez, A., and Archanjo, C.J., 1996, Shear zone-controlled magma emplacement or magma-assisted nucleation of shear zones? Insights from northeast Brazil: *Tectonophysics*, v. 262, p. 349–364, doi: 10.1016/0040-1951(96)00007-8.
- Pe-Piper, G., Koukouvelas, I., and Piper, D.J.W., 1998, Synkinematic granite emplacement in shear zone: The Pleasant Hill pluton, Canadian Appalachian: *Geological Society of America Bulletin*, v. 110, no. 4, p. 523–536, doi: 10.1130/0016-7606(1998)110<0523:SGEIAS>2.3.CO;2.
- Phillips, R.J., and Searle, M.P., 2007, Macrostructural and microstructural architecture of the Karakoram fault: Relationship between magmatism and strike-slip fault: *Tectonics*, v. 26, p. TC3017, doi: 10.1029/2006TC001946.
- Phillips, R.J., Parrish, R.R., and Searle, M.P., 2004, Age constraints on ductile deformation and long-term slip rates along the Karakoram fault zone, Ladakh: *Earth and Planetary Science Letters*, v. 226, p. 305–319, doi: 10.1016/j.epsl.2004.07.037.
- Pons, J., Barbey, P., Dupuis, D., and Léger, J.M., 1995, Mechanisms of pluton emplacement and structural evolution of a 2.1 Ga juvenile continental crust: The Birimian of southwestern Niger: *Precambrian Research*, v. 70, p. 281–301, doi: 10.1016/0301-9268(94)00048-V.
- Rabinowicz, M., and Vigneresse, J.L., 2004, Melt segregation under compaction and shear channeling: Application to granitic magma segregation in a continental crust: *Journal of Geophysical Research*, v. 109, B04407, doi: 10.1029/2002JB002372.
- Ravikant, V., 2006, Utility of Rb-Sr geochronology in constraining Miocene and Cretaceous events in the eastern Karakoram, Ladakh, India: *Journal of Asian Earth Sciences*, v. 27, p. 534–543, doi: 10.1016/j.jseas.2005.05.007.
- Rolland, Y., and Pêcher, A., 2001, The Pangong granulites of the Karakoram fault (western Tibet): Vertical extrusion within a lithosphere-scale fault? *Comptes Rendus de l'Académie des Sciences, Serie II, Fascicule A—Sciences de la Terre et des Planètes*, v. 332, no. 6, p. 363–370.
- Roman-Berdiel, T., Gapais, D., and Brun, J.-P., 1997, Granite intrusion along strike-slip zones in experiment and nature: *American Journal of Science*, v. 297, p. 651–678.
- Rutter, E.H., Faulkner, D.R., Brodie, K.H., Phillips, R.J., and Searle, M.P., 2007, Rock deformation processes in the Karakoram fault zone, Eastern Karakoram, Ladakh, NW India: *Journal of Structural Geology*, v. 29, p. 1315–1326, doi: 10.1016/j.jsg.2007.05.001.
- Sawyer, E.W., 1999, Criteria for the recognition of partial melting: *Physical and Chemistry of the Earth, Ser. A*, v. 24, no. 3, p. 269–279, doi: 10.1016/S1464-1895(99)00029-0.
- Searle, M.P., Weinberg, R.F., and Dunlap, W.J., 1998, Transpressional tectonics along the Karakoram fault zone, northern Ladakh, in Holdsworth, R.E., and Strachan, R.A., eds., *Continental Transpressional and Transtensional Tectonics*: Geological Society of London Special Publication 135, p. 307–326.
- Tikoff, B., and Teyssier, C., 1992, Crustal-scale, en-echelon “P-shear” tensional bridges: A possible solution to the batholithic room problem: *Geology*, v. 20, p. 927–930, doi: 10.1130/0091-7613(1992)020<0927:CSEEPS>2.3.CO;2.
- Valli, F., Nicolas, A., Leloup, P.H., Sobel, E.R., Maheo, G., Lacassin, R., Guillot, S., Li, H., Tapponnier, P., and Xu, Z., 2007, Twenty million years of continuous deformation along the Karakoram fault, western Tibet: A thermochronological analysis: *Tectonics*, v. 26, p. TC4004, doi: 10.1029/2005TC001913.
- Valli, F., Leloup, P.H., Paquette, J.-L., Arnaud, N., Li, H., Tapponnier, P., Lacassin, R., Guillot, S., Liu, D., Deloule, E., Xu, Z., and Maheo, G., 2008, New U-Th/Pb constraints on timing of shearing and long-term slip-rate on the Karakoram fault: *Tectonics*, doi: 10.1029/2007TC002184 (in press).
- Vigneresse, J.L., 1995, Control of granite emplacement by regional deformation: *Tectonophysics*, v. 249, p. 173–186, doi: 10.1016/0040-1951(95)00004-7.
- Weinberg, R.F., 1999, Mesoscale pervasive melt migration: Alternative to dyking: *Lithos*, v. 46, no. 3, p. 393–410, doi: 10.1016/S0024-4937(98)00075-9.
- Weinberg, R.F., and Dunlap, W.J., 2000, Growth and deformation of the Ladakh Batholith, northwest Himalayas: Implications for timing of continental collision and origin of calc-alkaline batholiths: *The Journal of Geology*, v. 108, p. 303–320, doi: 10.1086/314405.
- Weinberg, R.F., and Mark, G., 2008, Magma migration, folding and disaggregation of migmatites in the Karakoram shear zone, Ladakh, NW India: *Geological Society of America Bulletin*, v. 120, 7/8, 994–1009, doi: 10.1130/B26227.1.
- Weinberg, R.F., and Searle, M.P., 1998, The Pangong injection complex, Indian Karakoram: A case of pervasive granite flow through hot viscous crust: *Journal of the Geological Society of London*, v. 155, p. 883–891, doi: 10.1144/gsjgs.155.5.0883.
- Weinberg, R.F., Dunlap, W.J., and Whitehouse, M., 2000, New field, structural and geochronological data from the Shyok and Nubra valleys, northern Ladakh: Linking Kohistan to Tibet, in Khan, R., Treloar, P.J., and Searle, M.P., eds., *Tectonics of the Nanga Parbat Syntaxis and the Western Himalaya*: Geological Society of London Special Publication 170, p. 253–275.
- Weinberg, R.F., Sial, A.N., and Mariano, G., 2004, Plutons and shear zones in the Borborema Province, Brazil: *Geology*, v. 32, p. 377–380, doi: 10.1130/G20290.1.

MANUSCRIPT RECEIVED 4 NOVEMBER 2007

REVISED MANUSCRIPT RECEIVED 12 FEBRUARY 2008

MANUSCRIPT ACCEPTED 29 FEBRUARY 2008

PRINTED IN THE USA



Hybridization of granitic magmas in the source: The origin of the Karakoram Batholith, Ladakh, NW India

H. Reichardt ^{a,*}, R.F. Weinberg ^a, U.B. Andersson ^b, C.M. Fanning ^c

^a School of Geosciences, Monash University, Clayton, VIC 3800, Australia

^b Laboratory for Isotope Geology, Swedish Museum for Natural History, Box 50007, SE-104 05 Stockholm, Sweden

^c Research School of Earth Sciences, The Australian National University, Mills Road, Canberra ACT 0200, Australia

ARTICLE INFO

Article history:

Received 17 April 2009

Accepted 22 November 2009

Available online 2 December 2009

Keywords:

Karakoram Shear Zone

Karakoram Batholith

Crustal anatexis

Magma mixing

Radiogenic isotopes

ABSTRACT

Many magmatic bodies have a hybrid isotopic signature suggesting that somewhere during genesis, transport and emplacement, magmas assimilated other rocks or mixed with other magmas. Where and how hybridization takes place is seldom documented. Here, we investigate a magmatic system in the Eastern Karakoram, Ladakh, NW India, comprising an anatectic zone, and a network of sheets, stocks and plutons exposed in the Pangong Metamorphic Complex within the Karakoram Shear Zone, as well as the Karakoram Batholith. These granitic rocks have an isotopic signature indicative of a mixture between mantle and crustal sources. In the anatectic region, calc-alkaline granitoids and their meta-sedimentary country rocks underwent water-fluxed partial melting at upper amphibolite facies between 20 and 14 Ma ago. Anatexis gave rise to leucosomes and intrusive rocks that have a range in composition from leucotonalite to leucogranite. Those related to the partial melting of calc-alkaline rocks contain hornblende, whereas those related to Bt-psammites contain two micas \pm garnet. Leucosomes rooting in different source rocks merge with each other and homogenize as they link up to form a hierarchy of magma channels, feeding into stocks, plutons and ultimately into the Karakoram Batholith. This interpretation is supported by Sr and Nd isotopes. Initial $^{87}\text{Sr}/^{86}\text{Sr}$ and ϵ_{Nd} values are distinct for each of the magma protoliths in the anatectic zone and for the magmatic products. Calc-alkaline granitoids have initial $^{87}\text{Sr}/^{86}\text{Sr} = 0.7042$ to 0.7077 and $\epsilon_{\text{Nd}} = +0.6$ to $+2.4$, indicative of a slightly depleted mantle source region. This is in contrast to the meta-sedimentary rocks that yield initial $^{87}\text{Sr}/^{86}\text{Sr} = 0.7115$ to 0.7161 and $\epsilon_{\text{Nd}} = -10.0$ to -9.6 , suggesting a stronger crustal component. Leucogranitic rocks, including a variety of leucosomes in the anatectic zone and samples from the Karakoram Batholith, yield intermediate values of initial $^{87}\text{Sr}/^{86}\text{Sr} = 0.7076$ to 0.7121 and $\epsilon_{\text{Nd}} = -3.6$ to -7.1 that can be modelled by mixing of the two source rocks. The hybrid signature of leucosomes and their similarity to intrusive leucogranites indicate that magma hybridization must have taken place within the source region as a result of the confluence of magmas to form the escape channels. We conclude that the voluminous leucogranites of the Miocene Karakoram Batholith result from water-fluxed intracrustal melting of sources with crustal and mantle signatures, and that mixing occurred within the source.

© 2009 Elsevier B.V. All rights reserved.

1. Introduction

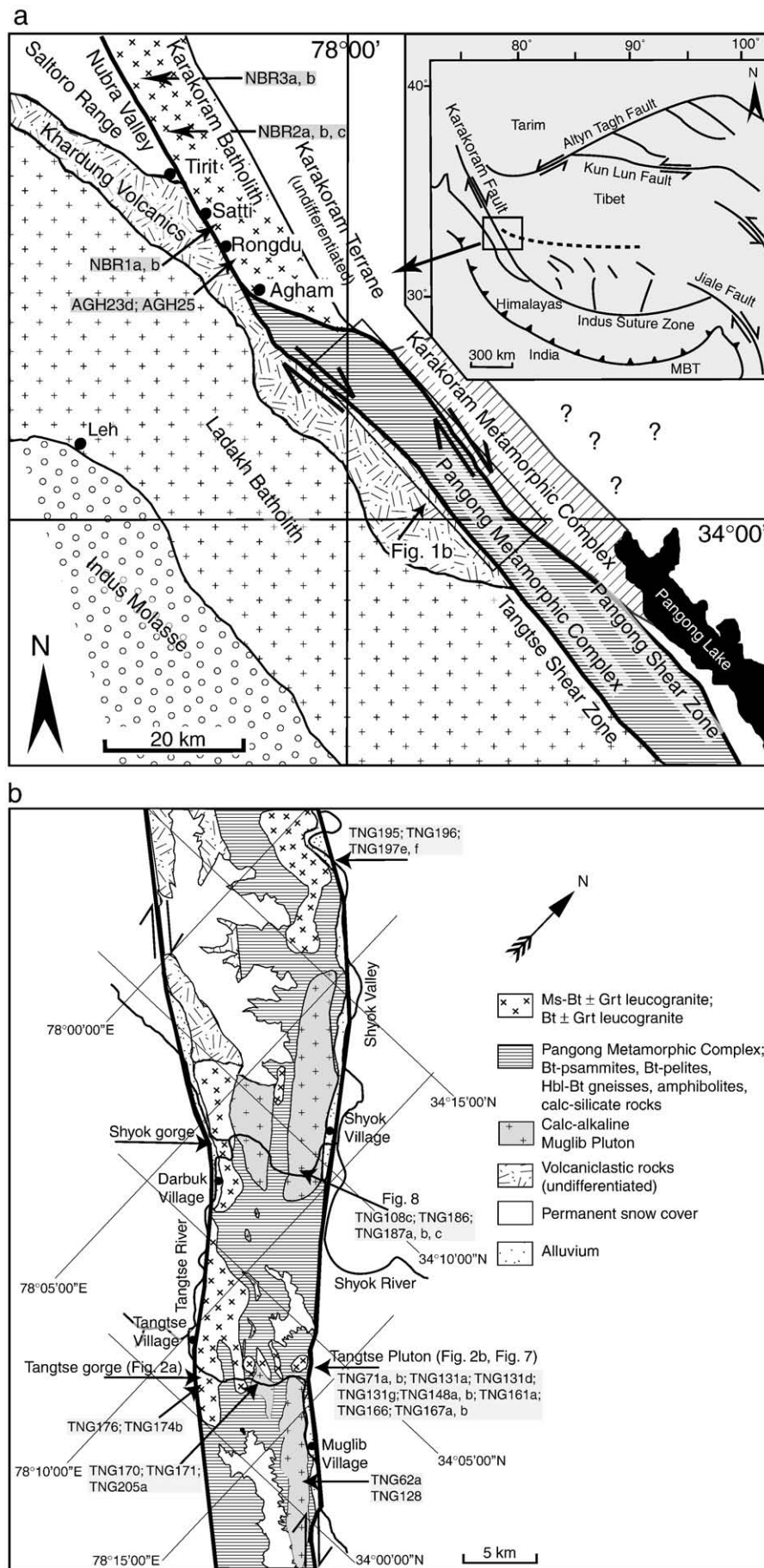
Granitic magma generation in continental collision zones can involve various source rocks and takes place under a range of conditions. Isotopic compositions of magmatic bodies are widely applied to trace their origin as the source rocks leave their isotopic fingerprint on the magmas (e.g. Beard et al., 2005). Granitoids with isotopic signatures intermediate between those of crustal and mantle sources, indicate that mixing of different magmas may have been involved (e.g. Andersson, 1991; Guillot and Le Fort, 1995; Hawkesworth and Vollmer, 1979). Generally, Himalayan Miocene leucogranites are examples of crustal melting with clear crustal isotopic signature (Deniel et al., 1987;

Le Fort et al., 1987; Guillot and Le Fort, 1995). Broadly contemporaneous leucogranites of the Karakoram Range in the western parts of the Himalayan orogen, however, have isotopic signatures intermediate between mantle and crust (Schärer et al., 1990; Searle et al., 1992; Crawford and Searle, 1992; Mahéo et al., 2002; Mahéo et al., 2009). The signature was explained by Mahéo et al. (2002) as resulting from break-off of the subducted Indian lithosphere causing higher heat flow from the asthenosphere and melting of metasomatised mantle of the Asian lithosphere. These melts then mixed with crustal melts. Mixing of magmas derived from a mantle and a crustal source has also been suggested by Crawford and Searle (1992) and Rex et al. (1988) who concluded that mantle-derived lamprophyre dykes found in the Karakoram could have influenced crustal magmas.

In the Tangtse-Shyok region of the Pangong Range within the Karakoram Shear Zone, in Ladakh, NW India (Fig. 1), migmatites are

* Corresponding author.

E-mail address: Henning.Reichardt@sci.monash.edu.au (H. Reichardt).



associated with leucogranite intrusions (Weinberg and Searle, 1998; Weinberg and Mark, 2008; Weinberg et al., 2009). Leucosomes are linked to leucogranites that form a complex intrusive sheet network linked to stocks and plutons that extend along the shear zone towards the Karakoram Batholith to the NW (Fig. 1a). In this paper, we present new geochemical, isotopic and geochronological data which support a link between magma migration and mixing processes that took place in the exposed migmatitic crustal source. This has led to the hybrid isotopic signature of the Karakoram Batholith. In the following, we introduce the Karakoram Shear Zone and describe the migmatites and their field relationships with leucogranite intrusions, including an overview of their geochemistry. Sr–Nd isotope and U–Pb SHRIMP results are then used to test field-based interpretations and to support regional-scale inferences.

2. Regional geology

The Karakoram Shear Zone lies in the central part of the Karakoram Fault and separates the Karakoram Terrane to the NE, from the Ladakh Terrane to the SW (Fig. 1a) (e.g. Raz and Honegger, 1989; Searle et al., 1998; Weinberg and Dunlap, 2000). The Karakoram Shear Zone itself is part of a crustal-scale, possibly lithospheric-scale (Lacassin et al., 2004; Rolland and Pêcher, 2001) strike–slip fault system that accommodates the northward push of the Indian plate into Eurasia and is characterized by dextral strike–slip motion, trending NW–SE, traceable for at least 700 km. The Karakoram Shear Zone in the Pangong Range area, in NE Ladakh is bounded by two roughly parallel mylonitic shear strands (Fig. 1a, b). The Tangtse Shear Zone (SW strand) dips 70° NE and separates the Pangong Metamorphic Complex (PMC) to the NE from the Ladakh Batholith to the SW. The Pangong Shear Zone (NE strand) is sub-vertical to steeply dipping SW, and separates the PMC from rocks of the Karakoram Terrane and the Karakoram Metamorphic Complex (KMC). The Karakoram Batholith crops out alongside the Nubra Valley to the NE of the Karakoram Shear Zone.

South of the PMC, the Ladakh Batholith granitoids comprise mainly Bt–Hbl granodiorites, commonly with mafic magmatic enclaves. The overlying Kardhung Volcanics are extrusive equivalents of the granitoids. This batholith is part of the Ladakh–Kohistan arc system with crystallization ages between 49 and 103 Ma (Honegger et al., 1982; Weinberg and Dunlap, 2000; Upadhyay et al., 2008; Ravikant et al., 2009). The PMC comprises a calc–alkaline granitoid suite, a meta–sedimentary rock sequence and leucogranite intrusions.

The calc–alkaline suite is dominated by a large body that we refer to as the Muglib Batholith. It is comprised mainly of Hbl–Bt–granodiorite, Bt–granodiorite and diorite. It extends at least from the area close to the Pangong Lake northwestwards to the Shyok Valley and links up discontinuously to the Tirit granite at the northeastern flanks of the Saltoro Range in the Nubra Valley further NW (Weinberg et al., 2000) through a number of dioritic–granodioritic bodies (Fig. 1a, b). The Muglib Batholith thus crops out for at least 85 km along strike of the Karakoram Shear Zone. The meta–sedimentary sequence comprises Bt–psammmites, Bt–pelites, Bt–Hbl gneisses ranging to amphibolites and calc–silicate rocks. Minor beds of marble crop out in the Tangtse Shear Zone (Dunlap et al., 1998; Weinberg and Searle, 1998; Phillips et al., 2004). The calc–alkaline granitoids and meta–sedimentary sequence are migmatized, giving rise to leucogranite intrusions (Weinberg et al., 2009). Leucogranites, including pegmatitic dykes, are mostly two mica ± garnet leucogranites and Bt–leucogranites, and have crystallization ages between 19.1 ± 1.1 Ma (Ravikant et al., 2009) and 13.7 ± 0.2 Ma (Phillips et al., 2004).

The Karakoram Metamorphic Complex (KMC), NE of the Pangong Range consists mainly of pelitic Grt–St-bearing Bt–schists, amphibolites and marbles (Searle and Tirrul, 1991; Dunlap et al., 1998). The

Karakoram Batholith crops out along strike of the Pangong Range and of the Karakoram Shear Zone further NW in the Nubra Valley as a 6 to 7 km wide band (Fig. 1a; Searle et al., 1998; Weinberg et al., 2000).

Strain in the PMC is strongly partitioned into the main mylonitic shear strands and deformation intensity decreases away from these. Fold axes of isoclinal folds within the PMC plunge moderately (20–30°) towards NW (320–345°). A continuous schistosity is defined by aligned biotite and, when present, hornblende. It generally trends 320–330° and has a stretching lineation defined by biotite and stretched quartz grains plunging gently to moderately (generally 10–40°, rarely horizontal) towards NW in amphibolite facies rocks. Consistent dextral S–C–C' fabrics throughout the PMC indicate dextral transpressional shearing with a NE-side-up component (Searle et al., 1998). A greenschist facies overprint is locally evident along the mylonitic Pangong Shear Zone where Ms, Ep and Chl (mineral abbreviations after Kretz, 1983) stretching lineations plunge moderately SE, indicating fault reactivation with a NE-side-down component. Evidence for present-day movements in the area has been reported only in one locality from the Pangong Shear Zone, whereas the Tangtse Shear Zone seems to be inactive (Brown et al., 2002; Rutter et al., 2007). There are wide variations in the estimation of total offset and the current slip rate along the Karakoram Shear Zone (see Valli et al., 2007 for discussion). Estimates of recent movements are in the range of 4 ± 1 mm/a (Brown et al., 2002), 3.4 ± 5 mm/a (Jade et al., 2004) or as low as 1 ± 3 mm/a (Wright et al., 2004).

3. Methodology

3.1. Geochemical analysis

For major element and trace element analysis, pulverized whole rock samples were analyzed after preparation of fused discs and pressed pellets, respectively, in a Bruker–AXS S4 Pioneer XRF Spectrometer at the Advanced Analytical Centre (AAC) of James Cook University. In Table 1 and appendix A, only samples labeled with * were analyzed for trace elements by XRF. For all other samples, trace elements were analyzed using a Thermo Finnigan X series II, quadrupole ICP–MS. Sample solutions were produced from approximately 50 mg of sample powder using high pressure digestion methods. ICP–MS count rates were externally standardized by means of calibration curves based on the USGS standard reference material AGV-1 and RGM-1 following Eggins et al. (1997) for their trace element contents. Drift corrections were applied by the combined use of In, Bi as internal standards. Reproducibility on replicate analyses and accuracy was in the order of 5% for all elements.

3.2. Rb–Sr and Sm–Nd isotope geochemistry

Radiogenic isotope analytical work was carried out in the VIEPS facilities at the University of Melbourne, following procedures described in detail by Maas et al. (2005). The isotopic data were obtained with a NU Plasma multi-collector ICP–MS coupled to a CETAC Aridus desolvating nebulizer operated at an uptake rate of 40 µl/min. Typical sensitivity in this set-up is in the range of 100–130 V/ppm Sr or Nd. Instrumental mass bias was corrected by normalizing to $^{88}\text{Sr}/^{86}\text{Sr} = 8.37521$ and $^{146}\text{Nd}/^{145}\text{Nd} = 2.0719425$ (equivalent to $^{146}\text{Nd}/^{144}\text{Nd} = 0.7219$, Vance and Thirlwall, 2002), using the exponential law as part of an online iterative spike-stripping/internal normalization procedure. Data are reported relative to the accepted values for the standards: La Jolla $^{143}\text{Nd}/^{144}\text{Nd} = 0.511860$ and SRM987 $^{86}\text{Sr}/^{87}\text{Sr} = 0.710230$. This secondary normalization yields the following results for international standards ($\pm 2\text{sd}$): BCR-1 $^{143}\text{Nd}/^{144}\text{Nd} = 0.512641 \pm 18$, BHVO-1 $^{143}\text{Nd}/^{144}\text{Nd} = 0.512998 \pm 18$, JNdi-1 $^{87}\text{Sr}/^{86}\text{Sr} = 0.512113 \pm 22$; and for $^{86}\text{Sr}/^{87}\text{Sr}$ E&A Sr = 0.708005 ± 47 , BCR-1 = 0.705016 ± 46 , BHVO-1 = 0.703478 ± 36 . These results

Fig. 1. (a) Geological sketch map of the Eastern Karakoram, based on Weinberg and Searle (1998). For explanations see text. Locations for samples from the Karakoram Batholith are shown. (b) Geological overview map of the Karakoram Shear Zone and sample locations.

Table 1

Analysis of representative samples.

Type	Leucogranite Tangtse Pluton				In situ leucosome		Hbl-bearing leucosome		Leucogranite Dyke	
Sample	TNG166	TNG71a*	TNG167a	TNG161a	TNG170	TNG171	TNG60d	AGH23a	TNG174b	TNG186
Coordinates	34°04'10.5"N 78°13'39.4"E	34°03'42.6"N 78°13'52.2"E	34°03'57.7"N 78°13'37.2"E	34°02'35.6"N 78°13'16.0"E	34°02'50.1"N 78°13'02.7"E	34°03'25.3"N 78°14'13.3"E	34°25'10.6"N 77°49'23.5"E	34°01'26.7"N 78°12'12.9"E	34°08'41.8"N 78°08'17.8"E	
Major elements wt.%										
SiO ₂	70.83	73.40	74.10	73.55	72.09	75.53	62.3	58.1	72.11	71.16
TiO ₂	0.29	0.09	0.17	0.06	0.13	0.06	0.57	0.70	0.19	0.22
Al ₂ O ₃	15.55	14.90	15.33	14.89	15.96	14.72	16.3	12.5	16.24	15.41
Fe ₂ O ₃ t	1.57	0.63	0.93	0.59	0.71	0.39	2.30	4.61	1.15	1.37
MnO	0.03	0.02	0.01	0.02	0.01	0.01	0.06	0.13	0.01	0.02
MgO	0.33	bd	0.26	0.26	0.26	0.26	1.31	3.88	0.48	0.40
CaO	1.79	1.71	1.97	1.73	2.37	2.37	2.65	8.05	3.99	2.09
Na ₂ O	4.02	3.73	3.66	3.90	4.33	3.57	1.68	1.92	3.68	3.28
K ₂ O	4.50	4.76	4.15	3.76	2.98	2.94	10.1	6.53	1.69	4.56
P ₂ O ₅	0.09	0.02	0.03	0.01	0.03	0.02	0.40	2.06	0.07	0.09
LOI	0.46	0.77	0.39	0.33	0.47	0.34	0.46	0.59	0.41	0.44
Total	99.45	99.95	101.00	99.07	99.34	100.20	98.1	99.0	99.99	99.04
A/CNK	1.06	1.03	1.09	1.09	1.09	1.10	0.88	0.50	1.07	1.09
Mg/(Fe ⁺ Mg)	0.29	0.00	0.36	0.47	0.42	0.57	0.53	0.63	0.45	0.37
Trace elements ppm										
Sc	1.3	bd	1.2	0.6	0.5	0.3	6.1	16.4	1.0	2.0
Ba	1963.1	849	641.2	80.4	1360.1	1320.4	8279.9	4136.1	533.3	1500.7
Ti	973.8	593	687.9	112.5	553.2	185.8	2551.2	4068.8	830.5	966.2
V	14.0	7	6.9	bd	9.1	2.9	38.0	75.4	10.9	15.7
Cr	bd	23	bd	bd	1.7	0.3	36.6	60.9	0.9	0.7
Mn	153.4	69	97.5	52.1	41.4	39.4	348.7	928.0	67.4	125.2
Co	38.5	1	55.9	26.2	68.6	79.4	20.3	35.1	67.6	46.7
Ni	0.9	4	0.3	-0.6	3.1	1.0	28.2	39.2	1.4	1.3
Cu	7.6	14	0.4	0.2	39.7	7.8	31.6	66.0	2.6	3.4
Zn	29.5	24	27.1	18.5	8.4	6.1	38.7	86.1	28.8	26.9
Ga	23.2	16	13.2	4.0	20.0	21.8	165.3	13.9	12.3	21.5
Pb	86.6	55	55.5	62.2	15.7	14.2	85.4	30.2	24.7	34.1
Rb	321.0	156	172.8	176.4	52.1	57.4	440.9	151.4	80.4	140.6
Sr	741.1	398	433.1	162.1	1090.0	816.2	1083.2	903.4	542.5	438.8
Y	5.3	2	2.3	2.1	1.0	1.4	20.9	29.9	3.2	3.9
Zr	54.9	39	18.4	14.3	6.5	6.6	39.7	30.4	8.4	23.0
Nb	7.8	4	2.8	7.2	1.3	0.5	9.7	21.2	2.4	4.2
Th	58.6	bd	4.1	0.6	0.8	2.2	93.3	21.3	27.3	27.0
U	8.4	bd	1.0	0.6	0.1	0.2	6.5	3.7	0.8	1.0
Rb/Sr	0.43	0.39	0.40	1.09	0.05	0.07	0.41	0.17	0.15	0.32

compare well with data based on TIMS from other laboratories (e.g. Maas and McCulloch, 1991; Tanaka et al., 2000; Raczek et al., 2003). Typical within-run precisions (2 σ) are ± 0.000010 ($^{143}\text{Nd}/^{144}\text{Nd}$) and ± 0.000020 ($^{86}\text{Sr}/^{87}\text{Sr}$), while external precision (reproducibility, 2 σ) based on the results for secondary standards is ± 0.000020 (Nd) and ± 0.000040 (Sr). External precision for $^{87}\text{Rb}/^{86}\text{Sr}$ and $^{147}\text{Sm}/^{144}\text{Nd}$ obtained by isotope dilution is $\pm 0.5\%$ and $\pm 0.2\%$, respectively. Parent/daughter ratios obtained by Q-ICP-MS (Monash University) for unspiked samples have uncertainties of $\pm 2\%$ to $\pm 3\%$ for $^{87}\text{Rb}/^{86}\text{Sr}$ and $\pm 3\%$ to $\pm 5\%$ for $^{147}\text{Sm}/^{144}\text{Nd}$, respectively.

The Sm–Nd and Rb–Sr analytical work of the samples from the Ladakh Batholith (marked with ** in Table 5) were performed at the Laboratory for Isotope Geology at the Swedish Museum of Natural History and followed the analytical procedure reported in Andersson et al. (2002). The average of measurements of the LaJolla Nd standard during the measurements of samples LEH40 and LEH52 was 0.511843 ± 13 (1 σ , $n=13$), and during measurements of the other samples 0.511844 ± 5 (1 σ , $n=10$). No correction was applied. Similarly, an average of the measurements of the SRM987 Sr standard during measurements of the samples was 0.710245 ± 32 (1 σ , $n=16$). No correction was applied.

Age corrections (18–100 Ma) for the samples analyzed here are generally small, amounting to <1 unit for ϵ_{Nd} and ~ 0.00100 (mostly much less) for $^{87}\text{Sr}/^{86}\text{Sr}$. The propagated error for initial ϵ_{Nd} is $\sim \pm 0.5$

unit and 0.00007 or less for initial $^{87}\text{Sr}/^{86}\text{Sr}$. Propagated errors for samples analyzed unspiked (i.e. with Rb/Sr and Sm/Nd by Q-ICP-MS) are similar. The decay constants used are: ^{87}Rb $1.42 \times 10^{-11}/\text{yr}$; ^{147}Sm $6.54 \times 10^{-12}/\text{yr}$.

3.3. U–Pb SHRIMP analysis

Zircon and titanite grains were separated from whole rock samples using standard crushing, washing, heavy liquid (density 2.96 and 3.3), and paramagnetic procedures. The zircon and titanite concentrates were hand picked and placed onto double-sided tape, mounted in epoxy together with chips of the reference zircons (Temora, and SL13) and titanite (BLR-1), sectioned approximately in half, and polished. Sample TNG148b was analyzed *in situ* in a polished thin section. Reflected and transmitted light photomicrographs were obtained for all zircons. Cathodoluminescence (CL) and Scanning Electron Microscope (SEM) images were prepared for all zircon grains; back scattered SEM (BSE) images were prepared for the titanite grains. These CL and BSE images were used to decipher the internal structures of the sectioned grains and to ensure that the $\sim 20 \mu\text{m}$ SHRIMP spot was wholly within a single age component within the sectioned grains.

The U–Th–Pb analyses were made using the SHRIMP II at the Research School of Earth Sciences, The Australian National University, Canberra, Australia, following procedures given in Williams (1998,

Pegmatite Dyke			Leucogranite Shyok Valley			Karakoram Batholith			
TNG187a	TNG187b	TNG187c	TNG195	TNG196	TNG197e	Leucogranite			
	34°08'48.6"N		34°18'06.8"N	34°18'07.2"N	34°17'39.6"N	AGH25a	NBR1b	NBR2a	NBR3b
	78°08'26.9"E		78°00'46.2"E	78°00'46.6"E	78°02'02.9"E	34°27'04.4"N	34°29'06.0"N	34°37'54.6"N	34°46'27.5"N
						77°45'53.1"E	77°44'20.0"E	77°38'24.1"E	77°32'45.7"E
Major elements wt.%									
75.12	74.35	75.41	70.79	73.31	71.91	72.3	73.40	72.92	73.83
0.05	0.05	0.07	0.32	0.17	0.22	0.27	0.22	0.24	0.20
14.14	14.01	14.21	15.40	14.92	15.61	14.9	14.89	14.92	14.07
0.74	1.04	0.72	1.70	0.98	1.17	1.88	1.42	1.51	1.39
0.05	0.06	0.03	0.04	0.02	0.02	0.03	0.02	0.04	0.03
0.26	0.26	0.26	0.45	0.26	0.27	0.43	0.29	0.28	0.26
1.52	1.38	1.65	2.19	1.65	2.17	2.61	1.60	1.77	1.68
4.11	3.54	3.85	3.87	3.91	4.15	4.03	3.79	3.80	3.18
3.30	4.36	3.73	3.77	4.27	3.66	2.26	3.64	3.65	4.11
bd	0.01	bd	0.10	0.04	0.05	0.07	0.06	0.09	0.07
0.21	0.22	0.49	0.47	0.37	0.35	0.80	0.64	0.86	0.80
99.47	99.25	100.41	99.07	99.88	99.58	99.6	99.95	100.07	99.60
1.08	1.07	1.06	1.07	1.06	1.06	1.08	1.14	1.11	1.10
0.41	0.33	0.42	0.34	0.34	0.31	0.31	0.29	0.27	0.27
Trace elements ppm									
2.6	2.3	1.2	1.1	1.1	1.7	2.1	1.8	8.0	1.9
21.8	51.8	93.2	1404.6	893.4	997.1	860.2	679.2	1000.5	789.8
182.7	151.4	206.1	990.9	665.7	903.2	688.3	742.8	3946.8	723.3
3.2	5.3	1.9	16.1	11.7	14.6	4.5	10.9	76.2	6.5
bd	bd	bd	bd	bd	0.1	55.2	bd	9.9	bd
382.0	387.0	170.3	188.8	114.3	130.0	144.3	132.7	476.3	160.4
65.5	60.7	67.1	27.4	44.0	37.5	69.3	0.9	8.1	0.9
0.1	0.0	0.6	1.6	1.0	1.3	1.0	bd	12.3	bd
6.0	2.4	1.8	2.1	6.0	9.1	2.7	0.9	36.1	bd
12.3	13.4	9.5	29.6	21.1	26.6	17.8	20.0	48.2	26.5
4.7	4.3	4.6	17.8	16.8	17.0	14.4	11.9	17.5	13.4
50.9	49.5	40.7	69.7	89.0	60.1	52.3	35.7	37.4	40.5
145.8	162.1	131.2	140.6	219.4	164.1	161.5	201.1	208.7	201.3
66.3	78.4	121.2	546.2	563.5	597.5	146.8	363.2	501.3	336.8
15.7	16.7	6.3	5.2	2.2	3.5	8.6	6.2	13.8	10.1
27.7	63.9	10.2	27.8	29.5	48.6	31.5	30.8	95.2	41.6
2.6	2.9	1.9	6.3	3.2	4.7	8.5	6.4	12.5	8.5
4.0	7.3	1.2	40.4	31.6	27.5	15.8	15.6	20.0	20.2
2.0	1.9	0.5	4.0	6.9	2.5	4.2	1.4	4.9	3.5
2.20	2.07	1.08	0.26	0.39	0.27	1.1	0.55	0.42	0.60

(continued on next page)

and references therein). Each analysis consisted of 6 scans through the mass range, with a U–Pb reference grain analyzed for every three unknown analyses. The data have been reduced using the SQUID Excel Macro of Ludwig (2001).

For the zircon analyses, the U/Pb ratios have been normalized relative to a value of 0.0668 for the Temora reference zircon, equivalent to an age of 417 Ma (see Black et al., 2003). Uncertainties in the U–Pb calibration were 0.40% for TNG62a and TNG131a analytical sessions, and 1.18% for *in situ* analysis of TNG148b. The U–Pb ratios for titanite were normalized relative to the BLR-1 standard (1051 Ma, Aleinikoff et al., 2007). Uncertainties in the U–Pb calibrations were 0.43% for titanite SHRIMP sessions TNG131a and TNG148a.

Uncertainties given for individual analyses (ratios and ages) are at the one sigma level (Tables 2–4). Tera and Wasserburg (1972) concordia plots, probability density plots with stacked histograms and weighted mean $^{206}\text{Pb}/^{238}\text{U}$ age calculations were carried out using ISOPLOT/EX (Ludwig, 2003).

4. Field relations and anatexis in the Tangtse and Darbuk–Shyok areas

The Tangtse and Darbuk–Shyok gorges are cut by the Tangtse River roughly perpendicular to strike of the Karakoram Shear Zone, 20 km apart. Here, a mid-crustal section including the main lithologies of the PMC is exposed between the Tangtse Shear Zone and the Pangong

Shear Zone (Fig. 2a). These migmatized rocks will be described here following the terminology suggested by Sawyer (2008).

4.1. Meta-sedimentary sequence

This sequence comprises Bt–psammites, Bt–pelites, Bt–Hbl gneisses ranging to amphibolites, and calc–silicate rocks. These rock types are interlayered at the scale of tens of meters to hundreds of meters. Bt–psammites and Bt–pelites are generally characterized by the mineral assemblage Bt + Pl + Qtz ± Grt, and muscovite occurs in retrograde shear zones. Common accessory phases are Ap + Ttn + Mag + Mnz + Aln + Zrn. We found sillimanite in only one sample of PMC meta-sedimentary rocks, but its occurrence has also been reported by Rolland and Pêcher (2001). Calc–silicate rocks generally contain Cpx + Hbl + Pl + Qtz ± Bt ± Cc.

Whilst calc–silicate rocks and mafic amphibolites (SiO₂ < 50 wt %) do not present evidence for anatexis, Bt–psammites and Bt-bearing amphibolites have leucosomes that are interpreted to be the remainders of crystallized melt that segregated from the melanosome. Diffuse leucosome patches are common, and layer-parallel leucosomes in stromatic migmatites have melanosome rims that consist mostly of biotite. Leucosomes in migmatitic Bt–psammites range in composition from leucotonalite to leucogranite and commonly contain garnet. Leucosomes in the Hbl-rich gneissic to amphibolitic

Table 1 (continued)

Type	Muglib Batholith					Pangong Metamorphic Complex			
	Granodiorite		Diorite		Gabbro	Bt-psammite		Amphibolite	Calc-silicate
Sample	TNG131a*	TNG207	TNG169a	TNG205a	AGH5	TNG131d*	TNG167b	TNG108c*	TNG208
Coordinates	34°03'38.8"N	34°03'01.4"N	34°02'40.3"N	34°02'38.3"N	34°18'47.7"N	34°03'38.8"N	34°03'40.4"N	34°08'42.0"N	34°01'33.5"N
	78°13'52.1"E	78°13'41.3"E	78°13'07.8"E	78°13'25.4"E	77°52'03.8"E	78°13'52.1"E	78°13'52.7"E	78°08'18.5"E	78°12'01.7"E
Major elements wt.%									
SiO ₂	67.50	68.23	61.95	54.91	52.4	61.60	60.99	52.82	52.49
TiO ₂	0.56	0.50	0.70	1.37	1.10	0.83	0.82	1.01	0.64
Al ₂ O ₃	16.30	15.26	14.29	17.56	19.8	17.00	16.97	15.55	14.69
Fe ₂ O ₃ t	3.49	3.05	5.18	8.04	7.91	6.56	6.85	8.94	5.77
MnO	0.09	0.07	0.15	0.13	0.15	0.11	0.10	0.15	0.11
MgO	1.57	1.22	4.55	3.01	2.93	2.84	3.27	7.18	3.74
CaO	3.16	2.85	6.46	5.90	7.89	5.23	3.77	10.03	15.00
Na ₂ O	4.37	3.17	3.01	3.81	3.22	1.82	2.00	3.47	0.98
K ₂ O	2.85	4.57	2.47	2.97	1.04	3.02	3.25	0.73	3.41
P ₂ O ₅	0.22	0.19	0.14	0.50	0.27	0.16	0.15	0.09	0.15
LOI	0.50	0.57	0.93	0.82	2.92	1.06	1.59	0.36	2.03
Total	100.62	99.65	99.83	99.00	99.6	100.17	99.74	100.30	98.99
A/CNK	1.02	0.99	0.74	0.87	0.95	1.08	1.24	0.63	0.45
Mg/(Fe+Mg)	0.47	0.44	0.64	0.43	0.42	0.46	0.49	0.61	0.56
Trace elements ppm									
Sc	9	5.4	19.9	12.7	17.5	22	11.5	37	16.2
Ba	337	379.7	586.5	540.1	154.0	448	255.1	19	396.5
Ti	4103	2121.4	3833.4	7373.2	5423.7	7362	3270.7	5844	3419.7
V	87	49.7	103.7	123.5	193.0	186	95.1	235	119.0
Cr	63	21.1	74.8	12.7	20.9	178	124.8	220	102.9
Mn	790	415.1	1053.4	859.2	910.1	909	497.3	1183	737.8
Co	7	36.2	45.1	27.6	18.5	20	43.4	47	22.7
Ni	32	13.4	53.5	16.7	7.2	62	76.5	57	48.9
Cu	17	6.3	21.5	47.7	23.2	24	20.1	84	12.8
Zn	81	38.4	62.6	86.7	73.3	112	72.1	61	73.2
Ga	20	8.9	12.6	14.4	17.6	20	6.5	15	9.4
Pb	43	20.5	12.4	12.2	5.0	29	20.7	8	25.5
Rb	199	161.1	49.4	124.1	26.5	168	253.5	10	153.9
Sr	379	413.3	547.6	568.6	497.3	159	96.6	132	339.7
Y	19.00	17.6	18.8	24.3	20.2	28	20.7	25	22.4
Zr	164	18.8	11.5	58.6	7.9	185	6.7	86	11.2
Nb	27	15.0	18.2	25.5	5.7	25	12.8	9	11.1
Th	15	15.2	1.1	11.2	1.8	12	12.9	2	10.6
U	bd	2.2	2.1	1.1	0.3	bd	2.1	bd	1.8
Rb/Sr	0.53	0.39	0.09	0.22	0.05	1.06	2.62	0.08	0.45

rocks of this sequence commonly contain large poikilitic hornblende crystals (Fig. 3a).

In the central part of the Tangtse gorge there are metatexites and diatexites (indicated in cross section, Fig. 2a) that have melanosomes ranging compositionally from Hbl–Bt–schists to amphibolitic gneisses. Leucosomes in these rocks are Bt–leucogranites, Hbl–Bt–leucogranites and leucotonalites. Interplay between folding, shearing and magma migration in these meta- and diatexites has been described by Weinberg and Mark (2008). Typically, layer-parallel leucosomes in metatexites are linked with leucosomes parallel to the axial plane in folds. Folded leucosomes also cut through fold limbs and connect to leucosomes of different layers (Fig. 4). Fold hinges are truncated by axial planar shearing which further facilitates leucosome interconnection. Disruption of melanosomes, especially in the diatexites leads to a large range of compositions and a heterogeneous rock where distinction between leucosome and melanosome is blurred. In either meta- or diatexite the exact nature of the protolith is obscured by compositional changes related to melt extraction.

4.2. Calc-alkaline granitoids

The main facies of the Muglib Batholith is a medium to coarse-grained titanite bearing Hbl–Bt–granodiorite, commonly with Ap + Aln + Zrn as accessory minerals and decimetric mafic magmatic enclaves. A continuous foliation is defined by aligned Hbl, Bt and Ttn grains. Within the main facies, there are up to 100 m long lenses of Hbl–Cpx diorite. A Bt–

granodiorite occurs at the margins of the batholith and forms a border facies which crops out close to the Pangong Shear Zone near Muglib Village (Fig. 1b), and also intrudes the meta-sedimentary country rocks as dykes.

Migmatization of the Muglib Batholith is evident in the Bt–granodiorite border facies, in patches of the main facies as well as in the Hbl–Cpx diorite lenses. Leucosomes parallel to the dominant foliation parallel to the Karakoram Shear Zone are continuous with crosscutting leucosomes, thus forming a network interpreted to represent a melt flow network during anatexis (Weinberg and Searle, 1998). Melanosome rims are generally present and consist of mostly biotite and hornblende around leucosomes. Up to 3 cm large euhedral poikilitic hornblende crystals in leucosomes are common especially in diorites but rare in the Hbl-free border facies. In these migmatitic diorites, leucosomes that dominantly consist of Hbl megacrysts and Kfs (Fig. 3b) are interpreted as a residual assemblage after the melt was extracted.

4.3. Leucogranites

Leucogranites are ubiquitous in the Karakoram Shear Zone either as dykes, stocks on the scale of tens to hundreds of meters or kilometer-sized plutons (Fig. 1b, 2) such as the Darbuk Pluton, a sheared Ms–Bt ± Grt–leucogranite (Fig. 1b) or the Tangtse Pluton which is related to the Pangong Injection Complex that is depicted in Fig. 2b (Weinberg and Searle, 1998; Weinberg et al., 2009). The

Table 2
U–Pb SHRIMP data; sample TNG62a.

Zircon analysis													
Coordinates		34°02'16.8"N 78°14'57.7"E											
Grain. spot	U (ppm)	Th (ppm)	Th/U	²⁰⁶ Pb*	²⁰⁴ Pb/ ²⁰⁶ Pb	±	f ₂₀₆ %	²³⁸ U/ ²⁰⁶ Pb	±	²⁰⁷ Pb/ ²⁰⁶ Pb	±	²⁰⁶ Pb/ ²³⁸ U	Radiogenic age (Ma)
													²⁰⁶ Pb/ ²³⁸ U ±
1.1	924	516	0.56	7.6	0.000084	–	0.05	104.82	1.19	0.0477	0.0009	0.0095	0.0001 61.2 0.7
1.2	358	277	0.78	3.5	–	–	0.23	88.01	1.12	0.0493	0.0014	0.0113	0.0001 72.7 0.9
2.1	2137	1398	0.65	20.9	0.000093	–	<0.01	87.73	1.11	0.0473	0.0008	0.0114	0.0001 73.1 0.9
2.2	421	317	0.75	4.0	–	–	0.14	91.00	1.16	0.0485	0.0014	0.0110	0.0001 70.4 0.9
3.1	136	100	0.74	1.2	0.001987	–	0.31	93.94	1.38	0.0498	0.0024	0.0106	0.0002 68.1 1.0
4.1	403	294	0.73	3.9	0.000515	–	0.04	89.54	1.15	0.0478	0.0014	0.0112	0.0001 71.6 0.9
5.1	185	118	0.64	1.8	0.000872	–	0.40	89.50	1.37	0.0506	0.0020	0.0111	0.0002 71.3 1.1
6.1	123	109	0.89	1.1	0.000938	–	0.39	93.46	1.68	0.0505	0.0027	0.0107	0.0002 68.3 1.2
7.1	227	159	0.70	2.2	0.000981	–	0.62	90.68	1.33	0.0523	0.0019	0.0110	0.0002 70.3 1.0
8.1	229	252	1.10	2.2	0.000518	–	0.26	88.05	1.29	0.0495	0.0018	0.0113	0.0002 72.6 1.1
9.1	385	273	0.71	3.8	–	–	0.75	88.10	1.14	0.0534	0.0032	0.0113	0.0002 72.2 1.0
10.1	171	163	0.95	1.7	0.001165	–	<0.01	86.10	1.50	0.0466	0.0021	0.0116	0.0002 74.5 1.3
11.1	239	163	0.68	2.3	0.000502	–	0.27	90.65	1.38	0.0495	0.0018	0.0110	0.0002 70.5 1.1
11.2	2525	1941	0.77	24.5	–	–	0.01	88.56	0.93	0.0475	0.0005	0.0113	0.0001 72.4 0.8
12.1	298	226	0.76	2.8	0.001338	–	0.22	90.01	1.23	0.0491	0.0016	0.0111	0.0002 71.1 1.0
12.2	1458	909	0.62	13.2	–	–	<0.01	94.82	1.04	0.0473	0.0008	0.0105	0.0001 67.6 0.7
13.1	365	355	0.97	3.4	–	–	0.01	91.69	1.22	0.0475	0.0015	0.0109	0.0001 69.9 0.9
13.2	1157	742	0.64	11.0	0.000018	–	0.01	90.01	1.00	0.0475	0.0008	0.0111	0.0001 71.2 0.8
14.1	278	421	1.52	2.7	–	–	0.03	89.34	1.26	0.0477	0.0017	0.0112	0.0002 71.7 1.0
15.1	470	331	0.70	4.4	0.000711	–	0.47	91.03	1.14	0.0511	0.0013	0.0109	0.0001 70.1 0.9
16.1	526	286	0.54	5.0	0.000199	–	0.08	90.25	1.52	0.0481	0.0012	0.0111	0.0002 71.0 1.2
16.2	390	324	0.83	3.7	–	–	0.27	90.49	1.17	0.0496	0.0014	0.0110	0.0001 70.7 0.9
17.1	677	612	0.90	6.6	0.000189	–	0.19	88.15	1.03	0.0490	0.0018	0.0113	0.0001 72.6 0.9

f₂₀₆ % denotes the percentage of ²⁰⁶Pb that is common Pb.

Tangtse Pluton is approximately 1.3 km in length, has an outcrop height of ~600 m (Fig. 2b), and is a result of the amalgamation of multiple magma sheets that intruded Bt-psammmites and which are still preserved as screens inside the pluton. Leucogranite sheets in the Pangong Injection Complex are most likely derived from a combination of local and intrusive magma sheets (Weinberg and Searle 1998, Weinberg et al., 2009). The pluton is petrographically heterogeneous consisting mainly of medium-grained Bt-leucogranite, Ms-Bt ± Grt leucogranite and coarse-grained Grt-Ms-leucogranite. Accessory minerals are commonly Ap, Zrn, Mnz, Aln and Grt. Only rarely, small and strongly corroded hornblende crystals are found.

The leucogranites are generally deformed and show S–C fabrics, and in some biotite-rich examples Bt-foliae that wrap around feldspar crystals or form asymmetric tails thereby defining dextral S–C–C' fabrics. In some cases, deformation fabrics are not apparent in hand specimen, because micas are lacking, but are visible under the microscope. Microstructures, however, reveal dextral S–C fabrics.

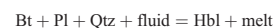
4.4. Syndeformational melting

Leucosomes in shear bands suggest that these are either the loci of incipient partial melting or that melt migrated into and accumulated in these zones (Fig. 5). Like this structure, a number of field relationships between melt, faults, shear zones and folds have been interpreted to result from synkinematic melting (Weinberg and Mark, 2008). A common feature found in many of the least deformed leucogranite sheets is shown in Fig. 6 where a broad dextral S–C fabric is defined by the alignment of feldspar lozenges. The interstitial finer-grained Qtz and Pl are only weakly deformed and are interpreted as having crystallized directly from a melt, indicating synkinematic magma crystallization. We therefore take the view here that anatexis was contemporaneous with deformation. This was also the interpretation by Rolland et al. (2009) based on microstructural relationships, and contradicts the pre-kinematic view presented by Phillips et al. (2004).

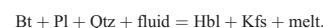
Deformation outlasted magmatism, continuing as the rock mass cooled to temperatures below 250 °C, as documented in microstructures in the Muglib area (Rutter et al., 2007) and Shiquanhe area further SE in the Karakoram Shear Zone (Valli et al., 2007). This low temperature deformation is reflected by porphyroclasts of K-feldspar and plagioclase in leucogranites with rims of fine-grained, sheared and recrystallized Kfs + Pl + Qtz (Fig. 6).

4.5. Water-fluxed melting

The presence of large, poikilitic hornblende crystals in leucosomes in calc-alkaline granodiorites and diorites (Fig. 3, 6) and the lack of other obvious peritectic minerals, suggests melting in the presence of a H₂O-rich fluid phase (Lappin and Hollister, 1980; Kenah and Hollister, 1983; Mogk, 1992). This interpretation is also supported by the lack of peritectic minerals in leucosomes in Bt-psammmites (Weinberg and Mark, 2008). Mogk (1992) stressed the importance of water infiltration in order to form Hbl-bearing leucosomes in migmatites and proposed that shear zones form pathways for H₂O-rich fluids. Accordingly, in the melting experiments of Gardien et al. (2000) hornblende was found as a crystallizing phase only when water was added. We suggest that the melting reactions proposed by McLellan (1988) and Lappin and Hollister (1980) account for hornblende-bearing leucosomes at calculated temperatures between 675 and 750 °C and 6 to 8 kbar,



or



Based on mineral paragenesis and thermobarometry, Rolland and Pêcher (2001) proposed that peak metamorphic temperatures in the Tangtse area reached 700 ± 20 °C at 7 ± 1 kbar, i.e. just below the onset of muscovite dehydration melting and well below

Table 3
U–Pb SHRIMP data; sample TNC131a.

Zircon analysis													
Sample	TNC131a												
Coordinates	34°03'38.8"N 78°13'52.1"E												
Grain, spot	U (ppm)	Th (ppm)	Th/U	²⁰⁶ Pb* (ppm)	²⁰⁶ Pb/ ²³⁸ Pb	±	<i>f</i> ₂₀₆ %	²³⁸ U/ ²⁰⁶ Pb	±	²⁰⁷ Pb/ ²⁰⁶ Pb	±	²⁰⁶ Pb/ ²³⁸ U	±
Radiogenic age (Ma)													
													±
1.1	1696	1160	0.68	15.3	0.000129	–	<0.01	95.31	1.06	0.0472	0.0007	0.0105	0.0001
1.2	465	349	0.75	4.3	0.000176	–	0.28	92.15	1.15	0.0496	0.0013	0.0108	0.0001
2.1	553	551	1.00	5.2	0.000033	–	<0.01	90.89	1.19	0.0469	0.0012	0.0110	0.0001
2.2	258	184	0.71	2.4	0.000764	–	0.01	90.87	1.28	0.0475	0.0017	0.0110	0.0002
3.1	412	333	0.81	4.0	0.000571	–	0.34	88.57	1.12	0.0502	0.0013	0.0113	0.0001
4.1	134	185	1.38	1.2	–	–	0.28	92.72	1.61	0.0496	0.0025	0.0112	0.0001
5.1	643	600	0.93	6.3	0.000494	–	0.23	87.96	1.04	0.0493	0.0011	0.0113	0.0001
6.1	4364	4115	0.94	43.1	–	–	<0.01	87.01	0.90	0.0474	0.0004	0.0115	0.0001
7.1	54	55	1.01	0.5	0.003931	–	1.32	87.83	2.08	0.0580	0.0039	0.0112	0.0003
8.1	554	425	0.77	5.2	0.000254	–	0.33	91.85	1.12	0.0500	0.0012	0.0109	0.0001
9.1	451	333	0.74	4.2	0.000383	–	<0.01	91.89	1.16	0.0468	0.0013	0.0109	0.0001
9.2	303	139	0.46	2.9	–	–	0.17	88.97	1.21	0.0488	0.0015	0.0112	0.0002
10.1	325	202	0.62	3.1	0.001032	–	1.59	90.45	1.22	0.0600	0.0017	0.0109	0.0001
10.2	516	301	0.58	5.0	0.000040	–	0.20	87.88	1.07	0.0490	0.0012	0.0114	0.0001
11.1	244	244	0.97	2.5	0.000403	–	0.02	87.42	1.24	0.0477	0.0017	0.0114	0.0002
12.1	262	166	0.63	2.5	0.000520	–	0.27	90.75	1.28	0.0496	0.0017	0.0110	0.0002
12.2	250	170	0.68	2.3	0.000106	–	0.15	94.03	1.35	0.0486	0.0018	0.0106	0.0002
13.1	418	227	0.54	3.8	0.000424	–	0.32	93.91	1.20	0.0499	0.0014	0.0106	0.0001
14.1	506	433	0.86	4.9	–	–	0.03	89.51	1.09	0.0477	0.0012	0.0112	0.0001
15.1	113	175	1.55	1.1	–	–	<0.01	90.61	1.66	0.0466	0.0027	0.0110	0.0002
16.1	3055	2050	0.67	30.0	0.000070	–	0.08	87.39	0.91	0.0481	0.0005	0.0114	0.0001
17.1	196	106	0.54	1.8	0.001090	–	0.14	91.30	1.40	0.0486	0.0020	0.0109	0.0002
Zircon included in titanite													
2.1	593	273	0.46	6.8	0.013439	–	26.44	74.46	0.93	0.2569	0.0316	0.0099	0.0006
Titanite analysis													
1.1	406	48	0.12	1.7	0.031001	–	57.9	202.99	2.87	0.4805	0.0064	0.0021	0.0003
2.1	146	29	0.20	0.9	0.028931	0.002476	54.0	141.04	2.41	0.4690	0.0084	0.0033	0.0004
3.1	180	7	0.04	0.9	0.034459	0.002420	64.4	167.62	2.71	0.4928	0.0081	0.0021	0.0003
3.2	37	396	10.61	0.6	0.021536	0.002722	40.0	55.11	1.34	0.4282	0.0096	0.0109	0.0010
4.1	98	6	0.06	0.7	0.034500	0.002938	64.4	116.85	2.20	0.6005	0.0110	0.0030	0.0006
5.1	107	71	0.67	0.8	0.035582	0.002774	66.4	108.33	1.98	0.5921	0.0107	0.0031	0.0006
5.2	34	456	13.49	0.6	0.027273	0.002768	50.7	45.15	1.11	0.4566	0.0096	0.0109	0.0013
6.1	88	65	0.73	1.0	0.020407	0.001886	38.0	72.92	1.31	0.3152	0.0059	0.0085	0.0006
7.1	64	466	7.30	1.0	0.030482	0.002392	56.7	57.19	1.13	0.5689	0.0092	0.0076	0.0010
7.2	91	27	0.30	0.8	0.031392	0.002969	58.6	101.37	2.01	0.5523	0.0107	0.0041	0.0006
8.1	99	369	3.73	1.1	0.013155	0.001402	24.5	74.71	1.30	0.2358	0.0046	0.0101	0.0004
8.2	54	671	12.47	0.9	0.029445	0.002516	54.8	53.98	1.16	0.5018	0.0092	0.0084	0.0010
6.2	57	435	7.62	0.7	0.017611	0.002039	32.8	66.93	1.38	0.2997	0.0066	0.0100	0.0007
9.1	35	430	12.21	0.6	0.027630	0.002883	51.4	52.11	1.28	0.4160	0.0093	0.0093	0.0012
9.2	57	398	7.00	0.8	0.034492	0.002761	64.3	59.77	1.24	0.5771	0.0100	0.0060	0.0010
10.1	87	420	4.81	1.0	0.013854	0.001558	25.8	72.01	1.30	0.2584	0.0051	0.0103	0.0005
10.2	44	411	9.30	0.6	0.025447	0.002662	47.3	58.69	1.34	0.4184	0.0098	0.0090	0.0010
11.1	34	369	10.75	0.5	0.027740	0.002921	51.6	54.33	1.34	0.4124	0.0092	0.0089	0.0011
11.2	45	394	8.75	0.7	0.028876	0.002621	53.7	53.24	1.18	0.5294	0.0107	0.0087	0.0011
12.2	497	50	0.10	1.6	0.028322	0.001868	52.9	260.51	3.68	0.4760	0.0068	0.0018	0.0002
13.1	151	8	0.05	1.0	0.034971	0.002753	65.3	136.17	2.38	0.5833	0.0100	0.0025	0.0005
13.2	48	437	9.05	0.7	0.028979	0.002682	53.9	55.55	1.22	0.4381	0.0094	0.0083	0.0011
14.1	49	425	8.65	0.7	0.023750	0.002314	44.2	62.23	1.37	0.3423	0.0076	0.0090	0.0008
14.2	52	447	8.61	0.7	0.024840	0.002444	46.2	61.30	1.32	0.4416	0.0087	0.0088	0.0009
14.3													5.5

*f*₂₀₆ % denotes the percentage of ²⁰⁶Pb that is common Pb.

biotite dehydration melting. Rolland et al. (2009) concluded that a small thermal increase initiated muscovite dehydration melting in the Tangtse area. However, this is unnecessary when considering external water influx. In this case, melting is expected to begin at the water saturated solidus for pelites and quartzofeldspathic rocks, which is essentially similar to that of the haplogranitic system $Qtz + Ab + Or + H_2O$ with temperatures as low as 650 °C (Clemens and Vielzeuf, 1987; Holtz et al., 1992). Water influx can create significant amounts of melt, depending on the size of the infiltrated (shear-) zone (Mogk, 1992; Genier et al. 2008). Possible sources for infiltrating water are hydrated, low-grade metamorphosed sedimentary rocks of the Karakoram Metamorphic Complex, overthrust by the Pangong Metamorphic Complex (Weinberg and Mark, 2008).

In summary, field relations suggest widespread partial melting of two major rock sequences, meta-sedimentary and calc-alkaline rocks, in the presence of a water-rich fluid contemporaneous with deformation. In the process, a large network of magmatic bodies developed, linking nearly *in situ* leucosomes with a large network of magma sheets and bodies.

5. Evidence for magma hybridization in migmatites

In the PMC, different rock types that underwent anatexis are interlayered on the scale of meters to hundreds of meters (Figs. 2, 3). This provides an opportunity for magmas from different sources to interact early in their migration history as they travel through an expanding channel network. In the following, we describe two field examples where this might have happened.

5.1. Base of Tangtse Pluton

At the exposed base of the Tangtse Pluton, an irregular sheet of calc-alkaline Bt–granodiorite of the Muglib Batholith border facies intrudes Bt–psammite (Fig. 7). Both rock types have undergone partial melting. This is evidenced in the Bt–psammite by chaotically folded leucosomes and leucosome patches comprised of Ms–Bt ± Grt–leucogranite with melanosome rims consisting mostly of biotite and small amounts of Pl + Qtz + Grt (Fig. 7c, f).

In the Bt–granodiorite sheet anatexis is evidenced by leucosome patches with diffuse boundaries with the melanosome that form an irregular network of Bt ± Grt–leucogranite pockets and veins, feeding into a larger leucosome with width varying up to one meter (Fig. 7b). Although sometimes difficult to distinguish, the neosome is coarser-grained and more felsic than the paleosome. Melanosome rims bordering the leucosomes are absent. Isolated rafts of Bt–granodiorite with diffuse boundaries are found in the large leucosome (Fig. 7d). Garnet is heterogeneously distributed in the leucosome and absent in the melanosome except for high concentrations on wispy schlieren of biotite dragged from the Bt–psammite at the contact with the partially molten Bt–granodiorite sheet. The presence of garnet and biotite–garnet schlieren from the Bt–psammite in the leucosome suggests it is a hybrid formed by merging of magma from the Bt–granodiorite with magma from the Bt–psammite. If this is so, then the pre-existing granodiorite gave rise to a magma channelway that was used by leucosomes from both rock types. In order to test this hypothesis, we sampled the different rock types in this and adjoining outcrops to study their isotopic composition.

5.2. Leucogranite dykes in the Darbuk–Shyok gorge

In the Darbuk–Shyok gorge (Fig. 1b), mainly pegmatitic Bt ± Ms ± Grt leucogranite dykes cut across interlayered amphibolites and calc-silicate rocks, calc-alkaline diorites of the Muglib Batholith, but also merge continuously with *in situ* leucosomes in dioritic protoliths (Fig. 8). Diorite gneisses show leucosome patches with

euhedral hornblende poikiloblasts and diffuse margins to the melanosome, interpreted to represent *in situ* leucosomes. These leucosomes are generally parallel to tectonic foliation and compositional layering and have melanosome rims consisting of mostly Hbl + Bt, forming a stromatic migmatite. These Hbl-bearing leucosomes are connected with the crosscutting Bt ± Ms ± Grt–leucogranite dykes and, in the field and in thin section, the contact is seamless (Fig. 8b). In parts of this outcrop, large amounts of magma disrupt pre-existing layering in the calc-alkaline protolith and form a diatexite migmatite (Fig. 8c). Continuity between *in situ* leucosome in the dioritic protolith and intrusive dykes suggest contemporaneity of dyke and local anatexis.

6. Major and Trace Element Geochemistry

We carried out major and trace element analysis on 88 samples of the main lithologies of the PMC, including 58 leucogranitic samples from the Karakoram Shear Zone and Karakoram Batholith. In general, Fe_2O_3 , MgO, TiO_2 and CaO contents of source rocks and leucogranites in the Karakoram Shear Zone and Karakoram Batholith correlate negatively with SiO_2 , K_2O and SiO_2 show no clear trend. Leucogranites have SiO_2 contents between 64.0 wt% and 76.2 wt% and are dominantly mildly peraluminous (A/CNK 1.02 to 1.16; Fig. 9a). In the alkali–lime vs. SiO_2 diagram (Fig. 9b), the source rocks follow the calc-alkalic to alkali–calcic trend and almost all leucogranite samples lie in the field of peraluminous leucogranites as defined in Frost et al. (2001). The different rock types define different fields depending on their Fe_2O_3 + MgO + TiO_2 content (Fig. 9c). While the ferromagnesian and titaniferous phases are concentrated in the calc-alkaline diorites, Bt–psammite, Bt–pelites and melanosome samples, the calc-alkaline granodiorites and diatexites form an intermediate group. The leucogranites have the lowest Fe_2O_3 + MgO + TiO_2 contents (< 2.15 wt %). K_2O contents of leucogranites are usually high between 4 and 5 wt%, ranging from 0.94 wt% to 5.63 wt%. High, and variable, K_2O concentrations suggest K-feldspar accumulation trends in leucogranites. CaO + Na_2O concentrations in leucogranites range from 3.41 wt % to 9.89 wt % (not shown in Fig. 9).

The high K_2O content of 10.1 wt% in a leucosome sample of a Muglib Batholith migmatite (sample TNG60d in Table 1) is the result of K-feldspar accumulation in the Hbl-bearing leucosomes in Hbl–Bt diorite (Fig. 3b) in accordance with petrographic observations. Rb correlates positively with K_2O (Fig. 10a), but not with Fe_2O_3 and TiO_2 , suggesting that Rb contents are mainly controlled by the amount of K-feldspar and not by muscovite or biotite in the leucogranites. High Ba and Sr concentrations suggest feldspar crystallization leading to relatively quartz-poor but feldspar-rich leucogranites with a cumulate character (Fig. 10b). Feldspar accumulation as a result of Rayleigh fractionation is shown in the calculated trace element contents in the added curves of Fig. 10b. Relatively low Rb contents result in low Rb/Sr ratios, generally below one. The Tangtse Pluton (Fig. 2) appears to be an example of this; a magma that has started to crystallize close to the source.

7. Geochronology

In order to constrain the relation between timing of protolith crystallization, anatexis and leucogranite intrusion, we dated zircon and titanite grains from two samples of potential source rocks and two leucogranite samples using U–Pb SHRIMP analysis. We selected a melanosome (sample TNG62a), rich in hornblende and biotite as well as titanite, apatite and zircon. This sample was taken from a migmatized part of the Muglib Batholith ~3 km along strike to the SE of the Tangtse Pluton. The second sample (TNG131a) is a Bt–granodiorite sheet, interpreted as Muglib Batholith border facies, from the outcrop at the base of the Tangtse Pluton in Fig. 7b. For age determination of

Table 4

U–Pb SHRIMP data; sample TNG148a, TNG148b.

Sample TNG148a															
Coordinates		34°03'40.4"N 78°13'52.7"E													
Grain. spot	U (ppm)	Th (ppm)	Th/U	²⁰⁶ Pb* (ppm)	²⁰⁴ Pb/ ²⁰⁶ Pb	±	f ₂₀₆ %	²³⁸ U/ ²⁰⁶ Pb	±	²⁰⁷ Pb/ ²⁰⁶ Pb	±	²⁰⁶ Pb/ ²³⁸ U	±	Radiogenic age (Ma)	
														²⁰⁶ Pb/ ²³⁸ U	±
1.1	208	790	3.80	1.8	0.040139	0.002097	74.9	98.65	4.94	0.6528	0.0315	0.0025	0.0006	16.4	3.7
2.1	352	47	0.13	2.5	0.037675	0.002185	70.3	122.82	1.63	0.5935	0.0060	0.0024	0.0005	15.5	2.9
3.1	237	45	0.19	2.1	0.038220	0.002227	71.3	98.95	1.40	0.6388	0.0068	0.0029	0.0006	18.6	3.7
4.1	158	171	1.08	2.1	0.049082	0.002556	91.6	65.07	0.98	0.7046	0.0074	0.0013	0.0011	8.3	6.8
4.2	474	206	0.44	3.0	0.035915	0.001540	67.1	134.34	1.74	0.5603	0.0054	0.0025	0.0003	15.8	2.2
5.1	305	50	0.16	2.2	0.041903	0.002224	78.3	120.02	1.63	0.6085	0.0064	0.0018	0.0005	11.7	3.2
6.1	455	115	0.25	3.1	0.034043	0.001693	63.6	127.73	1.62	0.5746	0.0061	0.0029	0.0004	18.4	2.3
6.2	262	40	0.15	2.1	0.037824	0.001839	70.6	109.40	1.56	0.6410	0.0071	0.0027	0.0005	17.3	3.0
6.3	127	875	6.88	1.7	0.044925	0.002325	83.8	65.53	1.09	0.6986	0.0088	0.0025	0.0010	15.9	6.1
7.1	357	35	0.10	2.5	0.035071	0.001621	65.5	123.36	1.65	0.5812	0.0060	0.0028	0.0004	18.0	2.4
8.1	254	43	0.17	2.1	0.038986	0.001901	72.8	102.82	1.48	0.6308	0.0071	0.0026	0.0005	17.0	3.3
9.1	249	26	0.11	2.1	0.041786	0.001999	78.0	103.02	1.50	0.6532	0.0077	0.0021	0.0005	13.7	3.5
10.1	221	224	1.01	1.8	0.039211	0.002012	73.2	105.52	1.55	0.6406	0.0075	0.0025	0.0005	16.3	3.3
10.2	207	20	0.10	2.2	0.041973	0.002220	78.3	82.02	1.28	0.6695	0.0083	0.0026	0.0007	17.0	4.6
11.1	185	63	0.34	1.6	0.037226	0.002174	69.5	100.15	1.57	0.6379	0.0083	0.0030	0.0006	19.6	3.5
12.1	252	24	0.09	2.1	0.039991	0.003275	74.7	104.59	1.52	0.6200	0.0072	0.0024	0.0007	15.6	4.5
13.1	220	30	0.13	2.0	0.040177	0.001954	75.0	94.86	1.40	0.6460	0.0073	0.0026	0.0006	17.0	3.7
14.1	527	288	0.55	3.3	0.034685	0.001475	64.8	138.82	1.78	0.5499	0.0054	0.0025	0.0003	16.3	2.1
15.1	209	88	0.42	1.9	0.042656	0.002092	79.6	92.08	1.38	0.6374	0.0075	0.0022	0.0006	14.2	4.0
Zircon analysis															
Zircon included within titanite grains in sample TNG148a															
1.1	3034	1861	0.61	11.6	0.020867	0.002902	35.17	224.30	2.95	0.3245	0.0299	0.0029	0.0002	18.6	1.1
2.1	5655	2607	0.46	14.9	0.001053	0.000248	0.92	326.41	3.52	0.0537	0.0008	0.0030	0.0000	19.5	0.2
Sample TNG148b															
Zircon analyzed <i>in situ</i> in polished thin section															
24-1	1425	4	0.003	3.7	0.004420	0.001228	5.5	329.6	6.0	0.0895	0.0051	0.0029	0.0001	18.5	0.4
24-2	5784	3703	0.64	35.2	0.026992	0.002627	49.8	141.2	2.2	0.4406	0.0144	0.0036	0.0002	22.9	1.0
29-1	2060	1304	0.63	148.2	0.051735	0.000951	96.4	11.941	0.136	0.8127	0.0091	0.0030	0.0018	19.6	11.6
29-2	1464	2858	1.95	5.7	0.020839	0.002127	37.0	222.1	6.8	0.3389	0.0198	0.0028	0.0001	18.3	0.9
29-3	1709	823	0.48	4.4	0.006514	0.001335	8.3	333.7	5.0	0.1121	0.0062	0.0027	0.0000	17.7	0.3
29-4	1251	1503	1.20	163.2	0.054529	0.000701	97.6	6.588	0.073	0.8266	0.0198	0.0036	0.0047	23.1	30.1
47-1	2006	1015	0.51	5.5	0.000608	0.000248	2.2	313.2	4.3	0.0640	0.0020	0.0031	0.0000	20.1	0.3
47-2	672	1095	1.63	1.6	0.001152	0.000628	1.0	362.5	7.4	0.0546	0.0042	0.0027	0.0001	17.6	0.4
47-3	1116	2284	2.05	3.5	0.012479	0.001932	23.2	271.6	4.5	0.2294	0.0075	0.0028	0.0001	18.2	0.4

f₂₀₆ % denotes the percentage of ²⁰⁶Pb that is common Pb.

leucogranites we chose two samples from the Tangtse Pluton, one for zircon and one for titanite analysis (sample TNG148a and TNG148b).

7.1. Age of the Muglib Batholith

Zircons from samples TNG62a and TNG131a are prismatic, either translucent or pinkish in colour and between 150 µm and 500 µm in length, on average 200 µm. Cathodoluminescence (CL) imaging shows dominantly oscillatory zoning with little evidence for inherited cores, or overgrowths. These are interpreted to represent igneous zoning. A total of 23 areas have been analyzed on 17 zircon grains from sample TNG62a (melanosome), where 18 analyses form a dominant bell-shaped age probability distribution with a weighted mean ²⁰⁶Pb/²³⁸U age of 71.4 ± 0.6 Ma (MSWD = 1.14, Fig. 11a; Table 2). One analysis is slightly older whilst the remaining four analyses and are interpreted to have lost radiogenic Pb; for example analysis 1.1 in Table 2. The mean age of 71.4 ± 0.6 Ma is interpreted to represent a single population indicating the magmatic crystallization age of the Hbl–Bt–granodiorite.

Sample TNG131a corresponds to the Bt–granodiorite border facies that intruded Bt–psammities (Fig. 7b). As for the previous sample, the zircon grains are dominated by relatively simple igneous oscillatory zoning as seen under CL, although some discordant central areas may reflect a more complicated igneous crystallization history. A total of 22 areas were analyzed from 17 zircon grains (Fig. 11b; Table 3). An analysis was also made on a zircon included within a titanite grains

during the same SHRIMP session. It yielded a significantly younger ²⁰⁶Pb/²³⁸U date of ~63 Ma but the area has likely lost radiogenic Pb and hence was not included in the following discussion or age calculation. The zircon ²⁰⁶Pb/²³⁸U ages are slightly dispersed ranging between ~67 and ~74 Ma. The probability density distribution appears bimodal with a more prominent peak at about 70 Ma and another at about 73 Ma, with some younger analyses considered to reflect radiogenic Pb loss. The older group at ~73 Ma may indicate that there was an early period of magmatic zircon crystallization, but with the dominant zircon having crystallized at 70.5 ± 0.6 Ma (mean weighted ²⁰⁶Pb/²³⁸U age of 14 analyses, MSWD = 1.03; Fig. 11b). This age is overlapping within error but slightly younger than the 71.4 ± 0.6 Ma for sample TNG62a, and confirms that both intrusions relate to the same magmatic event.

The titanite grains have a light brown colour, are mostly anhedral to subhedral and are between 100 and 250 µm in diameter. In some grains the BSE images show a faint oscillatory zoning, whereas most grains have irregular internal structures, often with a slightly darker, central phase, irregularly surrounded by a lighter BSE component (Fig. 12b). Twenty four areas have been analyzed on 14 titanite grains (Fig. 13c; Table 3). As is common in metamorphic titanite, there are high amounts of common Pb and so the calculated radiogenic ratios and ages have high uncertainties compared to the U–Pb zircon data. In the Tera–Wasserburg plot of Fig. 13a, discordia lines have been fitted to the common Pb uncorrected data. It can be seen that there is an

Table 5
Rb–Sr and Sm–Nd isotopes.

Sample	Type / location	Coordinates	Rb ppm	Sr ppm	$^{87}\text{Rb}/^{86}\text{Sr}$	$^{87}\text{Sr}/^{86}\text{Sr}$	Sm ppm	Nd ppm	$^{147}\text{Sm}/^{144}\text{Nd}$	$^{143}\text{Nd}/^{144}\text{Nd}$	ϵ_{Nd} now	$^{87}\text{Sr}/^{86}\text{Sr}$ at 18 Ma	$^{143}\text{Nd}/^{144}\text{Nd}$ at 18 Ma	ϵ_{Nd} at 18 Ma
TNG 71a	Grt–Ms–Bt leucogranite, Tangtse Pluton	34°03'42.6"N 78°13'52.2"E	157.72	406.39	1.123	0.71066	0.65	3.21	0.1224	0.51233	–6.05	0.7104	0.51231	–5.9
TNG 71b	Ms–Bt leucogranite, Tangtse Pluton	34°03'42.6"N 78°13'52.2"E	131.43	455.57	0.835	0.71048	1.20	6.92	0.1048	0.51234	–5.79	0.7103	0.51233	–5.6
TNG 148a	Bt leucogranite, Tangtse Pluton	34°03'40.4"N 78°13'52.7"E	145.57	1046.06	0.403	0.70993	2.94	18.36	0.0966	0.51231	–6.42	0.7098	0.51230	–6.2
TNG 148b	Bt leucogranite, Tangtse Pluton	34°03'40.4"N 78°13'52.7"E	149.88	1528.89	0.284	0.70868	4.45	29.30	0.0917	0.51235	–5.58	0.7088	0.51234	–5.3
TNG 131 g	Pegmatitic leucosome, Tangtse Pluton	34°03'38.8"N 78°13'52.1"E	119.76	351.52	0.986	0.70904	0.50	2.51	0.1202	0.51244	–3.80	0.7088	0.51243	–3.6
TNG 170*	Leucosome, Tangtse gorge	34°02'35.6"N 78°13'16.0"E	52.14	1089.96	0.138	0.70544	0.53	2.97	0.1071	0.51268	0.90	0.7054	0.51267	1.1
TNG 186	Leucogranite dyke, Darbuk–Shyok gorge	34°08'41.8"N 78°08'17.8"E	140.62	438.78	0.926	0.71234	4.53	29.49	0.0929	0.51239	–4.76	0.7121	0.51238	–4.5
TNG 187a	Pegmatite dyke, Darbuk–Shyok gorge	34°08'48.6"N 78°08'26.9"E	109.87	73.56	4.322	0.70979	0.42	0.93	0.2757	0.51242	–4.34	0.7087	0.51238	–4.5
TNG 187b	Pegmatite dyke, Darbuk–Shyok gorge	34°08'48.6"N 78°08'26.9"E	131.98	98.23	3.888	0.70968	1.80	5.73	0.1902	0.51241	–4.37	0.7087	0.51239	–4.4
AGH23a*	Hbl–earring leucosome, Nubra Valley	34°25'10.6"N 77°49'23.5"E	151.40	903.40	0.485	0.70897	14.35	81.59	0.1064	0.51228	–7.02	0.7088	0.51227	–6.8
AGH25a	Grt–Ms–Bt leucogranite, Nubra Valley	34°27'04.4"N 77°45'53.1"E	158.44	155.61	2.946	0.70831	1.99	12.03	0.1003	0.51235	–5.60	0.7076	0.51234	–5.4
NBR1b*	Ms–Bt leucogranite, Nubra Valley	34°29'06.0"N 77°44'20.0"E	201.14	363.24	1.600	0.70809	2.86	16.05	0.1079	0.51234	–5.80	0.7077	0.51233	–5.6
NBR2a*	Ms–Bt leucogranite, Nubra Valley	34°37'54.6"N 77°38'24.1"E	208.66	501.35	1.203	0.70855	4.44	24.47	0.1097	0.51230	–6.66	0.7082	0.51228	–6.5
NBR3b*	Ms–Bt leucogranite, Nubra Valley	34°46'27.5"N 77°32'45.7"E	201.27	336.80	1.727	0.70963	3.55	20.27	0.1060	0.51226	–7.32	0.7092	0.51225	–7.1
TNG 62a	Melanosome, SW Muglib	34°02'16.8"N 78°14'57.7"E	122.37	538.39	0.658	0.70783	7.30	43.29	0.1019	0.51266	0.37	0.7077	0.51265	0.6
TNG 128	Calc-alkaline Hbl–Bt–granodiorite, SW Muglib	33°59'08.3"N 78°18'37.8"E	120.43	575.26	0.605	0.70523	5.41	32.32	0.1011	0.51266	0.43	0.7051	0.51265	0.6
TNG 169a*	Calc-alkaline diorite, Tangtse gorge	34°02'40.3"N 78°13'07.8"E	49.42	547.63	0.261	0.70528	3.18	13.46	0.1428	0.51275	2.17	0.7052	0.51273	2.3
TNG 98a	Calc-alkaline Hbl–Bt–granodiorite, Darbuk–Shyok gorge	34°09'23.1"N 78°08'52.0"E	116.76	573.49	0.589	0.70562	5.48	35.28	0.0939	0.51267	0.53	0.7055	0.51265	0.8
AGH5*	Calc-alkaline gabbro, Pangong Range	34°18'47.7"N 77°52'03.8"E	26.52	497.28	0.154	0.70421	3.63	15.39	0.1427	0.51276	2.28	0.7042	0.51274	2.4
TNG 70a	Bt–psammite, Tangtse Pluton	34°03'41.6"N 78°13'53.2"E	255.15	250.40	2.949	0.71251	5.35	28.11	0.1150	0.51214	–9.81	0.7118	0.51212	–9.6
TNG 131d	Bt–psammite, Tangtse Pluton	34°03'38.8"N 78°13'52.1"E	183.68	155.69	3.416	0.71700	6.21	32.64	0.1148	0.51211	–10.22	0.7161	0.51210	–10.0
TNG 112	Pelite, Shyok Valley	34°12'19.6"N 78°07'55.9"E	168.65	299.82	1.628	0.71188	6.45	32.52	0.1198	0.51212	–10.10	0.7115	0.51211	–9.9
PNG03b	Pelite, Tangtse Valley	33°57'53.5"N 78°23'46.0"E	168.22	147.66	3.299	0.71698	5.44	29.33	0.1120	0.51212	–10.12	0.7161	0.51211	–9.9
TNG 108c	Amphibolite, Darbuk–Shyok gorge	34°08'42.0"N 78°08'18.5"E	4.04	125.56	0.093	0.70477	2.40	6.92	0.2098	0.51309	8.82	0.7047	0.51307	8.8
LEH40**	Ladakh Batholith, Leh	Leh region	not available	0.339		0.70485	3.13	14.21	0.1331	0.51267	0.66	0.7048	0.51266	0.8
LEH55**	Ladakh Batholith, Leh	Leh region	159.00	95.00	4.843	0.70782	1.10	5.86	0.1131	0.51262	–0.29	0.7066	0.51261	–0.1
LEH29**	Ladakh Batholith, Leh	Leh region	49.00	219.00	0.647	0.70465	1.87	9.81	0.1152	0.51274	1.93	0.7045	0.51272	2.1
LEH38a**	Ladakh Batholith, Gyamsa	Leh region	85.00	119.00	2.066	0.70555	1.69	11.51	0.0888	0.51270	1.27	0.7050	0.51269	1.5
LEH38b**	Ladakh Batholith, Gyamsa	Leh region	79.00	188.00	1.216	0.70545	5.30	22.64	0.1416	0.51272	1.54	0.7051	0.51270	1.7
LEH52**	Ladakh Batholith, Gyamsa	Leh region	30.40	350.00	0.251	0.70485	8.49	36.85	0.1392	0.51270	1.13	0.7048	0.51268	1.3

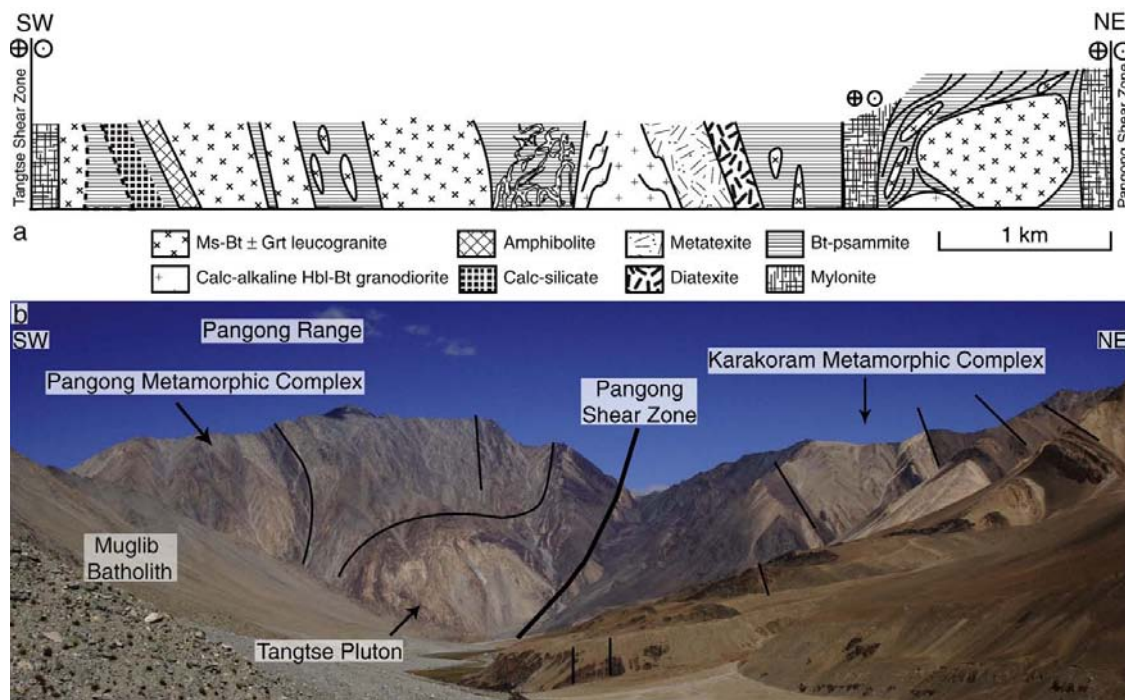


Fig. 2. (a) Schematic cross section through the Tangtse gorge roughly perpendicular to strike of the Karakoram Shear Zone. The Tangtse Shear Zone separates the Pangong Metamorphic Complex (PMC) from the Ladakh Batholith to the SW. The Pangong Shear Zone bounds the PMC from the Karakoram Metamorphic Complex to the NE. (b) Photograph of the NE end of the Tangtse gorge (looking NW). Calc-alkaline Muglib Batholith (lower left) and leucogranitic Tangtse Pluton (centre) in the Pangong Range. The Tangtse Pluton intrudes Bt-psammite of the PMC. Grt-St-Hbl-schists and marbles (bright colors) of the upper greenschist/lower amphibolite facies Karakoram Metamorphic Complex (KMC) were overthrust by the PMC during dextral transpressive movement.

older grouping that forms a linear array, intersecting the concordia at 65 ± 3 Ma. A second, sub-parallel group is slightly younger (~ 55 Ma), and then other analyses range down to ~ 11 Ma. The oldest calculated age is younger than that calculated from zircons of the same sample, the likely true magmatic age, and either is spurious or relates to a cooling event post initial magmatism. An early metamorphic event due to continued calc-alkaline intrusion is also possible. The relative probability plot of common Pb corrected $^{206}\text{Pb}/^{238}\text{U}$ ages highlights the two older age components with a scattered younger cluster peaking between ~ 11 and 21 Ma (Fig. 13c). It is not possible to calculate a meaningful age date for this younger, metamorphic titanite, but it is indicative of a metamorphic crystallization event broadly contemporaneous with anatexis (see below).

7.2. Age of the leucogranites from the Tangtse Pluton

Initially zircons were not recovered from the standard mineral separation applied to sample TNG148a. Titanites were separated similarly to the Bt-granodiorite sample. They have a light brown colour, are mostly anhedral to subhedral and are between 100 and 250 μm large. BSE images show weak oscillatory zoning, more common than in titanites from sample TNG131a, while irregular structures are not as prominent. We interpret the BSE internal structure to reflect compositional differences during magmatic growth as opposed to core and rim structures. Zircon inclusions are common. A total of 19 areas on 15 titanite grains from sample TNG148a have been analyzed (Fig. 13d; Table 4). The analyses are

significantly enriched in common Pb with many measured $^{207}\text{Pb}/^{206}\text{Pb}$ ratios ≥ 0.55 , and ranging to ~ 0.70 . Interpolation to a radiogenic end-member is therefore tenuous. However, it is possible to calculate a 3-dimensional linear fit to this common Pb enriched data and this provides a lower intercept at 16.7 ± 1.0 Ma (MSWD = 1.4, 19 analyses). A weighted mean of common Pb corrected $^{206}\text{Pb}/^{238}\text{U}$ ages gives 16.4 ± 1.4 Ma (MSWD = 0.4, 19 analyses). Two zircon inclusions within the same titanite separate were also analyzed (Table 4), and have $^{206}\text{Pb}/^{238}\text{U}$ ages of 18.6 ± 1.1 Ma and 19.5 ± 0.2 Ma, respectively. These zircon grains have very high U concentrations ~ 3000 ppm and ~ 5650 ppm, respectively, and so the radiogenic $^{206}\text{Pb}/^{238}\text{U}$ ages are unreliable by SHRIMP (see Williams and Hergt, 2000).

From a second sample from the same outcrop (TNG148b), nine areas on 3 zircon grains were analyzed *in situ* in a polished thin section. As with the zircon included within the titanite, the U concentrations range to very high values (~ 5785 ppm). However, lower, more reasonable U concentrations are recorded, and 5 analyses with ≤ 1710 ppm U have a weighted mean $^{206}\text{Pb}/^{238}\text{U}$ age of 18.0 ± 0.4 Ma (MSWD = 1.09, Fig. 13e; Table 4). It should be noted that the zircon grain with ~ 3000 ppm U that is included in titanite has a $^{206}\text{Pb}/^{238}\text{U}$ age within uncertainty of the titanite age. Thus, overall the zircon records a slightly older age than that obtained from titanite with high common Pb.

8. Rb-Sr and Sm-Nd isotope geochemistry

In order to track the origin and mixing of magmas from different sources as inferred in the field, we analyzed Rb-Sr and Sm-Nd

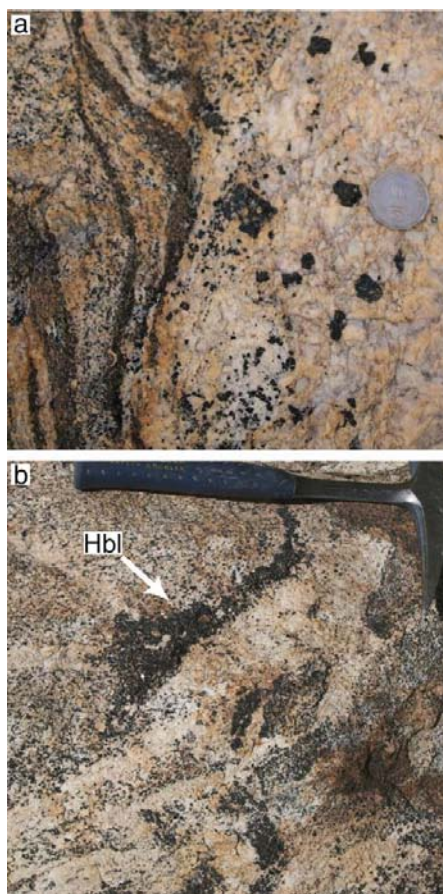


Fig. 3. (a) Up to ~1 cm poikilitic hornblende crystals in leucosome in metatexite. (b) Accumulation of hornblende crystals in leucosome network in calc-alkaline Hbl-Bt-granodiorite of the Muglib Batholith.

isotopes of rocks that we interpret to represent magma sources and those that represent melting products, i.e. the leucogranites. We used 18 Ma for recalculation of initial $^{87}\text{Sr}/^{86}\text{Sr}$ and $^{143}\text{Nd}/^{144}\text{Nd}$ ratios for leucogranites. This is the most likely crystallization age based on U–Pb



Fig. 4. Leucosomes in folded amphibolite. Melt must have been present at the time of deformation, because the folded layer-parallel leucosome cuts across the fold limb but stays in continuity with layer-parallel leucosomes on the opposite limb.



Fig. 5. Shear band in stromatic migmatite developed in calc-alkaline diorite. A leucosome forms within the shear band that runs from the upper left to the lower right. Layer-parallel leucosomes have diffuse boundaries with the leucosome in the shear band in the central part. The dark layer (melanosome) in the upper part of the photograph (tip of hammer) is continuous across the shear zone. The thick coarse-grained layer-parallel leucosome in the lower part of the photograph is nearly truncated by the shear zone, indicating that it formed earlier. However, the thinned out right part of the leucosomes almost connects to the counterpart on the left hand side.

SHRIMP data for such rocks (Searle et al., 1998 and our new analyses). For direct comparison with the products of anatexis, we also calculated the isotope data of source rocks and those of the Ladakh Batholith to that time.

8.1. Results

Initial $^{87}\text{Sr}/^{86}\text{Sr}$ between 0.7042 and 0.7077 and initial ϵ_{Nd} values between 0.6 and 2.4 for calc-alkaline granitoids of the Muglib Batholith indicate a mantle origin with a slight crustal influence, or juvenile crustal sources (Table 5, Fig. 14). For comparison we analyzed six samples from the Ladakh Batholith close to Leh (Fig. 1a). These yielded essentially identical $^{87}\text{Sr}/^{86}\text{Sr}_i$ ranging between 0.7045 and 0.7066 and $\epsilon_{\text{Nd}i}$ ranging between -0.1 and 2.1 . The overlap with the values for the Muglib Batholith indicates a possible genetic relationship (see discussion below). In contrast, meta-sedimentary rocks of the PMC yielded $^{87}\text{Sr}/^{86}\text{Sr}_i$ between 0.7115 and 0.7161 that indicate longer crustal residence and $\epsilon_{\text{Nd}i}$ that show limited variation between -10.0 and -9.6 (Table 5, Fig. 14). Thus, the protoliths recognized in the field have significantly different isotopic compositions.

The leucogranites, including *in situ* leucosomes interpreted to represent melt products in the PMC have $^{87}\text{Sr}/^{86}\text{Sr}_i$ ranging from 0.7086 to 0.7121, and $\epsilon_{\text{Nd}i}$ values between -3.6 and -6.2 . Similar values were obtained for four Ms-Bt \pm Grt-leucogranite samples from the Karakoram Batholith collected in the Shyok and Nubra River confluence area and in the Nubra Valley (Fig. 1a) at approximately

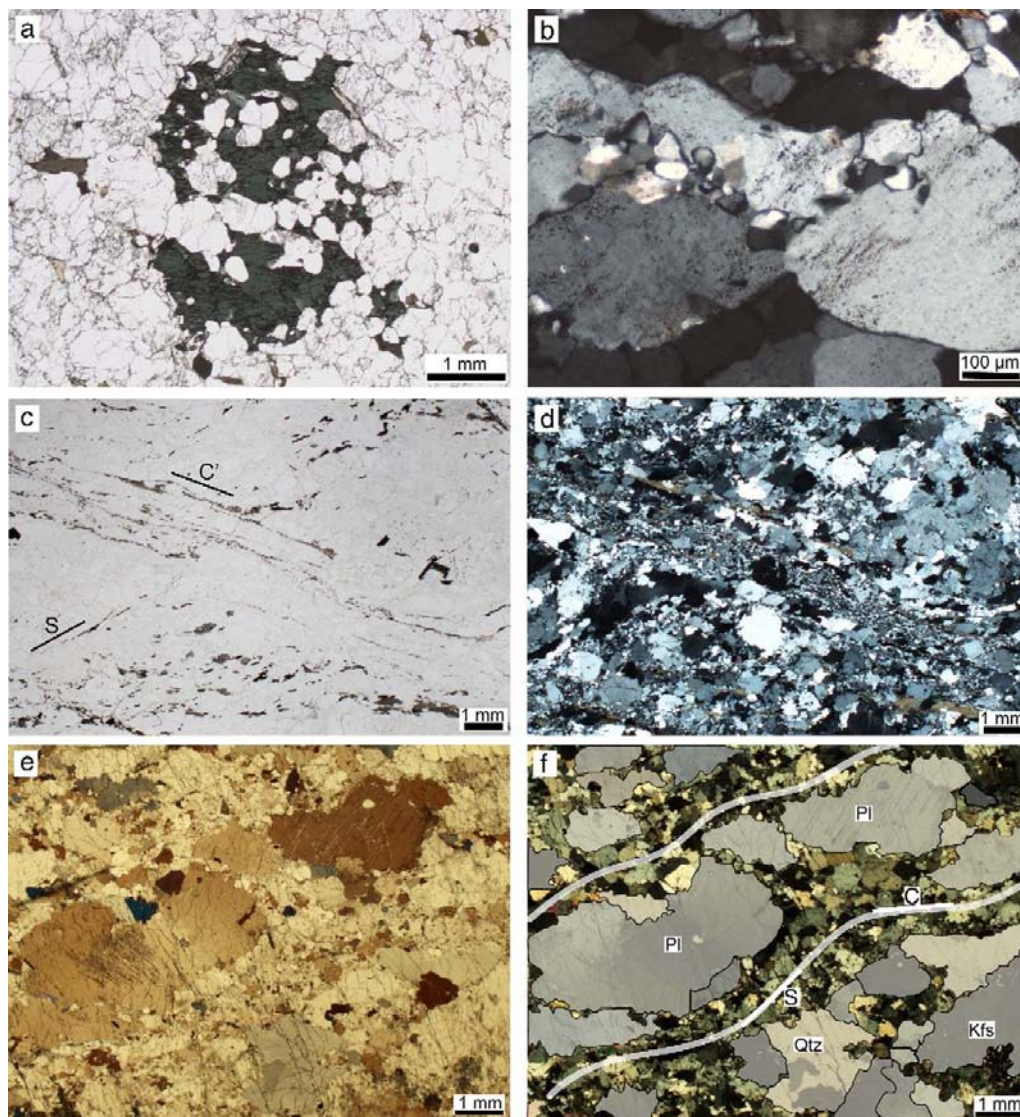


Fig. 6. Photomicrographs. (a) Hornblende crystal in tonalitic leucosome of a diatexite in the Tangtse gorge. The poikilitic texture suggests that the hornblende is peritectic. Plane-polarized light. (b) Recrystallization of deformed K-feldspar grains in a shear band in Bt ± Grt leucogranite. Cross-polarized light. (c) and (d) C-type shear band in Bt ± Grt leucogranite indicating dextral shear sense. Plane-polarized light and cross-polarized light, respectively. (e) Plagioclase and K-feldspar phenocrysts and fine-grained Qtz, Pl and Kfs in Grt–Ms–Bt leucogranite. Polarizer is only half turned in. (f) Same as in (e) but with crossed polarizer and line drawing to illustrate that the fine grains define a dextral C–S fabric. This fabric is interpreted to have been developed before complete crystallization of the magma.

60 km, 65 km, 85 km and almost 100 km distance from the Tangtse gorge ($^{87}\text{Sr}/^{86}\text{Sr}_i = 0.7076$ to 0.7092 and $\epsilon_{\text{Ndi}} = -5.4$ to -7.1). In the region of Rongdu (Fig. 1a) in the Shyok Valley, we have mapped a kilometer-wide Hbl–leucogranite body within the Karakoram Batholith similar in field appearance to Hbl-bearing leucosomes of the Tangtse migmatites. An enclave of calc-alkaline diorite migmatite was collected from within this body. Analysis of the hornblende-bearing leucosome of this sample (AGH23a in Table 5), which is petrographically and geochemically comparable to leucosomes in Hbl–Cpx diorites of the Muglib Batholith close to Muglib (sample TNG60d in Table 1), yielded isotope values similar to those of the Karakoram Batholith.

In the ϵ_{Ndi} vs. $^{87}\text{Sr}/^{86}\text{Sr}_i$ diagram (Fig. 14), leucogranites from the PMC and the Karakoram Batholith define a field with intermediate values between those of the calc-alkaline granitoids and meta-sedimentary rocks. In a simple two end-member mixing calculation, this field lies within hyperbolic curves between samples we infer to be representative of source rocks (Fig. 14). While ϵ_{Ndi} values of leucogranites show only little variation, $^{87}\text{Sr}/^{86}\text{Sr}_i$ scatter over a wider range.

Like the majority of leucogranite samples analyzed, those collected from the two outcrops described above (Figs. 7 and 8) also yielded intermediate signatures between those of calc-alkaline granitoids and meta-sedimentary rocks. The pegmatitic leucosome in the outcrop in

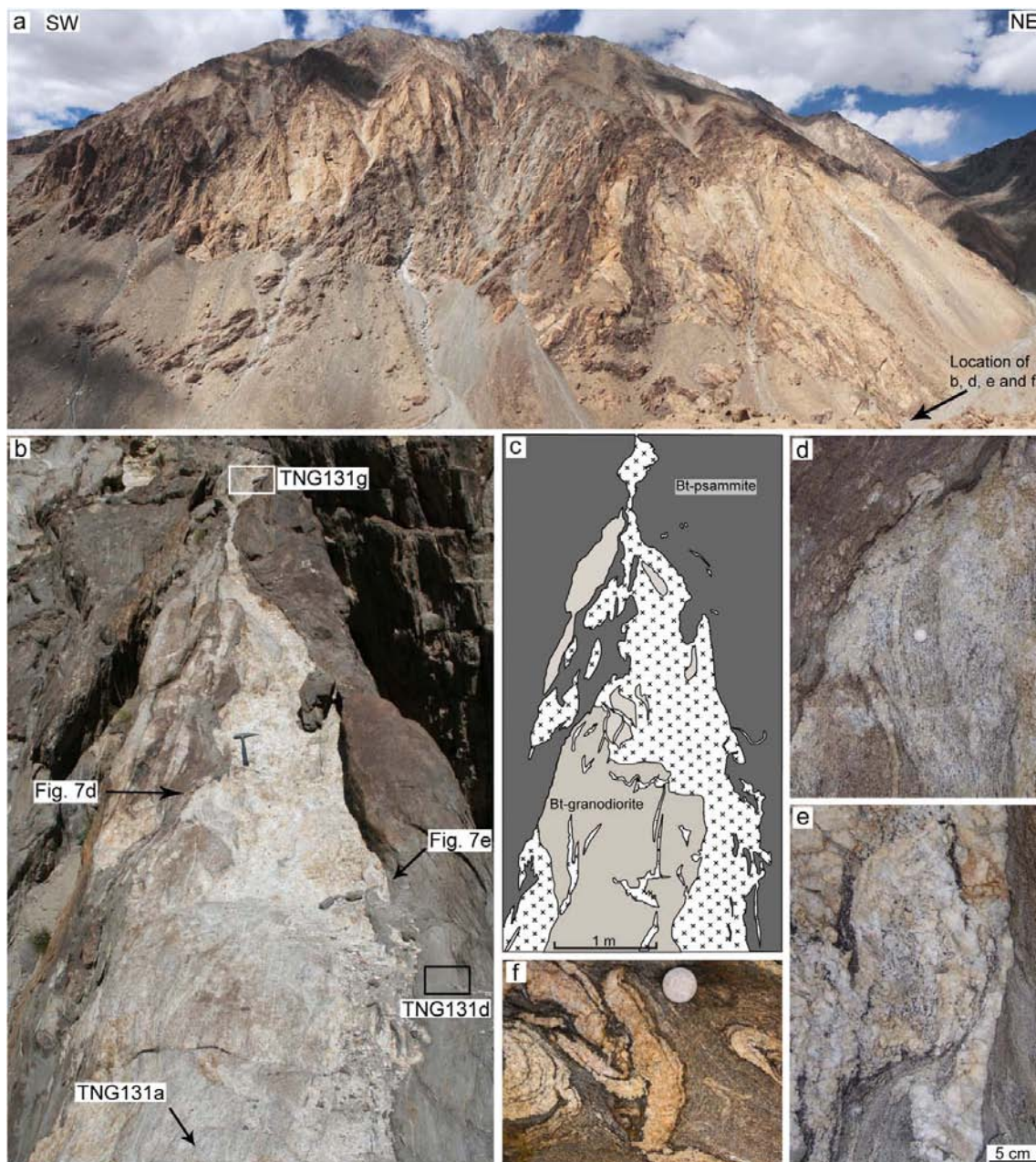


Fig. 7. Outcrops at the base of the Tangtse Pluton indicative of magma hybridization in the source. (a) Pangong Injection Complex and Tangtse Pluton looking NW. Dark rocks are Bt-psammites of the PMC, and light rocks are leucogranites. (b) Migmatite outcrop at the foot of the Tangtse Pluton. Leucosomes in a calc-alkaline Bt-granodiorite (lower centre; sample TNG131a; Zircon age = 70.5 ± 0.6 Ma) show diffuse boundaries with the leucosome (sample TNG131g, Table 2) in the centre of the photo which is connected to the leucogranite sheets that form the Tangtse Pluton. The surrounding Bt-psammite (sample TNG131d, Table 2) is also migmatitic. (c) Line drawing of (b). (d) Detail of (b); *in situ* leucosomes in Bt-granodiorite merge with the large pegmatitic leucosome. The Bt-granodiorite also forms rafts (towards right side of photograph). (e) Detail of (b); entrained wispy schlieren of Bt-psammite containing garnet. (f) Detail of folded leucosomes in Bt-psammite. Thin melanosome rims around leucosomes consist mostly of biotite.

Fig. 7b (sample TNG131g in Table 5) yielded a $^{87}\text{Sr}/^{86}\text{Sr}_i$ of 0.7088, and a $\epsilon_{\text{Nd}i}$ value of -3.6 . These are similar to isotope values obtained from two Ms-Bt \pm Grt-leucogranite samples from leucogranite sheets such as in

Fig. 7c (TNG71a and TNG71b in Table 5) and two other Bt-leucogranite samples from the Tangtse Pluton close to the outcrop in Fig. 7 (TNG148a and TNG148b in Table 5).

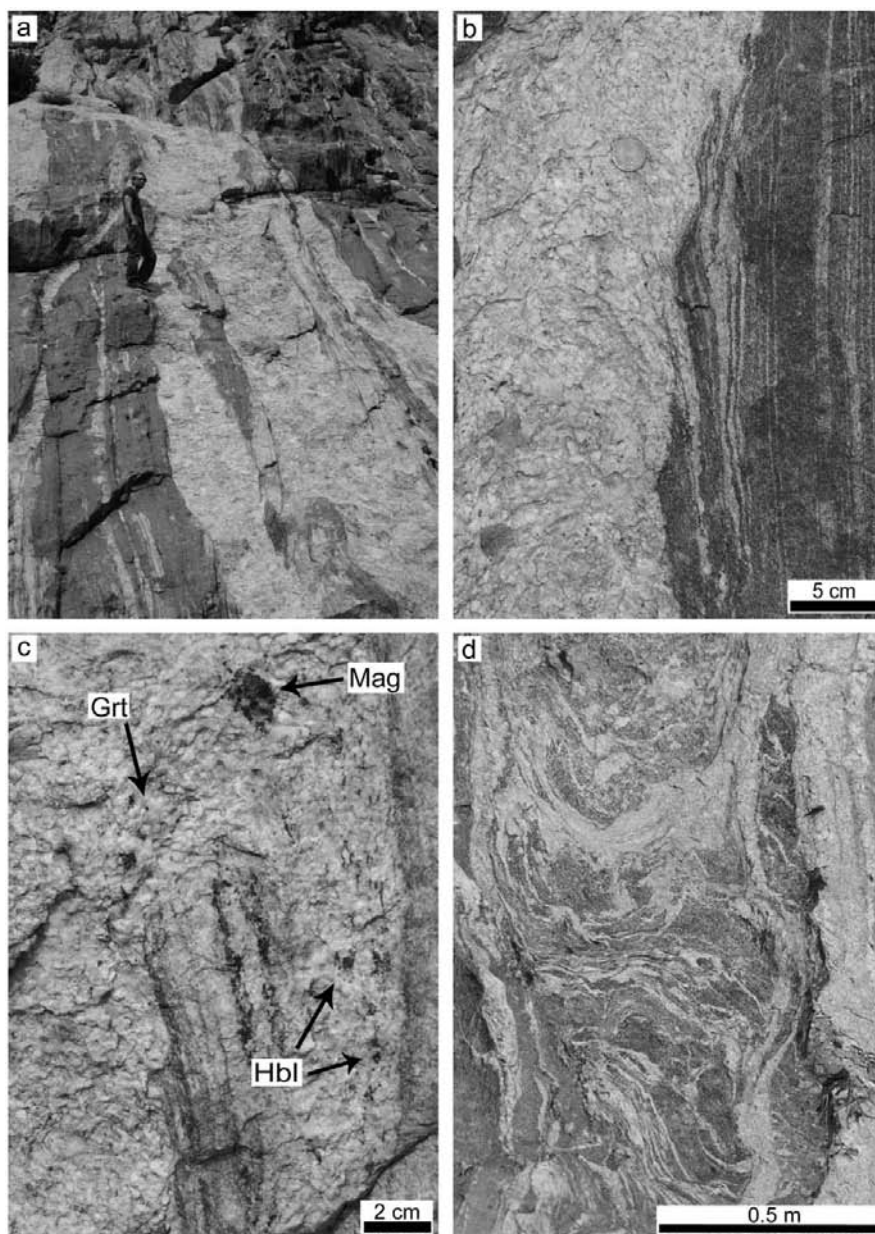


Fig. 8. (a) Pegmatitic leucogranite dykes intrude Hbl-Bt-gneiss in the Darbuk-Shyok gorge (samples TNG187a and TNG187b in Table 2). (b) Continuity between layer-parallel *in situ* Hbl-bearing leucosomes and crosscutting large garnet-bearing leucogranite dyke. *In situ* leucosomes generally have thin melanosome rims and are sometimes connected to leucosomes patches that have diffuse boundaries to the melanosome. (c) Seamless merging between dyke and *in situ* Hbl-bearing leucosome. Garnet crystals and cluster of magnetite in pegmatitic Grt-Bt-leucogranite dyke. The dyke continues to the upper left side of the photograph. (d) Diatexite migmatite. The pegmatitic leucogranite dyke that borders the diatexite migmatite is continuous with leucosomes in migmatite.

The isotope values of samples from two pegmatitic Grt-Ms-Bt-leucogranite dykes from the outcrop in Fig. 8 (TNG187a, TNG187b in Table 5) also show intermediate values ($^{87}\text{Sr}/^{86}\text{Sr}_i = 0.7087$ for both samples, $\epsilon_{\text{Ndi}} = -4.5$ and -4.4 , respectively). A Ms-Bt leucogranite dyke (TNG186 in Table 5) that intrudes calc-silicate rocks close by, has a comparable ϵ_{Ndi} value of -4.5 , but a remarkably high $^{87}\text{Sr}/^{86}\text{Sr}_i$ of 0.7121.

Whilst the majority of leucosomes show this intermediate signature, a Ms-Bt leucogranite sample (TNG170, Table 5) collected from within a metatexite in the centre of the Tangtse gorge has isotope values close to those for a patchy melanosome in diorite ($^{87}\text{Sr}/^{86}\text{Sr}_i = 0.7052$ and $\epsilon_{\text{Ndi}} = 2.3$) in the same outcrop (TNG169a in Table 5). These values are similar to those of the calc-alkaline source rocks ($^{87}\text{Sr}/^{86}\text{Sr}_i = 0.7054$ and

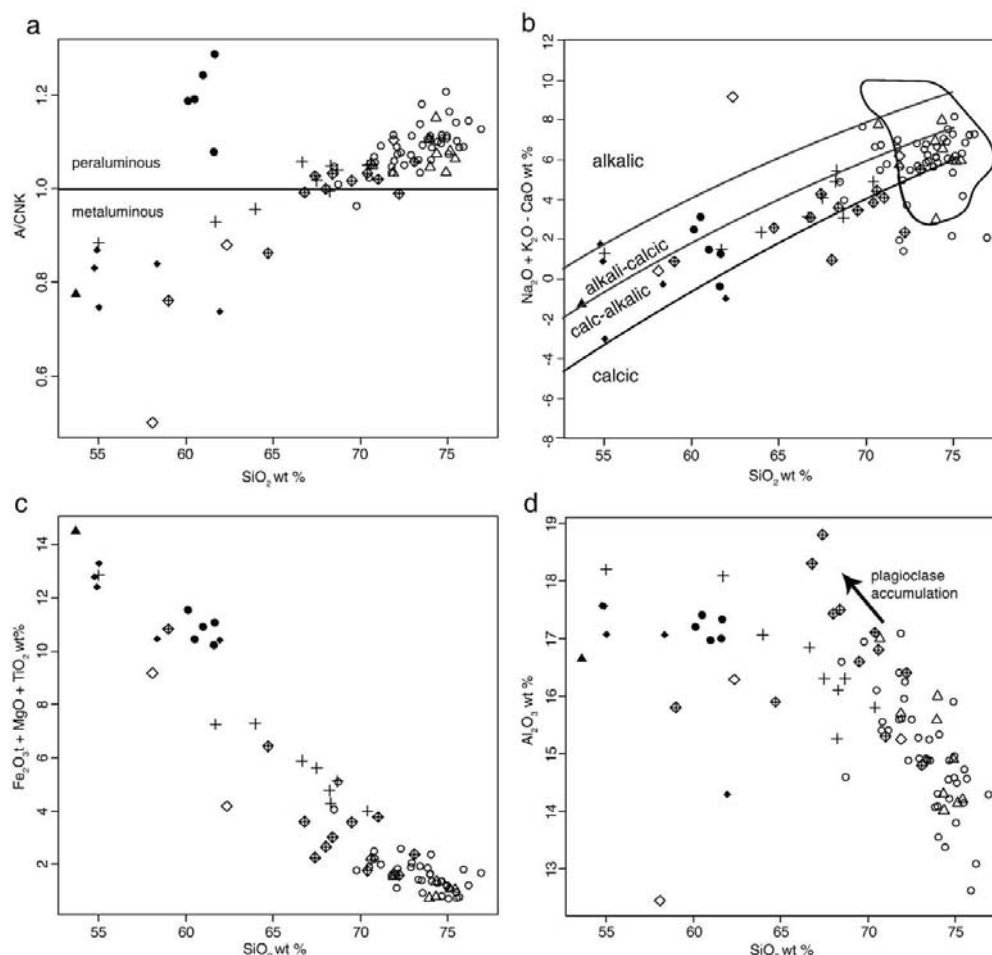


Fig. 9. Variations of major element concentrations of whole rock samples expressed as oxide weight percent. See explanations in text. (b) Alkali-lime vs. SiO₂ diagram after Frost et al. (2001). Rocks of the PMC that show no signs of anatexis are not included. Filled triangle: amphibolite gneiss (possibly andesitic protolith); filled diamonds: calc-alkaline diorites; filled circles: Bt-psammities and Bt-pelites; crosses: calc-alkaline granodiorites; open diamonds with crosses: diatexites; open triangles: pegmatitic leucogranite dykes; open diamonds: Hbl-Kfs leucosome; open circles: leucogranites. The arrow in (d) indicates plagioclase accumulation. $N = 87$.

$\epsilon_{\text{Nd}} = 1.1$), and indicates that in this particular case the leucosome was not hybridized.

An exceptional amphibolite gneiss sample (SiO₂ = 52.82 wt %) of the PMC (TNG108c in Table 5) has an isotope signature ($^{87}\text{Sr}/^{86}\text{Sr}_i = 0.7047$, $\epsilon_{\text{Nd}} = 8.8$) close to the field of present-day prevalent mantle (Zindler and Hart, 1986). This sample is isotopically and geochemically comparable to Kohistan-Ladakh island arc lavas (Northern Group, type 2 lavas in Rolland et al. 2002).

9. Discussion

9.1. Geochemical characteristics: comparison to other Miocene Himalayan leucogranites

Leucogranites of the broader Karakoram region are remarkably different from the High Himalayan leucogranites studied in Nepal (e.g. Deniel et al., 1987; Le Fort et al., 1987). High Himalayan leucogranites are generally strongly peraluminous, have high Rb/Sr ratios and high $^{87}\text{Sr}/^{86}\text{Sr}$ (0.74–0.82), whereas Karakoram leucogranites are mildly

peraluminous, have low Rb/Sr ratios and $^{87}\text{Sr}/^{86}\text{Sr}$ (0.71 to 0.72; Crawford and Windley, 1990). The leucogranites we studied in the Karakoram Shear Zone are geochemically comparable to the latter with A/CNK between 1.02 and 1.16, Rb/Sr ratios on average below one, and $^{87}\text{Sr}/^{86}\text{Sr}_i$ (0.7086 to 0.7121). Muscovite dehydration melting leads to high Rb/Sr ratios in the melt (Inger and Harris, 1993), whereas the low Rb/Sr ratios of the Karakoram rocks are most likely the result of H₂O-fluxed melting because plagioclase will melt preferably over biotite or muscovite (Patiño Douce and Harris, 1998).

9.2. Significance of water-fluxed melting

The significance of water-fluxed melting synchronous with deformation for crustal differentiation has been discussed for the European Alps (e.g. Burri et al., 2005; Berger et al., 2008). Most experimental work in the literature has been undertaken for fluid absent conditions where the limiting factor for melt production is the abundance of water-bearing phases, e.g. muscovite, in the source rock (see discussion in Clemens, 2006). This is in contrast with water-fluxed melting, where the

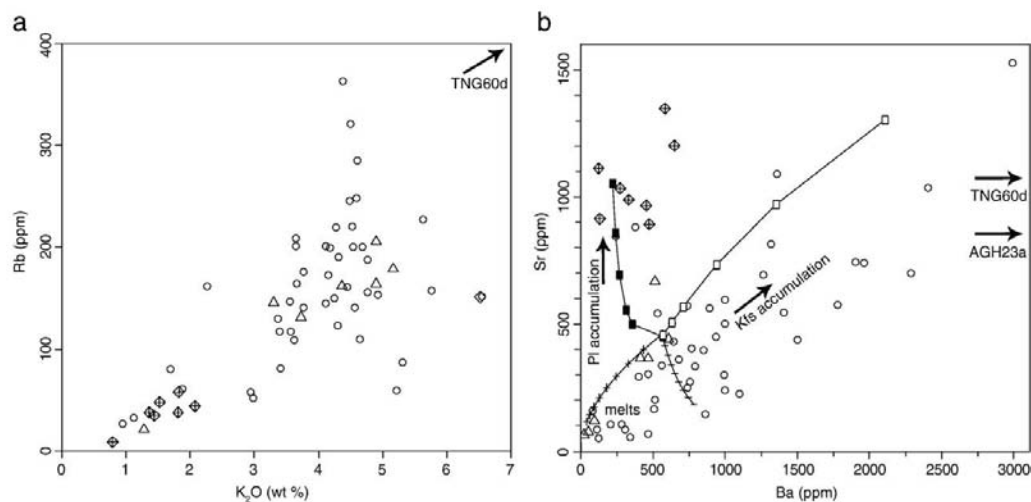


Fig. 10. (a) Rb contents correlate positively with K₂O in leucogranites, interpreted as the result of K-feldspar accumulation. Sample TNG60d (Hbl-Kfs leucosome) with extremely high K₂O (10.1 wt %) and Rb (441 ppm) concentrations is not shown ($N=60$). (b) Ba vs. Sr in leucogranites. High Ba and Sr concentrations indicate feldspar cumulates. The Hbl-Kfs leucosome samples TNG60d (Ba = 8280 ppm and Sr = 1083 ppm) and AGH23a (Ba = 4136 ppm and Sr = 903 ppm) are not shown for scaling reasons. The curves represent model calculations for fractionation and accumulation. Starting composition is leucosome TNG71b (Ba = 565 ppm and Sr = 448 ppm). Plus and minus symbols represent modelled compositions of residual liquids after Raleigh fractionation of K-feldspar and plagioclase, respectively, in 5% increments (5%, 10%, 15%... fractionated minerals). Open and filled squares represent modelled compositions of cumulates after Raleigh fractionation of K-feldspar and plagioclase, respectively, for different degrees of accumulation $F=0.1\ldots0.8$. Partition coefficients (K_d) after Arth (1976). Calculation after Rollinson (1993). See Fig. 9 for symbols. $N=59$.

availability of free water is the main limiting factor and melting would continue as long as water is brought into the system, for example via a shear zone (e.g. Mogk, 1992; Genier et al., 2008). In the Karakoram Shear Zone these processes operate on a large scale, potentially giving rise to magma volumes of batholith dimensions.

9.3. Age relations between leucogranites and the Muglib Batholith

Titanite and zircon grains from the two leucogranite samples dated yielded slightly different ages: 16.4 ± 1.4 Ma for titanite (sample TNG148a; Fig. 13d), compared to 18.0 ± 0.4 Ma for zircon (sample TNG148b; Fig. 13e). Because the titanite is strongly enriched in common Pb and hence less reliable, we consider the 18.0 ± 0.4 Ma zircon age as most closely reflecting the crystallization age of the Tangtse Pluton. Despite the slight differences, the two results overlap within error. However, ID-TIMS zircon age data of the Tangtse Pluton (the Muglib dome of Phillips and Searle, 2007) yielded 15.1 ± 0.6 Ma (Phillips and Searle, 2007). Other age results for leucogranite intrusions in the Tangtse area include 15.6 ± 0.1 Ma for a sample within the Tangtse Shear Zone (Phillips et al., 2004), 18.0 ± 0.6 Ma for a Grt–Ms–Bt–leucogranite sampled close to Tangtse (Searle et al., 1998), and between 16.6 ± 0.2 Ma and 19.1 ± 1.1 Ma from Ms–Bt–leucogranite samples collected close to Darbuk (Ravikant et al., 2009). A similar Ar–Ar age of 18 Ma was obtained for amphibole in an amphibolite sample from the Tangtse area (Rolland et al., 2009). Late-stage pegmatite dykes from the Tangtse Shear Zone yielded an even younger U–Pb zircon age of 13.7 ± 0.2 Ma (Phillips et al., 2004), but it is not clear whether these younger intrusions result from *in situ* melting of the anatexitic rocks exposed in that area or whether they are intrusive rocks generated elsewhere. Due to the general spread in ages, we conclude that magmatism in the region lasted at least between 20 and 13.5 Ma and that the difference in ages found for the Tangtse Pluton (18.0 ± 0.4 Ma and 15.1 ± 0.6 Ma) indicates the duration of its growth.

The younger ages of leucogranites in the Karakoram Shear Zone are comparable to samples from the Karakoram Batholith. A leucogranite sample collected close to Satti in the Nubra Valley, NW

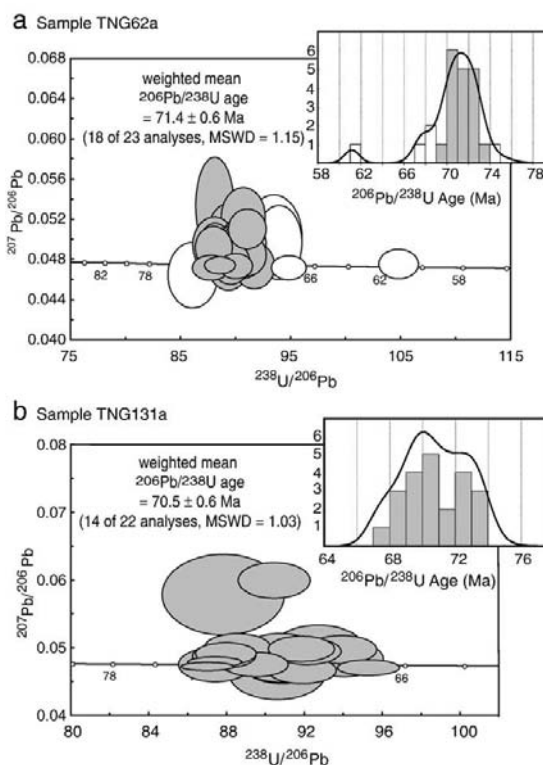


Fig. 11. Tera-Wasserburg concordia diagrams for sample TNG62a and sample TNG131a (Zrn). Inserts are histograms of relative age probability vs. number of spots in U–Pb SHRIMP analysis. Error ellipses are 68.3% confidence. (a) Zircons from the melanosome of a Hbl–Bt–granodiorite (sample TNG62a). (b) Zircons from a Bt–granodiorite (sample TNG131a).

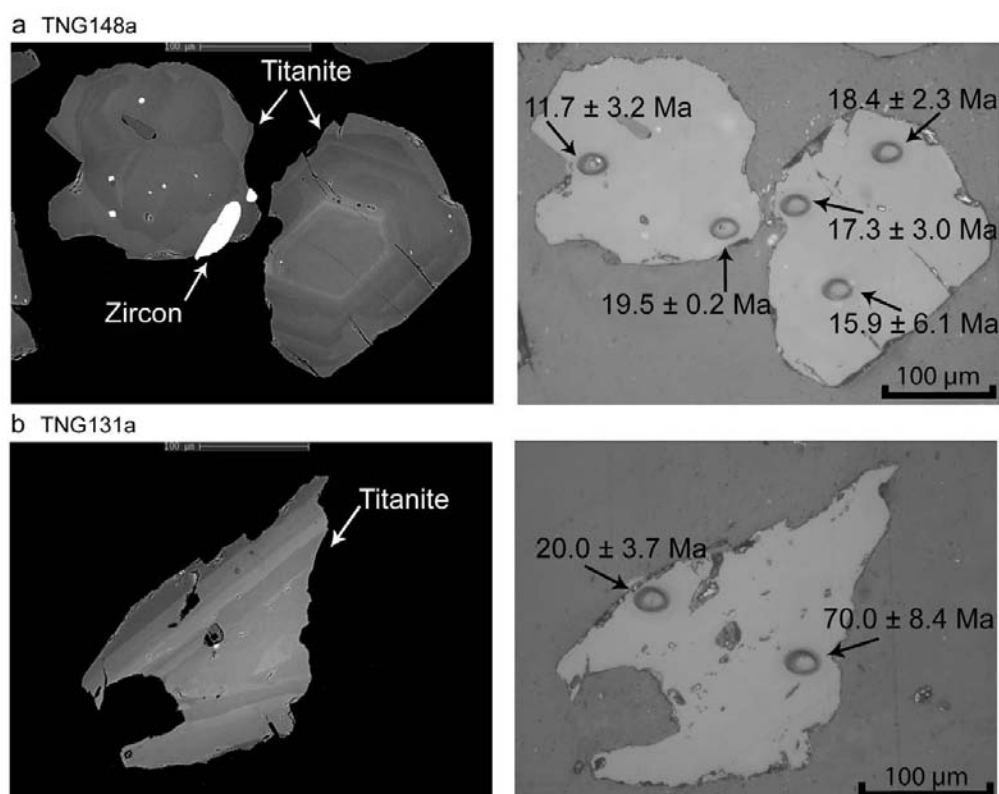


Fig. 12. (a) BSE image (left) and post-analysis photograph (right) of titanite grains from sample TNG148a. Note that the zircon inclusion yielded an older age than that of the surrounding titanite (see also Table 4). (b) BSE image (left) and post-analysis photograph (right) of a titanite grain from sample TNG131a. Ages are indicated for each analyzed spot (see also Table 3).

of the Pangong Metamorphic Complex, yielded a zircon SHRIMP crystallization age of 15.0 ± 0.4 Ma (Weinberg et al., 2000), similar to a mylonitic leucogranite also from Satti (ID-TIMS zircon age 15.9 ± 0.1 Ma; Phillips et al., 2004). A late-stage leucogranite dyke from this batholith collected further NW along strike of the Nubra Valley yielded ID-TIMS zircon age of 13.7 ± 0.3 Ma (Phillips et al., 2004).

The crystallization ages of the calc-alkaline Muglib Batholith obtained here, at 71.4 ± 0.6 Ma (sample TNG62a) and 70.5 ± 0.6 Ma (sample TNG131a), overlap with a Rb–Sr age of 72 ± 8 Ma (Ravikant, 2006) for a Hbl–Bt–granodiorite sample close to Muglib village, while Ravikant (2006) obtained a Rb–Sr age of 118 ± 15 Ma for a migmatitic granodiorite in the Tangtse gorge. A U–Pb SHRIMP zircon age of 68 ± 1 Ma was determined for the calc-alkaline Tirit granite at the confluence of the Shyok and Nubra Rivers by Weinberg et al. (2000). This suggests that a series of calc-alkaline bodies, possibly forming a continuous batholith that runs from Muglib along the Pangong Range and at the feet of the Saltoro Range in the Nubra Valley were emplaced between 67 and 72 Ma, possibly extending back to c. 120 Ma.

Titanite analyses of the Bt–granodiorite at the base of the Tangtse Pluton (Fig. 7b; sample TNG131a) yielded two age populations (Fig. 13c). The older group, 60–65 Ma, may represent early metamorphism in the Muglib Batholith, related to the heat from intrusion of late phases of calc-alkaline magmatism or, to slow cooling through the blocking temperature of titanite. The fact that the younger age range of ~11 to 21 Ma overlaps with the crystallization ages of the anatectic leucogranites of the Tangtse Pluton supports our interpretation that magma derived from anatexis of the Muglib Batholith contributed to form the Miocene leucogranite intrusions in the area.

This interpretation is further supported by the presence of 63.0 ± 0.8 Ma zircon cores in Miocene leucogranites from Tangtse (Searle et al., 1998). In the same study, a migmatitic orthogneiss, probably related to the Muglib Batholith, showed two age groups. The older group with a mean weighted U–Pb age of 106.3 ± 2.3 Ma was interpreted as the crystallization age of the orthogneiss, and the younger group with ages ranging between 22 and 15 Ma as the result of metamorphic growth during migmatization (Searle et al., 1998).

9.4. Origin of the Muglib Batholith

Considering the temporal and compositional similarities between the Tirit granite and the Muglib Batholith, and the extent of our mapping in the region (Fig. 1), we suggest that a Cretaceous calc-alkaline body crops out semi-continuously for at least 85 km along the Karakoram Shear Zone: from SE of Muglib and northwestwards along the Pangong Range to the Nubra–Shyok confluence where it links with the Tirit granite along the northeastern side of the Saltoro Range (Weinberg et al., 2000). These magmatic rocks are also temporally, chemically and isotopically similar to the Ladakh Batholith which crops out immediately south of the Karakoram Shear Zone (Weinberg and Dunlap, 2000; Upadhyay et al., 2008; Ravikant et al., 2009).

The Ladakh Batholith resulted from subduction-related calc-alkaline magmatism which ceased as a result of the collision with India ca. 50 Ma (Schärer et al., 1984; Weinberg and Dunlap, 2000; Upadhyay et al., 2008). Crystallization ages range between 49 Ma and 103 Ma, broadly coincident with those determined for the the Muglib–Tirit bodies with ages centered around 70 Ma. Ravikant et al.

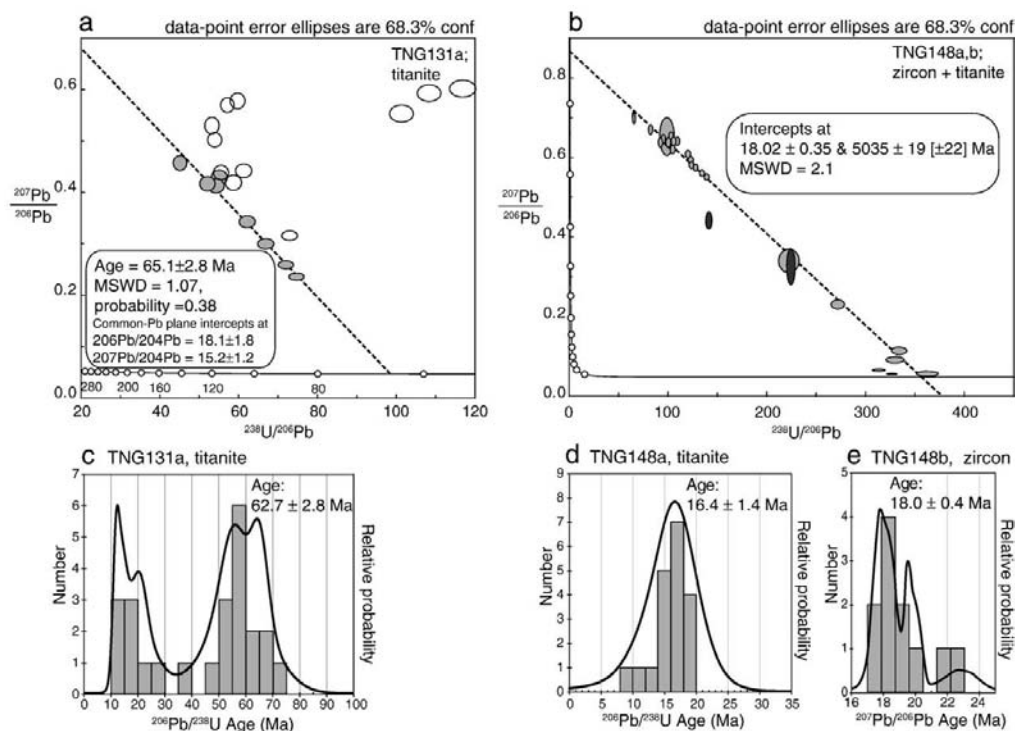


Fig. 13. (a) Concordia constrained linear 3-D isochron for sample TNG131a (Ttn). (b) Concordia diagram for samples TNG148a (Ttn) and TNG148b (Zrn) plotted together. (c) Histogram of titanite analyses of sample TNG131a. (d and e) Histogram of titanite and zircon analyses of samples TNG148a and TNG148b, respectively.

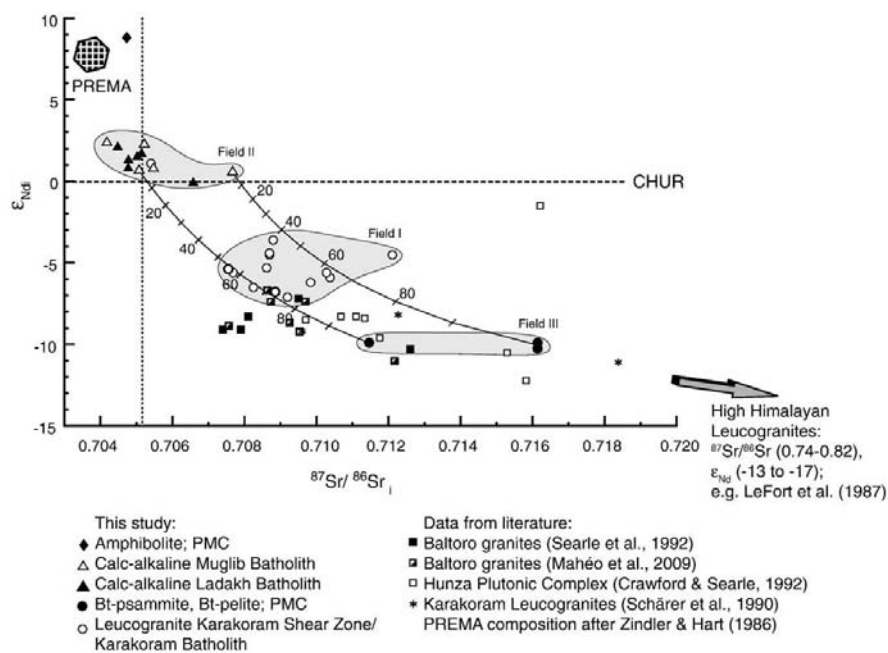


Fig. 14. $^{87}\text{Sr}/^{86}\text{Sr}_i$ vs. ϵ_{Nd} diagram calculated at 18 Ma. Curves are calculated mixing lines between end-member isotopic compositions of calc-alkaline granitoids and meta-sedimentary rocks. The grey fields mark the range of isotopic compositions for leucogranites (field I) and source rocks (field II and III).

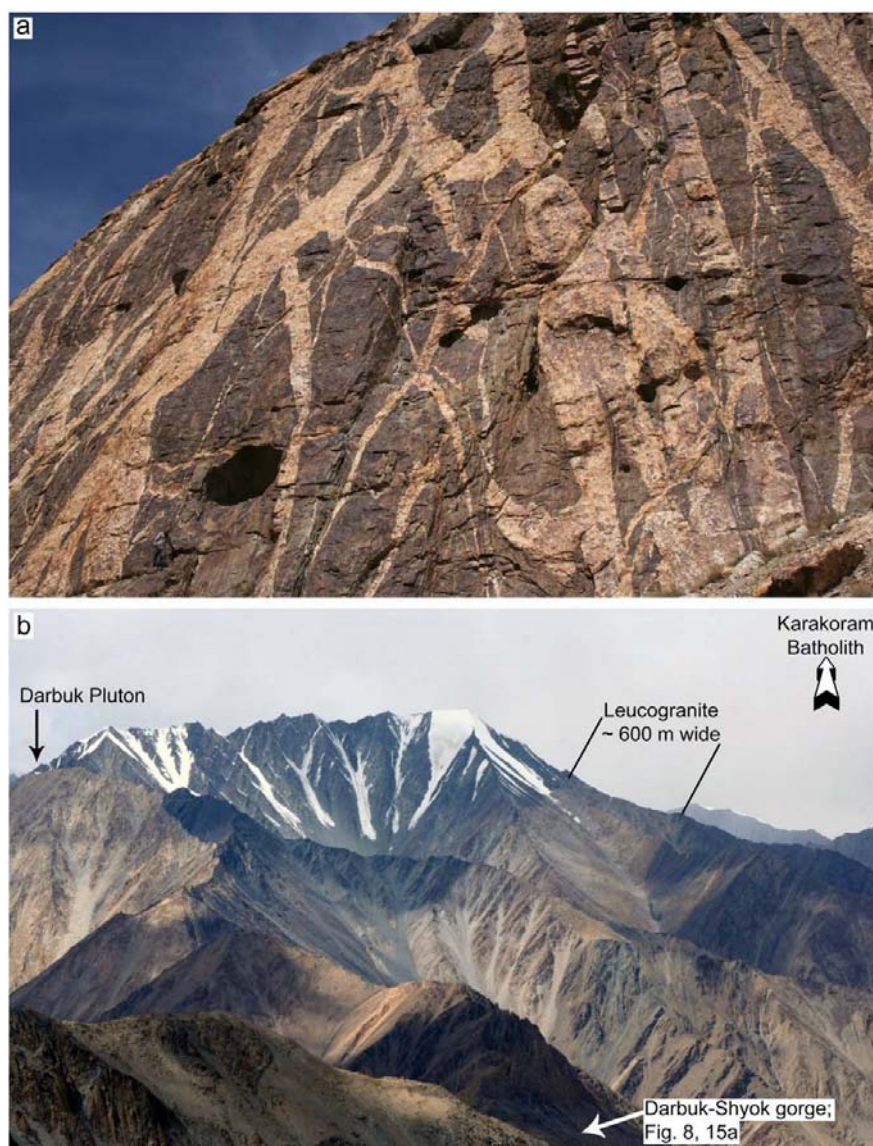


Fig. 15. Magma transport out of the source region. (a) Leucogranite dyke network in calc-silicate rocks the Darbuk-Shyok gorge. The dykes on this photo are up to ~5 m wide and merge and split seamlessly. Person on lower left of photograph as scale (below and left of shadow). (b) Pangong Range looking NW, showing an elongated leucogranite body 600 m thick (light band) that can also be seen in satellite images. Viewpoint is Pangong Range close to the Tangtse Pluton. The band can be followed into the Darbuk-Shyok gorge, where the dyke network in (a) and Fig. 8 are exposed (closer to viewer). The leucogranite pluton on the left hand side is connected to the dyke network. The far ridge of the leucogranite band is 15 km along strike from viewpoint.

(2009) concluded that the Ladakh Batholith formed in two magmatic stages, one between 83 and 103 Ma and the other between 50 and 67 Ma. The 67–72 Ma age of the Muglib Batholith and Tirit granite (Weinberg et al., 2000; Ravikant 2006) thus represent the upper end of the younger group. Calc-alkaline intrusions around 70 Ma are at odds with the model of 'flat subduction' of Neotethyan lithosphere that resulted in a cessation of magmatic activity at the South Tibetan margin in the period between 60 and 70 Ma (Wen et al., 2008). However, given the large distance to the study area in Ladakh, this

discrepancy might indicate diachronous changes along the subduction zone.

Both the Ladakh and Muglib Batholiths have an identical isotopic signature indicative of mantle derivation with only minor crustal influence, or derivation from crustal rocks that themselves have short crustal pre-histories. Based on these similarities we suggest that the calc-alkaline Muglib Batholith, including the Tirit granite, and the Ladakh Batholith are effectively part of the same island arc, developed south of the Asian margin.

9.5. Linking source to sink

9.5.1. Field relations

In migmatites of the Tangtse gorge region, layer-parallel leucosomes in folds merge with axial planar leucosomes thus forming an interconnected melt flow network and demonstrating contemporaneity of anatexis with folding and shearing (Weinberg and Mark 2008). The network that arises allows for contemporaneous migration and mixing of magmas from different sources as demonstrated by the features documented at the base of the Tangtse Pluton (Fig. 7) and the Darbuk–Shyok gorge (Fig. 8), and supported by the isotope systematics (Fig. 14).

Moving up from outcrop scale, an interconnected network of leucogranite sheets, each several meters wide, is well developed in interlayered amphibolites and calc-silicate rocks hundreds of meters wide at the SW end of the Tangtse gorge and in the Darbuk–Shyok gorge over 13 km along strike (Fig. 15a). A large-scale network is also developed in the anatectic calc-alkaline and meta-sedimentary rocks, but is much more irregular in terms of sheet orientations and widths (see also the Pangong Injection Complex of Weinberg and Searle, 1998). We interpret these networks as large-scale magma pathways through both anatectic and non-anatectic rocks.

This system of intrusive sheets is related to a number of kilometer-sized leucogranite plutons in the Karakoram Shear Zone, such as the Tangtse and Darbuk Plutons (Fig. 1b, 2) and the ~600 m wide sheeted body through the centre of the Pangong Range in Fig. 15b. The anastomosing sheet network, plutons and sheeted bodies are together interpreted as the magma transfer zone between the source and the Karakoram Batholith that crops out to the NW of the Pangong Range (Fig. 15b). This interpretation is supported by our mapping closer to the Karakoram Batholith and by isotopic similarity from the source all the way to the Karakoram Batholith. At Agham, further NW of the Tangtse–Darbuk area and at the southern tip of the Karakoram Batholith, leucogranite dykes partly retrogressed to greenschist facies, intrude strongly deformed chlorite and muscovite schists as well as gabbroic rocks of the Muglib Batholith. Leucogranites here have the same isotopic composition as in the source area (sample AGH25a, Table 5). Further NW, the exposed contact between the Karakoram Batholith and its footwall in Rongdu is characterized by a network of mylonitized leucogranite sheets. Thus, sheets of essentially similar leucogranites can be followed from their source in the Pangong Range to the Karakoram Batholith over 80 km along strike.

This link between the source zone and the batholith is further supported by the presence of a kilometer-wide zone of Hbl-bearing leucogranites, including partly disrupted decimetric to metric enclaves of migmatitic Hbl–Cpx–diorite inside the Karakoram Batholith near Rongdu. These Hbl-bearing leucogranites are similar to those documented in the source region near Muglib, and the migmatitic diorite enclaves are similar to the anatectic diorites of the Muglib Batholith and are interpreted to represent blocks of the migmatitic source. As seen above, the leucosomes in these dioritic enclaves yielded a hybrid signature similar to the rest of the Karakoram Batholith, rather than the pure signature of the Muglib Batholith (sample AGH23a, Table 5).

Along the NE-side of the Nubra Valley, the Karakoram Batholith is emplaced in greenschist facies meta-sedimentary rocks and meta-volcanic rocks (e.g. Weinberg et al. 2000; Phillips et al., 2004), and thus exposes a higher structural crustal level than the deeply exhumed upper amphibolite facies rocks of the PMC. Interestingly, the width of the Karakoram Batholith, as partly interpreted from satellite images, is similar to the width of the Pangong Range measured between the Tangtse and the Pangong shear zones (Figs. 1, 2). If the Karakoram Batholith intruded synkinematically (Mahéo et al., 2004) as has also been demonstrated for the Tangtse Pluton and other leucogranites along the Karakoram Fault (Lacassin et al., 2004; Rolland et al. 2009; Weinberg et al., 2009), its measured displacement does not measure the full displacement on the Karakoram Shear Zone.

The southernmost tip of the Karakoram Batholith currently crops out ~40 km from the northernmost significant migmatite area in the Darbuk–Shyok gorge (Fig. 1a, b). Given the dextral movement on the shear zone, the Karakoram Batholith in Ladakh would have been further away from the migmatite area at the time of anatexis. The link between the anatectic rocks exposed in the PMC and the Karakoram Batholith demonstrated here does not necessarily imply that voluminous magma from this particular source found its way to the now exposed batholith, but rather suggests that the Karakoram Batholith was fed mostly from a source similar to the one exposed in the PMC.

9.5.2. Implications of the isotopic signatures

Initial $^{87}\text{Sr}/^{86}\text{Sr}$ and ϵ_{Nd} values of the leucogranites and leucosomes from the Pangong Range are intermediate between those of the meta-sedimentary rocks of the Pangong Metamorphic Complex and the Muglib Batholith, the likely magma sources. In the $^{87}\text{Sr}/^{86}\text{Sr}$ vs. ϵ_{Nd} diagram (Fig. 14), these intermediate values lie in a field defined by hyperbolic mixing curves between representative end-member compositions. It is interesting to notice that leucosomes, interpreted to be roughly *in situ*, also have mixed signatures (samples TNG71a, TNG131g; Table 5). The only exception is a tonalitic leucosome sample (sample TNG170, Table 5) from a metatexite migmatite in the central part of the Tangtse gorge. It yields isotopic values similar to a patchy melanosome in diorite (sample TNG169a) in the same outcrop and also to other samples of the Muglib Batholith. These findings suggest that in general, mixing occurred at an early stage in the migration history of the magmas.

These hybrid leucogranites exposed close to the source have similar values to those in intrusive sheets or plutons in the vicinity, as well as to those of the Karakoram Batholith (samples AGH25a, NBR1b, NBR2a and NBR3b in Table 5) supporting our field-based interpretation that the system is effectively connected from the source in the Pangong Range to the Karakoram Batholith. This is further supported by Hf isotope data, which suggest a similar origin for the leucogranites

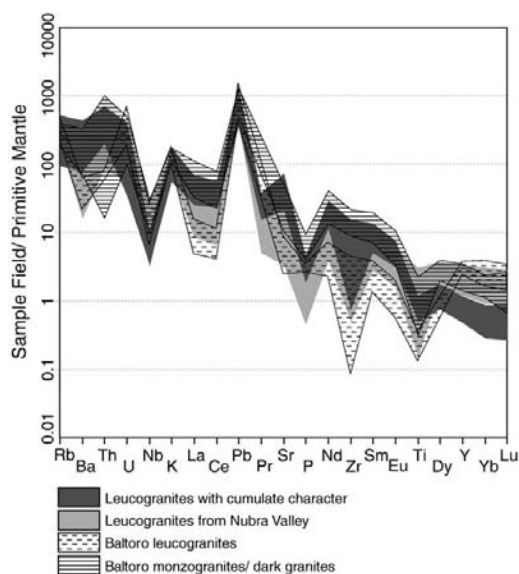


Fig. 16. Comparison of averaged subsets of leucogranite samples to available data for Baltoro granites. Samples are normalized to primitive mantle composition (Sun and McDonough, 1989). Leucogranites with cumulate character (high Sr and Ba): $N=9$; leucogranites from Nubra Valley: $N=9$; Baltoro leucogranites: $N=5$ (Searle et al., 1992); Baltoro monzogranites: $N=4$ (Searle et al., 1992); Baltoro dark granites: $N=5$ (Debon et al., 1986; Mahéo et al., 2002).

in the Karakoram Shear Zone and granitoids of similar ages of the Karakoram Batholith (Ravikant et al., 2009). We therefore conclude that magmas derived from the meta-sedimentary sequence and the calc-alkaline Muglib Batholith mixed early in their migration, and that this mixed magma gave rise to the Karakoram Batholith.

9.6. Similar leucogranite intrusions elsewhere in the Karakoram?

The Hunza Plutonic Unit and the Baltoro Batholith in Pakistan mark the NW continuation of the Karakoram Batholith (Crawford and Windley, 1990; Searle et al., 1992; Searle et al., 1998; Sirmal, 1986). The Baltoro Batholith is mostly composed of Bt ± Ms ± Grt-monzogranites and leucogranites that show mineralogical and geochemical similarities to the leucogranites of the Karakoram Shear Zone and the Karakoram Batholith (Searle et al., 1992), and are only slightly older (U–Pb zircon age 21 ± 0.5 Ma; Parrish and Tirrul, 1989). Trace element concentrations of our granites compare well to those of the Baltoro granite (Fig. 16; Crawford and Windley, 1990; Mahéo et al., 2009), suggesting a genetic link across the Pakistan–India border and across the Karakoram Shear Zone. Comparison of isotopic data in Fig. 14 further supports this link. Here we have included isotope data for the Karakoram and Baltoro granites, and granites of the Hunza Plutonic Unit from previous studies. Some of the Baltoro and Hunza samples overlap with our data, but others tend to show lower ϵ_{Nd} and some samples show higher $^{87}\text{Sr}/^{86}\text{Sr}_i$ values.

The isotope data for the Hunza and Baltoro granitoids can be explained using the same two source rocks inferred to have produced the Karakoram Batholith, but require more input from the meta-sedimentary sequence carrying the crustal signature. Whilst the Karakoram Batholith requires 40–70 % input from magmas derived from the meta-sedimentary rocks, the Hunza and Baltoro granitoids require more than 70 %. Exceptions are samples from Karakoram granites in Pakistan that show an even stronger crustal signature. Schärer et al. (1990) proposed, based on zircon and monazite inheritance and Pb, Sr and Nd isotopes that likely sources of these granites are the meta-sedimentary rocks of the Karakoram Metamorphic Complex in that region.

Alternative sources for the origin of the isotopic signature of granites in the Hunza and Baltoro areas have been suggested by Mahéo et al. (2002) and Mahéo et al. (2009). These include melting of metasomatized mantle in which melting was induced by asthenospheric upwelling after an inferred slab break-off of the subducted Indian plate, at the time of magmatism in the Karakoram and South Tibet. This component is indicated by the presence of lamprophyres cropping out in the area and which would have provided the heat for crustal melting or mixed with other magma sources to produce the leucogranites (Mahéo et al., 2009). Further, Mahéo et al. (2009) proposed partial melting of Cretaceous, calc-alkaline mafic to dioritic lower crust to account for the Baltoro granitic magmatism.

Multiple alternatives may be and have been proposed for interpreting essentially the same isotopic signatures. We argue that field relations allow us to directly document the process of magma generation and migration from the anatectic terrane exposed in the Pangong Metamorphic Complex, comprising a Late Cretaceous island arc batholith and its meta-sedimentary country rocks, to the Miocene leucogranites of the Karakoram Batholith.

10. Conclusions

In the Karakoram Shear Zone, anatexis of Late Cretaceous calc-alkaline granodiorites and diorites of the Muglib Batholith and of meta-sedimentary rocks of the Pangong Metamorphic Complex took place during deformation and as a result of water-fluxed melting. Magmas from this heterogeneous source formed an extensive network of channels, across a number of scales, which allowed for

extraction. The initial $^{87}\text{Sr}/^{86}\text{Sr}$ and ϵ_{Nd} values of leucosomes, leucogranite sheets, stocks and plutons in the Karakoram Shear Zone are similar to those of the Karakoram Batholith and vary between 0.7086 to 0.7121 and -7.1 to -3.6 , respectively. This is a hybrid signature between the two sources identified in the anatectic zone. We conclude therefore that the Karakoram Batholith is a result of melting of a heterogeneous source in the presence of a water-rich fluid, and that the mixing of these different magmas took place already within the source region.

Acknowledgements

We would like to thank Yann Rolland and Vadlamani Ravikant for constructive reviews and Olav Eklund for handling of the paper in the editing process. We also thank Bruce Schaefer for helpful discussions on isotope geochemistry, Roland Maas for carrying out isotope analysis, as well as Massimo Raveggi for help with ICP-MS analysis. This paper is part of the PhD thesis of the first author.

Appendix A. Supplementary data

Supplementary data associated with this article can be found, in the online version, at doi:10.1016/j.lithos.2009.11.013.

References

- Aleinkoff, J.N., Wintsch, R.P., Tollo, R.P., Unruh, D.M., Fanning, C.M., Schmitz, M.D., 2007. Ages and origins of rocks of the Killingworth Dome, south-central Connecticut; implications for the tectonic evolution of southern New England. *American Journal of Science* 307 (1), 63–118.
- Andersson, U.B., 1991. Granitoid episodes and mafic/felsic magma interaction in the Svecofennian of the Fennoscandian Shield, with main emphasis on the approximately 1.8 Ga plutonics. *Precambrian Research* 51 (1–4), 127–149.
- Andersson, U.B., Neymark, L.A., Billström, K., 2002. Petrogenesis of Mesoproterozoic (Subjotnian) rapakivi complexes of central Sweden; implications from U–Pb zircon ages, Nd, Sr and Pb isotopes. *Transactions of the Royal Society of Edinburgh: Earth Sciences* 92 (3–4), 201–228.
- Arth, J.G., 1976. Behavior of trace elements during magmatic processes; a summary of theoretical models and their applications. *Journal of Research of the U. S. Geological Survey* 4 (1), 41–47.
- Beard, J.S., Ragland, P.C., Crawford, M.L., 2005. Reactive bulk assimilation; a model for crust–mantle mixing in silicic magmas. *Geology* 33 (8), 681–684.
- Berger, A., Burri, T., Alt-Epping, P., Engi, M., 2008. Tectonically controlled fluid flow and water-assisted melting in the middle crust: an example from the Central Alps. *Lithos* 102 (3–4), 598–615.
- Black, L.P., Kamo, S.L., Allen, C.M., Aleinkoff, J.N., Davis, D.W., Korsch, R.J., Foudoulis, C., 2003. TEMORA 1; a new zircon standard for Phanerozoic U–Pb geochronology. *Chemical Geology* 200 (1–2), 155–170.
- Brown, E.T., Bendick, R., Bourles, D.L., Gaur, V., Molnar, P., Raisbeck, G.M., Yiou, F., 2002. Slip rates of the Karakoram fault, Ladakh, India, determined using cosmic ray exposure dating of debris flows and moraines. *Journal of Geophysical Research B: Solid Earth* 107 (9), 1–7.
- Burri, T., Berger, A., Engi, M., 2005. Tertiary migmatites in the Central Alps: regional distribution, field relations, conditions of formation and tectonic implications. *Schweizerische Mineralogische und Petrographische Mitteilungen* 85 (2–3), 215–232.
- Clemens, J.D., 2006. Melting of the continental crust: fluid regimes, melting reactions, and source rock fertility. In: Brown, M., Rushmer, T. (Eds.), *Evolution and Differentiation of the Continental Crust*. Cambridge University Press, New York, NY, United States, pp. 296–330.
- Clemens, J.D., Vielzeuf, D., 1987. Constraints on melting and magma production in the crust. *Earth and Planetary Science Letters* 86 (2–4), 287–306.
- Crawford, M.B., Searle, M.P., 1992. Field relationships and geochemistry of pre-collisional (India–Asia) granitoid magmatism in the central Karakoram, northern Pakistan. *Tectonophysics* 206 (1–2), 171–192.
- Crawford, M.B., Windley, B.F., 1990. Leucogranites of the Himalaya/Karakoram: implications for magmatic evolution within collisional belts and the study of collision-related leucogranite petrogenesis. *Journal of Volcanology and Geothermal Research* 44 (1–2), 1–19.
- Debon, F., Zimmermann, J.L., Bertrand, J.M., 1986. Le granite du Baltoro (batholite axial du Karakoram, nord Pakistan): une intrusion subalcaline d'âge Miocene Supérieur. *Comptes Rendus de l'Académie des Sciences, Paris, Serie II* 303 (6), 463–468.
- Deniel, C., Vidal, P., Fernandez, A., Le Fort, P., Peucat, J.J., 1987. Isotopic study of the Manaslu granite (Himalaya, Nepal): inference on the age and source of Himalayan leucogranites. *Contributions to Mineralogy and Petrology* 96 (1), 78–92.
- Dunlap, W.J., Weinberg, R.F., Searle, M.P., 1998. Karakoram fault zone rocks cool in two phases. *Journal of the Geological Society* 155 (6), 903–912.
- Eggins, S.M., Woodhead, J.D., Kinsley, L.P.J., Mortimer, G.E., Sylvester, P., McCulloch, M.T., Hergt, J.M., Handler, M.R., 1997. A simple method for the precise determination of

- >=40 trace elements in geological samples by ICPMS using enriched isotope internal standardisation. *Chemical Geology* 134 (4), 311–326.
- Gardien, V., Thompson, A.B., Ulmer, P., 2000. Melting of biotite + plagioclase + quartz gneisses; the role of H (sub 2) O in the stability of amphibole. *Journal of Petrology* 41 (5), 651–666.
- Genier, F., Bussy, F., Epard, J.-L., Baumgartner, L., 2008. Water-assisted migmatization of metagraywackes in a Variscan shear zone, Aiguilles-Rouges massif, western Alps. *Lithos* 102 (3–4), 575–597.
- Guillot, S., Le Fort, P., 1995. Geochemical constraints on the bimodal origin of High Himalayan leucogranites. *Lithos* 35 (3–4), 221–234.
- Hawkesworth, C.J., Vollmer, R., 1979. Crustal contamination versus enriched mantle: ¹⁴³Nd/¹⁴⁴Nd and ⁸⁷Sr/⁸⁶Sr evidence from the Italian volcanics. *Contributions to Mineralogy and Petrology* 69 (2), 151–165.
- Holtz, F., Pichavant, M., Barbey, P., Johannes, W., 1992. Effects of H (sub 2) O on liquidus phase relations in the haplogranite system at 2 and 5 kbar. *American Mineralogist* 77 (11–12), 1223–1241.
- Honegger, K., Dietrich, V., Frank, W., Gansser, A., Thöni, M., Trommsdorff, V., 1982. Magmatism and metamorphism in the Ladakh Himalayas (the Indus-Tsangpo suture zone). *Earth and Planetary Science Letters* 60, 253–292.
- Inger, S., Harris, N., 1993. Geochemical constraints on leucogranite magmatism in the Langtang Valley, Nepal Himalaya. *Journal of Petrology* 34 (2), 345–368.
- Jade, S., Bhatt, B.C., Yang, Z., Bendick, R., Gaur, V.K., Molnar, P., Anand, M.B., Kumar, D., 2004. GPS measurements from the Ladakh Himalaya, India: preliminary tests of plate-like or continuous deformation in Tibet. *Geological Society of America Bulletin* 116, 1385–1391.
- Kenah, C., Hollister, L.S., 1983. Anatexis in the Central Gneiss Complex. In: Atherton, M.P., Cribble, C.D. (Eds.), *Migmatites, Melting, and Metamorphism*. Shiva, Nantwich, pp. 142–162.
- Kretz, R., 1983. Symbols for rock-forming minerals. *American Mineralogist* 68, 277–279.
- Lacassin, R., Valli, F., Arnod, N., Leloup, P.H., Paquette, J.L., Haibling, L., Tapponnier, P., Chevalier, M.-L., Guillot, S., Mahéo, G., Zhiglin, X., 2004. Large-scale geometry, offset and kinematic evolution of the Karakoram Fault, Tibet. *Earth and Planetary Science Letters* 219, 255–269.
- Lappin, A.R., Hollister, L.S., 1980. Partial melting in the Central Gneiss Complex near Prince Rupert, British Columbia. *American Journal of Science* 280 (6), 518–545.
- Le Fort, P., Cuney, M., Deniel, C., France-Lanord, C., Sheppard, S.M.F., Upreti, B.N., Vidal, P., 1987. Crustal generation of the Himalayan leucogranites. *Tectonophysics* 134 (1–3), 39–57.
- Ludwig, K.R., 2001. SQUID 1.02, A user's manual. Berkeley Geochronology Center Special Publication 2.
- Ludwig, K.R., 2003. User's manual for Isoplot/Ex, Version 3.0, A geochronological toolkit for Microsoft Excel. Berkeley Geochronology Center Special Publication 4.
- Maas, R., Kamenetsky, M.B., Sobolev, A.V., Kamenetsky, V.S., Sobolev, N.V., 2005. Sr, Nd, and Pb isotope evidence for a mantle origin of alkali chlorides and carbonates in the Udachnaya Kimberlite, Siberia. *Geology* 33 (7), 549–552.
- Maas, R., McCulloch, M.T., 1991. The provenance of Archean clastic metasediments in the Narryer Gneiss Complex, Western Australia; trace element geochemistry, Nd isotopes, and U–Pb ages for detrital zircons. *Geochimica et Cosmochimica Acta* 55 (7), 1915–1932.
- Mahéo, G., Blichert-Toft, J., Pin, C., Guillot, S., Pêcher, A., 2009. Partial melting of mantle and crustal sources beneath South Karakoram, Pakistan: implications for the Miocene geodynamic evolution of the India–Asia convergence zone. *Journal of Petrology* 50 (3), 427–449.
- Mahéo, G., Guillot, S., Blichert-Toft, J., Rolland, Y., Pêcher, A., 2002. A slab breakoff model for the Neogene thermal evolution of South Karakoram and South Tibet. *Earth and Planetary Science Letters* 195 (1–2), 45–58.
- Mahéo, G., Pêcher, A., Guillot, S., Rolland, Y., Delacourt, C., 2004. Exhumation of Neogene gneiss domes between oblique crustal boundaries in south Karakoram, northwest Himalaya, Pakistan. *Special Paper — Geological Society of America* 380, 141–154.
- McLellan, E.L., 1988. Migmatite structures in the Central Gneiss Complex, Boca de Quadra, Alaska. *Journal of Metamorphic Geology* 6 (4), 517–542.
- Mogk, D.W., 1992. Ductile shearing and migmatization at mid-crustal levels in an Archean high-grade gneiss belt, northern Gallatin Range, Montana, USA. *Journal of Metamorphic Geology* 10 (3), 427–438.
- Parrish, R.R., Tirrul, R., 1989. U–Pb age of the Baltoro granite, northwest Himalaya, and implications for monazite U–Pb systematics. *Geology* 17 (12), 1076–1079.
- Patiño Douce, A.E., Harris, N., 1998. Experimental constraints on Himalayan anatexis. *Journal of Petrology* 39 (4), 689–710.
- Phillips, R.J., Parrish, R.R., Searle, M.P., 2004. Age constraints on ductile deformation and long-term slip rates along the Karakoram fault zone, Ladakh. *Earth and Planetary Science Letters* 226, 305–319.
- Phillips, R.J., Searle, M.P., 2007. Macrostructural and microstructural architecture of the Karakoram fault; relationship between magmatism and strike-slip faulting. *Tectonics* 26 (3) art. no. TC3017.
- Raczek, I., Jochum, K.P., Hofmann, A.W., 2003. Neodymium and strontium isotope data for USGS reference materials BCR-1, BCR-2, BHVO-1, BHVO-2, AGV-1, AGV-2, GSP-1, GSP-2 and eight MPI-DING reference glasses. *Geostandards Newsletter* 27 (2), 173–179.
- Ravikant, V., 2006. Utility of Rb–Sr geochronology in constraining Miocene and Cretaceous events in the eastern Karakoram, Ladakh, India. *Journal of Asian Earth Sciences* 27 (4), 534–543.
- Ravikant, V., Wu, F.-Y., Ji, W.-Q., 2009. Zircon U–Pb and Hf isotopic constraints on petrogenesis of the Cretaceous–Tertiary granites in eastern Karakoram and Ladakh, India. *Lithos* 110 (1–4), 153–166.
- Raz, U., Honegger, K., 1989. Magmatic and tectonic evolution of the Ladakh Block from field studies. *Tectonophysics* 161, 107–118.
- Rex, A.J., Searle, M.P., Tirrul, R., Crawford, M.B., Prior, D.J., Rex, D.C., Barnicoat, A.C., 1988. The geochemical and tectonic evolution of the central Karakoram, North Pakistan. *Philosophical Transactions of the Royal Society of London, Series A: Mathematical and Physical Sciences* 326 (1589), 229–255.
- Rolland, Y., Picard, C., Pêcher, A., Lapierre, H., Bosch, D., Keller, F., 2002. The Cretaceous Ladakh arc of NW Himalaya-slab melting and melt–mantle interaction during fast northward drift of Indian Plate. *Chemical Geology* 182 (2–4), 139–178.
- Rolland, Y., Mahéo, G., Pêcher, A., Villa, I.M., 2009. Syn-kinematic emplacement of the Pangong metamorphic and magmatic complex along the Karakoram Fault (N Ladakh). *Journal of Asian Earth Sciences* 34 (1), 10–25.
- Rolland, Y., Pêcher, A., 2001. The Pangong granulites of the Karakoram Fault (western Tibet): vertical extrusion within a lithosphere-scale fault? *Comptes Rendus de l'Académie des Sciences, Serie II, Sciences de la Terre et des Planètes* 332 (6), 363–370.
- Rollinson, H.R., 1993. Using geochemical data; evaluation, presentation, interpretation. Longman Scientific & Technical, Harlow, United Kingdom. 352 pp.
- Rutter, E.H., Faulkner, D.R., Brodie, K.H., Phillips, R.J., Searle, M.P., 2007. Rock deformation processes in the Karakoram fault zone, Eastern Karakoram, Ladakh, NW India. *Journal of Structural Geology* 29 (8), 1315–1326.
- Sawyer, E.W., 2008. Atlas of migmatites. The Canadian Mineralogist. Special Publication, Mineralogical Association of Canada, Ottawa, ON, Canada. 371 pp.
- Schärer, U., Copeland, P., Harrison, T.M., Searle, M.P., 1990. Age, cooling history, and origin of post-collisional leucogranites in the Karakoram Batholith; a multi-system isotope study. *Journal of Geology* 98 (2), 233–251.
- Schärer, U., Hamet, J., Allègre, C.J., 1984. The Transhimalaya (Gangdese) plutonism in the Ladakh region: a U–Pb and Rb–Sr study. *Earth and Planetary Science Letters* 67 (3), 327–339.
- Searle, M.P., Crawford, M.B., Rex, A.J., 1992. Field relations, geochemistry, origin and emplacement of the Baltoro granite, Central Karakoram. *Transactions of the Royal Society of Edinburgh: Earth Sciences* 83, 519–538.
- Searle, M.P., Tirrul, R., 1991. Structural and thermal evolution of the Karakoram crust. *Journal of the Geological Society of London* 148 (1), 65–82.
- Searle, M.P., Weinberg, R.F., Dunlap, W.J., 1998. Transpressional tectonics along the Karakoram Fault Zone, northern Ladakh. In: R.E. Holdsworth and R.A. Strachan (Editors), *Continental Transpressional and Transtensional Tectonics*. Geological Society of London Special Publication 135, 307–326.
- Srimal, N., 1986. India–Asia collision: implications from the geology of the eastern Karakoram. *Geology* 14, 523–527.
- Sun, S.S., McDonough, W.F., 1989. Chemical and isotopic systematics of oceanic basalts; implications for mantle composition and processes. *Geological Society of London Special Publication* 42, 313–345.
- Tanaka, T., Togashi, S., Kamioka, H., Amakawa, H., Kagami, H., Hamamoto, T., Yuhara, M., Orihashi, Y., Yoneda, S., Shimizu, H., Kunimaru, T., Takahashi, K., Yanagi, T., Nakano, T., Fujimaki, H., Shinjo, R., Asahara, Y., Tanimizu, M., Dragusanu, C., 2000. JNd1-1; a neodymium isotopic reference in consistency with LaJolla neodymium. *Chemical Geology* 168 (3–4), 279–281.
- Tera, F., Wasserburg, G.J., 1972. U–Th–Pb systematics in three Apollo 14 basalts and the problem of initial Pb in lunar rocks. *Earth and Planetary Science Letters* 14 (3), 281–304.
- Upadhyay, R., Frisch, W., Siebel, W., 2008. Tectonic implications of new U–Pb zircon ages of the Ladakh Batholith, Indus suture zone, northwest Himalaya, India. *Terra Nova* 20 (4), 309–317.
- Valli, F., Arnaud, N., Leloup, P.H., Sobel, E.R., Mahéo, G., Lacassin, R., Guillot, S., Li, H., Tapponnier, P., Xu, Z., 2007. Twenty million years of continuous deformation along the Karakoram fault, western Tibet: a thermochronological analysis. *Tectonics* 26 (4) art. no. TC4004.
- Vance, D., Thirlwall, M., 2002. An assessment of mass discrimination in MC-ICPMS using Nd isotopes. *Chemical Geology* 185 (3–4), 227–240.
- Weinberg, R.F., Dunlap, W.J., 2000. Growth and deformation of the Ladakh Batholith, Northwest Himalayas; implications for timing of continental collision and origin of calc-alkaline batholiths. *Journal of Geology* 108 (3), 303–320.
- Weinberg, R.F., Dunlap, W.J., Whitehouse, M., 2000. New field, structural and geochronological data from the Shyok and Nubra valleys, northern Ladakh: linking Kohistan to Tibet. In: A. Khan, P.J. Treloar and M.P. Searle (Eds.), *Tectonics of the Nanga Parbat Syntaxis and the Western Himalaya*. Geological Society of London Special Publication 170, 253–275.
- Weinberg, R.F., Mark, G., 2008. Magma migration, folding, and disaggregation of migmatites in the Karakoram shear zone, Ladakh, NW India. *Geological Society of America Bulletin* 120 (7–8), 994–1009.
- Weinberg, R.F., Mark, G., Reichardt, H., 2009. Magma ponding in the Karakoram shear zone, Ladakh, NW India. *Geological Society of America Bulletin* 121 (1–2), 278–285.
- Weinberg, R.F., Searle, M.P., 1998. The Pangong Injection Complex, Indian Karakoram: a case of pervasive granite flow through hot viscous crust. *Journal of the Geological Society of London* 155 (5), 883–891.
- Wen, D.-R., Liu, D., Chung, S.-L., Chu, M.-F., Ji, J., Zhang, Q., Song, B., Lee, T.-Y., Yeh, M.-W., Lo, C.-H., 2008. Zircon SHRIMP U–Pb ages of the Gangdese Batholith and implications for Neotethyan subduction in southern Tibet. *Chemical Geology* 252 (3–4), 191–201.
- Williams, I.S., 1998. U–Th–Pb geochronology by ion microprobe. *Reviews in Economic Geology* 7, 1–35.
- Williams, I.S., Hergt, J.M., 2000. U–Pb dating of Tasmanian dolerites; a cautionary tale of SHRIMP analysis of high-U zircon. *Beyond 2000. New Frontiers in Isotope Geoscience* 185–188.
- Wright, T.J., Parsons, B., England, P.C., Fielding, E.J., 2004. InSAR observations of low slip rates on the major faults of western Tibet. *Science* 305 (5681), 236–239.
- Zindler, A., Hart, S.R., 1986. Chemical geodynamics. *Annual Review of Earth and Planetary Sciences* 14, 493–571.